이 학 박 사 학 위 논 문

Synthesis and Gas Storage Application of Porous Metal-Organic Frameworks and Nanomaterials

다공성 금속-유기 골격체와 나노물질의 합성 및 가스 저장에의 응용 연구

2014년 2월

서울대학교 대학원

화학부 무기화학 전공

임 대 운

Synthesis and Gas Storage Application of Porous Metal-Organic Frameworks and Nanomaterials

By

Dae Woon Lim

Supervisor: Prof. Myunghyun Paik Suh

A Thesis for the Ph.D. Degree

in Inorganic Chemistry

Department of Chemistry

Graduate School

Seoul National University

February, 2014

이 학 박 사 학 위 논 문

Synthesis and Gas Storage Application of Porous Metal-Organic Frameworks and Nanomaterials

다공성 금속-유기 골격체와 나노 물질의 합성 및 가스 저장에의 응용 연구

지도교수 백 명 현

이 논문을 이학박사학위논문으로 제출함

2013년 12월

서울대학교 대학원

화학부 무기화학 전공

임 대 운

임대운의 박사학위 논문을 인준함

2014년 2월

위 원 장 강 관 [illegible]

부 위 원 장 백 명 현 (인)

위 원 천 진 우

위 원 강 자 헌

위 원 이 동 환 (인)

Abstract

PART I. Hydrogen Storage in Metal - Organic Framework Incorporating Crown Ether Moieties: Cation Inclusion

A doubly interpenetrated metal-organic framework (MOF) incorporating a 18-crown-6 ether (18C6) moiety, $Zn_5(\mu_3\text{-}OH)_2(TBADB\text{-}18\text{-}Cr\text{-}6)_2 \cdot 4DMF] \cdot 13DMF \cdot 4H_2O$ (SNU-200), has been synthesized. SNU-200 not only provides binding sites with various cations (K^+, NH_4^+, methyl viologen(MV^{2+}), and Eu^{3+}) but also exhibits characteristic gas sorption property depending on the bound cation. Despite the inclusion of the cations, SNU-200 retains the structure and the surface areas of MOF do not decreased. The MOF undergoes single-crystal to single crystal transformations upon cation binding together with the inclusion or coordination of the counter anion in the pores or at the metal site, respectively. To investigate the effect of the crown ether moiety and metal ions incorporated in the MOF on gas sorption properties, the adsorption-desorption isotherms were measured for N_2, H_2, CO_2, and CH_4 gases at various temperatures. SNU-200' shows a higher isosteric heat (Q_{st}) of the H_2 adsorption (7.70 $kJmol^{-1}$) compared to other Zn based MOFs. Among the cation inclusions, K^+ is the best for enhancing the Q_{st} of the H_2 adsorption (9.92 $kJmol^{-1}$) as well as the adsorption selectivity of CO_2/N_2 (22.6).

Keywords: metal-organic framework • hydrogen storage • crown ether • isosteric heat • electro static field • cation inclusion • single - crystal to single – crystal transformation

PART II. Fabrication of Magnesium Nanocrystal in Highly Porous Materials for Hybrid Hydrogen Storage by Physi- and Chemisorption

A 3D porous metal-organic frameworks, $[Zn_4O(atb)_2]\cdot 22DMF\cdot 9H_2O$ (SNU-90), have been prepared by the solvothermal syntheses from $Zn(NO_3)_2$ and aniline-2,4,6-tribenzoate (atb) ligand. SNU-90 is a non-interpenetrated (6,3)-connected net of a *qom* topology, similar to MOF-177 generating 3D channels. SNU-90 has Brunauer-Emmett-Teller (BET) and the Langmuir surface area of 4244 m^2g^{-1} and 4914 m^2g^{-1}, respectively.

Hexagonal-disk shaped magnesium nanocrystals of size 40 - 100 nm were embedded in a highly porous metal-organic framework, $[Zn_4O(atb)_2]$ (**SNU-90'**), where atb is aniline-2,4,6-tribenzoate, via chemical vapor deposition of $Mg(cp)_2$ followed by thermal decomposition at 473 K under argon atmosphere. The shape and location of Mg nanocrystals were confirmed by HRTEM and tomography. Mg@MOF adsorbs hydrogen gas both by physi- and chemi- sorptions. The physisorption capacity at 77 K decreased as the amount of Mg embedded in MOF increased. However, the heat of H_2 adsorption was increased from 4.55 $kJmol^{-1}$ up to 11.6 $kJmol^{-1}$ with increasing amount of Mg in the MOF. The hydrogen uptake capacity of the MOF at 298 K and 80 bar was also improved by the Mg nanocrystals from 0.45 wt% to 0.54 wt%. The Mg nanocrystals embedded in the MOF lowered the chemisorption temperature of hydrogen to 473 K, compared to 573 - 673 K for bare Mg powder of 50 - 100 μm. At 473 K and 30 bar, Mg@SNU-90 with a 10.5 wt% loaded amount of Mg chemisorbs hydrogen up to 0.71 wt%, which corresponds to 7.5 wt% of H_2 adsorption in Mg alone.

Highly porous covalent organic framework (Porous Aromatic Framework, PAF-1) has prepared by Ni catalyzed cross-coupling reaction of tetrakis (4-bromophenyl) methane. PAF-1 represents the diamondoid structure which consists of phenyl ring. It shows a high surface area (BET, 5640 m^2g^{-1}), exceptional thermal/ hydrothermal stability and the super hydrophobicity.

The Mg nanocrystals (Mg NCs) were prepared in PAF-1 by reduction of Mg precursor that was vapor-deposited in the pore. The Mg of 11.87 wt% is included in PAF-1. The size of Mg NCs in PAF-1 is in a wide range from 17 to 400 nm, and it was characterized by HRTEM, and PXRD patterns. On exposure Mg NCs @PAF-1 to air for 10 days, the PXRD peak of Mg NCs still indicate a pure Mg peaks without any oxidation in nanosized Mg. In N_2 and H_2 gas sorption, as Mg incorporated in the PAF-1, surface area, pore volume, and H_2 uptake capacity at 77 K and 1 atm decreased. However, the zero-coverage isosteric heats of the H_2 adsorption is increased from 4.0 $kJmol^{-1}$ to 5.8 $kJmol^{-1}$.

Keywords: metal-organic framework • covalent organic framework • Magnesium • Nanocrystal • hydrogen storage • chemisorption • physisorption

Table of contents

PART I

HYDROGEN STORAGE IN METAL - ORGANIC FRAMEWORK INCORPORTAING CROWN ETHER MOIETIES: CATION INCLUSION

I.1. Introduction

Porous metal - organic frameworks (MOFs) or porous coordination polymers (PCPs) have been received great attention due to their various applications[1] such as gas storage and separation,[2-9] catalysis,[10-11] and fabrication of nanoparticles.[12-16] These potential applications of MOFs are attributed to their large internal surface areas and tunable pore functionality.

Hydrogen is a promising candidate for future energy carrier. H_2 has a high energy density as well as eco-friendly property. However, it is not easy to use as an energy source due to safety problems. In order to use it as a fuel, a compact, safe, and efficient storage system should be developed. Porous metal-organic frameworks have been considered as a potential H_2 storage material because it is able to storage large amounts of H_2 at low temperature and high pressure (>7 wt%).[17-19] However, at ambient temperature, the uptake amounts of H_2 by MOFs suddenly fall down. The reason is that MOFs adsorb the H_2 based on the physisorption with weak interaction energy (< 20 $kJmol^{-1}$). In order to overcome this weak point, there have a lot of efforts such as creation of open metal site (vacant coordination site),[20-24] functionalization of ligand,[25-28] fabrication of metal nanoparticles,[12,13,29] and inclusion of metal ion[30-34] or organic compound[35] to increase interaction energy between MOFs and H_2. The U.S department of energy sets the target for H_2 storage. The 2017 H_2 storage targets are 5.5 wt % in gravimetric capacity, 40 gL^{-1} of volumetric capacity at an operating temperature of -40 ~ 60 ^oC under a maximum delivery pressure of 100 atm.[36] None of the materials have met yet the DOE (Department of Energy, US) target of 2017.

In this part, synthesis of carboxylate based MOFs, how to calculate the

isosteric heat of H_2, and strategy to increase isosteric heat of H_2 are presented. Especially, hydrogen storage in MOFs affected by electrostatic field of ligand and metal cation inclusion will be discussed base on the experimental data.

I.1.1. Synthesis of Metal-Organic Frameworks

The MOFs have been synthesized by the solvothermal reactions of metal salts and organic building blocks in high boiling organic solvents such as DMF, DMA, and DEF, generally at 80 ^{o}C - 130 ^{o}C. In general, solubility restrictions for the reagents can be minimized by high temperature reaction conditions of the solvothermal synthesis. Sometime mixed solvents systems are useful to control the solution polarity, and rate of product crystallization. For example, to reduce the rate of crystallization during the synthesis, acid solvent can be added. To construct the various structures of MOFs, it mainly depends on the combination of the metal salts and organic building blocks as well as the type of solvent, reaction temperature, and rate of crystal growth. The combination of Zn(II) or Cu(II) with various carboxylate ligands are the most commonly used for synthesis of MOFs. Various carboxylic acids as well as heterocyclic compounds containing nitrogen donors are used as the organic building blocks for the construction of MOFs. Gas sorption and guest recognition properties of MOFs depend on the structure, especially not only pore size and shape but also pore surface. Yaghi and O'keeffe have reported a review about the topology of MOFs constructed by metal ion and organic ligand.[37]

I.1.1.1. Carboxylate base MOFs[2]

The most common and well known MOFs reported are made up of

carboxylate ligands with various metal ions such as Zn, Cu, Mn, Co, Cr, Ni, lanthanide metals, and alkali metals. Especially, the MOF-5 constructed by dicarboxylic acid and Zn(II) ion is extensively studied by Yaghi and co-workers. In addition, they prepared isoreticural structure MOFs (IRMOFs) with various functional groups.[38-40] Most of them show high surface area and large pore volume. The most representative secondary building units (SBUs) constructed by metal ion and carboxylic acid ligand is Zn_4O and $Cu_2(CO_2)_4$ cluster. IRMOF series consist of Zn_4O secondary building units (SBUs) with octahedral geometry. Six carboxylates connected to four Zn(II) ions to form the cubic network structure with 3D channel. (Figure 1)

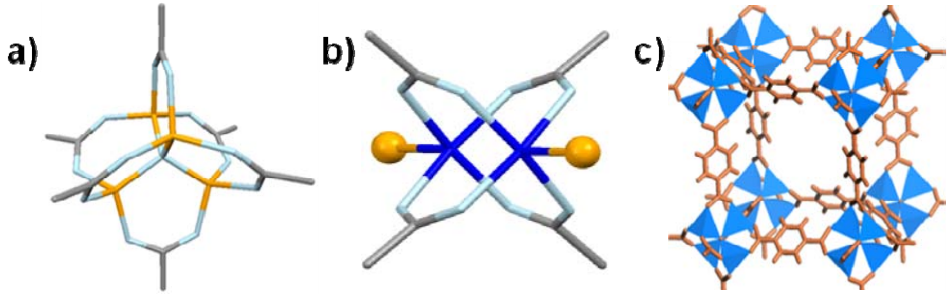

Figure 1. Secondary Building Units(SBUs) and MOF-5 structure. a) Zn_4O SBUs. b) paddle-wheel SBUs. c) MOF-5 cubic framework.

The control of pore size and surface area of IRMOFs was efficiently carried out by adjusting the number of benzene rings in the dicarboxylate ligand[41] and attaching the functional groups on the aromatic ring. MOF-5 shows very high gas sorption capacities, which adsorb 9.8 wt% of H_2 at 90 bar and 77 K.

MOFs prepared by tricarboxylic acid ligand and Zn_4O SBUs show a high surface area and void volume. MOF-200 and MOF-177 are the well-known examples.[17] In MOF-200 and MOF-177, 4,4',4''-(benzene-1,3,5-triyl-tris (benzene-4,1-

diyl)) tribenzoate (BBC) and 4,4',4"-benzene-1,3,5-triyltribenzoate (BTB) linked to each Zn_4O unit to form a (6, 3) connected net (Figure 2). MOF-200 and MOF-177 have a Langmuir surface area of 10400 m^2/g and 5340 m^2/g and has a pore volume of 3.59 and 1.89 cm^3/g, respectively, which are the highest values among the MOFs.

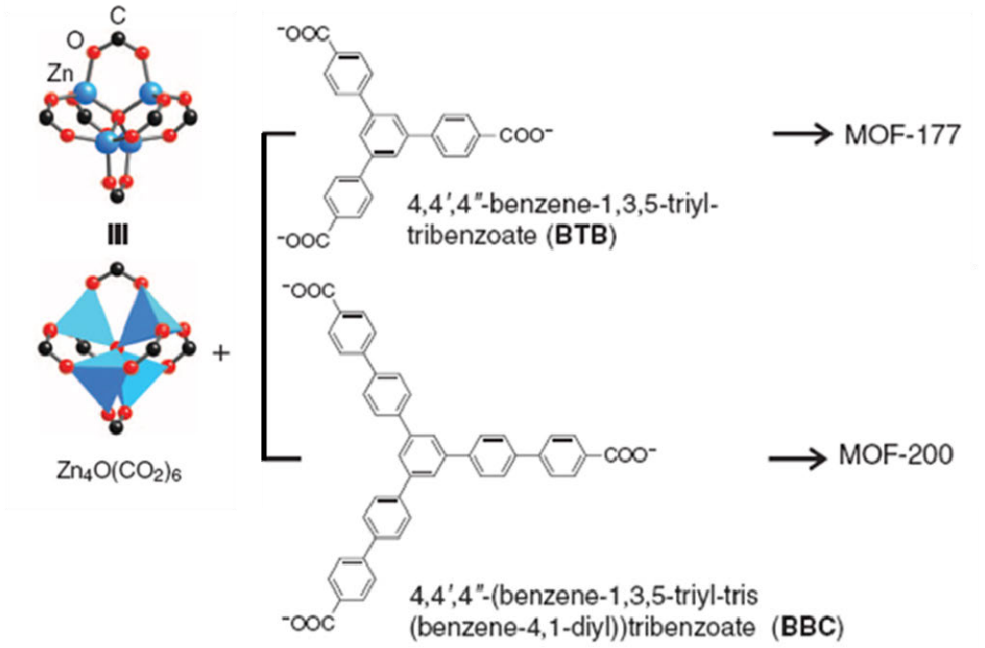

Figure 2. $Zn_4O(CO_2)_6$ unit is connected with organic liker to form MOFs.[17]

There are many other reports about MOFs which is formed by Zn_4O SBU and polycarboxylic acids. For instance, UMCM-2, MOF-205 and MOF-210 are synthesized by mixing Zn(II) ion, the di- and tri- carboxylate ligand (Figure 3). These kinds of materials represent the mesoporous properties which might be useful for hydrogen storage after modification of internal surface in order to improve the interaction energy between hydrogen and frameworks

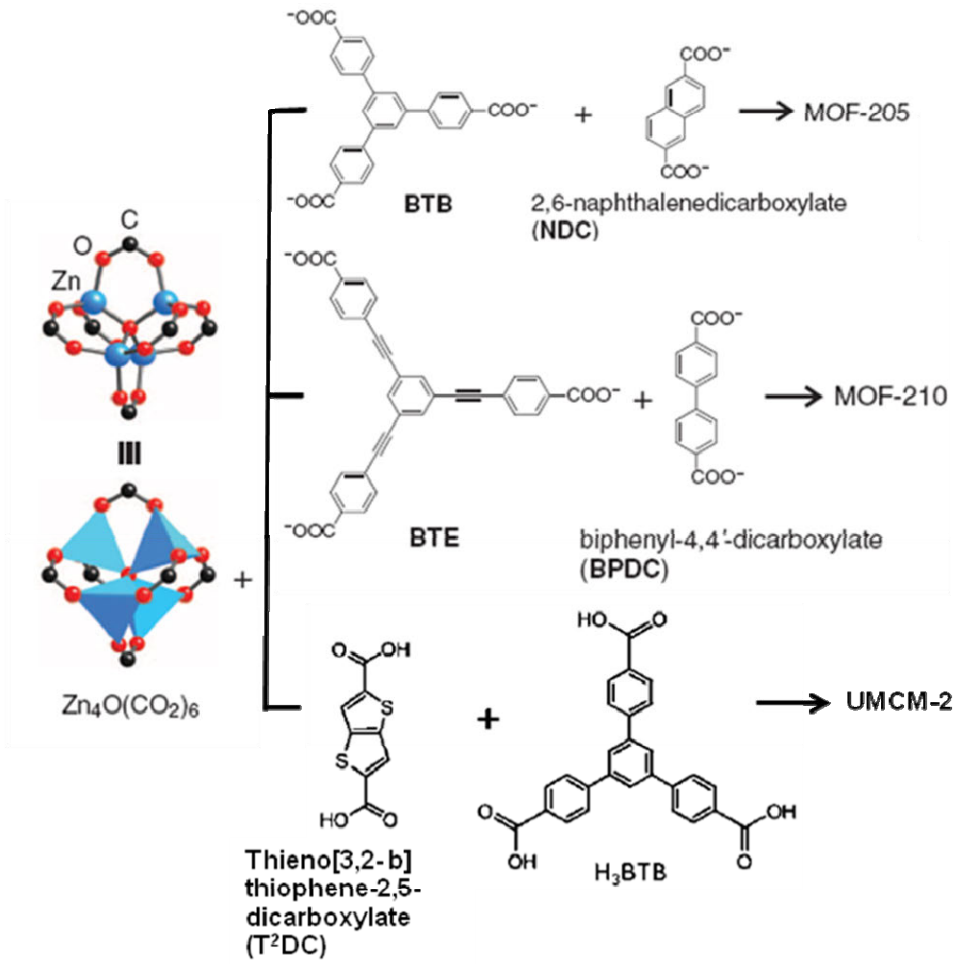

Figure 3. $Zn_4O(CO_2)_6$ unit is connected with multiple carboxylic acid liker to form MOFs.[17,42]

MOFs formed by Cu(II) ion and carboxylic acid ligands has been classified another interesting structure, because it used to form square paddle wheel type $[Cu_2(COO)_4]$ secondary building unit (Figure 1). In general, axial sites of paddle wheel type secondary building units occupied by the coordinated solvent molecules. However, the coordinated solvents molecules are simply removed by heating and evacuation without any structure decompositions. This activation process produced the open metal site on the metal cluster (Figure 4). The open metal site generates a high surface areas as well as strong interaction sites with gas molecules. Thus

normally MOFs with open metal sites indicate the higher H_2 uptake amounts than those of without open metal site.[43,44] Paddle wheel type's SBU is easily observed in the present of isophthalate organic ligand and Cu(II) ion.[18,44-46]

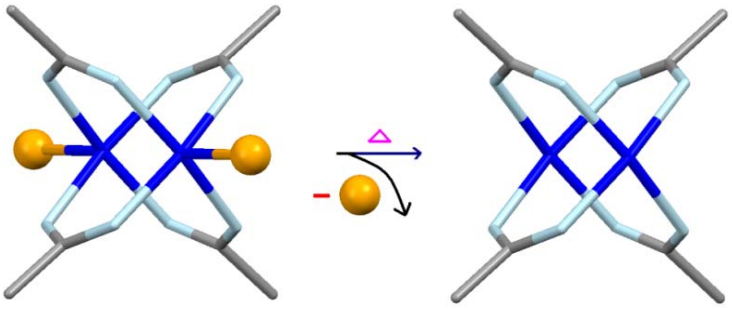

Figure 4. Creation of open metal sites on $Cu_2(CO_2)_4$ paddle wheel SBUs by removal of coordinated solvent s molecules.[2]

One of the oldest MOF based on the copper paddle wheel SBUs is HKUST-1, constructed by Cu paddle wheel SBU connecting with benzene-1,3,5-tricarboxylate.[47] HKUST -1 contains an intersecting three dimensional system of large square pore (9 Å x 9 Å) and have a pore volume of 0.333 cm^3g^{-1} and Langmuir surface are of 917.6 m^2g^{-1}. Hupp's group has reported a MOF (NU-100) which shows the largest surface area (BET: 6143 m^2g^{-1}) and the highest H_2 uptake amounts (excess: 9.95 wt%, total 16.5 wt%) among the Cu- paddle wheel type's MOFs.[18] There are several reports related to the paddle wheel SBUs based on the Zn(II) ion. Suh's group has published two kind of Zn paddle wheel type's MOFs, $[Zn_2(abtc)(dmf)_2]_3$ and $[Zn_2(BPnDC)_2(dabco)]$.[48,49] Even though Zn paddle wheel SBU is similar to Cu paddle wheel SBUs, compared to each other, Zn MOF tend to be unstable on guest removal[48] because Zn – Zn distance is longer (3.007(2) Å) than Cu-Cu distances (2.669(1) Å) in paddle structure. It means that there is no significant interaction

between Zn(II) ion in the paddle wheel SBU due to the sum of vander waals radii of Zn(II) is 2.80 Å.[49,50]

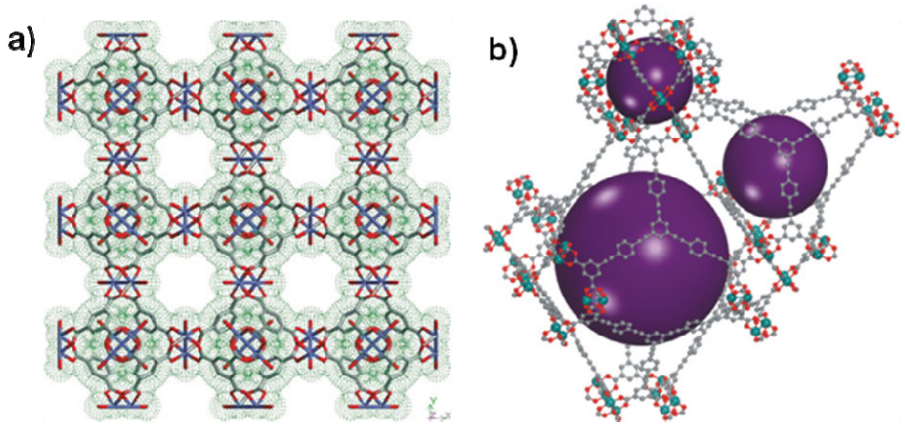

Figure 5. X-ray structure of a) HKUST-1 and b) NU-100.[18,47]

When the 2-dimensional (2D) network is formed by dicarboxylate with paddle wheel SBUs, axial site of paddle wheel SBUs can be connected by second ligand with nitrogen donating group, such as 4,4'-bipyridine (4,4'-bpy) or 3,6-di(4-pyridyl)-1,2,4,5-tetrazine (bpta), to construct a 3-dimensional (3D) networks.[49,51-53] The second ligand used to call "pillar" and these networks are more stable compared to the solvent coordinated paddle wheel framework.[54] In addition, interpenetration and pore size change by pillar ligand lead to selective adsorption toward guest molecules and gases.[51,53]

Some MOFs have prepared by various metal ions such as Cr(III),[21,55,56] In(III),[57-59] Co(II),[22,60,61] Mg(II),[41,62,63] Ni(II)[64] with carboxylic acid ligand. These compounds not only have different structure but also indicate the efficient H_2 adsorption properties. For instance, MIL-101 (MIL-101, $Cr_3OH(BDC)_3$) is well known compounds which have a high porousity and chemical stability. It shows a high H_2 uptake amounts (6.1 wt%, 77 K and 80 bar) and a high isosteric heat of H_2

adsorption (10 kJmol^{-1}) at low loading.

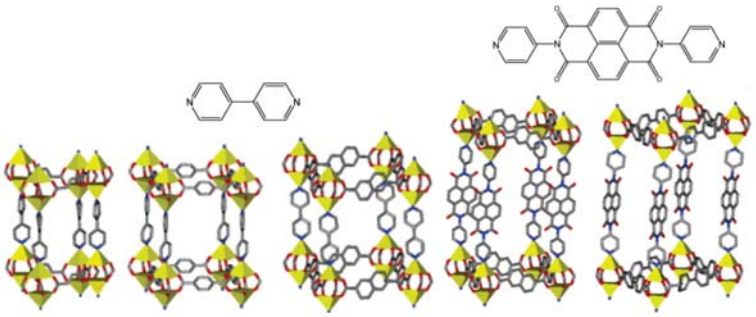

Figure 6. Pillared Zinc Paddle wheel Frameworks.[52]

In the synthesis of carboxylate MOFs, solvent system can be a critical factor to form the structure of MOF that consequently affect the properties of MOF. Suh's group reported two different kinds of MOFs synthesized from Zn(II) and H_3NTB (4,4',4"-nitrobenzoic acid) ligand.[65,66] Depending on the solvent system, one prepared in DEF, EtOH, and H_2O consists of Zn_4O SBUs linked by NTB^{3-} and another synthesized in the only EtOH has a Zn_3 cluster linked by NTB^{3-}. Although they use same metal salt and organic building block, Due to the different structure resulted, they show different gas sorption properties.

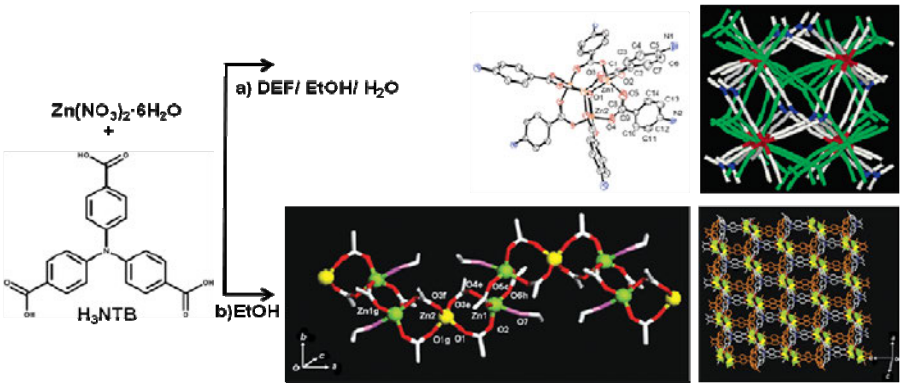

Figure 7. Two different frameworks formed from Zn(II) and NTN^{3-} in different solvent system. a) $[Zn_4O(NTB)_2]\cdot 3DEF\cdot EtOH$.[65] b) $[Zn_3(NTB)_2\ (EtOH)_2]\cdot 4EtOH$.[66]

I.1.2. Increase Isosteric Heat of Hydrogen Adsorption

Although porous metal-organic frameworks have been attracting attention as a potential H_2 storage material, it is challenging problem to store the acceptable density of hydrogen in MOFs by physisorption at ambient temperature and a proper operating pressure. Up to recently, MOFs have achieved an extremely large surface area and useful uptake amount of H_2 at cryogenic temperature. However, none of MOFs can satisfy the DOE target. In order to design the MOFs as the optimal H_2 adsorbent, several dominant factors should be considered. H_2 uptake correlated with isosteric heat of H_2 adsorption (Q_{st}), surface areas, and pore volume at different extent of loading amounts of H_2. There have been some computational studies to expect the effect of Q_{st}, surface area and pore volumes in H_2 adsorption. Bhatia and Mayer reported[67] that even though increase of Q_{st} is necessary, too much increasing the heat of adsorption leads to low gas delivery due to too much adsorption at discharge pressure. They estimated that optimal Q_{st} is 15.1 $kJmol^{-1}$ for delivery at ambient temperature and 1.5 - 30 bar. Snurr's group has carried out the molecular simulation of H_2 adsorption for a series of 10 isoreticular MOF at 77 K and up 120 bar.[33] The results represent that H_2 uptake correlated with Q_{st} at low loading of H_2, with surface area at intermediate loading, and with free volume of MOF at highest pressure. In addition, they performed these correlations for absolute/ excess H_2 adsorption at room temperatures up to 120 bar.[34] These results propose that free volume in absolute H_2 adsorption is a most important factor at 298 K and entire pressure as well as Q_{st} correlated well with excess H_2 adsorption at 298 K and low pressure. Base on these correlations, they make a plot that provides a requirement of Q_{st} and free volume to meet the H_2 storage target. According to this plot, in order to accomplish H_2 uptake

capacities of 6 wt% at room temperature, new material should attain the Q_{st} of 10 - 15 kJmol^{-1} and free volume of 1.6 - 2.4 cm^{3}g^{-1} at the same time. Garrone *et al.* propose that optimum H_2 storage and delivery at the range of pressure (1.5 – 30 bar) and ambient temperature required Q_{st} of 22-25 kJmol^{-1}.[68] Up to date Bae *et al.* demonstrated that a reasonable Q_{st} for maximum H_2 storage at 120 bar and delivery at 1.5 bar is ~ 20 kJmol^{-1} at 298 K.[69]

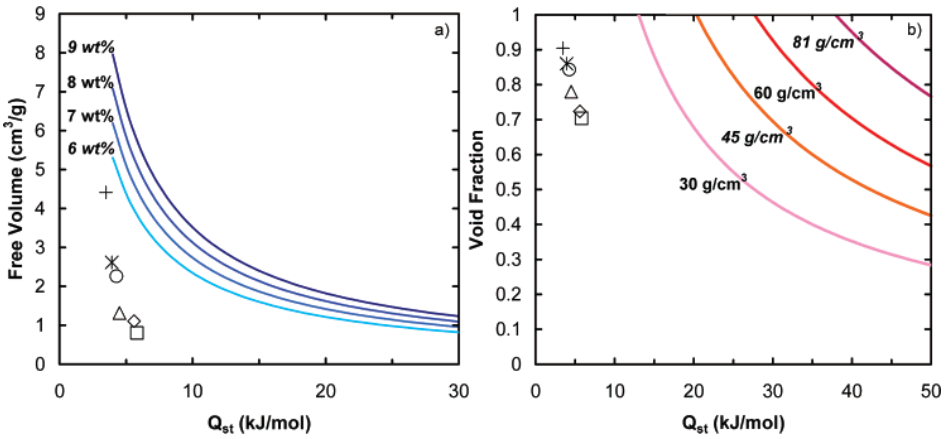

Figure 8. a) Requirements for target gravimetric loadings at 120 bar and 298 K. b) Requirements for target volumetric loadings at 120 bar and 298 K. Δ, IRMOF-1; ◇, IRMOF-9; ∗, IRMOF-10; ○, IRMOF-14; + , IRMOF-16; □, Cu-BTC.[34]

As considered these computational studies for H_2 storage and delivery at ambient temperature and entire pressure, it presents that the DOE target is able to be satisfied even at room temperature, if Q_{st} for H_2 is significantly enhanced in MOFs with large free volume. Therefore, development of strategy to increase the heat of adsorption for H_2 without any free volume loss is major issue in H_2 storage.

I.1.2.1. Calculation of Isosteric Heat of H_2 adsorption[2]

The interaction enthalpy between a MOF and H_2 molecules, the isosteric heat (Q_{st}) of hydrogen adsorption, can be calculated from the H_2 adsorption isotherms

measured at two independent temperatures, usually 77 and 87 K by fitting the data to *virial* equation or the *Langmuir - Freundlich* equation. The calculation provides the isosteric heat of H_2 adsorption depending on the adsorbed amounts of H_2, even though it can not give information about the position and the number of H_2 adsorption sites. The zero-coverage isosteric heat corresponds to the interaction energy between the H_2 molecule and the strongest interaction site of the MOF.

Three different methods have been used for estimating the isosteric heat of the H_2 adsorption.

Method 1. The *virial*-type equation (eq 1) is used to fit the gas sorption data, which is composed of parameters a_i and b_i that are independent of temperature.[60,71] In eq 1, P is pressure, N is the amount adsorbed H_2 gas, T is temperature, and m and n represent the number of coefficients required to adequately describe the isotherms. Adsorption isotherms measured at two different temperatures are fit to the equation by using the statistical programs such as *R* statistical software package.[72] To estimate the values of the isosteric heat of H_2 adsorption, eq 2 is applied, where R is the universal gas constant.

$$\ln P = \ln N + \frac{1}{T}\sum_{i=0}^{m} a_i N^i + \sum_{i=0}^{m} b_i N^i \quad (1)$$

$$Q_{st} = -R\sum_{i=0}^{m} a_i N^i \quad (2)$$

Method 2. The following *virial*-type equation[73] (eq 3) is used to fit the adsorption data at a fixed temperature. In eq 3, P is pressure, N is amount of adsorbed gas, and A_0,

A_1, etc. are virial coefficients. A_0 is related to the adsorbate-adsorbent interactions, whereas A_1 describes adsorbate-adsorbate interactions. Q_{st} for H_2 adsorption is calculated as a function of surface coverage by using *Clausius-Clapeyron* equation (eq 4), where *R* is the gas constant.

$$\ln(N/P) = A_0 + A_1N + A_2N^2 + A_3N^3 \ldots\ldots \quad (3)$$

$$Q_{st} = R\ln(\frac{P_1}{P_2})\frac{T_1T_2}{T_2 - T_1} \quad (4)$$

Method 3. *Langmuir-Freundlich* equation[74] (eq 5) is used to fit the adsorption data at a fixed temperature. In eq 5, *N* is amount of adsorbed gas, N_m is amount of adsorbed gas at saturation, *P* is pressure, and *B* and *t* are the constants. The *Langmuir-Freundlich* equation can be rearranged to eq 6, and the isosteric heat of H_2 adsorption is obtained by using eq 4.

$$\frac{N}{N_m} = \frac{BP^{(1/t)}}{1 + BP^{(1/t)}} \quad (5)$$

$$P = \left(\frac{N/N_m}{B - BN/N_m}\right)^{1/t} \quad (6)$$

We have to note that there are potential pitfalls in using each of the different types of fitting routines for deriving the isosteric heat of H_2 adsorption. **Methods 1** and **2** allow a series of Q_{st} values to be obtained as a function of n. Minimal deviations are observed for all experimental points measured over a wide range of pressure. The most salient feature of these *virial* equations is that they would allow extrapolation to zero coverage of H_2, therefore allowing the determination of this value at zero

coverage. However, the *Langmuir-Freundlich* (or other semiempirical routines) method results in gross overestimation of the adsorption enthalpy if extrapolation is made down to zero coverage, since this approach does not reduce to Henry's Law and leads to the largest error at zero coverage. This overestimation is in fact responsible for many high adsorption enthalpy values reported in the literature. On the other hand, fits using the *virial* equation can be overinterpreted if polynomials of too high order are used indiscriminately. The important value in that case is that of the lowest order polynomial coefficient. If a standard deviation in that fit is too large, the fit value is meaningless. However, this fact is unfortunately often disregarded by researchers in the field. Despite this, *virial* analysis is better and more mathematically consistent since it reduces to Henry's Law, although it gives lower values of the heat of adsorption.

I.1.2.2. Creation of Active Open Metal Sites

There are many reports about the H_2 storage that focused on MOFs with uncoordinated site, which is called as "open metal site", "exposed metal site", or "accessible metal site". This site has been well known as a strongly attractive site toward the introduced guest or gases. Thus, creation of open metal sites becomes one of the good strategies to enhance the Q_{st} for H_2 without any free volume loss. In order to introduce the exposed metal sites in MOFs, removal of coordinated solvent molecules on metal cluster[70,75] or synthesis of MOFs with metalloligand such as porphyrins, and salen ligands are utilized.[76]

In order to elucidate interaction of the exposed metal site and H_2 in Mg^{2+} and Ni^{2+}, Kosa *et al.* performed first principle calculation on a square pyramidal cluster

model with the exposed M^{2+} site and CH_3OCH_3 or OCH_3^- ligands.[77] In the results, Mg^{2+} site shows very weak interaction energy (< 1 $kJmol^{-1}$) and Ni^{2+} site strongly binds H_2 with binding energy up to 24 $kJmol^{-1}$. It is attribute to transition metals interact with H_2 via electron donation of σ(H-H) electrons to some empty orbital on the metal and back-donation of the electron density from the metal to the σ*(H-H) orbital.

Suh's group has compared a difference of the H_2 storage capacity depending on whether isoreticular structure MOFs obtains open metal site or not.[48] They synthesized two compounds, $[\{Zn_2(abtc)(dmf)_2\}_3]\cdot 4H_2O\cdot 10dmf$ and $[\{Cu_2(abtc)(H_2O)_2\}_3]\cdot 10dmf\cdot 6$ (1,4-dioxane), (H_4abtc=1,1'-azobenzene-3,3',5,5'-tetracarboxylic acid). By heating two crystals, MOFs without open metal sites, $[\{Zn_2$-$(abtc)(dmf)_2\}_3]$ (1a; SNU-4) and $[\{Cu_2(abtc)(dmf)_2\}_3]$ (2a; SNU-5'), as well as a MOF with open metal site, $[\{Cu_2(abtc)\}_3]$ (2b; SNU-5), are prepared. 2b with open metal sites exhibits higher pore volume and surface areas than 1a, 2a without open metal sites. Furthermore, in H_2 adsorption at 77 K and 1 atm, 2b adsorbs H_2 of 2.84 wt% indicating a high Q_{st} value of 11.60 $kJmol^{-1}$ whereas 1a and 2a show H_2 uptake capacity of 2.07 wt%, 1.83 with Q_{st} of 7.24 and 6.53 $kJmol^{-1}$, respectively. They supposed that the existence of open metal sites not only gives a high surface area but also enhances H_2 uptake amounts.

Zhou and co-worker reported the similar results which show the enhancing H_2 uptake amounts by alignment of open copper site in MOF.[78] Two Cu – mdip (mdip = 5,5'-methylene-di-isophthalate) MOFs (PCN-12, and PCN12') that are polymorphs where the MOFs consist of paddlewheel SBU occupied vertices of a cuboctahedron (PCN-12) and a rhombicuboctahedron (PCN-12'). Although two Cu -MOFs possess

the open metal sites, one indicate the open metal aligned within each cage, whereas another shows out of alignment of the open metal sites. The alignment of open metal sites significantly affected the H_2 gas sorption properties (Figure 9). The H_2 uptake amounts of PCN-12 and PCN12' are 3.05 wt% and 2.40 wt%. This notable enhancement of H_2 uptake amount can be attributed to the packed alignment of open metal sites in each cuboctahedral cage.

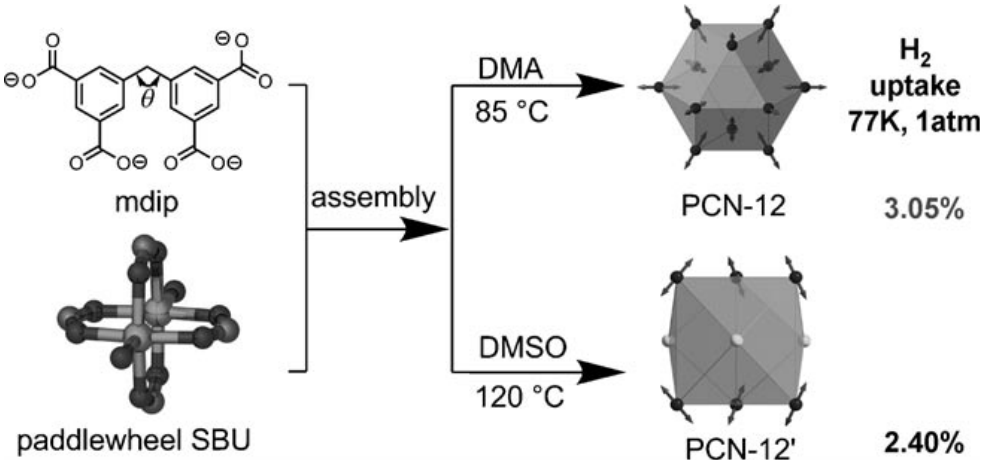

Figure 9. The synthesis, open metal site alignment, and hydrogen uptake of the two MOF polymorphs: PCN-12 and PCN-12'[78]

Dinca *et al.* directly demonstrated that H_2 bind at coordinatively unsaturated metal site by neutron powder diffraction.[70,75] They synthesized sodalite structure type's MOFs from Mn^{2+} and Cu^{2+} with 1,3,5-Tris(2*H*-tetrazol-5-yl)benzene hydrochloride ($H_3BTT{\cdot}2HCl$), $[Mn(DMF)_6]_3[(Mn_4Cl)_3(BTT)_8(H_2O)_{12}]_2 \cdot 42DMF \cdot 11H_2O \cdot 20CH_3OH$, and $H[Cu(DMF)_6][(Cu_4Cl)_3(BTT)_8(H_2O)_{12}] \cdot 3.5HCl \cdot 12H_2O \cdot 16CH_3OH$, respectively (Figure 10). The MOFs obtain the $[M_4Cl]^{7+}$ (M= Mn^{2+} and Cu^{2+}) squares SBUs connected by triangular BTT^{3-} ligand. Water ligands that can potentially be removed, occupy the one coordination site on each metal ion. After exchange the guest molecules with CH_3OH, H_2O and CH_3OH molecules is

eliminated by evacuation and heating. Neutron Diffraction measurements were taken at 3.5 - 4 K with various deuterium loadings. They identify four strong binding sites

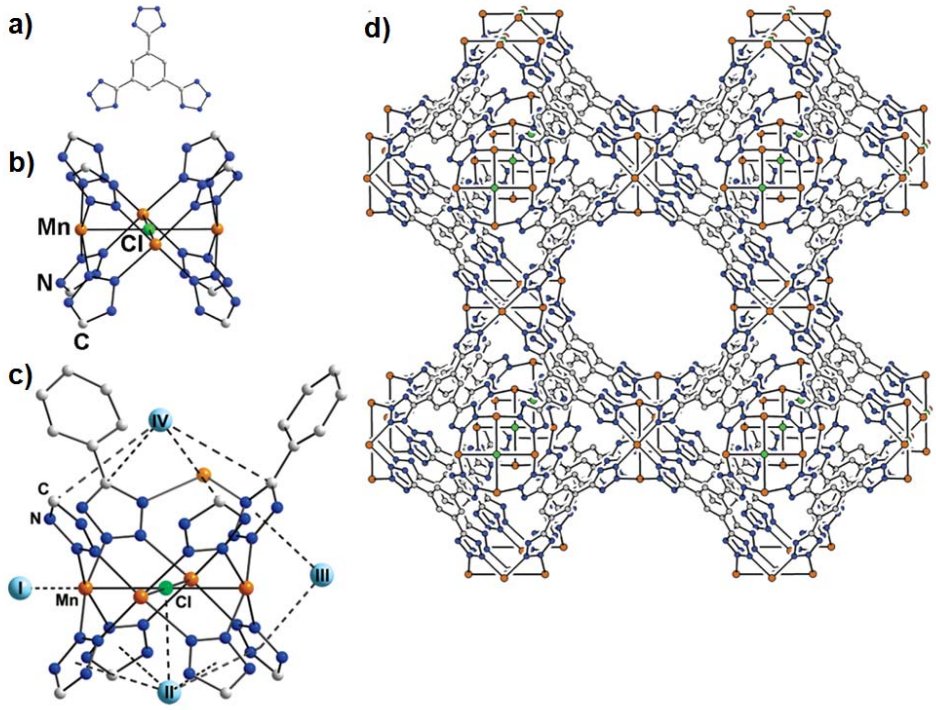

Figure 10. Portions of the crystal structure of $[Mn(DMF)_6]_3[(Mn_4Cl)_3(BTT)_8(H_2O)_{12}]_2 \cdot 42DMF \cdot 11H_2O \cdot 20CH_3OH$ a) molecular structure of the tritopic ligand, 1,3,5-Tris(2*H*-tetrazol-5-yl)benzene Hydrochloride ($H_3BTT \cdot 2HCl$) b) a square-planar Mn_4Cl cluster surrounded by eight tetrazolate rings c) Initial D_2 adsorption sites within $[Mn(CH_3OH)_6]_3[(Mn_4Cl)_3(BTT)_8\ (CH_3OH)_{12}]_2 \cdot 42CH_3OH$. Light blue spheres represent D_2 centroids, while the transparent orange sphere shows the position of a partially occupied, extra framework Mn^{2+} ion site. d) a cube of eight such units sharing square Mn_4Cl faces.[70]

in materials (Figure 9c and Figure 10). When they increased the D_2 loading amounts, D_2 molecules located in first the most attractive site (site I), and then next strongest site and possible sites which are labeled as site I→ II→ III→ IV.

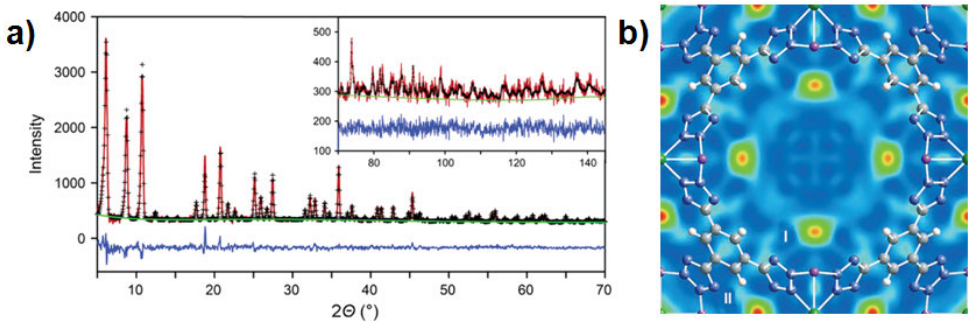

Figure 11. a) Rietveld refinement of neutron powder diffraction data for a loading of 12 D_2 molecules per formula unit of $Mn_3[(Mn_4Cl)_3(BTT)_8(CH_3OH)_{10}]_2$. Green lines, crosses, and red lines represent the background, calculated, and experimental diffraction patterns, respectively. The blue line shows the difference between experimental and calculated patterns. The final Rietveld fit parameter was χ^2 = 0.985.[70] b) Difference Fourier map after loading 12 D_2 molecules per formula unit within $HCu[(Cu_4Cl)_3(BTT)_8] \cdot 3.5HCl$ at 4 K, calculated from powder neutron diffraction data. The view is down a fourfold rotational axis. Red maxima indicate the centroids of the adsorbed D_2 molecules; adsorption sites I and II are labeled.[75]

NU-100 synthesized from $Cu(NO_3)_2.2.5H_2O$ and 5-tris[1,3-carboxylic acid -5-(4(ethynyl)phenyl)]ethyl]-benzen in DMF/HBF_4 at 75 ^oC for 24 h represented a large surface area (BET, 6143 m^3g^{-1}) and a high pore volume (2.82 cm^2g^{-1}) with open metal sites.[18] The excess uptake amounts of H_2 for NU-100 is 18.2 mg g^{-1} at 1 bar. In addition, at 56 bar and 77 K, it adsorbs the H_2 of 99.5 mg g^{-1} with total H_2 uptake of 164 mg g^{-1} at 70 bar and 77 K. The heat of adsorption for H_2 is 6.1 $kJmol^{-1}$. All H_2 gas adsorption data of MOFs with the open metal sites reported so far is summarized in Table 1. According to all MOFs data reported so far, MOFs with open metal sites indicate a higher average Q_{st} value of 1.0 kJ mol^{-1} than that of MOFs without open metal sites.[2]

Table 1. H_2 gas sorption data of carboxylate based MOFs with open metal sites.[2]

MOF		surface area/ $m^2\ g^{-1}$ BET	Langmuir	pore size/ Å	pore volume/ $cm^3\ g^{-1}$	hydrogen storage capacity[a] P/bar	T/K	gravimetric/ wt %	volumetric/ $g\ L^{-1}$	Q_{st}/ $kJ\ mol^{-1}$
					Dicarboxylic Acid					
$Mg_2(dobdc)$	MOF-74(Mg)	1510				1	77	2.2		10.3
						15(100)	77	3.2 (4.9)	(49)	
						(100)	298	(0.8)	(7.5)	
$Cr_3OF(BDC)_3$	MIL-101		5500	8.6	1.9	6080	77	6.1	1.84	10
							298	0.43		
Mn(NDC)		191		6.1	0.068	1	77	0.57		
$Fe_3O(tfbdc)_3$			635			1	77	0.9		
$NaNi_3(OH)(sip)_2$		700				1	77	0.94		10.4
$Ni(dhtp)_2$			1083		0.41	70	77	1.8		
						70	298	0.3		
Cu(peip)		1560	1780		0.696	1	77	2.51		6.63
						40	77	4.14		
						100	298	0.46		
Cu(pmip)		1490	1690		0.605	1	77	2.36		7.24
$Cu_6O(tzi)_3(NO_3)$		2847	3223		1.01	1	77	2.4		9.5
Zn(peip)		1660	1880		0.667	1	77	2.27		6.56
$Zn_2(dhtp)$	MOF-74, CPO-27-Zn	783	1132		0.39	1	77	1.77		8.3
		950	1072			26.1	77	2.21	27.6	
		870				30	77	2.8		8.8
$Zn_3(BDC)_3(Cu(pyen))$					0.26	1	77	0.66		12.3
$Zn_3(OH)(cdc)_{2.5}$		152		5		1	77	2.1		7
$Y_2(pdc)_3$		676				1	77	1.32		
$Sm_2Zn_3(oxdc)_6$		719			0.31	34	77	1.19		
						35	298	0.54		
$Er_2(3,5\text{-}pdc)_3$		427				1	77	0.68		
					Tricarboxylic Acid					
$Cr_3(BTC)_2$		1810	2040			1	77	1.9		7.4
$Cr_3OF(BTC)_2$	MIL-100		2700	25, 29	1	73.3	298	0.15	1.04	6.3
						90	77	3.28	23	
$Cr_3OF(ntc)_{1.5}$	MIL-102		42	4.4	0.12	35	77	1		6
						35	298	0.05		
$Fe_4O_2(BTB)_{8/3}$		1121	1835		0.69	1	77	2.1		
$H_2[Co_4O(TATB)_{8/3}]$	PCN-9		1355	6.5	0.51	1	77	1.53		10.1
$Cu_3(TATB)_2$ (catenated)	PCN-6		3800	5	1.456	1	77	1.9		
						50	77	7.2		6.2
$Cu_3(TATB)_2$ (noncatenated)	PCN-6′		2700		1.045	1	77	1.35		6
						50	77	4.2		
$Cu_3(bhtc)_2$	UMCM-150	2300	3100		1	1	77	2.1		7.3
						45	77	5.7	36	
Y(BTC)						1	77	1.57		7.3
						10	77	2.1	28.8	
$Mo_3(BTC)_2$	TUDMOF-1	1280	2010		0.67	1	77	1.75		
Dy(BTC)		655		6		1	77	1.32		
					Tetracarboxylic Acid					
$Co_2(H_2O)_2(MTB)$	SNU-15′					1	77	0.74		15.1
$Cu_2(bdpb)$	PMOF-3	1879	2489			1	77	2.47		
$Cu_2(bptc)$	MOF-505		1830	6.5	0.63	1	77	2.47		
	NOTT-100	1670			0.68	1	77	2.59	(38.9)	6.3
						20	77	(4.02)		
$Cu_2(tptc)$	NOTT-101	2247		7.3	0.89	1	77	2.52	43.6	5.3
						20	77	6.06		
$Cu_2(qptc)$	NOTT-102	2932		8.3	1.14	1	77	2.24	41.1	5.4
						20	77	6.07		

Cu_2(L, tetracarboxylate)	NOTT-103	2929		8	1.142	1	77	2.63		5.71
						20	77	(6.51)		
						60	77	(7.78)		
	NOTT-105	2387		7.3	0.898	1	77	2.52		5.77
						20	77	(5.40)		
	NOTT-106	1855		7.3	0.798	1	77	2.29		6.34
						20	77	(4.50)		
	NOTT-107	1822		7	0.767	1	77	2.26		6.70
						20	77	(4.46)		
	NOTT-109	1718		6.9	0.705	1	77	2.33		
						20	77	(4.15)		
	NOTT-110	2960		8	1.22	1	77	2.64		5.68
						55	77	5.43	46.8	
	NOTT-111	2930		8	1.19	1	77	2.56		6.21
						48	77	5.47	45.4	
Cu_2(aobtc)	PCN-10	1407	1779		0.67	1	77	2.34	18	6.8
						3.5	30	6.84	52.5	
						45	300	0.25		
Cu_2(sbtc)	PCN-11	1931	2442		0.91	1				
						3.5	30	7.89	59.1	
						45	77	5.23	39.2	
$Cu_2(C_{2v}$-mdip)	PCN-12′	1577	1962		0.73	1	77	2.4	20.4	
$Cu_6(C_s$-mdip$)_2(C_{2v}$-mdip)	PCN-12	1943	2425		0.94	1	77	3.05	23.2	
Cu_2(adip)	PCN-14	1753				1	77	2.7		8.6
						45	77	4.42	36.6	
Cu_2(ebdc)	PCN-16	2273	2800		1.06	1	77	2.6		
						~45	77	5.1		
Cu_2(ebdc)	PCN-16′	1760	2200		0.84	1	77	1.7		
						~28	77	2.9		
Cu_2(PMTB)	PCN-21	2718	4485		1.54	1	77	1.6		
Cu_2(abtc)	JUC-62				0.89	40	77	4.71	53	
	SNU-5		2850		1	1	77	2.84		
						50	77	5.22		
Cu_2(TCM)	SNU-21S		905	6.6, 9.2	0.31	1	77	1.95		6.65
						70	77	4.37		
						70	298	0.26		
	SNU-21H		695	6.3, 10.7	0.25	1	77	1.64		6.09
						70	77	4.36		
						70	298	0.18		
Cu_2(bdcppi)	SNU-50′	2300	2450	11	1.08	1	77	2.1		7.1
						60	77	5.53 (7.86)		
						61	298	0.399 (0.980)		
Cu_2(BDDC)		2357	3111		1.113	0.95	77	1.64	15	6.9
						17(31)	77	3.98(4.60)	36(41)	
Cu_2(tcpdep)			733			1	77	0.8		
$Cu_2(C_{2h}$-TCPPDA)			504			1	77	1.2		
$Cu_2(D_{2h}$-TCPPDA)			626			1	77	1.4		
Zn_2(btatb)		1370				1	77	2.2		8.1
In_3O(abtc$)_{1.5}(NO_3)$	*soc*-MOF		1417	7.65, 5.95	0.5	1.2	77	2.61		6.5
				Hexacarboxylic						
Cu_3(abtt)	NOTT-114	3424			1.36	1	78	2.28		
						30 (60)	78	5.0 (6.8)	(41.6)	5.3
Cu_3(BHB)	UTSA-20	1156		3.4, 8.5		1	77	2.9		
						15	77	4.1		
Cu_3(btei)	PCN-61	3000	3500		1.36	1	77	2.25	12.6	6.36
						33	77	6.24	35	
						90	298	0.667	3.74	
Cu_3(btti)	NOTT-119	4118			2.35	1	77	1.4		7.3
Cu_3(btti)	PCN-69	3989			2.173	1	77	1.7		8.14
						60	77	5.22		
Cu_3(ntbd)	NOTT-115	3394			1.38	1	78	2.42		
						33(60)	78	5.6 (7.5)	(49.3)	5.8

Cu_3(ntei)	PCN-66	4000	4600	1.63	1	77	1.79	7.98	6.22
					45	77	6.65	29.6	
					90	298	0.785	3.5	
Cu_3(ptei)	PCN-68	5109	6033	2.13	1	77	1.87	7.2	6.09
					50	77	7.32	28	
					90	298	1.01	4.1	
Cu_3(tbtt)	NOTT-113	2970		1.25	1	78	2.39		
					30 (60)	78	5.1 (6.7)	(42.5)	5.9
Cu_3(ttei)	NU-100	6143		2.82	1	77	1.82		6.1
					56(70)	77	9.95(16.4)		
Cu_3(L, hexacarboxylate)	NOTT-112	3800			1	78	2.3		5.64
					35—40 (77)	77	7.07 (10)	(50.3)	
	PMOF-2(Cu)	3730	4180		1	77	2.29		9.2
					30 (50)	77	5 (7)	(39.2)	
				Octacarboxylic Acid					
Cu_4(L)	NOTT-140	2620		1.07	1	77	2.5		4.15
					20	77	(6)		

This table comes from a published paper.[2]

I.1.2.3. Post-Synthetic Modifications[2]

The properties of MOFs such as surface area, pore volume and gas storage can be changed by modification of surface in MOFs. The modification of MOFs have achieved before or after the synthesis of MOFs. The prefunctionalization method is a manner to synthesize MOFs with ligand incorporating a special functional group that offers the change of the chemical properties in the MOF surface or strong attraction sites for guest molecules. In early stage of MOF chemistry, the prefunctionalization strategy was used frequently, especially for the introduction of -NH_2,-CH_3,-Br, etc. on the framework, which leads to form the series of IRMOFs.[79] Similarly, a family of ZIFs[80] and MILs[81,82] were prepared by prefunctionalization. However, a major problem of this strategy is the limitation of the synthesis of MOFs by solvothermal synthesis. Under the solvothermal synthesis to form MOFs, the thermally labile functional groups could be dissociated or participated in the coordination to metal ion providing the undesirable nanoporous structures. Fortunately, postsynthetic modification, as alternative of prefunctionalization, has attractive attention to introduce the functional group into MOFs. After synthesis of MOFs, changing the

state of MOFs such as covalent bond modification in ligand,[83,84] cation exchange of anion framework[85] or fabrication of metal nanoparticles in MOFs[12,13,29] is called postsynthetic modifications (PSM). The concept of postsynthetic modification initially described by Hoskins and Robson in 1990.[86] In 2007, Wang and Cohen modified free -NH_2 groups present in IRMOF-3 by the reaction with acetic anhydride.[83,84] When they attempt to modify the ligand for 5 days, the percent conversion of IRMOF-3 is >80 % estimated by ^{1}H NMR and structure of framework was retained.

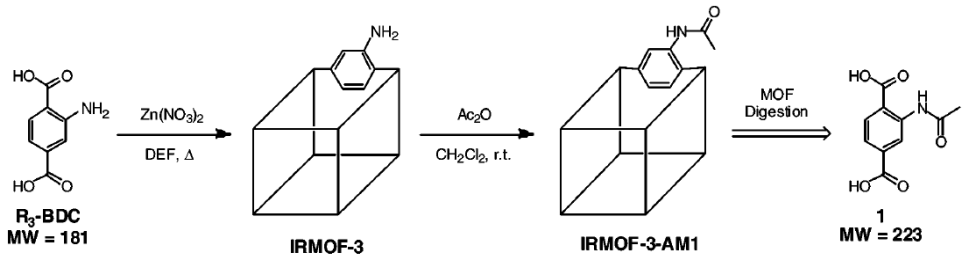

Figure 12. Process of post-synthetic modification in IRMOF-3.[84]

Mulfort *et al.*[87] replaced the proton of the hydroxyl group of ligand in a MOF with an alkali metal ions by postsynthetic modification. Someone synthesize an anionic framework including counter-cations located in the pore and then exchange counter-cations with metal cations.[83] Now postsynthetic modification is widely utilized in order to change the properties of a MOF for applications in gas storage and catalysis. A recent review by Cohen *et al.* offers some elaborate ideas about the postsynthetic modification of MOFs.[88-90] By postsynthetic modification, the framework can be functionalized without altering the framework structure. In addition, the introduction of functional group that is able to coordinate in the framework allows the incorporation of new metal ions, which increase the available open metal sites and thus enhance the total H_2 storage capacity. Such studies can be used to fine-tune the

framework structure, metal centers, and functional groups of the ligands for the development of MOFs for ambient temperature H_2 storage.

I.1.2.3.1. Ligand Functionalization

Postsynthetic modifications (PSM) can be broadly classified as a covalent PSM, dative PSM, and postsynthetic deprotection (PSD) (Figure 12).[90] These PSM is distinguished by chemical bond type during the PSM reaction. The definition of covalent PSM is to form a new covalent bond by use of a reagent in a heterogeneous, postsynthetic manner. Dative PSM is defined as a formation of metal-ligand bond by use of a reagent in a heterogeneous, postsynthetic manner. Finally PSD is defined as a cleavage of a chemical bond in the framework during the postsynthetic modification.

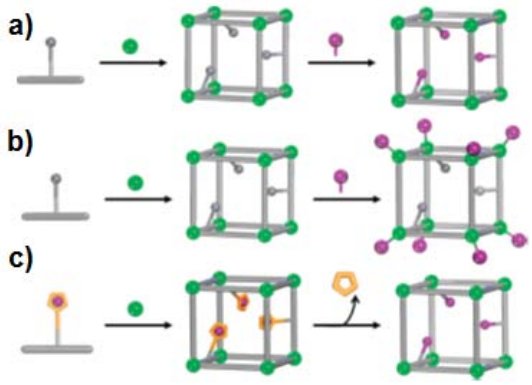

Figure12. Generic schemes for a) covalent PSM b) dative PSM c) postsynthetic deprotection (PSD).[90]

In this part, covalent PSM will be discussed. To form the covalent bond in ligand by PSM, a variety of chemical reactions were reported such as amide coupling,[25,83,91] imine condensation,[26,92,93] bromination,[27] and click reaction etc.[28,94] Coast *et al.* reported amide coupling as a postsynthetic modification.[25] They synthesized a new MOF, $\{[Gd_2(N\text{-}BDC)_3(dmf)_4]\}_n$ (MOF-LIC-1), from gadolinium nitrate with 2-amino

-1,4 benzene dicarboxylic acid in DMF. Amine functional group of MOF-LIC-1 reacts with acetic acid to have a channel modified MOFs. The amide functional group is observed in the single crystal X-ray structure.

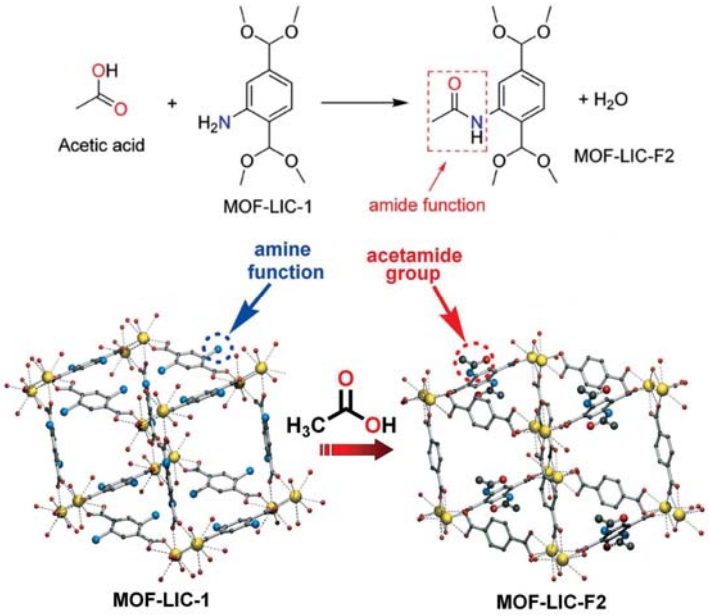

Figure 13. Reaction scheme and of MOF-LIC-1 with acetic acid.[25]

Similarly, Cohen's group has published amide coupling reaction as a postsynthetic modification to tune the hydrogen adsorption properties.[84] They used three MOFs, IRMOF-3, UMCM-1-NH_2, and DMOF-1-NH_2 which have a amine group in the organic building block (Figure 14). The amino group reacts with alkyl anhydrides or isocyanates resulting in amide or urea functional group. The conversion of functional group is controlled by reactant concentration or reaction time. Even though the surface area of MOFs is reduced depending on the nature of substituents, it indicates that hydrogen uptake capacity and heat of adsorption are enhanced. The hydrogen sorption properties and isosteric heat of all compounds are summarized in Table 2. As compared the aromatic ring substitution with alkyl chain substitution,

aromatic ring substitution shows higher enhancement of the hydrogen uptake capacity and Q_{st} values. They supposed that the added phenyl groups have a specific interaction with H_2 molecules.

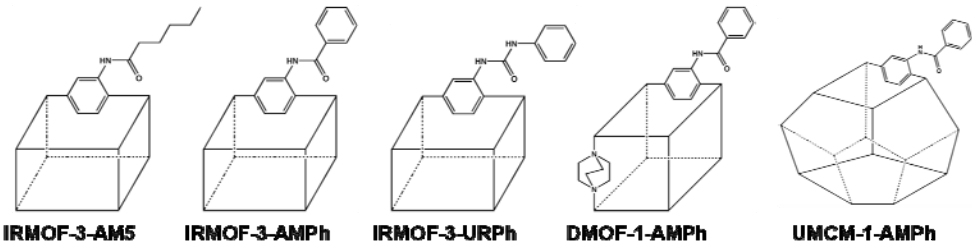

Figure 14. Schematic representation of the five modified MOFs utilized in post synthetic modification study.[84]

Table 2. A summary of hydrogen sorption properties of three distinct MOFs upon postsynthetic modification.[84]

Compound	Conversion	SA_{BET}/ m^2g^{-1}	H_2/ wt%[a]	ΔH_{ads}/ kJ mol^{-1}[b]
IRMOF-3	*N/A*	2639±61	1.52±0.02	5.3±0.3
AMP-a	32%	2267	1.73	5.3
AMP-b	44%	2052	1.73	5.7
AMP-c	70%	1657	1.68	6.0
URPh	41±5%	1940±52	1.54±0.06	5.7±0.3
AM-5	86±5%	1239±46	1.21±0.02	5.7±0.3
UMCM-1-NH_2	*N/A*	3917±137	1.35±0.05	4.6±0.4
AMPh	76±1%	3770±93	1.54±0.04	5.2±0.2
DMOF-1-NH_2	*N/A*	3770±93	2.08±0.01	5.6
AMPh	63±1%	913±37	1.69±0.05	7.0±0.1

[a]Gravimetric uptake at 77 K and 1 atm. [b]Heat of adsorption at zero coverage calculated from the virial-type equation

I.1.2.3.2. Inclusion of Metal Cation or Organic Molecules in the Frameworks

As mentioned previously, hydrogen storage in porous materials has faced with difficulty of storage capacity at ambient temperature and low adsorption enthalpy. To exploit metal-organic frameworks with the enhanced heat of H_2 adsorption, it is performed to replace cation included in the anionic framework or to add metal ion into the neutral frameworks, respectively. The included extra metal ions are able to interact with H_2 molecules more strongly.

According to the theoretical studies, Li-doped MOFs significantly improve H_2 uptake capacities at ambient conditions (Figure 15).[95,96] Another theoretical study on alkali metal ion doped zeolitic imidazole frameworks also showed significant improvement of H_2 uptake at room temperature.[97] In ZIFs, the alkali-metal ions bind to the five-membered ring rather than to six-membered rings. Li-ZIF-70 totally stores up to 3.08 wt% of H_2, Na-ZIF-70 to 2.19 wt% of H_2, and K-ZIF-70 to 1.62wt% of H_2 at 298 K and 100 bar, which are much higher than 0.74 wt% of H_2 for pristine ZIF-70. It shows that the dopant effect follows the order of Li-ZIF > Na-ZIF > K-ZIF. The binding energies of the first H_2 to the doped alkali- metals are 23.45 kJ mol^{-1} for Li^+, 12.20 kJ mol^{-1} for Na^+, and 5.39 kJ mol^{-1} for K^+ ($Li^+ > Na^+ > K^+$), as they are calculated using the second-order Møller-Plesset ab initio method.[98]

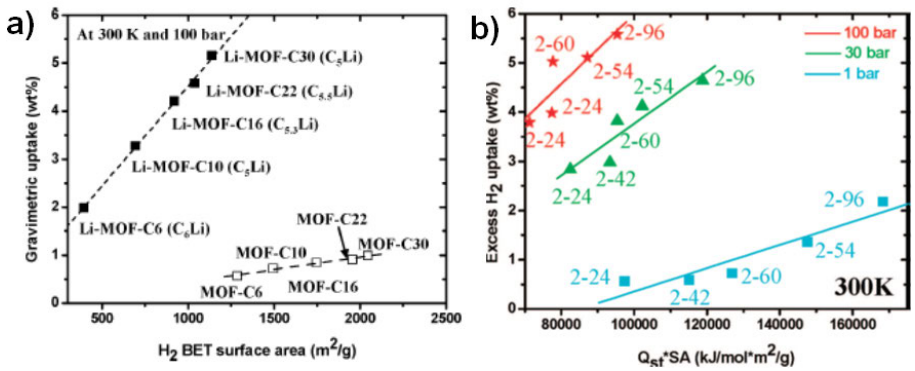

Figure 15. a) Gravimetric H_2 uptake at 300 K and 100 bar plotted against BET surface area for MOFs and Li-MOFs systems. b) Relationship between H_2 uptake in IRMOF-Li at 300K and multiple value of adsorption (Q_{st}) and Surface area (SA). This shows that both surface area and the ratio of Li to C are important for high performance.[95,96]

Dinca and Long reported the exchange of extra Mn^{2+} ions in $Mn_3[(Mn_4Cl)_3(BTT)_8(CH_3OH)_{10}]_2$ with various cations (Li^+, Cu^+, Fe^{2+}, Co^{2+}, Ni^{2+}, Cu^{2+}, Zn^{2+}) which result in the isostructural framework.[99] The total number of exchanged guest cations is similar to among the all samples; 4.0, 4.7, 3.0, 5.0, 5.0, and 5.0 for Fe^{2+}, Co^{2+}, Ni^{2+}, Cu^{2+}, Zn^{2+}, and Li^+, respectively. In hydrogen gas sorption properties, all samples represented similar H_2 uptake capacities (Table 3). However, the uptake slopes at low coverage are significantly different from each other. These results indicated that H_2 molecules bind the strongest site presented in metal cations. Co^{2+} exhibits the highest heat of adsorption for hydrogen (10.5 $kJmol^{-1}$) (Figure 16).

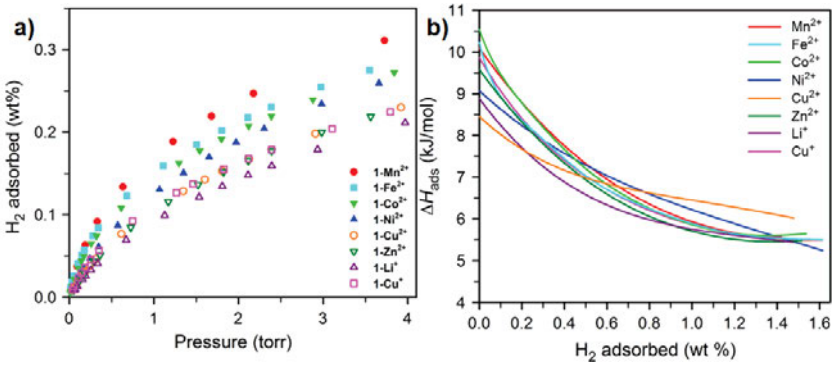

Figure 16. a) H_2 adsorption isotherm at 77 K, and b) Heat of adsorption for H_2.[99]

Table 3. Composition and H_2 sorption properties of cation exchanged compound.[99]

Compound [a]	M/Mn ratio (expt/found)[a]	SA_{BET} (m^2/g)	H_2 ads (wt %)[b]	Q_{st} (kJ/mol)
$Mn_3[(Mn_4Cl)_3(BTT)_8]_2$	N/A	2057(5)	2.23	5.5-10.1
$Fe_3[(Mn_4Cl)_3(BTT)_8]_2FeCl_2$	0.169/0.170	2033(5)	2.21	5.5-10.2
$Co_3[(Mn_4Cl)_3(BTT)_8]_21.7CoCl_2$	0.210/0.210	2096(5)	2.12	5.6-10.5
$Ni_{2.75}Mn_{0.25}[(Mn_4Cl)_3(BTT)_8]_2$	0.121/0.121	2110(5)	2.29	5.2-9.1
$Cu_3[(Cu_{2.9}Mn_{1.1}Cl)_3(BTT)_8]_22CuCl_2$	3.925/3.999	1695(5)	2.02	6.0-8.5
$Zn_3[(Zn_{0.7}Mn_{3.3}Cl)_3(BTT)_8]_22ZnCl_2$	0.553/0.546	1927(5)	2.10	5.5-9.6
$Li_{3.2}Mn_{1.4}[(Mn_4Cl)_3(BTT)_8]_20.4LiCl$	0.017/0.017	1904(5)	2.06	5.4-8.9
$Mn_3[(Mn_4Cl)_3(BTT)_8]_20.75CuPF_6$	*N/A*	1911(5)	2.00	5.6-9.9

[a]Based on the relative ratio of Mn^+/Mn^{2+} as determined using ICP-AA and on C, H, and N analysis [b]Obtained at 77 K and 900 torr. [c] Determined using a virial fit to the 77 and 87 K H_2 adsorption isotherms.

Hartmann *et al*. also exchanged the protons of hydroxyl pendants in [Al(OH)(BDC-OH)], MIL-53(Al) with lithium by using lithium diisopropylamide (LDA).[100] By chemical analysis, it was found that 15% of the acidic framework protons were exchanged with lithium. The apparent Langmuir (BET) surface area of Li-MIL-53(Al) was 1450 m^2g^{-1} (1384 m^2g^{-1}), which is 180 m^2g^{-1} smaller than that of

the original MOF. The H_2 uptake capacities at 77 K and 1 bar were 0.5 wt% and 1.7 wt% for undoped MIL-53(Al)-OH and Li-doped Li-MIL-53(Al), respectively. The enhancement of the H_2 storage in Li-MIL-53(Al) was not only due to the lithium doping but also due to the temperature-induced structural transformation. The isosteric heat of H_2 adsorption clearly demonstrated the impact of Li^+ doping on hydrogen sorption. Compared with the undoped compound which has an adsorption enthalpy of 5.8 - 4.4 $kJmol^{-1}$, Li-MIL-53(Al) has a heat of H_2 adsorption of 11.6 - 6.4 kJ mol^{-1}, which approaches the theoretical maximum value of ca. 13 kJ mol^{-1}.[101]

Instead of metal cation inclusion, Suh's group performed inclusion of organic molecules, crown ether moiety, in the highly porous metal organic framework (SNU-6) (Figure 17).[35] In this case, 18- crown-6(18C6) and 15-crown-5(15C5) that are capable of providing electrostatic field in MOFs, are selected as a inclusion guests. The optimal amount of 18- crown-6(18C6) has a stronger effect that that of 15-crown-5(15C5) in the enhancement of Q_{st} of H_2(SNU-6, 7.74 $kJmol^{-1}$; 1.2(18C6)@SNU-6, 10.5 $kJmol^{-1}$; 0.3(15C5)@SNU-6, 9.07 $kJmol^{-1}$). The enhancement of Q_{st} in crown ether inclusion is higher than that (ca. 1.1 kJ mol^{-1}) of inclusion of alkali or alkaline-

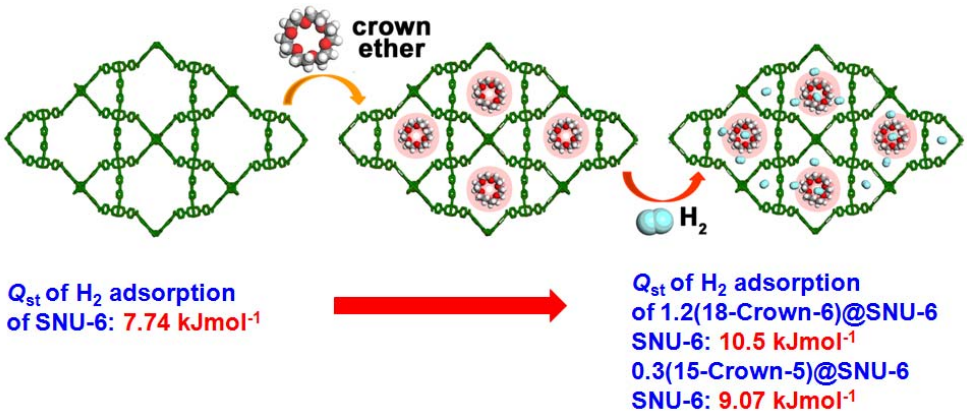

Figure 17. Scheme for inclusion of crown ether moiety in SNU-6

earth metal ions. In addition, it is comparable to those by the open metal sites in a MOF.

I.2. Experimental Section

General. All chemicals and solvents used in the syntheses were of reagent grade and used without further purification. 4,4',5,5'-tetrabenzoic acid dibenzo-18-crown-6 (H_4TBADB-18-Cr-6) was prepared by using Suzuki-Miyaura coupling method.[102] NMR spectra were measured on a Bruker Spectrospin spectrometer. Infrared spectra were recorded with a Perkin–Elmer Spectrum One FT-IR spectrophotometer. Elemental analyses were performed by Perkin–Elmer 2400 series II CHN analyzer. Thermogravimetric analysis (TGA) and differential scanning calorimetry (DSC) were performed under N_2(g) at a scan rate of 3 °C min-1 with Q50 and Q10 model devices from TA Instruments, respectively. Powder X-ray diffraction (PXRD) data were obtained on a Bruker New D8 diffractometer at 40 kV and 40 mA for Cu Kα (λ = 1.54050 Å) with a scan speed of 5^o min^{-1} and a step size of 0.02° in 2θ. For quantitative metal ion analysis, inductively coupled plasma-atomic emission spectrometry (ICP-AES) was performed on a Perkin-Elmer Optima-4300 DV instrument in Seoul National University, National Center for Inter – University Research Facilities.

Synthesis of 4,4',5,5'-terabenzoic acid dibenzo-18-crown-6 (H_4TBADB-18-Cr-6)

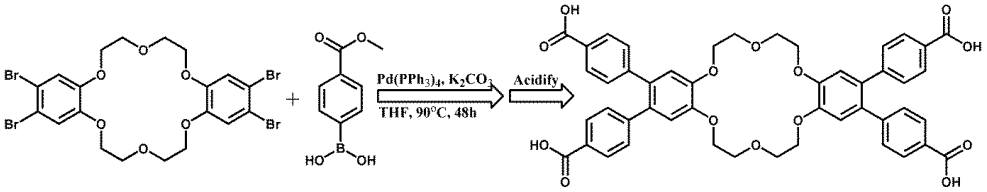

Figure 17. Synthetic scheme of 4,4',5,5'-terabenzoic acid dibenzo-18-crown-6

(H_4TBADB-18-Cr-6) ligand.

4,4'5,5'-terabenzoic acid dibenzo-18-crown-6 (H_4TBADB-18-Cr-6) was synthesized by using Suzuki-Miyaura coupling reaction.[102] $Pd(PPh_3)_4$ (0.201 g, 0.174 mmol), 4,4',5,5'-tetrabromodibenzo-18-crown-6 (2.059 g, 3.034 mmol), and K_2CO_3 (2.099g, 15.188 mmol) were dissolved in purified anhydrous THF, and stirred for 10 min. 4-methoxycarbonylphenyl boronic acid (2.258 g, 12.548 mmol), which was dissolved in methanol (15 mL), was added to the solution, and heated at 90 ^oC for 48 h. After being cooled to room temperature, the solution was concentrated in a rotary evaporator, and the deep-brown residue was extracted with chloroform. The solution was washed with water, and then dried over anhydrous magnesium sulfate. The resulting solution was concentrated to provide dark brown residue, which was recrystallized with ethyl acetate and chloroform. White powder was obtained by recrystallization. FT-IR (Nujol): $\nu_{O-C=O}$, 1720 cm^{-1}, $\nu_{c=c}$, 1606, ν_{c-o-c}, 1255. ^1H NMR (300 MHz, DMSO): δ 7.78 (d, 8H), 7.22 (d, 8H), 7.03 (s, 4H), 4.22 (s, 8H), 3.88 (s, 8H) ppm. Anal. calcd. for ($C_{48}H_{40}O_{14}$): C 68.57, H 4.79, N 0.00; Found: C 68.08, H 4.75, N 0.05.

Preparation of $[Zn_5(OH)_2(TBADB\text{-}18\text{-}Cr\text{-}6)_2 \cdot 4DMF] \cdot 13DMF \cdot 12H_2O$ (SNU-200). $Zn(NO_3) \cdot 6H_2O$ (1.01 g, 5.33 mmol) and H_4TBADB-18-Cr-6 (0.301 g, 0.358 mmol) were dissolved in DMF/H_2O (50:1, v/v). The solution was placed in a glass serum bottle that was capped with a silicon stopper and aluminum seal, and then heated at 80 ^oC for 24 h. On cooling to room temperature, white crystals formed, which were filtered off, washed briefly with mother liquor. FT-IR (Nujol): $\nu_{C=O}$(DMF), 1664 cm^{-1}. Anal. calcd (%). for $[Zn_5(OH)_2(TBADB\text{-}18\text{-}Cr\text{-}6)_2 \cdot 4DMF] \cdot 13DMF \cdot 12H_2O$: C 50.85,

H 5.69, N 6.86; Found: C 50.83, H 5.82, N 6.79.

Preparation of $[Zn_5(OH)_2(TBADB\text{-}18\text{-}Cr\text{-}6)_2]$ (SNU-200'). Prior to activation, the crystals of as- synthesized $[Zn_5(OH)_2(TBADB\text{-}18\text{-}Cr\text{-}6)_2 \cdot 4DMF] \cdot 13DMF \cdot 12H_2O$, which were still in the mother liquor, were transferred to a vial (20 mL). The mother liquor was decanted, and the crystals were washed briefly with DMF (4 x 15 mL). The crystals were placed inside the supercritical dryer together with the solvent, and the drying chamber was sealed. The temperature and pressure of the chamber were raised to 40 ^oC and 200 bar with CO_2, above the critical point (31 ^oC, 73 atm) of CO_2. The chamber was vented at a rate of 10 mL min^{-1}, and then filled with CO_2 again. The cycles of refilling with CO_2, pressurizing, and venting were repeated for 4 h. After drying, the closed container with the dried crystals was transferred to a glove bag to prevent the crystals from exposure to air. FT-IR (KBr pellet): $\nu_{O\text{-}C=O}$, 1599; $\nu_{C=C}$, 1521; $\nu_{O\text{-}C\text{-}O(ether)}$, 1125 cm^{-1}. Anal. calcd (%). for $[Zn_5(OH)_2(TBADB\text{-}18\text{-}Cr\text{-}6)_2]$: C 56.67, H 3.94, N 0.00; Found: C 55.67, H 3.94, N 0.28.

Preparation of $K^+ \subset$SNU-200'$\cdot SCN^-$. As-synthesized SNU-200 (200 mg) was washed with fresh DMF and immersed in the DMF solution (20 mL) of 0.1 M KSCN. The solution was replenished 10 times for 3 days. Before the analysis of the sample, the crystals were immersed in fresh DMF solvent to eliminate the extra salts included in the pores of the MOF, and then activated with supercritical CO_2. FT-IR (KBr pellet): $\nu_{Zn\text{-}N\text{-}C}$, 2087; $\nu_{C=C}$, 1521 cm^{-1}. Anal. calcd (%). for $[Zn_5(OH)_2(TBADB\text{-}18\text{-}Cr\text{-}6)_2K_2SCN_2]$: C 52.81, H 3.35, N 1.26; Found: C 53.09, H 3.19, N 0.85.

Preparation of NH_4^+⊂SNU-200'·Cl^-. The synthesized SNU-200 was washed with fresh DMF and immersed in the DMF/H_2O (50:1, v/v) solution of 0.01 M NH_4Cl. The solution was replenished more than 10 times for 3 days. Before the analysis of the sample, the crystals were immersed in fresh DMF solvent to eliminate the extra salts included in the pores of the MOF, and then activated with supercritical CO_2. Anal. calcd (%). for $[Zn_5(OH)_2(TBADB\text{-}18\text{-}Cr\text{-}6)_2]\cdot[NH_4Cl]_{2.17}$: C 53.61, H 3.88, N 1.41; Found: C 53.34, H 3.95, N 1.43.

Preparation of MV^{2+}⊂SNU-200'·$2Cl^-$. As-synthesized SNU-200 was washed with mother liquor and immersed in the DMF/H_2O (50:1, v/v) solution of 0.01 M of methyl viologen dichloride for 3 days. The solution was replenished more than 10 times for 3 days. Before the analysis of the sample, the crystals were immersed in fresh DMF solvent to eliminate the extra salts included in the pores of the MOF, and then activated with supercritical CO_2. Anal. calcd (%)for $[Zn_5(OH)_2(TBADB\text{-}18\text{-}Cr\text{-}6)_2]\cdot[C_{12}H_{14}N_2Cl_2]_{0.72}$: C 56.62, H 3.82, N 0.90; Found: C 57.36, H 3.93, N 0.89.

Preparation of Eu^{3+}⊂SNU-200'·$3Cl^-$. As-synthesized SNU-200 was washed with mother liquor and immersed in the DMF/H_2O (50:1, v/v) solution of 0.01 M of $EuCl_3$ for 3 days. The solution was replenished more than 10 times for 3 days. Before the analysis of the sample, the crystals were immersed in fresh DMF solvent to eliminate the extra salts included in the pores of the MOF, and then activated with supercritical CO_2. Anal. calcd (%)for $[Zn_5(OH)_2(TBADB\text{-}18\text{-}Cr\text{-}6)_2]\cdot[EuCl_3]\cdot(DMF)_{1.457}$: C 50.24, H 3.53, N 0.85; Found: C 51.96, H 3.58, N 0.88.

Theoretical determination of biding sites for methyl viologen dichloride in SNU-200. To predict the preferential location of methyl viologen dichloride as guests within the pores, we carried out location simulations by using a Sorption module of Material Studio.[103] Metropolis Monte Carlo method was selected for the calculation of the global minimum location. Universal force field (UFF) was chosen for energy calculation.

X-ray Crystallography. The diffraction data of $[Zn_5(OH)_2(TBADB\text{-}18\text{-}Cr\text{-}6)_2\cdot 4DMF]\cdot 13DMF\cdot 12H_2O$ (SNU-200) and $[Zn_5(OH)_2(TBADB\text{-}18\text{-}Cr\text{-}6)_2\cdot(KSCN)_2\cdot(H_2O)_4]$ ($K^+\subset$SNU-200$\cdot SCN^-$) $[Zn_5(OH)_2(TBADB\text{-}18\text{-}Cr\text{-}6)_2\cdot(NH_4)_2]\cdot Cl_2$ ($NH_4^+\subset$SNU-200$\cdot Cl^-$) were collected with synchrotron radiation (λ= 0.8000 and 0.69999 Å) on a ADSC Quantum-210 detector at 2D (SMC) with a silicon (111) double-crystal monochromator at the Pohang Accelerator Laboratory (PAL), Korea. For the collection of X-ray diffraction data of $[Zn_5(OH)_2(TBADB\text{-}18\text{-}Cr\text{-}6)\cdot 4DMF]\cdot 13DMF\cdot 12H_2O$, the crystal was coated with paratone oil immediately. The crystal was maintained at 100 K by the cryostream during the collection of the X-ray data. The ADSC Quantum-210 CCD program (Ver. 1.96)[104] was used for data collection and HKL3000 (Ver.730r)[105] was used for cell refinement, reduction, and absorption correction. The structures were solved by direct methods[106] and refined by full-matrix least-squares refinement using the SHELXS-97 computer program.[107] The hydrogen atoms were positioned geometrically by using a riding model. The electron densities of the disordered guest molecules were flattened by using *SQUEEZE* option of *PLATON*.[108] Therefore, the guest molecules in crystals were determined on the basis of IR spectroscopy, elemental analyses, and TGA. Although electron densities

associated with guest molecules could not be observed, residual electron densities found around the ligand were flattened by using *SQUEEZE* option of *PLATON*, which provided slightly lower *R* values than those determined without using *SQUEEZE* option.

CCDC-920678(SNU-200), 922626(K^+⊂SNU-200·SCN^-) and 949494(NH_4^+⊂SNU-200·Cl^-) contains the supplementary crystallographic data of this paper. These data can be obtained free of charge from The Cambridge Crystallographic Data Centre via www.ccdc.cam.ac.uk/data_request/cif.

Low Pressure Gas Sorption. The gas adsorption–desorption experiments were carried out on SNU-200', K^+⊂SNU-200'·SCN^-, NH_4^+⊂SNU-200'·Cl^-, MV^{2+}⊂SNU-200'·$2Cl^-$ and Eu^{3+}⊂SNU-200'·$3Cl^-$ by using an automated micropore gas analyzer Autosorb-3B (Quantachrome Instruments). All gases used were of 99.999% purity. The N_2 isotherms were measured at 77 K, and H_2 sorption isotherms were monitored at 77 K and 87 K, at each equilibrium pressure by the static volumetric method. After the gas sorption measurement was finished, weight of the sample was measured precisely. Surface area was determined from N_2 adsorption isotherm at 77 K by using the Brunauer-Emmett-Teller (BET) model by taking the data in the range P/P_0 = 0.11 – 0.005 for SNU-200', 0.07-0.002 for K^+⊂SNU-200'·SCN^-, 0.07-0.002 for NH_4^+⊂SNU-200'·Cl^-, and 0.09-0.001 for MV^{2+}⊂SNU-200'·$2Cl^-$. Pore volume was determined by using the Dubinin-Radushkevich (DR) equation. CO_2 and CH_4 sorption isotherms were measured at 195 K, 273 K, and 298 K.

Estimation of Isosteric Heat of the H_2 Adsorption. The isosteric heats of H_2 adsorption were estimated for SNU-200', $K^+ \subset$SNU-200'·SCN^-, $NH_4^+ \subset$SNU-200'·Cl^-, $MV^{2+} \subset$SNU-200'·$2Cl^-$ and $Eu^{3+} \subset$SNU-200'·$3Cl^-$ from the H_2 sorption data measured at 77 K and 87 K. A virial-type expression was used eq (1), which is composed of parameters a_i and b_i that are independent of temperature.[109]

In eq (1), P is pressure (atm), N is the amount adsorbed H_2 gas (mg g^{-1}), T is temperature (K), and m and n represent the number of coefficients required to adequately describe the isotherms. An equation was fit using the *R* statistical software package.[110]

To estimate the values of the isosteric heat of H_2 adsorption, eq (2) was applied, where R is the universal gas constant.

Calculation of Isosteric Heats of CO_2 and CH_4 Adsorption. The isosteric heats of CO_2 and CH_4 adsorption was estimated by fitting the adsorption isotherms at 195, 273, and 298 K to *Langmuir-Freundlich* equation (eq 7) In eq 7, P is pressure (atm), N is the amount adsorbed gas (mmolg^{-1}), N_m is the amount adsorbed gas at saturation, and b and c are constants. The isosteric heats of CO_2 and CH_4 adsorption were calculated by applying these fits to *Clausius-Clapeyron* equation (eq 8).

$$N = \frac{N_m b P^{1/c}}{1 + b P^{1/c}} \qquad (7)$$

$$\frac{\partial(\ln P)}{\partial(1/T)} = -\frac{Q_{st}}{R} \qquad (8)$$

Calculation of Adsorption Selectivity by Ideal Adsorbed Solution Theory (IAST).

The CO_2/N_2 and CO_2/CH_4 selectivity were calculated by using ideal adsorbed solution theory (IAST)[111,112] for SNU-200', $K^+ \subset$SNU-200'·SCN^- $NH_4^+ \subset$SNU-200'·Cl^-, and $MV^{2+} \subset$SNU-200'·$2Cl^-$. IAST is able to estimate the adsorption equilibrium of the binary gas mixture from the single-component isotherms. In order to calculate the adsorption selectivity for CO_2 over N_2 or CO_2 over CH_4, The idealized gas mixtures composed of 0.15 bar CO_2 and 0.85 bar N_2 for flue gas and 0.5 bar CO_2 and 0.5 bar CH_4 for landfill gas. According to IAST,

$$y_1 + y_2 = 1 \quad (9)$$

$$x_1 + x_2 = 1 \quad (10)$$

$$p_{\mathrm{mix}} y_1 = p_1^{\mathrm{o}} x_1 \quad (11)$$

$$p_{\mathrm{mix}} y_2 = p_2^{\mathrm{o}} x_2 \quad (12)$$

$$\pi_1^{\mathrm{o}} = \frac{RT}{A} \int_0^{p_1^{\mathrm{o}}} n_1(p) d \ln p \quad (13)$$

$$\pi_2^{\mathrm{o}} = \frac{RT}{A} \int_0^{p_2^{\mathrm{o}}} n_2(p) d \ln p \quad (14)$$

$$\pi = \pi_1^{\mathrm{o}} = \pi_2^{\mathrm{o}} \quad (15)$$

where y_i is the mole fraction of component i in the bulk gas mixture, x_i is the mole fraction of component i in adsorbed gas mixture, p_{mix} is the total pressure of the bulk gas mixture, p_1^{o} is the bulk pressure of pure component i that corresponds to the spreading pressure p of the binary mixture, R is the universal gas constant, T is adsorption temperature, A is surface area of the adsorbent, $n_i(p)$ is amount adsorbed at pressure p for pure component i.

Using Equations 9 – 15, the following equation can be obtained:

$$\int_0^{\frac{p_{mix}y_1}{x_1}} n_1(p)d\ln p = \int_0^{\frac{p_{mix}y_2}{1-x_1}} n_2(p)d\ln p \quad (16)$$

Total adsorbed amount of the gas mixture (n_Δ) is calculated by the following equation:

$$\frac{1}{n_\Delta} = \frac{1}{n_1(p_1^o)} + \frac{1}{n_2(p_2^o)} \quad (17)$$

where $n_1(p_1^o)$ is the amount of component 1 adsorbed at spreading pressure p in the absence of component 2, and $n_2(p_2^o)$is the amount of component 2 adsorbed at spreading pressure p in the absence of component 1. The adsorption amount for the component i (n_i^Δ) in the binary mixture adsorption is calculated using the following equation:

$$n_1^\Delta = n_\Delta x_1 \quad (18)$$

$$n_2^\Delta = n_\Delta x_2 \quad (19)$$

Adsorption selectivity of component 1 over component 2 (S_{12}) is calculated using the following equation:

$$S_{12} = \frac{x_1 y_2}{x_2 y_1} \quad (20)$$

I.3. Result and Discussion

X-ray structure and properties of SNU-200, K^+⊂SNU-200·SCN^-, and NH_4^+⊂ SNU-200·Cl^-

Colorless crystals of SNU-200 have been synthesized by heating a mixture of $Zn(NO_3)_2 \cdot 6H_2O$ and H_4TBADB-18-Cr-6 in DMF/H_2O at 80 °C for 24 h. The X-ray crystal structure of SNU-200 exhibits a doubly interpenetrated 3D network generating 1D channels (8.4 Å) that extend along the *c*-axis. In a pore, two 18C6 face each other

(Figure 18). There are three crystallographically independent Zn(II) centers (Zn1, Zn2, and Zn3), and they are linked by an OH^- bridge as well as eight different carboxylates to form a Zn_5 cluster unit with the inversion center at Zn3. (Figure 19). The Zn1 and Zn3 have an octahedral coordination geometry [∠O-Zn1-O, av. 89.63 (0.04) and ∠O-Zn3-O, av. 89.85 (0.04)] and Zn2 has a tetrahedral geometry [∠O-Zn2-O, av. 109.66 (0.06)]. Two DMF solvent molecules are coordinated at Zn1. The solvents

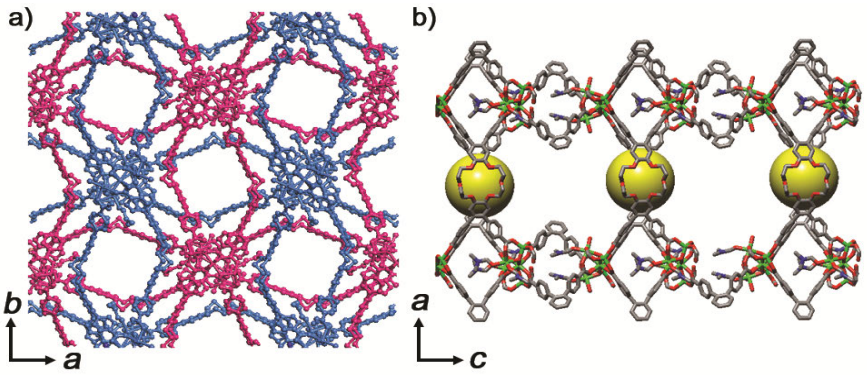

Figure 18. Single crystal X-ray structure of SNU-200 a) Doubly interpenetrated networks are represented in two different colors b) Single frame of SNU-200. The atoms of Zn, C, O, and N are shown in green, black, red, and blue, respectively Hydrogen atoms are omitted for clarity.

accessible void volume estimated by PLATON is 39.2% of the whole structure.

The X-ray structure of $K^+\subset$SNU-200·SCN^- indicates that two DMF molecules and one carboxyl oxygen coordinated at Zn1 in the pristine MOF are replaced with one SCN^- anion, which alters the coordination geometry of Zn1 from octahedral to tetrahedral [∠N-Zn1-O, av. 111.46 (0.13) and ∠O-Zn1-O, av. 107.66 (0.19)] (Figure 19). The Zn1 coordinates SCN^- via N atom as confirmed by a CN peak appearing at 2087 cm^{-1} in the IR spectrum (Figure 20). K^+ ion is located 0.0764(0.0061) Å above the mean plane made of six oxygen atoms of 18C6 and it is

coordinated with two water molecules at the axial site (Figure 21 and Figure 22).[113] Upon activation of the K^+ bound SNU-200, water molecules bound to the K^+ ion were removed (Figure 23). By the inductively coupled plasma (ICP) analysis data, it was found that 92% of 18C6 in the MOF bound K^+ ions.

In the X-ray structure of $NH_4^+ \subset$SNU-200·Cl^-, the coordination modes of the Zn ions in the Zn_5 cluster are same as that of SNU-200. The NH_4^+ ion is positioned 1.577 (0.035) Å above the mean plane of 18C6. The NH_4^+ ion forms hydrogen bonds with the oxygen atoms of the crown ether with an average N--O distance of 2.949 (0.067) Å. The Cl^- counter anions are also found in the channels. The elemental analysis data indicate that 1.09 NH_4^+ molecules exist per 18C6, implying that 100% of 18C6 in the MOF bind NH_4^+ cations.

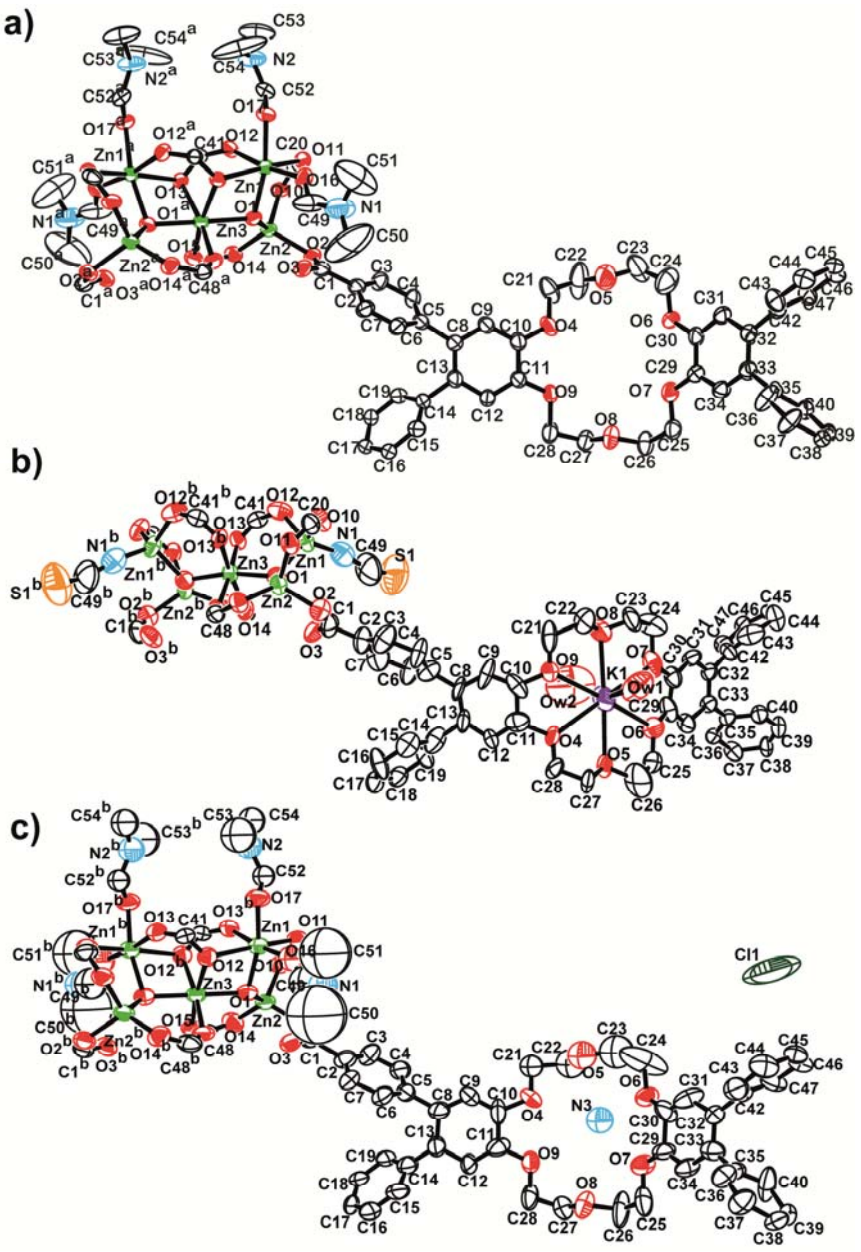

Figure 19. ORTEP drawings with the atomic numbering scheme. a) As synthesized SNU-200. b) $K^+ \subset$SNU-200·SCN^-. c) $NH_4^+ \subset$SNU-200·Cl^-. Symmetry operations: a, -x, -y+1, z; b -x+1, -y, z. The atoms of Zn, C, O, N, Cl, and S are represented by green, black, red, blue, and yellow spheres, respectively. Hydrogen atoms are omitted for clarity.

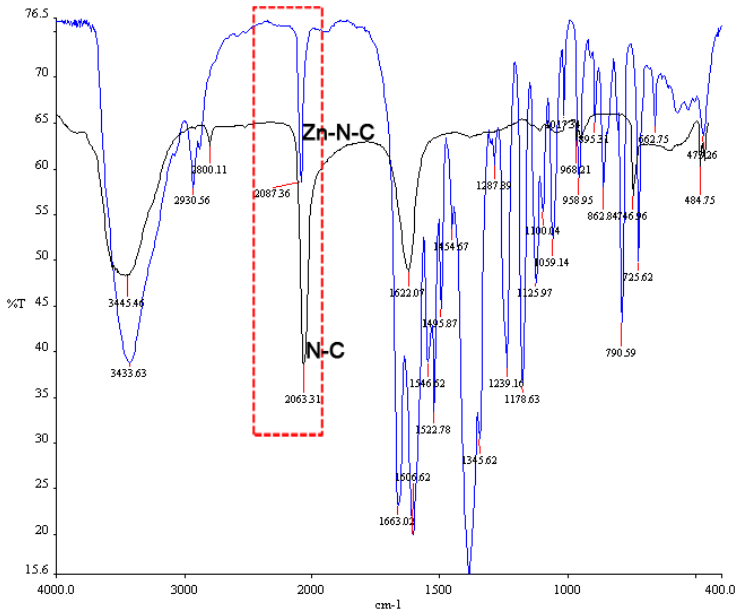

Figure 20. Infrared spectra of $K^+\subset$SNU-200 SCN^-(blue) and KSCN (black).

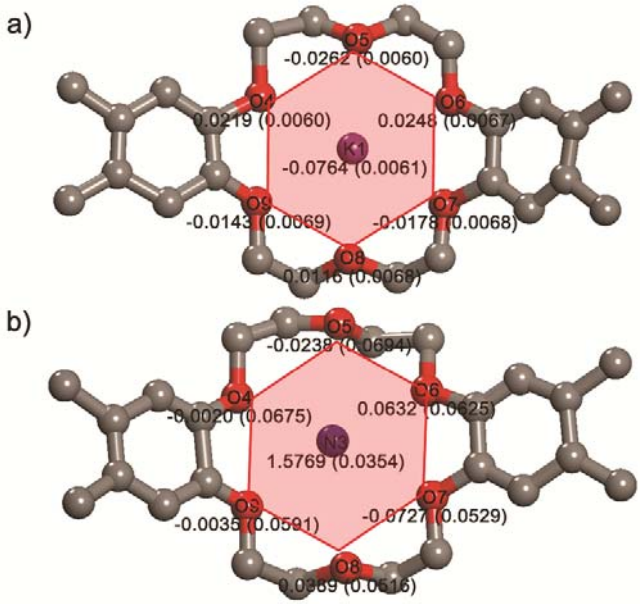

Figure 21. Distance of K^+ and NH_4^+ from the mean plane (O4, O5, O6, O7, O8, and O9) of the 18-crown-6 ether in a) $K^+\subset$SNU-200 SCN^-, and b) $NH_4^+\subset$SNU-200·Cl^-.

In $MV^{2+}\subset$SNU-200·2Cl^-, SNU-200 also maintained single crystallinity during the immersion in a DMF solution of highly concentrated methyl viologen (ca. 0.01 M). However, even with the synchrotron X-ray diffraction data collected at 100 K, the included methyl viologen species could not be located because of the thermal disorder. Therefore, the ‘‘locate simulations’’ was performed by using a sorption module of Materials Studio. The Metropolis Monte Carlo method was chosen for the calculation of the global minimum locations. Universal force field (UFF) was selected for the energy calculation, and the charge equilibration (QEq) method was used for the calculation of point atomic charges. The results indicate that SNU-200 can accommodate a maximum of 4 methyl viologen molecules per unit cell (1 molecule per formula unit of SNU-200). MV^{2+} resides beside the 18-crown-6 moiety and is stabilized by van der Waals forces and electrostatic interactions (Figure 22).

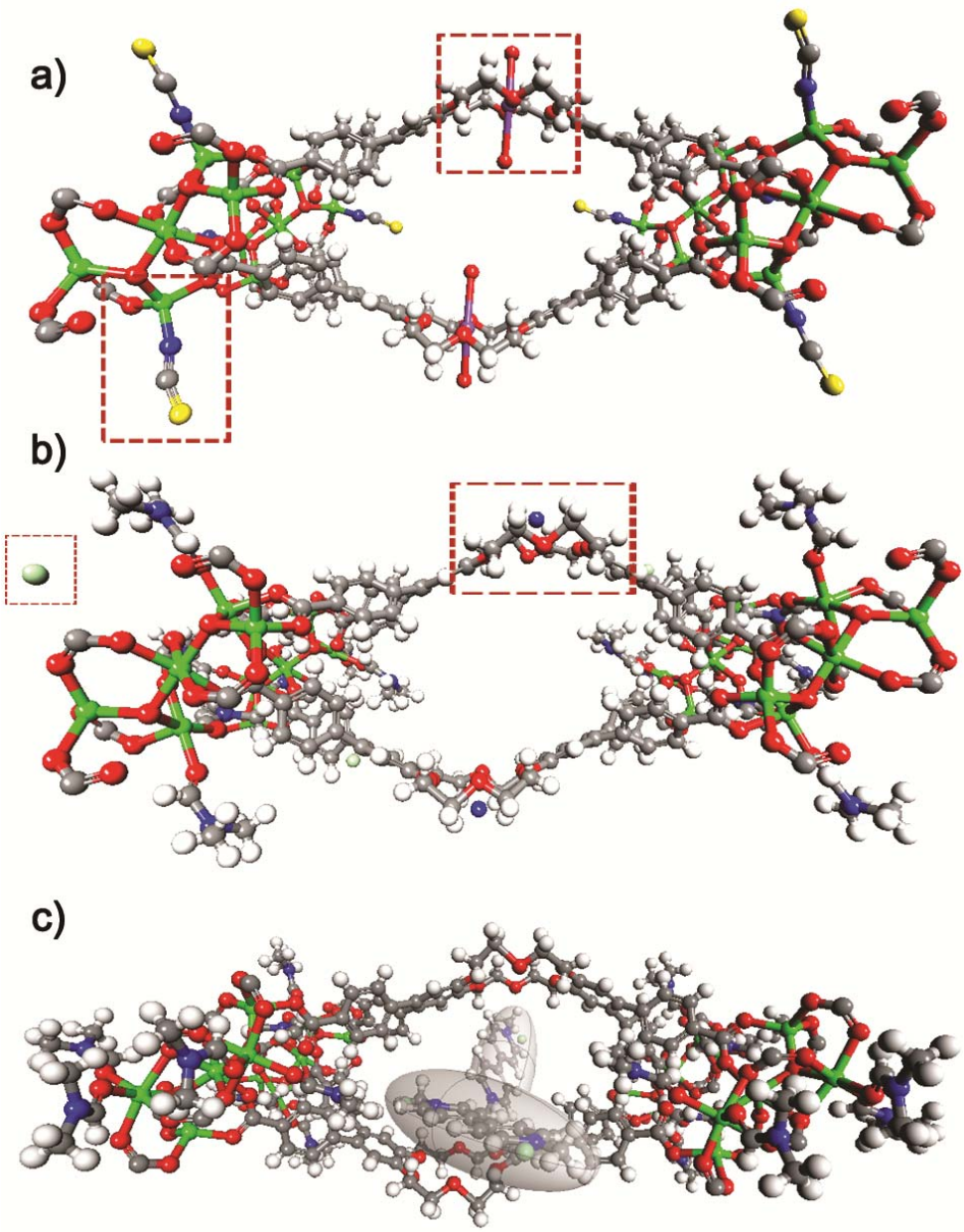

Figure 22. X-ray single crystal structures of a) $K^+ \subset$SNU-200·SCN^- and b) $NH_4^+ \subset$ SNU-200·Cl^-. c) "located simulation" structure of $MV^{2+} \subset$SNU-200·$2Cl^-$ matched to PXRD data. The atoms of Zn, C, H, O, N, Cl and S are shown by green, black, white, red, blue, pale green and yellow spheres, respectively.

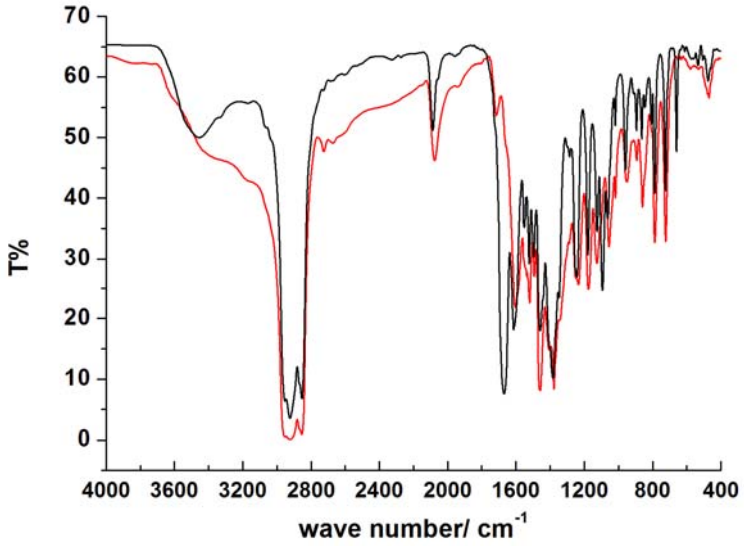

Figure 23. Infrared spectra (Nujol mull) of $K^{+}\subset$SNU-200 SCN^{-} before (black) and after (red) the removal of guest solvent.

Thermogravimetric analysis (TGA) data of **SNU-200** reveal 41.0% weight loss at 25 ^{o}C ~ 300 ^{o}C, which corresponds to the loss of all coordinated DMF and guest solvent molecules (calcd. 41.75 % for 13DMF and $12H_2O$), and no chemical decomposition occurs up to 350 ^{o}C (Figure 24).

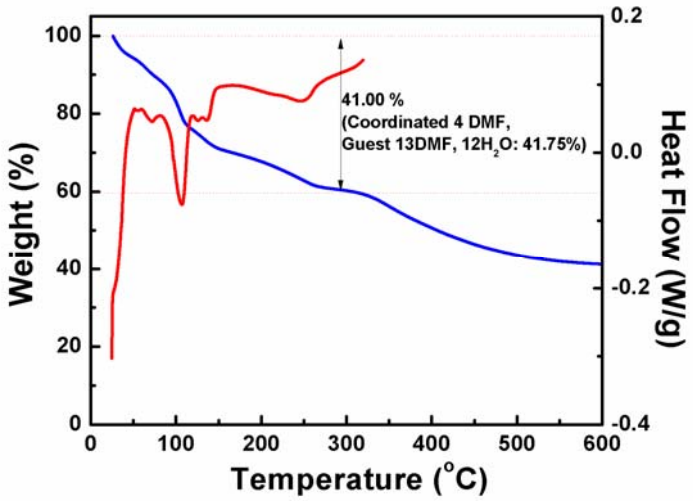

Figure 24. TGA/DSC traces of SNU-200.

The powder X-ray diffraction analysis

The powder X-ray diffraction (PXRD) patterns also indicate that the structure of SNU-200 is maintained even after the cation binding and the counter anion inclusion from KSCN, NH_4Cl, methyl viologen dichloride and $EuCl_3$ inside or near the crown ether moiety. (Figure 25). After activation of the compounds, the PXRD patterns of SNU-200 and $MV^{2+}\subset$SNU- 200·$2Cl^-$ are slightly broadened together with the shift of the peaks to higher angle region (Figure 26). However, the PXRD patterns of K^+ and NH_4^+ bound MOFs show their better crystalline properties than the activated SNU-200, and $MV^{2+}\subset$SNU- 200·$2Cl^-$ indicating that cation binding in 18C6 prevents shrinkage of the framework. The PXRD pattern for the simulated structure of MV^{2+} loaded SNU-200 is coincident with the measured data of $MV^{2+}\subset$SNU-200·$2Cl^-$. The new peaks at the low angle regions must correspond to the MV^{2+} guest molecules (Figure 26). All compounds were observed to be air sensitive.

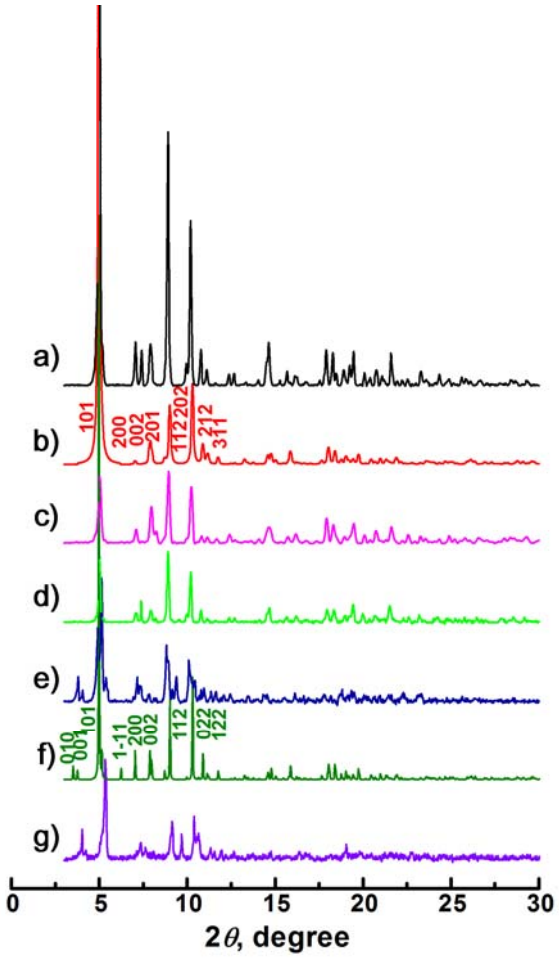

Figure 25. Powder X-ray diffraction patterns of as-synthesized samples. a) SNU-200. b) Simulated pattern of SNU-200 based on the X-ray single crystal data. c) $K^+ \subset$SNU-200·SCN^-. d) $NH_4^+ \subset$SNU-200·Cl^-. e) $MV^{2+} \subset$SNU-200·$2Cl^-$. f) Theoretically simulated pattern for $MV^{2+} \subset$SNU-200·$2Cl^-$. g) $Eu^{3+} \subset$SNU-200·$3Cl^-$.

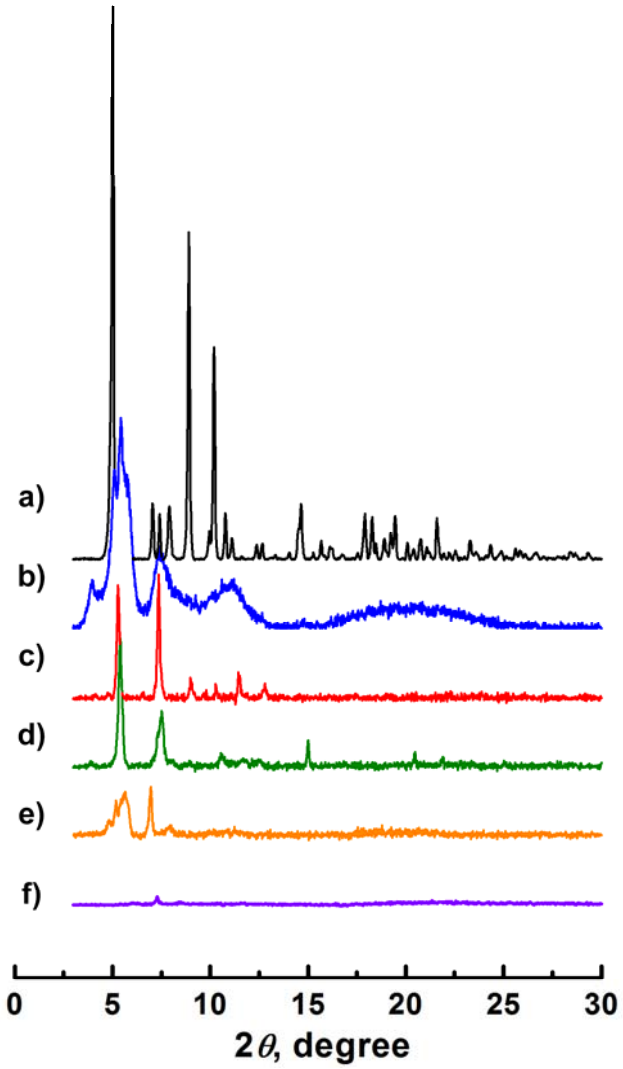

Figure 26. Powder X-ray diffraction patterns for the activated samples with supercritical CO_2 fluid. a) As-synthesized SNU-200, b) activated SNU-200, c) activated $K^+ \subset$SNU-200·SCN^-, d) activated $NH_4^+ \subset$SNU-200·Cl^-, and e) activated $MV^{2+} \subset$SNU-200·$2Cl^-$. f) activated SNU-200 after exposure to air for 2h.

Gas sorption analysis

To verify the porosity of the activated samples of SNU-200, $K^+\subset$SNU-200·SCN^-, $NH_4^+\subset$SNU-200·Cl^-, $MV^{2+}\subset$SNU-200·2Cl-, and $Eu^{3+}\subset$SNU-200·3Cl- the adsorption-desorption isotherms were measured for N_2, H_2, CO_2, and CH_4 gases at various temperatures (Table 4 and Table 5). The N_2 gas sorption isotherms of all samples show a type I curve, characteristic of the microporous materials (Figure 27). The BET surface areas of the compounds including the cations are slightly higher than that of SNU-200. Despite the inclusion of cations in the framework, the surface area does not decrease since the cations are included inside of the crown ether moieties.

Table 4. H_2 sorption properties of SNU-200' and cation ⊂SNU-200'

Compound	Cation/ Ligand ratio	SA_{BET} / m^2g^{-1}	H_2 uptake / wt%	Q_{st} of H_2/ $kJmol^{-1}$
SNU-200'	N/A	736.4	1.06(77 K)[d] 0.72(87 K)[d] 0.26 (298 K)[e]	7.70
$K^+\subset$SNU-200'·SCN^-	0.92[a](1.00)[c]	822.6	1.19(77 K)[d] 0.78(87 K)[d] 0.28 (298 K)[e]	9.92
$NH_4^+\subset$SNU-200'·Cl^-	1.09[b](1.00)[c]	818.2	1.09(77 K)[d] 0.71(87 K)[d]	6.41
$MV^{2+}\subset$SNU-200'·2Cl^-	0.36[b](0.50)[c]	934.9	0.86(77 K)[d] 0.54 (87 K)[d]	7.62
$Eu^{3+}\subset$SNU-200'·3Cl^-	0.51[a]		0.75(77 K)[d] 0.51 (87 K)[d]	7.98

[a]based on the ICP data (found). [b]based on the elemental analysis (found) data.
[c]theoretical calculation value (mol $_{cation}$/mol $_{ligand}$). [d]1 atm. [e]70 bar.

Table 5. CO_2 and CH_4 sorption properties of SNU-200', $K^+\subset$SNU-200'·SCN^-, $NH_4^+\subset$SNU-200'·Cl^-, $MV^{2+}\subset$SNU-200'·$2Cl^-$ and $Eu^{3+}\subset$SNU-200'·$3Cl^-$

Compound	Temp (K)	CO_2 uptake ($mmolg^{-1}$)	Q_{st} of CO_2 ($kJmol^{-1}$)	CH_4 uptake ($mmolg^{-1}$)	Q_{st} of CH_4 ($kJmol^{-1}$)
SNU-200'	195	8.41	29.9-25.7	3.40	36.9 - 19.3
	273	2.70		0.84	
	298	1.52		0.51	
$K^+\subset$SNU-200'·SCN^-	195	9.67	23.0-25.1	4.18	19.9 - 17.9
	273	2.93		0.74	
	298	1.54		0.43	
$NH_4^+\subset$SNU-200'·Cl^-	195	8.93	23.0-24.6	4.02	21.4 - 18.4
	273	2.53		0.68	
	298	1.43		0.41	
$MV^{2+}\subset$SNU-200'·$2Cl^-$	195	11.0	27.4-25.6	2.75	34.9 -19.3
	273	2.00		0.55	
	298	1.12		0.31	
$Eu^{3+}\subset$SNU-200'·$3Cl^-$	273	1.68	-	0.44	-
	298	0.95		0.25	

At low pressure H_2 adsorption isotherms, which were measured at 77 K and 87 K under 1 atm (Figure 27), SNU-200' uptakes H_2 of 1.06 wt% (77 K) and 0.72 wt% (87 K) with a improved isosteric heat (Q_{st}) of 7.70 $kJmol^{-1}$ compared to common Zn-MOFs (4.1 - 6.2 kJmol-1).[114-117] Interestingly, $K^+\subset$SNU-200'·SCN^- has the highest H_2 uptake capacity of 1.19 wt% (77 K) and 0.78 wt% (87 K) among the compounds, although its surface area is smaller than that of $MV^{2+}\subset$SNU-200'·$2Cl^-$. The zero-coverage isosteric heats of the H_2 adsorption, which are estimated from the isotherms at 77 K and 87 K by using the virial equation, increase from 7.70 $kJmol^{-1}$ for SNU-200' to 9.92 kJ mol^{-1} for $K^+\subset$SNU-200'·SCN^- (Table 4, Figure 28). This enhancement (2.22 kJ mol^{-1}) by the inclusion of the K^+ ion in the present MOF is

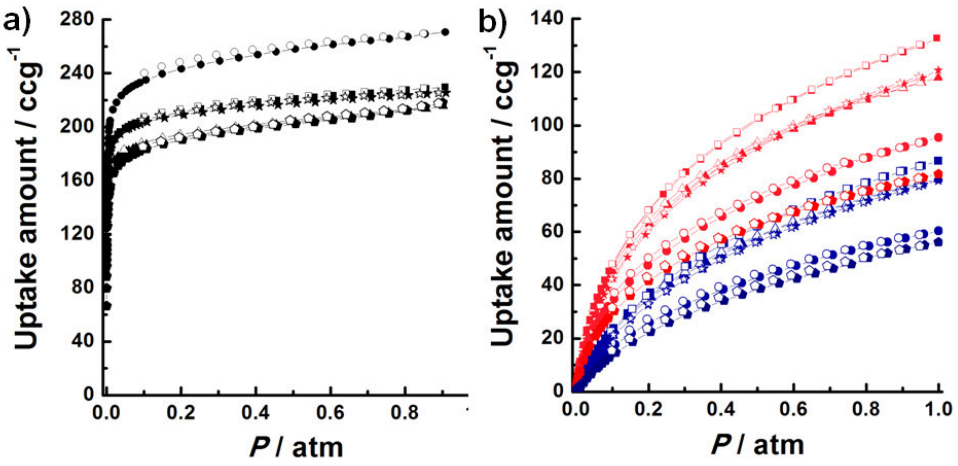

Figure 27. N_2 and H_2 gas sorption isotherms of SNU-200'(triangle), $K^+\subset$SNU-200·SCN^-(square), $NH_4^+\subset$SNU-200·Cl^-(diamond), $MV^{2+}\subset$SNU-200·$2Cl^-$(circle) and $Eu^{3+}\subset$SNU-200·$3Cl^-$(pentagon). a) N_2 at 77 K. b) H_2 at 77 K (red) and 87 K (blue). Filled shape: adsorption; open shape: desorption.

much higher than that (ca. 1.1 kJ mol^{-1}) reported previously for the MOF including alkali metal or alkali earth metal ions, which still coordinated solvent molecules.[118] The enhancement of the H_2 adsorption energy in the present $K^+\subset$SNU-200'·SCN^- is attributed to the K^+ cation containing empty coordination sites that are generated by the removal of coordinated water molecules on activation of the sample.

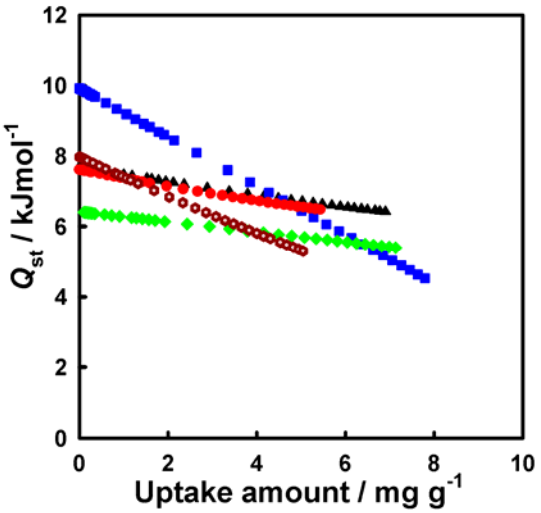

Figure 28. Isosteric heat of the H_2 adsorption in SNU-200' (black, triangle), $K^+ \subset$SNU-200·SCN^- (blue, square), $NH_4^+ \subset$SNU-200·Cl^- (green, diamond), $MV^{2+} \subset$SNU-200·$2Cl^-$ (red, circle) and $Eu^{3+} \subset$SNU-200·$3Cl^-$ (brown, hexagon dotted).

To determine the interaction energy between the adsorbed H_2 molecules and $K^+ \subset$SNU-200'·SCN^-, a location simulation was performed by using a sorption module of Materials Studio. The results indicate that at low coverage of H_2, the H_2 molecule is located beside the K^+ ion in the crown ether moiety with the highest electrostatic interaction energy (61.904 kcal mol^{-1}) (Figure 29). At high pressure and 298 K, H_2 adsorption amount of $K^+ \subset$SNU-200'·SCN^- is slightly higher than SNU-200' (0.28 wt% for $K^+ \subset$SNU-200'·SCN and 0.26 wt%). (Figure 30)

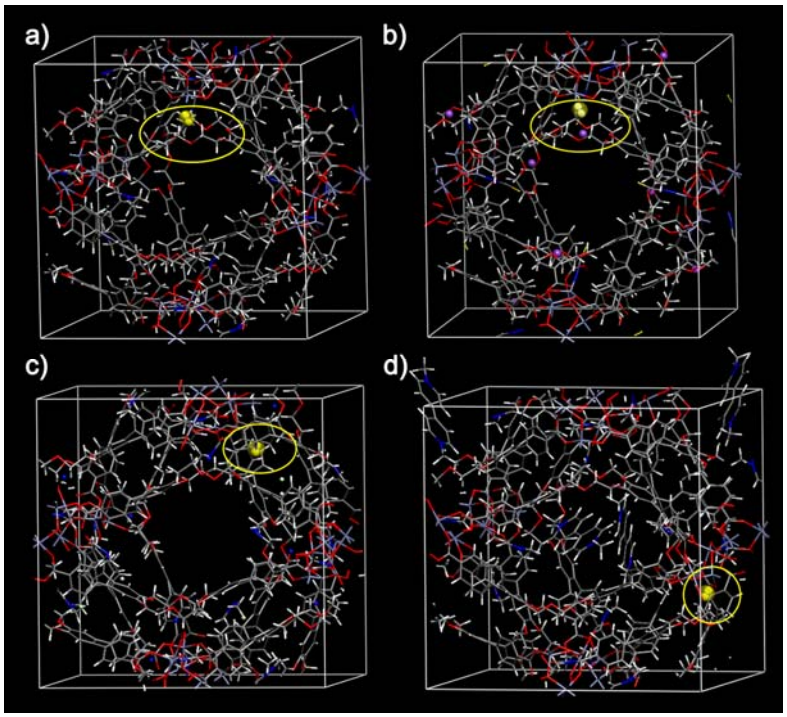

Figure 29. Positions of hydrogen molecules in a) SNU-200, b) $K^+ \subset$SNU-200·SCN^-, c) $NH_4^+ \subset$SNU-200·Cl^-, and d) $MV^{2+} \subset$SNU-200·$2Cl^-$ determined by locate simulations at low coverage. The calculated interaction energies of hydrogen molecules with the frameworks are as follows.

SNU-200' [kcal /mol]	$K^+ \subset$SNU-200'·SCN^- [kcal /mol]	$NH_4^+ \subset$SNU-200'·Cl^- [kcal /mol]	$MV^{2+} \subset$SNU-200'·$2Cl^-$ [kcal /mol]
Non-bond energy: -14.632	Non-bond energy: -58.474	Non-bond energy: -32.0705	Non-bond energy: -34.600
Hydrogen bond: 0.000	Hydrogen bond: 0.000	Hydrogen bond: 0.000	Hydrogen bond: 0.000
van der Waals: -3.593	van der Waals: 3.4296	van der Waals: -1.316	van der Waals: 14.848
Electrostatic: -11.039	Electrostatic: -61.904	Electrostatic: -30.759	Electrostatic: -49.448

Metropolis Monte Carlo method was used for the calculation of the global minimum location. Universal force field (UFF) was chosen for energy calculation. The charge equilibration (Q_{Eq}) method was used for the calculation of atomic point charge.

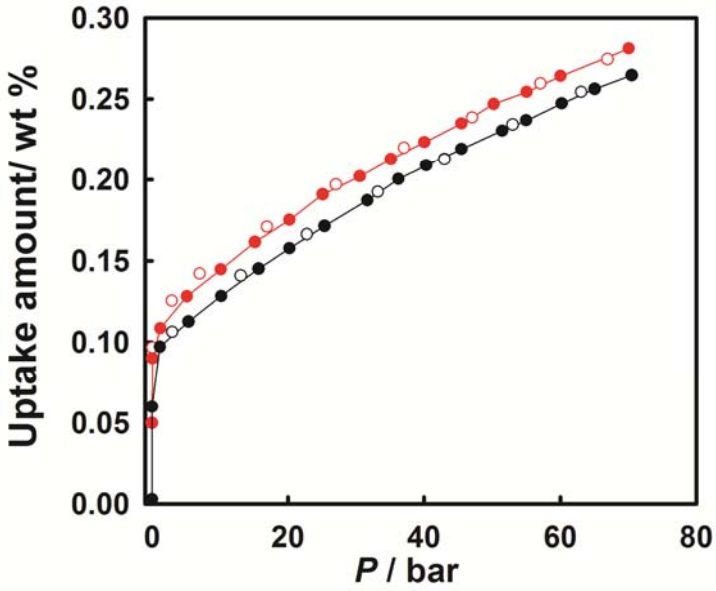

Figure 30. H_2 gas sorption isotherms at high pressure and 298 K for SNU-200' (black) and $K^+\subset$SNU-200'·SCN (red). Filled shape: adsorption; open shape: desorption.

Contrary to the H_2 adsorption isotherms, the CO_2 adsorption isotherms measure at 195 K under 1 atm indicate that the uptake capacities of various samples depend on their surface areas and increase in the order of SNU-200' < $NH_4^+\subset$SNU-200'·Cl^-, < $K^+\subset$SNU-200'·SCN^- < $MV^{2+}\subset$SNU-200·$2Cl^-$ (Table 5) However, at 298 K, pristine SNU-200 adsorbs comparable amount of CO_2 to that of $MV^{2+}\subset$SNU-200'·$2Cl^-$, even though SNU-200 has ca. 200 m^2g^{-1} smaller surface area (Table 4 and Table 5). In addition, pristine SNU-200 shows has the highest heats of the CO_2 adsorption (29.9 kJ mol^{-1}) and the CH_4 adsorption (36.9 kJ mol^{-1}) among all samples, indicating that the cation bound samples are less effective for CO_2 and CH_4 uptakes (Figure 31 and Figure 32). The selectivities of CO_2/N_2 and CO_2/CH_4 adsorption were calculated by the Ideal adsorbed solution theory (IAST).[111] The results indicate that

$K^+ \subset$SNU-200·SCN^- has the highest selectivity (22.59) for CO_2 adsorption over N_2 and $MV^{2+} \subset$SNU-200·$2Cl^-$ has the highest selectivity (4.94) for CO_2 adsorption over CH_4 among all samples (Figure 33 and Figure 34).

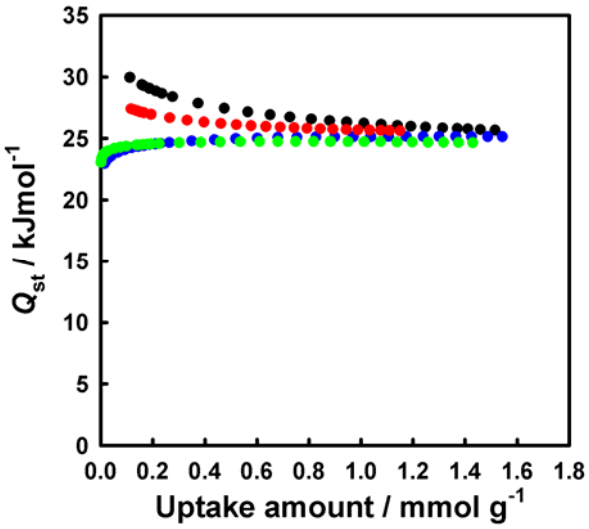

Figure 31. Isosteric heat of the CO_2 adsorption in SNU-200' (black), $K^+ \subset$SNU-200'·SCN^- (blue), $NH_4^+ \subset$SNU-200'·Cl^- (green), and $MV^{2+} \subset$SNU-200'·$2Cl^-$ (red).

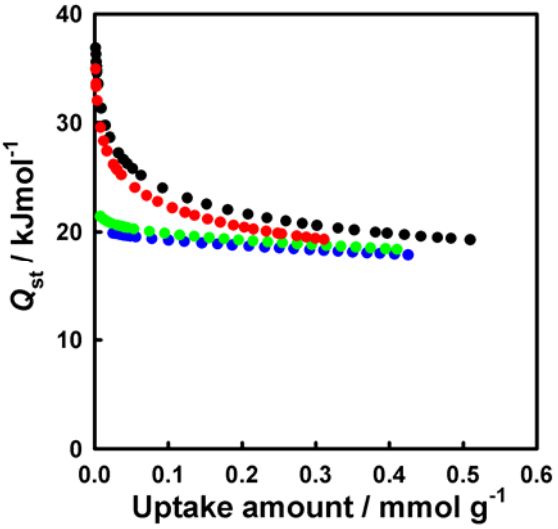

Figure 32. Isosteric heat of the CH_4 adsorption in SNU-200' (black), $K^+ \subset$SNU-200'·SCN^- (blue), $NH_4^+ \subset$SNU-200'·Cl^- (green), and $MV^{2+} \subset$SNU-200'·$2Cl^-$ (red).

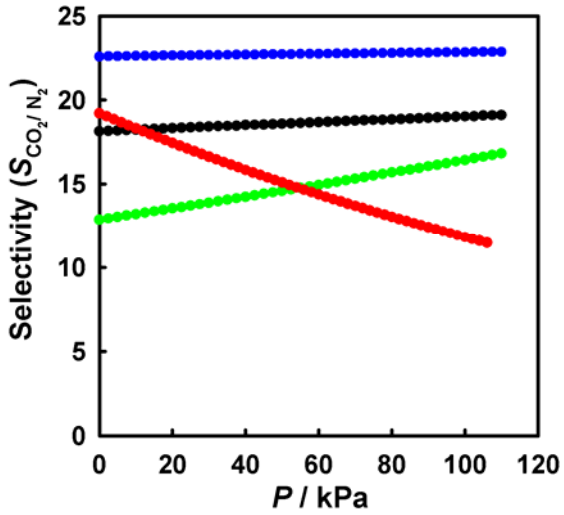

Figure 33. Selectivity of CO_2 adsorption over N_2 calculated by IAST method for SNU-200' (black), K^+⊂SNU-200'·SCN^- (blue), NH_4^+⊂SNU-200'·Cl^- (green), and MV^{2+}⊂SNU-200'·$2Cl^-$ (red).

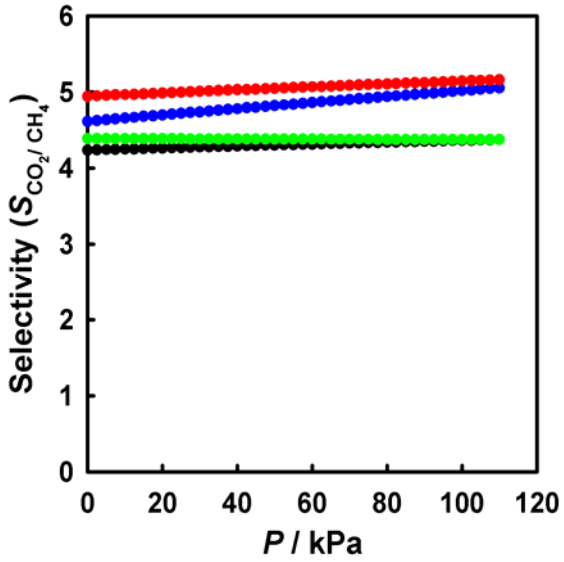

Figure 34. Selectivity of CO_2 adsorption over CH_4 calculated by IAST method for SNU-200' (black), K^+⊂SNU-200'·SCN^- (blue), NH_4^+⊂SNU-200'·Cl^- (green), and MV^{2+}⊂SNU-200'·$2Cl^-$ (red).

I.4. Conclusions

We prepared a MOF incorporating 18C6 crown ether moiety in the framework (SNU-200), which provides specific binding sites for K^+, NH_4^+, and MV^{2+} cations. Although there have been several reports only for the synthesis of rotaxane type MOFs containing crown ether moieties that are incapable of binding any guests, upon binding of the cations, SNU-200 underwent single-crystal to single-crystal transformations, and the X-ray structures of the cation bound MOFs could be determined. Interestingly, the results demonstrate how the gas (N_2, H_2, CO_2, and CH_4) adsorption properties of the MOFs are affected by the 18C6 incorporated in the framework and the bound cations, which provide electrostatic field interactions with the adsorbate gas molecules. The surface areas of the cation bound SNU-200 do not decrease compared to that of pristine SNU-200, since the cations are bound inside the 18C6. Compared with the general Zn type MOFs, pristine SNU-200 has a higher isosteric heat of the H_2 adsorption. Furthermore, the K^+ ion bound MOF exhibits the highest Q_{st} value of H_2 adsorption (9.92 kJ mol^{-1}) among the samples in this work. It also shows the highest CO_2/ N_2 adsorption selectivity (IAST), despite that the fact that pristine SNU-200 has the highest heat of the CO_2 and CH_4 adsorption. The present result demonstrates a new strategy to develop MOFs that have great potential for energy and environmental applications.

Supporting Information

Table I.S1. Crystallographic Data for as synthesized samples of SNU-200, $K^+ \subset$SNU-200·SCN^-, and $NH_4^+ \subset$SNU-200·Cl^- (Squeezed).

	SNU-200	$K^+ \subset$SNU-200·SCN^-	$NH_4^+ \subset$SNU-200·Cl^-
Formula	$C_{108}H_{102}N_4O_{34}Zn_5$	$C_{98}H_{74}K_2N_2O_{34}S_2Zn_5$	$C_{108}H_{110}Cl_2N_6O_{34}Zn_5$
crystal system	Tetragonal	Tetragonal	Tetragonal
space group	$P\bar{4}21c$	$P\bar{4}21c$	$P\bar{4}21c$
fw	2326.79	2292.76	2433.77
a [Å]	25.107(4)	25.556(4)	25.122(4)
c[Å]	23.531(5)	22.751(5)	23.412(5)
V [$Å^3$]	14833(4)	14859(4)	14776(4)
Z	4	4	4
ρ_{calcd} [g cm^{-3}]	1.042	1.025	1.094
T [K]	100	100	100
λ [Å]	0.800	0.69999	0.70000
μ [mm^{-1}]	0.857	0.936	0.898
goodness-of-fit (F^2)	1.054	0.830	0.996
F(000)	4800	4672	5024
reflections collected	101231	19985	77017
independent reflections	14532[*R*(int)=0.0590]	11120[*R*(int)= 0.0472]	11786[R(int)= 0.0628]
completeness to θ, %	99.6	84.3	78.0
data/parameters/restraints	14532 / 0 / 681	11120 / 6 / 627	11786 / 19 / 652
θ range for data collection, deg	2.04 to 29.59	1.57 to 29.43	1.60 to 26.30

diffraction limits (*h*, *k*, *l*)	-30≤*h*≤30, -30≤*k*≤30, -28≤*l*≤28	-35≤h≤35, -22≤k≤19, -30≤l≤30	-31≤h≤28, -28≤k≤28, -28≤l≤28
refinement method	Full-matrix least-squares on F^2	Full-matrix least-squares on F^2	Full-matrix least-squares on F^2
R_1[a], wR_2[b] [I>2σ(I)]	R_1 = 0.0634, wR_2 = 0.1921	R_1 = 0.0740, wR_2 = 0.1961	R_1 = 0.0966, wR_2 = 0.2583
R_1[a], wR_2[b] (all data)	R_1 = 0.0703, wR_2 = 0.1982	R_1 = 0.1606, wR_2 = 0.2170	R_1 = 0.1204, wR_2 = 0.2724
largest diff. peak, hole [e·Å^{-3}]	1.100, -0.766	0.497, -0.329	0.771 and -0.559

$R = \Sigma||Fo| - |Fc||/\Sigma|Fo|$. [b] $wR(F^2) = [\Sigma w(Fo^2 - Fc^2)^2/\Sigma w(Fo^2)^2]^{½}$ where $w = 1/[\sigma^2(Fo^2) + (0.1536P)^2 + (0.00)P]$, $P = (Fo^2 + 2Fc^2)/3$ for SNU-200, [b] $wR(F^2) = [\Sigma w(Fo^2 - Fc^2)^2/\Sigma w(Fo^2)^2]^{½}$ where $w = 1/[\sigma^2(Fo^2) + (0.1343P)^2 + (0.00)P]$, $P = (Fo^2 + 2Fc^2)/3$ for $K^+\subset$SNU-200·SCN^- [b] $wR(F^2) = [\Sigma w(Fo^2 - Fc^2)^2/\Sigma w(Fo^2)^2]^{½}$ where $w = 1/[\sigma^2(Fo^2) + (0.2000P)^2 + (0.00)P]$, $P = (Fo^2 + 2Fc^2)/3$ for $NH_4^+\subset$SNU-200·Cl^-.

Table I.S2. bond lengths (Å) and angles (°) for SNU-200.

C(5)-C(4)	1.340(8)	C(54)-N(2)	1.377(14)
C(5)-C(6)	1.390(8)	O(2)-C(1)	1.260(7)
C(5)-C(8)	1.522(8)	O(2)-Zn(2)	1.965(4)
C(22)-C(21)	1.386(14)	O(3)-C(1)	1.265(6)
C(22)-O(5)	1.74(2)	O(12)-Zn(1)	2.076(3)
C(23)-O(5)	1.392(14)	O(13)-Zn(3)	2.218(3)
C(23)-C(24)	1.524(15)	O(13)-Zn(1)#4	2.273(3)
C(24)-O(6)	1.478(13)	O(14)-Zn(2)	1.935(4)
C(25)-O(7)	1.412(8)	O(15)-Zn(3)	2.122(4)
C(25)-C(26)	1.502(8)	O(16)-Zn(1)	2.064(4)
C(41)-O(12)	1.257(5)	O(17)-Zn(1)	2.034(3)
C(41)-O(13)	1.266(5)	C(1)-C(2)	1.517(8)
C(41)-C(38)#1	1.488(6)	C(2)-C(7)	1.324(9)
C(42)-C(47)	1.371(8)	C(2)-C(3)	1.371(8)
C(42)-C(43)	1.448(9)	C(3)-C(4)	1.429(8)
C(42)-C(32)	1.482(8)	C(6)-C(7)	1.376(8)
C(43)-C(44)	1.374(9)	C(8)-C(13)	1.346(8)
C(44)-C(45)	1.361(9)	C(8)-C(9)	1.388(7)
C(45)-C(46)	1.372(9)	C(9)-C(10)	1.376(8)
C(45)-C(48)#2	1.519(8)	C(10)-O(4)	1.340(7)
C(46)-C(47)	1.379(9)	C(10)-C(11)	1.419(8)
C(48)-O(15)	1.215(6)	C(11)-O(9)	1.355(6)
C(48)-O(14)	1.282(6)	C(11)-C(12)	1.382(8)
C(48)-C(45)#3	1.519(8)	C(12)-C(13)	1.438(8)
C(49)-O(16)	1.123(9)	C(13)-C(14)	1.485(7)
C(49)-N(1)	1.374(14)	C(14)-C(19)	1.373(9)
C(50)-N(1)	1.537(19)	C(14)-C(15)	1.382(9)
C(51)-N(1)	1.35(2)	C(15)-C(16)	1.359(8)
C(52)-O(17)	1.232(6)	C(16)-C(17)	1.413(9)
C(52)-N(2)	1.312(8)	C(17)-C(18)	1.380(8)
C(53)-N(2)	1.456(10)	C(17)-C(20)#5	1.504(7)

C(18)-C(19)	1.373(8)	C(35)-C(40)	1.379(8)
C(20)-O(10)	1.241(8)	C(35)-C(36)	1.415(9)
C(20)-O(11)	1.258(7)	C(36)-C(37)	1.374(9)
C(20)-C(17)#6	1.504(7)	C(37)-C(38)	1.387(8)
C(21)-O(4)	1.416(10)	C(38)-C(39)	1.354(7)
C(26)-O(8)	1.435(7)	C(38)-C(41)#7	1.488(6)
C(27)-O(8)	1.377(7)	C(39)-C(40)	1.393(7)
C(27)-C(28)	1.507(9)	O(1)-Zn(2)	1.941(3)
C(28)-O(9)	1.495(8)	O(1)-Zn(3)	2.006(3)
C(29)-C(34)	1.362(7)	O(1)-Zn(1)	2.026(3)
C(29)-O(7)	1.363(7)	O(10)-Zn(2)	1.939(3)
C(29)-C(30)	1.388(8)	O(11)-Zn(1)	2.135(3)
C(30)-O(6)	1.360(6)	Zn(1)-O(13)#4	2.273(3)
C(30)-C(31)	1.435(10)	Zn(1)-Zn(3)	3.1566(8)
C(31)-C(32)	1.400(8)	Zn(3)-O(1)#4	2.006(3)
C(32)-C(33)	1.361(8)	Zn(3)-O(15)#4	2.122(4)
C(33)-C(34)	1.361(8)	Zn(3)-O(13)#4	2.218(3)
C(33)-C(35)	1.475(7)	Zn(3)-Zn(1)#4	3.1566(8)

C(4)-C(5)-C(6)	119.1(5)	C(48)-O(14)-Zn(2)	123.8(3)
C(4)-C(5)-C(8)	121.7(5)	C(48)-O(15)-Zn(3)	140.5(4)
C(6)-C(5)-C(8)	119.1(5)	C(49)-O(16)-Zn(1)	132.5(7)
C(21)-C(22)-O(5)	93.2(10)	C(52)-O(17)-Zn(1)	120.2(3)
O(5)-C(23)-C(24)	107.0(11)	C(51)-N(1)-C(49)	116.2(10)
O(6)-C(24)-C(23)	105.6(9)	C(51)-N(1)-C(50)	111.2(19)
O(7)-C(25)-C(26)	108.0(5)	C(49)-N(1)-C(50)	127.5(18)
O(12)-C(41)-O(13)	123.6(4)	C(52)-N(2)-C(54)	119.1(7)
O(12)-C(41)-C(38)#1	116.2(4)	C(52)-N(2)-C(53)	120.0(7)
O(13)-C(41)-C(38)#1	120.2(4)	C(54)-N(2)-C(53)	119.6(8)
C(47)-C(42)-C(43)	117.2(6)	O(2)-C(1)-O(3)	125.6(5)
C(47)-C(42)-C(32)	123.4(6)	O(2)-C(1)-C(2)	118.2(4)
C(43)-C(42)-C(32)	119.4(5)	O(3)-C(1)-C(2)	116.2(5)
C(44)-C(43)-C(42)	119.6(6)	C(7)-C(2)-C(3)	120.6(5)

C(45)-C(44)-C(43)	121.1(6)	C(7)-C(2)-C(1)	121.2(5)
C(44)-C(45)-C(46)	120.0(6)	C(3)-C(2)-C(1)	118.2(5)
C(44)-C(45)-C(48)#2	119.4(5)	C(2)-C(3)-C(4)	119.2(6)
C(46)-C(45)-C(48)#2	120.6(5)	C(5)-C(4)-C(3)	119.5(5)
C(45)-C(46)-C(47)	120.5(5)	C(7)-C(6)-C(5)	120.5(6)
C(42)-C(47)-C(46)	121.6(6)	C(2)-C(7)-C(6)	120.7(6)
O(15)-C(48)-O(14)	125.9(5)	C(13)-C(8)-C(9)	119.6(5)
O(15)-C(48)-C(45)#3	118.3(5)	C(13)-C(8)-C(5)	122.2(5)
O(14)-C(48)-C(45)#3	115.8(5)	C(9)-C(8)-C(5)	118.2(5)
O(16)-C(49)-N(1)	127.0(11)	C(10)-C(9)-C(8)	122.8(5)
O(17)-C(52)-N(2)	123.8(6)	O(4)-C(10)-C(9)	125.6(5)
C(1)-O(2)-Zn(2)	121.0(3)	O(4)-C(10)-C(11)	117.0(5)
C(23)-O(5)-C(22)	103.6(9)	C(9)-C(10)-C(11)	117.4(5)
C(41)-O(12)-Zn(1)	138.4(3)	O(9)-C(11)-C(12)	124.9(5)
C(41)-O(13)-Zn(3)	122.0(3)	O(9)-C(11)-C(10)	113.9(5)
C(41)-O(13)-Zn(1)#4	128.6(3)	C(12)-C(11)-C(10)	121.1(5)
Zn(3)-O(13)-Zn(1)#4	89.31(11)	C(11)-C(12)-C(13)	118.4(5)
C(8)-C(13)-C(12)	120.7(5)	C(32)-C(33)-C(35)	122.7(5)
C(8)-C(13)-C(14)	125.1(5)	C(34)-C(33)-C(35)	117.6(5)
C(12)-C(13)-C(14)	113.8(5)	C(33)-C(34)-C(29)	124.2(5)
C(19)-C(14)-C(15)	117.1(5)	C(40)-C(35)-C(36)	115.9(5)
C(19)-C(14)-C(13)	120.1(6)	C(40)-C(35)-C(33)	122.4(5)
C(15)-C(14)-C(13)	122.8(5)	C(36)-C(35)-C(33)	121.4(5)
C(16)-C(15)-C(14)	122.8(6)	C(37)-C(36)-C(35)	122.4(6)
C(15)-C(16)-C(17)	119.6(6)	C(36)-C(37)-C(38)	119.9(5)
C(18)-C(17)-C(16)	117.5(5)	C(39)-C(38)-C(37)	118.7(5)
C(18)-C(17)-C(20)#5	122.1(5)	C(39)-C(38)-C(41)#7	122.6(4)
C(16)-C(17)-C(20)#5	120.4(5)	C(37)-C(38)-C(41)#7	118.5(5)
C(19)-C(18)-C(17)	121.2(6)	C(38)-C(39)-C(40)	121.8(5)
C(14)-C(19)-C(18)	121.5(6)	C(35)-C(40)-C(39)	121.3(5)
O(10)-C(20)-O(11)	126.7(5)	Zn(2)-O(1)-Zn(3)	118.24(17)
O(10)-C(20)-C(17)#6	116.6(5)	Zn(2)-O(1)-Zn(1)	111.57(15)

O(11)-C(20)-C(17)#6	116.6(6)	Zn(3)-O(1)-Zn(1)	103.06(14)
C(22)-C(21)-O(4)	113.8(11)	C(10)-O(4)-C(21)	119.9(6)
O(8)-C(26)-C(25)	107.8(5)	C(30)-O(6)-C(24)	113.8(6)
O(8)-C(27)-C(28)	108.5(5)	C(29)-O(7)-C(25)	116.1(4)
O(9)-C(28)-C(27)	103.8(6)	C(27)-O(8)-C(26)	110.9(4)
C(34)-C(29)-O(7)	124.4(5)	C(11)-O(9)-C(28)	114.2(4)
C(34)-C(29)-C(30)	117.6(5)	C(20)-O(10)-Zn(2)	119.8(4)
O(7)-C(29)-C(30)	117.9(5)	C(20)-O(11)-Zn(1)	125.1(3)
O(6)-C(30)-C(29)	121.0(5)	O(1)-Zn(1)-O(17)	167.71(14)
O(6)-C(30)-C(31)	119.2(5)	O(1)-Zn(1)-O(16)	96.64(16)
C(29)-C(30)-C(31)	119.7(5)	O(17)-Zn(1)-O(16)	88.99(17)
C(32)-C(31)-C(30)	119.0(6)	O(1)-Zn(1)-O(12)	91.13(14)
C(33)-C(32)-C(31)	119.8(6)	O(17)-Zn(1)-O(12)	83.75(15)
C(33)-C(32)-C(42)	124.0(5)	O(16)-Zn(1)-O(12)	172.00(16)
C(31)-C(32)-C(42)	116.2(5)	O(1)-Zn(1)-O(11)	96.18(13)
C(32)-C(33)-C(34)	119.6(5)	O(17)-Zn(1)-O(11)	94.28(14)
O(16)-Zn(1)-O(11)	94.25(16)	O(15)#4-Zn(3)-O(15)	96.3(2)
O(12)-Zn(1)-O(11)	82.99(14)	O(1)-Zn(3)-O(13)	100.65(12)
O(1)-Zn(1)-O(13)#4	76.96(12)	O(1)#4-Zn(3)-O(13)	78.65(12)
O(17)-Zn(1)-O(13)#4	91.82(12)	O(15)#4-Zn(3)-O(13)	169.83(12)
O(16)-Zn(1)-O(13)#4	93.73(15)	O(15)-Zn(3)-O(13)	88.15(14)
O(12)-Zn(1)-O(13)#4	89.86(12)	O(1)-Zn(3)-O(13)#4	78.65(12)
O(11)-Zn(1)-O(13)#4	170.03(13)	O(1)#4-Zn(3)-O(13)#4	100.65(12)
O(1)-Zn(1)-Zn(3)	38.24(9)	O(15)#4-Zn(3)-O(13)#4	88.15(14)
O(17)-Zn(1)-Zn(3)	129.49(11)	O(15)-Zn(3)-O(13)#4	169.83(12)
O(16)-Zn(1)-Zn(3)	113.41(12)	O(13)-Zn(3)-O(13)#4	88.97(17)
O(12)-Zn(1)-Zn(3)	74.03(9)	O(1)-Zn(3)-Zn(1)#4	140.38(9)
O(11)-Zn(1)-Zn(3)	126.08(11)	O(1)#4-Zn(3)-Zn(1)#4	38.70(9)
O(13)#4-Zn(1)-Zn(3)	44.64(8)	O(15)#4-Zn(3)-Zn(1)#4	123.80(10)
O(14)-Zn(2)-O(10)	107.06(17)	O(15)-Zn(3)-Zn(1)#4	104.90(11)
O(14)-Zn(2)-O(1)	111.78(14)	O(13)-Zn(3)-Zn(1)#4	46.05(7)
O(10)-Zn(2)-O(1)	112.45(14)	O(13)#4-Zn(3)-Zn(1)#4	79.88(8)

O(14)-Zn(2)-O(2)	114.35(16)	O(1)-Zn(3)-Zn(1)	38.70(9)
O(10)-Zn(2)-O(2)	106.45(16)	O(1)#4-Zn(3)-Zn(1)	140.38(9)
O(1)-Zn(2)-O(2)	104.74(15)	O(15)#4-Zn(3)-Zn(1)	104.90(11)
O(1)-Zn(3)-O(1)#4	179.05(18)	O(15)-Zn(3)-Zn(1)	123.80(10)
O(1)-Zn(3)-O(15)#4	88.34(14)	O(13)-Zn(3)-Zn(1)	79.88(8)
O(1)#4-Zn(3)-O(15)#4	92.30(14)	O(13)#4-Zn(3)-Zn(1)	46.05(7)
O(1)-Zn(3)-O(15)	92.30(14)	Zn(1)#4-Zn(3)-Zn(1)	104.88(3)
O(1)#4-Zn(3)-O(15)	88.34(14)		

Symmetry transformations used to generate equivalent atoms:

#1 y+1/2, x+1/2, z+1/2 #2 x, y-1, z #3 x, y+1, z

#4 -x, -y+1, z #5 -y+1/2, -x+1/2, z-1/2

#6 -y+1/2, -x+1/2, z+1/2 #7 y-1/2, x-1/2, z-1/2

Table I.S3. bond lengths (Å) and angles (°) for K⊂SNU-200SCN⁻.

C(1)-O(2)	1.161(16)	C(48)-O(15)	1.331(7)
C(1)-O(3)	1.354(17)	C(48)-O(14)	1.338(8)
C(1)-C(2)	1.450(14)	C(48)-C(45)#2	1.365(9)
C(2)-C(7)	1.367(18)	C(49)-N(1)	1.36136(16)
C(2)-C(3)	1.486(19)	C(49)-S(1)	1.4497(2)
C(3)-C(4)	1.492(19)	O(1)-Zn(1)	1.941(7)
C(4)-C(5)	1.40(2)	O(1)-Zn(2)	1.951(6)
C(6)-C(5)	1.242(17)	O(1)-Zn(3)	2.027(7)
C(6)-C(7)	1.48(2)	O(2)-Zn(2)	1.920(10)
C(23)-O(8)	1.299(12)	O(12)-C(41)	1.267(12)
C(23)-C(24)	1.569(13)	O(12)-Zn(1)	1.966(9)
C(23)-K(1)	3.473(12)	O(13)-C(41)	1.217(12)
C(24)-O(7)	1.598(11)	O(13)-Zn(3)	2.079(8)
C(26)-O(5)	1.494(7)	O(14)-Zn(2)	1.934(6)
C(26)-C(25)	1.507(15)	O(15)-Zn(3)	2.166(7)
C(27)-C(28)	1.412(13)	OW1-K(1)	2.839(18)
C(27)-O(5)	1.454(11)	OW2-K(1)	2.827(19)
C(27)-K(1)	3.496(11)	K(1)-O(7)	2.663(8)
C(29)-O(6)	1.315(14)	K(1)-O(4)	2.727(7)
C(29)-C(30)	1.369(13)	K(1)-O(9)	2.752(9)
C(29)-C(34)	1.443(15)	K(1)-O(6)	2.770(9)
C(30)-C(31)	1.373(16)	K(1)-O(5)	2.782(9)
C(30)-O(7)	1.450(14)	K(1)-O(8)	2.785(9)
C(42)-C(43)	1.351(15)	K(1)-C(28)	3.531(13)
C(42)-C(47)	1.400(14)	C(5)-C(8)	1.51(2)
C(42)-C(32)	1.487(14)	C(8)-C(13)	1.315(17)
C(43)-C(44)	1.409(17)	C(8)-C(9)	1.324(19)
C(44)-C(45)	1.281(15)	C(9)-1(0)	1.340(18)
C(45)-C(46)	1.340(14)	C(11)-C(12)	1.298(17)
C(45)-C(48)#1	1.365(9)	C(11)-1(0)	1.418(17)
C(46)-C(47)	1.382(14)	C(11)-O(4)	1.511(16)

C(12)-C(13)	1.387(17)	C(32)-C(33)	1.369(13)
C(13)-C(14)	1.532(19)	C(33)-C(35)	1.418(13)
C(14)-C(19)	1.334(17)	C(33)-C(34)	1.481(14)
C(14)-C(15)	1.414(17)	C(35)-C(40)	1.383(13)
C(15)-C(16)	1.386(17)	C(35)-C(36)	1.415(13)
C(16)-C(17)	1.281(16)	C(36)-C(37)	1.439(14)
C(17)-C(18)	1.382(15)	C(37)-C(38)	1.433(13)
C(17)-C(20)#3	1.550(16)	C(38)-C(39)	1.381(14)
C(18)-C(19)	1.294(15)	C(38)-C(41)#5	1.510(15)
C(20)-O(11)	1.214(13)	C(39)-C(40)	1.402(13)
C(20)-O(10)	1.248(13)	C(41)-C(38)#6	1.510(15)
C(20)-C(17)#4	1.550(16)	1(0)-O(9)	1.424(14)
C(21)-O(9)	1.404(17)	N(1)-Zn(1)	1.8907(14)
C(21)-C(22)	1.535(18)	O(10)-Zn(1)	1.987(8)
C(22)-O(8)	1.456(13)	O(11)-Zn(2)	1.917(9)
C(25)-O(6)	1.427(15)	Zn(3)-O(1)#7	2.027(7)
C(28)-O(4)	1.337(13)	Zn(3)-O(13)#7	2.079(8)
C(31)-C(32)	1.384(13)	Zn(3)-O(15)#7	2.166(7)

O(2)-C(1)-O(3)	127.0(12)	C(46)-C(45)-C(48)#1	119.8(10)
O(2)-C(1)-C(2)	124.6(16)	C(45)-C(46)-C(47)	116.1(10)
O(3)-C(1)-C(2)	108.1(15)	C(46)-C(47)-C(42)	122.7(11)
C(7)-C(2)-C(1)	132.1(16)	O(15)-C(48)-O(14)	108.0(4)
C(7)-C(2)-C(3)	108.2(13)	O(15)-C(48)-C(45)#2	124.4(7)
C(1)-C(2)-C(3)	119.5(15)	O(14)-C(48)-C(45)#2	127.6(7)
C(2)-C(3)-C(4)	129.5(13)	N(1)-C(49)-S(1)	156.810(2)
C(5)-C(4)-C(3)	109.5(14)	Zn(1)-O(1)-Zn(2)	109.1(3)
C(5)-C(6)-C(7)	122.3(14)	Zn(1)-O(1)-Zn(3)	116.7(3)
C(2)-C(7)-C(6)	124.0(13)	Zn(2)-O(1)-Zn(3)	112.4(3)
O(8)-C(23)-C(24)	117.4(9)	C(1)-O(2)-Zn(2)	119.0(10)
O(8)-C(23)-K(1)	48.4(6)	C(41)-O(12)-Zn(1)	124.2(7)
C(24)-C(23)-K(1)	87.2(5)	C(41)-O(13)-Zn(3)	130.4(6)
C(23)-C(24)-O(7)	101.7(6)	C(48)-O(14)-Zn(2)	126.1(4)

O(5)-C(26)-C(25)	100.6(6)	C(48)-O(15)-Zn(3)	144.7(4)
C(28)-C(27)-O(5)	106.0(8)	O(7)-K(1)-O(4)	176.2(3)
C(28)-C(27)-K(1)	79.8(7)	O(7)-K(1)-O(9)	124.2(3)
O(5)-C(27)-K(1)	49.5(5)	O(4)-K(1)-O(9)	57.6(3)
O(6)-C(29)-C(30)	123.2(13)	O(7)-K(1)-O(6)	58.6(3)
O(6)-C(29)-C(34)	119.3(15)	O(4)-K(1)-O(6)	119.4(3)
C(30)-C(29)-C(34)	116.9(11)	O(9)-K(1)-O(6)	175.6(3)
C(29)-C(30)-C(31)	124.0(12)	O(7)-K(1)-O(5)	118.0(3)
C(29)-C(30)-O(7)	112.2(12)	O(4)-K(1)-O(5)	60.1(2)
C(31)-C(30)-O(7)	123.8(13)	O(9)-K(1)-O(5)	117.7(3)
C(43)-C(42)-C(47)	117.1(11)	O(6)-K(1)-O(5)	59.4(3)
C(43)-C(42)-C(32)	122.1(11)	O(7)-K(1)-O(8)	62.5(3)
C(47)-C(42)-C(32)	120.8(11)	O(4)-K(1)-O(8)	119.2(3)
C(42)-C(43)-C(44)	118.8(12)	O(9)-K(1)-O(8)	61.7(3)
C(45)-C(44)-C(43)	121.4(12)	O(6)-K(1)-O(8)	121.0(3)
C(44)-C(45)-C(46)	123.8(10)	O(5)-K(1)-O(8)	177.1(4)
C(44)-C(45)-C(48)#1	116.2(12)	O(7)-K(1)-OW2	86.7(7)
O(4)-K(1)-OW2	90.1(7)	O(9)-K(1)-C(28)	77.4(3)
O(9)-K(1)-OW2	86.7(6)	O(6)-K(1)-C(28)	99.7(3)
O(6)-K(1)-OW2	90.2(6)	O(5)-K(1)-C(28)	40.4(2)
O(5)-K(1)-OW2	93.3(6)	O(8)-K(1)-C(28)	139.0(3)
O(8)-K(1)-OW2	83.8(7)	OW2-K(1)-C(28)	92.4(7)
O(7)-K(1)-OW1	84.0(3)	OW1-K(1)-C(28)	103.0(4)
O(4)-K(1)-OW1	99.7(3)	C(23)-K(1)-C(28)	156.7(3)
O(9)-K(1)-OW1	83.5(3)	C(27)-K(1)-C(28)	23.2(2)
O(6)-K(1)-OW1	100.5(3)	C(6)-C(5)-C(4)	126.2(15)
O(5)-K(1)-OW1	107.2(3)	C(6)-C(5)-C(8)	113.9(18)
O(8)-K(1)-OW1	75.7(4)	C(4)-C(5)-C(8)	119.9(14)
OW2-K(1)-OW1	159.5(7)	C(13)-C(8)-C(9)	115.3(14)
O(7)-K(1)-C(23)	44.8(3)	C(13)-C(8)-C(5)	125.5(15)
O(4)-K(1)-C(23)	137.6(3)	C(9)-C(8)-C(5)	119.1(18)
O(9)-K(1)-C(23)	80.4(3)	C(8)-C(9)-1(0)	126.1(17)

O(6)-K(1)-C(23)	102.9(3)	C(12)-C(11)-1(0)	124.1(15)
O(5)-K(1)-C(23)	161.2(3)	C(12)-C(11)-O(4)	123.1(13)
O(8)-K(1)-C(23)	20.4(3)	1(0)-C(11)-O(4)	112.8(16)
OW2-K(1)-C(23)	93.0(7)	C(11)-C(12)-C(13)	114.8(13)
OW1-K(1)-C(23)	67.7(4)	C(8)-C(13)-C(12)	125.1(14)
O(7)-K(1)-C(27)	137.5(3)	C(8)-C(13)-C(14)	121.8(14)
O(4)-K(1)-C(27)	41.7(2)	C(12)-C(13)-C(14)	111.6(15)
O(9)-K(1)-C(27)	97.6(3)	C(19)-C(14)-C(15)	115.3(14)
O(6)-K(1)-C(27)	80.3(3)	C(19)-C(14)-C(13)	126.2(15)
O(5)-K(1)-C(27)	23.4(2)	C(15)-C(14)-C(13)	118.0(16)
O(8)-K(1)-C(27)	157.4(3)	C(16)-C(15)-C(14)	117.1(14)
OW2-K(1)-C(27)	104.9(7)	C(17)-C(16)-C(15)	126.0(14)
OW1-K(1)-C(27)	94.2(3)	C(16)-C(17)-C(18)	113.3(13)
C(23)-K(1)-C(27)	161.9(4)	C(16)-C(17)-C(20)#3	123.9(14)
O(7)-K(1)-C(28)	158.3(3)	C(18)-C(17)-C(20)#3	122.4(13)
O(4)-K(1)-C(28)	19.8(2)	C(19)-C(18)-C(17)	124.0(13)
C(18)-C(19)-C(14)	123.1(14)	C(9)-1(0)-C(11)	113.6(14)
O(11)-C(20)-O(10)	130.1(11)	C(9)-1(0)-O(9)	130.0(18)
O(11)-C(20)-C(17)#4	118.4(12)	C(11)-1(0)-O(9)	116.4(16)
O(10)-C(20)-C(17)#4	111.5(12)	C(49)-N(1)-Zn(1)	166.17(4)
O(9)-C(21)-C(22)	112.6(13)	C(28)-O(4)-C(11)	118.1(10)
O(8)-C(22)-C(21)	103.3(10)	C(28)-O(4)-K(1)	116.5(6)
O(6)-C(25)-C(26)	114.1(11)	C(11)-O(4)-K(1)	119.9(8)
O(4)-C(28)-C(27)	115.7(12)	C(27)-O(5)-C(26)	105.3(5)
O(4)-C(28)-K(1)	43.7(5)	C(27)-O(5)-K(1)	107.0(6)
C(27)-C(28)-K(1)	77.0(7)	C(26)-O(5)-K(1)	113.4(4)
C(30)-C(31)-C(32)	119.2(11)	C(29)-O(6)-C(25)	122.2(12)
C(33)-C(32)-C(31)	123.3(10)	C(29)-O(6)-K(1)	116.3(9)
C(33)-C(32)-C(42)	122.1(10)	C(25)-O(6)-K(1)	117.6(7)
C(31)-C(32)-C(42)	114.6(11)	C(30)-O(7)-C(24)	112.6(9)
C(32)-C(33)-C(35)	122.4(10)	C(30)-O(7)-K(1)	122.4(9)
C(32)-C(33)-C(34)	116.4(10)	C(24)-O(7)-K(1)	120.7(4)

C(35)-C(33)-C(34)	121.1(11)	C(23)-O(8)-C(22)	110.8(10)
C(29)-C(34)-C(33)	120.0(11)	C(23)-O(8)-K(1)	111.2(8)
C(40)-C(35)-C(36)	119.5(9)	C(22)-O(8)-K(1)	109.9(8)
C(40)-C(35)-C(33)	118.3(10)	C(21)-O(9)-1(0)	114.2(11)
C(36)-C(35)-C(33)	121.9(10)	C(21)-O(9)-K(1)	114.9(7)
C(35)-C(36)-C(37)	118.6(10)	1(0)-O(9)-K(1)	120.1(9)
C(38)-C(37)-C(36)	120.2(11)	C(20)-O(10)-Zn(1)	128.8(8)
C(39)-C(38)-C(37)	118.7(11)	C(20)-O(11)-Zn(2)	124.6(8)
C(39)-C(38)-C(41)#5	123.1(10)	N(1)-Zn(1)-O(1)	114.0(2)
C(37)-C(38)-C(41)#5	118.1(11)	N(1)-Zn(1)-O(12)	110.1(2)
C(38)-C(39)-C(40)	120.5(10)	O(1)-Zn(1)-O(12)	106.3(3)
C(35)-C(40)-C(39)	121.8(10)	N(1)-Zn(1)-O(10)	108.8(3)
O(13)-C(41)-O(12)	128.6(10)	O(1)-Zn(1)-O(10)	107.7(3)
O(13)-C(41)-C(38)#6	121.9(10)	O(12)-Zn(1)-O(10)	110.0(4)
O(12)-C(41)-C(38)#6	109.0(11)	O(11)-Zn(2)-O(2)	99.4(4)
O(11)-Zn(2)-O(14)	108.6(3)	O(13)#7-Zn(3)-O(13)	95.9(4)
O(2)-Zn(2)-O(14)	117.0(4)	O(1)#7-Zn(3)-O(15)#7	86.4(2)
O(11)-Zn(2)-O(1)	109.3(3)	O(1)-Zn(3)-O(15)#7	84.7(3)
O(2)-Zn(2)-O(1)	105.1(4)	O(13)#7-Zn(3)-O(15)#7	173.9(3)
O(14)-Zn(2)-O(1)	116.1(3)	O(13)-Zn(3)-O(15)#7	87.3(3)
O(1)#7-Zn(3)-O(1)	167.4(4)	O(1)#7-Zn(3)-O(15)	84.7(3)
O(1)#7-Zn(3)-O(13)#7	98.8(3)	O(1)-Zn(3)-O(15)	86.4(2)
O(1)-Zn(3)-O(13)#7	89.7(3)	O(13)#7-Zn(3)-O(15)	87.3(3)
O(1)#7-Zn(3)-O(13)	89.7(3)	O(13)-Zn(3)-O(15)	173.9(3)
O(1)-Zn(3)-O(13)	98.8(3)	O(15)#7-Zn(3)-O(15)	89.9(4)

Symmetry transformations used to generate equivalent atoms:

#1 x, y+1, z #2 x, y-1, z # 3 -y+1/2, -x+1 /2, z+1/2

#4 -y+1/2, -x+1/2, z-1/2 #5 -y+1/2, -x+3/2, z+1 /2

#6 -y+3/2, -x+1/2, z-1/2 #7 -x+1, -y, z

Table I.S4. bond lengths (Å) and angles (°) for NH_4^+⊂SNU-200SCN⁻.

C(1)-O(2)	1.24(10)	C(50)-N(1)	1.4100(2)
C(1)-O(3)	1.29(10)	C(51)-N(1)	1.5547(2)
C(1)-C(2)	1.49(10)	C(52)-O(17)	1.24(11)
C(2)-C(7)	1.26(12)	C(52)-N(2)	1.32(13)
C(2)-C(3)	1.39(15)	C(53)-N(2)	1.43(11)
C(7)-C(6)	1.44(13)	C(54)-N(2)	1.44(15)
C(21)-O(4)	1.37(6)	O(2)-Zn(2)	1.94(6)
C(21)-C(22)	1.6049(2)	O(4)-C(10)	1.38(11)
C(22)-O(5)	1.39(10)	O(6)-C(30)	1.33(10)
C(23)-O(5)	1.4(2)	O(7)-C(29)	1.27(10)
C(23)-C(24)	1.41(11)	O(9)-C(11)	1.44(11)
C(24)-O(6)	1.4(2)	O(10)-C(20)	1.27(10)
C(25)-O(7)	1.40(14)	O(10)-Zn(2)	1.91(5)
C(25)-C(26)	1.65(15)	O(11)-C(20)	1.22(10)
C(26)-O(8)	1.56(14)	O(11)-Zn(1)	2.10(5)
C(27)-O(8)	1.37(13)	O(12)-C(41)	1.25(8)
C(27)-C(28)	1.45(14)	O(12)-Zn(3)	2.19(5)
C(28)-O(9)	1.43(12)	O(12)-Zn(1)	2.31(5)
C(42)-C(43)	1.33(12)	O(13)-C(41)	1.24(8)
C(42)-C(47)	1.43(13)	O(13)-Zn(1)#3	2.09(6)
C(42)-C(32)	1.46(10)	O(14)-Zn(2)	1.93(7)
C(43)-C(44)	1.45(15)	O(15)-Zn(3)	2.11(6)
C(44)-C(45)	1.32(13)	O(16)-Zn(1)	2.023(9)
C(45)-C(46)	1.29(13)	O(17)-Zn(1)	2.06(6)
C(45)-C(48)#1	1.50(14)	C(3)-C(4)	1.40(13)
C(46)-C(47)	1.47(13)	C(4)-C(5)	1.26(13)
C(48)-O(14)	1.23(11)	C(5)-C(6)	1.33(18)
C(48)-O(15)	1.30(10)	C(5)-C(8)	1.50(13)
C(48)-C(45)#2	1.50(14)	C(8)-C(9)	1.35(12)
C(49)-O(16)	1.17923(16)	C(8)-C(13)	1.47(12)
C(49)-N(1)	1.4333(2)	C(9)-C(10)	1.31(13)

C(10)-C(11)	1.43(15)	C(33)-C(35)	1.46(12)
C(11)-C(12)	1.33(13)	C(35)-C(36)	1.28(12)
C(12)-C(13)	1.44(12)	C(35)-C(40)	1.33(13)
C(13)-C(14)	1.43(12)	C(36)-C(37)	1.43(14)
C(14)-C(19)	1.36(12)	C(37)-C(38)	1.43(13)
C(14)-C(15)	1.39(14)	C(38)-C(39)	1.36(11)
C(15)-C(16)	1.36(14)	C(38)-C(41)#6	1.48(10)
C(16)-C(17)	1.27(14)	C(39)-C(40)	1.46(14)
C(17)-C(18)	1.32(12)	C(41)-C(38)#7	1.48(10)
C(17)-C(20)#4	1.55(11)	O(1)-Zn(2)	1.92(6)
C(18)-C(19)	1.39(12)	O(1)-Zn(3)	2.00(5)
C(20)-C(17)#5	1.55(11)	O(1)-Zn(1)	2.04(5)
C(29)-C(30)	1.45(10)	Zn(1)-O(13)#3	2.09(6)
C(29)-C(34)	1.45(12)	Zn(1)-Zn(3)	3.155(11)
C(30)-C(31)	1.30(14)	Zn(3)-O(1)#3	2.00(5)
C(31)-C(32)	1.44(13)	Zn(3)-O(15)#3	2.11(6)
C(32)-C(33)	1.42(11)	Zn(3)-O(12)#3	2.19(5)
C(33)-C(34)	1.40(12)	Zn(3)-Zn(1)#3	3.155(11)

O(2)-C(1)-O(3)	125(7)	C(50)-N(1)-C(51)	121.672(12)
O(2)-C(1)-C(2)	122(7)	C(49)-N(1)-C(51)	119.263(7)
O(3)-C(1)-C(2)	113(8)	C(52)-N(2)-C(53)	116(8)
C(7)-C(2)-C(3)	115(9)	C(52)-N(2)-C(54)	130(10)
C(7)-C(2)-C(1)	127(8)	C(53)-N(2)-C(54)	113(9)
C(3)-C(2)-C(1)	118(8)	C(1)-O(2)-Zn(2)	122(5)
C(2)-C(7)-C(6)	124(10)	C(21)-O(4)-C(10)	115(7)
O(4)-C(21)-C(22)	98(3)	C(23)-O(5)-C(22)	108(10)
O(5)-C(22)-C(21)	96(6)	C(30)-O(6)-C(24)	120(10)
O(5)-C(23)-C(24)	122(10)	C(29)-O(7)-C(25)	114(7)
C(23)-C(24)-O(6)	116(10)	C(27)-O(8)-C(26)	105(9)
O(7)-C(25)-C(26)	103(10)	C(28)-O(9)-C(11)	115(6)
O(8)-C(26)-C(25)	98(9)	C(20)-O(10)-Zn(2)	121(6)
O(8)-C(27)-C(28)	106(10)	C(20)-O(11)-Zn(1)	128(5)

O(9)-C(28)-C(27)	107(8)	C(41)-O(12)-Zn(3)	124(5)
C(43)-C(42)-C(47)	123(8)	C(41)-O(12)-Zn(1)	129(5)
C(43)-C(42)-C(32)	121(9)	Zn(3)-O(12)-Zn(1)	89.1(18)
C(47)-C(42)-C(32)	116(8)	C(41)-O(13)-Zn(1)#3	140(5)
C(42)-C(43)-C(44)	118(9)	C(48)-O(14)-Zn(2)	126(6)
C(45)-C(44)-C(43)	123(9)	C(48)-O(15)-Zn(3)	139(6)
C(46)-C(45)-C(44)	119(9)	C(49)-O(16)-Zn(1)	140.3(2)
C(46)-C(45)-C(48)#1	120(9)	C(52)-O(17)-Zn(1)	118(6)
C(44)-C(45)-C(48)#1	121(8)	C(2)-C(3)-C(4)	119(10)
C(45)-C(46)-C(47)	125(10)	C(5)-C(4)-C(3)	125(10)
C(42)-C(47)-C(46)	113(9)	C(4)-C(5)-C(6)	116(10)
O(14)-C(48)-O(15)	124(10)	C(4)-C(5)-C(8)	123(9)
O(14)-C(48)-C(45)#2	119(8)	C(6)-C(5)-C(8)	120(10)
O(15)-C(48)-C(45)#2	117(9)	C(5)-C(6)-C(7)	119(10)
O(16)-C(49)-N(1)	127.072(5)	C(9)-C(8)-C(13)	118(8)
O(17)-C(52)-N(2)	122(10)	C(9)-C(8)-C(5)	123(8)
C(50)-N(1)-C(49)	108.833(2)	C(13)-C(8)-C(5)	119(8)
C(10)-C(9)-C(8)	125(9)	C(33)-C(32)-C(31)	113(8)
C(9)-C(10)-O(4)	128(10)	C(33)-C(32)-C(42)	123(7)
C(9)-C(10)-C(11)	118(9)	C(31)-C(32)-C(42)	123(8)
O(4)-C(10)-C(11)	115(9)	C(34)-C(33)-C(32)	121(8)
C(12)-C(11)-C(10)	123(8)	C(34)-C(33)-C(35)	118(7)
C(12)-C(11)-O(9)	122(8)	C(32)-C(33)-C(35)	121(8)
C(10)-C(11)-O(9)	115(9)	C(33)-C(34)-C(29)	122(8)
C(11)-C(12)-C(13)	119(9)	C(36)-C(35)-C(40)	119(8)
C(14)-C(13)-C(12)	118(8)	C(36)-C(35)-C(33)	121(9)
C(14)-C(13)-C(8)	124(8)	C(40)-C(35)-C(33)	120(9)
C(12)-C(13)-C(8)	117(8)	C(35)-C(36)-C(37)	121(9)
C(19)-C(14)-C(15)	116(8)	C(36)-C(37)-C(38)	119(8)
C(19)-C(14)-C(13)	125(9)	C(39)-C(38)-C(37)	119(7)
C(15)-C(14)-C(13)	119(10)	C(39)-C(38)-C(41)#6	123(7)
C(16)-C(15)-C(14)	119(10)	C(37)-C(38)-C(41)#6	118(7)

C(17)-C(16)-C(15)	126(10)	C(38)-C(39)-C(40)	115(8)
C(16)-C(17)-C(18)	117(7)	C(35)-C(40)-C(39)	124(9)
C(16)-C(17)-C(20)#4	123(9)	O(13)-C(41)-O(12)	121(7)
C(18)-C(17)-C(20)#4	120(8)	O(13)-C(41)-C(38)#7	118(7)
C(17)-C(18)-C(19)	123(8)	O(12)-C(41)-C(38)#7	121(7)
C(14)-C(19)-C(18)	120(8)	Zn(2)-O(1)-Zn(3)	118(3)
O(11)-C(20)-O(10)	126(8)	Zn(2)-O(1)-Zn(1)	112(2)
O(11)-C(20)-C(17)#5	119(8)	Zn(3)-O(1)-Zn(1)	103(2)
O(10)-C(20)-C(17)#5	115(9)	O(16)-Zn(1)-O(1)	97.0(14)
O(7)-C(29)-C(30)	121(8)	O(16)-Zn(1)-O(17)	89(2)
O(7)-C(29)-C(34)	124(7)	O(1)-Zn(1)-O(17)	167(2)
C(30)-C(29)-C(34)	115(8)	O(16)-Zn(1)-O(13)#3	173.8(16)
C(31)-C(30)-O(6)	122(9)	O(1)-Zn(1)-O(13)#3	89(2)
C(31)-C(30)-C(29)	119(8)	O(17)-Zn(1)-O(13)#3	86(3)
O(6)-C(30)-C(29)	118(8)	O(16)-Zn(1)-O(11)	95.7(16)
C(30)-C(31)-C(32)	128(9)	O(1)-Zn(1)-O(11)	96(2)
O(17)-Zn(1)-O(11)	96(2)	O(15)-Zn(3)-O(15)#3	95(3)
O(13)#3-Zn(1)-O(11)	82(2)	O(1)#3-Zn(3)-O(12)#3	81(2)
O(16)-Zn(1)-O(12)	95.0(12)	O(1)-Zn(3)-O(12)#3	99.6(18)
O(1)-Zn(1)-O(12)	77(2)	O(15)-Zn(3)-O(12)#3	89.0(18)
O(17)-Zn(1)-O(12)	90(2)	O(15)#3-Zn(3)-O(12)#3	171.6(19)
O(13)#3-Zn(1)-O(12)	88(2)	O(1)#3-Zn(3)-O(12)	99.6(18)
O(11)-Zn(1)-O(12)	168(2)	O(1)-Zn(3)-O(12)	81(2)
O(16)-Zn(1)-Zn(3)	113.2(3)	O(15)-Zn(3)-O(12)	171.6(19)
O(1)-Zn(1)-Zn(3)	38.3(15)	O(15)#3-Zn(3)-O(12)	89.0(18)
O(17)-Zn(1)-Zn(3)	128.3(19)	O(12)#3-Zn(3)-O(12)	88(2)
O(13)#3-Zn(1)-Zn(3)	72.8(16)	O(1)#3-Zn(3)-Zn(1)#3	39.0(15)
O(11)-Zn(1)-Zn(3)	125.5(16)	O(1)-Zn(3)-Zn(1)#3	141.2(13)
O(12)-Zn(1)-Zn(3)	43.9(13)	O(15)-Zn(3)-Zn(1)#3	104.1(16)
O(10)-Zn(2)-O(14)	108(3)	O(15)#3-Zn(3)-Zn(1)#3	124.7(15)
O(10)-Zn(2)-O(1)	112(2)	O(12)#3-Zn(3)-Zn(1)#3	47.0(13)
O(14)-Zn(2)-O(1)	112(2)	O(12)-Zn(3)-Zn(1)#3	79.5(13)

O(10)-Zn(2)-O(2)	105(2)	O(1)#3-Zn(3)-Zn(1)	141.2(13)
O(14)-Zn(2)-O(2)	116(2)	O(1)-Zn(3)-Zn(1)	39.0(15)
O(1)-Zn(2)-O(2)	105(2)	O(15)-Zn(3)-Zn(1)	124.7(15)
O(1)#3-Zn(3)-O(1)	180(3)	O(15)#3-Zn(3)-Zn(1)	104.1(16)
O(1)#3-Zn(3)-O(15)	88(2)	O(12)#3-Zn(3)-Zn(1)	79.5(13)
O(1)-Zn(3)-O(15)	92(2)	O(12)-Zn(3)-Zn(1)	47.0(13)
O(1)#3-Zn(3)-O(15)#3	92(2)	Zn(1)#3-Zn(3)-Zn(1)	106.0(4)
O(1)-Zn(3)-O(15)#3	88(2)		

Symmetry transformations used to generate equivalent atoms:

#1 x, y+1, z #2 x, y-1, z # 3 -x+1, -y, z

#4 y+1/2, x-1/2, z+1/2 #5 y+ 1/2, x-1/2, z-1/2 #6 y+1/2, x+1/2, z+1/2

#7 y- 1/2, x-1/2, z-1/2

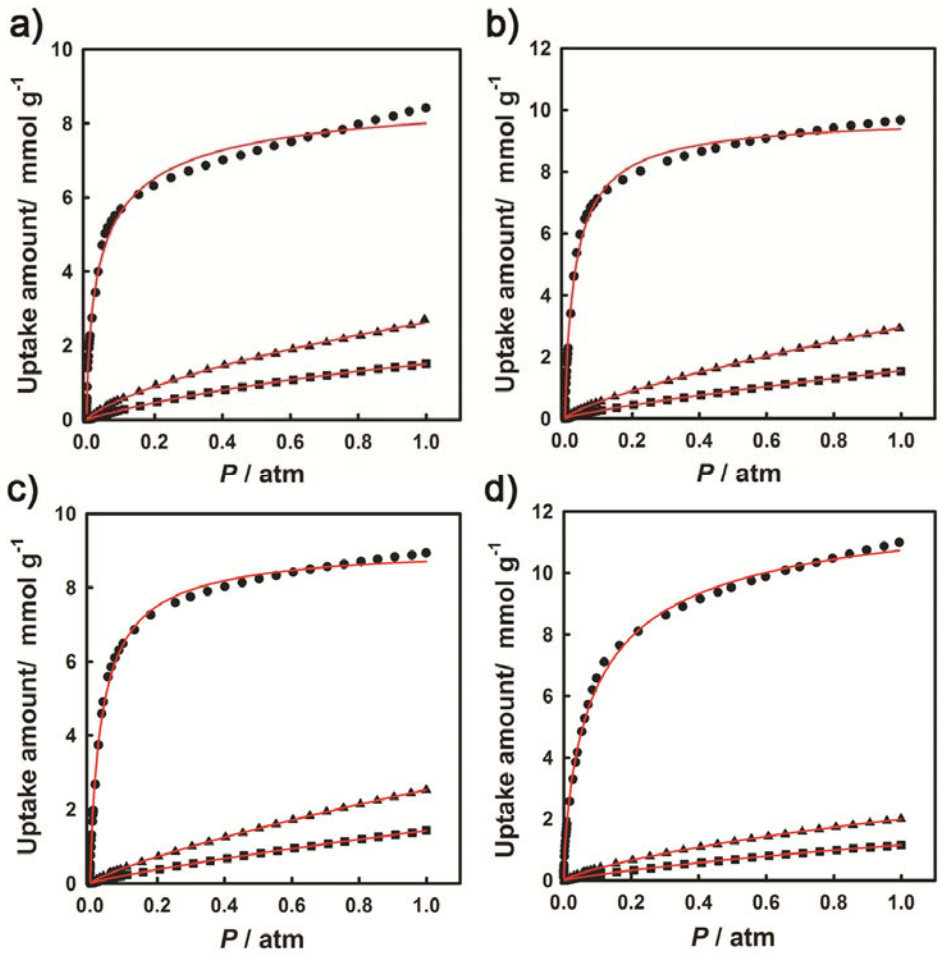

Figure I.S1. CO_2 gas adsorption isotherms measured at 195 K (circle), 273 K (triangle), and 298 K (square). a) SNU-200', b) $K^+ \subset$SNU-200'·SCN^-, c) $NH_4^+ \subset$SNU-200'·Cl^-, and d) $MV^{2+} \subset$SNU-200'·$2Cl^-$. The solid lines correspond to the best fits to the *Langmuir–Freundlich* equation.

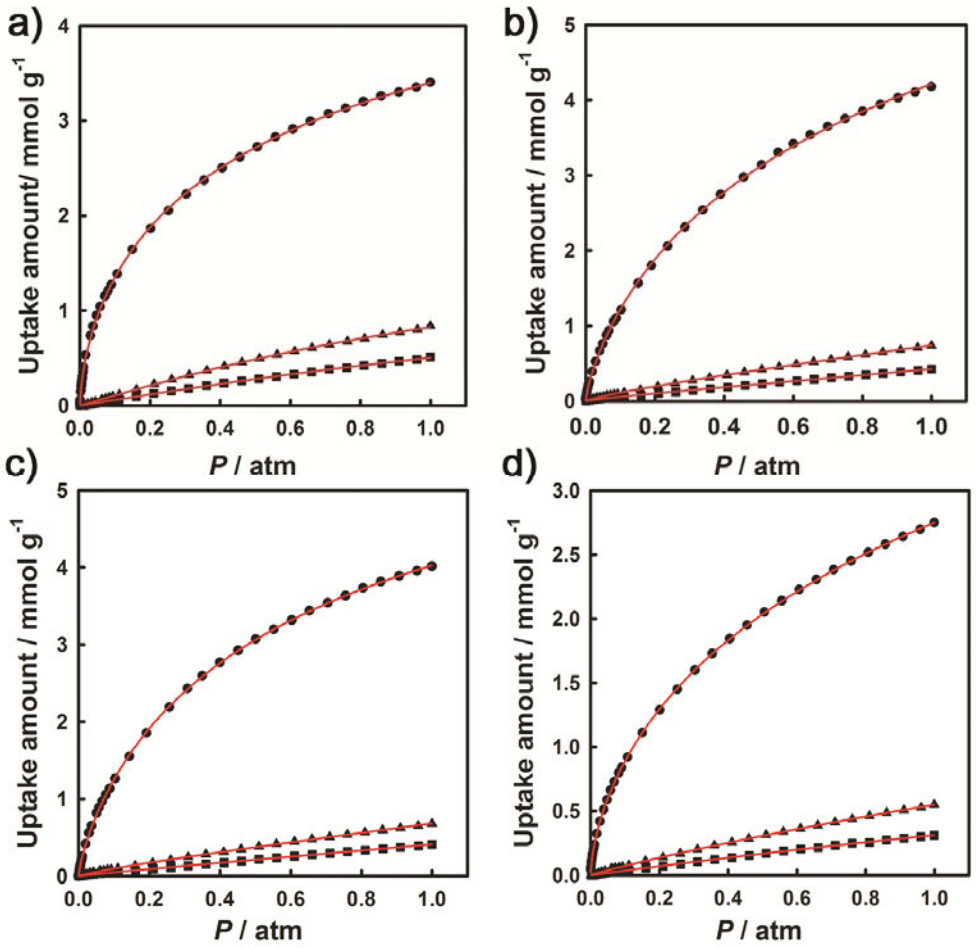

Figure I.S2. CH_4 gas adsorption isotherms of a) SNU-200', b) $K^+\subset$SNU-200'·SCN^-, c) $NH_4^+\subset$SNU-200'·Cl^-, and d) $MV^{2+}\subset$SNU-200'·$2Cl^-$ at 195 K (circle), 273 K (triangle), and 298 K (square). The solid red lines correspond to the best fits to *Langmuir–Freundlich* equation.

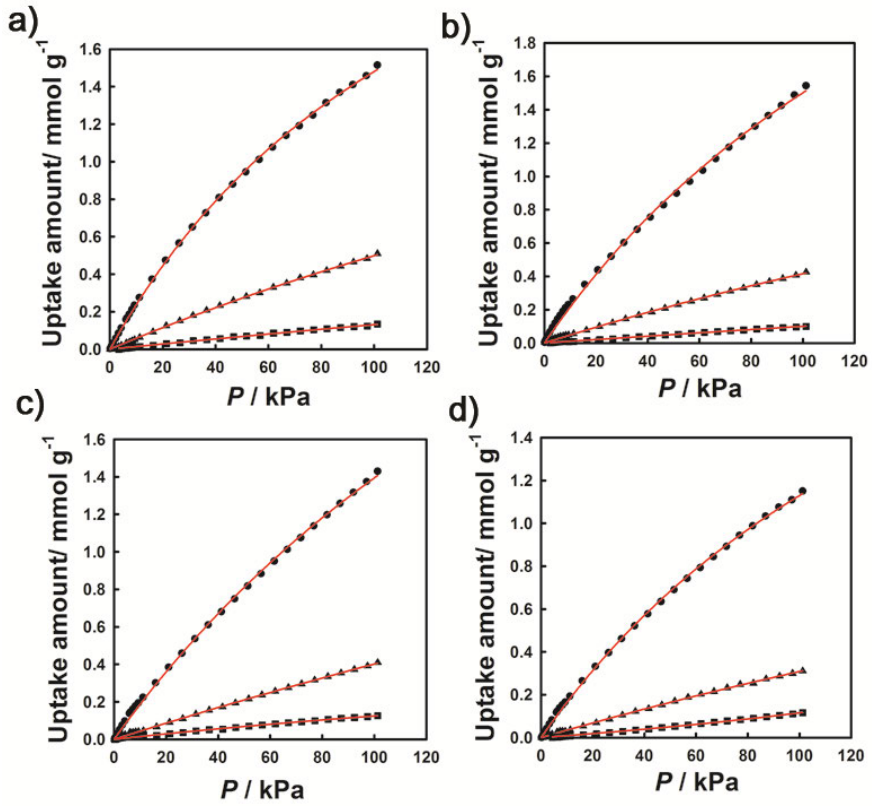

e)

	SNU-200'	$K^+ \subset$SNU-200'·SCN^-	$NH_4^+ \subset$SNU-200'·Cl^-	$MV^{2+} \subset$SNU-200'·$2Cl^-$
a	0.0254 (CO_2)	0.0226 (CO_2)	0.0193 (CO_2)	0.0173 (CO_2)
	0.0060 (CH_4)	0.0049 (CH_4)	0.0044 (CH_4)	0.0035 (CH_4)
	0.0014 (N_2)	0.0010 (N_2)	0.0015 (N_2)	0.0009 (N_2)
b	0.0072 (CO_2)	0.0051 (CO_2)	0.0039 (CO_2)	0.0053 (CO_2)
	0.0020 (CH_4)	0.0018 (CH_4)	0.0009 (CH_4)	0.0014 (CH_4)
	0.0007 (N_2)	0.0003 (N_2)	0.0022 (N_2)	-0.0023 (N_2)
R^2	0.9999 (CO_2)	0.9987 (CO_2)	0.9993 (CO_2)	0.9995 (CO_2)
	0.9996 (CH_4)	0.9983 (CH_4)	0.9991 (CH_4)	0.9995 (CH_4)
	0.9965 (N_2)	0.9983 (N_2)	0.9946 (N_2)	0.9980 (N_2)

Figure I.S3. Gas adsorption isotherms of CO_2 (circle), CH_4 (triangle) and N_2 (square) at 298 K in a) SNU-200', b) $K^+ \subset$SNU-200'·SCN^-, c) $NH_4^+ \subset$SNU-200'·Cl^-, and d) $MV^{2+} \subset$SNU-200'·$2Cl^-$. e) Langmuir fit parameters for CO_2, CH_4, and N_2 adsorption isotherms at 298 K.

PART II

FABRICATION OF MAGNESIUM NANOCRYSTAL IN HIGHLY POROUS MATERIALS FOR HYBRID HYDROGEN STORAGE BY PHYSI- AND CHEMISORPTION

II.1. Introduction

The depletion of fossil fuel supply and global warming by emission of CO_2 gas have demanded a renewable and clean alternative energy source. Hydrogen is a most promising candidate to replace the carbon based energy. Hydrogen has nearly three times higher energy density than carbon based energy (33.3 kWh kg^{-1} (123 MJ kg^{-1}) for hydrogen and 11.1 kWh kg^{-1} (47.2 MJ kg^{-1}) for gasoline.) and emits no CO_2 gas after combustion. Although hydrogen is considered as a perfect source, it is not facial to use for energy due to the safety problem. In order to use it as a fuel, a compact, safe, and efficient hydrogen storage system should be developed. Hydrogen is able to be store as 1) pressurized gas 2) cryogenic liquid and 3) solid state with materials by physishorption and chemisorption.

As a physisorption materials, metal - organic frameworks (MOFs) or porous coordination polymers (PCPs) and covalent - organic frameworks (COFs) have attracted great attention as potential hydrogen storage materials due to their high porousity and surface area.[2,119-121] MOFs and COF are able to uptake a large amount of hydrogen (> 7 wt%) at 77 K and high pressures.[120,121] However, at room temperature, the H_2 storage capacities of MOFs drop down to less than 1 wt% because interaction energies between the frameworks and H_2 are very low (4 – 8 kJ mol^{-1}).

Metal hydride is representative as a chemisorptions materials which mean that metal atoms binds with the hydrogen molecule to form chemical bonds under the high pressure and temperature with more strong interaction energy than that of physisortion materials.[122] In metal hydride, hydrogen is adsorbed as two different phase (α- and β-pahse) in the host metal lattice. α and β-pahse means that hydride is partially formed(α- pahse) or fully formed (β-pahse). For instance, the light metal such

as Mg, Na, Be, Li, B and Al generate a variety of metal hydride compound. Especially. Mg indicates the substantial stuedies as the hydrogen storage material due to the their high hydrogen strorage capacity, low cost, and abundant amount of source. MgH_2 represent a high energy density (9 MJ/kg) and H_2 capacitiy of 7.6 wt%. However, in dehydrogenation, MgH_2 need to supply a high temperature (>300 ^oC) and Mg has a high reactivity toward oxygen.[123,124] Herein, we report that impregnation of metal nanoparticles in porous materials for hybird hydrogen storage by physisorption and chemisorption.

II.2. Physisorption and Chemisorption for Hydrogen Storage[2]

Hydrogen can be stored as a solid state with materials by phyisortion or chemisorption manner. In physisorbed hydrogen storage materials, H_2 molecules are adsorbed on the surface of the pores of the materials. According to IUPAC, physisorption (physical adsorption) is the adsorption in which the forces involved are intermolecular forces (van der Waals forces) of the same kind as those responsible for the imperfection of real gases and the condensation of vapors and which do not involve a significant change in the electronic orbital patterns of the species involved.[125,126] Physisorption processes are reversible since no activation energy is involved and the interaction energy is very low. In materials such as metal-organic frameworks, porous carbons, zeolites, clathrates, and organic polymers, H_2 is physisorbed on the surface of the pores. In these classes of materials, the H_2 storage capacity mainly depends on the surface area and pore volume. The main limitation of use of these sorbents as H_2 storage materials is weak van der Waals interaction energy between H_2 and the surface of the sorbents. Therefore, many of the physisorption based materials have high storage capacities at liquid nitrogen temperature and high pressures, but their capacities become very low at ambient temperature and pressure. Research is being directed toward the synthesis of highly porous materials that would have enhanced interaction energies with gaseous H_2. The advantage of these materials is the fast adsorption and desorption kinetics.

In chemisorption-based materials, hydrogen is chemically bonded to the storage medium. According to the IUPAC, chemisorptions (chemical adsorption) is the adsorption that results from chemical bond formation (strong interaction) between the adsorbent and the adsorbate in a monolayer on the surface.[127] The formation and

stability of such materials highly depend on the pressure and temperature. Chemisorption process may not be reversible as relatively high activation energy exists in the adsorption and desorption process. On-board hydride materials and offboard regenerable hydride materials belong to this class. On-board reversible hydride materials include interstitial metal hydrides, covalently bound metal hydrides, metal amides, borohydrides, etc. These store dissociated hydrogen either covalently or as interstitially bound hydrogen, and release hydrogen by endothermic process. The storage materials can be directly recharged with hydrogen in situ on a vehicle, since endothermic release allows for exothermic rehydrogenation during on-board recharging of the hydrogen storage materials under reasonable temperature and pressure (below 300 ^{o}C and below 200 bar). Off-board regenerable hydride materials store dissociated hydrogen as covalently bound hydrogen materials, and they release hydrogen exothermically and involve complex offboard chemical processes for regeneration that cannot be performed on board a vehicle. Materials in this class are the hydrocarbons, ammonia borane, and alane.

II.3. Various Method for Preparation of Metal Nanoparticles in Metal - Organic Frameworks or Covalent - Organic Frameworks[128]

General synthetic methods of metal nanoparticles (M-NPs) in a porous solid matrix are the impregnation of a metal precursor in a porous solid, followed by reduction of the metal precursor to metal(0) atoms, which aggregate to M-NPs within the solid matrix. The precursor molecules that are most frequently used for the production of

M-NPs are chlorides or nitrates salts of the corresponding transition metal ions. In addition, organometallic complexes are often used as precursors in solid grinding or infiltration method.[129] In general, metal precursors included in MOFs are reduced with hydrogen gas, hydrazine, or $NaBH_4$ to generate MNPs, and the reduction process is often performed at high temperature, followed by the washing step. In some cases, ethanolic solution or methanol: supercritical CO_2 has also been used as a reducing agent to load NPs within the MOF.[130] The reduction conditions should be determined depending on the properties of the included precursor as well as the stability of the host matrix during the reduction processes.

II.3.1. Immersion of the Redox Active MOFs in Metal Salt Solution[128]

Contrary to the conventional methods, Suh's group developed new fabrication methods of M-NPs in PCPs, which produced M-NPs without using any capping or reducing agents and with no heating process at all.[13-16,131] They used redox active PCPs as supports for M-NPs and immersed them in the solutions of metal salts such as $AgNO_3$, $NaAuCl_4$, and $Pd(NO_3)_2$. They prepared redox active PCPs by using redox active building blocks. Redox active sites of the redox active building blocks may be at the organic ligands or at the metal centers such as Ni(II) sites in the Ni(II) macrocyclic complexes. As soon as metal ions are diffused to the redox active PCPs, they are reduced to metallic nanoparticles and the redox active building blocks in the PCPs are oxidized. The maxium amount of metal NPs formed can be easily predicted since the redox reactions between the redox active networks and metal ions are stoichiometric.

In most of the cases, the redox active PCPs retain their network structures even after the foramtion of metal NPs that are commonly much larger than the pore size of the PCPs. The most important advantages of this method are that the amount of M-NPs loaded in the PCP can be controlled by the immersion time of the host solid in the metal ion solution while the size of the M-NPs is independent of the concentration of the metal ion solution, temperature, and the type of the solvents.

Suh's group employed various Ni(II) square-planar macrocyclic complexes as redox active metal building blocks to construct redox-active PCPs.[14-16,131] Ni(II) macrocyclic complexes were prepared by simple one-pot template Schiff base condensation reactions.[132] They synthesized PCPs by self-assembly of thus prepared Ni(II) macrocyclic complexes and multidentate organic ligands containing carboxylate donor groups. The axial sites of Ni(II) ion of the macrocyclic complex with square planner geometry are coordinated by the carboxylate ligand to generate octahedral geometry; thus Ni(II) macrocyclic complex simply can be a linear linker to connect the organic ligand with its specific geometry in the construction of PCPs. By selecting the organic building blocks, multidimensional PCPs whose topology can be easily predicted from the geometry of organic ligand are constructed with various topologies. The octahedral Ni(II) macrocylic complexes can be easily oxdized to Ni(III) species.[132] The oxidation potential of Ni(II) to Ni(III) in the monomacrocyclic complexes ranges +0.90 – +0.93 V vs. SCE in the acetonitrile solutions.[132] When the PCPs constructed of Ni(II) macrocyclic complexes in octahedral coordination mode react with appropriate noble metal ions, resulting in the oxidized PCPs with Ni(III) macrocyclic species and metal(0) nanoparticles. Various Ni(II) macrocyclic complexes employed in construction of redox active PCPs are shown in (Figure 35).[14-

[16,130] The self-assembly of $(NiL_1)(ClO_4)_2$ (NiL_1^{2+} = $[Ni(C_{10}H_{26}N_6)]^{2+}$) and Na_2bpdc ($bpdc^{2-}$ = 4,4'-biphenyldicarboxylate) in a H_2O/pyridine mixture resulted in

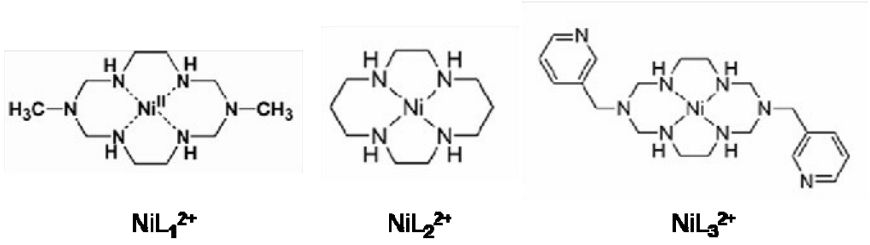

Figure. 35 Chemical structures of Ni(II) macrocyclic complexs as redox active species.[128]

$[(NiL_1)_3(bpdc)_3]\cdot 2pyridine\cdot 6H_2O$ (1), in which linear coordination polymer chains pack as a double network of threefold braids to generate 1D channels with honeycomb- shaped windows (effective pore size, 7.3 Å).[14] When desolvated host 1 was immersed in the methanolic solution of $AgNO_3$ (8.0 x 10-2 M) at room temperature for 10 min, Ag NPs (ca. 3 nm in diameter) were formed in solid 1. Inclusion of Ag(I) ions into 1 resulted in the oxidation of incorporated Ni(II) species to Ni(III) and simultaneous reduction of Ag(I) to Ag(0), followed by the nucleation and growth to Ag NPs. The redox reaction between Ag(I) and Ni(II) species were proved by the electron paramagnetic resonance (EPR) spectroscopy indicating the presence of d^7 Ni(III) species ($g\perp > g\|$) together with the X-ray photoelectron spectroscopy (XPS) showing the coexistance of Ni(III) and Ag(0). Elemental analysis data for the solid composite isolated after immersion of 1 in the AgNO3 solution for 10 min indicated that the reaction stoichiometry of Ni(II) ion in the host matrix and $AgNO_3$ was 1:1, proving that the redox reaction is quantitative (100%). Since the host framework became positively charged after the redox reaction, it included free NO_3^- anions as shown by the 1382 cm^{-1} peak in the IR spectra. The powder X-ray

diffraction (PXRD) patterns indicated that the framework structure was retained even after the formation of Ag NPs, and the peaks corresponding to Ag NPs were extremely weak due to very small sized NPs and too small amount of Ag compared with the amount of the host solid. Introducing well-designed building blocks to PCPs, the single-step preparation method for M-NPs in the solid support was successfully developed without using reducing agents and stabilizing agents at room temperature. The average size of the M-NPs was independent of immersion time, concentration of the metal salts, type of solvents, and temperature. Most interestingly, despite the formation of the metal nanoparticles, PXRD patterns of the network were intact, suggesting that network structures were unaltered by the metal NPs that are much bigger than aperture size of the networks. This was because even if all metal NPs broke down the networks, less than 10% of the whole framework would be destroyed and thus most of the network would be retained. By the similar methods, Au and Pd NPs were also fabricated in the redox active PCPs. Two dimensional square grid coordination network $[(NiL_2)_2(bptc)]\cdot 2H_2O$ (**2**) was assembled from $(NiL_2)(ClO_4)_2$ (L_2 = 1,4,8,11-tetraazacyclotetradecane) and H_4bptc ($bptc^{4-}$ = 1,1'-biphenyl-2,2',6,6'-tetracarboxylate). When **2** was immersed in EtOH solutions of $AgNO_3$ and $NaAuCl_4$ for 5 min, Ag NPs (3.7 ± 0.4 nm) and Au NPs (ca. 2 nm), respectively, were formed in the network.[15] In **2**, two dimensional layers of about 1 nm thickness were stacked with an interlayer spacing of 9.3 Å, through which $AgNO_3$ or $NaAuCl_4$ were diffused and then their metal ions were reduced to Ag(0) and Au(0) NPs, respectively. Within 5 min of immersion in the 0.1 – 0.3 M of metal ion solution, redox reaction between the metal ions and network occurred quantitatively, and all Ni(II) macrocyclic species were oxidized to Ni(III) to form Ag(0) NPs (ca. 4 nm) and Au(0) NPs (ca. 2 nm). This

was characterized by elemental analyses, which indicated the inclusion of counter anion NO_3^- and Cl^-, respectively. To fabricate small-sized Pd NPs in the PCPs, two redox active PCPs, $[(NiL_2)_2(mtb)]\cdot 8H_2O\cdot 4dmf$ (mtb^{4-} = methanetetrabenzoate, dmf = *N*,*N'*-dimethylformamide) (**3**) and $[(NiL_3)_2(tcm)]\cdot 5dmf\cdot 8H_2O$ ($L_3 = C_{20}H_{32}N_8$; tcm^{4-} = tetrakis[4-(carboxyphenyl)oxamethyl]methane) (**4**) were prepared by the self-assembly of corresponding Ni(II) macrocyclic complexes and organic building blocks.[16,130] The PCP **3** has a fourfold interpenetrated diamondoid network generating 1D channels with ink-bottle-type pores having a big cavity (13.4 x 13.4 Å) connected with narrow necks (2.05 x 2.05 Å).[16] Immersion of the desolvated solid of **3** in the acetonitrile solution of $Pd(NO_3)_2$ resulted in 2 nm-sized Pd NPs by autoredox reaction between Ni(II) macrocyclic species incorporated in the network and Pd(II) ions. Similarly, network **4** constructed by doubly interpenetrated rhombic grids that generate 1D channels (effective window size, 4.5 x 2.1 Å) also produced Pd NPs of 3 nm size.[130]

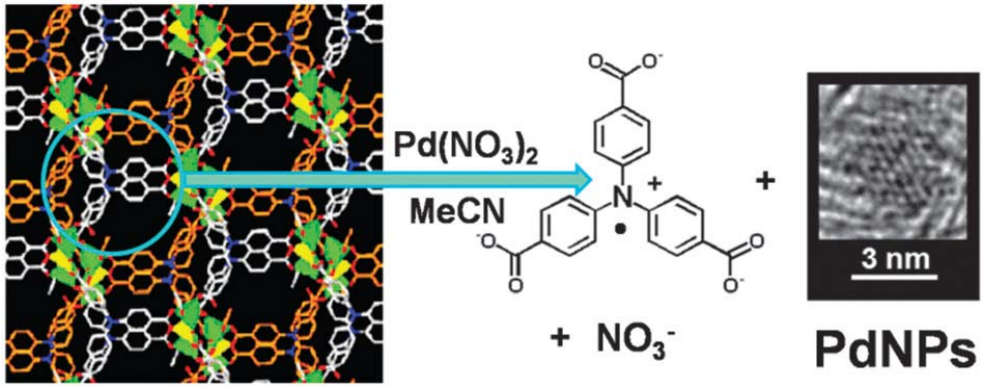

Figure 36. Reaction of a MOF incorporating redox-active organic species, 4,4',4''-nitrilotrisbenzoate (ntb^{3-}), with Pd^{2+} ions.[128]

Suh's group also prepared redox active PCPs by using redox active organic building

blocks.[13] Since 4,4',4"-nitrilotrisbenzoate (ntb^{3-}) can be readily oxidized to amine radical, the PCP constructed from ntb^{3-} becomes redox active as shown in Figure. 36. When porous MOF, $[Zn_3(ntb)_2(EtOH)_2]\cdot 4EtOH$ (EtOH = ethyl alcohol) (**5**),[66] which was synthesized from the solvothermal reaction of H_3ntb and $Zn(NO_3)_2$, was immersed in the acetonitrile solution of $Pd(NO_3)_2$ (1.0×10^{-3} M) for 30 min, the Pd(0) NPs of size 3.0 ± 0.4 nm were formed in the channels (aperture size, 7.7 Å) of the MOF.[13] The EPR spectrum indicated that MOF was oxidized to the positively charged network with nitrogen radical. The amount of Pd NPs loaded in the MOF could be controlled by the immersion time in the metal ion solution, which in turn affected the H_2 uptake. The MOF embedded with 3 wt% Pd NPs adsorbed the highest amount of H_2 at 77 K and 1 atm. Since this formation reaction of Pd NPs is a stoichiometric redox reaction between Pd(II) ions and the ntb^{3-} units of the host (Pd^{II}: ntb^{3-} = 1:2), a maximum of 9.05 wt% of Pd NPs can be formed if all of the ntb^{3-} units in the host are oxidized with palladium(II) ions. The PXRD pattern was retained intact even after the formation of Pd NPs that are larger than the channel size. This can be explained by the small volume ratio of Pd NPs produced versus the framework skeleton: even if all 3 wt% Pd NPs destroyed the framework, according to the calculation, a maximum of 0.7% by volume of the framework skeleton could be destroyed.

This synthetic method for fabrication of M-NPs in PCPs via autoredox reaction has superior advantages that neither a reducing agent nor a capping ligand is necessary, and the bare (naked) M-NPs are incorporated in porous host solids, which could be the leading candidates for heterogeneous catalysts as well as gas storage materials. Furthermore, the amount of M-NPs fabricated in PCPs can be controlled by the immersion time of the solid in metal ion solution and the concentration of the metal

salts. The redox reaction can provide 100% stoichiometric product. Although the resulting M-NPs often have larger diameters than the aperture size of the MOFs, the original structures of the frameworks are retained. The disadvantage is that the host solid should be oxidized and thus counter anions should be included in the pores, which reduces the surface area that are important for adsorption of gases and adsorbates.

Recently, it has been reported that when Rb-CD MOF and Cs-CD-MOF (CD = -cyclodextrin), which contain OH^- counter ions, were immersed in the acetonitrile solution of $AgNO_3$ and $HAuCl_4$, respectively, Ag NPs of 2.0 nm size and Au NPs of 3-4 nm size were formed.[133] In these cases, either OH^- counter ions included in the frameworks or cooperatively with the cyclodextrin units reduce the metal salt precursors to their respective NPs. While Ag NPs were deposited throughout the entire MOF crystal, Au NPs were located predominantly in the core of the crystal. The contents of deposited M-NPs increase on either increasing the time of soaking or with increasing the concentration of the metal precursors. By combination of the deposition modes of Ag and Au, core/shell NPs@CD-MOF was also synthesized. By immersion of MOF crystals first in $HAuCl_4$ solution, a core of Au NPs (>90%) was prepared, which was washed with acetonitrile and then immersed in $AgNO_3$ solution to deposit

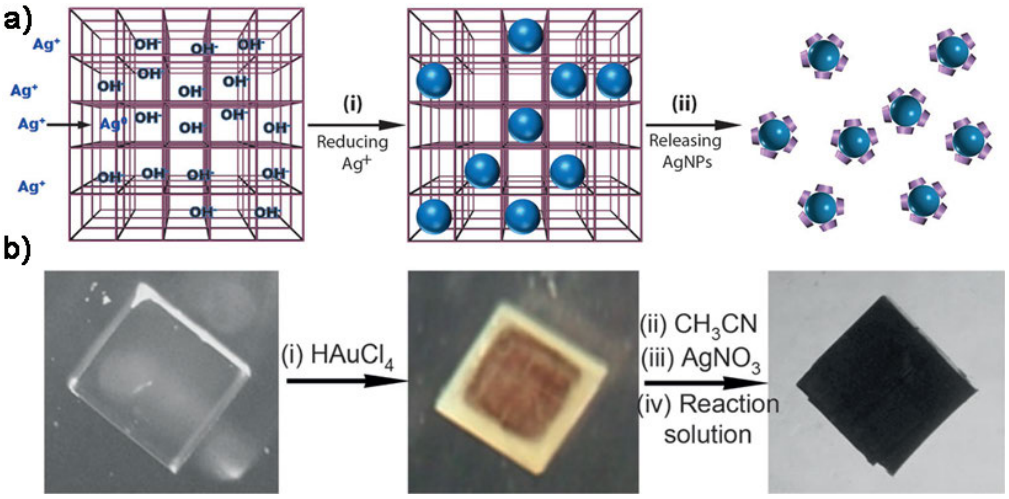

Figure 37. a) Scheme illustrating the diffusion and reduction of Ag+ ions within CD-MOFs, as well as the release of the Ag NPs formed when the MOF crystal is dissolved in water. b) Optical images of Rb-CD-MOF first loaded with Au NPs in the core region, and then with Ag NPs in the shell region.[133]

Ag NPs (>90%) in the shell region. The relative dimensions of the Ag-rich and the Au-rich regions could be adjusted by changing the core size, as shown in Figure 37. Although the reduction of metal salts proceeds much faster in MeOH than in MeCN, MeOH could not be used because it caused degradation of the MOF scaffolds

II.3.2. Chemical Vapor Deposition of Organometallic Compounds Followed by Hydrogenolysis[128]

Chemical vapor deposition (CVD) of volatile organometallic precursors has been used for preparation of the metallic or metal oxide thin film on the two-dimensional supports. This technique, however, has been applied not only to “flat surface”[134] but also to “internal surface” of the porous materials[135] to prepare the nanocomposite materials including metal complexes or metal clusters. In this technique, a dried MOF

and a volatile metal precursor are placed in two separate glass vials in a Schlenk tube. The tube is evacuated, sealed, and kept at proper temperature depending on the vapor pressure of the metal precursor under static vacuum (1 Pa). Upon infiltration of metal precursor into the MOFs, the crystal colors of MOFs would be changed. When hydrogenolysis of composite materials is followed to reduce the metal precursors, M-NPs incorporated in the MOFs are generated.[136-138] The various organometallic complexes that have appropriate sizes to enter into the cavities of the MOFs were used as precursors for CVD (Figure 38). When the vapor of [(η^5-C_5H_5)Pd(η^3-C_3H_5)] (A), [(η^5-C_5H_5)Cu(PMe_3)] (B), and [(CH_3)Au(PMe_3)] (C), respectively, were introduced to MOF-5 that has a pore diameter of 8 Å, in the static vacuum (1 Pa) at room temperature, metal precursors were embedded into MOF-5, as characterized by PXRD, elemental analysis, IR spectra, and solid state ^{13}C magic-angle spinning (MAS) NMR

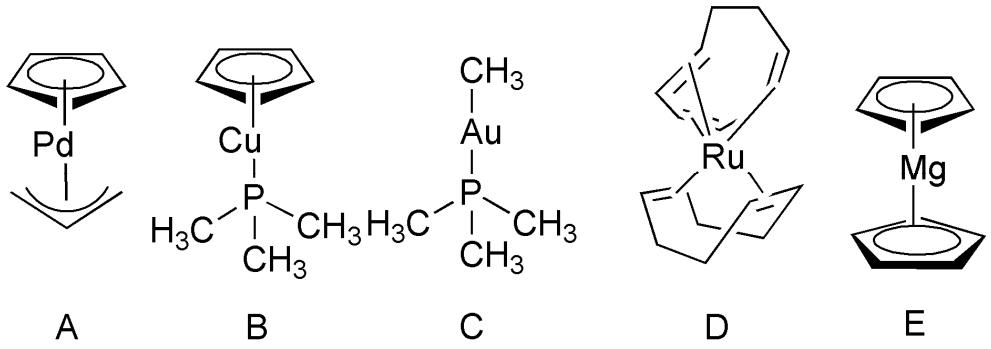

Figure 38. Organometallic precursors for chemical vapor deposition.

spectra.[136] The resulting A@MOF-5, B@MOF-5, and C@MOF-5, were treated with H_2 stream at the temperatures of hydrogenolysis (Pd for 23 ^oC, Cu for 150 ^oC, and Au for 190 ^oC), the "naked" metal-nanoclusters were formed. The size of the resulting M-NPs were 1.4 ± 0.1 nm for Pd@MOF-5, 3 – 4 nm for Cu@MOF-5, and 5 – 20 nm for Au@MOF-5. The polydispersity of Au NPs was explained by the high mobility of

reduced Au nuclei in the open MOF-5 structure. In the PXRD pattern of Pd@MOF-5, characteristic peaks of MOF-5 framework were significantly reduced, but the gas sorption data afforded Langmuir surface area of 1,600 m^2g^{-1}, indicating that the framework of Pd@MOF-5 was still highly porous. In addition, instead of thermally induced hydrogenolysis, UV photolysis of the metal precursor infiltrated in MOF-5 was carried out by using high pressure Hg lamp, which alternatively generated very small Pd and Cu NPs (1-2 nm) in the MOF-5 under much milder conditions.

As an alternative to MOFs, a covalent organic framework (COF) was used as the support for fabricating Pd NPs[139] Fischer's group prepared the Pd@COF-102 nanocomposite by the gas-phase infiltration of [Pd(η^3-C_3H_5)(η^5-C_5H_5)] into COF-102 and subsequent photodecomposition. As a results, Pd nanoparticles of 2.4±0.5 nm are distributed in the COF-102. The resulting material Pd@COF-102 exhibited enhanced hydrogen uptake by a factor of 2–3 at room temperature and 20 bar, compared to pristine COF. The enhancement was attributed to Pd-hydride formation as well as hydrogenation of organic residues originating from the metal precursor, as evidenced by MAS ^{13}C NMR. Similarly, Ru precursor, [Ru(cod)(cot)] (D, cod = 1,5-cyclooctadiene, cot = 1,3,5-cyclooctatriene) was loaded into MOF-5 by CVD method.[137] The homogeneous distribution of D in MOF-5 framework was ascertained by cross sectional photo as well as TEM images of D@MOF-5 crystals. The PXRD of D@MOF-5 showed the intact host structure even after inclusion of volatile Ru precursor D. Subsequent hydrogenolysis of the adsorbed D yielded Ru NPs of size 1.5 – 1.7 nm embedded in the MOF.[137] In the hydrogenolysis reaction, the mild conditions such as 25 ^oC for 30 min did not lead to the quantitative formation of Ru NPs. ^{13}C MAS NMR spectra indicated that hydrogenolysis of cot ligand in D was performed

prior to cod ligand. Partially hydrogenated precursor D was converted to a [(cod)Ru(0)] fragment, and the Ru(0) atom formed new coordination bond with a benzene ring of terephthalate in the host framework. Therefore, hydrogenolysis under the mild conditions at 25 ^{o}C could not generate M-NPs. To obtain Ru@MOF-5 from D@MOF-5 quantitatively, the hydrogenolysis should be conducted under 3 bar H_2 at 150 ^{o}C for a longer period time, 48h. Quantitative hydrogenolysis of D and removal of all volatile byproduct from MOF-5 were confirmed by ^{13}C MAS NMR and FT-IR spectra. After complete decomposition of Ru precursor D, the material Ru NPs@MOF-5 was obtained. In addition, this method was used to prepare Ni NPs in a mesoporous MOF, MesMOF-1 ($Tb_{16}(TATB)_{16}$, TATB = triazine-1,3,5-tribenzoate) (Figure.39).[138] After gas-phase loading of nickelocene in MesMOF-1, the sample was treated with hydrogen gas at 95 ^{o}C for 5 h, which yielded cyclopentane and Ni NPs included in MesMOF-1. When the residual cyclopentane molecules were removed by washing with methanol, Ni NPs@MesMOF-1 resulted. Depending on the loading time of the precursor, amount of Ni NPs fabricated in MesMOF-s could be controlled.

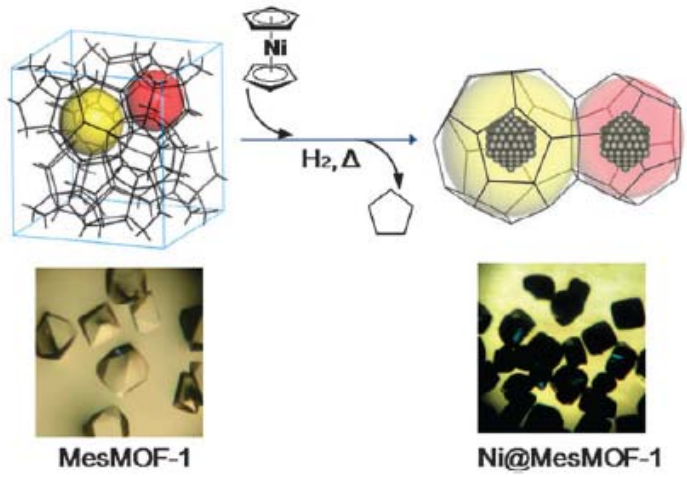

Figure 39. Preparation of Ni@MesMOF-1.[138]

This CVD method was also employed for the preparation of bimetallic nanoparticles such as FePt, PdPt, and RuPt in a MOF by loading MOF-5 with combination of two different MOCVD precursors.[140] In a Schlenk tube, dry MOF and two metal precusros were placed, and the tube was evacuated (10-3 mbar), sealed, and kept at room temperature for several hours. The simultaneous loading of two different metal presursors in MOF-5 was verified by ^{13}C MAS NMR spectroscopy, PXRD and elemental/AAS (atomic absorption spectroscopy) analyses After hydrogen treatment, the composite material of MOF-5 incorporating bimetallic nanoalloy was obtained. In this reaction, the selection of proper temperature for hydrogenolysis is important, because if mild conditions are applied to avoid decomposition of the host framework MOF-5, both precursors could not be reduced to bimetallic alloy nanoparticles. To achieve quantitative co-hydrogenolysis of the precursors, when the harsh condition was applied, the hydrogenation of bdc linkers in MOF-5 occured to yield *cis*/*trans*-1,4-cyclohexane dicarboxylic acid.

II.3.3. Encapsulation of Presynthesized Metal Nanoparticles in MOFs[128]

Presynthesized metal NPs that are capped by stabilizing agents can be encapsulated in MOFs by introducing NPs to the synthetic solution containing molecular building blocks for MOFs. When individually capped-NPs are encapsulated in MOFs, the size of NPs can be easily controlled, and agglomeration of nanoparticles can be restricted in the host framework. Hupp and Huo *et al.* reported encapsulation of the PVP (polyvinylpyrrolidone)-capped nanomaterials with various sizes, shapes, and compositions in a zeolitic imidazolate framework, ZIF-8 (Figure. 40).[141] PVP has been

widely used to synthesize various nanomaterials to control the size and shape as well as to stabilize them in polar solvents. By mixing PVP-capped Au NPs with the methanolic solution of zinc nitrate and 2-methylimidazole, Au@ZIF-8 was isolated by centrifugation. After isolation, the supernatant did not contain Au NPs, implying that

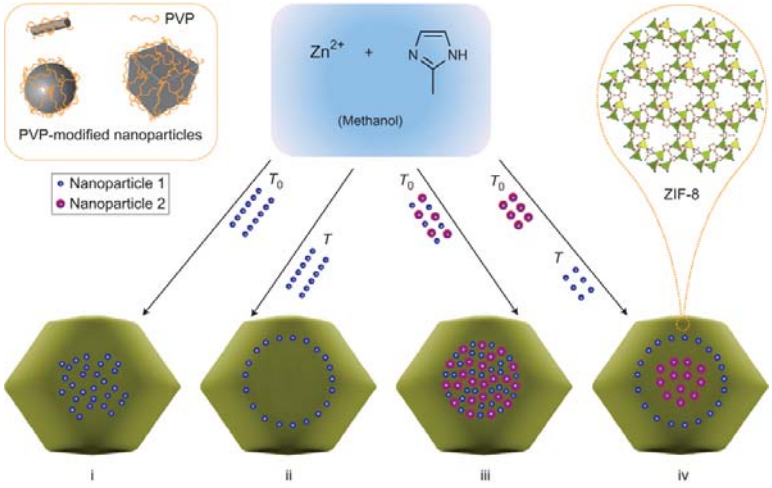

Figure 40. Scheme of the controlled encapsulation of nanoparticles in ZIF-8 crystals. Through surface modification with surfactant PVP, nanoparticles of various sizes, shapes and compositions can be encapsulated in a well-dispersed fashion in ZIF-8 crystals, which formed by the assembly of zinc ions and imidazolate ligands.[141]

almost all NPs were encapsulated in ZIF-8. This strategy was successfully extended to other nanomaterials such as Pt, CdTe, Fe_3O_4 and lanthanide-doped $NaYF_4$ nanoparticles, and Ag cubes, polystyrene spheres, β-FeOOH rods and lanthanide-doped $NaYF_4$ rods, whose surfaces were modified by PVP.[141]

II.4. Experimental Section

General. All chemicals and solvents used in the syntheses were of reagent grade and used without further purification. H_3atb (aniline-2,4,6-tribenzoic acid) was

synthesized by using Suzuki-Miyaura coupling reaction.[102] All preparations and manipulations of dried MOF, $MgCp_2$, and magnesium nanocrystals were performed under an argon atmosphere by using Schlenk lines or a dry box. Infrared spectra were recorded with a Perkin–Elmer Spectrum One FT-IR spectrophotometer. NMR spectra were measured on a Bruker Spectrospin 300 spectrometer and AVANCE 400 WB. UV/Vis diffuse reflectance spectra were recorded on a Perkin–Elmer Lambda 35 UV/Vis spectrophotometer. Elemental analyses were performed with a Perkin–Elmer 2400 series II CHN analyzer. Thermogravimetric analysis (TGA) and differential scanning calorimetry (DSC) were performed under N_2(g) at a scan rate of 5 °C min^{-1} with Q50 and Q10 model devices, respectively, from TA Instruments. Powder X-ray diffraction (PXRD) data were recorded on a Bruker D5005 diffractometer at 40 kV and 40 mA for Cu Kα (λ = 1.54050 Å) with a scan speed of 5^o min^{-1} and a step size of 0.02^o in 2θ. Inductively coupled plasma atomic emission spectroscopy (ICP-AES) was recorded with a PerkinElmer Optima-4300 DV. High Resolution TEM (HRTEM) images and energy-dispersive X-ray spectra (EDS) were obtained with JEM-3000F (JEOL) and JEM-3010 (JEOL) that were equipped with an Oxford INCA EDS unit. Electron tomography experiments were performed on a Tecnai G2 Spirit microscope, operated at 120 kV in Korea basic science institute. Temperature programmed desorption-mass spectroscopy (TPD-MS) data were recorded on IGA-Mass (IGA-001, HPR-30), Hiden Analytical Ltd.

Synthesis of aniline-2,4,6-tribenzoic acid (H_3atb). Aniline-2,4,6-tribenzoic acid (H_3atb) was synthesized by using Suzuki-Miyaura coupling reaction. $Pd(PPh_3)_4$ (0.4012 g, 0.3472 mmol), 2,4,6-Tribromaniline (3.070 g, 9.308 mmol), and K_2CO_3

(4.015g, 29.05 mmol) were dissolved in purified anhydrous THF (150 mL), and stirred for 10 minutes. To the solution, was added a methanol solution (15 mL) of 4-methoxycarbonylphenyl boronic acid (5.015 g, 27.93 mmol), and the solution was heated at 90 ^{o}C for 48 h. After being cooled to room temperature, the solution was concentrated in a rotary evaporator, and the resulting deep-greenish residue was extracted with methylene dichloride (300 mL). The solution was washed with water and brine solution, and dried over anhydrous magnesium sulfate. The resulting solution was concentrated, which resulted light greenish residue. The product was purified by a column chromatography using silica as adsorbent and methylene dichloride as eluent. FT-IR (Nujol): $\nu_{O-C=O}$, 1690 cm^{-1}, ν_{H-N-H}, 1606. ^{1}H NMR (300 MHz, DMSO-d^{6}): δ 8.08 (d, *J* = 8 Hz, 4H), 7.96 (d, *J* = 8 Hz, 2H), 7.83 (d, *J* = 8 Hz, 2H), 7.72 (d, *J* = 8 Hz, 4H), 7.49 (s, 2H) 4.69 (s, 2H) ppm. Elemental analysis (%). Found: C, 66.09; H, 4.38; N, 2.88. Calculated for $C_{27}H_{19}NO_6 \cdot 2H_2O$: C, 66.25; H, 4.74; N, 2.86.

Synthesis of $[Zn_4O(atb)_2] \cdot 22DMF \cdot 9H_2O$ (SNU-90). $Zn(NO_3) \cdot 6H_2O$ (1.01 g, 5.33 mmol) and H_3atb (0.311 g, 0.686 mmol) were dissolved in *N*,*N*-dimethylformamide (DMF, 40 mL). The solution was placed in a glass serum bottle that was capped with a silicon stopper and aluminum seal, and then heated at 80 ^{o}C for 24 h. On cooling to room temperature, yellowish crystals formed, which were filtered off and washed briefly with anhydrous DMF. FT-IR (Nujol): $\nu_{C=O}$(DMF), 1664 cm^{-1}; ν_{H-N-H}, 1606; UV/vis (diffuse reflectance, λ_{max}): 390 nm. Luminescence (solid): λ_{max} = 468 nm (excitation at λ_{max} = 390 nm). Elemental analysis (%). Found: C, 48.66; H, 6.74; N, 11.38. Calculated for $(Zn_4C_{54}H_{24}N_2O_{13}) \cdot 22(C_3H_7NO) \cdot 9H_2O$: C, 48.88; H, 6.97; N,

11.40.

Preparation of $[Zn_4O(atb)_2]$ (SNU-90') by treatment of SNU-90 with supercritical CO_2. Prior to activation, the crystals of as synthesized $[Zn_4O(atb)_2]\cdot 22DMF\cdot 9H_2O$, which were still in the mother liquor, were transferred to a vial (20 mL). The mother liquor was decanted, and the crystals were washed briefly with anhydrous DMF (4 x 15 mL). The crystals were placed inside the supercritical dryer together with the solvent, and the drying chamber was sealed. The temperature and pressure of the chamber were raised to 40 ^oC and 200 bar with CO_2, above the critical point (31 ^oC, 73 atm) of CO_2. The chamber was vented at a rate of 15 mL min^{-1}, and then filled with CO_2 again. The cycles of refilling with CO_2, pressurizing, and venting were repeated for 4 h. After drying, the closed container with the dried crystals was transferred to a glove bag to prevent the crystals from exposure to air. FT-IR (KBr pellet): $\nu_{O-C=O}$, 1599; $\nu_{C=C}$, 1521 cm^{-1}. Elemental analysis (%). Found: C, 54.65; H, 2.68; N, 1.84. Calculated for $Zn_4C_{54}H_{24}N_2O_{13}$: C, 55.04; H, 2.74; N, 2.38.

Preparation of Covalent Organic Frameworks (PAF-1)

Highly porous covalent organic framework (Porous Aromatic Framework, PAF-1) reported by Zhu's group in 2009 has prepared by Ni catalyzed cross-coupling reaction of tetrakis (4-bromophenyl) methane.[121]

Preparation of Mg nano crystals embedded in SNU-90'

Bis(cyclopentadienyl)magnesium, $MgCp_2$, was purchased from STREM. A small bottle containing SNU-90' (0.45 g, 3.85 x 10^{-4} mol) was placed in a Schlenk tube,

which contained $MgCp_2$ (0.35 g, 2.26 x 10^{-3} mol) under an argon atmosphere (Table 6). The chemical vapor deposition of $MgCp_2$ within SNU-90' was performed by two different methods. For the samples of Mg@SNU-90'a and Mg@SNU-90'b, the temperature of the reaction tube that was filled with argon was increased to 80 ^{o}C, which was then maintained for 1 day and 3 days, respectively. For Mg@SNU-90'c, pre-vacuum (10^{-3} mbar) state was maintained in the reaction bottle at room temperature, and then the temperature was raised to 80 ^{o}C for 3 h to deposit the vapor of $MgCp_2$ in SNU-90'. After deposition of $MgCp_2$ in the MOF, the samples were transferred to other Schlenk tubes in the dry box filled with argon, and then the tubes were immersed for ca. 3 h in the oil bath whose temperature was already maintained at 200 ^{o}C. This gave rise to thermal decomposition of $MgCp_2$ that produced Mg nanocrystals. The organic decomposition products were removed from the samples by evacuation (10^{-6} bar) at room temperature for 24 h, which afforded various samples of Mg@SNU-90' with different amounts of loaded Mg nanocrystals. Amounts of Mg included in SNU-90' were determined by inductively coupled plasma atomic emission spectroscopy (ICP-AES) recorded with a PerkinElmer Optima-4300 DV as well as elemental analysis data.

Table 6. Sample preparations and ICP data for Various Mg@SNU-90'.

Sample	SNU-90', mg (mol)	$MgCp_2$, mg (mol)	ICP data, Mg/Zn (mole/mole)
Mg@SNU-90'a	460 (3.93 x10^{-4})	369 (2.38 x10^{-3})	0.15
Mg@SNU-90'b	445 (3.80 x10^{-4})	345 (2.23 x10^{-3})	0.85
Mg @SNU-90'c	453 (3.87 x10^{-4})	364 (2.36 x10^{-3})	1.40

Preparation of Mg nano crystals embedded in PAF-1

PAF-1 prepared by previous report was placed in a Schlenk tube, which contained $MgCp_2$ (0.35 g, 2.26 x 10^{-3} mol) under an argon atmosphere. The pre-vacuum (10^{-3} mbar) state was maintained in the Schlenk tube at room temperature, and then the temperature was raised to 80 ^oC for 3 h to deposit the vapor of $MgCp_2$ in PAF-1. $MgCp_2$@PAF-1 was reduced with Li^+(naphthalenide-) in the tetrahydrofuran solution with stirring for 10 min or overnight. After reduction, the samples were rinsed with a fresh anhydrous THF. The reduction process was carried out under an argon atmosphere in a dry box at room temperature. Amounts of Mg included in PAF-1 were determined by inductively coupled plasma atomic emission spectroscopy (ICP-AES) recorded with a PerkinElmer Optima-4300 DV.

X-ray Crystallography. The diffraction data of $[Zn_4O(atb)_2]\cdot 22DMF\cdot 9H_2O$ (SNU-90) were collected at 150 K with an Enraf–Nonius Kappa CCD diffractometer (Mo Ka, λ=0.71073, graphite monochromator). For the collection of X-ray diffraction data of SNU-90, the guest molecules of the crystal was exchanged with anhydrous toluene for two days, during which time the anhydrous toluene was replenished several times. One of the crystals was coated with Paratone oil immediately. Preliminary orientation matrices and unit cell parameters were obtained from the peaks of the first 10 frames and then refined by using the whole data set. Frames were integrated and corrected for Lorentz and polarization effects using DENZO.[105] The scaling and global refinement of crystal parameters were performed by using SCALEPACK.[105] No adsorption correction was made. The crystal structure was solved by direct method[106] and refined by full matrix least-squares refinement using the SHELXS-97 computer program.[107]

The positions of all non-hydrogen atoms were refined with anisotropic displacement factors. The hydrogen atoms were positioned geometrically and refined by using a riding model. There were two independent Zn_4O clusters which were statistically disordered over two sites. The site occupancy factors were given as 0.5 for Zn(1) atom, which sat on a three-fold crystallographic axis, and 0.16667 for Zn(2) atom, which sat in a general position. The site occupancy factors were given as 0.49683 for Zn(3) atom, 0.51917 for Zn(4) atom, 0.50317 for Zn(5) atom, and 0.48083 for Zn(6) atom. The site occupancy factors were given as 0.5 for O(5A), O(5B), O(6A), O(6B), O(9A), and O(9B) atoms. All amine functional groups were also given with site occupancy factors; 0.33333 for N(1A), N(1B), N(1C), and 0.16667 for N(2). The electron densities of the disordered guest molecules were flattened by using *SQUEEZE* option of *PLATON*.[108] Therefore, the guest molecules in SNU-90 were determined based on the IR spectra, elemental analyses, and TGA results. Although electron densities associated with guest molecules could not be observed, residual electron densities found around the phenyl rings of atb^{3-} were flattened by using *SQUEEZE* option of *PLATON*,[108] which provided a slightly lower *R* value than that determined without *SQUEEZE*. These data can be obtained free of charge from The Cambridge Crystallographic Data Centre via www.ccdc.cam.ac.uk/data_request/cif. (CCDC 846696)

Low Pressure Gas Sorption Measurements. The gas adsorption–desorption experiments were carried out by using an automated micropore gas analyzer, Autosorb-3B (Quantachrome Instruments). All gases used were of 99.999% purity. The N_2 sorption isotherms were measured at 77 K. The H_2 sorption isotherms were monitored at 77 K and 87 K at each equilibrium pressure by the static volumetric

method. After the gas sorption measurement was finished, the weight of the sample was measured precisely. Surface area was determined from N_2 adsorption isotherm measured at 77 K by using the Brunauer-Emmett-Teller (BET) and the Langmuir models, taking the data in the range P/P_0 = 0.01 – 0.1 (BET) and 0.005 – 0.3 (Langmuir), respectively. Pore volume was determined by using the Dubinin-Radushkevich (DR) equation.

Estimation of Isosteric Heats of the H_2 Physical Adsorption. The isosteric heats of the H_2 adsorption were estimated by using the H_2 sorption data measured at 77 K and 87 K. A virial-type expression was used [eq (1)], which is composed of parameters a_i and b_i that are independent of temperature.[109,70] In eq (1), P is pressure (atm), N is the amount adsorbed H_2 gas (mg g^{-1}), T is temperature (K), and m and n represent the number of coefficients required to adequately describe the isotherms. An equation was fit using the *R* statistical software package.[110] To estimate the values of the isosteric heat of H_2 adsorption, eq (2) was applied, where R is the universal gas constant.

High Pressure Gas Sorption Measurements. High-pressure H_2 gas sorption isotherms of SNU-90', Mg@SNU-90'a and Mg@SNU-90'c were measured by the gravimetric method using a Rubotherm MSB (magnetic suspension balance) apparatus. The H_2 physical adsorption isotherms for SNU-90' and Mg@SNU-90'a were measured at 77 K and 298 K. The H_2 chemisorption in Mg@SNU-90'c were measured at 323 K and 415 K. The H_2 absorptions at 473 K in the samples of Mg@SNU-90' were measured with High Pressure Volumetric Analyzer (HPVA-100), VTI Corp. Gases used were of 99.999% purity, and the traces of moisture contained in

the gas was removed by using a drying trap filled with 5 Å molecular sieves, which was purchased from the Chromatography Research Supplies (model 500). Desolvated solids of SNU-90', Mg@SNU-90'a, and Mg@SNU-90'c (more than 300 mg) were quickly introduced to the gas sorption apparatus and then activated by evacuation at 100 ^{o}C. Prior to gas sorption measurements, the He isotherm (up to 80 bar) was measured at 298 K to obtain the volume of the framework skeleton. The excess sorption isotherms were measured and corrected for the buoyancy of the system and sample. The buoyancy correction of the sample was made by multiplying the volume of the framework skeleton by the density of the corresponding gas at each pressure and temperature.[142]

II.5. Results and Discussion[12]

Mg nanocrystals in Metal Organic Framework.

X-ray strucuture of SNU-90

Yellow crystals of $[Zn_4O(atb)_2]\cdot 22DMF\cdot 9H2O$ (SNU-90), where atb is aniline-2,4,6-tribenzoate, were synthesized by heating a mixture of $Zn(NO_3)_2$ and H_3atb in dimethylformamide (DMF). The X-ray single crystal structure of SNU-90 indicated a non-interpenetrated (6,3)-connected net of a qom topology, similar to MOF-177[142] (Figures 41).

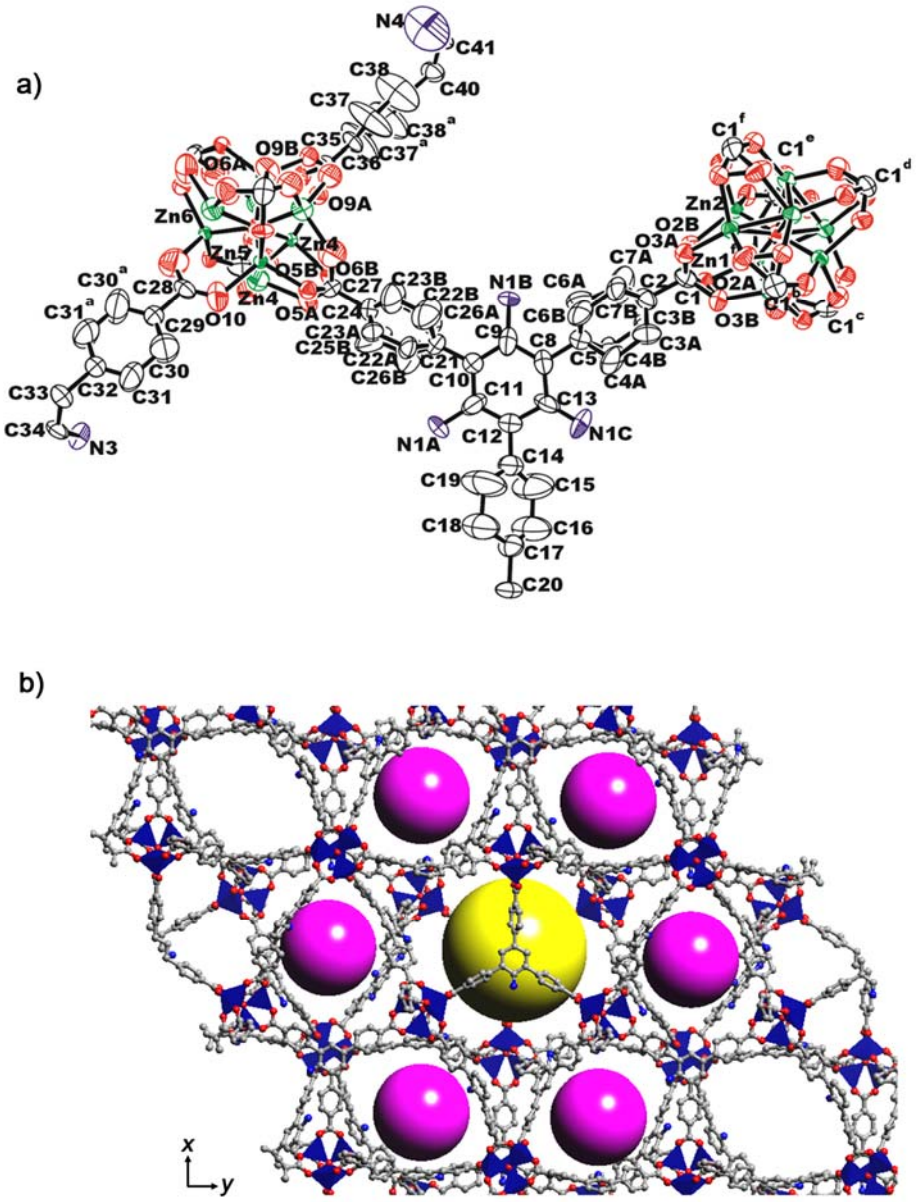

Figure 41. X-ray crystal structure of $[Zn_4O(atb)_2]\cdot 22DMF\cdot 9H_2O$ (SNU-90). a) An ORTEP drawing with the atomic numbering scheme. The atoms are represented by 30% possibility thermal ellipsoids. Symmetry operations: a, x, x-y, -z+1/2; b, x+1, x-y, -z+3/2; c, y-x+1, y, -z+3/2; d, -y+1, -x+1, -z+1; e, -y+1, x-y, z; f, y-x+1, -x+1, z. b) The 3D framework structure. The atoms of zinc, carbon, oxygen, and nitrogen are shown by dark blue octahedron, black, red, and blue spheres, respectively. Hydrogen atoms are omitted for clarity.

When the guest solvent molecules in SNU-90 were removed by treatment with supercritical CO_2,[19,144] a guest-free $[Zn_4O(atb)_2]$ (SNU-90', NH_2-MOF-177) was resulted. To SNU-90', vapor of bis-cyclopentadienyl magnesium ($MgCp_2$) was deposited at 80 ^oC, and then the resulting $MgCp_2$@SNU-90' was thermally decomposed at 473 K under an argon atmosphere, which gave rise to Mg NCs embedded in SNU-90'. Fabrication of nanosize Mg by the thermal decomposition of $MgCp_2$ is unprecedented, although it was reported that reduction of $MgCp_2$ with Li^+(naphthalenide-) in the tetrahydrofuran solution of polymethylmethacryate resulted round shaped Mg nanoparticles.[145] By changing the reaction conditions during the deposition process of $MgCp_2$ such as the duration time and whether or not a pre-vacuum state was applied to the reaction vessel, we could control the loaded amounts of $MgCp_2$ in the MOF and obtained several samples embedded with different amounts of magnesium nanocrystals (Table 6). The samples Mg@SNU-90'a, Mg@SNU-90'b, and Mg@SNU-90'c were loaded with 1.26 wt%, 6.52 wt%, and 10.5 wt% of Mg NCs, respectively, as determined by inductively coupled plasma atomic emission spectroscopy (ICP-AES) (Table 7). The HRTEM images for various samples of Mg@SNU-90' showed hexagonal-disk shaped magnesium nanocrystals,[146,147] which

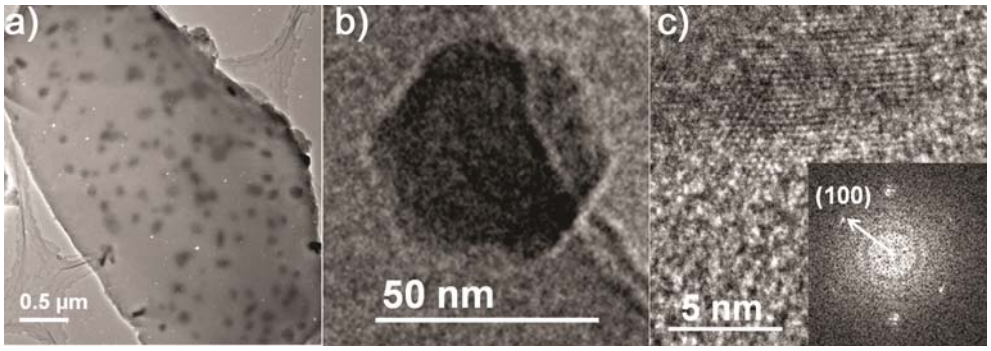

Figure 42. High resolution transmission electron microscopy (HRTEM) images. a)

Mg@SNU-90'b, b) A hexagonal shaped Mg nanocrystal and c) its edge image showing lattice fringes with a separation of 2.7871 Å, which corresponds to (100) d-spacing of Mg0 (2.7782 Å, JCPDS 04-0770). Inset: Selected area electron diffraction (SAED) pattern.

have a diagonal length of hexagon ranging 44 - 88 nm (average 60 ±18 nm) with a thickness ranging 16 – 61 nm (average 37± 12 nm) (Figure 42 and Figure 43). Fast Fourier transform (FFT) patterns for Mg NCs embedded in SNU-90' revealed a lattice fringe with a separation of 2.805 Å, which is in agreement with the (100) *d*-spacing of metallic Mg (2.7782 Å, JCPDS 04-0770). The size distribution of the Mg NCs was found to be very similar in all of the samples, even though there were significantly different amounts of Mg NCs embedded in the MOF. When Mg@SNU-90' was exposed to air for 3 weeks, the shape of the Mg NCs changed to a star shape having a lattice fringe with a separation of 2.1101 Å, which corresponds to the (200) d-spacing of MgO (2.1061Å, JCPDS 89-7746, Figure 43).

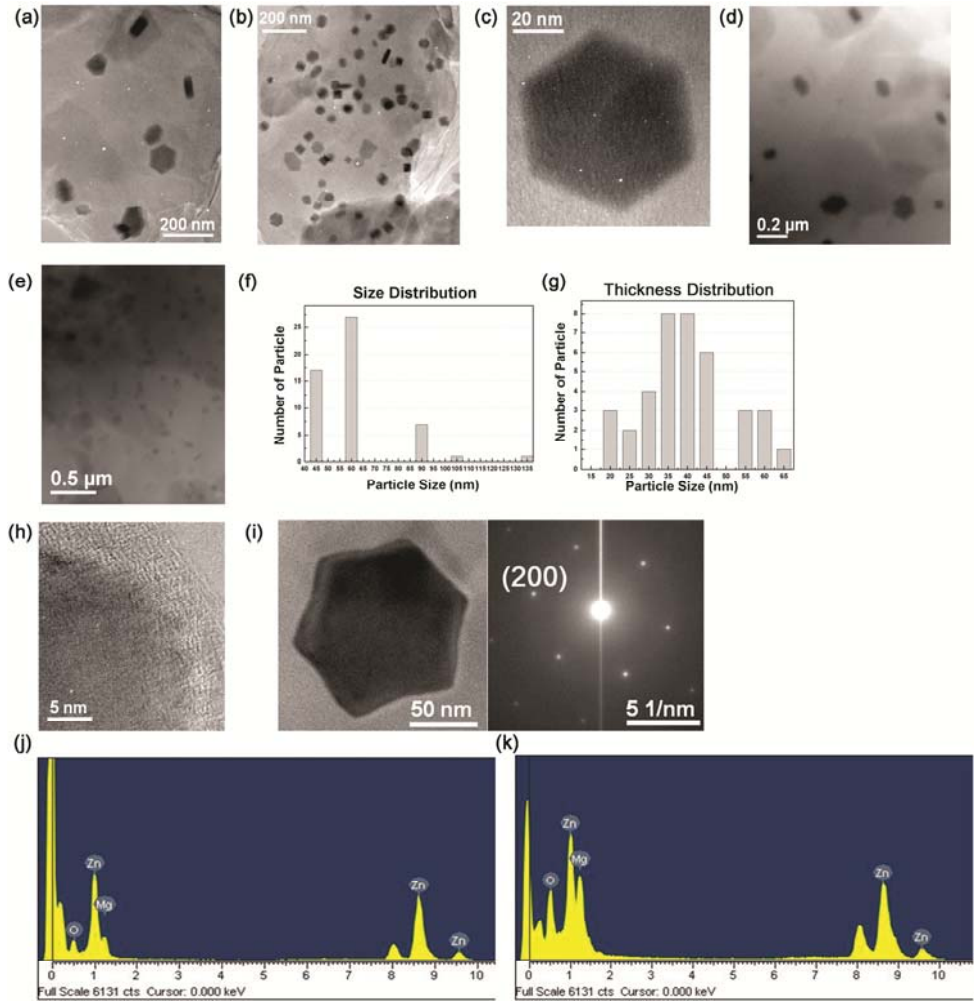

Figure 43. HRTEM images for a) Mg@SNU-90'a, b) Mg@SNU-90'b, c) a hexagonal shaped Mg nanocrystal of b, d) Mg@SNU-90'c, and e) Mg@SNU-90'c. f) Size distribution (diagonal length of hexagonal face) of Mg nanocrystals in a, b, and c. g) Thickness distribution of Mg nanocrystals. h) HRTEM image for Mg nanocrystals in Mg@SNU-90'b. i) A MgO nanocrystal resulted from exposure of Mg@SNU-90'b to air for 3 weeks, and its selected area electron diffraction pattern showing the lattice fringes with a separation of 2.1101 Å that is in agreement with (200) *d*-spacing of MgO (2.1061 Å, JCPDS 89-7746). j) EDS data for Mg@SNU-90'b. k) EDS data for Mg@SNU-90'c.

The XPS data of Mg@SNU-90' indicated that Mg^0 and Zn^{II} coexisted in the solid (Figure 44). The 2*p*3/2 and 2*p*1/2 peaks for ZnII appear at 1021 and 1044 eV,

respectively, similarly to the reported values of 1022 and 1045 eV.[148] A peak o f Mg at 50.6 eV is similar to the value (49.6 eV) reported previously for Mgo(2*p*).[149]

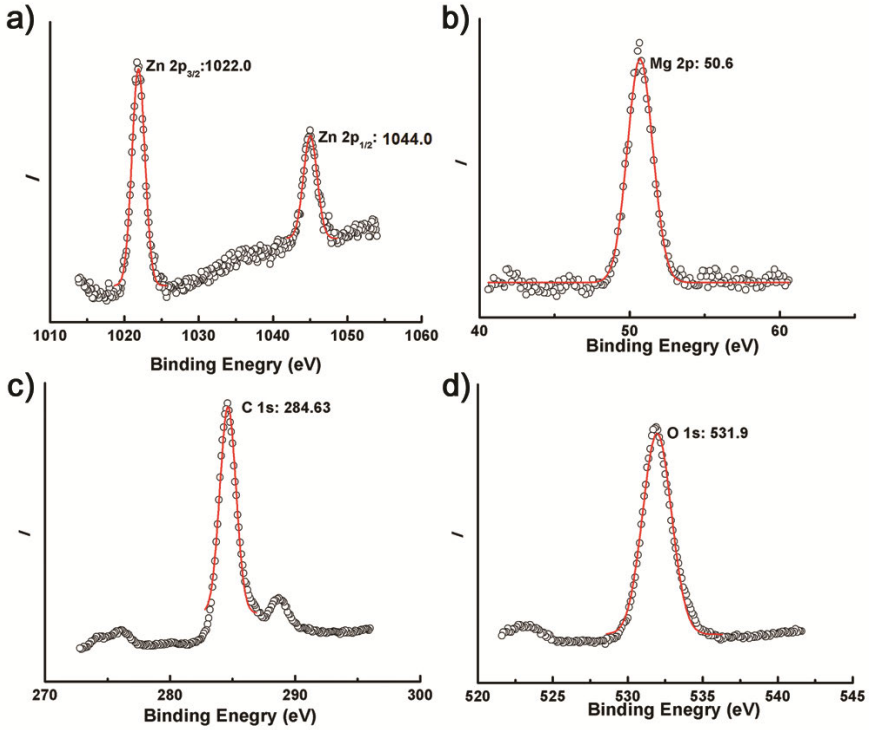

Figure 44. X-ray photoelectron spectra (XPS) of Mg @SNU-90'c. a) Peaks for Zn. b) Peaks for Mg. c) Peaks for carbon. d) Peaks for oxygen. The plots are fitted to Gaussian function. All Mg@**SNU-90**' samples loaded with different amounts of Mg nanocrystals show the same XPS data.

To verify that the Mg NCs were embedded inside the channels of the MOF, we performed electron tomography. From the TEM images that were collected with a 1° interval with the tilting angle of +40° ~ -40°, 3D images were constructed by using the IMOD program.[150] When the sample was tilted, the shape of a Mg NC was seen to change from hexagon to rectangle and from rectangle to hexagon, indicating that the Mg NCs were indeed embedded in the MOF (Figure 45).

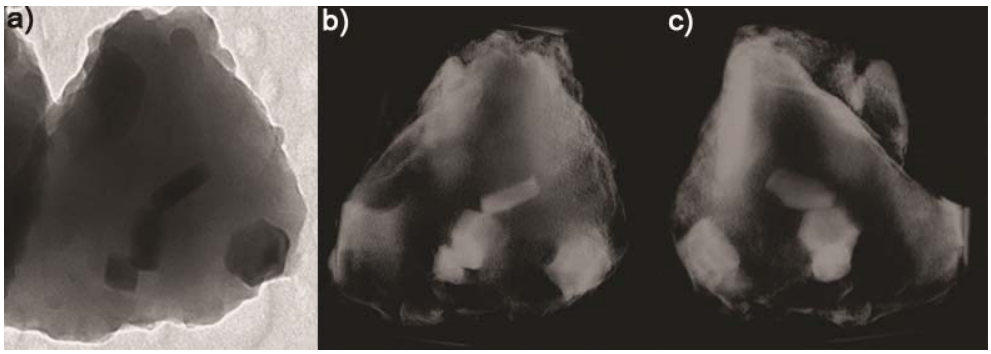

Figure 45. TEM and electron tomography images of Mg@SNU-90'b. a) TEM image. b) and c) Tomographically reconstructed images of Mg NCs embedded in SNU-90' at different angles.

The powder X-ray diffraction (PXRD) patterns showed that the structure of SNU-90' was maintained even after the formation of the Mg NCs, whose sizes were much larger than the channel size (12.9 Å x 9.6 Å) of the MOF (Figure 46). To understand this, we calculated the volume ratio of Mg NCs formed versus the network skeleton for Mg@SNU-90'c. Assuming that all Mg NCs destroyed the network skeleton, the Mg NCs would destroy a maximum 4.6 % of the network skeleton by volume. This value is too small to alter the PXRD pattern of the MOF. It was also previously reported that metal nanoparticles much bigger than the cavity sizes of the hosts were impregnated by maintaining the network structures.[13,14] The PXRD peaks of crystalline Mg should generally appear at 2θ = 32.2, 34.4, and 36.6° (Figure 47), but they were not observed for the present nanocomposites. The stronges peak of MOn exposure to air for 2 days, however, the PXRD pattern showed the peaks corresponding to MgO while retention of the framework structure of SNU-90' (Figure 46).

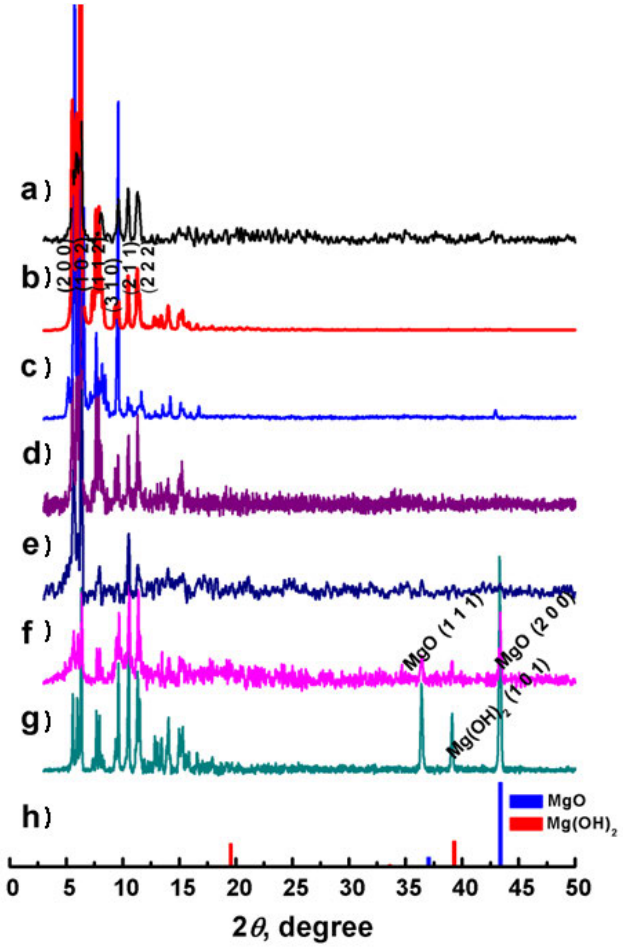

Figure 46. Powder X-ray diffraction patterns. a) SNU-90 as synthesized. b) The simulated PXRD pattern of SNU-90 derived from the single-crystal X-ray data. c) SNU-90' obtained from desolvation of SNU-90 by treatment with supercritical CO_2. d) Mg@SNU-90'b. e) Mg@SNU-90'c. f) Mg@SNU-90'c after air exposure for 2 days. g) Air exposed (for 2 days) sample of MgH_2@SNU-90' that resulted from the H_2 absorption in Mg@SNU-90'c. h) Reference peaks for MgO (JCPDS 89-7746) and $Mg(OH)_2$ (JCPDS 07-0239).

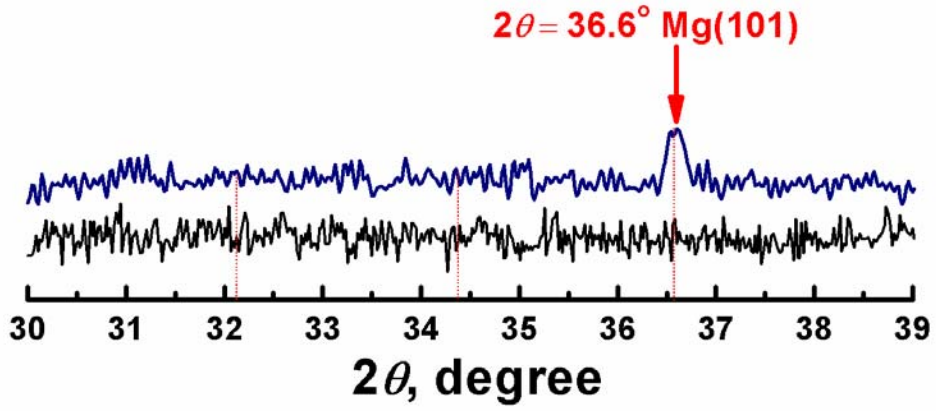

Figure 47. Powder X-ray diffraction patterns of as-synthesized SNU-90 (black) and Mg@SNU-90'c (blue) in the range of $2\theta = 30^{o} \sim 39°$.

Gas sorption analysis

The adsorption–desorption isotherms were measured for N_2 gas at 77 K and for H_2 gas at various temperatures on SNU-90', Mg@SNU-90'a, Mg@SNU-90'b, and Mg@SNU-90'c. The results are summarized in Table 7. The N_2 gas sorption isotherms of the four samples were type-I, characteristic of the microporous materials (Figure 48).

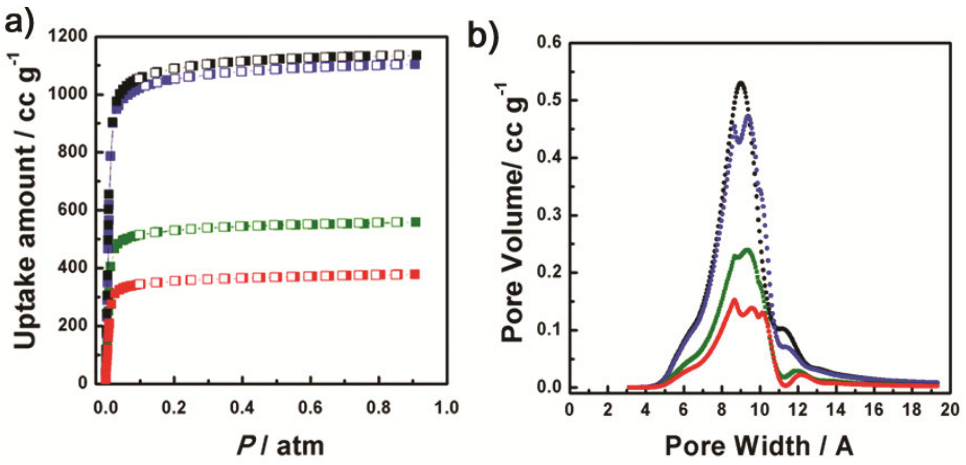

Figure 48. a)The N_2 gas sorption isotherms at 77 K. b) Pore size distributions estimated by Horvath-Kawazoe method. **SNU-90'** (black, ●), Mg@**SNU-90'a** (blue, ●), Mg@**SNU-90'b** (green, ●), and Mg@**SNU-90'c** (red, ●). Filled shape: adsorption.

Open shape: desorption.

Despite the presence of the NH_2 group in the ligand, the surface area, pore volume, and H_2 adsorption capacities of SNU-90' were similar to those of MOF-177.[143] Gas sorption data for various samples of Mg@SNU-90' showed that as the amount of Mg increased, the BET surface area, pore volume, and H_2 uptake capacity at 77 K and 1 atm decreased because Mg NCs occupied the surface and space of the pores in the MOF. At 298 K and high pressure, however, the H_2 uptake in Mg@SNU-90'a increased to 0.54 wt%, compared to 0.45 wt% in pristine SNU-90', suggesting that Mg NCs provide a positive effect on H_2 adsorption at 298 K (Figure 49).

Table 7. The N_2 and H_2 gas uptake data in SNU-90' and various samples of Mg@SNU-90'

compound		SNU-90'	Mg@SNU-90'a	Mg@SNU-90'b	Mg@SNU-90'c
Mg/Zn, mol/mol (wt%)		*N/A*	0.15 (1.26)	0.85 (6.52)	1.40 (10.5)
N_2 uptake, (cm^3g^{-1})		1135	1104	559	378
surface area, (m^2g^{-1})		4244[a] 4914[b]	4154[a] 4757[b]	2056[a] 2373[b]	1371[a] 1581[b]
pore volume, ($cm^{-3}g^{-1}$)		1.64[c]	1.47[c]	0.84[c]	0.36[c]
H_2 uptake, (wt%)	at 1 atm	1.21 (77 K) 0.74 (87 K)	1.24 (77 K) 0.65 (87 K)	0.72 (77 K) 0.40 (87 K)	0.60 (77 K) 0.47 (87 K)
	at high pressures (condition)	8.81 (77 K, 75 bar) 0.45 (298 K, 80 bar)	8.74 (77 K, 89 bar) 0.54 (298 K, 90 bar)	0.29 (473 K, 30 bar)	0.20 (323 K, 80 bar) 0.24 (415 K, 40 bar) 0.71 (473 K, 30 bar)
Q_{st}, (kJ mol^{-1})		4.55	5.68	7.24	11.6

[a]BET surface area, [b]Langmuir surface area, and [c]Pore volume estimated by using the Dubinin-Radushkevich (DR) equation

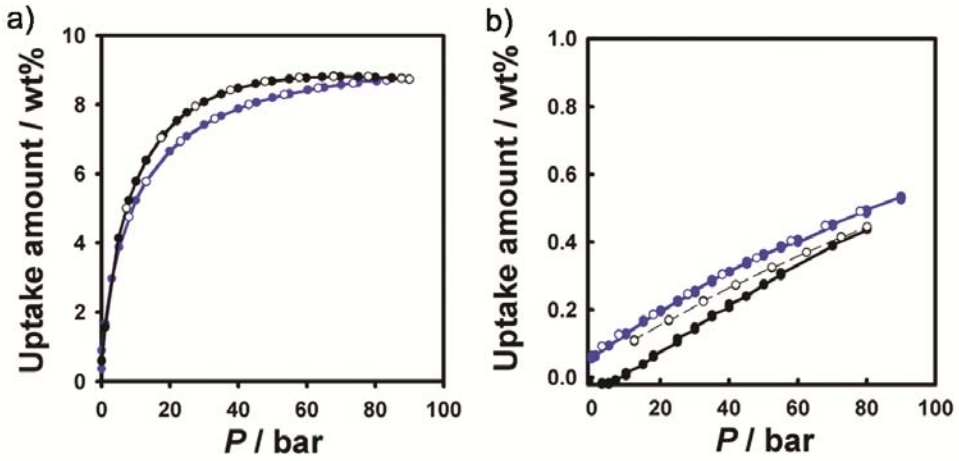

Figure 49. High pressure H_2 gas sorption isotherms for SNU-90' (black, ●) and Mg@SNU-90'a (violet, ●). a) At 77 K. b) At 298 K.

The zero-coverage isosteric heats of the H_2 adsorption, which were estimated from the H_2 adsorption isotherms measured at 77 K and 87 K, increased as the amount of Mg increased, up to 11.6 $kJmol^{-1}$ for Mg@SNU-90'c from 4.55 kJ mol^{-1} for SNU-90' (Figure 50).

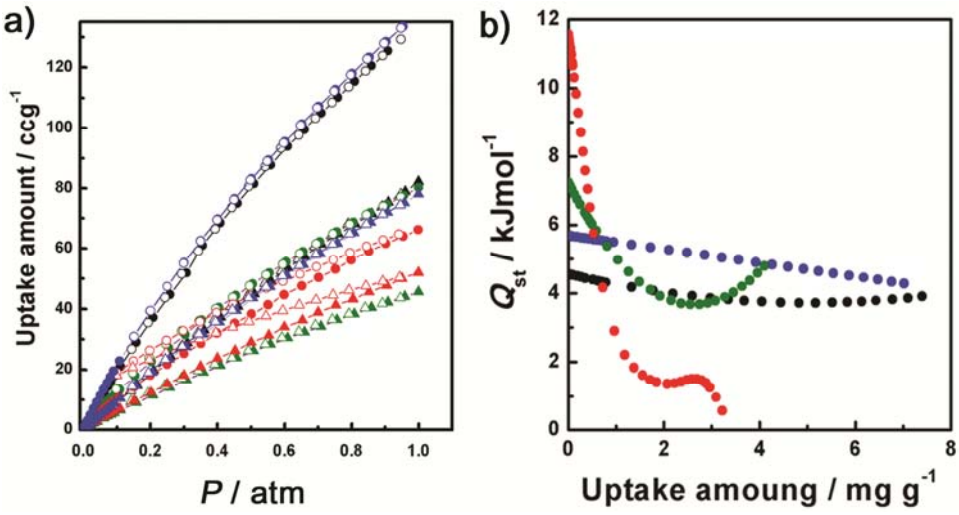

Figure 50. Physical adsorptions of H_2 in SNU-90' (black), Mg@SNU-90'a (blue), Mg@SNU-90'b (green), and Mg@SNU-90'c (red). a) The H_2 adsorption isotherms at 77 K (circles) and 87 K (triangles). Filled shape, adsorption; open shape, desorption. b) Isosteric heats of the H_2 adsorption. The samples of Mg@SNU-90'a, Mg@SNU-

90’b, and Mg@SNU-90’c contain 1.26 wt%, 6.52 wt%, and 10.5 wt%, respectively, of magnesium nanocrystals.

In order to observe the chemisorption ability of the embedded Mg NCs, we also measured the H_2 uptake in Mg@SNU-90’c at 323 K, 415 K, and 473 K under high pressures (Figure 51). Contrary to the physisorbed MOFs where H_2 uptake decreases at the elevated temperature, the H_2 chemisorption capacities of the present material increase as the temperature is raised.

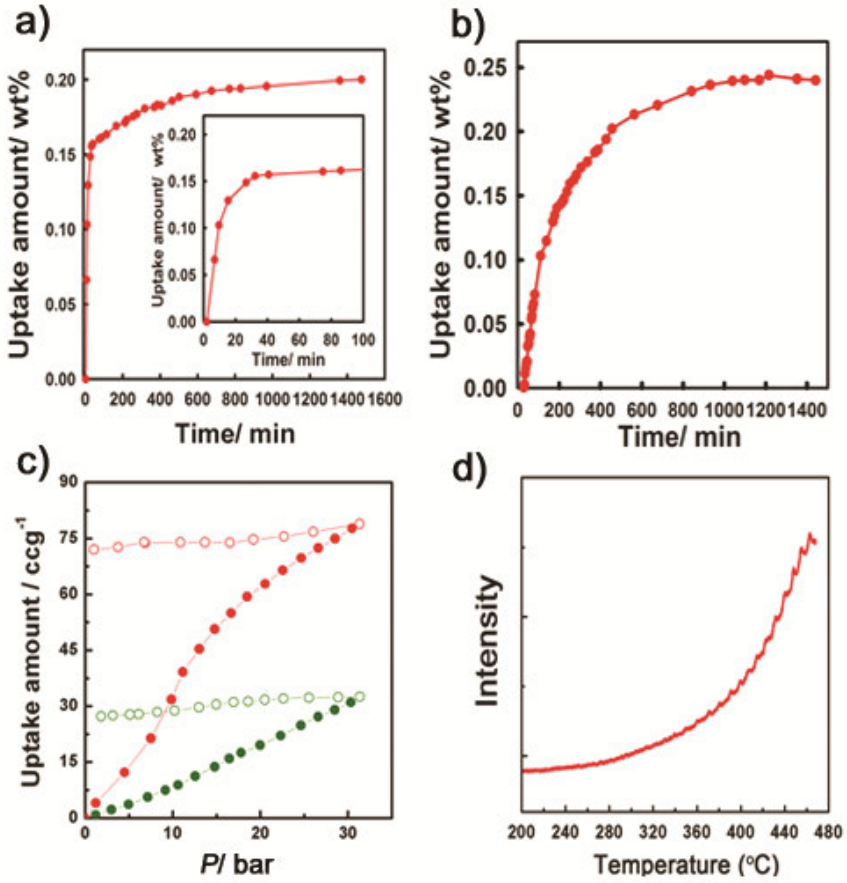

Figure 51. Chemical absorption of H_2 in Mg@SNU-90’c. a) The H_2 absorption kinetics at 325 K and 80 bar. Inset: data with a magnified time scale, b) The H_2 absorption kinetics at 415 K and 40 bar. c) The H_2 absorption isotherms at 473 K in Mg@SNU-90’b (green, ●) and Mg@SNU-90’c (red, ●). d) Temperature programmed

desorption mass spectroscopy (TPD-MS) data; m/e = 2, measured under argon.

The H_2 absorption capacities of Mg@SNU-90'c were 0.20 wt% at 323 K under the H_2 pressure of 80 bar, 0.24 wt% at 415 K under the H_2 pressure of 40 bar. At 473 K under 30 bar, the H_2 uptake capacity became 0.71 wt% (volumetric H_2 storage capacity, 3.1 g L^{-1}). This value for Mg@SNU-90'c is remarkably higher than that of Mg@SNU-90'b under the same condition (Table 7), despite that the former exhibits much lower surface area and pore volume due to the heavily loaded Mg. The fact that the H_2 uptake enhances with the elevated temperatures and the increased amount of Mg NCs confirms that the H_2 uptakes in Mg@SNU-90' at 323 K, 415 K, and 473 K are the chemisorption. These chemisorption temperatures are significantly lower (by > 200 K) than that (673 K under 10 bar) of bare Mg powder (50 - 100 μm).[151] If the H_2 uptake capacity of Mg alone is estimated from the data, it is 7.5 wt% at 473 K and 30 bar. Considering that the H_2 chemisorptioncapacity of pure Mg is 7.66 wt%, 99% of the Mg NCs in the sample chemisorbed H_2, which is much better than the results previously reported for Mg nanoparticles incorporated in a polymer[145] or in the form of bare Mg powder.[152]

The H_2 desorption properties of Mg @SNU-90'c were verified by the temperature programmed desorption mass spectroscopy (TPD-MS) (Figure 51d). The TPD-MS results indicated that H_2 was desorbed at T > 523 K and 1 atm. It should be noted that the intensities of H atom signals were exactly twice those of H_2 molecules (Figure 52). This suggests that all desorbed hydrogen sources were MgH_2, not from the MOF at all. The TG mass loss of Mg@SNU-90'c after H_2 absorption is also in good agreement with the TPD-MS data.

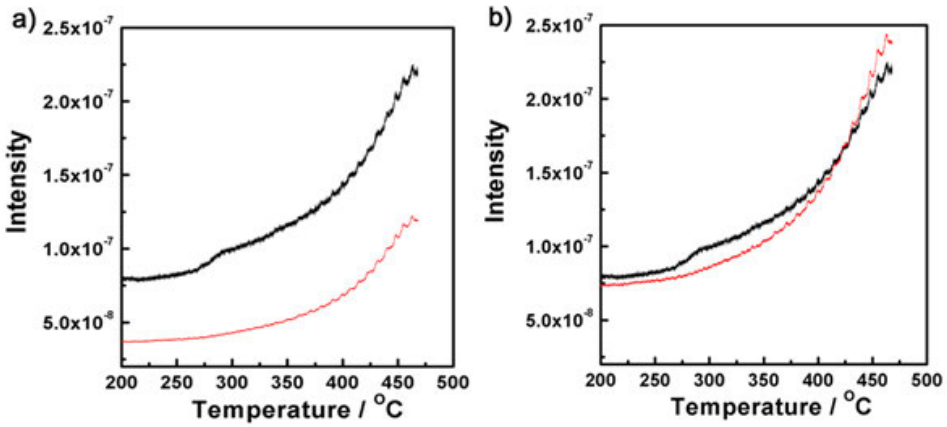

Figure 52. Temperature programmed desorption mass spectroscopy (TPD-MS) data for a) Mg @**SNU-90'c**; m/e = 1 (black, —), m/e = 2 (red, —). b) Comparison of the intensities for H atom (black, m/e = 1) and H_2 molecules (red, m/e = 2). The intensities of H atom are about two times greater than those of H_2 molecule.

The HRTEM images of Mg@SNU-90'c measured after the H_2 chemisorption at 473 K and 30 bar indicated that the crystal morphology of Mg was maintained but the crystal size was remarkably increased. The FFT pattern indicated the lattice fringe with a separation of 2.247 Å, which is in good agreement with the (110) *d*-spacing of β-MgH_2 (2.257 Å, JCPDS 35-1185, Figure 53). The MgH_2@SNU-90' shows the crystal size (diagonal length of hexagon) of average 142 ± 41 nm and thickness of average 83 ± 18 nm (Figure 53), ca. 2.3 times as large as those of Mg NCs. Considering that the volume of Mg should be increased only by 30% on hydride formation,30 this excessive expansion during the H_2 chemisorption process at high temperature and pressure can be explained by three dimensional Ostwald ripening, where the lager crystals take up the mobile atoms dissociated from the smaller crystals.[153] When MgH_2@SNU-90' was exposed to air, the PXRD data showed new peaks at 2θ = 36.8 and 42.8 deg, which correspond to MgO, and a new peak at 2θ = 38.0 deg that corresponds to $Mg(OH)_2$ (Figure 46).

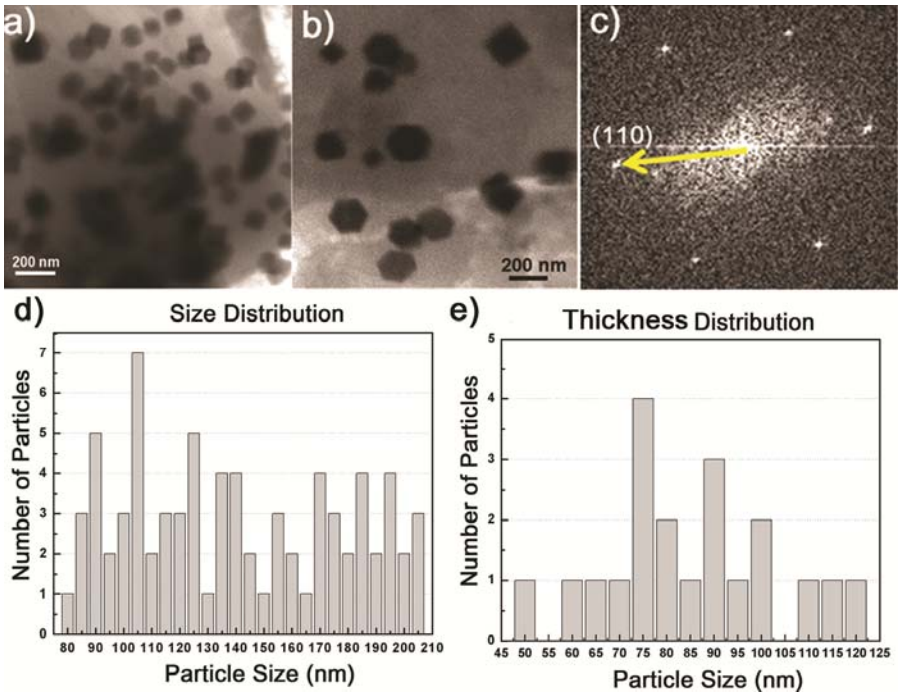

Figure 53. MgH_2 nanocrystals and distributions of the size and thickness of MgH_2 nanocrystals resulted from the H_2 absorption in Mg@SNU-90'c at 473 K and 30 bar. a), b) HRTEM images. c) Selected area electron diffraction (SAED) pattern of a crystal in b. A lattice fringe with a separation of 2.2474 Å is in agreement with (110) interplanar d-spacing of β-MgH_2 (2.2570 Å, JCPDS 35-1185). d) Size (diagonal length of hexagon): average 142 ± 41 nm. e) Thickness: average 83 ± 18 nm.

Thermogravimetric analysis (TGA) data of SNU-90 reveal 59.86.0% weight loss at 25 ^{o}C ~ 420 ^{o}C, which corresponds to the loss of all guest solvent molecules (calcd. 60.04 % for 22DMF and 9H_2O), and no chemical decomposition occurs up to 420 ^{o}C. The SNU-90' activated by supercritical CO_2 represents flat area up to decomposition temperature. (Figure 54)

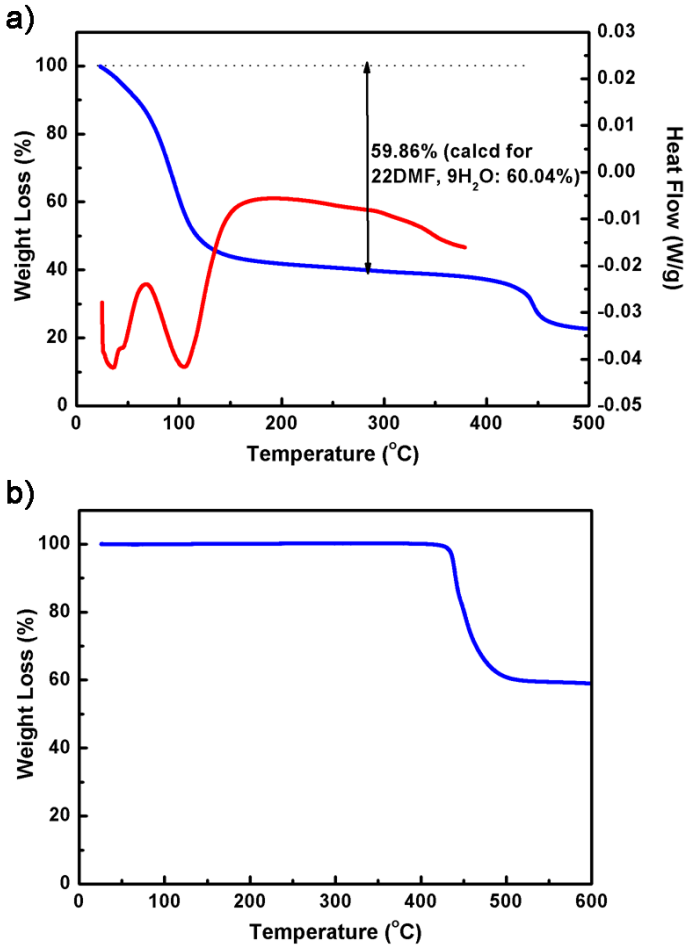

Figure 54. a). TGA/DSC traces for as-synthesized $[Zn_4O(atb)_2]\cdot 22DMF\cdot 9H_2O$ (SNU-90). b) TGA data of SNU-90' obtained from desolvation of SNU-90 by using supercritical CO_2.

The deposition of $MgCp_2$ in the MOF was confirmed by ^1H NMR The NMR spectra indicated the absence of cyclopentadiene (Cp) in the resulting nanocomposites (Figure. 55). Even after fabrication of Mg NPs and formation of MgH_2, Metal organic framework retains structure, and the organic ligand of SNU-90' was not hydrogenated as evidenced by the ^1H NMR spectra for the resulting nanocomposite that was dissolved in the mixture of DCl and d^6-DMSO.

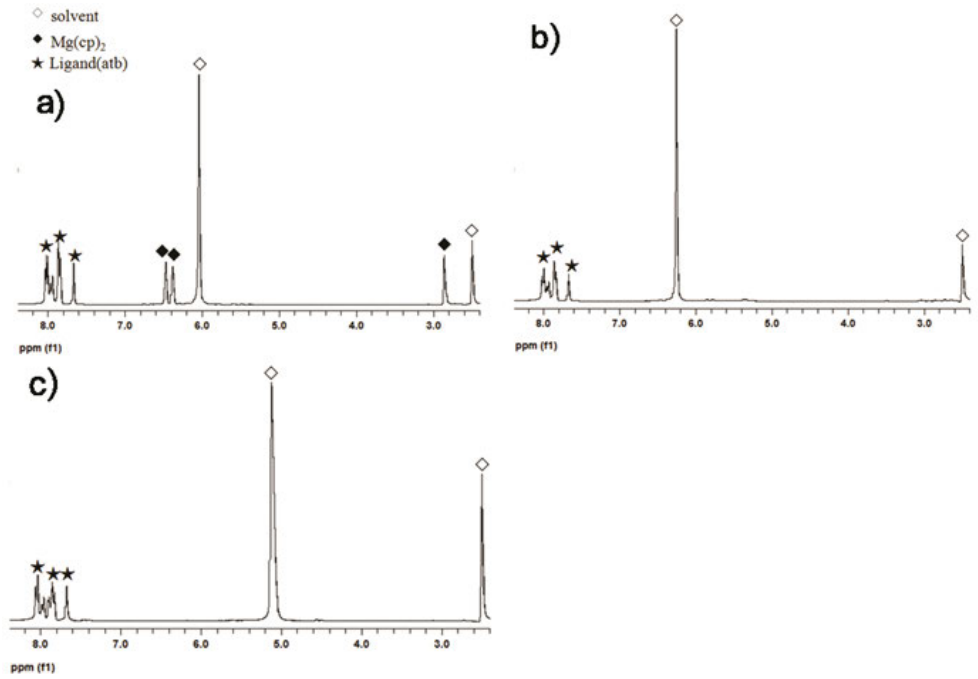

Figure 55. ^{1}H NMR spectra measured in the mixture of d_6-DMSO (dimethyl sulfoxide) and DCl. a) $MgCp_2$@SNU-90', b) Mg@SNU-90' that was obtained by thermal decomposition of $MgCp_2$@SNU-90'. The spectrum shows no peaks corresponding to Cp. c) MgH_2@SNU-90' resulted from the H_2 absorption in Mg@SNU-90'c at 473 K and 30 bar. The spectrum indicates that the organic ligand in SNU-90' was not hydrogenated.

To characterize the mechanism of MgH_2 formation, the H_2 uptake kinetic data for the initial 250 min of H_2 absorption in the Mg-vac@**SNU-90'** at 415 K and 40 bar were fitted to various Johnson-Mehl-Avrami (JMA) equations (eq. 21 - 24), where α is the hydrogenated fraction of Mg at time t and k is the phase transformation constant. The data were best fitted to equation (24) with $R^2 = 0.9920$, which suggests the diffusion controlled three-dimensional growth mechanism with decreasing interface velocity.

Table 8. Kinetic model equations applied for fitting the hydrogen absorption data.

Model equation		Description
$\alpha = kt$	(21)	Surface controlled (chemisorptions)[154]
$[-\ln(1-\alpha)]^{1/n} = kt$	(22)	n-dimensional growth of existing nuclei with constant interface velocity[155]
$1-(1-\alpha)^{1/n} = kt$	(23)	Contracting volume (CV)[154] n-dimensional growth with constant interface velocity
$1-(2\alpha/3)-(1-\alpha)^{2/3} = kt$	(24)	Contracting volume (CV) Three-dimensional growth diffusion controlled with decreasing interface velocity

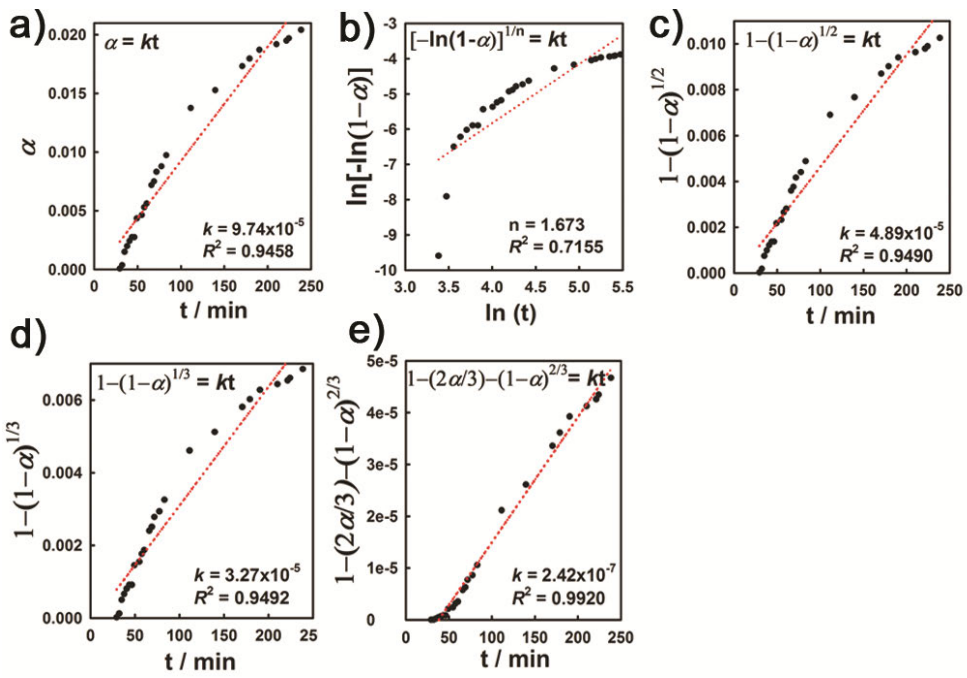

Figure 56. Kinetic models of hydride formation in Mg@SNU-90' nanocomposite. Hydrogen absorption data in Mg@SNU-90'c measured at 415 K and 40 bar (Figure 4b) (initial 250 min) were fit to Johnson-Mehl-Avrami (JMA) model equations.

The red dotted line represents a linear fit of the data to the equation. a) Surface

controlled (chemisorptions). b) n-dimensional growth of existing nuclei with constant interface velocity. c) 2-dimensional growth with constant interface velocity. d) 3-dimensional growth with constant interface velocity. e) 3-dimensional growth diffusion controlled with decreasing interface velocity.

Mg Nanocrystals in Porous Aromatic Framework (PAF-1)

The Mg nanocrystals (NCs) were fabricated in PAF-1 by chemical vapor deposition followed by chemical reduction (Mg@PAF-1).The sample of Mg@PAF-1 was loaded with 11.87 wt% of Mg contents. To varify the size and shape of Mg NCs, HR TEM is measured. In 10 min reduction sample, it represents a wide range of size distribution and irregular shape. The largest Mg NCs is rod shape with a length of 170.86 nm and width of 37.62 nm, however, the small size nanocrystals have 17.5 – 19.5.5 nm (Figure 57). This size is much smaller than that of Mg NCs@MOF. However, in overnight reduction sample, Mg NCs indicate hexagonal shape plate with diagonal length from 150 -400 nm.

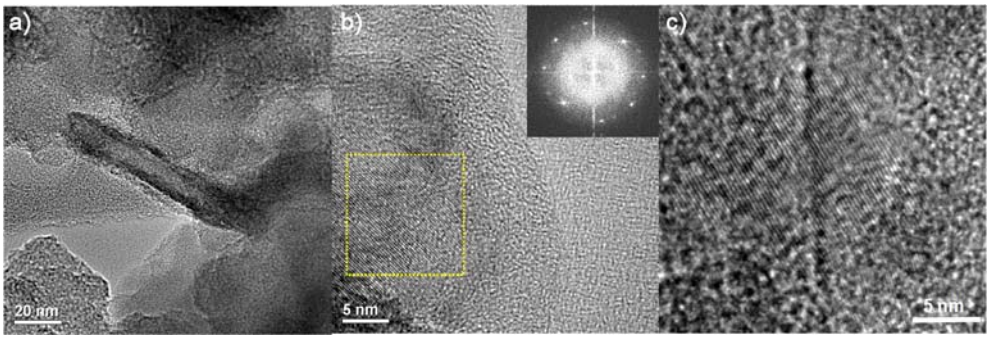

Figure 57. High resolution TEM images of Mg @PAF-1 (10 min reduction). a) rod shape MgNCs(170.86 x 37.62) b) and c) The small size of Mg NCs. Inset: selected area electron diffraction patter from yellow area.

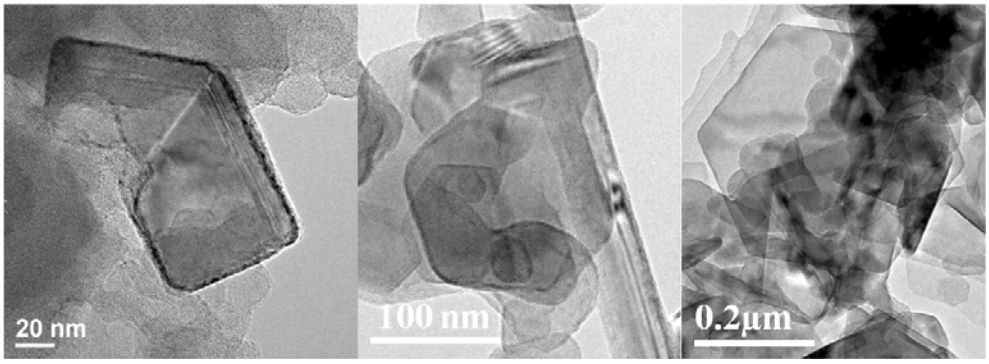

Figure 57. High resolution TEM images of Mg @PAF-1 (overnight reduction).

The powder X-ray diffraction (PXRD) patterns clearly showed formation of the Mg NCs. The PXRD peaks of crystalline Mg generally appear at 2θ = 32.2, 34.4, and 36.6°, they were definitely observed for the present nanocomposites. On exposure to air for 2 day, even after 10 days, the PXRD pattern of nanocomposit still retains crystalline Mg. It means that oxidation reaction by moistures does not happened in nanosized Mg due to the hydrophobic host porous material (Figure 58). It is a major difference from MOF incoporating Mg NCs. However, as the Mg@PAF-1 is immersed into H_2O directly, the peaks of $Mg(OH)_2$ are observed at at 18.29 ^{o} and 38.02 ^{o}.

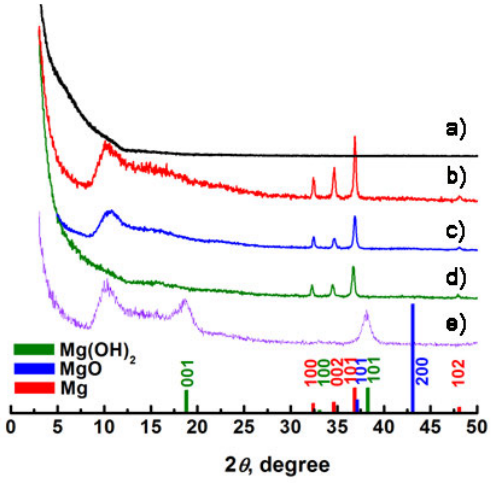

Figure 58. Powder X-ray diffraction patterns. a) After desolvation of PAF-1. b) Mg@PAF-1. c) Mg@PAF-1 after exposure to air for 2 days. d) Mg@PAF-1 after exposure to air for 10 days. e) after immersion of Mg@PAF-1 into water [$Mg(OH)_2$@PAF-1].

Gas sorption analysis

The adsorption–desorption isotherms were measured for N_2 gas at 77 K and for H_2 gas at 77 K and 87 K on PAF-1 and Mg@PAF-1. The N_2 gas sorption isotherms of two samples were type-I, characteristic of the microporous materials (Figure 59). The pristine PAF-1 represent the BET surface area of 5640 m^2g^{-1}. As the contents of Mg incorporated, the BET surface area, pore volume, and H_2 uptake capacity at 77 K and 1 atm decreased because Mg NCs occupied the surface and space of the pores in the PAF-1. The zero-coverage isosteric heats of the H_2 adsorption, which were estimated from the H_2 adsorption isotherms measured at 77 K and 87 K, increased as the amount of Mg increased, up to 4.0 $kJmol^{-1}$ for Mg@PAF-1 from 5.82 kJ mol^{-1} for PAF-1 (Figure 60). At low pressure less than 0.4 atm, Mg@PAF-1 indicate the higher H_2 uptake capacities than pristine PAF-1.

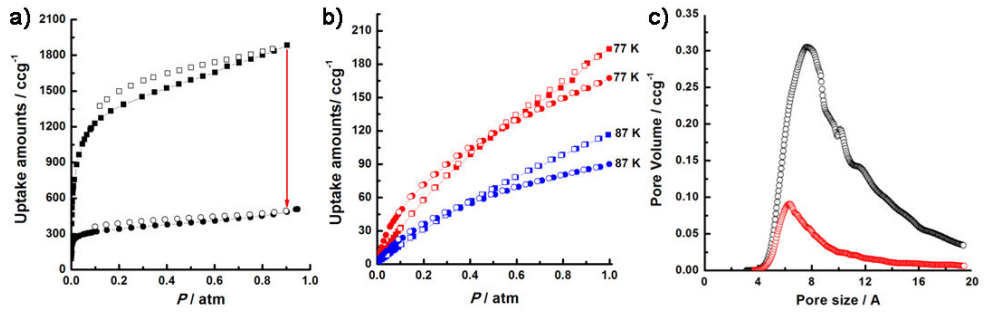

Figure 59. Gas sorption isotherm of N_2 and H_2 in PAF-1 (square) and Mg@PAF-1 (circle). a) The N_2 adsorption isotherms at 77 K. b) The H_2 adsorption isotherms at 77 K and 87 K. c) Pore size distribution of PAF-1 (black) and Mg@PAF-1 (red) (HK method). Filled shape, adsorption; open shape, desorption.

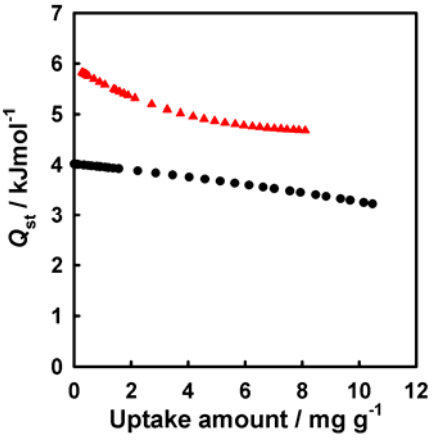

Figure 60. Isosteric heats of the H_2 adsorption. PAF-1(circle) and Mg@PAF-1 (triangle)

Table 9. The gas uptake data in PAF-1 and Mg@PAF-1.

Compound	PAF-1	Mg@PAF-1
Mg/Zn (wt%)	*N/A*	11.87
N_2 uptake, (cm^3g^{-1})	1885	506
S_{BET} (m^2g^{-1})	5640	1260.59
pore volume,	2.194	0.521

($cm^{-3}g^{-1}$) [a]			
H_2 uptake, (wt%)	at 1 atm	1.74 (77 K) 1.05 (87 K)	1.51 (77 K) 0.81 (87 K)
Q_{st}, (kJ mol^{-1})		4.0	5.82
CO_2 (mmol g^{-1})		51.06 (195 K) 2.24 (273 K) 1.26 (298 K)	50.62 (195 K) 2.17 (273 K) 1.11 (298 K)
CH_4, (wt%)		9.26 (195 K) 1.36 (273 K) 0.88 (298 K)	7.26 (195 K) 1.12 (273 K) 0.42 (298 K)

[a]Pore volume estimated by using the Dubinin-Radushkevich (DR) equation

II.5. Conclusion

We have reported for the first time simple method for fabrication of hexagonal-disk shaped magnesium nanocrystals (Mg NCs) within a MOF and COF. The fabrication of Mg nanocrystals inside MOFs and COF is unprecedented. The present nanocomposite is made by the thermal decomposition or chemical reduction of gas phase loaded air sensitive bis-cyclopentadienyl magnesium ($MgCp_2$), which is also unprecedented for production of nanosize Mg. The resulting Mg NCs@MOF is a hybrid hydrogen storage material that stores H_2 by both physical adsorption and chemisorption, exhibiting a synergistic effect to increase the isosteric heat of H_2 physisorption and to decrease the temperatures for chemi-sorption/desorption of H_2. In addion, as the Mg NCs is incoporated in PAF-1, it prevents Mg from oxidation by moisture. The present hybrid hydrogen storage material suggests a new strategy for H_2 storage and transport for the future. To develop the materials that are able to reach the DOE target, we are trying to further reduce the size of the Mg NCs and adjust the amount of loaded Mg in the selected physisorbed porous materials.

Supporting Information

Table II.S1. Crystallographic data for SNU-90

formula	$Zn_4\ C_{54}\ H_{24}\ N_2\ O_{13}$
crystal system	trigonal
space group	*P* -3 1c
fw	1170.23
a, Å	37.1796(6)
c, Å	29.9563(6)
V, Å3	35861.5(11)
Z	8
ρcalcd, g/cm3	0.433
temp, K	150
λ, Å	0.71073
μ, mm-1	0.547
GOF (F2)	1.070
F(000)	4688
reflections collected	56800
independent reflections	20255
	[*R*(int) = 0.1186]
completeness to θmax, %	98.3
data/parameters/restraints	20255 / 575 / 18
θ range for data collection, deg	1.10 to 24.79
diffraction limits (h, k, l)	$-43 \le h \le 43$
	$-37 \le k \le 37$
	$-21 \le l \le 35$
Refinement method	Full-matrix least-squares on F^2
R1a, wR2b [I>2σ(I)]	R_1 = 0.1149, wR_2 = 0.2760
R1 a, wR2b (all data)	R_1 = 0.1977, wR_2 = 0.3022
largest peak, hole, eÅ-3	0.472, -1.413

[a] $R = \Sigma||Fo| - |Fc||/\Sigma|Fo|$. [b] $wR(F^2) = [\Sigma w(Fo^2 - Fc^2)^2/\Sigma w(Fo^2)^2]^{1/2}$ where $w = 1/[\sigma^2(Fo^2) + (0.1227P)^2 + (0.00)P]$, $P = (Fo^2 + 2Fc^2)/3$. The residual electron densities were flattened by using *SQUEEZE* option of PLATON.

Table II.S2. bond lengths (Å) and angles (o) for SNU-90

C(28)-O(10)#1	1.216(6)	O(7A)-Zn(3)	1.926(8)
C(28)-O(10)	1.216(6)	O(8B)-C(20)	1.374(13)
C(28)-C(29)	1.502(12)	O(8B)-Zn(4)	1.885(11)
C(29)-C(30)#1	1.320(11)	O(8A)-C(20)#1	1.370(11)
C(29)-C(30)	1.320(11)	O(8A)-Zn(5)	1.920(7)
C(30)-C(31)	1.523(13)	O(5B)-C(27)	1.210(11)
C(31)-C(32)	1.272(10)	O(5B)-Zn(5)	1.942(9)
C(32)-C(31)#1	1.272(10)	O(9A)-Zn(3)	1.983(8)
C(32)-C(33)	1.572(11)	O(9B)-Zn(6)	1.843(10)
C(33)-C(34)	1.429(6)	O(10)-Zn(5)	1.951(7)
C(33)-C(34)#2	1.429(6)	O(10)-Zn(4)	2.392(8)
C(34)-N(3)	1.276(14)	C(23B)-C(22B)	1.32(3)
C(34)-C(33)#3	1.429(6)	C(23B)-C(24)	1.39(2)
C(35)-O(9A)#1	1.232(8)	C(26B)-C(21)	1.277(15)
C(35)-O(9A)	1.232(8)	C(26B)-C(25B)	1.38(3)
C(35)-O(9B)#1	1.292(11)	C(22B)-C(21)	1.44(2)
C(35)-O(9B)	1.292(11)	C(25B)-C(24)	1.25(2)
C(35)-C(36)	1.426(11)	N(1C)-C(13)	1.397(19)
C(36)-C(37)	1.227(10)	N(1B)-C(9)	1.525(14)
C(36)-C(37)#1	1.227(10)	C(1)-O(2A)	1.089(9)
C(37)-C(38)	1.509(14)	C(1)-O(2B)	1.185(9)
C(38)-C(39)	1.302(11)	C(1)-O(3A)	1.315(11)
C(39)-C(38)#1	1.302(11)	C(1)-O(3B)	1.390(12)
C(39)-C(40)	1.521(13)	C(1)-C(2)	1.580(9)
C(40)-C(41)#4	1.378(6)	C(2)-C(7A)	1.227(7)
C(40)-C(41)	1.378(6)	C(2)-C(3B)	1.261(6)
C(41)-N(4)	1.167(10)	C(2)-C(7B)	1.346(6)
C(41)-C(40)#5	1.378(6)	C(2)-C(3A)	1.404(7)
O(7B)-C(20)	1.160(19)	C(3A)-C(4A)	1.5257
O(7B)-Zn(6)	1.945(16)	C(4A)-C(5)	1.455(8)

O(7A)-C(20)	1.127(12)	C(5)-C(4B)	1.287(8)
C(5)-C(6B)	1.390(7)	O(1)-Zn(2)	1.822(2)
C(5)-C(6A)	1.500(7)	O(1)-Zn(1)#8	1.9901(12)
C(5)-C(8)	1.523(9)	O(1)-Zn(1)	1.9901(12)
C(6A)-C(7A)	1.5395	O(1)-Zn(1)#4	1.9901(12)
C(3B)-C(4B)	1.5379	O(1)-Zn(1)#9	1.9901(12)
C(6B)-C(7B)	1.5032	O(1)-Zn(1)#10	1.9901(12)
C(8)-C(13)	1.446(9)	O(1)-Zn(1)#11	1.9901(12)
C(8)-C(9)	1.457(10)	O(2A)-O(3B)	1.338(11)
C(13)-C(12)#6	1.474(10)	O(2A)-Zn(1)	1.938(8)
C(12)-C(11)#7	1.440(10)	O(2B)-Zn(2)	1.950(10)
C(12)-C(14)	1.469(9)	O(3A)-Zn(1)#11	1.895(8)
C(12)-C(13)#7	1.474(10)	O(3B)-Zn(1)#9	1.869(9)
C(11)-C(12)#6	1.440(10)	O(3B)-Zn(1)	2.335(9)
C(11)-C(10)	1.448(9)	O(4)-Zn(4)	1.915(3)
C(11)-N(1)	1.485(16)	O(4)-Zn(4)#1	1.915(3)
C(10)-C(9)	1.458(9)	O(4)-Zn(3)#1	1.928(3)
C(10)-C(21)	1.479(9)	O(4)-Zn(3)	1.928(3)
C(14)-C(15)	1.308(12)	O(4)-Zn(5)	1.949(3)
C(14)-C(19)	1.342(13)	O(4)-Zn(5)#1	1.949(3)
C(15)-C(16)	1.484(14)	O(4)-Zn(6)#1	1.976(3)
C(16)-C(17)	1.187(11)	O(4)-Zn(6)	1.976(3)
C(17)-C(18)	1.391(13)	O(6B)-Zn(3)	1.934(7)
C(17)-C(20)	1.533(10)	O(5A)-Zn(4)	1.987(13)
C(18)-C(19)	1.482(13)	O(6A)-C(27)#1	1.418(13)
C(20)-O(8A)#1	1.370(10)	O(6A)-Zn(6)	1.921(13)
C(27)-O(5A)	0.983(11)	Zn(1)-O(3B)#9	1.869(9)
C(27)-O(6B)	1.292(10)	Zn(1)-O(3A)#4	1.895(8)
C(27)-O(6A)#1	1.418(13)	Zn(1)-Zn(1)#9	2.189(2)
C(27)-C(24)	1.565(10)	Zn(1)-Zn(1)#8	2.702(2)
C(24)-C(23A)	1.258(15)	Zn(1)-Zn(1)#4	3.143(2)
C(24)-C(25A)	1.438(14)	Zn(1)-Zn(1)#11	3.143(2)

C(21)-C(22A)	1.285(14)	Zn(2)-O(2B)#4	1.950(10)
C(21)-C(26A)	1.430(15)	Zn(2)-O(2B)#11	1.950(10)
C(25A)-C(26A)	1.466(19)	Zn(4)-Zn(6)	3.141(2)
C(22A)-C(23A)	1.36(2)	Zn(5)-Zn(5)#1	3.134(2)
O(1)-Zn(2)#8	1.822(2)	Zn(6)-Zn(6)#1	3.112(4)

O(10)#1-C(28)-O(10)	129.5(11)	C(39)-C(38)-C(37)	116.3(12)
O(10)#1-C(28)-C(29)	115.3(6)	C(38)#1-C(39)-C(38)	120.0(16)
O(10)-C(28)-C(29)	115.3(6)	C(38)#1-C(39)-C(40)	120.0(8)
C(30)#1-C(29)-C(30)	123.3(14)	C(38)-C(39)-C(40)	120.0(8)
C(30)#1-C(29)-C(28)	118.4(7)	C(41)#4-C(40)-C(41)	120.4(11)
C(30)-C(29)-C(28)	118.4(7)	C(41)#4-C(40)-C(39)	119.8(6)
C(29)-C(30)-C(31)	116.2(11)	C(41)-C(40)-C(39)	119.8(5)
C(32)-C(31)-C(30)	120.5(10)	N(4)-C(41)-C(40)#5	120.2(5)
C(31)-C(32)-C(31)#1	122.1(13)	N(4)-C(41)-C(40)	120.2(5)
C(31)-C(32)-C(33)	118.9(7)	C(40)#5-C(41)-C(40)	119.6(11)
C(31)#1-C(32)-C(33)	118.9(7)	C(20)-O(7B)-Zn(6)	127.0(11)
C(34)-C(33)-C(34)#2	127.0(10)	C(20)-O(7A)-Zn(3)	128.3(8)
C(34)-C(33)-C(32)	116.5(5)	C(20)-O(8B)-Zn(4)	130.3(8)
C(34)#2-C(33)-C(32)	116.5(5)	C(20)#1-O(8A)-Zn(5)	131.0(6)
N(3)-C(34)-C(33)#3	123.5(5)	C(27)-O(5B)-Zn(5)	128.1(7)
N(3)-C(34)-C(33)	123.5(5)	C(35)-O(9A)-Zn(3)	133.3(7)
C(33)#3-C(34)-C(33)	113.0(10)	C(35)-O(9B)-Zn(6)	129.8(8)
O(9A)#1-C(35)-O(9A)	119.9(10)	C(28)-O(10)-Zn(5)	125.1(7)
O(9A)#1-C(35)-O(9B)#1	47.8(5)	C(28)-O(10)-Zn(4)	107.3(7)
O(9A)-C(35)-O(9B)#1	102.4(7)	Zn(5)-O(10)-Zn(4)	51.83(18)
O(9A)#1-C(35)-O(9B)	102.4(7)	C(22B)-C(23B)-C(24)	121(2)
O(9A)-C(35)-O(9B)	47.8(5)	C(21)-C(26B)-C(25B)	130(2)
O(9B)#1-C(35)-O(9B)	125.6(12)	C(23B)-C(22B)-C(21)	117(2)
O(9A)#1-C(35)-C(36)	120.0(5)	C(24)-C(25B)-C(26B)	112(2)
O(9A)-C(35)-C(36)	120.0(5)	O(2A)-C(1)-O(2B)	83.1(8)
O(9B)#1-C(35)-C(36)	117.2(6)	O(2A)-C(1)-O(3A)	134.2(8)

O(9B)-C(35)-C(36)	117.2(6)	O(2B)-C(1)-O(3A)	63.6(6)
C(37)-C(36)-C(37)#1	115.0(12)	O(2A)-C(1)-O(3B)	64.0(8)
C(37)-C(36)-C(35)	122.5(6)	O(2B)-C(1)-O(3B)	118.0(8)
C(37)#1-C(36)-C(35)	122.5(6)	O(3A)-C(1)-O(3B)	103.6(7)
C(36)-C(37)-C(38)	125.8(11)	O(2A)-C(1)-C(2)	115.8(7)
O(2B)-C(1)-C(2)	125.1(9)	C(13)-C(8)-C(9)	125.1(7)
O(3A)-C(1)-C(2)	109.1(7)	C(13)-C(8)-C(5)	116.6(7)
O(3B)-C(1)-C(2)	116.5(8)	C(9)-C(8)-C(5)	118.3(7)
C(7A)-C(2)-C(3B)	79.7(4)	N(1C)-C(13)-C(8)	125.3(12)
C(7A)-C(2)-C(7B)	74.1(4)	N(1C)-C(13)-C(12)#6	121.0(12)
C(3B)-C(2)-C(7B)	122.3(5)	C(8)-C(13)-C(12)#6	113.4(8)
C(7A)-C(2)-C(3A)	131.0(5)	C(11)#7-C(12)-C(14)	117.9(7)
C(3B)-C(2)-C(3A)	72.5(3)	C(11)#7-C(12)-C(13)#7	124.4(7)
C(7B)-C(2)-C(3A)	87.6(4)	C(14)-C(12)-C(13)#7	117.6(8)
C(7A)-C(2)-C(1)	117.7(6)	C(12)#6-C(11)-C(10)	119.1(8)
C(3B)-C(2)-C(1)	118.1(6)	C(12)#6-C(11)-N(1)	119.4(10)
C(7B)-C(2)-C(1)	119.6(6)	C(10)-C(11)-N(1)	120.7(10)
C(3A)-C(2)-C(1)	111.0(6)	C(11)-C(10)-C(9)	119.9(8)
C(2)-C(3A)-C(4A)	113.5(3)	C(11)-C(10)-C(21)	118.7(7)
C(5)-C(4A)-C(3A)	113.8(3)	C(9)-C(10)-C(21)	121.5(7)
C(4B)-C(5)-C(6B)	130.1(6)	C(8)-C(9)-C(10)	118.1(8)
C(4B)-C(5)-C(4A)	64.1(3)	C(8)-C(9)-N(1B)	119.6(9)
C(6B)-C(5)-C(4A)	90.7(5)	C(10)-C(9)-N(1B)	121.8(9)
C(4B)-C(5)-C(6A)	84.8(4)	C(15)-C(14)-C(19)	118.1(10)
C(6B)-C(5)-C(6A)	76.9(3)	C(15)-C(14)-C(12)	124.7(10)
C(4A)-C(5)-C(6A)	126.5(5)	C(19)-C(14)-C(12)	117.0(10)
C(4B)-C(5)-C(8)	116.6(6)	C(14)-C(15)-C(16)	120.2(12)
C(6B)-C(5)-C(8)	113.0(6)	C(17)-C(16)-C(15)	123.2(12)
C(4A)-C(5)-C(8)	114.7(6)	C(16)-C(17)-C(18)	119.1(11)
C(6A)-C(5)-C(8)	118.0(6)	C(16)-C(17)-C(20)	121.2(10)
C(5)-C(6A)-C(7A)	107.5(3)	C(18)-C(17)-C(20)	117.5(9)
C(2)-C(7A)-C(6A)	123.8(3)	C(17)-C(18)-C(19)	117.2(11)

C(2)-C(3B)-C(4B)	124.5(3)	C(14)-C(19)-C(18)	119.6(13)
C(5)-C(4B)-C(3B)	110.5(3)	O(7A)-C(20)-O(7B)	48.7(9)
C(5)-C(6B)-C(7B)	113.5(3)	O(7A)-C(20)-O(8A)#1	127.4(8)
C(2)-C(7B)-C(6B)	118.2(3)	O(7B)-C(20)-O(8A)#1	99.2(11)
O(7A)-C(20)-O(8B)	78.0(10)	C(22A)-C(21)-C(22B)	59.4(10)
O(7B)-C(20)-O(8B)	116.3(15)	C(26A)-C(21)-C(22B)	95.1(11)
O(8A)#1-C(20)-O(8B)	86.4(7)	C(26B)-C(21)-C(10)	129.0(16)
O(7A)-C(20)-C(17)	119.5(10)	C(22A)-C(21)-C(10)	122.6(11)
O(7B)-C(20)-C(17)	117.5(11)	C(26A)-C(21)-C(10)	118.4(10)
O(8A)#1-C(20)-C(17)	112.1(9)	C(22B)-C(21)-C(10)	115.6(14)
O(8B)-C(20)-C(17)	118.3(8)	C(24)-C(25A)-C(26A)	113.7(12)
O(5A)-C(27)-O(5B)	66.3(12)	C(21)-C(26A)-C(25A)	116.7(11)
O(5A)-C(27)-O(6B)	81.6(13)	C(21)-C(22A)-C(23A)	127.2(15)
O(5B)-C(27)-O(6B)	128.1(9)	C(24)-C(23A)-C(22A)	115.6(14)
O(5A)-C(27)-O(6A)#1	121.9(14)	Zn(2)#8-O(1)-Zn(2)	180.000(1)
O(5B)-C(27)-O(6A)#1	71.4(7)	Zn(2)#8-O(1)-Zn(1)#8	65.75(4)
O(6B)-C(27)-O(6A)#1	95.4(8)	Zn(2)-O(1)-Zn(1)#8	114.25(4)
O(5A)-C(27)-C(24)	125.4(12)	Zn(2)#8-O(1)-Zn(1)	114.25(4)
O(5B)-C(27)-C(24)	114.8(9)	Zn(2)-O(1)-Zn(1)	65.75(4)
O(6B)-C(27)-C(24)	117.0(8)	Zn(1)#8-O(1)-Zn(1)	85.50(7)
O(6A)#1-C(27)-C(24)	107.6(9)	Zn(2)#8-O(1)-Zn(1)#4	114.25(4)
C(25B)-C(24)-C(23A)	80.4(15)	Zn(2)-O(1)-Zn(1)#4	65.75(4)
C(25B)-C(24)-C(23B)	123.5(17)	Zn(1)#8-O(1)-Zn(1)#4	66.73(7)
C(23A)-C(24)-C(23B)	63.8(11)	Zn(1)-O(1)-Zn(1)#4	104.30(4)
C(25B)-C(24)-C(25A)	72.5(15)	Zn(2)#8-O(1)-Zn(1)#9	65.75(4)
C(23A)-C(24)-C(25A)	127.1(12)	Zn(2)-O(1)-Zn(1)#9	114.25(4)
C(23B)-C(24)-C(25A)	95.2(11)	Zn(1)#8-O(1)-Zn(1)#9	104.30(4)
C(25B)-C(24)-C(27)	115.7(16)	Zn(1)-O(1)-Zn(1)#9	66.73(7)
C(23A)-C(24)-C(27)	121.0(11)	Zn(1)#4-O(1)-Zn(1)#9	168.42(6)
C(23B)-C(24)-C(27)	119.9(13)	Zn(2)#8-O(1)-Zn(1)#10	65.75(4)
C(25A)-C(24)-C(27)	111.6(9)	Zn(2)-O(1)-Zn(1)#10	114.25(4)
C(26B)-C(21)-C(22A)	75.6(13)	Zn(1)#8-O(1)-Zn(1)#10	104.30(4)

C(26B)-C(21)-C(26A)	66.6(12)	Zn(1)-O(1)-Zn(1)#10	168.42(6)
C(22A)-C(21)-C(26A)	119.1(12)	Zn(1)#4-O(1)-Zn(1)#10	85.50(7)
C(26B)-C(21)-C(22B)	114.2(17)	Zn(1)#9-O(1)-Zn(1)#10	104.30(4)
Zn(2)#8-O(1)-Zn(1)#11	114.25(4)	Zn(3)-O(4)-Zn(5)#1	109.47(4)
Zn(2)-O(1)-Zn(1)#11	65.75(4)	Zn(5)-O(4)-Zn(5)#1	107.0(2)
Zn(1)#8-O(1)-Zn(1)#11	168.42(6)	Zn(4)-O(4)-Zn(6)#1	110.32(8)
Zn(1)-O(1)-Zn(1)#11	104.30(4)	Zn(4)#1-O(4)-Zn(6)#1	107.65(7)
Zn(1)#4-O(1)-Zn(1)#11	104.30(4)	Zn(3)#1-O(4)-Zn(6)#1	56.72(10)
Zn(1)#9-O(1)-Zn(1)#11	85.50(7)	Zn(3)-O(4)-Zn(6)#1	81.25(14)
Zn(1)#10-O(1)-Zn(1)#11	66.73(7)	Zn(5)-O(4)-Zn(6)#1	76.28(6)
C(1)-O(2A)-O(3B)	69.0(8)	Zn(5)#1-O(4)-Zn(6)#1	166.09(6)
C(1)-O(2A)-Zn(1)	125.9(7)	Zn(4)-O(4)-Zn(6)	107.65(7)
O(3B)-O(2A)-Zn(1)	89.0(6)	Zn(4)#1-O(4)-Zn(6)	110.32(7)
C(1)-O(2B)-Zn(2)	134.9(7)	Zn(3)#1-O(4)-Zn(6)	81.25(14)
C(1)-O(3A)-Zn(1)#11	124.7(6)	Zn(3)-O(4)-Zn(6)	56.72(10)
O(2A)-O(3B)-C(1)	47.0(5)	Zn(5)-O(4)-Zn(6)	166.09(6)
O(2A)-O(3B)-Zn(1)#9	117.6(7)	Zn(5)#1-O(4)-Zn(6)	76.28(6)
C(1)-O(3B)-Zn(1)#9	135.1(7)	Zn(6)#1-O(4)-Zn(6)	103.9(2)
O(2A)-O(3B)-Zn(1)	56.1(5)	C(27)-O(6B)-Zn(3)	130.3(6)
C(1)-O(3B)-Zn(1)	90.3(6)	C(27)-O(5A)-Zn(4)	132.5(13)
Zn(1)#9-O(3B)-Zn(1)	61.6(2)	C(27)#1-O(6A)-Zn(6)	128.9(9)
Zn(4)-O(4)-Zn(4)#1	116.3(2)	O(3B)#9-Zn(1)-O(3A)#4	106.6(4)
Zn(4)-O(4)-Zn(3)#1	166.39(8)	O(3B)#9-Zn(1)-O(2A)	107.7(4)
Zn(4)#1-O(4)-Zn(3)#1	68.15(6)	O(3A)#4-Zn(1)-O(2A)	111.2(4)
Zn(4)-O(4)-Zn(3)	68.15(6)	O(3B)#9-Zn(1)-O(1)	104.9(3)
Zn(4)#1-O(4)-Zn(3)	166.39(7)	O(3A)#4-Zn(1)-O(1)	112.5(3)
Zn(3)#1-O(4)-Zn(3)	110.7(2)	O(2A)-Zn(1)-O(1)	113.5(3)
Zn(4)-O(4)-Zn(5)	60.23(10)	O(3B)#9-Zn(1)-Zn(1)#9	69.8(3)
Zn(4)#1-O(4)-Zn(5)	82.45(14)	O(3A)#4-Zn(1)-Zn(1)#9	165.0(3)
Zn(3)#1-O(4)-Zn(5)	109.47(4)	O(2A)-Zn(1)-Zn(1)#9	83.6(3)
Zn(3)-O(4)-Zn(5)	110.07(4)	O(1)-Zn(1)-Zn(1)#9	56.64(3)
Zn(4)-O(4)-Zn(5)#1	82.45(14)	O(3B)#9-Zn(1)-O(3B)	90.9(4)

Zn(4)#1-O(4)-Zn(5)#1	60.23(10)	O(3A)#4-Zn(1)-O(3B)	146.1(4)
Zn(3)#1-O(4)-Zn(5)#1	110.07(4)	O(2A)-Zn(1)-O(3B)	34.9(3)
O(1)-Zn(1)-O(3B)	89.7(2)	O(8B)-Zn(4)-O(4)	110.4(4)
Zn(1)#9-Zn(1)-O(3B)	48.7(3)	O(8B)-Zn(4)-O(5A)	110.8(7)
O(3B)#9-Zn(1)-Zn(1)#8	76.5(3)	O(4)-Zn(4)-O(5A)	110.9(4)
O(3A)#4-Zn(1)-Zn(1)#8	85.8(3)	O(8B)-Zn(4)-O(10)	126.2(4)
O(2A)-Zn(1)-Zn(1)#8	159.6(3)	O(4)-Zn(4)-O(10)	95.0(2)
O(1)-Zn(1)-Zn(1)#8	47.25(3)	O(5A)-Zn(4)-O(10)	102.1(5)
Zn(1)#9-Zn(1)-Zn(1)#8	79.21(7)	O(8B)-Zn(4)-Zn(6)	74.7(3)
O(3B)-Zn(1)-Zn(1)#8	127.1(3)	O(4)-Zn(4)-Zn(6)	36.84(7)
O(3B)#9-Zn(1)-Zn(1)#4	119.6(3)	O(5A)-Zn(4)-Zn(6)	117.7(4)
O(3A)#4-Zn(1)-Zn(1)#4	74.7(3)	O(10)-Zn(4)-Zn(6)	124.58(18)
O(2A)-Zn(1)-Zn(1)#4	128.6(3)	O(8A)-Zn(5)-O(5B)	106.8(3)
O(1)-Zn(1)-Zn(1)#4	37.85(2)	O(8A)-Zn(5)-O(4)	108.0(2)
Zn(1)#9-Zn(1)-Zn(1)#4	94.22(2)	O(5B)-Zn(5)-O(4)	111.3(2)
O(3B)-Zn(1)-Zn(1)#4	121.7(2)	O(8A)-Zn(5)-O(10)	111.7(3)
Zn(1)#8-Zn(1)-Zn(1)#4	43.17(5)	O(5B)-Zn(5)-O(10)	109.1(3)
O(3B)#9-Zn(1)-Zn(1)#11	126.6(3)	O(4)-Zn(5)-O(10)	109.9(3)
O(3A)#4-Zn(1)-Zn(1)#11	121.6(3)	O(8A)-Zn(5)-Zn(5)#1	116.4(2)
O(2A)-Zn(1)-Zn(1)#11	76.6(3)	O(5B)-Zn(5)-Zn(5)#1	131.9(2)
O(1)-Zn(1)-Zn(1)#11	37.85(2)	O(4)-Zn(5)-Zn(5)#1	36.51(10)
Zn(1)#9-Zn(1)-Zn(1)#11	57.62(6)	O(10)-Zn(5)-Zn(5)#1	74.1(2)
O(3B)-Zn(1)-Zn(1)#11	62.0(2)	O(9B)-Zn(6)-O(6A)	109.2(5)
Zn(1)#8-Zn(1)-Zn(1)#11	84.95(3)	O(9B)-Zn(6)-O(7B)	107.1(5)
Zn(1)#4-Zn(1)-Zn(1)#11	60	O(6A)-Zn(6)-O(7B)	109.0(8)
O(1)-Zn(2)-O(2B)#4	109.5(3)	O(9B)-Zn(6)-O(4)	115.1(4)
O(1)-Zn(2)-O(2B)	109.5(3)	O(6A)-Zn(6)-O(4)	105.9(4)
O(2B)#4-Zn(2)-O(2B)	109.4(3)	O(7B)-Zn(6)-O(4)	110.3(7)
O(1)-Zn(2)-O(2B)#11	109.5(3)	O(9B)-Zn(6)-Zn(6)#1	77.1(3)
O(2B)#4-Zn(2)-O(2B)#11	109.4(3)	O(6A)-Zn(6)-Zn(6)#1	119.6(4)
O(2B)-Zn(2)-O(2B)#11	109.4(3)	O(7B)-Zn(6)-Zn(6)#1	126.8(8)
O(7A)-Zn(3)-O(4)	114.0(4)	O(4)-Zn(6)-Zn(6)#1	38.05(11)

O(7A)-Zn(3)-O(6B)	110.9(6)	O(9B)-Zn(6)-Zn(4)	124.1(4)
O(4)-Zn(3)-O(6B)	109.2(2)	O(6A)-Zn(6)-Zn(4)	123.0(4)
O(7A)-Zn(3)-O(9A)	107.9(4)	O(7B)-Zn(6)-Zn(4)	75.1(7)
O(4)-Zn(3)-O(9A)	108.3(2)	O(4)-Zn(6)-Zn(4)	35.51(6)
O(6B)-Zn(3)-O(9A)	106.3(3)	Zn(6)#1-Zn(6)-Zn(4)	61.42(5)

Symmetry transformations used to generate equivalent atoms:

#1 x,x-y,-z+1/2 #2 -y,x-y,z #3 -y,-x,-z+1/2

#4 -y+1,x-y,z #5 -y+1,-x+1,-z+1/2

#6 x-y,-y,z+1/2 #7 x-y,-y,z-1/2 #8 -y+1,-x+1,-z+3/2

#9 -x+y+1,y,-z+3/2 #10 x,x-y,-z+3/2

#11 -x+y+1,-x+1,z

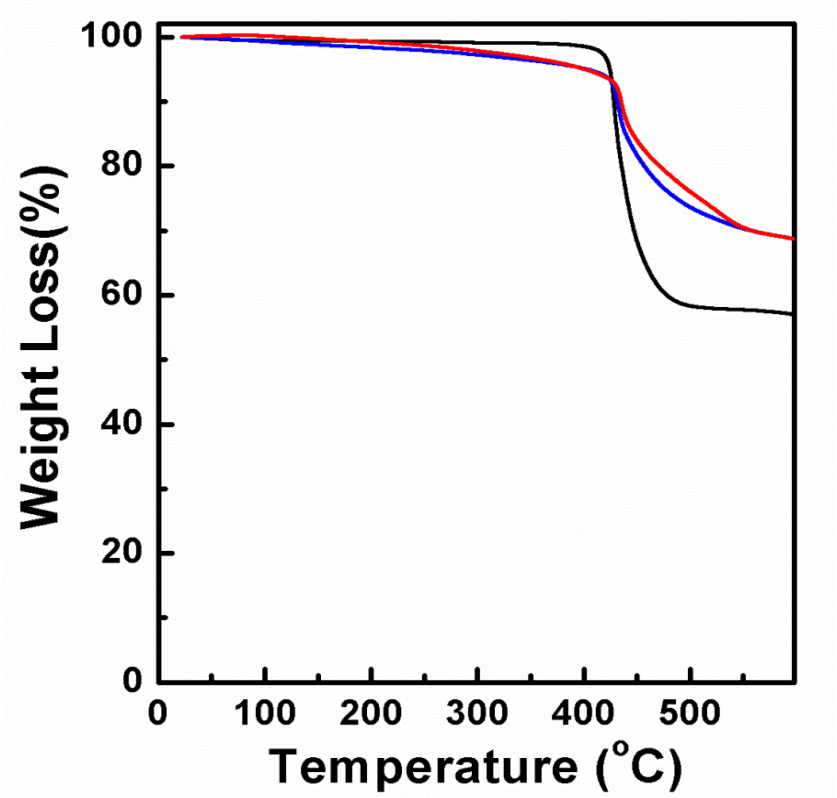

Figure II.S1. TGA traces for Mg@**SNU-90′c** before (red, –) and after (blue, –) chemisorption of H_2 gas at 200 °C and 30 bar, compared with that for Zn $_4O(atb)_2$ (SNU-90′, black) obtained from treatment with supercritical CO_2.

References

1. Furukawa, H.; Cordova, K. E.; O'Keeffe, M.; Yaghi, O. M. *Science*, **2013**, *341*, 1230444.
2. Suh, M. P.; Park, H. J.; Prasad, T. K.; Lim, D. -W.; *Chem. Rev.* **2012**, 112, 782.
3. Sumida, K; Rogow, D. L.; Mason, J. A.; McDonald, T. M.; Bloch, E. D.; Herm, Z. R.; Bae, T.-H.; J. Long, R. *Chem. Rev*., **2012**, *112*, 724.
4. Sculley, J.; Yuan, D.; Zhou, H. -C. *Energy Environ. Sci.* **2011,** *4*, 2721.
5. Park, H. J.; Suh, M. P. *Chem. Sci.* **2013**, *4*, 685.
6. Murray, L. J.; Dincă, M.; Long, J. R. *Chem. Soc. Rev.* **2009,** *38*, 1294.
7. Choi, H.-S.; Suh, M. P. *Angew. Chem. Int. Ed.* **2009**, *48*, 6865.
8. Li, J.-R.; Kuppler, R. J.; Zhou, H. -C. *Chem. Soc. Rev.* **2009**, *38*, 1477.
9. Cheon, Y. E.; Suh, M. P. *Chem. Commun.* **2009**, 2296.
10. Wu, C. -D.; Lin, W. *Angew.Chem. Int. Ed.* **2007**, *46*, 1075.
11. Uemura, T.; Kitaura, R.; Ohta, Y.; Nagaoka, M.; Kitagawa, S. *Angew. Chem. Int. Ed.* **2006**, *45*, 4112.
12. Lim, D.-W.; Yoon, J. W.; Ryu, K. Y.; Suh M. P. *Angew. Chem. Int. Ed.* **2012**, ,9814.
13. Cheon, Y. E.; Suh, M. P.; *Angew. Chem. Int. Ed.* **2009**, *48*, 2899.
14. Moon, H. R.; Kim, J. H.; Suh, M. P.; *Angew. Chem. Int. Ed.* **2005**, *44*, 1261.
15. Suh, M. P.; Moon, H. R.; Lee, E. Y.; Jang, S. Y. *J. Am. Chem. Soc.* **2006**, *128*, 4710.
16. Chen, Y. E.; Suh, M. P. *Chem. Euro. J.* **2008**, *14*, 3961.
17. Furukawa, H.; Ko, N.; Go, Y. B.; Aratani, N.; Choi, S. B.; Choi, E.;

Yazaydin, A. O.; Snurr, R. Q.; O'Keeffe, M.; Kim, J.; Yaghi, O. M. *Science* **2010**, *329*, 424.

18. Farha, O. K.; Yazaydin, A. O.; Eryazici, I.; Malliakas, C. D.; Hauser, B. G.; Kanatzidis, M. G.; Nguyen, S. T.; Snurr, R. Q.; Hupp, J. T. *Nat. Chem*. **2010**, *2*, 944.
19. Park, H. J.; Lim, D. -W.; Yang, W. S.; Oh, T. -R.; Suh, M. P. *Chem. -Eur. J.* **2011**, *17*, 7251.
20. Sumida, K.; Brown, C. M.; Herm, Z. R.; Chavan, S.; Bordiga, S.; Long, J. R. *Chem. Commun.* **2011**, *47*, 1157.
21. Latroche, M.; Suble, S.; Serre, C.; Mellot-Draznieks, C.; Llewellyn, P. L.; Lee, J. -H.; Chang, J. -S.; Jhung, S. H.; Ferey, G. *Angew. Chem., Int. Ed.* **2006**, 45, 8227.
22. Ma, S.; Zhou, H. -C. *J. Am. Chem. Soc.* **2006**, *128*, 11734.
23. Sumida, K.; Her, J. -H.; Dincă, M.; Murray, L. J.; Schloss, J. M.; Pierce, C. J.; Thompson, B. A.; FitzGerald, S. A.; Brown, C. M.; Long, J. R. *J. Phys. Chem. C* **2011**, *115*, 8414.
24. Cheon, Y. E.; Suh, M. P. *Chem. Commun*. **2009**, *45*, 2296.
25. Costa, J. S.; Gamez, P.; Black, C. A.; Roubeau, O.; Teat, S. J.; Reedijk, J. Eur. *J. Inorg. Chem.* **2008**, 1551.
26. Morris, W.; Doonan, C. J.; Furukawa, H.; Banerjee, R.; Yaghi, O. M. *J. Am. Chem. Soc.* **2008**, *130*, 12626.
27. Jones, S. C.; Bauer, C. A. *J. Am. Chem. Soc.* **2009**, *131*, 12516.
28. Goto, Y.; Sato, H.; Shinkai, S.; Sada, K. *J. Am. Chem. Soc.* **2008**, *130*, 14354.
29. Zlotea, C.; Campesi, R.; Cuevas, F.; Leroy, E.; Dibandjo, P.; Volkringer, C.;

Loiseau, T.; Ferey, G.; Latroche, M. *J. Am. Chem. Soc.* **2010**, *132*, 2991.

30. Kalidindi, S. B.; Fischer, R. A. *Phys. Status Solidi B,* **2013**, 250, 1119.

31. Furukawa, H.; Yaghi, O. M.; *J. Am. Chem. Soc.* **2009**, *131*, 8875.

32. Bhatia, S. K.; Myers, A. L. *Langmuir* **2006**, *22*, 1688.

33. Frost, H.; Duren, T.; Snurr, R. Q. *J. Phys. Chem. B* **2006**, *110*, 9565.

34. Frost, H.; Snurr, R. Q. *J. Phys. Chem. C* **2007**, *111*, 18794.

35. Park, H. J.; Suh, M. P. *Chem. Commun.* **2012**, 48, 3400.

36. http://www1.eere.energy.gov/hydrogenandfuelcells/storage/current_technology.html.

37. O'Keeffe, M.; Yaghi, O. M. *Chem. Rev.* **2012**, *112*, 675.

38. Rowsell, J. L.; Millward, A. R.; Park, K. S.; Yaghi, O. M. *J. Am. Chem. Soc.* **2004**, *126*, 5666.

39. Rowsell, J. L.; Yaghi, O. M. *J. Am. Chem. Soc.* **2006**, *128*, 1304.

40. Wong-Foy, A. G.; Matzger, A. J.; Yaghi, O. M. *J Am Chem Soc* **2006**, *128*, 3494.

41. Deng, H.; Grunder, S.; Cordova, K. E.; Valente, C.; Furukawa, H.; Hmadeh, M.; F. Gándara, Whalley, A. C.; Liu, Z.; Asahina, S.; Kazumori, H.; O'Keeffe, M.; Terasaki, O.; Stoddart, J. F.; Yaghi, O. M. *Science* **2012**, *336*, 1018.

42. Koh, K.; Wong-Foy, A. G.; Matzger, A. J. *J. Am. Chem. Soc.* **2009**, *131*, 4184.

43. Zhou, W.; Wu, H.; Yildirim, T. *J. Am. Chem. Soc.* **2008**,*130*, 15268.

44. Lin, X.; Telepeni, I.; Blake, A. J.; Dailly, A.; Brown, C. M.; Simmons, J. M.; Zoppi, M.; Walker, G. S.; Thomas, K. M.; Mays, T. J.; Hubberstey, P.;

Champness, N. R.; Schroder, M. *J. Am. Chem. Soc.* **2009**, *131*, 2159.

45. Yuan, D.; Zhao, D.; Sun, D.; Zhou, H. -C. *Angew. Chem., Int. Ed.* **2010**, *49*, 5357.

46. Sun, D.; Ma, S.; Simmons, J. M.; Li, J. -R.; Yuan, D.; Zhou, H. -C. *Chem. Commun.* **2010**, *46*, 1329.

47. Chui, S. S. Y.; Lo, S. M. F.; Charmant, J. P. H.; Orpen, A. G.; Williams, I. D. *Science* **1999**, *283*, 1148.

48. Lee, Y. -G.; Moon, H. R.; Cheon, Y. E.; Suh, M. P. *Angew. Chem. Int. Ed.* **2008**, *47*, 7741.

49. Park, H. J.; Suh, M. P. *Chem. Eur. J.* **2008**, *14*, 8812.

50. Bondi, A. *J. Phys. Chem.* **1964**, *68*, 441.

51. Chen, B.; Liang, C.; Yang, J.; Contreras, D. S.; Clancy, Y. L.; Lobkovsky, E. B.; Yaghi, O. M.; Dai, S. *Angew. Chem., Int. Ed.* **2006**, *45*, 1390.

52. Ma, B. -Q.; Mulfort, K. L.; Hupp, J. T. *Inorg. Chem.* **2005**, *44*, 4912.

53. Park, H. J.; Cheon, Y. E.; Suh, M. P. *Chem. Eur. J.* **2010**, *16*, 11662.

54. Horike, S.; Matsuda, R.; Tanaka, D.; Matsubara, S.; Mizuno, M.; Endo, K.; Kitagawa, S. *Angew. Chem., Int. Ed.* **2006**, *45*, 7226.

55. Ferey, G.; Mellot-Draznieks, C.; Serre, C.; Millange, F.; Dutour,J.; Surble, S.; Margiolaki, I. *Science* **2005**, *309*, 2040.

56. Ferey, G.; Serre, C.; Mellot-Draznieks, C.; Millange, F.; Surble, S.; Dutour, J.; Margiolaki, I. *Angew. Chem., Int. Ed.* **2004**, *43*, 6296.

57. Liu, Y.; Eubank, J. F.; Cairns, A. J.; Eckert, J.; Kravtsov, V. C.; Luebke, R.; Eddaoudi, M. *Angew. Chem., Int. Ed.* **2007**, *46*, 3278.

58. Yang, S. H.; Lin, X.; Blake, A. J.; Walker, G. S.; Hubberstey, P.; Champness,

N. R.; Schroder, M. *Nat. Chem.* **2009**, *1*, 487.

59. Qian, J.; Jiang, F.; Yuan, D.; Li, X.; Zhang, L.; Suab, K.; Hong, M. *J. Mater. Chem.* A, **2013**, *1*, 9075.

60. Li, Y.; Xie, L.; Liu, Y.; Yang, R.; Li, X. *Inorg. Chem.* **2008**, *47*, 10372.

61. Cheon, Y. E.; Suh, M. P. *Chem. Commun.*, **2009**, 2296.

62. Mallick, A.; Saha, S.; Pachfule, P.; Roy, S.; Banerjee, R. *J. Mater.Chem.* **2010**, *20*, 9073.

63. McDonald, T. M.; Lee, W. R.; Mason, J. A.; Weirs, B. M.; Hong, C. S.; Long, J. R. *J. Am. Chem. Soc.* **2012**, *134*, 7056.

64. Gedrich, K.; Senkovska, I.; Klein, N.; Stoeck, U.; Henschel, A.; Lohe, M. R.; Baburin, I. A.; Mueller, U.; Kaskel, S. *Angew. Chem. Int. Ed.* **2010**, *49*, 8489.

65. Lee, Y. E.; Jang, S. Y.; Suh, M. P. *J. Am. Chem. Soc.* **2005**, 127, 6374.

66. Suh, M. P.; Cheon, Y. E.; Lee, E. Y. *Chem.- Eur. J.* **2007**, 13, 4208.

67. Bhatia, S. K.; Myers, A. L. *Langmuir* **2006**, *22*, 1688.

68. Garrone, E.; Bonelli, B.; Arean, C. O. *Chem. Phys. Lett.* **2008**, *456*, 68.

69. Bae, Y. -S.; Snurr, R. Q. *Microporous Mesoporous Mater.* **2010**, *132*, 300.

70. Dinca, M.; Dailly, A.; Liu, Y.; Brown, C. M.; Neumann, D. A.; Long, J. R. *J. Am. Chem. Soc.* **2006**, *128*, 16876.

71. Czepirski, L.; Jagiello, *J. Chem. Eng. Sci.* **1989**, *44*, 797.

72. *R* program http://www.R-project.org.

73. Cole, J. H.; Everett, D. H.; Marshall, C. T.; Paniego, A. R.; Powl, J. C; Rodriguez-Reinoso, F. *J. Chem. Soc. Faraday Trans.* **1974**, *70*, 2154.

74. Yang, R. T. Gas Separation by Adsorption Process; Butterworth: Boston, **1997**.

75. Dinca, M.; Han, W. S.; Liu, Y.; Dailly, A.; Brown, C. M.; Long, J. R. *Angew. Chem. Int. Ed.* **2007**, *46*, 1419.

76. Jeon, Y. -M.; Armatas, G. S.; Heo, J.; Kanatzidis, M. G.; Mirkin, C. A. *Adv. Mater.* **2008**, *20*, 2105.

77. Kosa, M.; Krack, M.; Cheetham, A. K.; Parrinello, M. *J. Phys.Chem. C* **2008**, *112*, 16171.

78. Wang, X. -S.; Ma, S.; Forster, P. M.; Yuan, D.; Eckert, J.; Lopez, J. L.; Murphy, B. J.; Parise, J. B.; Zhou, H. -C. *Angew. Chem., Int. Ed.* **2008**, *47*, 7263.

79. Eddaoudi, M.; Kim, J.; Rosi, N.; Vodak, D.; Wachter, J.; O'Keeffe, M.; Yaghi, O. M. *Science* **2002**, *295*, 469.

80. Banerjee, R.; Phan, A.; Wang, B.; Knobler, C.; Furukawa, H.; O'Keeffe, M.; Yaghi, O. M. *Science*, **2008**, *319*, 939.

81. Ferey, G.; Mellot-Draznieks, C.; Serre, C.; Millange, F.; Dutour,J.; Surble, S.; Margiolaki, I. *Science* **2005**, *309*, 2040.

82. Ferey, G.; Serre, C.; Mellot-Draznieks, C.; Millange, F.; Surble, S.; Dutour, J.; Margiolaki, I. *Angew. Chem., Int. Ed.* **2004**, *43*, 6296.

83. Wang, Z.; Cohen, S. M. *J. Am. Chem. Soc.* **2007**, *129*, 12368.

84. Wang, Z.; Tanabe, K. K.; Cohen, S. M. *Chem.-Eur. J.* **2010**, *16*, 212.

85. Nouar, F.; Eckert, J.; Eubank, J. F.; Forster, P.; Eddaoudi, M. *J. Am. Chem. Soc.* **2009**, *131*, 2864.

86. Hoskins, B. F.; Robson, R. *J. Am. Chem. Soc.* **1990**, *112*, 1546.

87. Mulfort, K. L.; Farha, O. K.; Stern, C. L.; Sarjeant, A. A.; Hupp, J. T. *J. Am. Chem. Soc.* **2009**, *131*, 3866.

88. Wang, Z.; Cohen, S. M. *Chem. Soc. Rev.* **2009**, *38*, 1315.

89. Tanabe, K. K.; Cohen, S. M. *Chem. Soc. Rev.* **2011**, *40*, 498.

90. Cohen, S. M. *Chem. Rev.*, **2012**, *112*, 970.

91. Kawamichi, T.; Kodama, T.; Kawano, M.; Fujita, M. *Angew. Chem., Int. Ed.* **2008**, *47*, 8030.

92. Ingleson, M. J.; Barrio, J. P.; Guilbaud, J. -B.; Khimyak, Y. Z.; Rosseinsky, M. J. *Chem. Commun.* **2008**, *44*, 2680.

93. Burrows, A.; Frost, C.; Mahon, M.; Richardson, C. *Angew. Chem., Int. Ed.* **2008**, *47*, 8482.

94. Gadzikwa, T.; Farha, O. K.; Malliakas, C. D.; Kanatzidis, M. G.; Hupp, J. T.; Nguyen, S. T. *J. Am. Chem. Soc.* **2009**, *131*, 13613.

95. Han, S. S.; Goddard, W. A.; *J. Am. Chem. Soc.* **2007**, *129*, 8422.

96. Han, S. S.; Goddard, W. A. *J. Phys. Chem. C.* **2008**, 112, 13431.

97. Han, S. S.; Choi, S.-H.; Goddard, W. A. *J. Phys. Chem. C* **2011**, *115*, 3507.

98. Møller, C.; Plesset, M. S. *Phys. Rev.* **1934**, *46*, 618.

99. Dinca, M.; Long, J. R. *J. Am. Chem. Soc.* **2007**, *129*, 11172.

100. Himsl, D.; Wallacher, D.; Hartmann, M. *Angew. Chem., Int. Ed.***2009**, *48*, 4639.

101. Klontzas, E.; Mavrandonakis, A.; Tylianakis, E.; Froudakis, G. E. *Nano Lett.* **2008**, *8*, 1572.

102. Miyaura, N.; Suzuki, A. *Chem. Rev.*, **1995**, *95*, 2457.

103. Materials Studio v5.5, Accelrys Inc., San Diego, CA, 2010

104. Arvai, A. J.; Nielsen, C. ADSC Quantum-210 ADX Program, Area Detector System Corporation; Poway, CA, USA, 1983.

105. Otwinowski, Z.; Minor, W.; in Methods in Enzymology, ed. Carter, Jr., C. W.; Sweet, R. M. Academic Press, New York, 1997, vol. 276, part A, pp. 307.

106. G. M. Sheldrick, *Acta Crystallogr. A*, **1990**, *46*, 467.

107. Sheldrick, G. M. SHELXS-97. Program for the crystal structure refinement: (University of Gottingen, Gottingen, Germany (1997).

108. Spek, A. L. PLATON99 a multipurpose crystallographic tool: (Utrecht University: Utrecht, 1999).

109. Czepirski, L.; Jagiello, J. *Chem. Eng. Sci.***1989**, *44*, 797.

110. The software package is available online at http://www.r-project.org.

111. Myers, A. L.; Prausnitz, J. M. *AIChE J.* **1965**, *11*, 121.

112. Xie, L.-H.; Suh, M. P. *Chem. -Eur. J.* **2013**, *19*, 11590.

113. Steed, J. W. *Coord. Chem. Rev.*, **2001**, *215*, 171.

114. Panella, B.; Hirscher, M. *adv. Mater.* **2005**, 17, 538.

115. Lee, J. Y.; Olson, D. H.; Pan, L.; Emge, T. J.; Li, J. *Adv. Funct. Mater*. **2007**, *17*, 1255.

116. Zhou, W.; Wu, H.; Hartman, M. R.; Yildirim, T. *J. Phys. Chem. C* **2007**, *111*, 16131.

117. Hulvey, Z.; Sava, D. A.; Eckert, J.; Cheetham, A. K. *Inorg. Chem.* **2011**, *50*, 403.

118. Nouar, F.; Eckert, J.; Eubank, J. F.; Forster, P.; Eddaoudi, M. *J. Am. Chem. Soc.* **2009**, *131*, 2864.

119. Li, Y.; Yang, R.T. *AIChE J.* **2008**, 54, 269.

120. Han, S. S.; Furukawa, H.; Yaghi, O. M.; Goddard, W. A. *J. Am. Chem. Soc.*

2008, *130*, 11580.

121. Ben, T.; Ren, H.; Ma, S.; Cao, D.; Lan, J.; Jing, X.; Wang, W. Xu, J.; Deng, F.; Simmons, J. M.; Qiu, S.; Zhu, G. *Angew. Chem. Int. Ed.* **2009**, *48*, 9457.

122. Sakintuna, B.; Lamari-Darkrim, F.; Hirscher, M. *Int. J. Hydrogen Energy.* **2007**, 32, 1121.

123. Grochala, W.; Edwards, P. P. *Chem. Rev.* **2004**, *104*, 1283.

124. Imamura, H.; Masanari, K.; Kusuhara, M.; Katsumoto, H.; Sumi, T. Sakata, Y. *J. Alloys. Compds.* **2005**, *386*, 211.

125. Everett, D. H. *Pure Appl. Chem.* **1972**, *31*, 577.

126. Burwell, R L, Jr. *Pure Appl. Chem.* **1976**, *46*, 71.

127. Calvert, J. G. *Pure Appl. Chem.* **1990**, *62*, 2167.

128. Moon, H. R.; Lim, D. -W.; Suh, M. P. C*hem. Soc. Rev.* **2013**, *42*, 1807.

129. Schröder, F.; Fischer, R. A. *Top. Curr. Chem*, **2010**, *293*, 77.

130. Zhao, Y.; Zhang, J.; Song, J.; Li, J.; Liu, J.; Wu, T.; Zhang, P.; Han, B. *Green Chem.*, **2011**, *13*, 2078.

131. Moon, H. R.; Suh, M. P.; *Eur. J. Inorg. Chem.*, 2010, **24**, 3795.

132. Suh, M. P. *Adv. Inorg. Chem.*, **1996**, *44*, 93.

133. Wei, Y.; Han, S.; Walker, D. A.; Fuller, P. E.; Grzybowski, B. A. *Angew. Chem., Int. Ed.*, **2012**, *51*, 7435.

134. Hampden-Smith, M. J.; Kodas, T. T. *Chem. Vapor Depos.*, **1995**, *1*, 8.

135. Bowes, C. L.; Malek, A.; Ozin, G. A. *Chem. Vapor Depos.*, **1996**, *2*, 97.

136. Hermes, S.; Schröter, M. -K.; Schmid, R.; Khodeir, L.; Muhler, M.; Tissler, A.; Fischer, R. W.; Fischer, R. A. *Angew. Chem., Int. Ed*., **2005**, *44*, 6237.

137. Schroder, F.; Esken, D.; Cokoja, M.; van den Berg, M. W. E.; Lebedev, O. I.;

Tendeloo, G. V.; Walaszek, B.; Buntkowsky, G.; Limbach, H. -H.; Chaudret, B.; Fischer, R. A. *J. Am. Chem. Soc.*, **2008**, *130*, 6119.

138. Park, Y. K.; Choi, S. B.; Nam, H. J.; Jung, D. -Y.; Ahn, H. C.; Choi, K.; Furukawa, H.; Kim, J. *Chem. Commun.* **2010**, *46*, 3086.

139. Kalidindi, S. B.; Oh, H.; Hirscher, M.; Esken, D.; Wiktor, C.; Turner, S.; Tendeloo, G. V.; Fischer, R. A. *Chem.–Eur. J.*, **2012**, *18*, 10848.

140. Schroder, F.; Henke, S.; Zhang, X.; Fischer, R. A. *Eur. J. Inorg. Chem.*, **2009**, 3131.

141. Lu, G.; Li, S.; Guo, Z.; Farha, O. K.; Hauser, B. G.; Qi, X.; Wang, Y.; Wang, X.; Han, S.; Liu, X.; J. DuChene, S.; Zhang, H.; Zhang, Q.; Chen, X.; Ma, J.; Loo, S. C. J.; Wei, W. D.; Yang, Y.; Hupp, J. T. *Nature Chem.* **2012**, *4*, 310.

142. NIST chemistry webbook (thermophysical properties of fluid systems) http://webbook.nist.gov/chemistry/fluid.

143. Chae, H. K.; Siberio-Perez, D. Y.; Kim, J.; Go, Y.; Eddaoudi, M.; Matzger, A. J.; OKeeffe, M.; Yaghi, O. M.; *Nature* **2004**, *427*, 523.

144. Nelson, A. P.; Farha, O. K.; Mulfort, K. L.; Hupp, J. T.; *J. Am. Chem. Soc.* **2009**, *131*, 458.

145. Jeon, K. -J.; Moon, H. R.; Ruminski, A. M.; Jiang, B.; Kisielowski, C.; Bardhan, R.; Urban, J. J. *Nat. Mater.* **2011**, *10*, 286.

146. Kooi, B. J.; Palasantzas, G.; De Hosson, J. T. M.; *Appl. Phys.Lett.* **2006**, *89*, 161914.

147. Zhu, C.; Hosokai, S.; Matsumoto, I.; Akiyama, T.; *Cryst. Growth Des.* **2010**, *10*, 5123.

148. Fuggle, J. C., *Surf. Sci.* **1977**, *69*, 581.

149. Hunsicker, R. A.; Klier, K., *Chem Mater*. **2002**, *14*, 4807.

150. Mastronarde, D. N.; *J. Struct. Biol.* **1997**, *120*, 343.

151. Zaluska, A.; Zaluski, L.; J. Strom-Olsen, O.; *J. Alloys Compd.* **1999**, *288*, 217.

152. Sakintuna, B.; Lamari-Darkrim, F.; Hirscher, M.; *Int. J. Hydrogen Energy* **2007**, *32*, 1121.

153. Di Vece, M.; Grandjean, D.; Van Bael, M. J.; Romero, C. P.; Wang, X.; Decoster, S.; Vantomme, A.; Lievens, P.; *Phys. Rev. Lett.* **2008**, *100*, 236105.

154. Barkhordarian, G.; Klassen, T.; Bormann, R. *J Alloys Compd*. **2004**, *364*, 242.

155. Barkhordarian, G.; Klassen, T.; Bormann, R. *J Alloys Compd.* **2006**, *407*, 249.

Publications

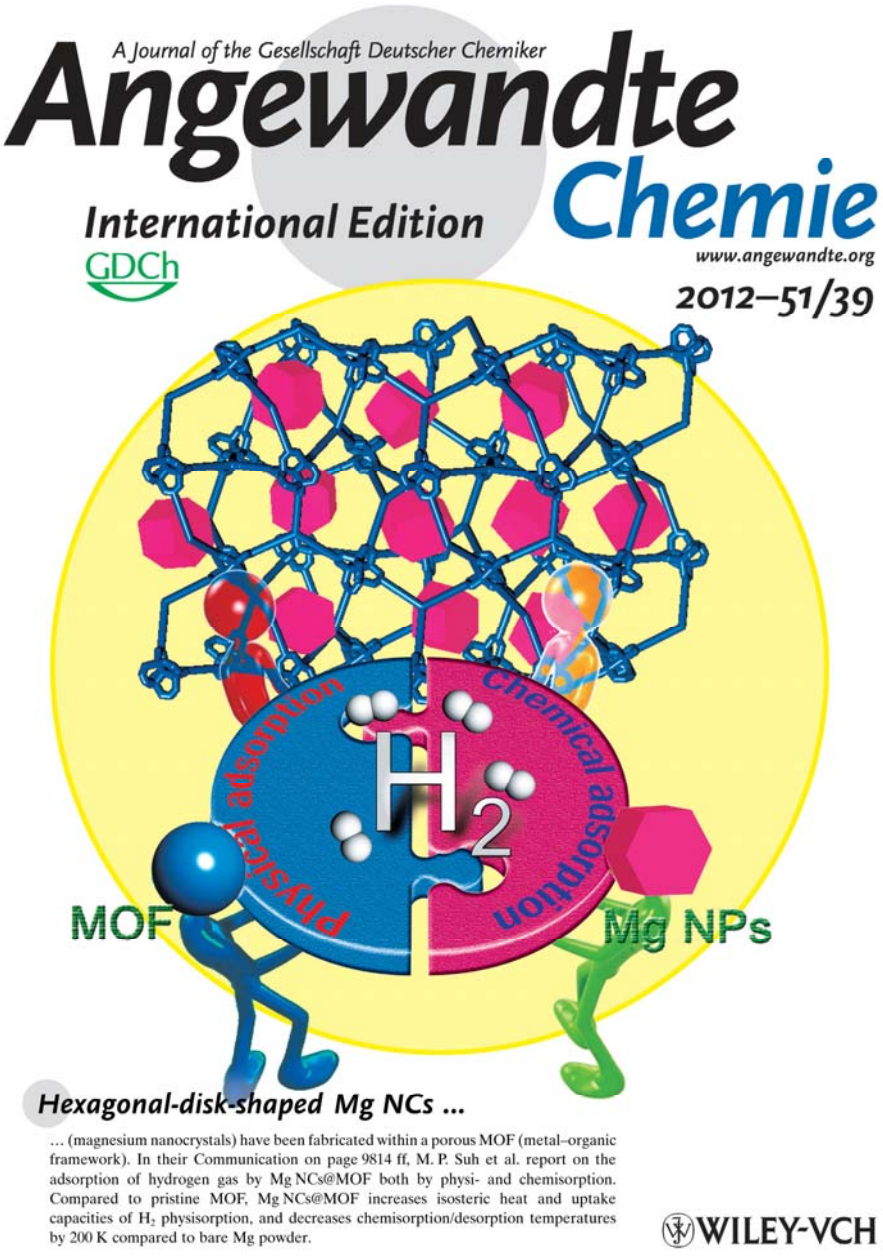

Hydrogen Storage

DOI: 10.1002/anie.201206055

Magnesium Nanocrystals Embedded in a Metal–Organic Framework: Hybrid Hydrogen Storage with Synergistic Effect on Physi- and Chemisorption**

*Dae-Woon Lim, Ji Woong Yoon, Keun Yong Ryu, and Myunghyun Paik Suh**

Hydrogen is considered to be a promising energy carrier for the future. In order to use it as a fuel, a compact, safe, and efficient hydrogen storage system should be developed. Porous metal–organic frameworks (MOFs) have attracted great attention as potential hydrogen storage materials,[1] because some MOFs can store large amount of H_2 (> 7 wt %) at 77 K and high pressures.[2] However, at room temperature, the H_2 storage capacities of MOFs drop to less than 1 wt % because interaction energies between the frameworks and H_2 are very low (4–8 kJ mol^{-1}). There have been efforts to enhance the H_2 storage capacities of MOFs at ambient temperature by methods such as tuning the ligand,[3] generation of open metal sites,[4] and embedding palladium nanoparticles.[5] Despite these modifications, the improvements were not very satisfactory, and none of the materials have yet met the target of the US Department of Energy (DOE) of 2017.

In search for a highly efficient material for H_2 storage, we have investigated the possibilities of hybrid materials that would be capable of storing H_2 by both physical adsorption and chemisorption. In particular, we have been interested in composite materials that consist of a MOF and magnesium nanoparticles. Magnesium chemisorbs H_2 at 773 K and 200 atm in the presence of MgI_2 catalyst.[6] Magnesium powder of 50–100 μm size made by ball milling slowly absorbs H_2 at 673 K and 10 bar.[7] The resulting magnesium hydride has a quite high dehydrogenation enthalpy (≈ 75 kJ per mol H_2),[8] and therefore heavy-metal catalysts should be used to reduce the H_2 desorption temperature and improve kinetics, but they still do not allow effective dehydrogenation.[9] In the presence of heavy-metal catalysts, the H_2 absorption and release temperatures decrease as a result of destabilization of the metal hydride when the particle size of magnesium is reduced.[10]

Nanosized magnesium particles have been synthesized by a variety of methods, such as ball-milling,[11] condensation of magnesium metal vapor,[12] plasma metal reaction,[13] infiltration of melted Mg in carbon material,[14] and sonoelectrochemistry[15] or chemical reduction of Mg precursors.[16] Some of the disadvantages of these methods are that they require a long process time, extremely high temperatures (898–1203 K), and electrically or chemically harsh conditions, and yet they provide inhomogeneous size distributions.

Herein we report a simple method for fabrication of hexagonal-disk-shaped magnesium nanocrystals (Mg NCs) within a MOF. The fabrication of Mg nanocrystals inside MOFs is unprecedented. Previously, small Ag, Au, Ni, Pd, Ru, or Pt nanoparticles (size, 1.4–10 nm) were prepared in MOFs by immersing redox-active MOFs in the metal-ion solutions[5,17] or by reducing the metal precursors deposited in the MOFs.[18] The present nanocomposite is made by the thermal decomposition of air-sensitive bis-cyclopentadienyl magnesium ($MgCp_2$) vapor in a MOF, leading to the deposition of MG NCs in the MOF, a method that is also unprecedented for production of nanosized Mg. The resulting Mg NCs@MOF is a hybrid hydrogen storage material that stores H_2 by both physical adsorption and chemisorption, exhibiting a synergistic effect to increase the isosteric heat of H_2 physisorption and decrease the temperatures for chemisorption/desorption of H_2.

Yellow crystals of $[Zn_4O(atb)_2]\cdot 22DMF\cdot 9H_2O$ (SNU-90), in which atb is aniline-2,4,6-tribenzoate, were synthesized by heating a mixture of $Zn(NO_3)_2$ and H_3(atb) in dimethylformamide (DMF). The X-ray single-crystal structure of SNU-90 indicated a non-interpenetrated (6,3)-connected net of a *qom* topology, similar to MOF-177[19] (see the Supporting Information, Figures S1 and S2). When the guest solvent molecules in SNU-90 were removed by treatment with supercritical CO_2,[2h,20] a guest-free $[Zn_4O(atb)_2]$ (SNU-90′, NH_2-MOF-177) was obtained.

Vapor of bis(cyclopentadienyl) magnesium ($MgCp_2$) was deposited in SNU-90′ at 80 °C, and the resulting $MgCp_2$@SNU-90′ was thermally decomposed at 200 °C under an argon atmosphere followed by evacuation, which gave rise to Mg NCs embedded in SNU-90′. Thus far it was unknown that the thermal decomposition of $MgCp_2$ results in

[a] D.-W. Lim, Prof. M. P. Suh
Department of Chemistry, Seoul National University
Seoul 151-747 (Republic of Korea)
E-mail: mpsuh@snu.ac.kr
Dr. J. W. Yoon
Catalysis Center for Molecular Engineering
Korea Research Institute of Chemical Technology (KRICT)
Jang-dong 100, Yuseong, Deajeon 305-600 (Republic of Korea)
K. Y. Ryu
Division of Electron Microscopic Research
Korea Basic Science Institute
113 Gwahangno, Daejeon 305-333 (Korea)

[**] This work was supported by the National Research Foundation of Korea (NRF) Grant funded by the Korean Government (MEST) (No. 2011-0031432 and No. 2012-0000651). D.-W. Lim acknowledges support by Hi Seoul Science Fellowship from Seoul Scholarship Foundation. We thank Dr. H. S. Jung in Korea Basic Science Institute for helping us to perform electron microscopy work.

Supporting information for this article is available on the WWW under http://dx.doi.org/10.1002/anie.201206055.

Table 1: N_2 and H_2 gas uptake data in SNU-90′ and various samples of Mg@SNU-90′.

Compound	mol_{Mg}/mol_{Zn} (wt%)	N_2 uptake [$cm^3 g^{-1}$]	Surface area [$m^2 g^{-1}$]		Pore volume [$cm^{-3} g^{-1}$]	H_2 uptake [wt%] at 1 atm	at high pressure	Q_{st} [$kJ mol^{-1}$]
SNU-90′	n.a.	1135	4244[a]	4914[b]	1.64[c]	1.21 (77 K)	8.81 (77 K, 75 bar)	4.55
						0.74 (87 K)	0.45 (298 K, 80 bar)	
Mg@SNU-90′a	0.15 (1.26)	1104	4154[a]	4757[b]	1.47[c]	1.24 (77 K)	8.74 (77 K, 89 bar)	5.68
						0.65 (87 K)	0.54 (298 K, 90 bar)	
Mg@SNU-90′b	0.85 (6.52)	559	2056[a]	2373[b]	0.84[c]	0.72 (77 K)	0.29 (473 K, 30 bar)	7.24
						0.40 (87 K)		
Mg@SNU-90′c	1.40 (10.5)	378	1371[a]	1581[b]	0.36[c]	0.60 (77 K)	0.20 (323 K, 80 bar)	11.6
						0.47 (87 K)	0.24 (415 K, 40 bar)	
							0.71 (473 K, 30 bar)	

[a] BET surface area. [b] Langmuir surface area, and [c] Pore volume estimated by using the Dubinin–Radushkevich (DR) equation. n.a. = not available.

nanosized Mg, although it was reported that reduction of $MgCp_2$ with Li^+(naphthalenide$^-$) in a solution of polymethylmethacryate in tetrahydrofuran afforded round-shaped Mg nanoparticles.[16] As for the mechanism of the thermal decomposition, formation of metal and two C_5H_5 radicals that might further dissociate or associate to the complex products, was predicted as an initial step based on the theoretical calculation.[21] However, in order to verify the mechanism in our case, further research should be carried out. By changing the reaction conditions during the deposition process of $MgCp_2$, such as the duration time and whether or not a prevacuum state was applied to the reaction vessel, we could control the loaded amounts of $MgCp_2$ in the MOF and obtained several samples embedded with different amounts of magnesium nanocrystals (Supporting Information, Table S1).

The samples, Mg@SNU-90′a, Mg@SNU-90′b, and Mg@SNU-90′c, were loaded with 1.26 wt%, 6.52 wt%, and 10.5 wt% of Mg NCs, respectively, as determined by inductively coupled plasma atomic emission spectroscopy (ICP-AES) (Table 1). The NMR spectra indicated the absence of cyclopentadiene (Cp) in the resulting nanocomposites (Supporting Information, Figure S3).

The HRTEM images for various samples of Mg@SNU-90′ showed hexagonal-disk-shaped magnesium nanocrystals,[22] which have a diagonal length of hexagon ranging 44–88 nm (average (60 ± 18) nm) with a thickness ranging 16–61 nm (average (37 ± 12) nm; see Figure 1 and Figure S4 in the Supporting Information). Although it was reported that hexagonal-disk-shaped Mg NCs could be formed when Mg powder was heated at temperatures higher than 500°C,[22b] in the present work, they are formed by heating $Mg(Cp)_2$@MOF at only 200°C. The formation of Mg NCs that are much bigger than the channel size (12.9 Å × 9.6 Å) of the MOF is attributed to the agglomerization of nanoparticles by heat during the thermal decomposition. Alternatively, it is simply caused by the degradation of the MOF under electron-beam irradiation during the observation by HRTEM.[23] The selected-area electron diffraction (SAED) patterns of Mg NCs embedded in SNU-90' showed lattice fringes separated by 2.7871 Å, which is in agreement with the (100) *d*-spacing of metallic Mg (2.7782 Å, JCPDS 04-0770). The size distribution of the Mg NCs was found to be very similar in all of the samples, even though there were significantly different amounts of Mg NCs embedded in the MOF. When Mg@SNU-90′ was exposed to air for three weeks, the shape of the Mg NCs changed to a star shape that has a lattice fringe with a separation of 2.1101 Å, which corresponds to the (200) *d*-spacing of MgO (2.1061 Å, JCPDS 89-7746; Supporting Information, Figure S4). XPS data of Mg@SNU-90′ indicated that Mg^0 and Zn^{II} coexisted in the solid (Supporting Information, Figure S5).

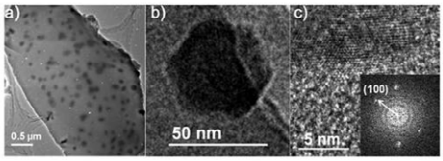

Figure 1. High-resolution transmission electron microscopy (HRTEM) images. a) Mg@SNU-90′b. b) A hexagonal-shaped Mg nanocrystal and c) its edge image showing lattice fringes with a separation of 2.7871 Å, which corresponds to (100) *d*-spacing of Mg^0 (2.7782 Å, JCPDS 04-0770). Inset: selected-area electron diffraction (SAED) pattern.

To verify that the Mg NCs were embedded inside the channels of the MOF, we performed electron tomography. From the TEM images that were collected with a 1° interval with the tilting angle of +40°–−40°, 3D images were constructed by using the IMOD program.[24] When the sample was tilted, the shape of a Mg NC changed from hexagon to rectangle and from rectangle to hexagon, thus indicating that the Mg NCs were indeed embedded in the MOF (Figure 2 and Supporting Video).

The powder X-ray diffraction (PXRD) patterns showed that the structure of SNU-90' was maintained even after the formation of Mg NCs, the sizes of which were much larger than the channel size (12.9 Å × 9.6 Å) of the MOF (Supporting Information, Figure S6). To understand this observation,

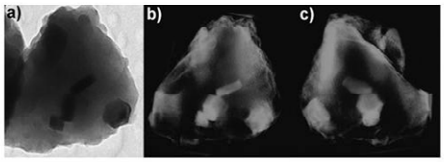

Figure 2. TEM and electron tomography images of Mg@SNU-90′b. a) TEM image. b) and c) Tomographically reconstructed images of Mg NCs embedded in SNU-90′ at different angles.

we calculated the ratio of the volumes of formed Mg NCs and the network skeleton for Mg@SNU-90′c. Assuming that all Mg NCs destroyed the network skeleton, the Mg NCs would destroy a maximum 4.6% of the network skeleton by volume. This value is too small to alter the PXRD pattern of the MOF. It was also previously reported that metal nanoparticles much bigger than the cavity sizes of the hosts were impregnated by maintaining the network structures.[15,17] The PXRD peaks of crystalline Mg should generally appear at $2\theta = 32.2$, 34.4, and 36.6°, but we could observe only a peak at 36.6°, which is the strongest peak of Mg (Figure S7). On exposure to air for two days, however, the PXRD pattern showed the peaks corresponding to MgO, with retention of the framework structure of SNU-90′.

The adsorption–desorption isotherms were measured for N_2 gas at 77 K and for H_2 gas at various temperatures on SNU-90′, Mg@SNU-90′a, Mg@SNU-90′b, and Mg@SNU-90′c (Figure 3 Table 1). The N_2 gas sorption isotherms of the four samples were of type I, which is characteristic for the microporous materials (Supporting Information, Figure S8.). Despite the presence of the NH_2 group in the ligand of SNU-90′, the surface area, pore volume, and H_2 adsorption capacities of SNU-90′ were similar to those of MOF-177.[19] Gas sorption data for various samples of Mg@SNU-90′ showed that as the amount of Mg increased, the BET surface area, pore volume, and H_2 uptake capacity at 77 K and 1 atm decreased, because Mg NCs occupied the surface and space of the pores in the MOF. At 298 K and high pressure, however, the H_2 uptake in Mg@SNU-90′a increased by 20%, to 0.54 wt% from 0.45 wt% in pristine SNU-90′, thus suggesting that Mg NCs provide a positive effect on H_2 adsorption at 298 K (Supporting Information, Figure S9). The zero-coverage isosteric heats of the H_2 adsorption, which were estimated from the H_2 adsorption isotherms measured at 77 K and 87 K, increased as the amount of Mg increased, up to 11.6 kJ mol^{-1} for Mg@SNU-90′c from 4.55 kJ mol^{-1} for SNU-90′ (Table 1, Figure 3).

In order to observe the chemisorption ability of the embedded Mg NCs, we also measured the H_2 uptake in Mg@SNU-90′c at 323 K, 415 K, and 473 K under high pressures (Figure 4). Contrary to the physisorbed MOFs, in which H_2 uptake decreases at the elevated temperature, the H_2 chemisorption capacities of the present material increase as the temperature is raised. The H_2 absorption capacities of Mg@SNU-90′c were 0.20 wt% at 323 K under the H_2 pressure of 80 bar, 0.24 wt% at 415 K under the H_2 pressure of 40 bar. At 473 K under 30 bar, the H_2 uptake capacity of Mg@SNU-90′c became 0.71 wt% (volumetric H_2 storage capacity, 3.1 g L^{-1}). This value is remarkably higher than that of Mg@SNU-90′b under the same conditions (Table 1), despite the former exhibiting a much lower surface area and pore volume because of the heavily loaded Mg. The fact that the H_2 uptake enhances with elevated temperatures and the increased amount of Mg NCs confirms that the H_2 uptakes in Mg@SNU-90′ at 323 K, 415 K, and 473 K are results of chemisorption. These chemisorption temperatures are significantly lower (by > 200 K) than that (673 K under 10 bar) of bare Mg powder of 50–100 μm in size.[7] If the H_2 uptake capacity of Mg alone is estimated from the data, it is 7.5 wt% at 473 K and 30 bar. Considering that the H_2 chemisorption capacity of pure Mg is 7.66 wt%, 99% of the Mg NCs in the sample chemisorb H_2, which is much better than any form of Mg previously reported, such as Mg nanoparticles incorporated in a polymer[16] and bare Mg powder.[25]

The H_2 desorption properties of Mg@SNU-90′c were verified by the temperature-programmed desorption mass spectroscopy (TPD-MS) analysis (Figure 4d). The TPD-MS results indicated that H_2 was desorbed at $T > 523$ K and 1 atm. It should be noted that the signal intensities of hydrogen atoms were exactly twice as strong as those of H_2 molecules (Supporting Information, Figure S10). This observation sug-

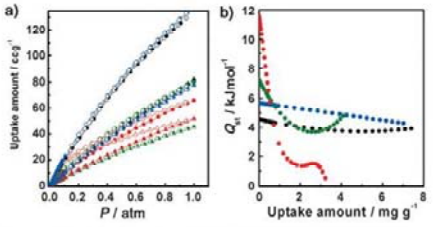

Figure 3. Physical adsorptions of H_2 in SNU-90′ (black), Mg@SNU-90′a (blue), Mg@SNU-90′b (green), and Mg@SNU-90′c (red). a) The H_2 adsorption isotherms at 77 K (circles) and 87 K (triangles). Filled shape: adsorption, open shape: desorption. b) Isosteric heats of the H_2 adsorption. The samples of Mg@SNU-90′a, Mg@SNU-90′b, and Mg@SNU-90′c contain 1.26 wt%, 6.52 wt%, and 10.5 wt%, respectively, of magnesium nanocrystals.

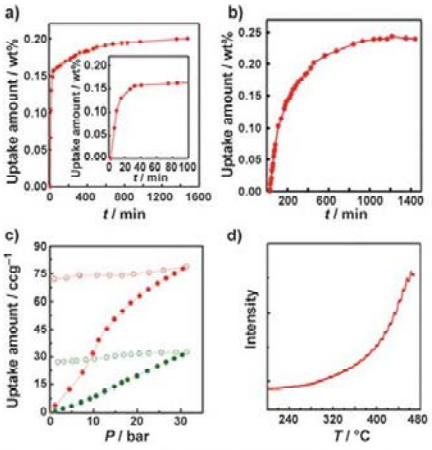

Figure 4. Chemical absorption of H_2 in Mg@SNU-90′c. a) H_2 absorption kinetics at 325 K and 80 bar. Inset: data with a magnified time scale. b) H_2 absorption kinetics at 415 K and 40 bar. c) H_2 absorption isotherms at 473 K in Mg@SNU-90′b (green) and Mg@SNU-90′c (red). Filled shapes: adsorption; open shapes: desorption. d) Temperature programmed desorption mass spectroscopy (TPD-MS) data; $m/e = 2$, measured under argon.

gests that all desorbed H_2 sources were MgH_2 not from the MOF at all. The TG mass loss of Mg@SNU-90′c after H_2 absorption is also in good agreement with the TPD-MS data (Supporting Information, Figure S11).

After the H_2 chemisorption at 473 K and 30 bar, the HRTEM images of Mg@SNU-90′c indicated that the crystal morphology of Mg was maintained but the crystal size was remarkably increased. The SAED pattern indicated the lattice fringe with a separation of 2.247 Å, which is in good agreement with the (110) *d*-spacing of β-MgH_2 (2.257 Å, JCPDS 35-1185, Supporting Information, Figure S12). The MgH_2@SNU-90′ shows the crystal size (diagonal length of hexagon) of average (142 ± 41) nm and thickness of average (83 ± 18) nm (Supporting Information, Figure S12), circa 2.3 times as large as those of Mg NCs. Considering that the volume of Mg should be increased by 30% on hydride formation,[26] this excessive expansion during the H_2 chemisorption processes at high temperature and pressure can be explained by the three-dimensional Ostwald ripening, in which the larger crystals take up the mobile atoms dissociated from the smaller crystals.[27] In addition, degradation of the MOF by electron beam during the TEM measurement plays a role in increasing the size of the MgH_2 crystal. Even after the formation of MgH_2, the organic ligands of SNU-90′ were not hydrogenated, as evidenced by the ^{1}H NMR spectra measured for the resulting nanocomposite that was dissolved in the mixture of DCl and $[D_6]Me_2SO$ (Supporting Information, Figure S3). When MgH_2@SNU-90′ was exposed to air, the PXRD pattern data showed new peaks at $2\theta = 36.8$ and 42.8 deg, which correspond to MgO, and a new peak at $2\theta =$ 38.0 deg that corresponds to $Mg(OH)_2$, (Supporting Information, Figure S6).

In conclusion, we have prepared for the first time Mg nanocrystals in a MOF, and showed that Mg NCs@MOF is a hybrid-hydrogen-storage material that has both physical adsorption and chemisorption properties, and exhibits synergistic effects to increase isosteric heat of the H_2 physisorption and to decrease the temperatures for chemisorption/desorption of H_2. The present hybrid-hydrogen-storage material suggests a new strategy for H_2 storage and transport for the future. To develop the materials that are able to reach the DOE target, we are trying to further reduce the size of the Mg NCs and adjust the amount of loaded Mg in the selected physisorbed porous materials, such as light-weighted MOFs or organic COFs.[28] In addition, we are trying to develop new methods to protect the material from oxidation through air.

Received: July 28, 2012
Published online: September 7, 2012

Keywords: chemisorption · magnesium · metal–organic frameworks · nanocrystals · physisorption

[1] a) M. P. Suh, H. J. Park, T. K. Prasad, D.-W. Lim, *Chem. Rev.* **2012**, *112*, 782–835; b) J. Sculley, D. Yuan, H.-C. Zhou, *Energy Environ. Sci.* **2011**, *4*, 2721–2735; c) L. J. Murray, M. Dincă, J. R. Long, *Chem. Soc. Rev.* **2009**, *38*, 1294–1314.

[2] a) H. Furukawa, N. Ko, Y. B. Go, N. Aratani, S. B. Choi, E. Choi, A. Özgür Yazaydın, R. Q. Snurr, M. O'Keeffe, J. Kim, O. M. Yaghi, *Science* **2010**, *329*, 424–428; b) H. J. Park, D.-W. Lim, W. S. Yang, T.-R. Oh, M. P. Suh, *Chem. Eur. J.* **2011**, *17*, 7251–7260.

[3] Z. Wang, K. K. Tanabe, S. M. Cohen, *Chem. Eur. J.* **2010**, *16*, 212–217.

[4] Y.-G. Lee, H. R. Moon, Y. E. Cheon, M. P. Suh, *Angew. Chem.* **2008**, *120*, 7855–7859; *Angew. Chem. Int. Ed.* **2008**, *47*, 7741–7745.

[5] Y. E. Cheon, M. P. Suh, *Angew. Chem.* **2009**, *121*, 2943–2947; *Angew. Chem. Int. Ed.* **2009**, *48*, 2899–2903; *Angew. Chem.* **2009**, *121*, 2943–2947.

[6] E. Wiberg, H. Goeltzer, R. Bauer, *Z. Naturforsch. B* **1951**, *6*, 394–395.

[7] A. Zaluska, L. Zaluski, J. O. Strom-Olsen, *J. Alloys Compd.* **1999**, *288*, 217–225.

[8] L. Schlapbach, A. Züttel, *Nature* **2001**, *414*, 353–358.

[9] J.-L. Bobet, E. Grigorova, M. Khrussanova, M. Khristov, D. Radev, P. Peshev, *J. Alloys Compd.* **2002**, *345*, 280–285.

[10] V. Bérubé, G. Radtke, M. Dresselhaus, G. Chen, *Int. J. Energy Res.* **2007**, *31*, 637–663.

[11] K.-F. Aguey-Zinsou, J. R. A. Fernandez, T. Klassen, R. Bormann, *Int. J. Hydrogen Energy* **2007**, *32*, 2400–2407.

[12] W. Li, C. Li, H. Ma, J. Chen, *J. Am. Chem. Soc.* **2007**, *129*, 6710–6711.

[13] X. Zhang, R. Yang, J. Yang, W. Zhao, J. Zheng, W. Tian, X. Li, *Int. J. Hydrogen Energy* **2011**, *36*, 4967–4975.

[14] P. E. de Jongh, R. W. P. Wagemans, T. M. Eggenhuisen, B. S. Dauvillier, P. B. Radstake, J. D. Meeldijk, J. W. Geus, K. P. de Jong, *Chem. Mater.* **2007**, *19*, 6052–6057.

[15] I. Haas, A. Gedanken, *Chem. Commun.* **2008**, 1795–1797.

[16] K.-J. Jeon, H. R. Moon, A. M. Ruminski, B. Jiang, C. Kisielowski, R. Bardhan, J. J. Urban, *Nat. Mater.* **2011**, *10*, 286–290.

[17] a) H. R. Moon, J. H. Kim, M. P. Suh, *Angew. Chem.* **2005**, *117*, 1287–1291; *Angew. Chem. Int. Ed.* **2005**, *44*, 1261–1265; b) M. P. Suh, H. R. Moon, E. Y. Lee, S. Y. Jang, *J. Am. Chem. Soc.* **2006**, *128*, 4710–4718; c) Y. E. Cheon, M. P. Suh, *Chem. Eur. J.* **2008**, *14*, 3961–3967; d) H. R. Moon, J. H. Kim, M. P. Suh, *Eur. J. Inorg. Chem.* **2010**, 3795–3803.

[18] a) M. Meilikhov, K. Yusenko, D. Esken, S. Turner, G. V. Tendeloo, R. A. Fischer, *Eur. J. Inorg. Chem.* **2010**, 3701–3714; b) Y. K. Park, S. B. Choi, H. J. Nam, D. Y. Jung, H. C. Ahn, K. Choi, H. Furukawa, J. Kim, *Chem. Commun.* **2010**, *46*, 3086–3088.

[19] H. K. Chae, D. Y. Siberio-Pérez, J. Kim, Y. Go, M. Eddaoudi, A. J. Matzger, M. O'Keeffe, O. M. Yaghi, *Nature* **2004**, *427*, 523–527.

[20] A. P. Nelson, O. K. Farha, K. L. Mulfort, J. T. Hupp, *J. Am. Chem. Soc.* **2009**, *131*, 458–460.

[21] A. G. Turnbull, *Aust. J. Chem.* **1967**, *20*, 2059–2067.

[22] a) B. J. Kooi, G. Palasantzas, J. T. M. De Hosson, *Appl. Phys. Lett.* **2006**, *89*, 161914; b) C. Zhu, S. Hosokai, I. Matsumoto, T. Akiyama, *Cryst. Growth Des.* **2010**, *10*, 5123–5128.

[23] R. J. T. Houk, B. W. Jacobs, F. E. Gabaly, N. N. Chang, A. A. Talin, D. D. Graham, S. D. House, I. M. Robertson, M. D. Allendorf, *Nano Lett.* **2009**, *9*, 3413–3418.

[24] D. N. Mastronarde, *J. Struct. Biol.* **1997**, *120*, 343–352.

[25] B. Sakintuna, F. Lamari-Darkrim, M. Hirscher, *Int. J. Hydrogen Energy* **2007**, *32*, 1121–1140.

[26] C. Zlotea, J. Lu, Y. Andersson, *J. Alloys Compd.* **2006**, *426*, 357.

[27] M. Di Vece, D. Grandjean, M. J. Van Bael, C. P. Romero, X. Wang, S. Decoster, A. Vantomme, P. Lievens, *Phys. Rev. Lett.* **2008**, *100*, 236105.

[28] a) A. P. Côté, A. I. Benin, N. W. Ockwig, A. J. Matzger, M. O'Keeffe, O. M. Yaghi, *Science* **2005**, *310*, 1166–1170; b) K. Sumida, M. R. Hill, S. Horike, A. Dailly, J. R. Long, *J. Am. Chem. Soc.* **2009**, *131*, 15120–15121.

Chem Soc Rev

RSC Publishing

TUTORIAL REVIEW

View Article Online
View Journal | View Issue

Fabrication of metal nanoparticles in metal–organic frameworks†

Cite this: *Chem. Soc. Rev.*, 2013, **42**, 1807

Received 8th August 2012

DOI: 10.1039/c2cs35320b

www.rsc.org/csr

Hoi Ri Moon,[a] Dae-Woon Lim[b] and Myunghyun Paik Suh*[b]

In this review, we highlight various preparative strategies and characterization methods for metal nanoparticles fabricated in porous metal–organic frameworks (MOFs) or porous coordination polymers (PCPs), and their applications in hydrogen storage and heterogeneous catalysis.

1. Introduction

Metal–organic frameworks (MOFs) are the materials that are constructed by connectivity of metal ions and multidentate organic building blocks. MOFs are also called porous coordination polymers (PCPs) or coordination polymer networks (CPNs).[1] Most of these solid materials possess well-defined pores and large internal surface areas. Although permanent porosity cannot be always generated in MOFs, it is a useful property for the applications. By selecting appropriate inorganic and organic building blocks, the rational design of framework structures having desired pore size and shape is feasible.[2] Easy functionalization and modification of the inner pore surface are also important features of MOFs.[3] Well-designed MOFs can be applied in gas storage and separation,[4] heterogeneous catalysis,[5] molecular recognition and sensing,[6] and optics.[7]

Recently, there have been extensive efforts to fabricate metal-nanoparticles (M-NPs) in MOFs to elicit the properties that are hardly achieved by the individual material.

The physical and chemical properties of M-NPs are different from those of bulk metals, such as thermal and electrical conductivities, which are manifested by delocalization of free electrons.[8] Since the high surface-area-to-volume ratio of M-NPs provides a large number of active sites, the size and shape control of M-NPs is the key to achieve enhanced reactivity.[9] However, as a consequence of the high surface energy and large surface area

[a] *Interdisciplinary School of Green Energy and KIER-UNIST Advanced Center for Energy, Ulsan National Institute of Science and Technology, Ulsan 689-798, Republic of Korea. E-mail: hoirimoon@unist.ac.kr; Fax: +82-52-217-2019; Tel: +82-52-217-2928*

[b] *Department of Chemistry, Seoul National University, Seoul 151-747, Republic of Korea. E-mail: mpsuh@snu.ac.kr; Fax: +82-2-886-8516; Tel: +82-2-880-7760*

† Part of the centenary issue to celebrate the Nobel Prize in Chemistry awarded to Alfred Werner.

Hoi Ri Moon

Hoi Ri Moon received her BS degree from the Department of Chemistry, Ewha Womans University (2001), and MS (2003) and PhD (2007) from Seoul National University under the direction of Professor Myunghyun Paik Suh. After postdoctoral work with Dr Jeffrey J. Urban at Lawrence Berkeley National Lab, she became an assistant professor at the Interdisciplinary School of Green Energy, Ulsan National Institute of Science and Technology (UNIST) in 2010. Her research interests are nanostructured inorganic materials for energy applications.

Dae-Woon Lim

Dae-Woon Lim received his BS (2009) degree in chemistry from DanKook University in Korea. He is currently a PhD student at Seoul National University, working on porous materials and nanocomposites for hydrogen storage under the guidance of Prof. Myunghyun Paik Suh.

of M-NPs, their thermodynamic stability is severely decreased, which obstructs the control of size and shape with high uniformity. Various synthetic methods have been exploited to obtain monodispersed and small-sized M-NPs. To control the nucleation and growth of M-NPs, an organic surfactant or a polymer has been introduced as a surface capping agent,[10] or M-NPs have been enclosed within an inorganic material such as silica to form a core–shell structure.[11]

Another approach is to produce M-NPs inside porous inorganic materials with defined pore size such as zeolites, mesoporous aluminosilicates, and other porous inorganic or organic materials.[12] In particular, MOFs have been utilized as supports for M-NPs since they control the limited growth of M-NPs in the confined cavities, and produce monodispersed M-NPs.[13]

Utilization of MOFs as supports for M-NPs has several advantages over other porous materials; their three dimensional pore structures, the presence of organic linkers that stabilize M-NPs, robust structural property in some cases, and moderate thermal stability. Various MOFs with different pore sizes and shapes can be prepared from a wide range of metal ions and organic linkers, and thus an appropriate MOF can be easily selected as a host matrix. In choosing a MOF for loading M-NPs, the structural stability of the MOF upon the precursor loading or reduction procedure should be considered. Furthermore, to maintain a high surface area of the MOF, caution must be taken in the reduction process not to block the pores by the NPs or by unwanted by-products formed. Although the encapsulation of M-NPs in MOF pores is expected to limit the particle growth, the precursor compound and the product can actually diffuse out through the pores of the host to form M-NPs on the surface of the MOF crystal, instead of being inside the pores. Therefore, the location of the M-NPs, on the surface of the crystal or inside of the pores, should be verified by experimental evidence. If MOFs have straight channels, they do not provide an adequate confinement effect, and thus there is a possibility that agglomeration may occur and M-NPs may escape through the pores. Therefore, it is necessary to develop novel porous MOFs that can be employed as supports for M-NPs for the improvement of efficiency.

Myunghyun Paik Suh

Myunghyun Paik Suh is a professor in the Department of Chemistry at Seoul National University. She received her BS from Seoul National University (1971) and PhD from the University of Chicago (1976), and started her career as an assistant professor at the Seoul National University in 1977. Her current research interest is the development of energy and environment related materials based on coordination chemistry and nanoscience. She is a member of the Korean Academy of Science and Technology, and has received the Korean Science Award offered by the President of Korea.

M-NPs@MOF can be applied to hydrogen storage[14,15] and heterogeneous catalysis, depending on the type of metal.[16–20] For example, Pd-NPs@MOF has shown enhanced hydrogen storage both at 77 K and at room temperature.[14] In particular, Mg-NPs@MOF adsorbs hydrogen by physisorption at low temperatures and by chemisorption at high temperatures, exhibiting a synergistic effect on both adsorptions.[21] The material increases isosteric heat of hydrogen physisorption and decreases significantly the hydrogen chemisorption/desorption temperatures compared to Mg powder. Furthermore, some M-NPs@MOFs have exhibited excellent catalytic activities in organic reactions due to the confinement effect of the substrates in a MOF as well as the limitation of the particles that remain constrained and do not grow further after catalytic reactions.

A couple of years ago, Fischer *et al.* published a wonderful review entitled "Metals@MOFs – Loading MOFs with Metal Nanoparticles for Hybrid Functions".[13] The paper described the preparation and characterization methods of M-NPs@MOF materials as well as some useful applications. In the present tutorial review, we embrace the recent progress in the development of M-NPs@MOF systems, including previously reviewed systems, and cover the advanced characterization techniques and more extensive applications. In particular, we discuss some important issues that have arisen in this field of research such as size control of M-NPs in MOFs, localized destruction of frameworks in M-NPs@MOFs, and location of M-NPs in MOFs.

2. Various methods of preparation

General synthetic methods to embed M-NPs in a porous solid matrix entail the impregnation of a metal precursor in a porous solid, followed by reduction of the metal precursor to metal(0) atoms, which aggregate into M-NPs within the solid matrix. The precursor molecules that are most frequently used for the production of M-NPs are chloride or nitrate salts of the corresponding transition metal ions. In addition, organometallic complexes are often used as precursors in the solid grinding or infiltration method.[22] In general, metal precursors included in MOFs are reduced with hydrogen gas, hydrazine, or $NaBH_4$ to generate M-NPs, and the reduction process is often performed at high temperature, followed by a washing step. In some cases, supercritical CO_2-methanolic solution has been used to load the precursor compound within a MOF, followed by a heating process.[23] The reaction conditions for fabricating M-NPs in MOFs should be determined depending on the properties of the included precursors as well as the stability of the host matrices during the reduction process. Since the size of the NPs is significantly affected by the loading time of the metal precursor and the reduction conditions, these conditions should be carefully controlled.

2.1 Simple immersion of redox active MOFs in metal salt solutions

Contrary to the conventional methods, Suh's group developed new fabrication methods for M-NPs in PCPs, which produced M-NPs without using any capping or reducing agents and with

no heating process at all.[14,24–27] They used redox active PCPs as supports for M-NPs and immersed them in the solutions of metal salts such as $AgNO_3$, $NaAuCl_4$, and $Pd(NO_3)_2$. They prepared redox active PCPs by using redox active building blocks. Redox active sites of the redox active building blocks may be at the organic ligands or at the metal centers such as Ni(II) sites in the Ni(II) macrocyclic complexes. As soon as metal ions are diffused into the redox active PCPs, they are reduced to metallic nanoparticles and the redox active building blocks in the PCPs are oxidized. The maximum amount of M-NPs formed can be easily predicted since the redox reactions between the redox active networks and metal ions are stoichiometric. In most of the cases, the redox active PCPs retain their network structures even after the formation of M-NPs that are commonly much larger than the pore size of the PCPs. The most important advantage of this method is that the amount of M-NPs loaded in the PCP can be controlled by the immersion time of the host solid in the metal ion solution, while the size of the M-NPs is unaffected by the immersion time, concentration of the metal ion solution, temperature, and the type of solvent.

Suh's group employed various Ni(II) square-planar macrocyclic complexes as redox active metal building blocks to construct redox-active PCPs.[24–27] The Ni(II) macrocyclic complexes were prepared by simple one-pot template Schiff base condensation reactions.[28] They synthesized PCPs by self-assembly of the Ni(II) macrocyclic complexes and multidentate organic ligands containing carboxylate donor groups. The Ni(II) ion of the macrocyclic complex has a square planar coordination geometry and coordinates to the carboxylate ligands through the axial positions to generate octahedral geometry. Therefore, the Ni(II) macrocyclic complex simply acts as *a linear linker* to connect the organic ligand in the construction of PCPs. By selecting organic building blocks of various topologies, PCPs whose topology can be easily predicted from the geometry of organic ligands are constructed. The octahedral Ni(II) macrocyclic complexes can be easily oxidized to Ni(III) species.[29] The oxidation potential of Ni(II) to Ni(III) in the monomacrocyclic complexes is in the range of +0.90–+0.93 V *vs.* SCE in acetonitrile solutions.[28] When the PCPs constructed from Ni(II) macrocyclic complexes in octahedral coordination mode react with appropriate noble metal ions, oxidized PCPs with Ni(III) macrocyclic species and metal(0) nanoparticles result. Various Ni(II) macrocyclic complexes employed in the construction of redox active PCPs are shown in Fig. 1.[24–27]

The self-assembly of $(NiL_4)(ClO_4)_2$ ($NiL_1^{2+} = [Ni(C_{10}H_{26}N_6)]^{2+}$) and Na_2bpdc ($bpdc^{2-}$ = 4,4′-biphenyldicarboxylate) in a H_2O–pyridine mixture resulted in $[(NiL_4)_3(bpdc)_3]\cdot 2pyridine\cdot 6H_2O$ (**1**), in which linear coordination polymer chains pack as a double network of threefold braids to generate 1D channels with honeycomb-shaped

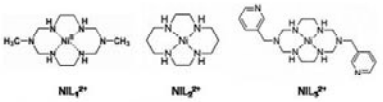

Fig. 1 Chemical structures of Ni(II) macrocyclic complexes as redox active species.

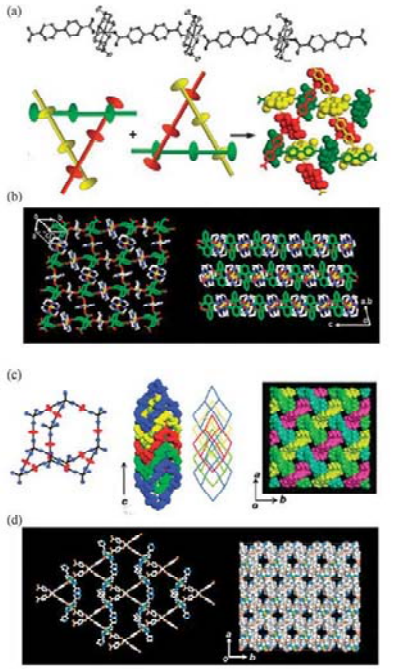

Fig. 2 X-ray structure of porous coordination polymer (a) $[(NiL_4)_3(bpdc)_3]\cdot 2pyr\cdot 6H_2O$ (**1**), (b) $[(NiL_5)_2(bpte)]\cdot 2H_2O$ (**2**), (c) $[(NiL_5)_2(mtb)]\cdot 8H_2O\cdot 4dmf$ (**3**), and (d) $[(NiL_6)_2(tcm)]\cdot 5dmf\cdot 8H_2O$ (**4**). Reprinted with permission from ref. 24–27.

windows (effective pore size, 7.3 Å) (Fig. 2a).[24] When desolvated host **1** was immersed in a methanolic solution of $AgNO_3$ (8.0×10^{-2} M) at room temperature for 10 min, Ag NPs (*ca.* 3 nm in diameter) were formed in solid **1**. Inclusion of Ag(I) ions into **1** resulted in the oxidation of incorporated Ni(II) species to Ni(III) and simultaneous reduction of Ag(I) to Ag(0), followed by the nucleation and growth of Ag NPs. The redox reaction between Ag(I) and Ni(II) species was proved by electron paramagnetic resonance (EPR) spectroscopy indicating the presence of d^7 Ni(III) species ($g_\perp > g_\parallel$) together with X-ray photoelectron spectroscopy (XPS) showing the coexistence of Ni(III) and Ag(0). Elemental analysis data for the solid composite isolated after immersion of **1** in $AgNO_3$ solution for 10 min indicated that the reaction stoichiometry of Ni^{II} in the host matrix and $AgNO_3$ was 1 : 1, proving that the redox reaction is quantitative. Since the host framework became positively charged after the redox reaction, it included free NO_3^- anions as shown by the unsplit 1382 cm^{-1}

peak in the IR spectra. The powder X-ray diffraction (PXRD) patterns indicated that the framework structure was retained even after the formation of Ag NPs, and the peaks corresponding to Ag NPs were extremely weak due to the very small sized NPs and too little Ag compared to the amount of the host solid. Introducing well-designed building blocks into PCPs, the single-step preparation method for M-NPs in the solid support was successfully developed without using reducing agents and stabilizing agents at room temperature. The average size of the M-NPs was independent of immersion time, concentration of the metal salts, type of solvents, and temperature. Most interestingly, despite the formation of the metal nanoparticles, PXRD patterns of the network were intact, suggesting that network structure was unaltered by the metal NPs that are much bigger than the aperture size of the network. This was because even if all M-NPs break down the network, less than 10% of the whole framework would be destroyed and thus most of the network would be retained.

By similar methods, Au and Pd NPs were also fabricated in the redox active PCPs. As shown in Fig. 2b, the two dimensional square grid coordination network $[(NiL_2)_2(bptc)]\cdot 2H_2O$ (**2**) was assembled from $(NiL_2)(ClO_4)_2$ (L_2 = 1,4,8,11-tetraazacyclotetradecane) and H_4bptc ($bptc^{4-}$ = 1,1′-biphenyl-2,2′,6,6′-tetracarboxylate). When **2** was immersed in EtOH solutions of $AgNO_3$ and $NaAuCl_4$ for 5 min, Ag NPs (3.7 ± 0.4 nm) and Au NPs (*ca.* 2 nm), respectively, were formed in the network.[25] In **2**, two dimensional layers of about 1 nm thickness were stacked with an interlayer spacing of 9.3 Å, through which $AgNO_3$ or $NaAuCl_4$ diffused and then their metal ions were reduced to Ag(0) and Au(0) NPs, respectively. Within 5 min of immersion in 0.1–0.3 M metal ion solution, redox reaction between the metal ions and the network occurred quantitatively, and all Ni(II) macrocyclic species were oxidized to Ni(III) to form Ag(0) NPs (*ca.* 4 nm) and Au(0) NPs (*ca.* 2 nm). This was characterized by elemental analyses, which indicated the inclusion of counter anions NO_3^- and Cl^-, respectively.

To fabricate small-sized Pd NPs in the PCPs, two redox active PCPs, $[(NiL_2)_2(mtb)]\cdot 8H_2O\cdot 4dmf$ (mtb^{4-} = methanetetrabenzoate, dmf = *N*,*N*′-dimethylformamide) (**3**) (Fig. 2c) and $[(NiL_3)_2(tcm)]\cdot 5dmf\cdot 8H_2O$ (L_3 = $C_{20}H_{33}N_8$; tcm^{4-} = tetrakis[4-(carboxyphenyl)-oxamethyl]methane) (**4**) (Fig. 2d), were prepared by the self-assembly of corresponding Ni(II) macrocyclic complexes and organic building blocks.[26,27] The PCP **3** has a fourfold interpenetrated diamondoid network generating 1D channels with ink-bottle-type pores having a big cavity (13.4 × 13.4 Å) connected with narrow necks (2.05 × 2.05 Å).[26] Immersion of the desolvated solid of **3** in an acetonitrile solution of $Pd(NO_3)_2$ resulted in 2 nm-sized Pd NPs by autoredox reaction between Ni(II) macrocyclic species incorporated in the network and Pd(II) ions. Similarly, network **4** constructed by doubly catenated rhombic grids that generate 1D channels (effective window size, 4.5 × 2.1 Å) also produced Pd NPs of 3 nm size.[27]

Suh's group also prepared redox active PCPs by using redox active organic building blocks.[14] Since 4,4′,4″-nitrilotrisbenzoate (ntb^{3-}) can be readily oxidized to the amine radical, the PCP constructed from ntb^{3-} becomes redox active as shown in Fig. 3.

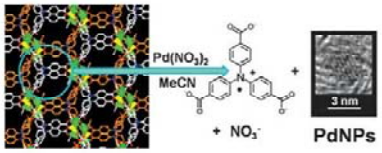

Fig. 3 Reaction of a MOF (**5**) incorporating redox-active organic species, 4,4′,4″-nitrilotrisbenzoate (ntb^{3-}), with Pd^{2+} ions. Reproduced with permission from ref. 14.

When a porous MOF, $[Zn_3(ntb)_2(EtOH)_2]\cdot 4EtOH$ (EtOH = ethyl alcohol) (**5**),[29] which was synthesized from the solvothermal reaction of H_3ntb and $Zn(NO_3)_2$, was immersed in the acetonitrile solution of $Pd(NO_3)_2$ (1.0×10^{-3} M) for 30 min, the Pd(0) NPs of size 3.0 ± 0.4 nm were formed in the channels (aperture size, 7.7 Å) of the MOF.[14] The EPR spectrum indicated that the MOF was oxidized to the positively charged network with the nitrogen radical. The amount of Pd NPs loaded in the MOF could be controlled by the immersion time in the metal ion solution, which in turn affected the H_2 uptake. The MOF embedded with 3 wt% Pd NPs adsorbed the highest amount of H_2 at 77 K and 1 atm. Since this formation reaction of Pd NPs is a stoichiometric redox reaction between Pd(II) ions and the ntb units of the host (Pd^{II} : ntb^{3-} = 1 : 2), a maximum of 9.05 wt% of Pd NPs can be formed if all of the ntb^{3-} units in the host are oxidized with palladium(II) ions. The PXRD pattern was retained intact even after the formation of Pd NPs that are larger than the channel size. This can be explained by the small volume ratio of Pd NPs produced *versus* the framework skeleton: even if all 3 wt% Pd NPs destroyed the framework, a maximum of 0.7% by volume of the framework skeleton could be destroyed according to the calculation.

This synthetic method for fabrication of M-NPs in PCPs *via* autoredox reaction has superior advantages such as neither a reducing agent nor a capping ligand is necessary, and the bare (naked) M-NPs are incorporated in porous host solids, which could be the leading candidates for heterogeneous catalysts as well as gas storage materials. Furthermore, the amount of M-NPs fabricated in PCPs can be controlled by the immersion time of the solid in metal ion solution and the concentration of the metal salts. The redox reaction can provide a 100% stoichiometric product. Although the resulting M-NPs often have larger diameters than the aperture size of the MOFs, the original structures of the frameworks are retained. The disadvantage is that the host solid should be oxidized and thus counter anions should be included in the pores, which reduces the surface area that is important for adsorption of gases and adsorbates.

Recently, it has been reported that when Rb-CD MOF and Cs-CD-MOF (CD = γ-cyclodextrin), which contain OH^- counter ions, were immersed in an acetonitrile solution of $AgNO_3$ and $HAuCl_4$, respectively, Ag NPs of 2.0 nm size and Au NPs of 3–4 nm size were formed.[30] In these cases, OH^- counter ions included in the frameworks either alone or cooperatively with the cyclodextrin units reduce the metal salt precursors to their

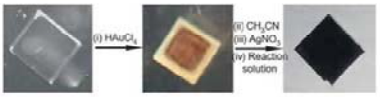

Fig. 4 Optical images of Rb-CD-MOF first loaded with Au NPs in the core region, and then with Ag NPs in the shell region. Reprinted with permission from ref. 30.

respective NPs. While Ag NPs were deposited throughout the entire MOF crystal, Au NPs were located predominantly in the core of the crystal. The amount of deposited M-NPs increases upon either increasing the time of soaking or increasing the concentration of the metal precursors. By combination of the deposition modes of Ag and Au, a core–shell NPs@CD-MOF was also synthesized. By immersion of MOF crystals first in $HAuCl_4$ solution, a core of Au NPs (>90%) was prepared, which was washed with acetonitrile and then immersed in $AgNO_3$ solution to deposit Ag NPs (>90%) in the shell region. The relative dimensions of the Ag-rich and the Au-rich regions could be adjusted by changing the core size, as shown in Fig. 4. Although the reduction of metal salts proceeds much faster in MeOH than in MeCN, MeOH could not be used because it caused degradation of the MOF scaffolds.

2.2 Chemical vapor deposition of organometallic compounds followed by hydrogenolysis

Chemical vapor deposition (CVD) of volatile organometallic precursors has been used for preparation of the metallic or metal oxide thin film on two-dimensional supports. This technique, however, has been applied not only to the "flat surface"[31] but also to the "internal surface" of the porous materials[32] to prepare the nanocomposite materials including metal complexes or metal clusters. In this technique, a dried MOF and a volatile metal precursor are placed in two separate glass vials in a Schlenk tube. The tube is evacuated, sealed, and kept at proper temperature depending on the vapor pressure of the metal precursor under static vacuum (1 Pa). Upon infiltration of the metal precursor into the MOF, the crystal colors of the MOF would be changed. When hydrogenolysis of the composite material is carried out to reduce the metal precursor, M-NPs incorporated in the MOF are generated.[33–35]

As shown in Fig. 5, various organometallic complexes that have appropriate sizes to enter into the cavities of the MOFs were used as precursors for CVD. When the vapor of $[(\eta^5\text{-}C_5H_5)Pd(\eta^3\text{-}C_3H_5)]$ (**A**), $[(\eta^5\text{-}C_5H_5)Cu(PMe_3)]$ (**B**), and $[(CH_3)Au(PMe_3)]$ (**C**), respectively, was introduced into MOF-5 that has a pore diameter of 8 Å, under static vacuum (1 Pa) at room temperature, metal precursors were embedded into MOF-5, as characterized by PXRD, elemental analysis, IR spectra, and solid state ^{13}C magic-angle spinning nuclear magnetic resonance (MAS NMR) spectra.[33] When the resulting **A**@MOF-5, **B**@MOF-5, and **C**@MOF-5 were treated with H_2 stream at the temperatures of hydrogenolysis (Pd for 23 °C, Cu for 150 °C, and Au for 190 °C), the "naked" metal-nanoclusters were formed. The sizes of the resulting M-NPs were 1.4 ± 0.1 nm for Pd@MOF-5, 3–4 nm for Cu@MOF-5, and 5–20 nm for Au@MOF-5. The polydispersity of Au NPs was explained by the high mobility of reduced Au nuclei in the open MOF-5 structure. In the PXRD pattern of Pd@MOF-5, characteristic peaks of the MOF-5 framework were significantly reduced, but the gas sorption data afforded a Langmuir surface area of 1600 $m^2\ g^{-1}$, indicating that the framework of Pd@MOF-5 was still highly porous. In addition, instead of thermally induced hydrogenolysis, UV photolysis of the metal precursor infiltrated in MOF-5 was carried out by using a high pressure Hg lamp, which alternatively generated very small Pd and Cu NPs (1–2 nm) in the MOF-5 under much milder conditions.

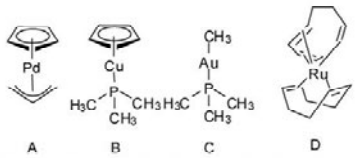

Fig. 5 Organometallic precursors for chemical vapor deposition.

Similarly, a Ru precursor, [Ru(cod)(cot)] (**D**, cod = 1,5-cyclooctadiene, cot = 1,3,5-cyclooctatriene), was loaded into MOF-5 by the CVD method.[34d] The homogeneous distribution of **D** in the MOF-5 framework was ascertained by a cross sectional photo as well as TEM images of **D**@MOF-5 crystals. The PXRD of **D**@MOF-5 showed the intact host structure even after inclusion of volatile Ru precursor **D**. Subsequent hydrogenolysis of the adsorbed **D** yielded Ru NPs of size 1.5–1.7 nm embedded in the MOF.[34d] In the hydrogenolysis reaction, mild conditions such as 25 °C for 30 min did not lead to the quantitative formation of Ru NPs. ^{13}C MAS NMR spectra indicated that hydrogenolysis of the cot ligand in **D** occurred prior to that of the cod ligand. The partially hydrogenated precursor **D** was converted to a [(cod)Ru(0)] fragment, and the Ru(0) atom formed a new coordination bond with a benzene ring of terephthalate in the host framework. Therefore, hydrogenolysis under mild conditions at 25 °C could not generate M-NPs. To obtain Ru@MOF-5 from **D**@MOF-5 quantitatively, the hydrogenolysis should be conducted under 3 bar H_2 at 150 °C for a longer period of time, 48 h. Quantitative hydrogenolysis of **D** and removal of all volatile byproducts from MOF-5 were confirmed by ^{13}C MAS NMR and FT-IR spectra. After complete decomposition of the Ru precursor **D**, the material Ru NPs@MOF-5 was obtained. In addition, this method was used to prepare Ni NPs in a mesoporous MOF, MesMOF-1 ($Tb_{16}(TATB)_{16}$, TATB = triazine-1,3,5-tribenzoate) (Fig. 6).[34c] After gas-phase loading of nickelocene in MesMOF-1, the sample was treated with hydrogen gas at 95 °C for 5 h, which yielded cyclopentane and Ni NPs included in MesMOF-1. When the residual cyclopentane molecules were removed by washing with methanol, Ni NPs@MesMOF-1 resulted. Depending on the loading time of the precursor, the amount of Ni NPs fabricated in MesMOF-s could be controlled.

This CVD method was also employed for the preparation of bimetallic nanoparticles such as FePt, PdPt, and RuPt in a MOF

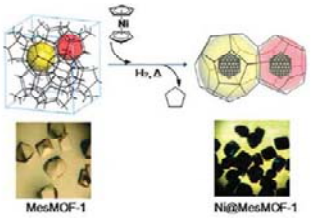

Fig. 6 Preparation of Ni@MesMOF-1. Reprinted with permission from ref. 34c.

by loading MOF-5 with a combination of two different metal–organic CVD precursors.[35] In a Schlenk tube, dry MOF-5 and two metal precursors were placed, and the tube was evacuated (10^{-3} mbar), sealed, and kept at room temperature for several hours. The simultaneous loading of two different metal precursors in MOF-5 was verified by ^{13}C MAS NMR spectroscopy, PXRD and elemental/AAS (atomic absorption spectroscopy) analyses. After hydrogen treatment, the composite material of MOF-5 incorporating a bimetallic nanoalloy was obtained. In this reaction, the selection of proper temperature for hydrogenolysis is important, because if mild conditions are applied to avoid decomposition of the host framework MOF-5, both precursors could not be reduced to bimetallic alloy nanoparticles. When harsh conditions were applied to achieve quantitative co-hydrogenolysis of the precursors, the hydrogenation of bdc linkers in MOF-5 occurred to yield *cis*/*trans*-1,4-cyclohexane dicarboxylic acid.

2.3 Chemical vapor deposition of an organometallic compound followed by thermal decomposition

Recently Suh's group reported that they fabricated hexagonal-disk shaped magnesium nanocrystals (Mg NCs) within a MOF by chemical vapor deposition followed by simple thermal decomposition without a hydrogenolysis step.[21] They deposited the vapor of bis-cyclopentadienyl magnesium ($MgCp_2$) in SNU-90′ at 80 °C. The resulting $MgCp_2$@SNU-90′ was thermally decomposed at 200 °C under an argon atmosphere, followed by removal of the organic by-products by evacuation. The reaction resulted in hexagonal-disk shaped Mg NCs embedded in SNU-90′. The absence of the organic traces for the decomposed bis-cyclopentadienyl was checked with the NMR spectra. The amount of Mg NCs embedded in the MOF could be controlled by the reaction conditions during the chemical vapor deposition of $Mg(Cp)_2$, such as length of the deposition time and whether or not the prevacuum state was maintained in the reaction bottle. The Mg nano disk had the diagonal length and the thickness of a hexagon, average 60 ± 18 nm and average 37 ± 12 nm, respectively.

Even though Mg NCs were much bigger than the channel size (12.9 Å × 9.6 Å) of the MOF, they were embedded inside the channels of the MOF as confirmed by TEM and electron tomography (Fig. 7). The powder X-ray diffraction (PXRD) patterns showed that the structure of SNU-90′ was maintained

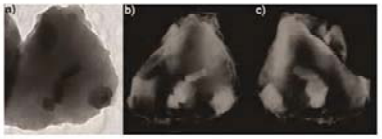

Fig. 7 TEM and electron tomography images of Mg@SNU-90′. (a) TEM image. (b) and (c) Tomographically reconstructed images of Mg NCs embedded in SNU-90′ at different angles. Reprinted with permission from ref. 21.

even after the formation of Mg NCs. When the Mg@MOF was exposed to air for 2 days, the PXRD pattern showed the peaks corresponding to MgO, with retention of the framework structure of SNU-90′.

2.4 Immersion of MOFs in metal salt solutions followed by reduction

This approach is based on the solution-phase technique. A porous support is immersed in the solution of a metal precursor. The metal precursor is mostly metal salt such as metal nitrate and chloride, and is completely dissolved in an organic solvent or sometimes in water. When the dried porous solid is soaked in the metal ion solution, the metal ions are infiltrated into the empty pores. The metal precursors should be carefully selected by considering the size of pores or channels of the MOF. After removal of the guest solvent molecules included in the host framework, the metal ions impregnated in the solid support are reduced by a reducing agent, typically H_2 gas, to obtain M-NPs embedded in the MOF.

Recently Latroche *et al.* adopted this technique to prepare Pd NPs (2.0 nm) embedded in a MOF, MIL-100(Al) (MIL represents Materials of Institut Lavoisier).[15] MIL-100(Al) has the 3D structure of cubic zeolitic MTN topology, with two types of large cavities (effective internal diameters: 2.1 and 2.5 nm, respectively), having a smaller window opening of size 8.7 Å (Fig. 8). Therefore, MIL-100(Al) is accessible by $[PdCl_4]^{2-}$ whose longest edge is 5.7 Å. MIL-100(Al) was immersed in a 10% (v/v) aqueous HCl solution of H_2PdCl_4, and then the impregnated Pd complex was reduced with Ar–H_2 flow at 553 K for 6 h. The Pd NPs impregnation in MIL-100(Al) was evidenced by PXRD, inductively coupled plasma (ICP), and transmission electron microscopy (TEM) images. In the PXRD of Pd@MIL-100(Al), additional peaks to those of the host framework were found at 40.2°, 46.5°, 68.2°, and 81.1°, which corresponded to an α phase of a Pd cubic cell ($Fm\bar{3}m$). Based on the N_2 adsorption–desorption isotherms for MIL-100(Al) and Pd@MIL-100(Al), it was revealed that the BET surface area and the total pore volume of the framework were greatly reduced upon loading of Pd NPs in MIL-100(Al), from 1200 to 380 $m^2\ g^{-1}$ and from 0.65 to 0.33 $cm^3\ g^{-1}$, respectively. This indicates that insertion of Pd NPs alters the pore structure of MIL-100(Al).

In particular, the incipient wetness method, which is also called the capillary impregnation or dry impregnation method, is one of the impregnation techniques that have been developed to

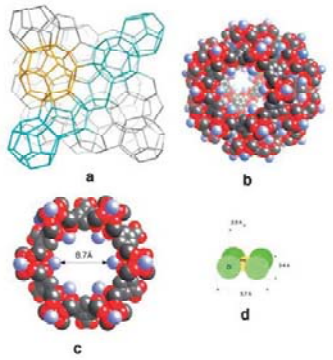

Fig. 8 (a) The MTN topology of MIL-100(Al): large cages are in yellow and small ones in turquoise. (b) Space-filling perspective view of the large cage of MIL-100(Al): carbon in gray, oxygen in red, terminal groups (water or OH) in pale blue. (c) Space-filling representation of the hexagonal window of the large cage (the same color codes as in panel b). (d) Size comparison of the $[PdCl_4]$ anion at the same scale. Reprinted with permission from ref. 15.

prepare heterogeneous catalysts. The solution of metal precursor, whose volume is the same as the total pore volume of the support, is added to the dried solid support. When the guest-free solid support and a definite amount of solution are mixed, capillary force leads the solution to fill the pores. Therefore, the incipient wetness method is called capillary impregnation or dry impregnation. The successive reduction reaction of the metal precursor generates M-NPs in the support. The proper choice of solvents, for example, water, polar, or nonpolar organic solvent, should be made based on the surface nature of the porous solid, so that the solution can be comfortably introduced into the pores of the porous solid. In this method, the loading amounts of metal are feasibly controllable by varying the concentrations of the precursor solution, and accordingly, the maximum loading amount is restricted by the solubility of the metal precursor in the solvent.[16]

Kaskel *et al.* introduced a similar method to embed Pd NPs in MOF-5.[36] The total volume of chloroform solution of $[Pd(acac)_2]$ (acac = acetylacetonate) was calculated from the pore volume of the desolvated MOF-5 (1.18 cc g^{-1}), and the exact amount of precursor solution was infiltrated into the empty space of MOF-5. The thermal (150 or 200 °C under vacuum) or hydrogen treatment (150 or 200 °C in H_2 flow) was conducted subsequently to reduce metal precursors to M-NPs. Various reduction conditions were applied to optimize the performance of the catalyst. During this hydrogen reduction, the benzene-1,4-dicarboxylate ligand was not hydrogenated as evidenced by ^1H and ^{13}C NMR spectra of Pd@MOF-5. The PXRD patterns measured after inclusion of $Pd(acac)_2$ and then reduction to Pd NPs in MOF-5 indicated that the 3D structure of MOF-5 remained unchanged.

Xu *et al.* have reported the fabrication of Pt-NPs in MIL-101(Cr) by using a "double solvent" method in order to avoid the aggregation of M-NPs on the external surface of the MOF.[37] The method involves immersion of a MOF in the metal salt solution, but it employs two different solvents, a hydrophilic solvent (water) and a hydrophobic solvent (hexane). The method minimizes the deposition of the precursor compound on the outer surface of the MOF. In the experimental process, the activated MOF was suspended in a large amount of dry *n*-hexane, to which was added the metal precursor (H_2PtCl_6) dissolved in water with a volume set equal to or less than the pore volume of the adsorbent (MIL-101). Because MIL-101(Cr) has a much larger inner surface area with hydrophilic character than the outer surface, the small amount of aqueous H_2PtCl_6 (equal to or less than pore volume) was readily incorporated into the pores by capillary force, which greatly minimizes the deposition of the precursor on the outer surface. After loading the precursor, the samples were treated with H_2–He stream at 200 °C for 5 h. By varying the concentration of the Pt precursor, various amounts of Pt NPs were loaded in MIL-101. The average size of Pt NPs formed was 1.8 ± 0.2 nm. The Pt@MIL-101 showed catalytic performance in various reactions such as ammonia borane hydrolysis, ammonia borane thermal dehydrogenation, and CO oxidation.

2.5 Immersion of MOFs in metal salt solutions followed by UV irradiation

It is possible to deposit M-NPs in the core of MOF crystallites by photochemical generation. For example, Ag@MOF-5 was prepared by photo catalytic reduction of Ag(I). When an ethanol solution of $AgNO_3$ was stirred in the presence of MOF-5 under UV irradiation, Ag NPs were formed in MOF-5.[38] The formation of Ag NPs in MOF-5 was evidenced by the color change of MOF-5 from white powder to dark brown-black. Similarly to the other observations, the PXRD pattern of Ag@MOF-5 indicated that MOF-5 structure was retained even after the formation of Ag NPs. The main advantage of the photochemical generation of M-NPs is the spatial resolution that can be achieved by using a light beam to effect the reduction leading to metallic particles. That is, by using this method, it may be possible to fabricate M-NPs in a specific part of the MOF crystal leaving the other part of the crystal without NPs. The photo catalytic reduction may be applied to prepare other noble metals. However, this photo catalytic reduction procedure is not generally applicable to all MOFs. This can be applied only to semiconducting MOFs. In contrast to the case of MOF-5, when MIL-53(Al) that contains the same terephthalate ligand but with Al^{3+} as a metal ion was used as a solid support, Ag NPs were not produced by similar photo irradiation. This is because MOF-5 is a semiconductor that is able to effect the photo catalytic reduction of noble metal ions, while MIL-53(Al) is not a semiconductor.

2.6 Impregnation of a metal salt in a photoactive MOF followed by visible light irradiation

Recently Lin *et al.* constructed photoactive MOFs that have the ability to generate Pt NPs by triethylamine (TEA)-mediated photoreduction.[18] The MOFs were prepared *via* a solvothermal reaction of

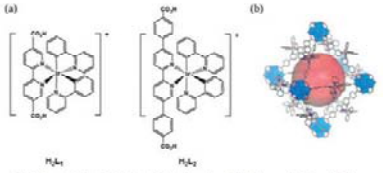

Fig. 9 (a) $[Ir(ppy)_2(bpy)]^+$-derived dicarboxylic acids H_2L_1 and H_2L_2. (b) The crystal structure of the photoactive MOF constructed from H_2L_2 and Zr^{4+}. Reprinted with permission from ref. 18.

$[Ir(ppy)_2(bpy)]^+$-derived dicarboxylic acids, H_2L_1 (L_1 = 2,2′-bipyridine-5,5′-dicarboxylate) and H_2L_2 (L_2 = 2,2′-bipyridine-5,5′-dibenzoate; ppy = 2-phenyl-pyridine; bpy = 2,2′-bipyridine) (Fig. 9a) with Zr^{4+}. The resultant MOFs, $Zr_6(\mu_3\text{-}O)_4(\mu_3\text{-}OH)_4(bpdc)_{5.94}(L_1)_{0.06}$ (**6**) and $Zr_6(\mu_3\text{-}O)_4(\mu_3\text{-}OH)_4(L_2)_6\cdot 64DMF$ (**7**), adopted the face centred cubic topology (fcu in classification of the Reticular Chemistry Structure Resource, available at http://rcsr.anu.edu.au) by connecting the $Zr_6(\mu_3\text{-}O)_4(\mu_3\text{-}OH)_4(carboxylate)_{12}$ secondary building units with the linear linker L_1 and L_2, respectively (Fig. 9b). The $[Ir^{III}(ppy)_2(bpy)]^+$ moiety in the MOFs can be excited by visible light to an excited state of $[Ir^{III}(ppy)_2(bpy)]^{+\bullet}$, which exhibits phosphorescence emission through an intersystem crossing. A mixture of K_2PtCl_4 and the MOF powder in a mixed solvent of tetrahydrofuran (THF)–TEA–H_2O was degassed and then irradiated with visible light from a 450 W Xe-lamp with a 420 nm cut-off filter. TEA reductively quenches the photo-excited $[Ir^{III}(ppy)_2(bpy)]^{+\bullet}$ to generate the reduced radical, $[Ir^{III}(ppy)_2(bpy^{\bullet-})]$, which reduces K_2PtCl_4 to form Pt nanoparticles within the host framework. Pt NPs with diameters of 2–3 nm in **6** and 5–6 nm in **7** were generated by an *in situ* photoreduction of K_2PtCl_4. Furthermore, the radicals can transfer electrons to the Pt NPs to reduce protons in water for hydrogen production. The PXRD pattern of Pt@MOF indicated that the framework structure was maintained even after loading of the Pt NPs.

2.7 Microwave irradiation on a MOF and metal precursor mixture

Although the reports existing so far are extremely rare, M-NPs can be fabricated on a MOF by microwave irradiation. By using the microwave-irradiation heating method, the activation of the pores of MIL-101 and the rapid chemical reduction of metal precursors were simultaneously performed in the presence of a reducing agent, which resulted in the formation of small Pd, Cu, and Pd–Cu nanoparticles of 2–3 nm within the pores and larger particles of 4–6 nm on the surface of the MIL-101 crystals.[20]

2.8 Grinding solid precursors with MOFs followed by hydrogenation

The solid grinding method is also an effective and facile route to fabricate M-NPs into porous materials.[17,39,40] Activated metal–organic frameworks which have accessible pore openings are ground together with volatile organometallic precursors in a mortar for several minutes at room temperature without using organic solvents. During grinding, the volatile precursor is sublimated and its vapor diffuses rapidly through the cavities of the MOF, which results in well-distributed deposition of the precursor. The metal precursor embedded in the porous MOF is treated with H_2 gas at high temperature, which produces very small M-NPs.

Haruta and Xu *et al.* reported several heterogeneous catalysts prepared by simple grinding of $[Au(acac)(CH_3)_2]$ (acac = acetylacetonate) and porous MOFs such as MOF-5, HKUST, ZIF-8, MIL-53(Al), and CPL-2.[17,39,40] Au NPs of size *ca.* 2 nm with small standard deviations, 2.2 ± 0.3 nm and 1.5 ± 0.7 nm, were fabricated in CPL-2 and MIL-53(Al), respectively. This is contrary to those obtained by a CVD method, which results in 3.0 ± 1.9 nm NPs with wider standard deviation in CPL-2.[41] Specific surface area of Au@CPL-2 prepared by the solid grinding method was reduced to 64 $m^2\ g^{-1}$ from 500 $m^2\ g^{-1}$ of as-synthesized CPL-2. This is attributed to the pore blocking by Au NPs as well as partial degradation of the porous structure. However, the PXRD pattern of Au@CPL-2 was the same as that of CPL-2, indicating that a large part of the host framework was still intact. The nanocomposites of small Au NPs and ZIF-8 show catalytic activity toward CO oxidation reaction to produce CO_2.[39]

2.9 Encapsulation of presynthesized metal nanoparticles in MOFs

Presynthesized metal NPs that are capped by stabilizing agents can be encapsulated in MOFs by introducing NPs into a synthetic solution containing molecular building blocks for MOFs. When individually capped-NPs are encapsulated in MOFs, the size of NPs can be easily controlled, and agglomeration of nanoparticles can be restricted in the host framework. Hupp and Huo *et al.* reported encapsulation of the PVP (polyvinylpyrrolidone)-capped nanomaterials with various sizes, shapes, and compositions in a zeolitic imidazolate framework, ZIF-8 (Fig. 10).[42] PVP has been widely used in the synthesis of various nanomaterials to control

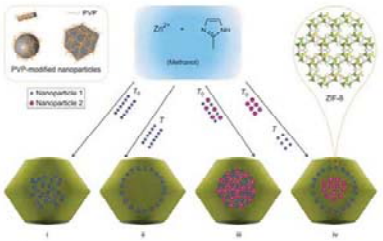

Fig. 10 Scheme of the controlled encapsulation of nanoparticles in ZIF-8 crystals. Through surface modification with surfactant PVP, nanoparticles of various sizes, shapes and compositions can be encapsulated in a well-dispersed fashion in ZIF-8 crystals, which formed by the assembly of zinc ions and imidazolate ligands. Reprinted with permission from ref. 42.

the size and shape as well as to stabilize them in polar solvents. By mixing PVP-capped Au NPs with a methanolic solution of zinc nitrate and 2-methylimidazole, Au@ZIF-8 was isolated by centrifugation. After isolation, the supernatant did not contain Au NPs, implying that almost all NPs were encapsulated in ZIF-8. This strategy was successfully extended to other nanomaterials such as Pt, CdTe, Fe_3O_4 and lanthanide-doped $NaYF_4$ nanoparticles, and Ag cubes, polystyrene spheres, β-FeOOH rods and lanthanide-doped $NaYF_4$ rods, whose surfaces were modified by PVP.[42]

3. Characterization of nanocomposites

Because M-NPs@MOFs is a complex system of organic–inorganic hybrid material, various analytical and spectroscopic tools should be employed for the characterization. During and/or after synthesis of the nanocomposites, both resultant nanoparticles and supporting MOFs should be carefully analyzed to explain the formation mechanism. The objects and tools for the characterization are listed below.

(1) Deposition of metal precursors within porous MOFs: inductively coupled plasma (ICP) spectroscopy, infrared (IR) spectroscopy, magic angle spinning (MAS) nuclear magnetic resonance (NMR) spectroscopy, elemental analysis, X-ray photoelectron spectroscopy (XPS).

(2) Morphology, size, distribution, and coordination environment of M-NPs: transmission electron microscopy (TEM), energy dispersive spectroscopy (EDS), extended X-ray absorption fine structure (EXAFS), ICP.

(3) Structural changes of MOFs after loading M-NPs: powder X-ray diffraction (PXRD) data.

(4) Features of nanocomposites: electron paramagnetic resonance (EPR), TEM, EDS, PXRD, ICP, BET measurement, XPS.

Loading of a volatile organometallic precursor, [Ru(cod)(cot)] (D, Fig. 5) (cod = 1,5-cyclooctadiene, cot = 1,3,5-cyclooctatriene), into MOF-5 by a CVD method was evidenced by solid state ^{13}C MAS NMR spectroscopy.[34a] As shown in Fig. 11, the carbon resonance signals indicated that the precursor D was included in MOF-5, and the nature of D was unchanged even after intercalation. Precursor D included in MOF-5 exhibited peaks with the chemical shifts very similar to those measured for pristine D in C_6D_6 rather than to those in the solid state. This means that D included in MOF-5 has high mobility, and behaves like being in the solution. The ^{13}C MAS NMR spectrum of D@MOF-5 after hydrogenolysis revealed that depending on the reaction temperature, degree of hydrogenation of D was varied. Under mild reduction conditions (25 °C, 30 min), Ru was still coordinated with the cot ligand, but it dissociated cod to interact with the bdc linker. Under harsh conditions (3 bar of H_2, 150 °C, 48 h), D@MOF-5 was quantitatively hydrogenized to yield Ru@MOF-5. In this case, MAS-NMR spectroscopy was used as a very powerful tool to elucidate the mechanism of formation of M-NPs in porous MOFs.

Transmission electron microscopy (TEM) is the most common and important technique to elucidate morphology, size, crystal structure, dispersity, and distribution of M-NPs within MOFs.

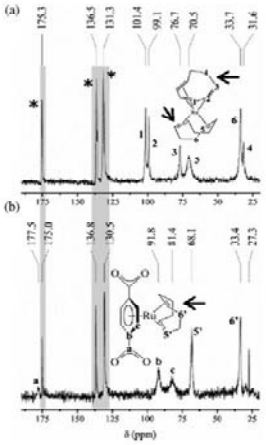

Fig. 11 ^{13}C MAS NMR spectra of D@MOF-5 before (a) and after (b) hydrogenolysis at 1 cc min^{-1} with H_2 at 25 °C for 30 min. Signals of MOF-5 are shaded. The carbon signals of MOF are marked with asterisks. Reprinted with permission from ref. 34a.

In addition to this, various tools such as high-resolution TEM (HR-TEM), selected area electron diffraction (SAED), high-angle annular dark-field scanning transmission electron microscopy (HAADF-STEM), tomography, energy dispersive spectroscopy (EDS), and electron energy loss spectroscopy (EELS) mapping can be utilized complementarily to explain the formation of M-NPs in MOFs clearly.

As shown in Fig. 12a, SAED combined with HR-TEM measurement for Pd NPs@4 indicated that the autoredox reaction between the included Pd^{II} ions and redox active PCP 4 yielded 2.9 ± 0.4 nm Pd NPs, which had a face-centered cubic (fcc) structure with a *d*(111) spacing of 0.23 nm. Small metal NPs less than 2 nm are more clearly seen in HAADF-STEM.[27] In Fig. 12b, small Au NPs with a mean diameter of 1.5 nm incorporated in MIL-53(Al) are clearly seen in the dark-field image obtained in STEM mode.[17] Although TEM is an essential tool to examine nano-sized materials, it has a limitation of providing only 2D information projected along the beam direction. In addition, it was demonstrated that rapid TEM-induced degradation of MOFs led to agglomeration of the initially formed small metal clusters, in particular Ag_3 clusters, into the stable and easily imaged bigger particles.[43]

As shown in Table 1, there are many reports indicating that M-NPs larger than the pore size of the MOF were formed. Therefore, the location of M-NPs deposited on MOFs has been a controversial issue. However, TEM cannot provide explicit solution to the dispute whether the M-NPs locate inside of the pores or only on the surface of the MOF. To address this issue,

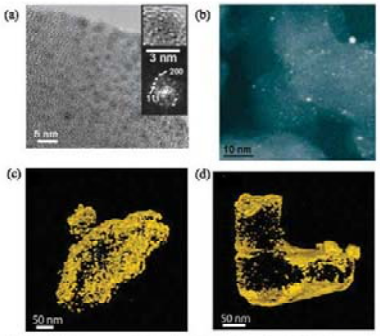

Fig. 12 (a) HR-TEM image and SAED for Pd NPs@**4**. (b) HAADF-STEM image of Au NPs@MIL-53(Al). Tomographically reconstructed images of (c) Pd NPs and (d) Ru NPs in MOF-5. Reprinted with permission from ref. 27 (a), ref. 17 (b), and ref. 44 (c and d).

the tomographic reconstruction of TEM images, which are taken using a 2° interval through the use of a penetrating e-beam, should be carried out to give 3D information. The electron tomography performed for Pd@MOF-5 and Ru@MOF-5 verified the position and distribution of the particles within the framework.[34a] As shown in Fig. 12c and d, the tomography images revealed that introduction of different kinds of metal precursors followed by reduction afforded various degrees of penetration and dispersion of the nanoparticles. The Pd NPs in Pd@MOF-5 had sizes ranging from 1 to 5 nm as evidenced by bright field TEM images, and the electron tomography indicated that Pd NPs with 1–3 nm size were distributed within the MOF-5 whereas larger particles/agglomerates were mostly located at the surface of MOF-5 (Fig. 12c).[44] In the TEM images of Ru@MOF-5, the particles seemed to be dispersed within MOF-5, but 3D tomographic reconstruction of Ru@MOF-5 revealed that particles were penetrated to only 20 nm depth of the host frameworks, and located at or close to the surface of the MOF-5 (Fig. 12d).[44]

The positions of Ag clusters incorporated in MOF-508 were also proved by tomography, which indicated that Ag clusters are permeated in the entire MOF matrix.[43] In this report, the authors claimed that the TEM electron beam rapidly (within several seconds) damages the framework structure of the soft material MOF, which facilitated aggregation of Ag nanoparticles resulting in NPs larger than the pore size of the MOF. To minimize this effect, during TEM measurement the specimen was cooled to *ca.* 100 K, and the beam was defocused. By comparison with TEM images of Ag@MIL-68(In) before and after e-beam damage, it was revealed that the beam significantly affected agglomeration of Ag NPs embedded in the MOF (Fig. 13). Even though the TEM technique was not appropriate to characterize as-synthesized Ag NPs, EPR spectroscopy confirmed the formation of Ag_4 clusters, which were small enough to be embedded in pores of MOFs. FT-IR analysis also indicated that the MOF provided a large kinetic barrier toward crystallization.

The possible structural changes of MOFs before and after loading M-NPs were monitored by PXRD patterns. As shown in Fig. 14, by the comparison of PXRD patterns, it was revealed that the original structure of **1** was maintained even after Ag NPs were generated in PCP **1** by the autoredox reaction between Ag(I) ions and Ni(II) species incorporated in **1**.[24] However, when the reaction time was prolonged, the PXRD pattern became weaker and broader, suggesting that the original host structure could be destroyed. During the autoredox reaction, the oxidation states of metal precursors as well as the metal ions in the host framework were studied by EPR and XPS analyses.[11,21–27]

EPR spectroscopy and XPS are also used to verify the M-NPs incorporated in MOFs. When a redox active PCP, $[(NiL_2)_2(bptc)]\cdot 2H_2O$ (**2**), was immersed in an EtOH solution of $NaAuCl_4\cdot 2H_2O$ for several min at room temperature, *ca.* 2 nm size Au NPs were formed in **2**.[25] The EPR spectrum measured for Au NPs@**2** showed the anisotropic signals at $g_\perp = 2.177$ and $g_\parallel = 2.026$, clearly indicating tetragonally distorted Ni(III) species (Fig. 15a). The XPS data (Fig. 15b) showed that Au(0) and Ni(III) species coexisted in the nanocomposites. These indicated that the Ni(II) species incorporated in **2** were oxidized to Ni(III) species, and simultaneously Au(III) was reduced to Au(0) atoms, which aggregated into Au NPs.

Although TEM is an effective technique to observe the morphology and size of metallic NPs, it has the limitation of resolution, and well-dispersed metal clusters less than 1 nm size cannot be distinguished by HAADF-STEM images as well as by bright-field TEM images. As shown in Fig. 16, EXAFS can precisely tell the size, coordination environment, and chemical form of very small metal clusters. By the solid-grinding method, Au clusters smaller than 1 nm were successfully intercalated in a porous Cd-MOF, but the ultrafine Au clusters could not be detected by TEM.[40] However, Au L_{III}-edge EXAFS revealed the presence of Au^0 and ultrafine gold clusters with the average atom number of 2.5. In addition, from this analysis, kinds of bonds between Au atoms and others and the coordination number of Au atoms could be determined. It was revealed that Au atoms interacted with F and O atoms of the host framework.

4. Important issues for M-NPs@MOF

On characterization of M-NPs@MOF, several important issues should be addressed such as (1) size control of M-NPs in MOFs, (2) size of M-NPs *vs.* cavity size of MOF, (3) localized destruction of the framework upon loading M-NPs, and (4) location of M-NPs in MOFs. Although these issues are related to each other, here we discuss them separately.

4.1 Size control of M-NPs: size of M-NPs *vs.* cavity size of MOF

Size of M-NPs loaded in the MOFs often cannot be easily controlled even under controlled experimental conditions. In the case of simple immersion of redox active PCPs in the metal salt solutions, the average size of the resulting M-NPs is independent of immersion time, concentration of the metal

Table 1 Preparation method, particles size, and application of various M-NP@MOFs

Section	Metal precursor[a] (loading amount, wt%)	MOF[b] (pore size, Å)	Preparation method (solvent)	Reduction method	Metal size (nm)	Application	Ref.
2.1	$AgNO_3$	$[Ni(C_{10}H_{26}N_6)]_3(bpdc)_3$ (7.3)	Impregnation (methanol)	Redox-active Ni^{II} macrocycle	3	—	24[c]
	$AgNO_3$	$[Ni(cyclam)]_2[bptc]$	Impregnation (ethanol)	Redox-active Ni^{II} macrocycle	3.7 ± 0.4	—	25[c]
	$AgNO_3$ $HAuCl_4$	Cs-CD-MOF/ Rb-CD-MOF (8)	Impregnation (acetonitrile)	OH^- counter ions in MOF	(Ag, 2 0. ± 4) (Au, 3–4)	—	30
	$NaAuCl_4{\cdot}2H_2O$	$[Ni(cyclam)]_2[bptc]$	Impregnation (ethanol)	Redox-active Ni^{II} macrocycle	2	—	25
	$Pd(NO_3)_2$ (1.0 wt%)	$[Ni(cyclam)]_2(mtb)]$ (2.05)	Impregnation (acetonitrile)	Redox-active Ni^{II} macrocycle	2.0 ± 0.6	—	26[c]
	$Pd(NO_3)_2$ (5.0 wt%)	$[Ni(C_{20}H_{32}N_8)]_2[tcm]$ (4.5 × 2.1)	Impregnation (acetonitrile)	Redox-active Ni^{II} macrocycle	2.9 ± 0.4	—	27[a]
	$Pd(NO_3)_2{\cdot}2H_2O$ (3.2 wt%)	$[Zn_3(ntb)_2(EtOH)_2]$ (7.7)	Impregnation (acetonitrile)	Redox active MOF	3.0 ± 0.4	Hydrogen storage	14
2.2	Au(CO)Cl (30 wt%)	ZIF-8/ZIF-90 (12)	Chemical vapor deposition	H_2, 2 bar, 100–130 °C	(ZIF-8) 3.2 ± 0.1 (ZIF-90) 1.4 ± 0.2	Oxidation of alcohols	34b[c]
	$(CH_3)Au(PMe_3)$ (48 wt%)	MOF-5	Chemical vapor deposition	H_2, 190 °C, 4 h	5–20	CO oxidation (inactive)	33
	$(\eta^5\text{-}C_5H_5)Cu(PMe_3)$ (13.8 wt%)	MOF-5	Chemical vapor deposition	H_2, 150 °C, 1 h	1–2	Methanol production from syngas	33
	$NiCp_2$	MesMOF-1 (1.5, 1.7)	Chemical vapor deposition	H_2, 95 °C, 5 h	—	Conversion of styrene to ethylbenzene	34c[c]
	$(\eta^5\text{-}C_5H_5)Pd(\eta^3\text{-}C_3H_5)$ (35.6 wt%)	MOF-5	Chemical vapor deposition	H_2, 23 °C, 30 min	1–2	Hydrogenation	33
	Ru(cod)(cot) (18.7 wt%)	MOF-5	Chemical vapor deposition	H_2, 3 bar, 150 °C	1.5–1.7	Oxidation of alcohols, hydrogenation of benzene	34a[c]
2.3	$MgCp_2$ (10.6 wt%)	SNU-90 (12.9 × 9.6)	Chemical vapor deposition	Thermal decomposition	60 ± 18	Hydrogen storage	21
2.4	$HAuCl_4$ (0.47–0.52 wt%)	MIL-101 (30)	Impregnation (water)	H_2, 200 °C, 2 h	9.8 ± 3.4	Oxidation of alcohols	19
	H_2PdCl_4 (10 wt%)	MIL-100(Al) (8.7)	Impregnation (water)	H_2, 353 K	1.8 ± 0.4	Hydrogen storage	15
	$Pd(acac)_2$ (20.9 wt%)	MOF-5 (7)	Incipient wetness ($CHCl_3$)	H_2, 80 °C	40	—	16
	$Pd(acac)_2$ (1.04 wt%)	MOF-5	Incipient wetness impregnation ($CHCl_3$)	Vacuum heating (150–200 °C)/ H_2 (150–200 °C)	—	Hydrogen storage/ hydrogenation	36[c]
	H_2PtCl_6	MIL-101(Cr) (12, 16)	Impregnation (water–hexane)	H_2, 200 °C, 5 h	1.8 ± 0.2	Ammonia borane hydrolysis/ CO oxidation	37
2.5	$AgNO_3$	MOF-5	Impregnation (ethanol)	UV irradiation	—	—	38
2.6	K_2PtCl_4	$Zr_6(\mu_3\text{-}O)_4(\mu_3\text{-}OH)_4(bpdc)_{5.94}(L_1)_{0.06}$	Impregnation (THF–TEA–H_2O)	Photoreduction Xe-lamp	2–3		18
		$Zr_6(\mu_3\text{-}O)_4(\mu_3\text{-}OH)_4(L_2)_6{\cdot}$ 64DMF (16)			5– 6		18
2.7	$Pd(NO_3)_2$ (4.9 wt%)/ $Cu(NO_3)_2$ (2.0 wt%)	MIL-101 (30)	Impregnation (water)	Hydrazine with microwave irradiation	2–3, 4–6	CO oxidation	20
2.8	$Me_2Au(acac)$	CPL-1 (4 × 6)	Solid grinding	H_2 120 °C, 2 h	—	Catalyst: oxidation of alcohols	17
		CPL 2 (6 × 8)			2.2 ± 0.3		
		MIL-53(Al) (8.5 × 8.5)			1.5 ± 0.7		
		MOF-5 (15 × 15)			—		
		Cu-BTC (11 × 11)			—		
	$(CH_3)_2Au(acac)$	ZIF-8	Solid grinding	H_2, 230 °C, 2.5 h	3.4 + 1.4	CO oxidation	39[c]
	$(CH_3)_2Au(acac)$ (1 wt%)	$[Cd_2(L)\cdot(H_2O)]{\cdot}0.5H_2O$	Solid grinding	H_2, 170 °C, 2 h	—	—	40
	5 wt% Pt supported on active carbon	MOF-5/IRMOF-8	Ground together		—	Hydrogen storage	47
2.9	Presynthesized M NPs M = Au, Pt, CdTe, Fe_3O_4, $NaYF_4$, Ag cubes, β-FeOOH	ZIF-8	Encapsulation of presynthesized metal nanoparticles	—	Au(13)/Pt (2.5, 3.3, 4.1)/ CdTe (2.8)/Fe_3O_4 (8)/ $NaYF_4$ (24)/Ag cubes (160)/β-FeOOH (22 × 160)	Catalyst, magnetic and optical material	42
Others	$AgNO_3$	Cu(BTC)/MOF-508/ MIL-68(In)	Impregnation (water–ethanol)	Ethanol	≤1	—	43[c]
	$HAuCl_4$ (0.47–0.52 wt%)	MIL-101 (30)		$NaBH_4$	2.3 ± 1.1/6.4 ± 2.6	Oxidation of alcohols	19

Table 1 (*continued*)

Section	Metal precursor[a] (loading amount, wt%)	MOF[b] (pore size, Å)	Preparation method (solvent)	Reduction method	Metal size (nm)	Application	Ref.
			Colloidal deposition (water)				
	$Pd(\eta^3\text{-}C_3H_5)(\eta^3\text{-}C_3H_5)$ (35 wt%)	MOF-5 (7)	Chemical vapor deposition	Photolysis UV light at RT	2.4 ± 0.2	—	16[c]
	$[PdCl_4]^{2-}$, $[PtCl_6]^{2-}$, $[AuCl_4]^-$	MIL-101(Cr) (12, 16)	Anion exchange	$NaBH_4$	2–4	Heck reaction	50
	$RuCl_3{\cdot}3H_2O$ (0.98 wt%)	La(1,3,5-BTC)·$6H_2O$	Colloidal deposition (supercritical CO_2–methanol)	Methanol	2	Hydrogenation	23

[a] Metal precursor = $NiCp_2$: Cp = cyclopentadienyl/[Ru(cod)(cot)]: cod = 1,5-cyclooctadiene; cot = 1,3,5-cyclooctatriene/$Pd(acac)_2$: acac = acetylacetonate. [b] MOF = $[Ni(C_{10}H_{28}N_4)]_3(bpdc)_3$: bpdc = [Ni(cyclam)]$_2$[bptc]: cyclam = 1,4,8,11-tetraazacyclotetradecane; H_4bptc = 1,1′-biphenyl-2,2′,6,6′-tetracarboxylic acid/Cs-CD-MOF; Rb-CD-MOF: CD = cyclodextrin/[Ni(cyclam)]$_2$(mtb): mtb = methanetetrabenzoic acid/$[Ni(C_{20}H_{32}N_8)]_2[tcm]$: tcm = tetrakis[4-(carboxyphenyl)oxamethyl]-methane/$[Zn_3(ntb)_2(EtOH)_2]$: ntb = 4,4′,4″-nitrilotrisbenzoate/ZIF-8: Zn(MeIM)$_2$: IM = imidazolate/ZIF-90: $Zn(ICA)_2$: ICA = imidazolate-2-carboxyaldehyde/MOF-5: $Zn_4O(bdc)_3$, bdc = benzene-1,4-dicarboxylate/MesMOF-1: $Tb_{16}(TATB)_{16}$: TATB = triazine-1,3,5-tribenzoate/SNU-90: $[Zn_4O(atb)_2]$·2DMF·$9H_2O$; atb = aniline-2,4,6-tribenzoate/MIL-101: $Cr_3F(H_2O)_2O[(O_2C)\text{–}C_6H_4\text{–}(CO_2)]_3{\cdot}nH_2O$/MIL-100(Al): $(Al_3O(OH)(H_2O)_2[btc]_2)\cdot 3nH_2O$; btc = benzene-1,3,5-tricarboxylate/$Zr_6(\mu_3\text{-}O)_4(\mu_3\text{-}OH)_4(bpdc)_{5.94}(L_1)_{0.06}$: L_1 = 2,2′-bipyridine-5,5′-dicarboxylate/$Zr_6(\mu_3\text{-}O)_4(\mu_3\text{-}OH)_4(L_2)_6$·64DMF: L_2 = 2,2′-bipyridine-5,5′-dibenzoate; ppy = 2-phenyl-pyridine; bpy = 2,2′-bipyridine/CPL-1: $[Cu_2(pzdc)_2(pyz)]_n$, pzdc = pyrazine-2,3-dicarboxylate, pyz = pyrazine/CPL-2: $[Cu_2(pzdc)_2(bpy)]_n$, bpy = 4,4′-bipyridine]/MIL-53(Al): $[Al(OH)(bdc)]_n$/Cu-BTC: $[Cu_3(btc)_2]_n$, btc = benzene-1,3,5-tricarboxylate/$[Cd_2(L)\cdot(H_2O)]\cdot 0.5H_2O$: L = 4,4′-(hexafluoroisopropylidene)diphthalate/MOF-508: Zn(BDC)(4,4′-Bipy)$_{0.5}$·(DMF)$(H_2O)_{0.5}$; BDC = 1,4-benzenedicarboxylic acid; 4,4′-Bipy = 4,4′-bipyridine MIL-68(In): In(OH)$(O_2C\text{–}C_6H_4\text{–}CO_2)$. [c] Ref. = ref. 13 includes the same data.

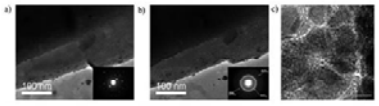

Fig. 13 Before and after TEM images of Ag@MIL-68(In). (a) TEM image of Ag@MIL-68(In) before significant electron beam damage. The inset is an SAED pattern of the MOF. (b) TEM image of Ag@MIL-68(In) after 1 min exposure, showing significant beam damage. The inset is an SAED pattern of the MOF and coalesced Ag. (c) HRTEM image of coalesced Ag particles. Reprinted with permission from ref. 43.

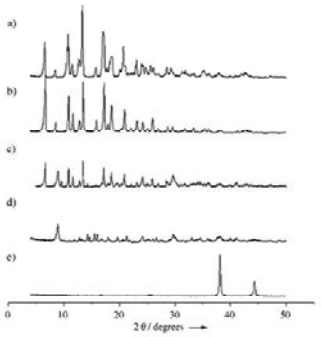

Fig. 14 PXRD patterns for (a) original host framework $[(NiL_1)_3(bpdc)_3]$·2pyr·$6H_2O$ (**1**), (b) desolvated host framework **1**, (c) desolvated host solid after immersion in a methanolic solution of $AgNO_3$ for 10 min, (d) after immersion for 18 h, and (e) host-free silver nanoparticles. Reprinted with permission from ref. 24.

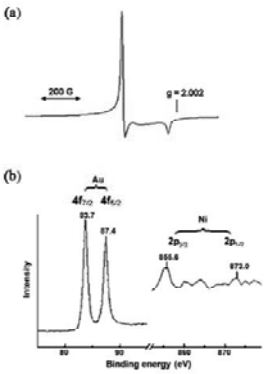

Fig. 15 (a) EPR spectrum of the solid that was isolated after $[(NiL_2)_3(bptc)]\cdot 2H_2O$ (**2**) was immersed in an EtOH solution of $NaAuCl_4{\cdot}2H_2O$ (3.4×10^{-2} M) for 20 min. Measured at 102 K; $g_\perp$ = 2.177 and $g_\parallel$ = 2.026. (b) XPS for the solid isolated after solid **2** (powder sample) was immersed in the EtOH solution of $NaAuCl_4{\cdot}2H_2O$ (3.4×10^{-2} M) for 5 min. Measured at room temperature. Reprinted with permission from ref. 25.

salts, type of solvents, and temperature.[14,24–27] The nature of metal seems to dominate the size distribution. Ag has a stronger tendency to aggregate than other noble metals such as Pd, Au, and Pt. The redox active PCPs commonly result in much larger M-NPs than the pore sizes of the PCPs, but the growth of M-NPs is still restricted by PCP matrices. This might be a compromise of the competition between the agglomeration tendency to lower the surface tension of M-NPs and the interaction of functional groups in MOFs with M-NPs, although they are not clearly

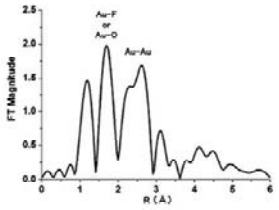

Fig. 16 Au L_{III}-edge FT-EXAFS spectrum for Au@Cd-MOF. The signal at approximately 1.2 Å is due to an experimental artifact. Reprinted with permission from ref. 40.

disclosed. The preparation of M-NPs whose sizes match with the pore sizes of MOFs has been rarely achieved by the functionalization of the MOF surface with strongly interacting groups.[34b] Two MOFs, ZIF-8 and ZIF-90, which have identical topology but different functional groups (methyl *vs.* aldehyde) at the organic linkers were chosen as the matrices to examine the role of the surface functional groups in the size control of Au NPs. The sizes (average <2 nm) of Au-NPs formed in ZIF-90 matched with the cavity size of ZIF-90, and very small, including Au_{55}, clusters were homogenously dispersed and stabilized inside the intact crystalline MOF matrix. The aldehyde groups in ZIF-90 act as the surfactant to prevent the growth of M-NPs and stabilize them more effectively compared with the nonfunctionalized and less interacting ZIF-8.

4.2 Localized destruction of frameworks

Robustness of the framework structures is very important for the application of M-NPs@MOFs. On preparation of M-NPs, chemical and thermal stabilities of the MOFs, acidity of metal precursor solutions, and loading amount of M-NPs affect the MOF structure. In the redox active PCP systems, despite the formation of the metal nanoparticles that are much bigger than the aperture size of the networks, the PXRD patterns indicated that the PCP networks were intact, suggesting that the network structures were unaltered by the formation of M-NPs.[24] This was because even if all M-NPs break down the network, only a small percentage of the framework would be destroyed and most of the network would be retained. However, as the immersion time increases, the original host framework can be destroyed as evidenced by PXRD, which might be attributed to the instability of the host in the solutions of metal precursors. The loading of M-NPs leads to a decrease in the surface area of MOFs because the M-NPs not only occupy the cavities of MOFs, but also increase the mass of the system.[34d] In particular, it has been demonstrated that electron beam irradiation during the TEM measurement also destroys the framework structure, which leads to the agglomeration of the particles. As mentioned earlier, in the case of Ag NPs, rapid TEM-induced degradation of MOFs led to agglomeration of the initially formed small Ag_3 clusters and resulted in stable and easily imaged bigger particles.[43]

4.3 Location of M-NPs in/on MOFs

M-NPs can be formed inside the cavities and/or on the external surface of MOFs. Although most of the M-NPs are fabricated inside the cavities of MOFs, some M-NPs can be formed on the surface of the MOFs. To locate the M-NPs, direct evidence should be provided by the TEM tomography technique as mentioned in the previous section. Although TEM is a powerful tool to elucidate the micro- and nano-structure of M-NPs@MOFs, TEM studies involving MOF materials should be performed with great care due to the instability of MOFs upon e-beam exposure.[34b,43] Recently, to avoid any possibilities of aggregation and to immobilize M-NPs inside the pores of MOFs, a double solvent method was employed by using a mixed solution system of hydrophilic and hydrophobic solvents.[37] This method resulted in successful fabrication of Pt NPs inside the pores of MIL-101(Cr) and minimized the deposition of the M-NPs on the outer surface. Zhang *et al.* prepared Ru NPs immobilized on the surface of a MOF. The material was prepared by dispersion of the MOF in a MeOH solution of $RuCl_3 \cdot 3H_2O$ and then introduction of supercritical CO_2, which was followed by heating at 200 °C for 5 h. Ru NPs were stabilized by interaction with the carboxylate groups of the MOF, and aggregation of the particles did not occur.[23] The strong interactions between the M-NPs and the MOF can generate enhanced catalytic activities of the material, compared with unsupported M-NPs.

5. Applications

5.1 Hydrogen storage

To apply MOFs as hydrogen storage materials, various efforts have been made such as pore size tuning,[45] generating accessible metal sites,[4a,46] and fabrication of M-NPs in the MOFs.[14,15,47] In particular, MOFs embedded with Pd NPs have been proven to have enhanced hydrogen uptake capacity at room temperature.[14,15,36,48] The phenomena have been explained by the spillover effect of Pd NPs that split H_2 molecules into hydrogen atoms before they are adsorbed in the MOF, although controversy still exists over the real mechanism. Some other mechanisms such as formation of Pd hydride and hydrogenation of the organic components in the MOFs should be considered as well, and the real mechanism should be proven by appropriate experiments. Besides Pd NPs, Mg NPs were fabricated in a MOF to prepare a hybrid hydrogen storage material.[21] The material Mg-NPs@MOF adsorbs hydrogen both by physi- and chemi-sorption, exhibiting a synergistic effect between them. It increases the isosteric heat of H_2 physisorption compared to pristine MOF and decreases the chemisorption/desorption temperatures by 200 °C compared to bare Mg powder. At 200 °C and 30 bar, 99% of Mg was converted to MgH_2, from which H_2 molecules could be released at $T > 250$ °C.[21]

Suh *et al.* reported that when Pd NPs (<5 nm) were fabricated in a MOF solid (**5**) by the redox reaction between Pd(II) ions and **5** incorporating redox active organic species (ntb^{3-}), the H_2 uptake capacity depended on the amount of Pd NPs loaded in the MOF.[14] The MOF loaded with 3 wt% Pd NPs showed significantly decreased N_2 and CO_2 uptake capacities because of the introduced counter anions (NO_3^-) and Pd NPs

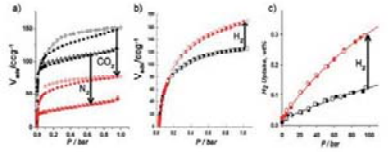

Fig. 17 Gas adsorption (solid symbols) and desorption (open symbols) isotherms for 3 wt% Pd NPs@$\mathbf{5}^{0.5,4}$-$(NO_3)_{0.54}$ (red) and for the apohost **5** (black). (a) N_2 adsorption at 77 K and CO_2 adsorption at 195 K. (b) H_2 (circles) at 77 K. (c) Excess amount of H_2 uptake at 298 K up to 95 bar. Reprinted with permission from ref. 14.

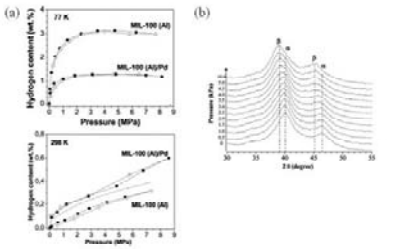

Fig. 18 (a) Comparison of H_2 adsorption (solid symbols) and desorption (open symbols) isotherms at 77 K and 298 K of MIL-100(Al) and Pd@MIL-100(Al). The dashed line is calculated from the addition of the quantity of H_2 required for the formation of the bulk β-Pd hydride and the amount of physisorbed H_2 by Pd-free MIL-100(Al). (b) *In situ* PXRD measured during the hydrogen adsorption in Pd NPs at room temperature and pressure up to 10 kPa, indicating formation of β-Pd hydride. Reprinted with permission from ref. 15.

that occupied the pore space of the oxidized MOF (Fig. 17a). Contrary to N_2 and CO_2 adsorptions, Pd-NPs (3 wt%)@SNU-3 (**5**) showed enhanced H_2 uptake capacities at 77 K and 1 atm as well as at room temperature. The H_2 uptake capacity at 77 K and 1 atm was increased to 1.48 wt% from 1.03 wt% for the pristine MOF (Fig. 17b). The H_2 uptake capacity at room temperature and 95 bar was increased to 0.30 wt% for the Pd NPs loaded sample, compared with 0.13 wt% for the pristine MOF (Fig. 17c). Considering the decreased surface area and the increase in the mass for the Pd loaded sample, the effective enhancement factor of H_2 uptake by Pd NPs was 350% at 77 K.[14] The effect of incorporated Pd NPs on increasing the H_2 uptake capacity was 230% at room temperature and 95 bar. Although the Pd NPs loaded in the MOF did not provide greater isosteric heat of H_2 adsorption than the pristine MOF, the increased hydrogen uptakes were explained by the spillover effect of Pd NPs, which dissociate H_2 molecules into H atoms before adsorption on the surface of the MOF.

Latroche and Ferey *et al.* also reported that the composite material Pd@MIL-100(Al), which was prepared by impregnation of a Pd precursor followed by treatment with hydrogen stream, showed increased hydrogen uptake at room temperature.[15] After loading 10 wt% Pd in MIL-100(Al), the hydrogen sorption capability at 77 K decreased as compared with that of MIL-100(Al), whereas maximum hydrogen capacity at 298 K increased as shown in Fig. 18a. The careful comparison of the hydrogen isotherms measured for MIL-100(Al) and MIL-100(Al)/Pd at 298 K reveals the different sorption properties. The isotherm of MIL-100(Al) at room temperature shows a linear trend, as generally reported for microporous material, but the isotherm of the Pd@MIL-100(Al) composite displays a steep increase below 0.1 MPa followed by a constant increase with pressure and an almost similar slope to that for the MIL-100(Al) isotherm. The different isotherm for Pd@MIL-100(Al) originates from the formation of Pd hydride during the H_2 adsorption at room temperature. *In situ* PXRD patterns measured during hydrogen uptake evidenced this, showing that increase in pressure from 0.5 to 4.5 kPa led to the formation of β-Pd hydride (Fig. 18b). When the sum of the quantity of H_2 required for formation of the bulk β-Pd hydride and the amount of physisorbed H_2 by Pd-free MIL-100(Al) was calculated (dashed lines in Fig. 18b), the actual uptake amount of the Pd@MIL-100(Al) composite exceeded it. It was explained that the spillover effect of Pd NPs took place, which promoted the dissociation of H_2 molecules into H atoms, to result in the enhanced hydrogen uptake capacity.

As an alternative to MOFs, a covalent organic framework (COF) was used as the support for fabricating Pd NPs.[48] Fischer's group prepared the Pd@COF-102 nanocomposite by the gas-phase infiltration of $[Pd(\eta^3\text{-}C_3H_5)(\eta^5\text{-}C_5H_5)]$ into COF-102 and subsequent photodecomposition. The resulting material Pd@COF-102 exhibited enhanced hydrogen uptake by a factor of 2–3 at room temperature and 20 bar, compared to pristine COF (Fig. 19). The enhancement was attributed to Pd-hydride formation as well as hydrogenation of organic residues originating from the metal precursor, as evidenced by MAS ^{13}C NMR.

Recently, Suh's group reported Mg-NCs@SNU-90′ as a hybrid hydrogen storage material. It adsorbed hydrogen by physisorption at low temperatures and by chemisorption at high temperatures, particularly showing the synergistic effect on both.[21]

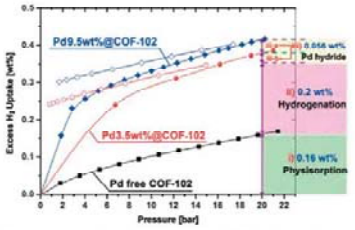

Fig. 19 Hydrogen sorption isotherms of pristine COF-102 (black), Pd(3.5 wt%)@COF-102 (red), and Pd(9.5 wt%)@COF-102 (blue) at 298 K. Reprinted with permission from ref. 48.

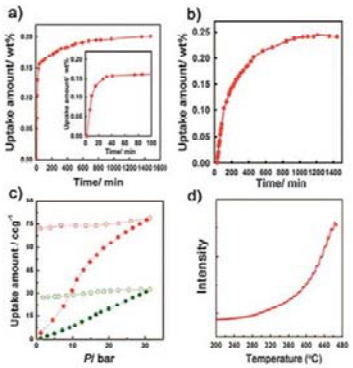

Fig. 20 Chemical adsorption of H_2 in Mg(10.5 wt%)@SNU-90′. (a) The H_2 absorption kinetics at 325 K and 80 bar. Inset: data with a magnified time scale. (b) The H_2 absorption kinetics at 415 K and 40 bar. (c) The H_2 adsorption isotherms at 473 K in Mg(6.52 wt%)@SNU-90′ (green, ●) and Mg(10.5 wt%)@SNU-90′ (red, ●). (d) Temperature programmed desorption mass spectroscopy (TPD-MS) data; $m/z = 2$, measured under argon. Reprinted with permission from ref. 21.

The hydrogen physisorption data for various samples of Mg@SNU-90′ showed that the BET surface area, pore volume, and H_2 uptake capacities at 77 K and 1 atm decreased as the amount of Mg embedded in MOF increased, because Mg NCs occupied the pore space of the MOF. However, the zero-coverage isosteric heat of H_2 physisorption increased as the amount of embedded Mg increased up to 11.6 kJ mol^{-1} for Mg(10.5 wt%)@SNU-90′ compared with 4.55 kJ mol^{-1} for SNU-90′. The hydrogen physisorption capacity in the MOF at 298 K and 80 bar also improved by *ca.* 20% due to the embedded Mg NCs. Contrary to the physisorption, the H_2 chemisorption capacities of the material increased as the temperature and the amount of loaded Mg increased. The hydrogen uptake capacity in Mg(10.5 wt%)@SNU-90′ at 473 K and 30 bar reaches 0.71 wt% (Fig. 20), which corresponded to 7.5 wt% H_2 adsorption in Mg alone, implying that 99% of Mg was converted to MgH_2 upon H_2 absorption. Desorption of H_2 occurred at 573 K and 1 atm, as evidenced by temperature programmed desorption mass spectroscopy. The Mg NCs embedded in the MOF lowered the H_2 chemisorption/desorption temperatures by >200 K than those of bare Mg(50–100 μm). After the H_2 chemisorption at 473 K and 30 bar, the HRTEM images of Mg@SNU-90′ indicated that the crystal morphology of Mg was maintained but the crystal size was remarkably increased. The excessive expansion during the H_2 chemisorption processes at high temperature and pressure can be explained by the three dimensional Ostwald ripening.

5.2 Heterogeneous catalysis

Some MOFs containing NPs have shown excellent activities in many organic reactions due to the confinement effect as well as the limitation of the particles that remain constrained avoiding growth after catalytic reactions. Recently, catalysis by M-NPs@MOF has been well reviewed,[49] and here we will briefly introduce various reactions catalyzed by M-NPs@MOF, classifying them by reaction types.

5.2.A Liquid phase catalytic reactions: aerobic oxidation of alcohols and olefin hydrogenation. Various supported metal nanoparticles have been utilized in a wide range of applications, especially catalysis.[50] Metal nanoparticle incorporated MOFs are one of the most promising heterogeneous catalysts. Among liquid phase catalytic reactions over M-NPs@MOF, the oxidation reaction of alcohol is the most well known reaction. Haruta *et al.* compared the catalytic activities and the product selectivities of Au NPs loaded in various MOFs in aerobic oxidation of alcohol.[17] Generally, the oxidation of benzyl alcohol yields a mixture of benzaldehyde and benzoic acid, and a base should be usually added to accelerate the reaction by deprotonating the alcohol. While Au/polymer gel showed low selectivity to produce 36% benzoic acid and 49% benzaldehyde, respectively, Au@MOF-5 and Au@MIL-53(Al) exhibited selective catalytic activity to produce methyl benzoate, and Au@Cu-PCPs showed high selectivity toward benzaldehyde. These phenomena were explained by the different degrees of surface acidity of each MOFs or PCPs, which tuned unique product selectivity. In addition, Au NPs in PCPs exhibited high catalytic activity in liquid phase benzyl alcohol oxidation even in the absence of base. The proposed mechanism for benzyl alcohol oxidation over Au@PCP is compared with that over Au/AC (AC: activated carbon) in Fig. 21.

Similarly, Au@MIL-101, which was prepared by deposition of Au-PVP colloids onto MIL-101, exhibited high catalytic activities in liquid-phase aerobic oxidation of various alcohols.[19] The catalyst Au@MIL-101 is very efficient because it can catalyze the aerobic

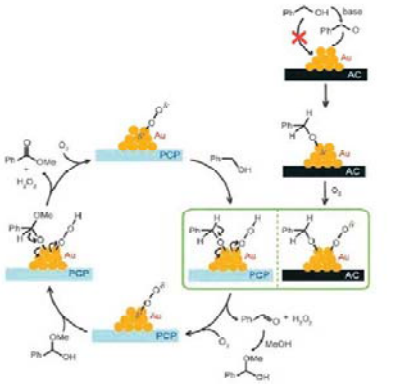

Fig. 21 Plausible pathways for benzyl alcohol oxidation over Au/PCPs and Au/AC. Reprinted with permission from ref. 17.

oxidation reaction in the absence of water or base. It was suggested that the highly dispersed Au NPs and the electron donating effect of aryl rings of substituted benzyl alcohols to the Au NPs within the large cages of the MIL-101 provided the high activity of the catalyst under the reaction conditions.

The other representative catalytic reaction over metal@PCPs is olefin hydrogenation. Pd NPs loaded in MOF-5 showed a high catalytic activity in styrene hydrogenation, which is comparable to that of Pd NPs on AC.[36] While large molecules such as 1-octene and *cis*-cyclooctene could not effectively access the pores resulting in low conversion, hydrogenation of styrene over Pd@MOF-5 produced ethylbenzene with high catalytic activity. By changing the reduction conditions, catalytic performance could be altered, and the treatment with H_2 stream at higher temperature afforded a positive effect on this reaction.

5.2.B Liquid phase catalytic reactions: C–C coupling reactions. C–C coupling reactions such as Suzuki–Miyaura, Ullmann, Heck, and Sonogashira coupling reactions are some of the most important and useful reactions in organic synthesis. Palladium-catalyzed C–C bond formations have been intensively studied, and Pd NPs incorporating MOFs were examined as C–C coupling catalysts. MIL series and surface modified MOFs were mainly used as supports due to their high stability in aqueous solution as well as in organic solvent (Fig. 22). The Pd@ED-grafted-MIL-101(Cr) and Pd@APS-grafted-MIL-101(Cr) (ED = ethylenediamine, APS = 3-aminopropyltrialkoxysilane), which were obtained by anion exchange reactions followed by $NaBH_4$ reduction in amine-functionalized MIL-101(Cr), had high activities in the Heck reaction of acrylic acid with iodobenzene. Their activities were comparable with that of a commercial Pd/C catalyst (1.09 wt% Pd) after a certain induction period (0.5–1 h).[51] Pd@MIL-101(Cr) showed good recyclability. It was also reported that Pd@MIL-101(Cr) catalyzed the one-pot cascade synthesis of methyl isobutyl ketone (MIBK) from acetone.[52] Pd@MIL-101(Cr) was also tested for Suzuki–Miyaura and Ullmann coupling reactions.[53] It catalyzed the coupling reaction between 4-chloroanisole and phenylboronic acid in the presence of various bases. This provided an important example since C–Cl bond activation requires much harsher reaction conditions than for the C–Br and C–I bonds. The catalytic activities of Pd@MIL-101(Cr) for Ullmann homocoupling reactions of various aryl chlorides were also examined in air as well as under a nitrogen atmosphere. The results revealed high reaction yield (>96%) under both reaction conditions. After the reaction, the Pd@MIL-101(Cr) catalyst was easily recovered and reused five times without any loss of efficiency.

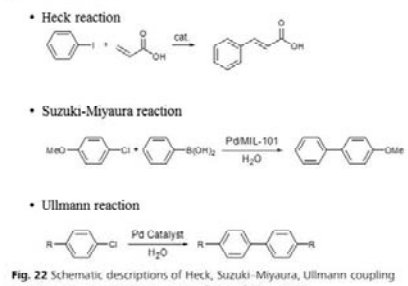

Fig. 22 Schematic descriptions of Heck, Suzuki–Miyaura, Ullmann coupling reactions. Reprinted with permission from ref. 51 and 53.

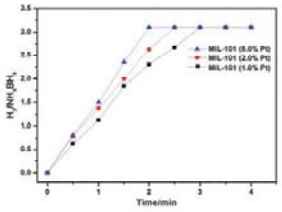

Fig. 23 Hydrogen generation from aqueous NH_3BH_3 in the presence of Pt@MIL-101 catalyst at room temperature. Pt : AB (molar ratio) = 0.0014, 0.0029, and 0.0071 at Pt loadings of 1.0, 2.0 and 5.0%, respectively. Reprinted with permission from ref. 37.

5.2.C Liquid phase ammonia borane hydrolysis. Ammonia borane is one of the promising hydrogen storage materials, from which H_2 can be released by either hydrolysis or pyrolysis. Xu *et al.* recently reported that Pt-NPs@MIL-101 (size of Pt NPs, average 1.8 ± 0.2 nm) catalyzed liquid phase ammonia borane (NH_3BH_3, AB) hydrolysis.[37] When the aqueous AB was introduced into the reaction flask containing Pt@MIL-101 with vigorous stirring, H_2 was produced from aqueous AB at room temperature (Fig. 23). The rate of hydrolysis of AB is 1.0×10^4 L_{H2} mol_{Pt}^{-1} min^{-1}, 2 times faster than that of 2 wt% Pt/γ-Al_2O_3, the most active Pt catalyst reported so far for this reaction. It was found that the productivity of H_2 over the Pt@MIL-101 catalyst remains unchanged after five runs, indicating the high durability of the catalyst. Since the byproduct (BO^{2-}) formed from AB hydrolysis is soluble in water, the spent fuel can be removed by washing with water and the catalyst can be reused.

5.2.D Gas phase catalytic reaction: CO oxidation. The liquid-phase catalytic reactions over pristine MOFs or M-NPs@MOFs have been actively exploited. However, their catalytic properties for gaseous reactions have been rarely reported. El-Shall *et al.* reported catalytic oxidation of CO to CO_2 by the bimetallic nanocatalyst systems incorporated into MIL-101.[19] The Pd NPs@MIL-101 catalyst containing 2.9 wt% Pd NPs showed the highest catalytic activity among catalysts with various amounts of Pd NPs, and small sized Pd nanocrystals mainly participated in the catalytic reaction. While Cu NPs@MIL-101 showed full conversion at high temperature (289 °C), the mixed Pd–Cu catalyst exhibited full conversion at 152 °C, revealing significantly enhanced catalytic function compared with the Cu NPs-only catalyst, which is possibly due to the formation of a PdCu nanoalloy (Fig. 24).

Xu *et al.* also reported the catalytic CO oxidation by Au NPs embedded in ZIF-8,[39] as well as by Pt NPs embedded in MIL-101.[37]

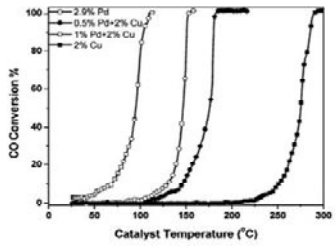

Fig. 24 CO oxidation to CO_2 on Pd, Cu, and mixed Pd–Cu nanocatalysts supported in MIL-101. Reprinted with permission from ref. 20.

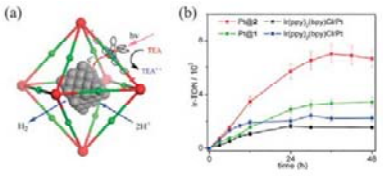

Fig. 25 (a) A scheme showing the synergistic photocatalytic hydrogen evolution process via photoinjection of electrons from the light-harvesting MOF framework into the Pt NPs. (b) Time-dependent hydrogen evolution curves. **1** and **2** in (b) indicate $Zr_6(\mu_3\text{-}O)_4(\mu_3\text{-}OH)_4(bpdc)_{5.94}(L_1)_{0.06}$ and $Zr_6(\mu_3\text{-}O)_4(\mu_3\text{-}OH)_4(L_2)_6{\cdot}64DMF$, respectively. Reprinted with permission from ref. 18.

For Au@ZIF-8, the CO oxidation activities improved with increasing amount of Au loaded in ZIF-8, as evidenced by the decrease of the temperature for 50% conversion of CO. For Pt@MIL-101, while MIL-101 exhibited no catalytic activity for CO oxidation in the temperature range 25–180 °C, the 5% Pt@MIL-101 started to show activity at 50 °C. The CO to CO_2 conversion increased suddenly at 100 °C and complete conversion occurred at 150 °C. Arrhenius plots showed that the activation energy was 40.7 kJ mol^{-1}. Pt@MIL-101 showed stable activity, keeping 100% CO conversion for 150 min at 175 °C. After catalytic reaction, the crystallinity of the Pt@MIL-101 host matrix remained unchanged with no large Pt particle aggregation.

5.2.e Photocatalytic hydrogen evolution. The Pt NPs loaded in photoactive MOFs, $Zr_6(\mu_3\text{-}O)_4(\mu_3\text{-}OH)_4(bpdc)_{5.94}(L_1)_{0.06}$ and $Zr_6(\mu_3\text{-}O)_4(\mu_3\text{-}OH)_4(L_2)_6$, were found to be efficient photocatalysts for hydrogen evolution from water, giving higher turnover frequencies and higher turnover numbers than those of the homogeneous analogs (Fig. 25).[18] The radicals, $[Ir^{III}(ppy)_2(bpy^{\bullet-})]$, generated in the MOFs by TEA-mediated photoreduction can transfer electrons to the entrapped Pt NPs to reduce protons of water. The highest hydrogen evolution turnover number (TON) based on Ir phosphors (Ir-TON) in 6 h was 1620, showing high photochemical quantum yield.

6. Concluding comments

In last few decades, dramatic advancement has been made in metal–organic frameworks. In particular, various synthetic strategies for incorporating M-NPs in porous MOFs have been developed, and the applications of those materials have been successfully demonstrated. By the choice of well-designed metal or organic molecular building blocks, redox-active PCPs could be synthesized, and the simple immersion of the redox-active PCPs in the metal precursor solutions produced M-NPs embedded in the PCPs at room temperature, in the absence of extra reducing agents and capping agents. In addition, to initially deposit metal precursors in the porous MOFs, other methods such as CVD, impregnation of metal solution, and solid-grinding have been also employed. When the reduction steps such as thermal hydrogenolysis were followed, various M-NPs@MOFs were yielded. Recently, fabrication of M-NPs in a MOF has been made by the irradiation of UV light on the metal ion impregnated MOF or by visible light irradiation on the metal ion included photoactive MOF. In addition, presynthesized M-NPs stabilized by a polymer are included in a MOF by synthesizing MOFs in the presence of the M-NPs capped by a polymer. The advantages of using MOFs as supports for M-NPs are the following: (1) the confinement effect of MOFs provides limited growth of M-NPs and generates rather uniform and small sized M-NPs, (2) the structural diversity of MOFs having different pore sizes and channel systems offers the choice of appropriate MOFs for M-NPs generation, (3) the organic parts of a MOF can interact with M-NPs and stabilize them without an extra stabilizing agent. Even though M-NPs bigger than the pore sizes are generally formed, the MOF frameworks are maintained in most of the cases. For this phenomenon, it has been argued that MOF frameworks are apt to be degraded upon TEM electron irradiation, which induces the agglomerization of the small metal clusters into bigger M-NPs. To characterize nanocomposites of M-NPs@MOFs, various techniques have been used such as ICP, IR, NMR, EPR spectroscopy, elemental analysis, EXAFS, XPS, TEM, electron tomography, and PXRD, which are described in this review. Using the resultant M-NPs@MOFs, enhanced hydrogen storage, liquid- and gas-phase catalytic reactions, and photocatalytic hydrogen evolution have been successfully demonstrated. In the coming years, more facile and inexpensive preparative methods for M-NPs@MOFs should be developed, and the multifaceted efforts would be accompanied to show the useful applications of these nanocomposites. Furthermore, the nanomaterials impregnated in MOFs should be extended from metals to a wide range of chalcogenides and pnictide semiconductors, and some transition-metal oxides.[54] Those nanocomposites would exhibit diverse functionalities, and they might provide environmentally benign and commercially useful catalyst systems. The fabrication of the various compounds in MOFs will be a highly promising field for the future.

Acknowledgements

This work was supported by National Research Foundation of Korea (NRF) Grant funded by the Korean Government (MEST)

(No. 2011-0031432 and No. 2012-0000651). H. R. Moon acknowledges financial support from NRF (No. 2011-0004358).

Notes and references

1 S. T. Batten, N. R. Champness, X.-M. Chen, J. Garcia-Martinez, S. Kitagawa, L. Ohrstrom, M. O'Keeffe, M. P. Suh and J. Reedijk, *CrystEngComm*, 2012, **14**, 3001–3004.
2 O. M. Yaghi, M. O'Keeffe, N. W. Ockwig, H. K. Chae, M. Eddaoudi and J. Kim, *Nature*, 2003, **423**, 705–714.
3 (*a*) K. L. Mulfort, O. K. Farha, C. L. Stern, A. A. Sarjeant and J. T. Hupp, *J. Am. Chem. Soc.*, 2009, **131**, 3866–3868; (*b*) J. Yang, A. Grzech, F. M. Mulder and T. J. Dingemans, *Chem. Commun.*, 2011, **47**, 5244–5246.
4 (*a*) Y.-G. Lee, H. R. Moon, Y. E. Cheon and M. P. Suh, *Angew. Chem., Int. Ed.*, 2008, **47**, 7741–7745; (*b*) Y. E. Cheon, J. Park and M. P. Suh, *Chem. Commun.*, 2009, 5436–5438; (*c*) H. J. Park and M. P. Suh, *Chem. Commun.*, 2010, **46**, 610–612; (*d*) H. R. Moon, N. Kobayashi and M. P. Suh, *Inorg. Chem.*, 2006, **45**, 8672–8676; (*e*) T. K. Kim and M. P. Suh, *Chem. Commun.*, 2011, **47**, 4258–4560; (*f*) H. J. Park, Y. E. Cheon and M. P. Suh, *Chem.–Eur. J.*, 2010, **16**, 11662–11669.
5 A. Corma, H. Garcia and F. X. L. i Xamena, *Chem. Rev.*, 2010, **110**, 4606–4655.
6 (*a*) A. Lan, K. Li, H. Wu, D. H. Olson, T. J. Emge, W. Ki, M. Hong and J. Li, *Angew. Chem., Int. Ed.*, 2009, **48**, 2334–2338; (*b*) J. Liu, F. Sun, F. Zhang, Z. Wang, R. Zhang, C. Wang and S. Qiu, *J. Mater. Chem.*, 2011, **21**, 3775–3778.
7 (*a*) I. T. Weber, A. J. G. de Melo, M. A. de M. Lucena, M. O. Rodrigues and S. A. Junior, *Anal. Chem.*, 2011, **83**, 4720–4723; (*b*) P. Horcajada, C. Serre, D. Grosso, C. Boissiere, S. Perruchas, C. Sanchez and G. Ferey, *Adv. Mater.*, 2009, **21**, 1931–1935.
8 J.-T. Lue, *J. Phys. Chem. Solids*, 2001, **62**, 1599–1612.
9 (*a*) K. L. Kelly, E. Coronado, L. L. Zhao and G. C. Schatz, *J. Phys. Chem. B*, 2003, **107**, 668–677; (*b*) A. R. Tao, S. Habas and P. Yang, *Small*, 2008, **4**, 310–325.
10 C. Burda, X. Chen, R. Narayanan and M. A. El-Sayed, *Chem. Rev.*, 2005, **103**, 1025–1102.
11 (*a*) K. Aslan, M. Wu, J. R. Lakowicz and C. D. Geddes, *J. Am. Chem. Soc.*, 2007, **129**, 1524–1525; (*b*) S. H. Joo, J. Y. Park, C.-K. Tsung, Y. Yamada, P. Yang and G. A. Somorjai, *Nat. Mater.*, 2009, **8**, 126–131.
12 (*a*) S. H. Joo, S. J. Choi, I. Oh, J. Kwak, Z. Liu, O. Terasaki and R. Ryoo, *Nature*, 2001, **412**, 169–172; (*b*) H. Song, R. M. Rioux, J. D. Hoefelmeyer, R. Komor, K. Niesz, M. Grass, P. Yang and G. A. Somorjai, *J. Am. Chem. Soc.*, 2006, **128**, 3027–3037.
13 M. Meilikhov, K. Yusenko, D. Esken, S. Turner, G. V. Tendeloo and R. A. Fischer, *Eur. J. Inorg. Chem.*, 2010, 3701–3714.
14 Y. E. Cheon and M. P. Suh, *Angew. Chem., Int. Ed.*, 2009, **48**, 2899–2903.
15 C. Zlotea, R. Campesi, F. Cuevas, E. Leroy, P. Dibandjo, C. Volkringer, T. Loiseau, G. Ferey and M. Latroche, *J. Am. Chem. Soc.*, 2010, **132**, 2991–2997.
16 D. Esken, X. Zhang, O. I. Lebedev, F. Schröder and R. A. Fischer, *J. Mater. Chem.*, 2009, **19**, 1314–1319.
17 T. Ishida, M. Nagaoka, T. Akita and M. Haruta, *Chem.–Eur. J.*, 2008, **14**, 8456–8460.
18 C. Wang, K. E. deKrafft and W. Lin, *J. Am. Chem. Soc.*, 2012, **134**, 7211.
19 H. Liu, Y. Liu, Y. Li, Z. Tang and H. Jiang, *J. Phys. Chem. C*, 2010, **114**, 13362–13369.
20 M. S. El-Shall, V. Abdelsayed, A. E. R. S. Khder, H. M. A. Hassan, H. M. El-Kaderi and T. E. Reich, *J. Mater. Chem.*, 2009, **19**, 7625–7631.
21 D.-W. Lim, J. W. Yoon, K. Y. Ryu and M. P. Suh, *Angew. Chem., Int. Ed.*, 2012, **51**, 9814–9817.
22 F. Schröder and R. A. Fischer, *Top. Curr. Chem.*, 2010, **293**, 77–113.
23 Y. Zhao, J. Zhang, J. Song, J. Li, J. Liu, T. Wu, P. Zhang and B. Han, *Green Chem.*, 2011, **13**, 2078–2082.
24 H. R. Moon, J. H. Kim and M. P. Suh, *Angew. Chem., Int. Ed.*, 2005, **44**, 1261–1265.
25 M. P. Suh, H. R. Moon, E. Y. Lee and S. Y. Jang, *J. Am. Chem. Soc.*, 2006, **128**, 4710–4718.
26 Y. E. Cheon and M. P. Suh, *Chem.–Eur. J.*, 2008, **14**, 3961–3967.
27 H. R. Moon and M. P. Suh, *Eur. J. Inorg. Chem.*, 2010, 3795–3803.
28 M. P. Suh, *Adv. Inorg. Chem.*, 1997, **44**, 93–146.
29 M. P. Suh, Y. E. Cheon and E. Y. Lee, *Chem.–Eur. J.*, 2007, **13**, 4208–4215.
30 Y. Wei, S. Han, D. A. Walker, P. E. Fuller and B. A. Grzybowski, *Angew. Chem., Int. Ed.*, 2012, **51**, 7435–7439.
31 M. J. Hampden-Smith and T. T. Kodas, *Chem. Vap. Deposition*, 1995, **1**, 8–23.
32 C. L. Bowes, A. Malek and G. A. Ozin, *Chem. Vap. Deposition*, 1996, **2**, 97–103.
33 S. Hermes, M.-K. Schröter, R. Schmid, L. Khodeir, M. Muhler, A. Tissler, R. W. Fischer and R. A. Fischer, *Angew. Chem., Int. Ed.*, 2005, **44**, 6237–6241.
34 (*a*) F. Schröder, D. Esken, M. Cokoja, M. W. E. van den Berg, O. I. Lebedev, G. V. Tendeloo, B. Walaszek, G. Buntkowsky, H.-H. Limbach, B. Chaudret and R. A. Fischer, *J. Am. Chem. Soc.*, 2008, **130**, 6119–6130; (*b*) D. Esken, S. Turner, O. I. Lebedev, G. V. Tendeloo and R. A. Fischer, *Chem. Mater.*, 2010, **22**, 6393–6401; (*c*) Y. K. Park, S. B. Choi, H. J. Nam, D.-Y. Jung, H. C. Ahn, K. Choi, H. Furukawa and J. Kim, *Chem. Commun.*, 2010, **46**, 3086–3088; (*d*) J. Hermannsdörfer and R. Kempe, *Chem.–Eur. J.*, 2011, **17**, 8071–8077.
35 F. Schrödcr, S. Henke, X. Zhang and R. A. Fischer, *Eur. J. Inorg. Chem.*, 2009, 3131–3140.
36 M. Sabo, A. Henschel, H. Fröde, E. Klemm and S. Kaskel, *J. Mater. Chem.*, 2007, **17**, 3827–3832.
37 A. Aijaz, A. Karkamkar, Y. J. Choi, N. Tsumori, E. Rönnebro, T. Autrey, H. Shioyama and Q. Xu, *J. Am. Chem. Soc.*, 2012, **134**, 13926–13929.
38 R. Ameloot, M. B. J. Roeffaers, G. D. Cremer, F. Vermoortele, J. Hofkens, B. F. Sels and D. E. De Vos, *Adv. Mater.*, 2011, **23**, 1788–1791.
39 H.-L. Jiang, B. Liu, T. Akita, M. Haruta, H. Sakurai and Q. Xu, *J. Am. Chem. Soc.*, 2009, **131**, 11302–11303.
40 H.-L. Jiang, Q.-P. Lin, T. Akita, B. Liu, H. Ohashi, H. Oji, T. Honma, T. Takei, M. Haruta and Q. Xu, *Chem.–Eur. J.*, 2011, **17**, 78–81.
41 (*a*) M. Okumura, S. Tsubota and M. Haruta, *J. Mol. Catal. A: Chem.*, 2003, **199**, 73–84; (*b*) M. Okumura, K. Tanaka, A. Ueda and M. Haruta, *Solid State Ionics*, 1997, **95**, 143–149.
42 G. Lu, S. Li, Z. Guo, O. K. Farha, B. G. Hauser, X. Qi, Y. Wang, X. Wang, S. Han, X. Liu, J. S. DuChene, H. Zhang, Q. Zhang, X. Chen, J. Ma, S. C. J. Loo, W. D. Wei, Y. Yang and J. T. Hupp, *Nat. Chem.*, 2012, **4**, 310–316.
43 R. J. T. Houk, B. W. Jacobs, F. E. Gabaly, N. N. Chang, A. A. Talin, D. D. Graham, S. D. House, I. M. Robertson and M. D. Allendorf, *Nano Lett.*, 2009, **9**, 3413–3418.
44 S. Turner, O. I. Lebedev, F. Schrodcr, D. Eskcn, R. A. Fischer and G. V. Tendeloo, *Chem. Mater.*, 2008, **20**, 5622–5627.
45 (*a*) S. Ma, D. Sun, M. Ambrogio, J. A. Fillinger, S. Parkin and H.-C. Zhou, *J. Am. Chem. Soc.*, 2007, **129**, 1858–1859; (*b*) J. L. Belof, A. C. Stern, M. Eddaoudi and B. Space, *J. Am. Chem. Soc.*, 2007, **129**, 15202–15210.
46 (*a*) M. Dincă and J. R. Long, *J. Am. Chem. Soc.*, 2007, **129**, 11172–11176; (*b*) S. S. Kaye and J. R. Long, *J. Am. Chem. Soc.*, 2005, **127**, 6506–6507; (*c*) K. L. Mulfor and J. T. Hupp, *J. Am. Chem. Soc.*, 2007, **129**, 9604–9605.
47 (*a*) Y. Li and R. T. Yang, *J. Am. Chem. Soc.*, 2006, **128**, 726–727; (*b*) Y. Li and R. T. Yang, *J. Am. Chem. Soc.*, 2006, **128**, 8136–8137.
48 S. B. Kalidindi, H. Oh, M. Hirscher, D. Esken, C. Wiktor, S. Turner, G. V. Tendeloo and R. A. Fischer, *Chem.–Eur. J.*, 2012, **18**, 10848–10856.
49 A. Dhakshinamoorthy and H. Garcia, *Chem. Soc. Rev.*, 2012, **41**, 5262–5284.
50 R. M. Crooks, M. Zhao, L. Sun, V. Chechik and L. K. Yeung, *Acc. Chem. Res.*, 2001, **34**, 181–190.
51 Y. K. Hwang, D.-Y. Hong, J.-S. Chang, S. H. Jhung, Y.-K. Seo, J. Kim, A. Vimont, M. Daturi, C. Serre and G. Férey, *Angew. Chem., Int. Ed.*, 2008, **47**, 4144–4148.
52 Y. Pan, B. Yuan, Y. Li and D. He, *Chem. Commun.*, 2010, **46**, 2280–2282.
53 B. Yuan, Y. Pan, Y. Li, B. Yin and H. Jiang, *Angew. Chem., Int. Ed.*, 2010, **49**, 4054–4058.
54 (*a*) M. Müller, S. Hermes, K. Kähler, M. W. E. van den Berg, M. Muhler and R. A. Fischer, *Chem. Mater.*, 2008, **20**, 4576–4587; (*b*) M. Müller, X. Zhang, Y. Wang and R. A. Fischer, *Chem. Commun.*, 2009, 119–121.

CHEMICAL REVIEWS

REVIEW

pubs.acs.org/CR

Hydrogen Storage in Metal–Organic Frameworks

Myunghyun Paik Suh,* Hye Jeong Park, Thazhe Kootteri Prasad, and Dae-Woon Lim

Department of Chemistry, Seoul National University, Republic of Korea

CONTENTS

1. INTRODUCTION

The decreasing fossil fuel supply and climate change caused by carbon dioxide emission have spurred an initiative to develop alternative fuels. Hydrogen is one of the most promising candidates for the replacement of current carbon-based energy sources. Hydrogen has an energy density much greater than gasoline and emits no carbon dioxide after burning. On a weight basis, hydrogen has nearly three times higher energy content than gasoline: lower heating values are 33.3 kWh kg^{-1} (123 MJ kg^{-1}) for hydrogen and 11.1 kWh kg^{-1} (47.2 MJ kg^{-1}) for gasoline, although on a volume basis the situation is reversed (8 MJ L^{-1} for liquid hydrogen versus 32 MJ L^{-1} for gasoline).

Free hydrogen does not occur naturally in quantity, and it should be generated from some other energy source by steam reformation of natural gas or other methods. Hydrogen is therefore an energy carrier (like electricity), not a primary energy source (like coal). For the advancement of hydrogen and fuel cell power technologies in transportation, stationary, and portable application, the research on hydrogen production, delivery, storage, and fuel cell technologies should be fully developed. Hydrogen storage is considered to be a key enabling technology.

In the case in which H_2 is used as a fuel in automobiles, 5–13 kg of H_2 would be consumed daily per ca. 300 miles driven. This implies a necessity to store a very large liquid or pressurized H_2 gas tank on board the vehicle. It would also require refilling everyday, which is neither safe nor practical. Therefore, the automobile and fuel cell industries have been searching for an efficient method to store and transport H_2. The U.S. Department of Energy (DOE) has set up the targets for on-board H_2 storage systems with the concept that higher efficiency fuel-cell power sources will replace current carbon-based energy source in future vehicles. The 2017 H_2 storage targets are 5.5 wt % in gravimetric capacity, 40 g L^{-1} of volumetric capacity at an operating temperature of −40–60 °C under a maximum delivery pressure of 100 atm. The targets are for a complete system, including tank, material, valves, regulators, piping, mounting brackets, insulation, added cooling capacity, and/or other balance-of-plant components.[1] None of the candidate materials developed so far has satisfied the DOE target yet.

Special Issue: 2012 Metal-Organic Frameworks

Received: July 22, 2011
Published: December 22, 2011

Wide ranges of materials have been tested as H_2 gas storage materials, which include metal hydrides,[2] complex hydrides,[3−6] chemical hydrides,[7−9] carbohydrates,[10] clathrates,[11] inorganic nanotubes,[12] organic materials,[13] sorbents such as metal-organic frameworks (MOFs) and carbon materials,[14−16] etc. There have been numerous reviews on the H_2 storage materials.[17−24] The main goal has been to find materials that adsorb hydrogen with H_2 density greater than the density of liquid H_2. The weight density of liquid hydrogen is as little as 70.8 kg m^{-3} at 20 K and atmospheric pressure, and 5 kg of H_2 occupies a fairly large volume of 56 m^3 under standard conditions.

There are various hydrogen storage materials. They can be divided into three categories based on the relative strength of the interaction of a storage material with hydrogen, which greatly affects the kinetics and thermodynamics of the hydrogen uptake and release: "physisorption materials", "on-board reversible hydrides", and "off-board regenerable hydrides" materials. In physisorbed hydrogen storage materials, H_2 molecules are adsorbed on the surface of the pores of the materials. According to IUPAC, physisorption (physical adsorption) is the adsorption in which the forces involved are intermolecular forces (van der Waals forces) of the same kind as those responsible for the imperfection of real gases and the condensation of vapors and which do not involve a significant change in the electronic orbital patterns of the species involved.[25,26] Physisorption processes are reversible since no activation energy is involved and the interaction energy is very low. In materials such as metal−organic frameworks, porous carbons, zeolites, clathrates, and organic polymers, H_2 is physisorbed on the surface of the pores. In these classes of materials, the H_2 storage capacity mainly depends on the surface area and pore volume. The main limitation of use of these sorbents as H_2 storage materials is weak van der Waals interaction energy between H_2 and the surface of the sorbents. Therefore, many of the physisorption based materials have high storage capacities at liquid nitrogen temperature and high pressures, but their capacities become very low at ambient temperature and pressure. Research is being directed toward the synthesis of highly porous materials that would have enhanced interaction energies with gaseous H_2. The positive side of these materials is the fast adsorption and desorption kinetics.

In chemisorption-based materials, hydrogen is chemically bonded to the storage medium. According the IUPAC, chemisorption (chemical adsorption) is the adsorption that results from chemical bond formation (strong interaction) between the adsorbent and the adsorbate in a monolayer on the surface.[27] The formation and stability of such materials highly depend on the pressure and temperature. Chemisorption process may not be reversible as relatively high activation energy exists in the adsorption and desorption process. On-board hydride materials and off-board regenerable hydride materials belong to this class.

On-board reversible hydride materials include interstitial metal hydrides, covalently bound metal hydrides, metal amides, borohydrides, etc. These store dissociated hydrogen either covalently or as interstitially bound hydrogen, and release hydrogen endothermically. The storage materials can be directly recharged with hydrogen in situ on a vehicle, since endothermic release allows for exothermic rehydrogenation during on-board recharging of the hydrogen storage materials under reasonable temperature and pressure (below 300 °C and below 200 bar). Interstitial metal hydrides are materials such as $LaNi_5H_x$. Covalent metal hydrides are discrete compounds such as MgH_2 and AlH_3, which have high gravimetric storage capacities, but the binding energies of these compounds are too weak or too strong to use as H_2 storage materials. Complex covalent hydrides are metal borohydrides and metal amides such as $LiBH_4$, $NaBH_4$, $Mg(BH_4)_2$, $LiNH_2$, and $Mg(NH_2)_2$. These have high gravimetric H_2 storage capacities but have the problem of high dehydrogenation temperature and irreversibility, and many catalysts are being tested for the use of such materials in reversible and moderate conditions.

Off-board regenerable hydride materials store dissociated hydrogen as covalently bound hydrogen materials, and they release hydrogen exothermically and/or involve complex off-board chemical processes for regeneration that cannot be performed on board a vehicle. Materials in this class are the hydrocarbons, ammonia borane, and alane. The hydrocarbons and alane release hydrogen endothermically, but high hydrogen pressures or the complexity of their rehydrogenation most likely will require an off-board process. Ammonia borane releases also a large amount of hydrogen rather exothermically, but it cannot be rehydrogenated readily at common pressures and temperatures.

As one of the promising hydrogen storage materials, MOFs have been extensively studied for the past decade. MOFs are crystalline materials consisting of metal ions linked together by organic ligands which generate micropores (<2 nm) and channels. Since MOFs are synthesized from metal ions and organic building blocks, the framework topology, pore size, and surface area can be readily tuned by the selection of molecular building blocks. MOFs generally have defined structures, permanent porosity, and high specific surface areas. Numerous MOFs with relatively small to very large surface areas have been reported. The highest excess H_2 storage capacity reported so far for MOFs is 99.5 mg g^{-1} at 56 bar and 77 K in NU-100 (NU = Northwestern University), which has a total capacity of 164 mg g^{-1} at 77 K and 70 bar.[28] The highest total H_2 storage capacity reported is 176 mg g^{-1} (excess 86 mg g^{-1}) in MOF-210 at 77 K and 80 bar.[29] These values are symbolic to the tremendous advancement in research on MOFs as H_2 storage materials. In 2003, the initial H_2 storage data were reported for MOF-5 (4.5 wt % at 77 K and 1 atm), which were prepared from benzene-1,4-dicarboxylate (BDC) and Zn(II) salt,[30] although it was found later that the maximum H_2 uptake varies from 1.3 to 5.2 excess wt % at 77 K depending on the preparation and handling conditions: Preparation and handling under N_2 atmosphere lead to H_2 uptake of excess 7.1 wt % at 77 K and 40 bar with total capacities of 10 wt % at 77 K and 100 bar, and 11.5 wt % at 77 K and 170 bar.[31] Since MOF-5 was reported, there have been numerous reports of porous MOFs, many of which have different framework topologies, and they showed relatively high H_2 storage capacities. Many researchers have employed various metal ions such as Zn(II), Cu(II), Mn(II), Cr(III), and lanthanides(III), and diverse types of ligands such as carboxylates, imidazolates, triazolates, tetrazolates for the construction of the MOFs. In recent years, researchers have modified the MOFs to increase the H_2 storage capacities.

Despite significant progresses in design and modification strategies for MOFs, we still encounter many problems in the development of practically applicable MOFs. Here, we review the representative MOFs that have been developed for H_2 storage and discuss the problems and prospects of MOFs as a H_2 storage material. Since there have been many review papers already published on hydrogen storage in MOFs, readers can find information from them also.[32−39]

2. DEFINITIONS AND TERMINOLOGIES USED FOR HYDROGEN STORAGE

2.1. Sorption and Desorption

Sorption is the nonspecific term that describes both adsorption and absorption. It is most often used when it is difficult or impossible to differentiate between adsorption and absorption or when both processes occur simultaneously. The reverse process of sorption is desorption. The sorption and desorption of the sorbate by the sorbent is a dynamic process.

2.2. Adsorption and Absorption

Adsorption is the enrichment or depletion of one or more components in an interfacial layer. Absorption occurs when the adsorbates are incorporated into the internal structure of the adsorbent. In absorption, the structure and/or the chemical nature of the absorbate and absorbent may be modified. Adsorption and absorption refer to the location of the sorbed species with respect to the sorbent, that is, surface and bulk, respectively.

2.3. Chemisorption and Physisorption

Chemisorption is a surface-specific phenomenon and occurs when the interaction force between a surface and an adsorbate is similar to that of chemical bonding in bulk compounds. Physisorption is restricted to adsorption and occurs when the forces involved are weak intermolecular forces of the same kind as those responsible for the nonideality of gases and the condensation of vapors. Weak intermolecular forces are also known as van der Waals forces. Physisorption does not involve a significant change in the electronic structure of the species involved. For a molecular adsorbate where no bond dissociation occurs, it is often difficult to draw a boundary in the energy landscape between strong physisorption and weak chemisorption. It is useful to make a distinction between molecular physisorption, in which the H−H bond in the gas phase is preserved in the sorbed state, and chemisorption, in which the H−H bond is broken during the sorption process. Chemisorption may occur only in a monolayer on a surface, whereas physisorption is usually accompanied by multilayer adsorption depending upon the temperature.

2.4. Langmuir Surface Area and BET Surface Area

According to IUPAC, the porous materials are classified by their pore sizes. Macroporous materials have a pore size larger than 500 Å, mesoporous materials have pore size in the range 20−500 Å, and microporous materials have a pore size less than 20 Å. The microporous materials can be classified into two classes, ultramicroporous (smaller than 7 Å) and supermicroporous (7−20 Å) materials. The adsorption of gases on these materials has different mechanisms. Most MOFs reported so far fall in the category of microporous materials. The ultramicropores are filled at very low relative pressure (P/P_0), directed by gas−solid interactions and the rates of adsorption highly depend on temperature. In supermicropores, in addition to gas−solid interactions, a cooperation effect exists. Because of the cooperation effect, pore filling occurs at relatively lower relative pressure. Pore filling occurs when it is energetically as favorable for a gas molecule to exist between the monolayers of gas in the center of the pore as it is to complete monolayer coverage.[40,41]

The Langmuir equation is generally applied to materials having uniform surfaces that form only a monolayer with the adsorbates. Most MOFs have different types of atomic surfaces, and the interactions with gases highly depend on the metal atoms as well as organic linkers. At a very low pressure region, the initial adsorption takes place at the strongest sites of the surface, and as the pressure increases the adsorption takes place at weaker sites. In materials with multiple pores, the narrow pores are filled first and the larger pores are filled at slightly higher pressure. Because of the localized adsorption in ultramicroporous MOFs, and multilayer adsorption in supermicroporous MOFs, which is attributed to pore filling effect at very low relative pressure, the use of the Langmuir equation in the estimation of the surface area of MOFs may not provide accurate results.

BET theory takes into account multilayer adsorption. The BET equation is used universally for the calculation of surface area as a standard method because of its simplicity. Recently, it has been shown that BET surface area calculated from the N_2 adsorption isotherm obtained by the Grand Canonical Monte Carlo (GCMC) simulation is very similar to the experimental BET surface area.[42] Care must be taken in using the BET equation to determine the surface area of the MOFs since the calculated surface area of the framework depends on the pressure range used in the calculation.[43]

The specific surface areas of MOFs are generally determined from the N_2 adsorption isotherms at 77 K. It is common to use the Langmuir or BET equation to calculate the surface area of MOFs. In almost all cases, the surface area calculated by the Langmuir equation is much larger than that by the BET equation. The Langmuir surface area reported for MOF-200 is 10400 $m^2 g^{-1}$ and the corresponding BET surface area is 4530 $m^2 g^{-1}$.[29] MOF-210 has a Langmuir surface area of 10400 $m^2 g^{-1}$ and BET surface of 6240 $m^2 g^{-1}$. MOF-205 has a Langmuir surface area of 6170 $m^2 g^{-1}$ and BET surface area of 4460 $m^2 g^{-1}$.[29] For MOF-200 and MOF-210, the reported crystal density was 0.25 g cm^{-3}, which is one of the lowest for MOFs. MOF-205 has a crystal density of 0.38 g cm^{-3}. It has been found that the MOFs with a larger crystal density show a smaller difference between the Langmuir and BET surface areas. The results suggest that as the void volume increases, the difference in the Langmuir and BET surface areas increases.

2.5. Excess and Total Adsorptions of Hydrogen

The high pressure H_2 uptakes are generally represented as excess and total adsorption amount. The excess adsorption, which is also known as the Gibbs excess, is the difference in the amounts of gas phase H_2 that would be present in the equivalent volume of the adsorbed phase in the presence and absence of adsorption.[44] The excess adsorption reaches saturation at high pressure and then decreases as the hydrogen gas density increases further, due to the incompressibility of H_2 gas in the pores. In general, for the H_2 adsorption capacity up to 1 bar, the excess and total adsorption amounts are nearly identical. However, for H_2 adsorption capacity at high pressure, the absolute amount of H_2 gas per unit volume of MOF also contains pressurized gas in the pores of MOFs, which are not adsorbed on the surface. The total amount can be derived from the excess adsorption isotherms and the total skeletal volume of the framework, which can be obtained from the He gas sorption isotherm.[31]

The total amount of adsorbed gas is expressed as follows.[45−47]

$$N_{tot} = N_{ex} + d_{gas} V_{pore} \quad (1)$$

where N_{tot} is the total adsorption in mg g^{-1}, N_{ex} is the excess adsorption in mg g^{-1} that is the quantity being measured, d_{gas} is

the compressed gas at a given temperature and pressure in g cm^{-3},

$$V_{pore} = \frac{1}{d_{bulk}} - \frac{1}{d_{skeletal}} \quad (2)$$

where V_{pore} is the pore volume in cm^3 g^{-1}, d_{bulk} is the crystallographic density of the sample, and $d_{skeletal}$ is the skeletal density of the material.

$$d_{skeletal} = m/V_{skeletal} \quad (3)$$

where m is the sample mass expressed in g, and $V_{skeletal}$ is the sample volume in cm^3, which is determined by using He expansion measured at 298 K up to 100 bar.

Generally, H_2 adsorption capacities in MOFs are represented in wt %, which can be expressed as (mass of H_2)/(mass of sample + mass of H_2). However, many researchers have omitted the term (mass of H_2) in the denominator, which should be avoided. For MOFs with low adsorption capacities, the omission of the term in the denominator may not make a difference, but as the H_2 adsorption capacity increases, it leads to overestimated wt %. Therefore, it is safe to use mg g^{-1} (mass in mg of H_2 adsorbed per gram of MOF) as a unit for the H_2 uptake capacity, and we encourage the use of mg g^{-1} instead of wt %.

2.6. Isosteric Heat of the Hydrogen Adsorption

The interaction enthalpy between a MOF and H_2 molecule, the isosteric heat (Q_{st}) of hydrogen adsorption, can be calculated from the H_2 adsorption isotherms measured at two independent temperatures, usually 77 and 87 K by fitting the data to virial equation or the Langmuir–Freundlich equation. The calculation provides the isosteric heat of H_2 adsorption depending on the adsorbed amounts of H_2, even though it cannot give information about the position and the number of H_2 adsorption sites. The zero-coverage isosteric heat corresponds to the interaction energy between the H_2 molecule and the strongest interaction site of the MOF.

Three different methods have been used for estimating the isosteric heat of the H_2 adsorption.

Method 1. The virial-type equation (eq 4) is used to fit the gas sorption data, which is composed of parameters a_i and b_i that are independent of temperature.[48,49] In eq 4, P is pressure, N is the amount adsorbed H_2 gas, T is temperature, and m and n represent the number of coefficients required to adequately describe the isotherms. Adsorption isotherms measured at two different temperatures are fit to the equation by using the statistical programs such as R statistical software package.[50] To estimate the values of the isosteric heat of H_2 adsorption, eq 5 is applied, where R is the universal gas constant.

$$\ln P = \ln N + \frac{1}{T}\sum_{i=0}^{m} a_i N^i + \sum_{i=0}^{m} b_i N^i \quad (4)$$

$$Q_{st} = -R\sum_{i=0}^{m} a_i N^i \quad (5)$$

Method 2. The following virial-type equation[51] (eq 6) is used to fit the adsorption data at a fixed temperature.

$$\ln(N/P) = A_0 + A_1 N + A_2 N^2 + A_3 N^3 + \cdots \quad (6)$$

In eq 6, P is pressure, N is amount of adsorbed gas, and A_0, A_1, etc. are virial coefficients. A_0 is related to the adsorbate–adsorbent interactions, whereas A_1 describes adsorbate–adsorbate interactions. Q_{st} for H_2 adsorption is calculated as a function of surface coverage by using Clausius–Clapeyron equation (eq 7), where R is the gas constant.

$$Q_{st} = R\ln\left(\frac{P_1}{P_2}\right)\frac{T_1 T_2}{T_2 - T_1} \quad (7)$$

Method 3. Langmuir–Freundlich equation[52] (eq 8) is used to fit the adsorption data at a fixed temperature. In eq 8, N is amount of adsorbed gas, N_m is amount of adsorbed gas at saturation, P is pressure, and B and t are the constants.

$$\frac{N}{N_m} = \frac{BP^{(1/t)}}{1 + BP^{(1/t)}} \quad (8)$$

The Langmuir–Freundlich equation can be rearranged to eq 9, and the isosteric heat of H_2 adsorption is obtained by using eq 7.

$$P = \left(\frac{N/N_m}{B + BN/N_m}\right) \quad (9)$$

We have to note that there are potential pitfalls in using each of the different types of fitting routines for deriving the isosteric heat of H_2 adsorption. Methods 1 and 2 allow a series of Q_{st} values to be obtained as a function of n. Minimal deviations are observed for all experimental points measured over a wide range of pressure. The most salient feature of these virial equations is that they would allow extrapolation to zero coverage of H_2, therefore allowing the determination of this value at zero coverage. However, the Langmuir–Freundlich (or other semiempirical routines) method results in gross overestimation of the adsorption enthalpy if extrapolation is made down to zero coverage, since this approach does not reduce to Henry's Law and leads to the largest error at zero coverage. This overestimation is in fact responsible for many high adsorption enthalpy values reported in the literature. On the other hand, fits using the virial equation can be overinterpreted if polynomials of too high order are used indiscriminately. The important value in that case is that of the lowest order polynomial coefficient. If a standard deviation in that fit is too large, the fit value is meaningless. However, this fact is unfortunately often disregarded by researchers in the field. Despite this, virial analysis is better and more mathematically consistent since it reduces to Henry's Law, although it gives lower values of the heat of adsorption.

3. DESIGN AND SYNTHESIS OF METAL–ORGANIC FRAMEWORKS FOR HYDROGEN STORAGE

MOFs have been successfully synthesized from solvothermal reactions with metal and organic building blocks in organic solvents, in particular, those that have high boiling points such as DMF and DEF, generally at 80–130 °C. In general, the high temperature reaction conditions of solvothermal syntheses eliminate the solubility restrictions for the reagents. Mixed solvents are sometimes used to control the solution polarity, solvent–ligand exchange kinetics, and rate of product crystallization. For example, to aid crystallization during synthesis, low boiling solvents such as ethanol and acetonitrile can be added.

MOFs can be constructed by various combinations of metal ions and ligands. Sometimes two different metal ions and a ligand are reacted to obtain new MOFs that contain two kinds of metal ions.[53,54] A metal ion can also be reacted with two different ligands.[29,55–57] Although the framework structure of a MOF mainly depends on the metal and organic building blocks, it can

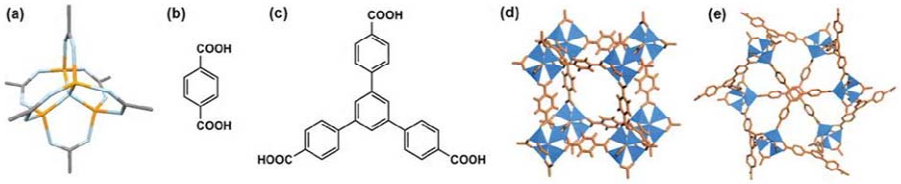

Figure 1. (a) $[Zn_4O]$ SBU. The carboxylic acid used in the synthesis of (b) MOF-5 and (c) MOF-177. The structures of (d) MOF-5 and (e) MOF-177.

also depend on the type of solvent, reaction temperature, and rate of crystal growth. If a solvent is included in the pores or coordinated at the metal ion of the framework, the type of solvent can completely change the framework structure. Subsequently, the properties of a MOF, such as gas sorption and guest recognition, depend on its structure, in particular, the size and shape of the pores and the chemical environment of the pore surface.

The most common metal ions used in the synthesis of MOFs are Zn(II) and Cu(II), but other transition metal ions such as those in the first transition series may be employed as metal building blocks. Various carboxylic acids as well as heterocyclic compounds containing nitrogen donors are used as the organic building blocks for the construction of MOFs. The excellent review by O'Keeffe and Yaghi has shown various possible topologies of MOFs that are constructed from metal and organic building blocks.[58]

3.1. Carboxylate-Based MOFs

MOFs can be synthesized by the solvothermal reaction of metal ions and various carboxylic acids. The network topology is established by the metal-carboxylate subunits as nodes and the organic linkers as struts. The great variety of organic ligands and metal ions that are employed in the synthesis provides a wide range of networks with various pore sizes and metal centers. The use of rigid organic carboxylates ligands in the synthesis of MOFs often leads to porous frameworks with exceptional robustness, and many of these MOFs do not collapse even after the removal of the guest solvent molecules that are incorporated during the synthesis. Various metal sources have been utilized in the synthesis of MOFs, such as Zn, Cu, Mn, Co, Cr, Ni, lanthanide metals, alkali metals, Mg, and Al, and the structures and properties of those MOFs have been reported. The hydrogen adsorption capacity slightly depends on the type of metal ion but is more generally correlated with the surface area and pore volume of the framework. The chemical or electronic environment of the pore surface is also important, modified by the presence of functional groups in the ligand and/or at the vacant coordination sites on metal ions. Some MOFs, in particular, Zn-carboxylate based MOFs, are known to be air-sensitive, with hydrogen gas sorption capacities decreasing upon exposure to air. This is most likely due to the degradation of the frameworks, and thus proper handling of the Zn-MOFs is required.[51]

MOFs synthesized from carboxylate ligands are among most commonly reported. Dicarboxylic acids, especially, have been extensively used in various syntheses. Since MOF-5 was synthesized from the solvothermal reaction of a Zn^{II} salt and 1,4-benzenedicarboxylic acid (BDC) in DEF,[59] a series of isoreticular MOFs (IRMOF) were prepared using various dicarboxylic acids.[60−62] The IRMOF series have cubic framework structures that generate varying size 3D channels. In their structures, $[Zn_4O]$ clusters were formed as the octahedral secondary building units (SBUs), which are connected with six carboxylate linkers to form a cubic network. The pore size and the surface area in the series were efficiently controlled by adjusting the length of the dicarboxylic acid and by the introduction of functional groups on the aromatic ring. Most of the IRMOFs showed high surface areas and large pore volumes. MOF-5 (IRMOF-1) has a BET surface area of 3800 $m^2\ g^{-1}$ and adsorbs excess 7.1 wt % of H_2 at 40 bar and 77 K, and is still considered to be one of the best hydrogen storage materials.[31] Because of the high surface area and large pore volume of MOF-5, many studies have been done on MOF-5, such as incorporation of various metal nanoparticles,[63−66] chromatography with a single crystal of MOF-5,[67] utilization as a template for porous carbon synthesis,[68] hydrogen spillover study,[69] etc. For example, in such a study, $Cr(CO)_3$ species were attached to the BDC rings of MOF-5 via postsynthetic modification. After the formation of piano stool complexes, the framework was still stable, crystalline, and microporous.[70]

MOFs constructed from $[Zn_4O]$ SBUs and tricarboxylate ligands are also very common and possess very high surface areas and large pore volumes. The well-known MOF-177 is constructed from $[Zn_4O]$ clusters and 4,4′,4″-benzene-1,3,5-triyl-tribenzoate (BTB), where each $[Zn_4O]$ unit is connected to six carboxylate groups and each tricarboxylate ligand connects to three $[Zn_4O]$ units to form a (6,3) connected net (Figure 1). MOF-177 has a BET surface area of 4750 $m^2\ g^{-1}$ and a pore volume of 1.59 $cm^3\ g^{-1}$, making it one of the most porous MOFs.[62,71] The compound adsorbs 7.5 wt % of H_2 at 77 K and 70 bar.[62] After the discovery of MOF-177, many highly porous MOFs having (6,3) net structures have been reported, and most of them show high surface areas. For example, MOF-200, which was constructed from $[Zn_4O]$ cluster and 4,4′,4″-[benzene-1,3,5-triyl-tris(benzene-4,1-diyl)]tribenzoate (BBC) has a BET surface area of 4530 $m^2\ g^{-1}$.[29]

Many other MOFs that are constructed of $[Zn_4O]$ octahedral SBUs and polycarboxylates were also reported, such as UMCM-2, MOF-205, and MOF-210, which are mesoporous materials.[29,72] These mesoporous materials might be useful for hydrogen storage after modification of the pores to enhance the interaction between hydrogen and the framework.

MOFs synthesized from copper and carboxylic acids are an interesting class of MOFs since they generally consist of a paddle-wheel type $[Cu_2(OOC)_4]$ SBU and a carboxylate linker (Figure 2). The typical MOF formed from a Cu(II) paddle-wheel SBU and BTC is HKUST-1, which shows a Langmuir surface of 917.6 $m^2\ g^{-1}$.[73] In paddle-wheel type SBUs, the axial positions are normally occupied by coordinated solvent molecules, which can be easily removed by heating and/or evacuation without destroying

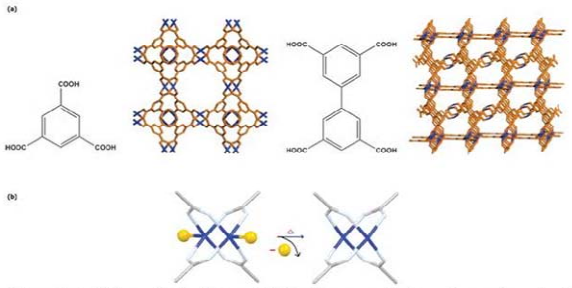

Figure 2. (a) The carboxylic acids employed in the synthesis of porous MOFs with open metal sites and respective networks. (b) Creation of open metal sites at the paddle-wheel SBU in a MOF by removal of coordinated solvent molecules.

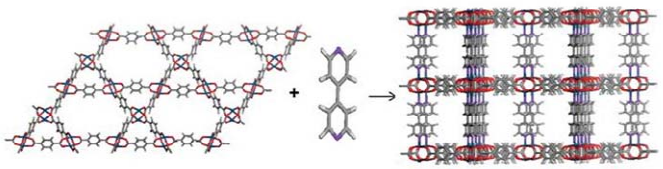

Figure 3. Schematic diagram showing the construction of a 3D MOF from the 2D layer formed of paddle-wheel SBUs and the second pillaring ligand. Color scheme: Zn, blue; O, red; N, violet; C, gray; H, light gray.

the framework structure, thus leading to the formation of open metal sites. MOFs with open metal sites generally provide high surface areas due to the reduction of framework mass as well as the stronger interaction between the metal sites and gas molecules, and thus generally adsorb higher amounts of H_2 gas.[74,75] A comparison of the H_2 gas sorption properties of MOFs having the same framework structures, in the presence and absence of the open metal sites, has also been reported.[76] In the presence of open metal sites, the MOF showed higher H_2 gas uptake capacities, mainly due to the mass reduction effect, but the H_2 gas capacities per volume of MOF samples were also higher (10−20%) than those without open metal sites.

As previously mentioned, MOFs made from $[Zn_2(OOC)_4]$ paddle-wheel SBUs often coordinate solvent molecules at the axial sites of the Zn ion, which can be removed by activation to generate open metal sites.[76] Furthermore, when two-dimensional (2D) networks constructed of dicarboxylate and square paddle-wheel units are connected with a second ligand, such as 4,4′-bipyridine (4,4′-bpy) or 3,6-di(4-pyridyl)-1,2,4,5-tetrazine (bpta), a 3D network can be constructed (Figure 3).[56,57,77−81] Many of these frameworks are interpenetrated and often show selectivity toward adsorption of the gases due to the molecular sieving effect of their pore sizes.

The representative MIL (MIL: material from Institute Lavoisier) series are constructed of trimeric chromium(III) octahedral cluster units and di- or tricarboxylates.[82−84] Many of the MIL frameworks are highly porous, and show high thermal and chemical stability. For example, MIL-101 adsorbs 6.1 wt % of H_2 at 77 K and 80 bar. The isosteric heat of H_2 adsorption is 10 kJ mol^{-1} at low H_2 loading. Many other highly porous materials have also been prepared from other metal ions such as In(III),[85−87] Co(II),[88,89] Mg(II),[90−92] Ni(II)[93] and have different structures and relatively high H_2 uptake capacities.

It must be emphasized that in the synthesis of carboxylate MOFs, the solvent system often greatly affects the structure of the MOF, which consequently affects the gas sorption properties. For example, Suh et al. prepared a porous MOF, $[Zn_4O(NTB)_2]_n \cdot 3nDEF\cdot n$EtOH, by using $Zn(NO_3)_2 \cdot 6H_2O$ and H_3NTB (4,4′,4″-nitrilotrisbenzoic acid) in a DEF, EtOH, and H_2O mixture.[94] In the structure, the $Zn_4O(CO_2)_6$ octahedral SBUs are linked by the NTB^{3-} units to form PdF_2 type (3,6)-connected nets, which are doubly interpenetrated to generate curved 3D channels (Figure 4). The compound maintained the single crystal nature even after removal of guest solvent molecules, and the desolvated framework $[Zn_4O(NTB)_2]_n$ exhibited permanent porosity, high thermal stability, blue luminescence, and high N_2, H_2, CO_2, and CH_4 gas storage capacities. In particular, it showed H_2 uptake capacity of 1.9 wt % at 77 K and 1 atm. When a similar solvothermal synthesis was carried out at 110 °C in a different solvent system consisting only of EtOH, a 3D network $[Zn_3(NTB)_2(EtOH)_2]_n \cdot 4n$EtOH was produced, which generated one-dimensional (1D) channels of honeycomb aperture.[95] On activation, the compound released the coordinating EtOH as well as guest EtOH molecules to result in the desolvated sample $[Zn_3(NTB)_2]_n$, which maintained the single crystallinity and showed H_2 uptake capacity of 1.0 wt % at 77 K and 1 atm.

3.2. Azolate-Based MOFs

Heterocyclic ligands such as imidazole, pyrazole, triazole, and tetrazole have been used in the synthesis of porous MOFs. The pK_a values of imidazole, pyrazole, triazole, and tetrazole are about 14.5, 14.2, 9.3, and 4.9, respectively.

Zeolitic imidazole frameworks (ZIFs) form neutral networks from the tetrahedrally coordinated zinc or cobalt centers and imidazolate linkers (Figure 5). The bridging angle of M−IM−M (IM = imidazolate) is similar to that of Si−O−Si angle in zeolites. These classes of compounds having zeolitic topology

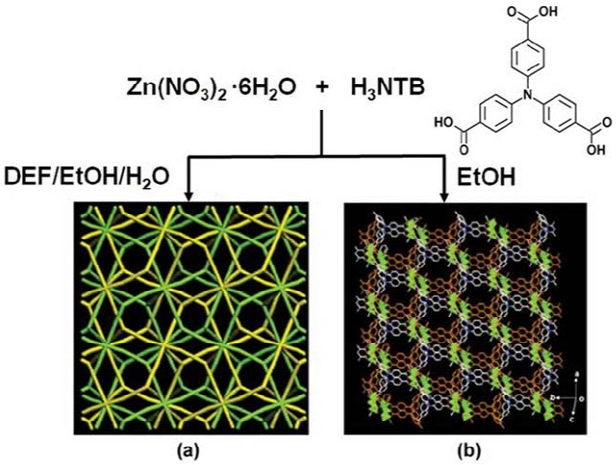

Figure 4. Two different frameworks formed from Zn(II) and NTB^{3-} in the different solvent systems. (a) A doubly interpenetrated PdF_2 structure of $[Zn_4O(NTB)_2]_n \cdot 3nDEF\cdot n$EtOH produced from DEF/EtOH/H_2O (5:3:2, v/v) mixture.[94] (b) The framework structure of $[Zn_3(NTB)_2(EtOH)_2]_n \cdot 4n$EtOH produced from EtOH.[95]

have high chemical and thermal stability. The structures of various ZIFs have been well documented,[96−99] and their gas storage properties have been reported.[100−103]

The H_2 storage capacities of several ZIFs have been reported. $Zn(MeIM)_2$ (ZIF-8) adsorbs 3.3 wt % of H_2 at 77 K and 30 bar, which is the highest H_2 adsorption capacity reported to date for ZIFs, indicating that ZIFs likely cannot be better H_2 storage materials than the carboxylate based MOFs. A recent review provides a detailed description of zeolitic imidazolate frameworks.[104]

Long and co-workers have reported a synthesis of Co(BDP)·2DEF·H_2O from the reaction of Co(II) ion and 1,4-benzenedi(4′-pyrazolyl) (BDP), which shows a high Langmuir surface area (2670 $m^2\ g^{-1}$) and a stepwise N_2 adsorption. It shows excess H_2 uptake capacities of 5.5 wt % at 10 bar and 50 K, and 3.1 wt % at 30 bar and 77 K.[105]

Triazolate-based MOFs are analogous to carboxylate-based MOFs with respect to their gas sorption properties. Triazole generally has a low pK_a value of about 9.3 and has different types of coordination modes depending on the degree of deprotonation. Gamez et al. provides a nice review on the triazoles, tetrazoles, and their possible coordination modes (Figure 6).[106] There are two different types of triazoles depending on the position of N on the ring, 1,2,3-triazole and 1,2,4-triazole.

Recently, Long and co-workers reported a triazolate-based framework $H_3[(Cu_4Cl)_3(BTTri)_8]$ (BTTri = 1,3,5-tris(1H-1,2,3-triazol-5-yl)benzene). The activated framework has exposed Cu^{2+} sites and shows a BET surface area of 1770 $m^2\ g^{-1}$ and a H_2 uptake capacity of 1.2 wt % at 1.2 bar and 77 K.[107] Most importantly, triazolate-based frameworks are stable in air, boiling water, and even acidic media. The framework FMOF-1 with the formula $\{Ag_2[Ag_4Tz_6]\}_n$ was synthesized from Ag(I) and 3,5-bis(trifluoromethyl)-1,2,4-triazolate and showed hysteretic

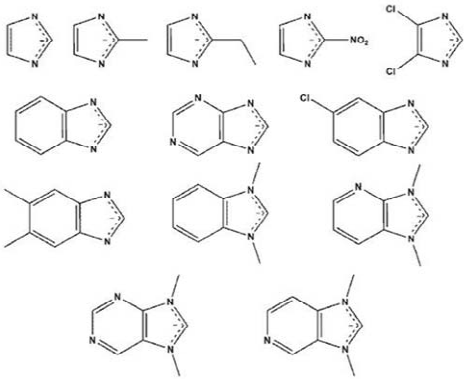

Figure 5. Various ligands used in the synthesis of zeolitic imidazolate frameworks.

adsorption of H_2 with a volumetric capacity of 41 kg m^{-3} at 77 K and 64 bar due to the fluoro-lined channels and cavities of the triazole framework.[108] In addition to the frameworks referred to here, many other porous triazolate-based frameworks exist.[109−111]

The tetrazolates are similar to carboxylic acids with respect to ligand acidity and planarity, and the tetrazole ring has a pK_a value of about 4.9. The presence of multiple N atoms gives rise to various types of coordination (Figures 7 and 8), which leads to the formation of a wide range of porous structures. There are many reports of tetrazolate-based MOFs,[48,112] a few of which

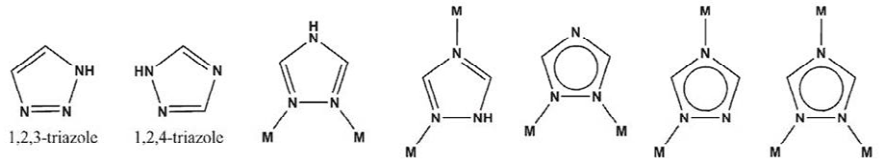

Figure 6. 1,2,3-Triazole, 1,2,4-triazole, and the coordination modes of 1,2,4-triazole and 1,2,4-triazolate.

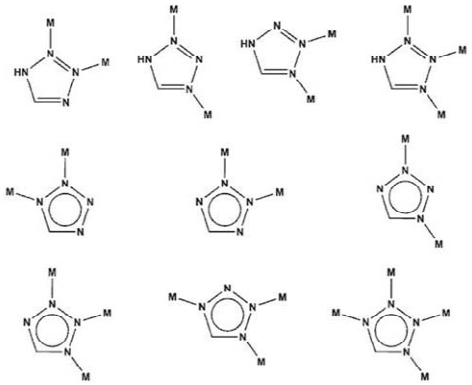

Figure 7. Coordination modes of tetrazole and tetrazolate.

contain open metals sites. Dincă and Long reported the synthesis and gas sorption properties of $Mn_3[(Mn_4Cl)_3(BTT)_8(CH_3OH)_{10}]_2$ (BTT = 1,3,5-benzenetristetrazolate), which showed a total H_2 uptake capacity of 6.9 wt % at 77 K and 90 bar and zero coverage isosteric heat of H_2 adsorption of 10.1 kJ mol^{-1}.[148] Neutron powder diffraction (NPD) data showed that H_2 molecules were directly bound to unsaturated Mn^{2+} centers within the framework. The guest Mn^{2+} ions in the framework can be exchanged with various cations such as Li^+, Cu^+, Fe^{2+}, Co^{2+}, Ni^{2+}, Cu^{2+}, and Zn^{2+}, and all of them are porous, showing relatively high H_2 uptakes ranging from 2.00 to 2.29 wt % at 77 K and 900 Torr.[112] The Co^{2+}-exchanged compound has zero coverage isosteric heat of 10.5 kJ mol^{-1}, which is slightly greater than that of the original sample. The reactions of Cu(II) and two similar tetrazole ligands, 1,3,5-tri-*p*-(tetrazol-5-yl)phenylbenzene (H_3TPB-3tz) and 2,4,6-tri-*p*-(tetrazol-5-yl)phenyl-*s*-triazine (H_3TPT-3tz), lead to the formation of noncatenated and catenated sodalite-type MOFs. The catenated framework shows relatively high stability toward desolvation and shows higher surface area and H_2 uptake. The total hydrogen uptake capacity of the catenated framework is 4.5 wt % at 80 bar and 77 K.[113] There are few other reports for the tetrazolate-based frameworks that show moderate H_2 uptake capacities ranging from 0.82 to 1.46 wt %.[114]

3.3. MOFs with Mixed Ligands

Porous MOFs that contain two different organic ligands within the same framework or those constructed of a ligand that contains two different coordinating functional groups can be synthesized. The most common and well-known MOFs

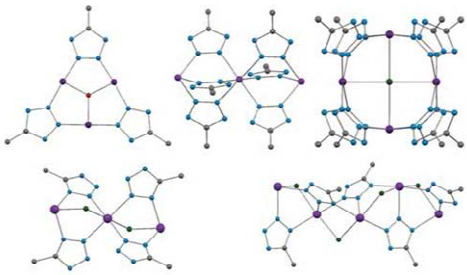

Figure 8. Various types of tetrazolate cluster units found in tetrazolate-based MOFs. Color code: violet, metal; green, Cl; red, O; blue, N; gray, C.

constructed from the combination of two different ligands are the 3D primitive cubic-type (α-Po) structures (Figure 9). In these MOFs, 2D layers are assembled from paddle-wheel cluster units $[M_2(O_2CR)_4]$ (M = Cu^{2+}, Zn^{2+}, and Co^{2+}) and dicarboxylate linkers. The 2D layers are linked with pillars to form 3D MOFs. The pore size and pore environment of these pillared square grid nets can be simply tuned by selecting the different combinations of dicarboxylates and pillar linkers. For example, Kim and co-workers reported the X-ray structures and gas sorption properties of a series of isomorphous MOFs that were systematically modulated from a prototype $[Zn_2(1,4\text{-bdc})_2(dabco)]$ by replacing 1,4-bdc with dicarboxylate linkers having aliphatic (tetramethylterephthalate, tmbdc), aromatic (1,4-naphthalenedicarboxylate, 1,4-ndc), or halogenic (tetrafluoroterephthalate, tfbdc) side groups on the phenyl ring of the ligands, and substituting 1,4-diazabicyclo[2.2.2]octane (dabco) with longer 4,4′-bpy.[115] Introduction of substituents on the phenyl ring of 1,4-bdc resulted in a significant decrease in the surface area. The H_2 adsorption isotherms showed similar uptake capacities, but the curves showed markedly different slopes in the low pressure ranges (P < 0.4 atm). The framework with the most crowded pore environment showed the fastest rise in H_2 uptake, indicating the highest affinity toward H_2 at low pressures. The authors proposed that a porous material with a surface area greater than 2000 m^2 g^{-1}, a void fraction greater than 60%, and free window sizes smaller than 6 Å might exhibit an excellent H_2 storage capacity.

When longer ligands were used in the construction of the primitive cubic net, multiply interpenetrated frameworks often resulted. Some of these multiply interpenetrating MOFs exhibit unusual stepwise gas adsorption and hysteretic desorption behavior due to the changes in the framework structures. Suh et al. reported a doubly interpenetrated (α-Po) net with 3D curved

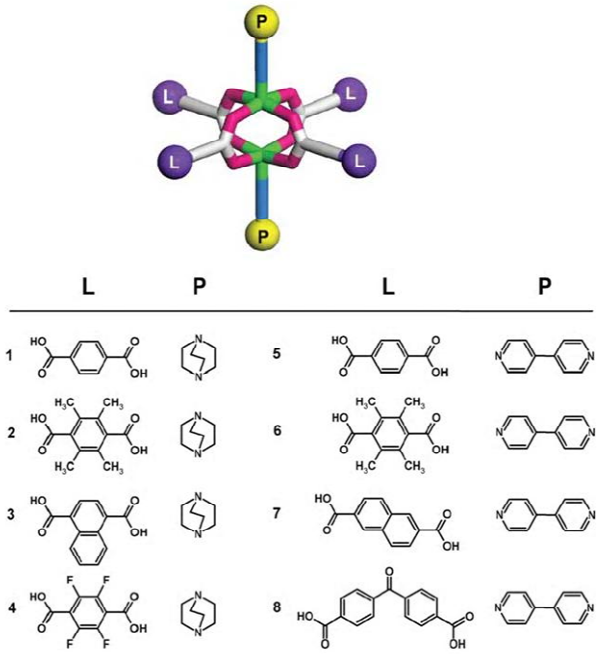

Figure 9. Linkers (L) and pillars (P) employed in the synthesis of 3D primitive cubic-type (α-Po) structures.

channels, $[Zn_2(BPnDC)_2(bpy)]_n$ (SNU-9), where BPnDC is 4,4′-benzophenone dicarboxylate.[116] In SNU-9, every binuclear Zn_2 unit is bridged by BPnDC1 and 4,4′-bpy to form a distorted square grid 2D network that runs parallel to the *ab* plane, while BPnDC2 acts as a pillar linking the layers along the *c* axis, which gives rise to a 3D framework. SNU-9 showed a three-step adsorption for N_2 and O_2 gases, and two-step adsorption for CO_2 and H_2 gases with large hysteresis on desorption, while it does not uptake CH_4 gas. SNU-9 has a Langmuir surface area of 1030 $m^2\ g^{-1}$, pore volume of 0.366 $cm^3\ g^{-1}$, and high gas uptake capacities for H_2, CO_2, and O_2 gases.

As a new method to develop highly porous MOF, Matzger and co-workers suggested coordination copolymerization of topologically different linkers with identical coordinating functionality.[72,117,118] They combined symmetrical dicarboxylate and tricarboxylate, which should be connected with $[Zn_4O]$ octahedral SBUs. For example, $[Zn_4O(BDC)(BTB)_{4/3}]$ (UMCM-1, UMCM = University of Michigan crystalline material) was obtained from BDC and BTB.[117] On the octahedral building unit, two BDC linkers are adjacent and the other four positions are occupied by BTB linkers, which construct an octahedral cage. When ditopic linker BDC was replaced with thieno[3,2-b]thiophene-2,5-dicarboxylate (T^2DC), 2,5-thiophenedicarboxylate (TDC), and NDC, different coodination modes formed, which provided the frameworks with different topologies, UMCM-2, UMCM-3, and MOF-205, respectively. All MOFs (UMCM-1, -2, -3, -4, -5, MOF-205, and MOF-210) prepared by this technique demonstrated BET surface areas ranging from 3500 to 6240 $m^2\ g^{-1}$ and the high pore volumes ranging from 1.64 to 3.60 $cm^3\ g^{-1}$.[29,118] UMCM-2, $\{[Zn_4O(T^2DC)(BTB)_{4/3}]\}$, showed high H_2 uptake (excess 68.8 mg g^{-1}) at 77 K and 46 bar. MOF-210 constructed from 4,4′,4″-[benzene-1,3,5-triyl-tris(ethyne-2,1-diyl)]tribenzoate (BTE) and biphenyl-4,4′-dicarboxylate (BPDC) exhibited excess H_2 uptake of 86 mg g^{-1} at 77 K and 56 bar with a total uptake of 176 mg g^{-1} at 77 K and 80 bar. This total H_2 uptake is the highest and excess is the second after NU-100 among the data ever reported for physisorption materials.

The ligand having two different coordinating functional groups has been also employed in the synthesis of porous MOFs. The representative example is pyridyl carboxylic acid such as isonicotinic acid[119] and pyridinedicaboxylic acid (Figure 10).[120] Recently, Su and Eddaoudi groups independently suggested a new pillaring strategy based on a ligand-to-axial approach by combining two previous methods, axial-to-axial and ligand-to-ligand pillaring.[121,122] They used trigonal heterofunctional ligand that is a functionalized isophthalic acid with N-donor (pyridyl of triazolyl) at the 5-position. From trigonal ligands (3-connected) and the common 6-coordinated paddle-wheel $[Cu_2(COO)_4L_2]$ motifs, (3,6)-connected 3D MOFs have been synthesized.

Recently, Chen and co-workers reported a new approach to construct interpenetrated microporous MOFs having primitive cubic net structures, which were constructed from the combination of pyridylcarboxylate and dicarboxylate linkers with paddle-wheel units (Figure 11).[123] $[Zn_2(PBA)_2(BDC)]\cdot 3DMF\cdot 4H_2O$ (UTSA-36; UTSA = University of Texas at San Antonio) was constructed from 4-(4-pyridyl) benzoic acid (PBA) and BDC

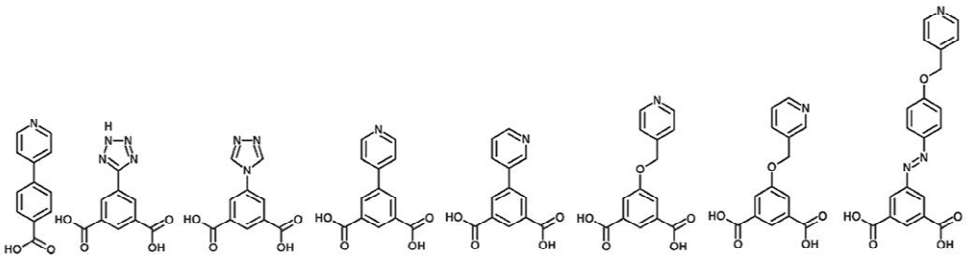

Figure 10. The ligands with two different functional groups.

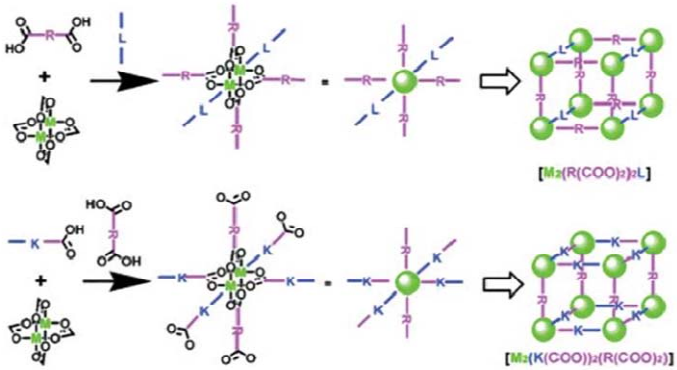

Figure 11. Two approaches for constructing the porous MOFs with primitive cubic net structure by using two different organic ligands. Reproduced with permission from ref 123. Copyright 2011 WILEY-VCH Verlag GmbH & Co. KGaA, Weinheim.

with a Zn salt. UTSA-36 is doubly interpenetrated to generate small pores of size 3.1−4.8 Å, which shows highly selective sorption of small hydrocarbons C_2H_2, C_2H_4, and C_2H_6 over CH_4. It has a Langmuir (BET) surface area of 806 $m^2 g^{-1}$ (495 $m^2 g^{-1}$), a pore volume of 0.33 $cm^3 g^{-1}$, and a H_2 uptake of 123 $cm^3 g^{-1}$ (1.1 wt %) at 77 K and 1 atm.

MOFs containing two different types of metal clusters can be also synthesized. Eddaoudi, Zaworotko, and co-workers reported $[Cu_6O(TZI)_3(H_2O)_9(NO_3)]$, which was constructed of two different Cu clusters and 5-tetrazolylisophthalic acid (H_3TZI).[124] The X-ray crystal structure revealed isophthalates and tetrazolates formed $[Cu_2(O_2CR)_4]$ paddle-wheels units and trigonal $[Cu_3O(N_4CR)_3]$ trimers. The framework showed a Langmuir (BET) surface area of 3223 (2847) $m^2 g^{-1}$, a total pore volume of 1.01 $cm^3 g^{-1}$, high H_2 storage capacity (2.4 wt % at 77 K and 1 atm) with high isosteric heat of 9.5 kJ mol^{-1}.

3.4. MOFs with Metal Complexes as Building Blocks

3.4.1. MOFs Based on Macrocyclic Complexes. Another class of compounds that might find application in hydrogen storage is the frameworks constructed from square-planar Ni(II) macrocyclic complexes and organic ligands. When the square-planar macrocyclic complexes are reacted with various types of carboxylates, such as linear dicarboxylates, trigonal tricarboxylates, square-type or tetrahedral-shaped tetracarboxylates, the Ni(II) ions of the macrocyclic complex coordinate oxygen atoms of the carboxylate at the axial sites of the macrocyclic plane to yield electronically neutral 1D, 2D, and 3D networks, respectively.[125−133] In such networks, the carboxylate ligands are located at the nodes and the macrocyclic complexes are positioned at the struts since the macrocyclic complexes simply act as linear linkers to connect the organic ligands (Figure 12). The synthetic strategies are previously well reviewed.[125,126]

The advantage of Ni(II) macrocyclic complexes in the construction of MOFs is that they can form grooves in the structures, which induce fits between the networks and often lead to robust frameworks. Moreover, the networks constructed of Ni(II) macrocyclic complexes are redox active because the Ni(II) ion of the macrocyclic complex can be oxidized to Ni(III) species or reduced to Ni(I) species, which are stabilized by the macrocyclic effect despite of the uncommon oxidation state. By using such redox-active properties, Suh's group oxidized the crystal of the network by using I_2, which resulted in an oxidized framework containing I_3^- anions.[128] On the basis of this knowledge, Suh's group developed the fabrication method of Ag, Au, and Pd nanoparticles in the pores of the networks by simple immersion of the redox-active porous crystals in the solutions of Ag(I), Au(III), and Pd(II) salts, respectively.[130−132,134] The MOF loaded with palladium nanoparticles showed enhanced hydrogen uptakes at 77 K as well as at room temperature.[134]

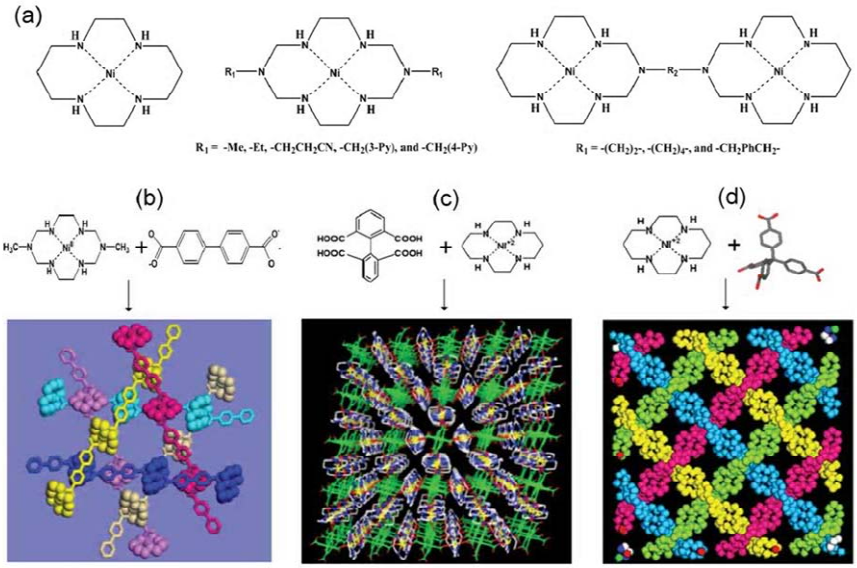

Figure 12. Typical examples of porous frameworks constructed from Ni(II) square-planar macrocyclic complexes and carboxylate ligands. (a) The employed Ni(II) macrocyclic complexes. (b) A robust 3D network formed by the packing of 1D coordination polymers in a double network of 3-fold braids.[129,130] (c) A 2D square-grid network.[131] (d) A 3D diamondoid network.[132]

The self-assembly of a Ni(II) macrocyclic complex and a linear dicarboxylate forms a linear coordination polymer, which is packed in a double network of 3-fold braids to construct an extremely robust 3D porous network. The single crystallinity and 3D packing structure were retained even after the removal of the solvent molecules by heating and evacuation. The network has a Langmuir surface area of 817 $m^2\ g^{-1}$ and pore volume of 0.37 $cm^3\ g^{-1}$. It adsorbs 1.1 wt % of H_2 at 1 atm and 77 K.[129]

In addition, 2D and 3D networks can be constructed from the Ni(II) macrocyclic complexes with tri- and tetracarboxylates. The 2D networks were prepared from Ni(II) macrocyclic complexes and tricarboyxlates.[135−138] In the case of large-sized tricarboxylates, multiple interwoven structures were formed.[138] The 2D bilayer network was prepared from BTC and a Ni(II) bismacrocyclic complex,[127,128] whose crystal behaves like a sponge, and thus shrinks and swells depending on the amount of guest solvent molecules included in the pores.

3D networks have been also prepared from Ni(II) macrocyclic complexes and tetracarboxylates. When the sizes of the tetracarboxylate ligands were very large, 8-fold, 4-fold, and doubly interpenetrated networks were generated (Figure 13).[132,133,139] The 4-fold network $\{[Ni(cyclam)]_2(MTB)\}_n$ (MTB = methanetetrabenzoate) showed a BET surface area of 141 $m^2\ g^{-1}$ (Langmuir = 154 $m^2\ g^{-1}$). At 77 K, the framework adsorbed 0.7 wt % of H_2 at 1 atm, and 1.25 wt % at 40 bar.

3.4.2. Metal-Cyanide Frameworks. Metal-cyanide frameworks are synthesized from the reaction of potassium hexacyanometallate with a different metal salt. For example, $Cu_3[Co(CN)_6]_2$ is synthesized from $K_3[Co(CN)_6]$ and $CuNO_3$ in an aqueous medium. These classes of MOFs have cubic network structures that are analogous to Prussian blue complex and are constructed of octahedral $[M(CN)_6]$ complexes linked by M^{2+} ions. The metal-cyanide frameworks have also been studied as potential hydrogen storage materials. Many of them contain accessible open metal sites, but the main limitation of these as porous materials is that the cyanide linker is too short to generate high porosity. In general, they have surface areas and pore volumes that are too small to adsorb a large amount of H_2 gas even at high pressures, except $Cu_3[Co(CN)_6]_2$ that adsorbs 2.61 wt % H_2 at 1 bar and 77 K with an isosteric heat of 6.9 kJ mol^{-1}.[140] The framework, $K_2Zn_3[Fe(CN)_6]_2$ showed a H_2 uptake capacity of 1.2 wt % at 77 K and 1.19 bar with 7.9−9.0 kJ mol^{-1} of the

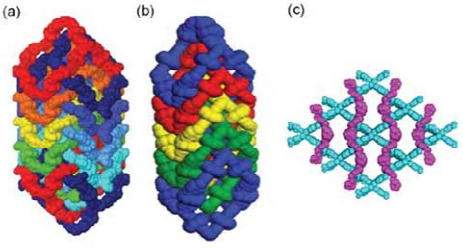

Figure 13. (a) 8-fold, (b) 4-fold, and (c) doubly interpenetrated networks constructed from various Ni(II) macrocyclic complexes and tetracarboxylate ligands. Figures adapted from refs 132, 133, and 139.

isosteric heat of H_2 adsorption.[141] Many metal-cyanide frameworks exist that have relatively good H_2 uptake capacities at low temperature, such as $M[Fe(CN)_5NO]$ (M = Co^{2+}, Ni^{2+}),[142] $M(L)[M'(CN)_4]$ (M, M′ = Co, Ni; Co, Pd; Co, Pt; Ni, Ni; Ni, Pd),[143] $M[M'(CN)_6]$ (M, M′ = Mn, Co; Fe, Co; Co, Co; Ni, Co; Cu, Co; Zn, Co),[144] $[Ga[Co(CN)_6]$, $Fe_4[Fe(CN)_6]_3$, $M_2[Fe(CN)_6]$ (M = Mn, Co, Ni, Cu), $Co_3[Co(CN)_5]_2$,[145] $Zn_3A_2[M(CN)_6]_2$ (A = K, Rb, Cs; M = Fe, Ru, Os).[146] A series nanoporous Prussian blue analogues, $M^{II}_3[Co^{III}(CN)_6]_2$ (M^{II} = Mn, Fe, Co, Ni, Cu, Zn, Cd), and their H_2 adsorption capacities were also reported.[147]

3.5. Post-Synthetic Modification

Functionalization of MOFs is a method to change properties of MOFs, such as surface area and pore volume. Moreover, one can include specific functional groups that can change chemical properties of the MOF surface or provide strong interaction sites for H_2. For example, one may include a hydroxyl group in the ligand and then exchange the proton of the hydroxyl group with an alkali metal ion.[148] One may also synthesize a negatively charged framework including counter-cations and then exchange the counter-cations with alkali or alkaline earth metal ions.[149] In addition to these, several other postsynthetic modifications exist, such as covalent modification,[150] framework reduction,[151] and doping with metal nanoparticles.[134,152]

The functionalization of a MOF can be accomplished before and after the synthesis of the MOF. One can attach a specific functional group to the ligand that can be used in the construction of the MOF. This is known as "prefunctionalization". During the earlier periods of MOF chemistry, the prefunctionalization approach was used widely, especially for the introduction of $-NH_2$, $-CH_3$, $-Br$, etc. on the framework, which leads to the formation of a series of structures widely known as IRMOFs.[59] Similar prefunctionalization strategies provided a series of ZIFs[100] and a family of MILs.[82,83] The main problem associated with the prefunctionalization strategy is the difficulty in synthesis. The labile functional groups can be dissociated during the harsh solvothermal reaction conditions, or the functional group may take part in the reaction to provide an unwanted nonporous structure.

In 1990, Hoskins and Robson suggested the idea of postsynthetic modification.[153] In 2007, Wang and Cohen modified free $-NH_2$ groups present in IRMOF-3 by the reaction with acetic anhydride.[154] The modification was partially (>80%) made in 5 days, and even after the modification, the framework structure was maintained. Now postsynthetic modification is widely used in order to change the properties of a MOF for applications in gas storage and catalysis. A recent review by Cohen et al. provides some elaborate ideas about the postsynthetic modification of MOFs.[155,156]

By postsynthetic modification, the framework can be functionalized without altering the framework structure. Organic linker part of the framework can be modified by covalent modification, and the metal centers of the framework can be modified with various ligands. In addition, MOFs can be modified by inserting extra metal ions or metal nanoparticles into the channels. The metal centers of the MOF can be modified by generating the open metal centers followed by coordinating the ligands that have amine or pyridine groups at the open metal centers. After the functionalization of the framework, the effect of the specific functional groups on the H_2 uptake capacity can be studied. In addition, the introduction of a coordinating functional group in the framework allows the incorporation of new metal ions or metal nanoparticles, which increase the available open metal sites and thus enhance the total H_2 storage capacity. Such studies can be used to fine-tune the framework structure, metal centers, and functional groups of the ligands for the development of MOFs for ambient temperature H_2 storage.

3.5.1. Modification of Metal Centers. The postsynthetic modification at the metal centers of a MOF is less common than modification of the organic parts. Férey and co-workers reported amine-grafting at open metal sites of the MOFs.[157] The postsynthetic amine grafting was employed in the synthesis of the chromium(III)-terephthalate MIL-101. The coordinated water molecules in MIL-101 were replaced with ethylene diamine (ED), diethylenetriamine (DETA), and 3-aminopropyltrialkoxysilane (APS) by heating the sample at 423 K followed by refluxing the sample with those amines. There was no change in the crystallinity, as indicated by the powder X-ray diffraction (PXRD) patterns. After grafting the amines, the BET surface area decreased from 4230 $m^2\ g^{-1}$ to 3555 $m^2\ g^{-1}$ and the pore size was reduced. One may note that the amine modified framework is able to incorporate $[PdCl_4]^{2-}$, $[PtCl_6]^{2-}$, and $[AuCl_4]^-$ in the lattice. When the MOF incorporating those metal complex was reduced, metal nanoparticles around 2−4 nm in size were produced in the MOF. It has been reported that nanoparticles embedded in MOF increases the H_2 storage capacity.[134,158] In the other report, Farha et al. have shown that the H_2 storage capacity of MOFs can be modified by postsynthetic incorporation of pyridine type coordinating ligands at the open metal site.[159] The H_2 uptake capacities of the modified frameworks become lower than that with open metal sites. The framework with open metal sites, Zn_2(btatb) (btatb = 4,4′,4″,4‴-benzene-1,2,4,5-tetrayltetrabenzoate), shows a BET surface area of 1370 $m^2\ g^{-1}$ and the H_2 uptake capacity of 2.2 wt % at 77 K and 1 bar.

Suh et al. reported postsynthetic substitution of coordinated water molecules with bidentate organic linkers, which changes the pore size and pore shape of the MOF, leading to changes in gas sorption properties. The coordinated water molecules in $[Zn_2(TCPBDA)(H_2O)_2]\cdot 30DMF\cdot 6H_2O\}$ (H_4TCPBDA = *N*,*N*,*N*′,*N*′-tetrakis(4-carboxyphenyl)biphenyl-4,4′-diamine) (SNU-30) were quantitatively substituted with 3,6-di(4-pyridyl)-1,2,4,5-tetrazine (bpta), which resulted in the new compound $[Zn_2(TCPBDA)(bpta)]\cdot 23DMF\cdot 4H_2O$ (SNU-31SC) where bpta is linked to two paddle-wheel type Zn_2 clusters, while maintaining single-crystallinity.[78] Unlike its pristine form, the bpta is significantly bent due to the steric constraints. The inserted bpta linker in SNU-31 can also be removed by immersion in DEF, which generates $[Zn_2(TCPBDA)(H_2O)_2]\cdot 23DEF$ (SNU-30SC) and again retains the single-crystallinity. The activated framework of SNU-30 (SNU-30′) adsorbed H_2, N_2, O_2, CO_2, and CH_4 gases. The BET surface area measured from the N_2 adsorption isotherm was 704 $m^2\ g^{-1}$ and the pore volume was 0.28 $cm^3\ g^{-1}$. At 1 atm, SNU-30′ has a H_2 uptake capacity of 1.42 wt % at 77 K and 0.72 wt % at 87 K. The framework has an isosteric heat of H_2 adsorption of 8.12−7.27 kJ mol^{-1}. At 77 K and 61 bar, the framework shows an excess H_2 uptake capacity of 2.75 wt % and total uptake of 3.27 wt %. At 298 K and 71 bar, the H_2 uptake capacity was 0.16 wt %. Interestingly, the postsynthetically modified framework did not adsorb H_2, N_2, O_2, CH_4 but selectively adsorbed CO_2.

3.5.2. Modification of Ligand Parts. The surface area, pore volume, and pore size of the MOFs can be modified by postsynthetic modification of the ligands. There are many reports in

which the ligand component of MOFs are modified without collapsing the framework. Many different types of postsynthetic covalent modification are reported, such as amide coupling,[154,160,161] imine condensation,[162−164] bromination,[165] click chemistry,[166,167] etc. Detailed description can be found in the recent reviews by Cohen et al.[155,156] Cohen et al. showed that H_2 uptake capacities of the MOFs could be modified by postsynthetic modification.[150] The amine groups in various MOFs were modified to amides groups. The resulting MOFs such as IRMOF-3-AMPh, IRMOF-3-URPh, and UMCM-1-AMPh showed increased H_2 storage capacities up to 1.73 wt %, 1.54 wt %, and 1.54 wt %, respectively, compared to those of IRMOF-3 (1.51 wt %) and UMCM-1-NH_2 (1.35 wt %) at 77 K and 1 atm. Detailed discussion can be found in section 4.2.2.

4. STRATEGIES FOR IMPROVING HYDROGEN STORAGE CAPACITIES IN METAL−ORGANIC FRAMEWORKS

It has been shown through calculations and experimental results that a qualitative linear relationship exists between the H_2 storage capacities at 77 K and the specific surface areas. In Figure 14, the high pressure H_2 uptake capacities of various MOFs are presented versus the surface areas. In general, the pore volume is proportional to the specific surface area. Therefore, in order to increase the H_2 uptake capacities at 77 K, higher specific surface area and higher pore volume should be created in the MOF. However, the H_2 storage capacity decreases sharply with increasing temperature, and none of the MOFs yet satisfies the proposed DOE target at room temperature. The MOFs are physisorption-based materials for H_2 storage, and their interaction energy with H_2 molecules is very weak. Q_{st} in the porous MOFs are in the range of 5−9 kJ mol^{-1}. SNU-15, which contains an open metal site at every Co(II), has the H_2 adsorption enthalpy of 15 kJ mol^{-1} at zero coverage, but it decreases sharply as the H_2 loading increases.[168] To extend the H_2 storage performance to ambient temperature, one should increase substantially the heat of H_2 adsorption in the MOF. The predicted average heat of H_2 adsorption, which is necessary for effective ambient temperature storage and release, is ca. 15 kJ mol^{-1}.[169,170]

Snurr and co-workers performed GCMC simulations to predict H_2 adsorption isotherms in a series of 10 isoreticular MOFs (IRMOFs) at 77 K.[171] The effects of surface area, free volume, and heat of adsorption on the H_2 uptake were investigated by the simulations over a wide range of pressures at 77 K on this set of materials that have the same framework topology and surface environment but with different pore sizes. The results reveal the existence of three adsorption regimes; at low pressure (loading), the H_2 uptake correlates with the heat of H_2 adsorption, at intermediate pressure (up to 30 bar) with the surface area, and at the high pressures (120 bar) with the free volume (Figure 15).

Later, Frost and Snurr tested these correlations at room temperature and analyzed the absolute (total) and excess adsorptions.[172] The results showed that the correlations that had been held for absolute H_2 adsorption at 77 K could not be applied for absolute H_2 adsorption at 298 K due to very weak adsorption energy between MOF and H_2. Even at low loadings, the absolute adsorbed amount of H_2 at 298 K mainly correlates with the free volume. They also found that at low loading the excess adsorption of H_2 at 298 K correlates well with the heat of adsorption again, but at high loadings, the adsorption correlates better with the surface area than with the free volume (Figure 16). They suggested that a reasonable goal of 9 wt % and 30 g L^{-1} could be obtained with MOFs that can provide an isosteric heat of 15 kJ mol^{-1}

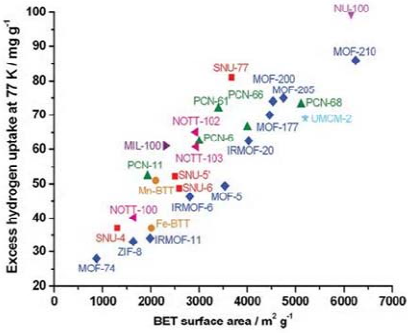

Figure 14. Excess high pressure H_2 uptake capacities at 77 K versus BET surface areas for some highly porous MOFs.

or higher while maintaining a free volume of 2.5 cm^3 g^{-1} and void fraction of 85%.

4.1. Increase in Surface Area and Pore Volume

Selected data for the H_2 uptake capacities and the surface areas of the MOFs reported so far are summarized in Tables 1 and 2. As shown in Figure 17, the H_2 uptake capacities at 77 K and 1 atm are related with the surface areas in the range of 100−2000 m^2 g^{-1}, but they hardly relate with the surface area when the surface area exceeds 2000 m^2 g^{-1}. It seems that at 1 atm of H_2 pressure, the surface area greater than 2000 m^2g^{-1} cannot be fully covered with H_2 molecules, since at low pressure, H_2 will preferentially bind on the sites that have large affinity for H_2. In addition, low-pressure H_2 adsorption may be influenced by other factors such as pore size, catenation, ligand functionalization, and open metal sites. For example, the H_2 uptake capacity at 77 K and 1 atm for doubly interpenetrating SNU-77 (1.80 wt %), which has a BET surface area of 3670 m^2 g^{-1} and a pore size of 8.0 Å,[173] is higher than that of MOF-177 (1.24 wt %) that has higher surface area (4750 m^2 g^{-1}) and larger pores (11.8 Å) in the noninterpenetrating (6,3)-connected net,[45] but it is lower than that of $[Zn_4O(NTB)_2]$ (SNU-1, 1.9 wt %) that has a much smaller surface area (1120 m^2 g^{-1}) and smaller pores (5.0 Å) in the doubly interpenetrating nets.[94] The factors influencing the H_2 uptake of porous MOFs will be discussed in the following sections. However, the H_2 uptake capacities at 77 K under high pressures show a quite nice qualitative relationship with the surface areas. As the surface area increases, the high pressure H_2 uptake capacity at 77 K increases.

4.1.1. Elongation of Ligands. The MOFs constructed from long organic ligands tend to collapse after removal of guest molecules. In addition, the longer ligands often lead to the framework interpenetration that gives rise to a reduced surface area or even a nonporous structure. However, some reports have shown that with a given framework topology, the surface area can be increased by using the elongated ligands. Suh and co-workers reported doubly interpenetrated pyr (pyrite) frameworks, $[Zn_4O(NTB)_2]$ (SNU-1)[94] and $[Zn_4O(TCBPA)_2]$ (SNU-77),[173] which were constructed from $[Zn_4O(COO)_6]$ octahedral secondary building units (SBUs) and tricarboxylates, NTB in the former and TCPBA in the latter. TCBPA is tris(4′-carboxybiphenyl)amine that is an extended form of NTB. Both frameworks

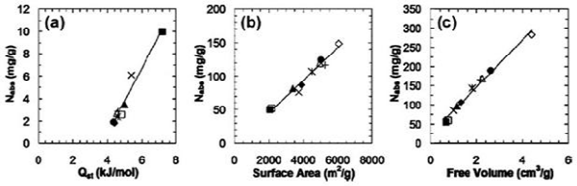

Figure 15. Simulated H_2 adsorption in a series of 10 IRMOFs at 77 K. (a) Adsorbed amounts at 0.1 bar vs isosteric heat of adsorption. (b) Adsorbed amounts at 30 bar vs accessible surface area. (c) Adsorbed amounts at 120 bar vs free volume. ♦, IRMOF-1; ■, IRMOF-4; ▲, IRMOF-6; x, IRMOF-7; *, IRMOF-8; ●, IRMOF-10; +, IRMOF-12; Δ, IRMOF-14; ◊, IRMOF-16; □, IRMOF-18. Reproduced with permission from ref 171. Copyright 2006 the American Chemical Society.

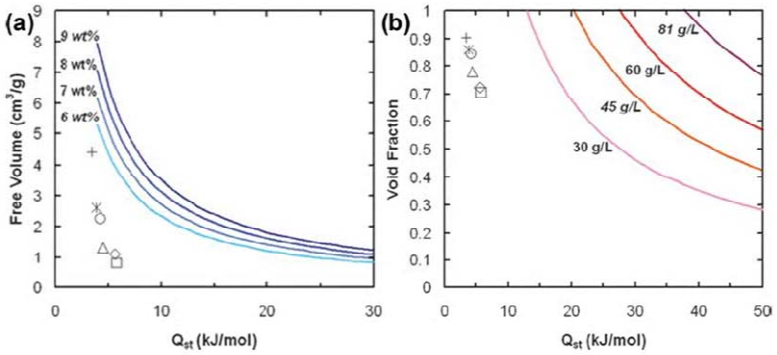

Figure 16. (a) Requirements for target gravimetric H_2 loadings at 120 bar and 298 K. (b) Requirements for target volumetric H_2 loadings at 120 bar and 298 K. Results for existing materials are marked with symbols: Δ, IRMOF-1; ◊, IRMOF-10; *, IRMOF-14; +, IRMOF-16; □, CuBTC. Reproduced with permission from ref 172. Copyright 2007 the American Chemical Society.

exhibit high permanent porosity, high thermal stability (up to 400 °C), guest-dependent luminescence, and single-crystal-to-single-crystal transformations, mainly rotational motions in response to removal of the guest molecules. The Langmuir surface area of SNU-77 is 4180 $m^2\ g^{-1}$, which is much higher than that (1121 $m^2\ g^{-1}$) of SNU-1.

Yaghi and co-workers also reported Zn_4O-based MOFs, MOF-177 and MOF-200, which are noninterpenetrating qom networks.[29] MOF-200 was prepared from BBC that is an elongated form of BTB employed in the synthesis of MOF-177. MOF-200 shows ultrahigh surface areas of 10 400 $m^2\ g^{-1}$ (Langmuir) and 4520 $m^2\ g^{-1}$ (BET) as determined by N_2 gas sorption data, while MOF-177 has surface areas of 5640 $m^2\ g^{-1}$ (Langmuir) and 4750 $m^2\ g^{-1}$ (BET).[45]

Schröder and co-workers reported an isostructural series of MOF having NbO type networks of $6^4 \cdot 8^2$ topology that were constructed from $[Cu_2(COO)_4]$ paddle-wheel configuration and tetracarboxylate ligands.[24] It was observed that elongation of the ligand dramatically increases pore diameter along the *c* axis from 10.0 Å in NOTT-100 to 32.0 Å in NOTT-102. As summarized in Table 3, the framework NOTT-100 that was synthesized from the shortest ligand shows the lowest BET surface area, pore volume, and pore size. The highest pore volume and BET surface area were obtained with NOTT-102 that incorporates the longest ligand.

An isoreticular series of rht topology with hexacarboxylate ligands have been also reported.[28,265,275,276] These MOFs contain the ligands having C_3 symmetry with three coplanar isophthalate moieties and the metal−organic polyhedra. The biggest hexacarboxylate reported is 5,5′,5″-(((benzene-1,3,5-triyltris(ethyne-2,1-diyl))tris(benzene-4,1-diyl))tris-(ethyne-2,1-diyl))triisophthalic acid (ttei). A solvothermal reaction of H_6ttei and $Cu(NO_3)_2 \cdot 2.5H_2O$ in DMF/HBF_4 afforded $[Cu_3(ttei)(H_2O)_3]_n$ (NU-100/PCN-610), whose X-ray crystal structure revealed noninterpenetrating (3,24)-connected framework formed from Cu_2-paddle-wheel units. Activated NU-100 prepared by a supercritical CO_2 drying method exhibits an ultra high BET surface area of 6143 $m^2\ g^{-1}$ and a pore volume of 2.82 $cm^3\ g^{-1}$. The excess H_2 uptake of NU-100 was 99.5 mg g^{-1} at 56 bar, and the total was 164 mg g^{-1} at 70 bar and 77 K. These values are the highest in excess among those of the MOFs reported so far, and second in total H_2 uptake after MOF-210. The reason why those MOFs from extended hexatopic ligand are stable is because of the formation of a special 3,24-connected network, which effectively reduces the pore opening and prevents the network interpenetration. This approach is an effective way to increase the MOFs' surface area without sacrificing their stability.

4.1.2. Catenation and Interpenetration. Catenation refers the physical entanglement of two or more identical frameworks.[277] It is also known as interpenetration, but interpenetration

Table 1. The H_2 Gas Sorption Data for MOFs without Open Metal Sites

		surface area/$m^2\ g^{-1}$				hydrogen storage capacity[a]					
MOF		BET	Langmuir	pore size/ Å	pore volume/ $cm^3\ g^{-1}$	P/ bar	T/ K	gravimetric/ wt %	volumetric/ $g\ L^{-1}$	Q_{st}/ $kJ\ mol^{-1}$	ref
$Be_{12}(OH)_{12}(BTB)_4$		4030	4400			1	77	1.6		5.5	174
						20(100)	77	6 (9.2)	(43)		
						95	298	(2.3)	(11)		
$Mg_3(HCO_2)_6$		150		4.5, 5.5	0.043	1	77	0.6			175
$Mg_3(NDC)_3$	TUDMOF-2	190	520	3.6		1	77	0.78		9.5	91
Al(OH)(BDC)	MIL-53(Al)	1100		8.5		16	77	3.8	37		176
$Al_{12}O(OH)_{18}(H_2O)_3$-$(Al_2(OH)_4)(BTC)_6$	MIL-96					3	77	1.91			177
$Sc(BDC)_3$		721		5.4	0.332	1	77	1.5			178
$[Sc_2(BPTC)(OH)_2]$	NOTT-400	1350		7.5	0.56	1	77	2.14		5.96	179
						20	77	(3.84)			
[Sc(TDA)(OH)]	NOTT-401	1514		6.2	0.66	1	77	2.31		6.65	179
						20	77	(4.44)			
$Mn(HCO_2)_2$		297		4.5		1	77	0.9			180
$Mn_3[(Mn_4Cl)_3(tpt\text{-}3tz)_8]_2$		1580	1700			25 (80)	77	3.7 (4.5)			113
$Fe_3(OH)(pbpc)_3$		1200				1	77	1.6			181
						20	77	3.05			
Co(BDP)			2670		0.93	30	77	3.1			105
Co(HBTC)(4,4′-bpy)		887		5, 8		72	77	2.05		7.0	89
						72	298	0.96			
Co(NDC)(4,4′-bpy)			115	5.1, 4.0	0.1	1	77	0.72			182
Co(ox)(4,4′-bpy)						1	77	0.1			183
$Co_2(6\text{-mna})_2$	CUK-2	420			0.17	1	77	0.66			184
$Co_2(BDC)_2(dabco)$		1595	2120		0.77	10	298	0.03			185
						44.2	77	4.11			186
						100	293	0.32			
$Co_3(BDC)_3(dabco)$		360	538		0.2	0.93	77	1	51.2		187
$Co_3(bpdc)_3(4,4'\text{-bpy})$		922		8	0.38	1	77	1.98		7.1	188
$Co_3(NDC)_3(dabco)$		1502	2293	4.5	0.82	1	77	2.45	29.8		187
						17.2	298	0.89	10.8		
$Co_3(2,4\text{-pdc})_2(OH)_2$	CUK-1	630			0.26	1	77	1.6			184
$[Co_9(BTC)_6(tpt)_2(H_2O)_{15}]$				8,6		1	77	0.89			189
Ni(cyclam)(bpydc)			817	5.8	0.37	1	77	1.1			129
Ni(HBTC)(4,4′-bpy)		1590		5, 8		72	77	3.42		8.8	89
						72	298	1.2			
Ni(ox)(4,4′-bpy)						1	77	0.16			183
$[Ni^{II}_2Ni^{III}(\mu_3\text{-}OH)(IN)_3(BDC)_{1.5}]_3$		571.0	888.3			1	77	1.47			190
$Ni_3(OH)(pbpc)_3$		1553				1	77	1.99			181
						20	77	4.15			
$Ni_3O(TATB)_2$	PCN-5		225		0.13	1	77	0.63			191
$Cu(bpy)(CF_3SO_3)_2$						1	40	1.4			192
$Cu(dccptp)(NO_3)$		268			0.113	1	77	1.34		6.12	193
						20	77	1.91	23.9		
$Cu(fma)(bpe)_{0.5}$				3.2, 2.0		1	77	0.8			194
$Cu(2\text{-pymo})_2$		350		2.9		1.2	77	0.86	13		195
$Cu(F\text{-pymo})_2$						1.2	90	0.56	10		196
$Cu(hfipbb)(h_2hfipbb)_{0.5}$						1	77	0.23			183
						48	298	1	14.7		197
$Cu_2(abtc)(DMF)_2$	SNU-5		1260		0.48	1	77	1.83			76
$Cu_2(BDC)_2(dabco)$		1461				1	77	1.8			198

dx.doi.org/10.1021/cr200274s |*Chem. Rev.* 2012, 112, 782–835

Table 1. Continued

MOF		surface area/$m^2\ g^{-1}$ BET	Langmuir	pore size/ Å	pore volume/ $cm^3\ g^{-1}$	hydrogen storage capacity[a] P/ bar	T/ K	gravimetric/ wt %	volumetric/ g L^{-1}	Q_{st}/ kJ mol^{-1}	ref
		1300	1703		0.63	33.7	77	2.7			186
						100	293	0.42			
$Cu_2(BPnDC)_2(4,4'\text{-bpy})$	SNU-6	2590	2910	14.0, 18.2	1.05	1	77	1.68	5.31	7.74	57
						70	77	4.87 (10.0)	15.4		
$Cu_3[(Cu_4Cl)_3(tpb\text{-}3tz)_8]_2\cdot 11CuCl_2$		1120	1200			30	77	2.8			113
$Zn(abdc)(bpe)_{0.5}$			100			1	77	0.62			80
$Zn(MeIM)_2$	ZIF-8	1630	1810		0.64	1	77	1.27			100
						55	77	3.01			
						1	77	1.3		4.5	199
						30	77	3.3			
						60	298	0.13			
$Zn(PhIM)_2$	ZIF-11					1	77	1.35			100
$Zn(BDC)(4,4'\text{-bpy})_{0.5}$	MOF-508		946	4.0, 4.0		1	77	0.8			56
$Zn(NDC)(bpe)_{0.5}$			303	5.1, 4.3	0.2	40	77	2	18		200
						65	298	0.3			
Zn(tbip)		256				1	77	0.75	54	6.7	201
$Zn_2(abtc)(DMF)_2$	SNU-4		1460		0.53	1	77	2.07			76
						50	77	3.7			
$Zn_2(BDC)(tmbdc)(dabco)$		1100	1670		0.59	1	77	2.08			115
$Zn_2(BDC)_2(dabco)$		1264				1	77	1.92			202
		1165	1488			83.2	77	3.17			186
						1	77	2.1		5.3	198
Zn(bpe)(tftpa)		512			0.203	1	77	1.04		6.2	203
$Zn_2(bpytc)$		313	424		0.15	4	77	1.1			204
$Zn_2(btatb)(DMF)_2$		796				1	77	1.2		7.4	159
$Zn_2(btatb)(Py)$		709				1	77	1.24			
$Zn_2(btatb)(MePy)$		370				1	77	0.59			
$Zn_2(btatb)(EtPy)$		309				1	77	0.57			
$Zn_2(btatb)(ViPy)$		473				1	77	1.04			
$Zn_2(btatb)(CF_3Py)$		388				1	77	0.57			
$Zn_2(cnc)_2(dpt)$			342		0.19	1	77	1.28		7.85	205
$Zn_2(NDC)_2(dabco)$		1000	1450		0.52	1	77	1.7			115
$Zn_2(NDC)_2(diPyNI)$		802			0.30	1	77	0.92		5.6	151
$Zn_2(tcpdep)$			252			1	77	0.2			206
$Zn_2(tfbdc)_2(dabco)$		1070	1610		0.57	1	77	1.78			115
$Zn_2(tmbdc)_2(4,4'\text{-bpy})$		1120	1740		0.62	1	77	1.68			
$Zn_2(tmbdc)_2(dabco)$		920	1400		0.5	1	77	1.85			
$Zn_3(bpdc)_3(4,4'\text{-bpy})$		792		8	0.33	1	77	1.74		7.1	188
$Zn_3(NTB)_2$			419	7.72	0.15	1	77	1			95
$Zn_3(TATB)_2(HCO_2)$			1100			1	77	1.3			207
$Zn_4O(adc)_3$	PCN-13		150	3.5	0.1	1	77	0.41			208
$[Zn_4O(azd)_3]$	MOF-646	925	1130			1	77	1.75	20.9	7.8	209
$Zn_4O(BBC)_2(H_2O)_3\cdot H_2O$	MOF-200	4530	10400		3.59	80	77	7.4(16.3)	(36)		29
$Zn_4O(BDC)_3$	MOF-5, IRMOF-1	2296	3840			50	77	4.7		3.8	210
						65	298	0.28			
						60	200	0.9			
						48	298	1.65	9.9		197
		3362				1	77	1.32			60
		3534	4171			45.4	77	4.95	30.8		62
			3080			30	77	4.3		4.1	211
						60	298	0.45			
		572	1014			67	298	0.2			212
						10	77	1.6			

dx.doi.org/10.1021/cr200274s |Chem. Rev. 2012, 112, 782-835

Table 1. Continued

MOF		surface area/$m^2\ g^{-1}$ BET	Langmuir	pore size/ Å	pore volume/ $cm^3\ g^{-1}$	hydrogen storage capacity[a] *P*/ bar	*T*/ K	gravimetric/ wt %	volumetric/ g L^{-1}	Q_{st}/ kJ mol^{-1}	ref
		2885			1.18	1	77	1.15			213
		3800	4400			40(100)	77	7.1 (10)	42.1 (66)		31
						1	77	1.32		4.8	61
			3080			30	77	4.3			211
						1	77	1.35			199
						35	77	5.75			
						60	298	0.3			
						1	77	4.5			30
$Zn_4O(BDC)_3$ (interpenetrated)	MOF-5		1130	6.7		1	77	2.0	23.3	7.6	214
						100	77	(2.8)	33		64
$Zn_4O(bpdc)_2$	IRMOF-9	1904	2613		0.9	1	77	1.17			61
$Zn_4O(Brbdc)_2$	IRMOF-2	1722	2544		0.88	1	77	1.21			61
$Zn_4O(BTB)_2$	MOF-177	4526				1	77	1.25			60
		4746	5640			70	77	7.5	32		62
		4750	5640		1.59	66	77	7.1	49		63
$Zn_4O(BTB)_{4/3}(NDC)$	MOF-205	4460	6170		2.16	80	77	7.0(12.0)	(46)		29
$Zn_4O(BTE)_{4/3}(BPDC)$	MOF-210	6240	10400		3.6	80	77	8.6(17.6)	(44)		
$Zn_4O(D_2\text{-TCPPDA})_{1.5}$			2095			1	77	0.8			215
$Zn_4O(dbdc)_2$	IRMOF-6	2476	3263		1.14	1	77	1.48			61
		2804	3305			45	77	4.63	31.7		62
$Zn_4O(dcbBn)_3$		396		4.5	0.13	48	298	0.98			216
$Zn_4O(dcdEt)_3$		502		4.7	0.2	48	298	1.12			
$Zn_4O(NH_2\text{-bdc})_2$	IRMOF-3	2446	3062		1.07	1	77	1.42			61
$Zn_4O(hpdc)_3$	IRMOF-11		1911			1	77	1.62			60
		1984	2337	9		33.7	77	3.4	26.7		62
$Zn_4O(NDC)_3$	IRMOF-8	890			0.45	1	77	1.45			202
		1466				1	77	1.50			60
			1818			15	77	3.6	20.9	6.1	211
						30	298	0.4	2.32		
$Zn_3O(NTB)_2$	SNU-1		1121	5	0.51	1	77	1.9			94
$Zn_4O(pyrdc)_2$	IRMOF-13	1551	2100		0.73	1	77	1.73			61
$Zn_4O(TCBPA)_2$	SNU-77H	3670	4180	8.1, 4.1	1.52	1	77	1.79	10.5	7.05	173
						90	77	8.1(11.0)	47.4		
						90	298	0.5(1.19)	2.93		
$Zn_3O(T^2DC)(BTB)_{4/3}$	UMCM-2	5200	6060			46	77	6.9		6.4	72
$Zn_4O(ttdc)_2$	IRMOF-20	3409	4346		1.53	1	77	1.35			61
		4024	4593			77.6	77	6.25	34.1		62
$Zn_3(trz)_4(1,4\text{-ndc})_2$		362				1	77	0.84			217
$Zn_3(trz)_4(2,6\text{-NDC})_2$		584				1	77	1.09			217
$Zn_6(BTB)_4(4,4'\text{-bipy})_3$	FJI-1	4043	4624	1.21		1	77	1.02		4.62	218
						37(62)	77	6.52(9.08)			
						65	298	0.43			
$Zn_7O_2(pda)_5(H_2O)_2$					0.17	71.43	298	1.01			219
$Pd(2\text{-pymo})_2$		600				1.2	77	1.3	18		195
$Pd(F\text{-pymo})_2$		600				1.2	77	1.15	18		220
$Ag_2[Ag_4(trz)_6]$	FMOF-1	810			0.324	64	77	2.33	41		221
$Cd_3(bpdc)_3$	JUC-48		880	25	0.19	100	298	1.1			222
						40	77	2.8	20		
$Cd(pymc)_2$	*rho*-ZMOF		1168		0.47	1	77	1.16		8.7	223
$[In(pmdc)_2Na_{0.36}K_{1.28}](NO_3)_{0.64}$	*sod*-ZMOF		616		0.25	1	77	0.9		8.4	223
$(In_3O)(OH)(adc)_2(IN)_2$		1496	1857			1	77	2.08		6.9	224
$(In_3O)(OH)(adc)_2(MIH_2IN)_2$		1716	2106			1	77	2.31		7.9	

Table 1. Continued

MOF		surface area/$m^2\ g^{-1}$ BET	Langmuir	pore size/ Å	pore volume/ $cm^3\ g^{-1}$	hydrogen storage capacity[a] P/ bar	T/ K	gravimetric/ wt %	volumetric/ $g\ L^{-1}$	Q_{st}/ $kJ\ mol^{-1}$	ref
$[CH_3NH_3][In_3O(bpdc)_3(HCO_2)_{3/2}(H_2O)]_2$	CPM-13	904	1441	7.02	0.487	1	77	1.0			225
$Yb_4(TATB)_{8/3}(SO_4)_2$	PCN-17	820			0.34	1	77	0.94			226

[a] The data in parentheses are total uptake amounts.

Table 2. The H_2 Gas Sorption Data for MOFs with Open Metal Sites

MOF		surface area/ $m^2\ g^{-1}$ BET	Langmuir	pore size/ Å	pore volume/ $cm^3\ g^{-1}$	hydrogen storage capacity[a] P/bar	T/K	gravimetric/ wt %	volumetric/ $g\ L^{-1}$	Q_{st}/ $kJ\ mol^{-1}$	ref
					Dicarboxylic Acid						
$Mg_2(dobdc)$	MOF-74(Mg)	1510				1	77	2.2		10.3	227
						15(100)	77	3.2 (4.9)	(49)		
						(100)	298	(0.8)	(7.5)		
$Cr_3OF(BDC)_3$	MIL-101		5500	8.6	1.9	6080	77	6.1	1.84	10	84
							298	0.43			
Mn(NDC)		191		6.1	0.068	1	77	0.57			228
$Fe_3O(tfbdc)_3$			635			1	77	0.9			229
$NaNi_3(OH)(sip)_2$		700				1	77	0.94		10.4	230
$Ni(dhtp)_2$			1083		0.41	70	77	1.8			231
						70	298	0.3			
Cu(peip)		1560	1780		0.696	1	77	2.51		6.63	232
						40	77	4.14			
						100	298	0.46			
Cu(pmip)		1490	1690		0.605	1	77	2.36		7.24	233
$Cu_6O(tzi)_3(NO_3)$		2847	3223		1.01	1	77	2.4		9.5	124
Zn(peip)		1660	1880		0.667	1	77	2.27		6.56	232
$Zn_2(dhtp)$	MOF-74, CPO-27-Zn	783	1132		0.39	1	77	1.77		8.3	61
		950	1072			26.1	77	2.21	27.6		62
		870				30	77	2.8		8.8	234
$Zn_3(BDC)_3(Cu(pyen))$					0.26	1	77	0.66		12.3	235
$Zn_3(OH)(cdc)_{2.5}$		152		5		1	77	2.1		7	236
$Y_2(pdc)_3$		676				1	77	1.32			237
$Sm_2Zn_3(oxdc)_6$		719			0.31	34	77	1.19			54
						35	298	0.54			
$Er_2(3,5\text{-}pdc)_3$		427				1	77	0.68			237
					Tricarboxylic Acid						
$Cr_3(BTC)_2$		1810	2040			1	77	1.9		7.4	238
$Cr_3OF(BTC)_2$	MIL-100		2700	25, 29	1	73.3	298	0.15	1.04	6.3	84
						90	77	3.28	23		
$Cr_3OF(ntc)_{1.5}$	MIL-102		42	4.4	0.12	35	77	1		6	239
						35	298	0.05			
$Fe_4O_2(BTB)_{8/3}$		1121	1835		0.69	1	77	2.1			240
$H_2[Co_3O(TATB)_{8/3}]$	PCN-9		1355	6.5	0.51	1	77	1.53		10.1	88
$Cu_3(TATB)_2$ (catenated)	PCN-6		3800	5	1.456	1	77	1.9			241
						50	77	7.2		6.2	242
$Cu_3(TATB)_2$ (noncatenated)	PCN-6′		2700		1.045	1	77	1.35		6	243
						50	77	4.2			242

dx.doi.org/10.1021/cr200274s |*Chem. Rev.* 2012, 112, 782–835

Table 2. Continued

		surface area/ $m^2\ g^{-1}$				hydrogen storage capacity[a]					
MOF		BET	Langmuir	pore size/ Å	pore volume/ $cm^3\ g^{-1}$	P/bar	T/K	gravimetric/ wt %	volumetric/ $g\ L^{-1}$	Q_{st}/ $kJ\ mol^{-1}$	ref
$Cu_3(bhtc)_2$	UMCM-150	2300	3100		1	1	77	2.1		7.3	244
						45	77	5.7	36		
Y(BTC)						1	77	1.57		7.3	245
						10	77	2.1	28.8		
$Mo_3(BTC)_2$	TUDMOF-1	1280	2010		0.67	1	77	1.75			246
Dy(BTC)		655		6		1	77	1.32			247
					Tetracarboxylic Acid						
$Co_2(H_2O)_2(MTB)$	SNU-15′					1	77	0.74		15.1	168
$Cu_2(bdpb)$	PMOF-3	1879	2489			1	77	2.47			248
$Cu_2(bptc)$	MOF-505		1830	6.5	0.63	1	77	2.47			249
	NOTT-100	1670			0.68	1	77	2.59	(38.9)	6.3	250
						20	77	(4.02)			75
$Cu_2(tptc)$	NOTT-101	2247		7.3	0.89	1	77	2.52	43.6	5.3	75, 250
						20	77	6.06			
$Cu_2(qptc)$	NOTT-102	2932		8.3	1.14	1	77	2.24	41.1	5.4	75, 250
						20	77	6.07			
$Cu_2(L_x$ tetracarboxylate)	NOTT-103	2929		8	1.142	1	77	2.63		5.71	75
						20	77	(6.51)			
						60	77	(7.78)			
	NOTT-105	2387		7.3	0.898	1	77	2.52		5.77	75
						20	77	(5.40)			
	NOTT-106	1855		7.3	0.798	1	77	2.29		6.34	75
						20	77	(4.50)			
	NOTT-107	1822		7	0.767	1	77	2.26		6.70	75
						20	77	(4.46)			
	NOTT-109	1718		6.9	0.705	1	77	2.33			75
						20	77	(4.15)			
	NOTT-110	2960		8	1.22	1	77	2.64		5.68	251
						55	77	5.43	46.8		
	NOTT-111	2930		8	1.19	1	77	2.56		6.21	251
						48	77	5.47	45.4		
$Cu_2(aobtc)$	PCN-10	1407	1779		0.67	1	77	2.34	18	6.8	252
						3.5	30	6.84	52.5		
						45	300	0.25			
$Cu_2(sbtc)$	PCN-11	1931	2442		0.91	1					252
						3.5	30	7.89	59.1		
						45	77	5.23	39.2		
$Cu_2(C_{2v}$-mdip)	PCN-12′	1577	1962		0.73	1	77	2.4	20.4		253
$Cu_6(C_s$-mdip$)_2(C_{2v}$-mdip)	PCN-12	1943	2425		0.94	1	77	3.05	23.2		253
$Cu_2(adip)$	PCN-14	1753				1	77	2.7		8.6	254
						45	77	4.42	36.6		
$Cu_2(ebdc)$	PCN-16	2273	2800		1.06	1	77	2.6			255
						~45	77	5.1			
$Cu_2(ebdc)$	PCN-16′	1760	2200		0.84	1	77	1.7			255
						~28	77	2.9			
$Cu_2(PMTB)$	PCN-21	2718	4485		1.54	1	77	1.6			256
$Cu_2(bdi)$	PCN-46	2500	2800		1.012	1	77	1.95		7.2	257
						32(97)	77	5.31(6.88)	34.7(45.7)		

dx.doi.org/10.1021/cr200274s |*Chem. Rev.* 2012, 112, 782–835

Table 2. Continued

MOF		surface area/ $m^2\ g^{-1}$ BET	Langmuir	pore size/ Å	pore volume/ $cm^3\ g^{-1}$	hydrogen storage capacity[a] P/bar	T/K	gravimetric/ wt %	volumetric/ g L^{-1}	Q_{st}/ kJ mol^{-1}	ref
Cu_2(abtc)	JUC-62				0.89	40	77	4.71	53		258
	SNU-5		2850		1	1	77	2.84			76
						50	77	5.22			
Cu_2(TCM)	SNU-21S		905	6.6, 9.2	0.31	1	77	1.95		6.65	259
						70	77	4.37			
						70	298	0.26			
	SNU-21H		695	6.3, 10.7	0.25	1	77	1.64		6.09	259
						70	77	4.36			
						70	298	0.18			
Cu_2(bdcppi)	SNU-50′	2300	2450	11	1.08	1	77	2.1		7.1	260
						60	77	5.53 (7.86)			
						61	298	0.399 (0.980)			
Cu_2(BDDC)		2357	3111		1.113	0.95	77	1.64	15	6.9	261
						17(31)	77	3.98(4.60)	36(41)		
Cu_2(tcpdep)			733			1	77	0.8			206
Cu_2(C_{2h}-TCPPDA)			504			1	77	1.2			262
Cu_2(D_{2h}-TCPPDA)			626			1	77	1.4			
Zn_2(btatb)		1370				1	77	2.2		8.1	205
In_3O(abtc)$_{1.5}$(NO_3)	*soc*-MOF		1417	7.65, 5.95	0.5	1.2	77	2.61		6.5	85
				Hexacarboxylic							
Cu_3(abtt)	NOTT-114	3424			1.36	1	78	2.28			263
						30 (60)	78	5.0 (6.8)	(41.6)	5.3	
Cu_3(BHB)	UTSA-20	1156		3.4, 8.5		1	77	2.9			264
						15	77	4.1			
Cu_3(btei)	PCN-61	3000	3500		1.36	1	77	2.25	12.6	6.36	265
						33	77	6.24	35		
						90	298	0.667	3.74		
Cu_3(btti)	NOTT-119	4118			2.35	1	77	1.4		7.3	266
						44 (60)	77	5.6 (9.2)	(37)		
Cu_3(btti)	PCN-69	3989			2.173	1	77	1.7		8.14	267
						60	77	5.22			
Cu_3(ntbd)	NOTT-115	3394			1.38	1	78	2.42			263
						33(60)	78	5.6 (7.5)	(49.3)	5.8	
Cu_3(ntei)	PCN-66	4000	4600		1.63	1	77	1.79	7.98	6.22	265
						45	77	6.65	29.6		
						90	298	0.785	3.5		
Cu_3(ptei)	PCN-68	5109	6033		2.13	1	77	1.87	7.2	6.09	265
						50	77	7.32	28		
						90	298	1.01	4.1		
Cu_3(tbtt)	NOTT-113	2970			1.25	1	78	2.39			263
						30 (60)	78	5.1 (6.7)	(42.5)	5.9	
Cu_3(ttei)	NU-100	6143			2.82	1	77	1.82		6.1	28
						56(70)	77	9.95(16.4)			
Cu_3(L, hexacarboxylate)	NOTT-112	3800				1	78	2.3		5.64	268
						35−40 (77)	77	7.07 (10)	(50.3)		
	PMOF-2(Cu)	3730	4180			1	77	2.29		9.2	269
						30 (50)	77	5 (7)	(39.2)		
				Octacarboxylic Acid							
Cu_4(L)	NOTT-140	2620			1.07	1	77	2.5		4.15	270
						20	77	(6)			

dx.doi.org/10.1021/cr200274s |*Chem. Rev.* 2012, 112, 782–835

Table 2. Continued

MOF		surface area/ $m^2 g^{-1}$ BET	Langmuir	pore size/ Å	pore volume/ $cm^3 g^{-1}$	hydrogen storage capacity[a] P/bar	T/K	gravimetric/ wt %	volumetric/ g L^{-1}	Q_{st}/ kJ mol^{-1}	ref
					Azolates						
$Mn_3[(Mn_4Cl)_3(BTT)_8]_2$	Mn-BTT	2100			0.795	1.2	77	2.2	43	10.1	48
						90	77	5.1 (6.9)	(60)		
						90	298	0.94	7.9		
$Mn_3[(Mn_4Cl)_3(BTT)_8]_2 \cdot 0.75CuPF_6$		1911	2072			1.2	77	2		9.9	112
$Fe_3[(Mn_4Cl)_3(BTT)_8]_2 \cdot FeCl_2$		2033	2201			1.2	77	2.21		10.2	112
$Fe_3[(Fe_4Cl)_3(BTT)_8(MeOH)_4]_2$	Fe-BTT	2010	2200			1.2	77	2.3		11.9	271
						13(95)	77	3.7(4.1)	(35)		
$Co_3[(Mn_4Cl)_3(BTT)_8]_2 \cdot 1.7CoCl_2$		2096	2268			1.2	77	2.12		10.5	112
$Ni_{2.75}Mn_{0.25}[(Mn_4Cl)_3(BTT)_8]_2$		2110	2282			1.2	77	2.29		9.1	112
Cu(BDT)		200				1	77	0.66			114
$Cu_3[(Cu_{2.9}Mn_{1.1}Cl)_3(BTT)_8]_2 \cdot 2CuCl_2$		1695	1778			1.2	77	2.02		8.5	112
$Cu_9(4\text{-TBA})_{10}(C_2H_5OH)$ 2		616	686			1	77	1.16			62
$Cu_2(4\text{-TBA})_2(DMF)(C_2H_5$ OH)		356	402	4.24		1	77	1.54			62
$Cu_2(2\text{-F-4-TBA})_2(DMF)_2$						1	77	0.67			62
$Cu_4(TTPM)_2 \cdot 0.7CuCl_2$		2506	2745			1	77	2.8			272
						20 (70)	77	4.1 (5.6)	(41)		
$HCu[(Cu_4Cl)_3(BTT)_8] \cdot 3.5HCl$	Cu-BTT	1710	1770			1.2	77	2.42		9.5	273
						20(70)	77	4.1 (~6)	38(53)		
						90	298	(0.46)			
$Zn_3(BDT)_3$		640				1.17	77	1.46		8.7	114
$Zn_3[(Zn_{0.7}Mn_{3.3}Cl)_3(BTT)_8]_2 \cdot 2ZnCl_2$		1927	2079			1.2	77	2.1		9.6	112
$[Zn_5Cl_4(BTDD)_3]$	MFU-4 L	2750		1.2, 1.86	1.15	20	77	4		5	274
						20	117	1.8			
$[Cd_2(Tzc)_2]$		230	339			1	77	0.55		11.4	55

[a] The data in parentheses are total uptake amounts.

commonly refers to a type of catenation in which a maximal displacement happens between the catenated frameworks. Interweaving is also a type of catenation where a minimal displacement occurs between the catenated frameworks.[278]

One can control the interpenetration of MOF by the rational design of the organic building blocks. In general, if big pores should be generated in a MOF that is synthesized from an extended organic building block, an interpenetrated framework often resulted, since nature prefers to form a compact structure and reduce the free space. A review by Batten and Robson introduces various types of interpenetrated networks.[279,280] Zhou et al. reported that catenation or noncatenation can be controlled by adding a template during the solvothermal synthesis. When oxalic acid was used as a template during the synthesis of MOF, a noncatenated framework was formed, while a catenated framework resulted in the absence oxalic acid.[243] Farha et al. have controlled the catenation of MOF by the rational design of the ligands. When they used a brominated ligand, a noncatenated framework was produced, while the use of a nonbrominated ligand yielded a catenated structure.[281] Zaworotko and co-workers controlled the interpenetration by adjusting the concentration and temperature in the synthesis. In the reaction of Cd^{2+} with 4,4′-bpy and BDC linkers, a noninterpenetrated framework was formed at low temperature and low concentration, while a doubly interpenetrated framework resulted at relatively high concentration and high temperature.[282] Fischer and co-workers reported that the catenation was controlled by liquid-phase epitaxy on an organic template.[283]

Catenation significantly affects the gas sorption properties. Zhou and co-workers compared the H_2 adsorption capacities of the MOFs that are chemically identical but with a catenated and noncatenated sturcture.[242,243] The catenated PCN-6 and noncatenated PCN-6′ have the general formula $Cu_3(TATB)_2$, and they were built from copper paddle-wheel units and 4,4′,4″-*s*-triazine-2,4,6-triyltribenzoate (TATB). The volumetric H_2 adsorption measurements for the samples activated at 50 °C showed that catenated PCN-6 adsorbed 1.74 wt %, while PCN-6′ adsorbed 1.35 wt % at 77 K and 1 atm. When the samples were activated at 150 °C the adsorption capacity increased slightly, PCN-6 to 1.9 wt % and PCN-6′ to 1.62 wt %. The larger improvement in H_2 adsorption of PCN-6′ was attributed the open metal sites. However, the open copper sites in PCN-6 were blocked because of the catenation, which leads to less improved H_2 adsorption. The catenated structures adsorb more H_2 gas than the noncatenated structures.

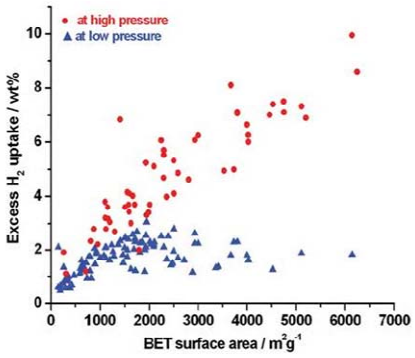

Figure 17. A plot showing the relationship between H_2 uptake capacities at 77 K and BET surface areas of various MOFs. Low pressure is 1 atm and high pressures are in the range of 10−90 bar.

The high pressure gas sorption data showed that the excess H_2 uptake of PCN-6 was 72 mg g^{-1} (6.7 wt %) at 77 K and 50 bar, while that of PCN-6′ is 42 mg g^{-1} (4.0 wt %). The total H_2 uptake capacity of PCN-6 was 95 mg g^{-1} (8.7 wt %) at 77 K and 50 bar and that of PCN-6′ was 58 mg g^{-1} (5.5 wt %). At 298 K and 50 bar, the excess H_2 adsorption capacities of PCN-6 and PCN-6′ were 9.3 mg g^{-1} (0.92 wt %) and 4.0 mg g^{-1} (0.40 wt %), and the total adsorption capacities were 15 mg g^{-1} (1.5 wt %) and 8.1 mg g^{-1} (0.80 wt %), respectively. At low coverage, PCN-6 (6.2−4.5 kJ mol^{-1}) and PCN-6′ (6.0−3.9 kJ mol^{-1}) have similar isosteric heats of the H_2 adsorption, but as the H_2 loading increases, catenated PCN-6 shows steadily higher H_2 adsorption enthalpies than those of PCN-6′. Inelastic neutron scattering measurement indicates that in both PCN-6 and PCN-6′, the first sites occupied by H_2 are the open metal sites, and as the H_2 loading increases, the interaction between H_2 molecules and the organic linkers becomes stronger in catenated PCN-6 than that in PCN-6′. These interesting results suggested that the catenation enhances H_2 uptake at room temperature.

Even though there was no direct comparison between the noncatenated and catenated frameworks, many catenated frameworks showed comparatively high H_2 uptake capacities. Long et al. employed two similar ligands, 1,3,5-tri-*p*-(tetrazol-5-yl)-phenylbenzene (H_3TPB-3tz) and 2,4,6-tri-*p*-(tetrazol-5-yl) phenyl-*s*-triazine (H_3TPT-3tz), to construct MOFs of Cu(II) and Mn(II), which afforded sodalite-type frameworks. The reaction of $CuCl_2 \cdot 2H_2O$ and H_3TPB-3tz yielded a noncatenated framework, $Cu_3[(Cu_4Cl)_3(TPB\text{-}3tz)_8]_2 \cdot 11CuCl_2 \cdot 8H_2O \cdot 120DMF$, while the reaction of $MnCl_2 \cdot 4H_2O$ and H_3TPT-3tz yielded the catenated framework $Mn_3[(Mn_4Cl)_3(TPT\text{-}3tz)_8]_2 \cdot 25H_2O \cdot 15CH_3OH \cdot 95DMF$. The activated sample of noncatenated Cu framework showed an H_2 uptake of 2.8 wt % at 77 K and 30 bar, while the catenated Mn framework showed a higher H_2 uptake of 3.7 wt % at 77 K and 25 bar with a total H_2 uptake of 4.5 wt % at 77 K and 80 bar. At 298 K, both of the frameworks showed comparable excess H_2 uptakes, 0.5 wt % at 68 bar. The isosteric heat of the noncatenated framework is 8.2 kJ mol^{-1}, and that of the catenated framework is 7.6 kJ mol^{-1}. The slightly higher isosteric heat in the noncatenated framework is attributed to the presence of exposed chloride anions of the $CuCl_2$ units.[113] The result indicates that not only the catenation but also the availability of exposed metal sites affects the hydrogen uptake properties.

It was also reported that $Zn_4O(dcdEt)_3$ and $Zn_4O(dcbBn)_3$ (dcdEt = 6,6′-dichloro-2,2′-diethoxy-1,1′-binaphthyl-4,4′-dibenzoate, dcbBn = 6,6′-dichloro-2,2′-dibenzyloxy-1,1′-binaphthyl-4,4′-dibenzoate), which have 4-fold interpenetrated structures, adsorb about 1.0 wt % of H_2 and 298 K and 48 bar due to the smaller pores that increased the H_2−host interactions.[216,284] Sometimes even if MOFs are highly interpenetrated, they show very low H_2 adsorption enthalpy. For example, the 3-fold interpenetrated 3D microporous MOFs $[Cu_3(4,4'\text{-bpy})_{1.5}(2,6\text{-NDC})_3]_n$ and $\{[Cu(bpe)_{0.5}(2,6\text{-NDC})] \cdot 0.5H_2O\}_n$ (bpe = 1,2-bis(4-pyridyl)ethane) have H_2 adsorption enthalpies of 3.7 and 4.5 kJ mol^{-1}, respectively. The Langmuir surface areas of the MOFs were very low due to the interpenetration, 113 $m^2\ g^{-1}$ and 337.5 $m^2\ g^{-1}$, respectively. The frameworks show low H_2 uptake capacities at 77 K and 15 bar, 0.88 wt % for the former and 0.96 wt % for the latter.[285]

Despite the above examples, catenation may reduce the free volume and thus have a detrimental effect on the high pressure H_2 storage. Sometimes it even leads to nonporous structures. The positive effect of catenation and interpenetration on hydrogen storage is due to a strengthened framework and narrower pore size. Theoretical calculations predict that interpenetration is beneficial for hydrogen storage at low temperature and low pressure, but at ambient temperature, the adsorption capacity decreases significantly.[286]

4.1.3. Mixed Ligand System. As described in section 4.1.1, the elongation of the organic linker can increase the surface area and pore volume. However, the strategy has a considerable disadvantage of multistep organic synthesis. For example, the organic building block (H_6ttei) used in the synthesis of NU-100 or PCN-610 was prepared by a 10-step procedure.[28,266]

Another approach for the preparation of the porous materials is to combine two types of ligands within the same structure. In many previous reports, 2D layers are assembled from bimetallic tetracarboxylate paddle-wheel units $M_2(O_2CR)_4$, whose axial sites are linked with the linear ditopic nitrogen donor linkers to construct 3D primitive cubic MOFs. This strategy of constructing pillared structures can afford highly porous frameworks. For example, SNU-6 is a framework built from BPnDC, 4,4′-bpy, and Cu(II).[57] The solvent-accessible volume for this material is 83.7% with a BET (Langmuir) surface area of 2590 (2910) $m^2\ g^{-1}$. The structure has very large pores with an effective size of 18.2 Å. The large pores result in modest H_2 uptake at 1 bar (1.68 wt % at 77 K) but high uptake at 70 bar (excess: 4.87 wt %, total: 10.0 wt %).

As mentioned in section 3.3, Matzger and co-workers provided an alternative strategy, which is coordination copolymerization of topologically different linkers with identical coordinating functionality.[118] $[Zn_4O(T^2DC)(BTB)_{4/3}]$ (UMCM-2) has BET and Langmuir surface areas of 5200 $m^2\ g^{-1}$ and 6060 $m^2\ g^{-1}$, respectively, and its excess H_2 storage capacity is 68.8 mg g^{-1} at 77 K and 46 bar. Yaghi and co-workers also used mixed BTB/NDC and BTE/BPDC to obtain MOF-205 and MOF-210, respectively.[29] Activated MOF-205 and MOF-210 showed extraordinarily high BET (and Langmuir) surface areas, 4460 (6170) $m^2\ g^{-1}$ and 6240 (10400) $m^2\ g^{-1}$, respectively. The BET surface area of MOF-210 is the highest reported so far for the crystalline materials. At 77 K, the excess and total H_2 uptake in MOF-210 are 86 mg g^{-1} at 56 bar and 176 mg g^{-1} at 80 bar, respectively, which are also the highest values at 77 K among data ever reported for physisorption materials.

It should be noted here that the high surface areas of MOFs synthesized by this coordination copolymerization do not come

Table 3. Effect of Elongation of Ligands on the Gas Sorption Properties

tricarboxylate	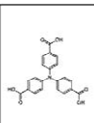	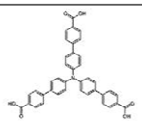	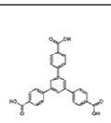	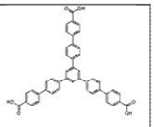	
metal	Zn^{II}				
topology	pyr	pyr	qom	qom	
MOFs	SNU-1	SNU-77	MOF-177	MOF-200	
surface area,[a] m^2g^{-1}	1121	4180 (3670)	5640 (4750)	10400 (4530)	
pore volume, cm^3g^{-1}	0.51	1.52	1.59	3.59	
tetracarboxylate			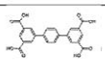	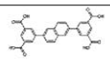	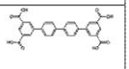
metal	Cu^{II}				
topology	NbO				
MOFs	NOTT-100	SNU-5'	NOTT-101	NOTT-103	NOTT-102
surface area,[a] m^2g^{-1}	(1640)	2850	(2316)	(2929)	(2942)
pore volume, cm^3g^{-1}	0.680	1.00	0.886	1.142	1.138
hexacarboxylate				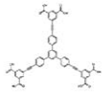	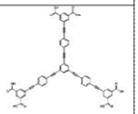
metal	Cu^{II}				
topology	rht				
MOFs	PCN-61	NOTT-112	PCN-66	PCN-68 NOTT-116	NU-100
surface area,[a] m^2g^{-1}	3500 (3000)	(3800)	4600 (4000)	6033 (5109)	6143
pore volume, cm^3g^{-1}	1.36	1.62	1.63	2.13	2.82

[a] Number in the parentheses is the BET surface area and the other is the Langmuir surface area.

from different chemical compositions of the ligands but from the novel framework topologies that are hard to achieve using only one ligand. In other words, using mixed carboxylate ligands will generate novel framework topology that may have huge porosity, independently of whether the ligands are O donors or N donors.

4.2. Increase in Isosteric Heat of Hydrogen Adsorption

Some MOFs with large surface areas meet the H_2 storage targets proposed by the U.S. Department of Energy (DOE), but only at cryogenic temperatures. None of the MOFs yet satisfy the targeted goals specified by the DOE in the United States for H_2 storage materials that should be developed by 2017. The materials should have at least 5.5 wt % of H_2 uptake ability for the whole system at moderate temperature and pressure. The main problem is that H_2 adsorption in MOFs is a physisorption, and the van der Waals interaction between H_2 and pore surface of MOFs is very weak. The H_2 uptake capacity at moderate temperatures falls down to less than 1/10 of the cryogenic value. To enhance the H_2 uptake at ambient temperature, strong adsorption sites should be incorporated into the pores. In addition, the pore surfaces/curvatures should be optimized for efficient H_2 packing.

As mentioned previously in section 4, Frost and Snurr have shown that the H_2 storage capacity at 298 K of a MOF can be

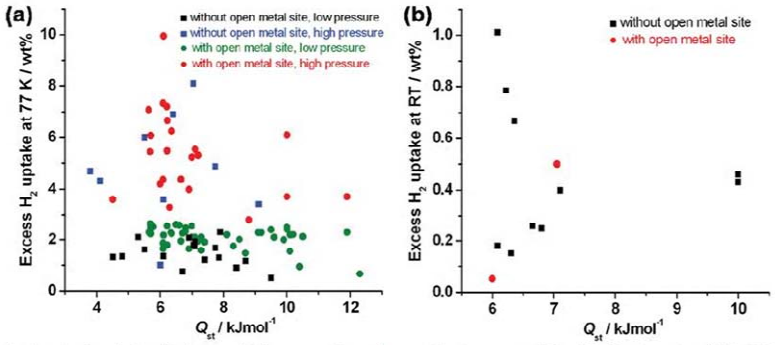

Figure 18. A plot showing the relationship between high pressure H_2 uptake capacities in excess and Q_{st} of the H_2 adsorption. (a) At 77 K. (b) At 298 K. Low pressure is 1 atm, and high pressures are in the range of 10−90 bar.

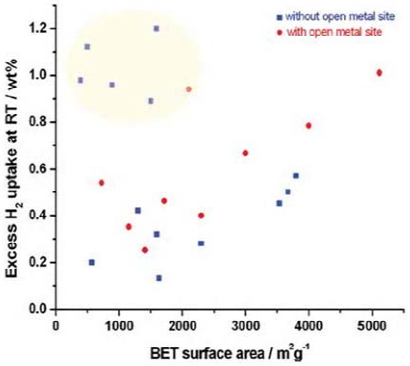

Figure 19. A plot of the room temperature H_2 uptake capacities vs BET surface areas of MOFs.

considerably increased at high pressures when the MOF has a high isosteric heat of H_2 adsorption, although big pore volume is the most important factor to achieve high H_2 adsorption capacity at high pressures.[172]

Recently, Bae and Snurr studied H_2 storage and delivery between 1.5−120 bar in a MOF. By using GCMC simulations, they estimated the optimal Q_{st} value for maximum H_2 delivery.[287] The deliverable capacity is the difference between the adsorbed amount of H_2 at high pressure and the adsorbed amount of H_2 at the discharge pressure (1.5 bar). The simulations demonstrated that the optimal Q_{st} is approximately 20 kJ mol^{-1}. However, Q_{st} of H_2 adsorption in most porous MOFs is in the range 5−9 kJ mol^{-1}.

Bhatia and Myers calculated that if the H_2 adsorption enthalpy is 6 kJ mol^{-1}, the optimal operating temperature of H_2 storage in microporous material is 131 K between 1.5 and 100 bar.[170] Therefore, to eliminate the need for a heavy and expensive cooling system, the H_2 affinity to MOFs should be increased. Various strategies have been made to increase the H_2 interactions with MOFs, such as creation of the open metal sites, introduction of cations generating strong electrostatic field within the cavities,

Table 4. Gas Sorption Data for HKUST-1

BET surface area, $m^2\ g^{-1}$	pore volume, $cm^3\ g^{-1}$	H_2 uptake, wt %	isosteric heat, kJ mol^{-1}	ref
1239	0.62	2.18[a]	6.1	202
1154		3.6,[b] 0.35[c]	4.5	210
1507	0.75	2.48[a]	6.8	61
1944		3.3[d]		62
	0.4	1.44[a]	6−7	183
		3.6[e]		289

[a] At 77 K and 1 bar. [b] At 77 K and 50 bar. [c] At 298 K and 65 bar. [d] At 77 K and 77 bar. [e] At 77 K and 10 bar.

doping with metal ions, fabrication of metal nanoparticles, and functionalization of the ligands that are exposed to the pores, which will be discussed in detail in the following sections.

In Figure 18, we have plotted reported data for the excess H_2 adsorption capacities of some MOFs at 77 and 298 K vs their Q_{st} values, to see if a relationship exists between them. As seen in Figure 18a, most of the MOFs have Q_{st} values in the range of 4−12 kJ mol^{-1}, and even if Q_{st} values are increased by several kJ mol^{-1}, they did not enhance the high pressure H_2 storage capacities at 77 K. However, at room temperature and high pressures (Figure 18b), there is a tendency that as the Q_{st} value increases, the excess H_2 adsorption capacity is increased, although there are not so many data for the statistics.

One of the reasons why there is no obvious relationship between hydrogen uptake capacities at 77 K and isosteric heats of hydrogen adsorption may be that the isosteric heats of H_2 adsorption represented are the low coverage data. When we refer to the impact of isosteric heat of adsorption, especially in the theoretical calculation study, we mean the average isosteric heat of adsorption instead of the one at very low hydrogen coverage. However, there is no commonly accepted method to determine the average isosteric heat of adsorption; almost all of the isosteric heats of adsorption reported so far are low coverage data.

4.2.1. Generation of Active Metal Sites in MOFs. On the basis of both experimental and computational studies, it has been shown that the coordinatively unsaturated metal centers ("open metal site", "exposed metal site", or "accessible metal site") enhance Q_{st} of the H_2 adsorption in a MOF because H_2

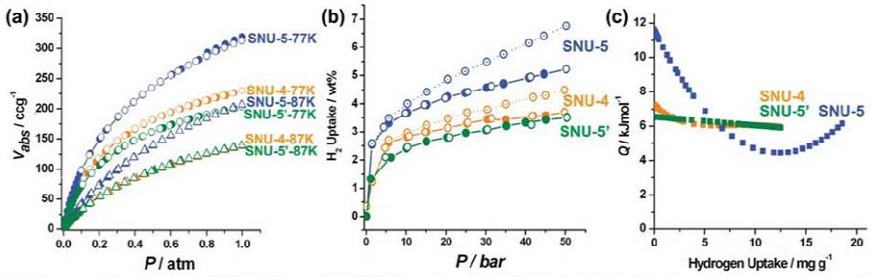

Figure 20. H_2 gas uptake properties of SNU-4 (orange), SNU-5′ (green), and SNU-5 (blue). (a) The H_2 adsorption isotherms measured at 77 K (circle) and 87 K (triangle) up to 1 atm of H_2. (b) Excess (solid line) and total (dotted line) H_2 adsorption isotherms at 77 K and high pressure. Filled shape: adsorption; open shape: desorption. (c) Isosteric heat of H_2 adsorption. SNU-4 and SNU-5′ have no accessible metal site, while SNU-5 has accessible metal sites. Reproduced with permission from ref 76. Copyright 2008 WILEY-VCH Verlag GmbH & Co. KGaA, Weinheim.

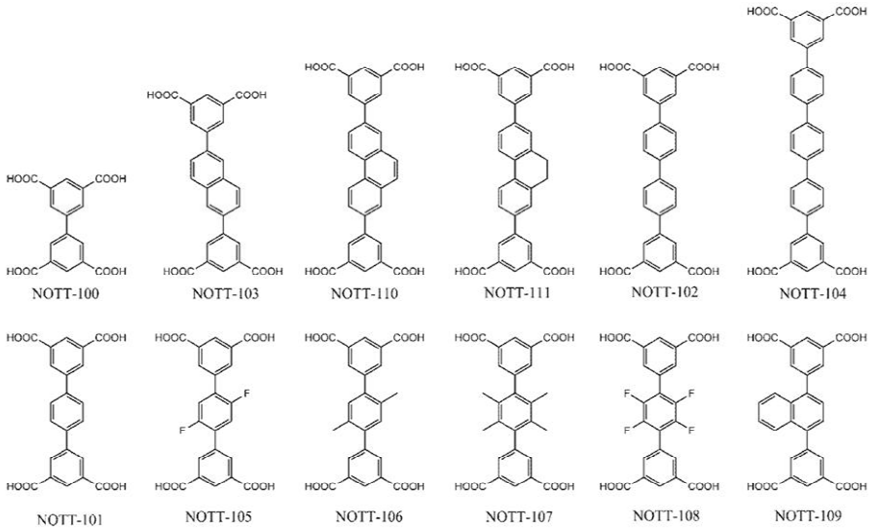

Figure 21. Various tetracarboxylic acids used in the synthesis of NOTT-series having NbO-net structure. NOTT-series generate open Cu(II) sites on activation.

molecules can directly interact with these sites. The metal−H_2 interactions in a MOF have been confirmed by neutron powder diffraction (NPD) experiments and inelastic neutron scattering (INS) spectroscopy.[48,275,288] The strategies for introducing open metal sites in the MOFs are the incorporation of metal clusters coordinating solvent molecules that are easily removable, the use of the metal building blocks that contain open metal sites, such as porphyrins, salens, etc., the attachment of organometallic complexes to the aromatic components of the struts,[70] and the electrostatic intercalation of metal complexes[112] or solvated (or unsolvated) metal cations in the anionic frameworks.[149]

In Figure 19, the excess H_2 uptake capacities at room temperature and high pressures are plotted against surface areas of various MOFs. The room temperature H_2 storage capacities of the MOFs with open metal sites are much higher than those without open metal sites, in particular when the surface areas are higher than 3000 $m^2 g^{-1}$. However, if the surface area is smaller than 3000 $m^2 g^{-1}$, the effect of the open metal sites on the room temperature H_2 storage capacities is rather minor. We will discuss the region marked by the yellow circle in Figure 19 in section 4.2.2.

4.2.1.1. Open Metal Sites at Secondary Building Units. The primary method for generating open metal sites consists of the synthesis of the MOF constructed of metal clusters coordinating solvent molecules as SBUs, which locate at the framework nodes, followed by removal of the coordinating solvent molecules by thermal evacuation. Most common SBUs for such purposes are the bimetallic paddle-wheel units of $M_2(O_2CR)_4$ (M = Cu^{2+}, Zn^{2+}, and Cd^{2+}), where solvent molecules are coordinated at the axial sites.

It was reported that open metal sites were generated in $[Cu_3(BTC)_2(H_2O)_3]_n$ (HKUST-1), which was constructed from benzene-1,3,5-tricarboxylate and Cu paddle-wheel SBUs.[73] The Langmuir and BET surface areas were 917.6 $m^2 g^{-1}$ and

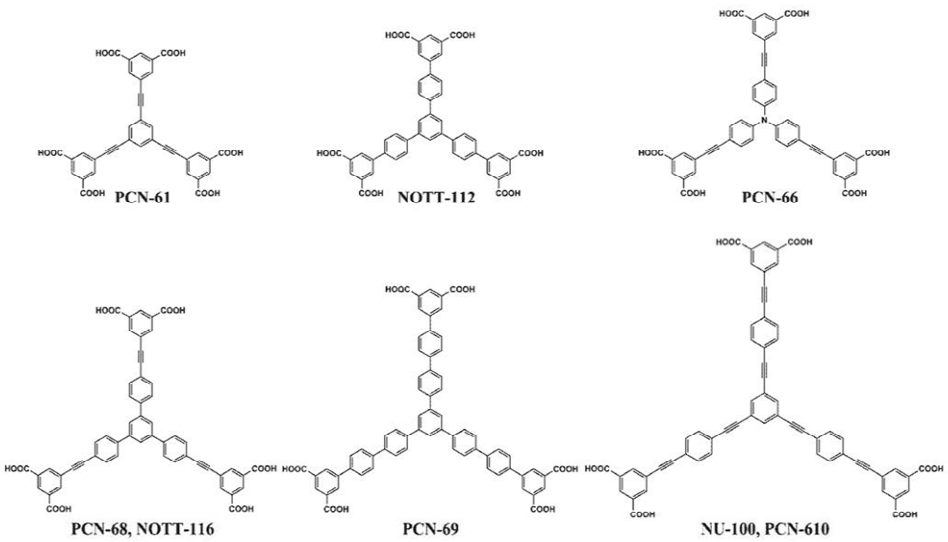

Figure 22. Various hexacarboxylic acid ligands used in the synthesis of polyhedral frameworks.

692.2 $m^2 g^{-1}$, respectively, with a total pore volume of 0.333 $cm^3 g^{-1}$. However, many other research groups later reported different values of the surface area, pore volume, H_2 storage capacity, and H_2 adsorption enthalpy, which are summarized in Table 4. We assume that the activation method, handling of the activated sample containing open metal sites, and method of gas sorption measurements might cause these differences. For example, Kaskel and coworkers have reported that the use of new pressure free synthesis, which means refluxing copper acetate and H_3BTC in DMF without sealing the reaction vessel during the synthesis, and by avoiding the nitrate precursor, produced better quality product without any impurities.[202] The new synthetic method led to greater micropore volume of 0.62 $cm^3 g^{-1}$ compared to a previous report of 0.41 $cm^3 g^{-1}$. This suggests that we have to be very careful in handling the activated MOFs that contain open metal sites in order to obtain the data that can be reproducible.

Suh's group made a comparison of the H_2 storage capacities for three isostructural MOFs with and without open metal sites. $[\{Zn_2(abtc)(dmf)_2\}_3]$ (SNU-4) and $[\{Cu_2(abtc)(dmf)_2\}_3]$ (SNU-5′) have no open metal site, whereas $[\{Cu_2(abtc)\}_3]$ (SNU-5) has open metal sites (abtc = 1,1′-azobenzene-3,3′,5,5′-tetracarboxylate).[76] The available surface area and pore volume in SNU-5 having open metal sites are 1.4−1.7 times greater than those of SNU-4 and SNU-5′. Furthermore, the H_2 sorption capacities of SNU-5 are much higher than those of SNU-4 and SNU-5′; at 77 K and 1 atm, the H_2 uptake capacities are 2.07 wt % for SNU-4, 1.83 wt % for SNU-5′, and 2.87 wt % for SNU-5. At 77 K and 50 bar, the excess adsorption capacities of SNU-4 and SNU-5 are 3.70 wt % and 5.22 wt %, respectively, with the total adsorption capacities of 4.49 wt % and 6.76 wt % (Figure 20). To exclude the reduced mass effect for the sample without coordinated solvent molecules, the H_2 adsorption capacities per volume of the MOFs were also compared, which still indicated that the MOF with open metal sites adsorbed a higher amount of H_2 gas (120%). The isosteric heats of H_2 adsorption for SNU-4, SNU-5′, and SNU-5 were 5.96−7.24, 5.91−6.53, and 4.43−11.60 kJ mol^{-1} respectively. The zero coverage isosteric heat of H_2 adsorption for SNU-5, 11.6 kJ mol^{-1}, is one of the highest values reported so far. However, the room temperature H_2 uptake capacity of SNU-5 is still not so satisfactory, 0.5 wt % at 100 bar. These results suggest that the presence of open metal sites in a MOF leads to the higher H_2 uptake capacity and higher isosteric heat of H_2 adsorption as well as a higher surface area and pore volume.

Similarly, Zhou et al. reported that alignment of open metal sites affects the H_2 adsorption. PCN-12 ($[Cu_6(C_s\text{-mdip})_2(C_{2v}\text{-mdip})(H_2O)_6]\cdot 3DMA\cdot 6H_2O$) and PCN-12′ ($[Cu_2(C_{2v}\text{-mdip})(H_2O)_2]\cdot 3DMSO$) are polymorphs formed from the Cu paddle-wheel SBUs and 5,5′-methylenediisophthalate (mdip).[253] The polymorphism occurred due to two extreme conformations, one in C_s and the other in C_{2v} symmetry. The structure consists of cuboctahedra, and in PCN-12 the open metal sites are aligned while in PCN-12′ the open metal sites are out of alignment. The dissimilar alignments of open metal sites significantly affected the hydrogen uptakes of these MOFs. The Langmuir surface areas of PCN-12 and PCN-12′ are 2425 and 1962 $m^2 g^{-1}$, and the pore volumes are 0.94 mL g^{-1} and 0.73 mL g^{-1}, respectively. The H_2 uptake capacities of PCN-12 and PCN-12′ are 3.05 wt % and 2.40 wt %, respectively, at 77 K and 1 atm. The inelastic neutron scattering spectrum of PCN-12 indicates that H_2 strongly prefers available Cu sites to other binding sites.

PCN-10 $\{Cu_2(abtc)(H_2O)_2\cdot 3DMA\}$ and PCN-11 $\{Cu_2(sbtc)(H_2O)_2\cdot 3DMA\}$, which are synthesized from azoxybenzene-3,3′,5,5′-tetracarboxylic acid (H_4azobtc) and *trans*-stilbene-3,3′,5,5′-tetracarboxylic acid (H_4sbtc), respectively, with Cu(II) paddle-wheel SBUs, are isostructural porous MOFs.[252] Both frameworks contain nanoscopic cages and generate coordinatively unsaturated metal centers on activation. PCN-10 and PCN-11 have Langmuir

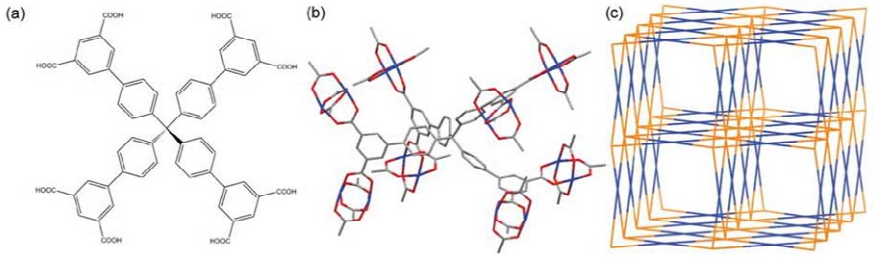

Figure 23. NOTT-140.[270] (a) Octacarboxylic acid employed in the synthesis, (b) connectivity of L^{8-} with eight Cu paddle-wheel units, and (c) (4,8)-connected scu topology of the framework.

surface areas of 1779 and 2442 $m^2\ g^{-1}$ with total pore volumes of 0.67 and 0.91 $cm^3\ g^{-1}$, respectively. At 77 K and 1 atm, PCN-10 shows a H_2 uptake capacity of 2.34 wt %, while PCN-11 shows a capacity of 2.55 wt %. The high pressure adsorption isotherms at 77 K show that the H_2 uptakes reach saturation at 20 atm, and the excess uptake capacities of PCN-10 and PCN-11 are 4.33 wt % and 5.05 wt %, respectively. This suggests that MOF with N═N double bonds has a slightly higher H_2 affinity than corresponding MOF with C═C double bonds.

A series of MOFs (NOTT-100—NOTT-111) were constructed from Cu(II) paddle-wheel SBUs and long tetracarboxylic acids (Figure 21).[75,250,251] On activation, all of them have similar structures and stoichiometry, except NOTT-104, which forms an interpenetrated structure and is unstable to desolvation. All MOFs show high H_2 uptake capacities due to the large pore volumes as well as the presence of copper open metal sites. The neutron powder diffraction data indicate that the open Cu(II) sites are the strongest adsorption sites in the pores, but the heat of H_2 adsorption is very similar in all sites in a MOF. In the series of MOFs, the heat of H_2 adsorption is affected by the ligand structure near the paddle-wheel SBUs. The high heat of adsorption at low H_2 loading was observed for NOTT-106 and NOTT-107, and it is due to the exposed Cu(II) sites as well as methyl groups exposed to the pores. The MOFs with functionalized pores with fluorine and methyl groups have lower pore volumes and lower H_2 capacities, and the heat of adsorption drops rapidly with increasing H_2 loading. The naphthalene ring in NOTT-103, and the phenanthrene group in NOTT-110 have a positive effect on the H_2 uptake, which may be due to the presence of a large aromatic surface.

The MOFs formed from hexacarboxylic acids and Cu paddle-wheel units are an interesting class of compounds. In these MOFs, large cavities are formed in the fused polyhedral frameworks (Figure 22). For example, NOTT-112, $[Cu_3(L)(H_2O)_3]\cdot 8DMSO\cdot 15DMF\cdot 3H_2O$, was constructed from 1,3,5-tris(3′,5′-dicarboxy[1,1′-biphenyl]-4-yl)benzene (L) and copper paddle-wheel SBUs, and it shows high H_2 uptake capacity.[268] The BET surface area of NOTT-112 was 3800 $m^2\ g^{-1}$, and the total pore volumes calculated from the N_2 and Ar isotherms were 1.62 $cm^3\ g^{-1}$ and 1.69 $cm^3\ g^{-1}$, respectively. It adsorbs 2.3 wt % of H_2 at 78 K and 1 bar. The high H_2 adsorption capacity at low pressure is attributed to the presence of exposed Cu(II) centers and the presence of the relatively small cages. The isosteric heat of H_2 adsorption is 5.64—4.74 kJ mol^{-1}. At high pressure, the excess H_2 uptake of NOTT-112 was 7.07 wt % at 35—40 bar, and the total uptake was 10.0 wt % at 77 bar. The high H_2 uptake is attributed to the high surface and large pore volume along with the presence of polyaromatic ligands.[290] NOTT-116, $[Cu_3(ptei)(H_2O)_3]\cdot 16DMF\cdot 26H_2O$, also shows high H_2 uptake, which was constructed from (5,5′-((5′-(4-((3,5-dicarboxyphenyl)ethynyl)phenyl)-[1,1′:3′,1″-terphenyl]-4,4″-diyl)-bis(ethyne-2,1-diyl))diisophthalic acid = H_6ptei) and copper paddle-wheel SBUs. The desolvated NOTT-116 contains open metal sites, and its apparent BET surface area is 4664 $m^2\ g^{-1}$. The framework has big pores with a pore-size distribution around 1.6, 2.0, and 2.6 nm. The total pore volume calculated from the Ar sorption isotherm is 2.17 $cm^3\ g^{-1}$, which is extraordinarily high for a porous MOF material. NOTT-116 adsorbs 1.9 wt % of H_2 at 78 K and 1 bar, and the isosteric heat of the H_2 adsorption is 6.7 kJ mol^{-1} at zero coverage. The high pressure volumetric H_2 sorption isotherm of desolvated NOTT-116 indicates an excess H_2 uptake capacity of 6.4 wt % at 77 K and 27 bar with the total uptake amounts of 9.2 wt % at 50 bar, which is lower than that of NOTT-112. This indicates that for mesoporous materials, a higher internal surface area and higher pore volume do not guarantee the higher H_2 adsorption capacity.[275]

NU-100 having the formula $[Cu_3(ttei)(H_2O)_3]_n$ was prepared from 1,3,5-tris[(1,3-carboxylic acid-5-(4-(ethynyl)phenyl))ethynyl]-benzene (H_6ttei) and copper paddle-wheel SBUs, which forms a noncatenated structure. Because of the elongated ligand and open Cu(II) sites in NU-100, BET surface area of activated NU-100 was 6143 $m^2\ g^{-1}$ and the total pore volume of NU-100 was 2.82 $cm^3\ g^{-1}$. The excess hydrogen uptake of NU-100 was 18.2 mg g^{-1} at 1 bar and 99.5 mg g^{-1} at 56 bar and at 77 K, with the total H_2 uptake of 164 mg g^{-1}at 70 bar and 77 K. The isosteric heat of H_2 adsorption is 6.1 kJ mol^{-1} at low loading.[28]

Zhou et al. have reported a series of isostructural MOFs, which were synthesized from dendritic hexacarboxylate ligands and copper paddle-wheel SBUs, namely, PCN-61 (5,5′,5″-benzene-1,3,5-triyltris(1-ethynyl-2-isophthalate), btei), PCN-66 (5,5′,5″-(4,4′,4″-nitrilotris(benzene-4,1-diyl)tris(ethyne-2,1-diyl))triisophthalate, ntei), PCN-68, H_6ptei), PCN-610 H_6ttei), and PCN-69 (5,5′,5″-(benzene-1,3,5-triyl-tris(biphenyl-4,4′-diyl)) triisophthalic acid, H_6btti).[265,267] On evacuation at 100 °C, the PCN series generate open Cu(II) sites. Among the desolvated PCNs, PCN-61, PCN-66, PCN-68, and PCN-69 showed remarkably high surface areas and H_2 uptake capacities, while PCN-610 was unstable on evacuation. At 77 K, the pressure of maximum H_2 adsorption increases from PCN-61 to PCN-68, coincident with the increase of the surface area, and the total H_2

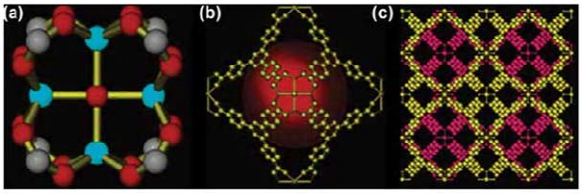

Figure 24. (a) The $Co_4(\mu_4\text{-}O)(carboxylate)_4$ SBU in PCN-9. Color scheme: C, gray; Co, aqua; and O, red. (b) Crystal structure of PCN-9 showing an octahedral cage; the red sphere represents void inside the cage. (c) View of the crystal structure of PCN-9 along the *a*-axis; the two interpenetrated networks are shown in gold and pink, respectively. All atoms are shown in arbitrary scales. Figure was adapted from ref 88. Copyright 2006 American Chemical Society.

uptake capacity reaches to 130 mg g^{-1} for PCN-68, which is one of the high gravimetric hydrogen uptake capacities reported so far. However, these frameworks have relatively low isosteric heats of H_2 adsorption at zero coverage, 6.36, 6.22, and 6.09 kJ mol^{-1} for PCN-61, PCN-66, and PCN-68, respectively, despite the presence of open Cu(II) sites. Even though the surface area of PCN-69 is greater than PCN-61, its H_2 uptake capacity is smaller than any of the series. However, PCN-69 shows a slightly higher isosteric heat (8.14 kJ mol^{-1}) at zero coverage because of the bent ligand creating pockets and concaves in the pores, which increases the interaction between the H_2 and host.

UTSA-20, $[Cu_3(BHB)(H_2O)_3]\cdot 6DMF\cdot 2.5H_2O$, was constructed from 3,3′,3″,5,5′,5″-benzene-1,3,5-triyl-hexabenzoic acid (BHB) and paddle-wheel type $Cu_2(COO)_4$ SBUs. Unlike the other MOFs, which are all based on the same 3,24-connected network, USTA-20 has a completely different structure of zyg topology.[264] The desolvated MOF has open Cu sites. It has a BET surface area of 1156 $m^2\ g^{-1}$ and H_2 uptake capacity of 2.9 wt % at 77 K and 1 bar. The high pressure adsorption isotherm shows excess H_2 uptake capacity of 4.1 wt % at 77 K and 15 bar, and this rather low uptake capacity must be due to the low surface area.

NOTT-140, $[Cu_4L(H_2O)_4]\cdot 10DMF\cdot C_4H_8O_2\cdot 8H_2O$, was constructed from copper paddle-wheel SBUs and octacarboxylic acid (4′,4‴,4⁗,4⁗′,4⁗″-methanetetrayltetrakis(([1,1′-biphenyl]-3,5-dicarboxylic acid))), which forms a 4,8-connected network comprised of octahedral and cuboctahedral cages (Figure 23).[270] The desolvated framework contains exposed Cu sites and shows total H_2 uptake capacity of 6.0 wt % at 20 bar at 77 K. The isosteric heat of H_2 adsorption was 4.15 kJ mol^{-1} at zero surface coverage. The relatively low isosteric heat is due to the different alignment of the vacant Cu sites. Contrary to other NOTT series that have the exposed Cu sites in the pores of the cages, NOTT-140 has the Cu sites that locate outside the cages, which results in reduced affinity for H_2.

The highest Q_{st} value of MOFs reported so far is 15 kJ mol^{-1} for $[Co^{II}_4(\mu\text{-}OH_2)_4(MTB)_2]_n$ (SNU-15′) prepared by heating of $[Co^{II}_4(\mu\text{-}OH_2)_4(MTB)_2(H_2O)_4]_n\cdot 13n DMF\cdot 11n H_2O$ (SNU-15) at 220 °C under a vacuum for 24 h.[168] SNU-15 has fluorite-like network generating 3D channels. In the as-synthesized MOF, each Co(II) ion coordinates terminal aqua ligand, and Co−Co distances are 3.550 Å and 3.428 Å. During the activation process, the coordinated water molecules were removed and the vacant coordination sites were created on every Co^{II} ion. The extraordinarily high isosteric heat of H_2 adsorption in SNU-15 might be attributed to the Co−Co distance that makes it possible for a H_2 molecule to bind in a side-on fashion.

An oxo-centered trigonal $[M_3(\mu_3\text{-}O)(COO)_6]$ unit (M = Cr^{3+}, Al^{3+}, $Fe^{2+/3+}$, Ni^{2+}, and In^{3+}) is the one of the most common carboxylate-bridged clusters. Every metal ion in $[M_3(\mu_3\text{-}O)(COO)_6]$ unit displays one potential open metal site. Férey and co-workers reported the H_2 sorption properties of metal-BDC M(OH)(BDC) containing Cr(III) and Al(III), denoted as MIL-53 (MIL = material from Institute Lavoisier), which are well-known as material exhibiting the breathing phenomenon upon guest removal and reintroduction.[176] The structure is formed of infinite *trans* corner-sharing octahedral $MO_4(OH)_2$ chains linked with each other through the BDC molecules to generate 1D lozenge-shape tunnels with a pore size of 8.5 Å. At 77 K under 1.6 MPa, MIL-53(Cr) shows a maximum H_2 adsorption capacity of 3.1 wt %, whereas MIL-53(Al) exhibits 3.8 wt % at the same pressure. The BET surface areas are 1020 $m^2\ g^{-1}$ and 1026 $m^2\ g^{-1}$ for MIL-53 (Al) and MIL-53 (Cr), respectively.

Two chromium carboxylate MOFs, $Cr_3OF(BTC)_2$ (MIL-100) and $Cr_3OF(BDC)_3$ (MIL-101) have totally different topologies from MIL-53.[84] They contain trimeric chromium(III) octahedral clusters coordinating removable terminal water molecules and thus provide potentially unsaturated metal sites. The resulting zeotype architectures were built by the connection of large hybrid supertetrahedron and generated very large mesopores. After removal of the guests, the accessible pore diameters are 25 and 29 Å for MIL-100, and 29 and 34 Å for MIL-101. Desolvated MIL-100 prepared by evacuating at 220 °C showed a Langmuir surface area of 2700 $m^2\ g^{-1}$ and a maximum H_2 uptake of 3.28 wt % at 77 K and 26.5 bar and 0.15 wt % at 298 K and 73 bar. In the case of MIL-101, two different treatments were applied to afford MIL-101a with H_2BDC and MIL-101b without H_2BDC in the pores. For MIL-101a, the Langmuir surface was 4000 $m^2\ g^{-1}$, and maximum H_2 adsorption capacities were 4.5 wt % at 77 K and 40 bar and 0.36 wt % at 298 K and 86 bar. For MIL-101b, the Langmuir surface was 5500 $m^2\ g^{-1}$, and maximum H_2 adsorption capacities were 6.1 wt % at 77 K and 80 bar and 0.43 wt % at 298 K and 86 bar. Furthermore, MIL-101b has high heat of H_2 adsorption (9.3−10.0 kJ mol^{-1}) at low coverage, which is larger than that (5.6−6.3 kJ mol^{-1}) of MIL-100. The high isosteric heat of H_2 adsorption in MIL-101b was explained by the presence of strong adsorption sites within the microporous supertetrahedra (ST), probably at each corner close to the trimers of chromium octahedra.

The cubic structure of $[In_3O(abtc)_{1.5}(H_2O)_3](NO_3)$ is built from trimers of corner-sharing octahedrally coordinated indium centers linked by abtc organic linkers.[85] The trimers contain three $[InO_5(H_2O)]$ octahedra sharing one central μ_3-oxo anion located on a 3-fold axis. In each octahedron, the apical position is occupied by a terminal water molecule, which can be

Table 5. The H_2 Adsorption Data for DMA-*rho*-ZMOF, Mg-*rho*-ZMOF, and Li-*rho*-ZMOF[149,292]

	DMA-*rho*-ZMOF	Mg-*rho*-ZMOF	Li-*rho*-ZMOF
H_2 uptake at 78 K and 0.95 atm, wt %	0.95	0.91	0.91
adsorbed H_2 (mol)/In atom	2.21	2.21	2.28
heat of adsorption, kJ mol^{-1}	8	9	9.1

Table 6. Compositions and Gas Sorption Properties of Cation-Exchanged Mn(II) Framework[112]

exchanged metal ion	formula[a]	M/Mn ratio	H_2 ads, wt %[b]	Q_{st}, kJ mol^{-1}[c]
	$Mn_3[(Mn_4Cl)_3(BTT)_8]_2$	N/A	2.23	10.1−5.5
Li^+	$Li_{3.2}Mn_{1.4}[(Mn_4Cl)_3(BTT)_8]_2 \cdot 0.4LiCl$	0.017	2.06	8.9−5.4
Cu^+	$Mn_3[(Mn_4Cl)_3(BTT)_8]_2 \cdot 0.75CuPF_6$	N/A	2.00	9.9−5.6
Fe^{2+}	$Fe_3[(Mn_4Cl)_3(BTT)_8]_2 \cdot FeCl_2$	0.17	2.21	10.2−5.5
Co^{2+}	$Co_3[(Mn_4Cl)_3(BTT)_8]_2 \cdot 1.7CoCl_2$	0.21	2.12	10.5−5.6
Ni^{2+}	$Ni_{2.75}Mn_{0.25}[(Mn_4Cl)_3(BTT)_8]_2$	0.121	2.29	9.1−5.2
Cu^{2+}	$Cu_3[(Cu_{7.9}Mn_{1.1}Cl)_3(BTT)_8]_2 \cdot 2CuCl_2$	3.999	2.02	8.5−6.0
Zn^{2+}	$Zn_3[(Zn_{0.7}Mn_{3.3}Cl)_3(BTT)_8]_2 \cdot 2ZnCl_2$	0.546	2.1	9.6−5.5

[a] Based on the relative ratio of M^{n+}/Mn^{2+}. [b] Measured at 77 K and 900 Torr. [c] Obtained by using a virial fit to the H_2 adsorption isotherms at 77 and 87 K.

removed by activation. Each trimer unit is linked by six separate organic linkers to produce a novel 3D structure having *soc* topology. The Langmuir surface area and pore volume of desolvated sample are 1417 $m^2\ g^{-1}$ and 0.50 $cm^3\ g^{-1}$, respectively. It adsorbs high amounts of H_2 gas, up to 2.61 wt % at 78 K and 1.2 atm and shows the invariable isosteric heat (6.5 kJ mol^{-1}) of the H_2 adsorption up to 1.8 wt % of loading, which indicates the homogeneity of the sorption sites up to this experimental loading (ca. 70% of the full loading of 2.61 wt % H_2 at 78 K and 1.2 atm). This result suggests the potential effects of open metal site, framework charge, and pore dimension on the energetics of sorbed H_2 molecules in MOFs.

Among heterocyclic azolate-based frameworks, Mn-BTT, $Mn_3[(Mn_4Cl)_3(BTT)_8(CH_3OH)_{10}]_2$, exhibited the highest surface area, H_2 uptake capacity, and isosteric heat of H_2 adsorption.[48] The X-ray crystal structure indicates that the chloride-centered square-planar $[Mn_4Cl]^{7+}$ units are linked with eight trigonal planar BTT^{3-} ligands to form the anionic, three-dimensional sodalite-type framework. The solvent molecules occupy the sixth coordination site on each Mn^{2+} ion, while charge balance is provided by Mn complexes. The desolvated Mn-BTT, which contains open metal sites, exhibited a BET surface area of 2100 $m^2\ g^{-1}$, excess (total) H_2 adsorption capacity of 5.1 wt % (6.9 wt %) at 77 K and 90 bar, and high zero-coverage isosteric heat of H_2 adsorption, 10.1 kJ mol^{-1}. On the contrary, $[Mn(DMF)_6]_3[(Mn_4Cl)_3(BTT)_8(DMF)_{12}]_2$, which is the isomorphous framework where all Mn^{2+} ions are coordinatively saturated with DMF molecules shows much lower zero-coverage enthalpy of H_2 adsorption, 7.6 kJ mol^{-1}. It adsorbs only total 3.9 wt % of H_2 at 77 K and 50 bar. These values indicate strong H_2 adsorption sites are available in Mn-BTT, which do not exist in $[Mn(DMF)_6]_3[(Mn_4Cl)_3(BTT)_8(DMF)_{12}]_2$. The neutron powder diffraction study reveals that this is directly related to H_2 binding at coordinatively unsaturated Mn^{2+} centers with a distance of 2.27 Å. The isostructural sodalite frameworks, $HCu[(Cu_4Cl)_3(BTT)_8] \cdot 3.5HCl$ (Cu-BTT)[273] and $Fe_3[(Fe_4Cl)_3(BTT)_8(MeOH)_4]_2$ (Fe-BTT),[271] also showed high zero-coverage H_2 binding enthalpy, 9.5 and 11.9 kJ mol^{-1}, respectively. The strongest binding site is located just 2.47 and 2.17 Å away from the exposed Cu^{2+} and Fe^{2+} metal sites, respectively.

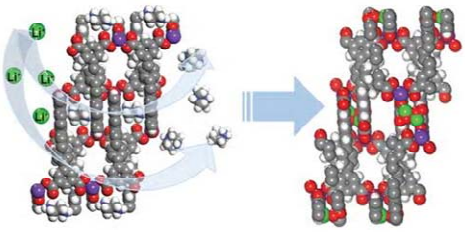

Figure 25. The X-ray structures of NOTT-200 (left) and NOTT-201 (right).[87] The H_2ppz^{2+} dications in the channel B of NOTT-200 can be completely exchanged with Li^+ ions in the channel C of NOTT-201. Color code: In, violet; Li, green; C, gray; N, blue; O, red; H, white.

$[Cu_6O(TZI)_3(H_2O)_9(NO_3)]$ (TZI = 5-tetrazolylisophthalate is a unique example consisting of two different types of metal clusters.[124] The X-ray crystal structure revealed the framework was constructed from truncated cuboctahedra (24 functionalized isophthalate ligands connected by 12 copper dimer centers, $[Cu_2(O_2CR)_4]$ paddle-wheels) connected to trigonal $Cu_3O(N_4CR)_3$ trimers through each tetrazolate (N_4CR) moiety. As mentioned previously, the solvent molecules are coordinated to the axial sites of each paddle-wheel unit. Each copper atom of $Cu_3O(N_4CR)_3$ trimer is coordinated to two nitrogen atoms (one from each of two tetrazolates), an oxygen (oxo) core, two oxygen atoms of two different equatorial water molecules to give square pyramidal geometry. The Langmuir (BET) surface area is 3223 (2847) $m^2\ g^{-1}$ and the total pore volume is 1.01 $cm^3\ g^{-1}$. H_2 capacity is up to 2.4 wt % at 77 K and 1 atm with the isosteric heat of 9.5 kJ mol^{-1} at the lowest coverage.

Another approach for generating the open metal sites is synthesis of MOF with entatic metal centers (EMCs). In contrast to the examples discussed above, the EMCs have the potential to bind the substrate without ligand removal. Ma and Zhou reported

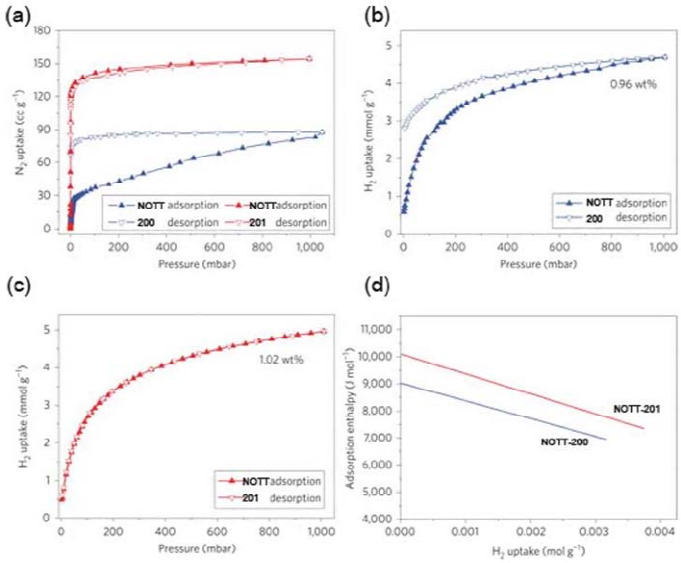

Figure 26. Gas adsorption isotherms of NOTT-200 and NOTT-201. (a) N_2 at 78 K. (b) H_2 for NOTT-200 at 78 K up to 1 bar. (c) H_2 for NOTT-201 at 78 K up to 1 bar. (d) Enthalpies of H_2 adsorption at low surface coverage. Reproduced with permission from ref 87. Copyright 2009 Macmillan Publishers Limited.

an MOF with EMCs, $H_2[Co_4O(TATB)_{8/3}]$, designated as PCN-9 (TATB = 4,4′,4″-*s*-triazine-2,4,6-triyltribenzoate, PCN = porous coordination network).[88] It adopts a square-planar $Co_4(\mu_4\text{-O})$ SBU, with a μ_4-oxo residing at the center of four Co atoms (Figure 24). All four Co atoms in the SBU are five-coordinate with square-pyramidal geometry, and the position below the square-plane formed of the four O atoms is in an entatic state and ready to bind a substrate to achieve octahedral coordination. The square-planar μ_4-oxo bridge found in PCN-9 is unique in a MOF. After desolvation, PCN-9 exhibits a Langmuir surface area of 1355 $m^2 g^{-1}$ and a pore volume of 0.51 $cm^3 g^{-1}$. The H_2 adsorption isotherm at 77 K indicates that PCN-9 has an uptake of 1.53 wt % at 1 atm. At low coverage, the heat of adsorption of PCN-9 for H_2 is 10.1 kJ mol^{-1}.

All H_2 adsorption data for the MOFs having open metal sites are summarized in Table 2. According to the collected data for the MOFs having open metal sites, the highest zero coverage isosteric heat of H_2 adsorption is 15 kJ mol^{-1} for SNU-15[168] and the next highest is 12.3 kJ mol^{-1} for $[Zn_3(BDC)_3(Cu(pyen))]$ (pyen = 5-methyl-4-oxo-1,4-dihydropyridine-3-carbaldehyde),[235] and the lowest is 4.15 kJ mol^{-1} for NOTT-140.[270] For all MOFs having open metal sites reported so far, the average value of isosteric heats of H_2 adsorption is 7.8 kJ mol^{-1} according to our calculation. These are greater than the values for the MOFs without open metal sites, in which the average value of isosteric heats of H_2 adsorption is 6.8 kJ mol^{-1}. Among all MOFs without open metal sites reported so far, the highest isosteric heat of H_2 adsorption is 9.5 kJ mol^{-1} for $Mg_3(NDC)_3$,[291] and the lowest is 3.8 kJ mol^{-1} for MOF-5.[210]

4.2.1.2. Introduction of Metal Ions in the Pores. As discussed in the previous section, in order to increase hydrogen storage capacity at ambient temperature, the interaction energy between H_2 and a MOF should be increased. The MOF should have a binding energy of 15−25 kJ mol^{-1} for satisfactory H_2 storage. One of the approaches to enhance the heat of H_2 adsorption is exchanging the counter-cations included in the anionic framework with metal ions that can interact with H_2 molecules more strongly.

Eddaoudi et al. have synthesized anionic zeolite-like frameworks, $[In_2(HImDC)_4\cdot(HPP^{2+})]_{24}\cdot 36DMF\cdot 192H_2O$ (*rho*-ZMOF, HImDC = 4,5-imidazoledicarboxylic acid, HPP = 1,3,4,6,7,8-hexahydro-2*H*-pyrimido[1,2-a]pyrimidine), $[In(HImDC)_2\cdot(HIM^+)]\cdot 4DMF\cdot CH_3CN\cdot 4H_2O$ (*sod*-ZMOF, HIM = protonated imidazole), and $[In(HImDC)_2\cdot(DMA^+)]_{48}$(DMA-*rho*-ZMOF, DMA = dimethylammonium).[149,292] They exchanged the cations included in the ZIFs, such as HPP^{2+}, HIM^+, and DMA^+, with Na^+, Li^+, and Mg^{2+} by immersion of the ZIFs in the solution of the metal salt and obtained the fully exchanged products at room temperature after 18 h. Contrary to their expectations, however, the H_2 uptake amount and the isosteric heat of H_2 adsorption were not significantly increased compared to those for the MOFs with open metal sites, even though they were higher than those of some neutral MOFs (Table 5). The X-ray structure of Mg-*rho*-ZIF indicated that Mg^{2+} ions were coordinatively saturated with six aqua ligands. The adsorption isotherms for three samples including DMA^+, Li^+, and Mg^{2+} were similar, since the exchanged metal cations retained the aqua ligands even after the activation and direct access of the H_2 molecules to the metal sites was impossible.

Long et al. also reported that Mn^{2+} ions in an anionic framework, $Mn_3[(Mn_4Cl)_3(BTT)_8]_2\cdot 10CH_3OH$, could be exchanged with a variety of metal ions such as Li^+, Cu^+, Fe^{2+},

Table 7. Theoretical H_2 Uptake Capacities of MOFs Doped with Li Atoms at 300 K and 10 MPa[296,297 a]

$Zn_4O(CO)_6$ Cubic lattice	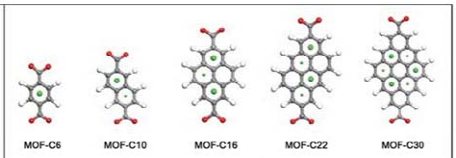 MOF-C6 MOF-C10 MOF-C16 MOF-C22 MOF-C30				
ratio C / Li H_2 uptake amount	C_6Li 2.0 wt%	C_5Li 3.3 wt%	$C_{5.3}Li$ 4.2 wt%	$C_{5.5}Li$ 4.6 wt%	C_9/ Li 5.2 wt%
$Zn_4O(CO)_6$ Hexagonal lattice	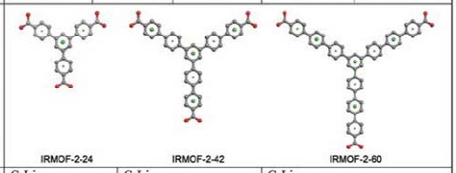 IRMOF-2-24 IRMOF-2-42 IRMOF-2-60				
ratio C / Li H_2 uptake amount	C_6Li 3.8 wt%	C_6Li 4.0 wt%	C_6Li 5.0 wt%		
$Zn_4O(CO)_6$ Hexagonal lattice	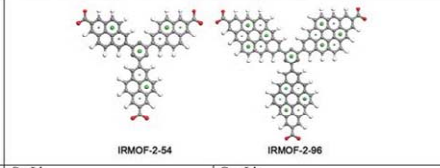 IRMOF-2-54 IRMOF-2-96				
Ratio of C / Li H_2 uptake amount	$C_{5.4}Li$ 5.1 wt%		$C_{5.05}Li$ 5.6 wt%		

[a] In each case the $Zn_4O(CO_2)_6$ connector couples to six aromatic linkers through the O−C−O common to each linker. The MOFs are named according to the number of aromatic carbon atoms. The large green atoms in the linkers represent Li atoms above the linkers while small green Li atoms lie below the linkers. The C_xLi ratio considers only aromatic carbon atoms.

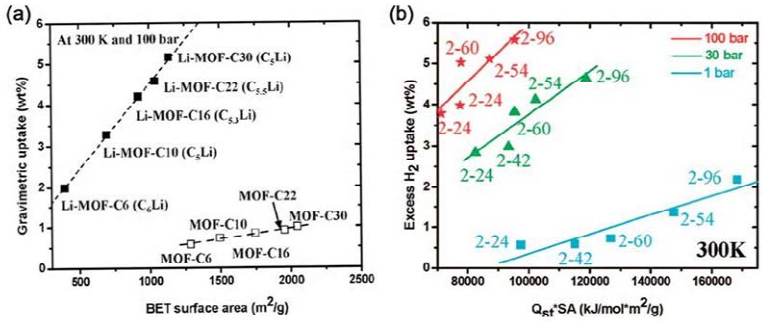

Figure 27. (a) Theoretical gravimetric H_2 uptakes at 300 K and 100 bar plotted against BET surface areas for MOFs and Li-MOFs systems. (b) Relationship between H_2 uptake in IRMOF-Li at 300 K and multiple value of Q_{st} and surface area (SA). This shows that both surface area and the ratio of Li to C are important for high performance. Reproduced with permission from refs 296 and 297. Copyright 2007 and 2008 American Chemical Society.

Co^{2+}, Ni^{2+}, Cu^{2+}, and Zn^{2+}.[112] The H_2 adsorption properties depending on the type and the amount of exchanged metal cations are summarized in Table 6. The total number of extra-framework cations including both charge-balancing and additional adsorbed species are not larger than five, and almost similar for all exchanged materials with Fe^{2+} (4.0), Co^{2+} (4.7), Ni^{2+} (3.0), Cu^{2+} (5.0), Zn^{2+} (5.0), and Li^+ (5.0), respectively (Table 6). The original material showed the isosteric heat of H_2 adsorption of

Table 8. The N_2 and H_2 Gas Adsorption Data for Alkali Metal Ion Doped MOFs, $Zn_2(NDC)_2(diPyNI)$, $Zn_2(NDC)_2(diPyNI)\cdot M$, $Zn_2(NDC)_2(diPyTz)$, and $Zn_2(NDC)_2(diPyTz)\cdot M$[293,294]

	M: diPyNI or diPyTz	BET surface area ($m^2\ g^{-1}$)	DR micropore volume ($cm^3\ g^{-1}$)	H_2/wt% (1 atm, 77 K)	Q_{st} range (kJ mol^{-1})
$Zn_2(NDC)_2(diPyNI)$	0.00	802	0.30	0.93	5.6−3.4 (av. 4.31)
$Zn_2(NDC)_2(diPyNI)\cdot Li$	0.06	676	0.34	1.23	6.3−5.6 (av. 5.96)
$Zn_2(NDC)_2(diPyNI)\cdot Na$	0.10	837	0.33	1.45	5.6−4.5 (av. 4.99)
$Zn_2(NDC)_2(diPyNI)\cdot K$	0.06	988	0.39	1.54	6.0−3.3 (av. 4.51)
$Zn_2(NDC)_2(diPyNI)\cdot K'$	0.26	813	0.32	1.42	5.6−3.7 (av 4.46)
$Zn_2(NDC)_2(diPyNI)\cdot K''$	0.84	382	0.15	0.75	5.1−4.0 (av. 4.45)
$Zn_2(NDC)_2(diPyTz)$	0.00	400	0.16	1.12	8.5−6.5
$Zn_2(NDC)_2(diPyTz)\cdot Li$	0.05	526	0.19	1.46	8.3−6.1
$Zn_2(NDC)_2(diPyTz)\cdot Na$	0.12	558	0.21	1.60	8.7−4.0
$Zn_2(NDC)_2(diPyTz)\cdot K$	0.07	509	0.20	1.51	8.9−4.4
$Zn_2(NDC)_2(diPyTz)\cdot Li^*$,[a]	0.35	163	0.07	0.54	9.0−5.0

[a] * represents different degree of the alkali metal ion doping.

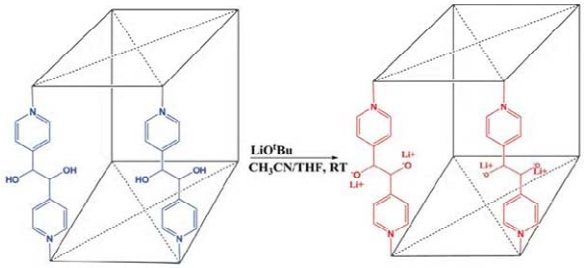

Figure 28. Metal alkoxide formation within a porous framework.[148]

10.1 kJ mol^{-1} and those cation-exchanged materials exhibited a large variation of the H_2 adsorption enthalpy for Li^+ (8.9 kJ mol^{-1}), Cu^+ (9.9 kJ mol^{-1}), Fe^{2+} (10.2 kJ mol^{-1}), Co^{2+} (10.5 kJ mol^{-1}), Ni^{2+} (9.1 kJ mol^{-1}), Cu^{2+} (8.5 kJ mol^{-1}), and Zn^{2+} (9.6 kJ mol^{-1}) respectively.

Champness and Schröder et al. reported an interesting investigation for the kinetics and hysteresis of the H_2 adsorption related with cation exchange.[87] $\{[H_2ppz][In_2(qptc)_2]\cdot 3.5DMF\cdot 5H_2O\}_\infty$ (NOTT-200), which was synthesized from In(III) and a tetracarboxylate ligand (qptc = 1,1′,4′,1″,4″,1‴-quaterphenyl-3,5,3‴,5‴-tetracarboxylate) in the presence of piperazine (ppz), has a doubly interpenetrated anionic structure with three kinds of channels with sizes of 6.6 Å × 4.4 Å (channel A), 4.3 Å × 4.1 Å (channel B), and 4.6 Å × 1.0 Å (channel C). The NH_2^+ group of the H_2ppz^{2+} located in channel B, which forms hydrogen bonds with the oxygen atoms of the ligands, was confirmed by single-crystal X-ray analysis (Figure 25). When the H_2ppz^{2+} cation was substituted with Li^+ by immersion of the MOF in a LiCl solution, $\{Li_{1.5}[H_3O]_{0.5}[In_2(L)_2]\cdot 11H_2O\}_\infty$ (NOTT-201) resulted. The structure of NOTT-201 showed an open channel B that must be blocked by the NH_2^+ group in NOTT-200. NOTT-200 showed big hysteretic N_2 and H_2 adsorption isotherms due to the kinetic trapping of H_2 and H_2ppz^{2+} blocking the channel B. However, NOTT-201 showed not only the typical Type-1 isotherms with no hysteresis but also enhanced H_2 adsorption capacity from 0.96 wt % to 1.02 wt % at 78 K and 1 bar as well as increased H_2 adsorption enthalpy from 9.0 kJ mol^{-1} to 10.1 kJ mol^{-1} (Figure 26). The result suggests that the postsynthetic cation exchange with a reasonable selection of cation size would increase the heat of H_2 adsorption as well as modulate the hysteretic adsorption behavior in an anionic framework.

Hupp et al. reported a MOF doped with 5 mol % Li^+ cations, which was obtained by the reaction of a doubly interpenetrated $[Zn_2(NDC)_2(diPyNI)]$ containing redox active ligand *N,N′*-di-(4-pyridyl)-1,4,5,8-naphthalenetetracarboxydiimide (diPyNI) with the suspension of Li in DMF. The Li^+-doped material showed the H_2 uptake of 1.63 wt % at 77 K and 1 atm, which is considerably higher than 0.93 wt % in the original material.[151] The heat of H_2 adsorption was also increased from 5.5 kJ mol^{-1} to 6.1 kJ mol^{-1} by the Li^+ ion doping. This rather small increase in the H_2 adsorption enthalpy is attributed to solvent molecules coordinated at the impregnated Li^+ ion, which cannot be completely removed by the activation. According to the authors' later report, more than one DMF molecules remained per Li^+ ion even after the activation by heating at 110 °C under vacuum for 24 h.[293,294] Therefore, the effect of the Li^+ was structural instead of electronic.

The reports demonstrating the enhancement of H_2 uptake by the impregnation of the metal ion in MOFs are very rare, but the examples described above suggest that other materials can be modified by a similar manner to enhance the hydrogen affinity. However, the effect of the impregnated metal ions would be rather minor because the degree of metal ion impregnation may be not so high and the doped metal ions would be usually coordinated with solvent molecules, which cannot be easily removed by the activation.

To exploit the system having enhanced heat of H_2 adsorption, theoretical studies were performed on metal-doped MOFs and

the results suggested significantly increased hydrogen sorption capacities.[295−303] For example, Goddard et al. reported that Li-doped MOFs can significantly improve H_2 uptake capacities at ambient conditions.[296,297] They examined the effect of metal doping in MOFs that have cubic and hexagonal lattices constructed from $[Zn_4O]$ SBUs with carboxylate links. In order to predict the structure and H_2 uptake behavior, quantum mechanics (QM) calculation and GCMC simulations have been used, respectively. The results suggest that Li atoms prefer to bind at the centers of the hexagonal aromatic rings, but Li atoms at the adjacent aromatic rings should locate on the opposite sides (Table 7). Furthermore, the doped Li atoms increase the amount of hydrogen storage in the MOFs. The simulated results for MOF-C6 and IRMOF-2-24 were compared with the experimental results of MOF-5[60] and MOF-177,[62] respectively. Further extension of the organic linker via increasing number of phenyl ring afforded more positive values by offering increased attractive sites for Li. According to these results, IRMOF-2-96 which has the biggest ligand showed a H_2 storage capacity of 6.5 wt % at 243 K and 100 bar. The ligands employed in the theoretical study and the predicted H_2 uptake amounts at ambient temperature and high pressure are summarized in Table 7 and Figure 27. Despite the interesting theoretical results, however, synthetic chemists would doubt whether those ligands could be really synthesized. In addition, a full charge was used on the Li in the calculations, but it may be overestimated even if we consider that some of the charge on Li should be used to interact with the framework.

Hupp et al. also reported a metal doping effect on the H_2 sorption properties of MOFs.[148,293,294] They reduced the organic linker of doubly interpenetrated $Zn_2(NDC)_2(diPyNI)$ and triply interpenetrated $Zn_2(NDC)_2(diPyTz)$ (diPyTz = 3,6-di(4-pyridyl)-1,2,4,5-tetrazine) with an alkali metal (Na, Li, and K) naphthalenides. The ligands in the frameworks were partially reduced (6−84%) and the alkali metal ions were concomitantly introduced to the MOFs as counter-cations.[293,294] All alkali metal doped MOFs exhibited enhanced N_2 and H_2 sorption properties. As summarized in Table 8, the alkali metal cation doping together with framework reduction significantly enhanced the H_2 uptake but modestly increased the binding energy of H_2 with the MOFs. This must be attributed to the solvent DMF molecules still bound to the doped metal ions (DMF/M^+ ratio = 0.28−1.8), as evidenced by ^1H NMR spectra. At 77 K and 1 atm, the reversible H_2 uptake increased with dopant cation size: 0.93 wt % for the pristine $Zn_2(NDC)_2(diPyNI)$, 1.23 wt % for $Zn_2(NDC)_2(diPyNI)\cdot Li$, 1.45 wt % for $Zn_2(NDC)_2(diPyTz)\cdot Na$, and 1.54 wt % for $Zn_2(NDC)_2(diPyNI)\cdot K$. It was noted that the improved N_2 and H_2 uptakes were not attributed to the direct access of the gas molecules to the doped metal cations, but due to the cation-induced displacement of the catenated structures. The order of average Q_{st} values for $Zn_2(NDC)_2(diPyNI)\cdot M$ is $Li^+ > Na^+ > K^+$, which corresponds to the ratio of cation charge to radius. This must be related with the strength of the interaction between the alkali cations and quadrupole moment of H_2. However, a triply interpenetrated framework, $Zn_2(NDC)_2(diPyTz)$, represented the different Q_{st} order ($K^+ > Na^+ > Li^+$). Although those results represent enhanced hydrogen uptakes at 77 K and 1 atm by doped metal cations, they did not show a direct relationship between hydrogen sorption capacities and heat of H_2 adsorption. This indicated that the catenated structures might interfere with the direct interaction between an alkali metal cation and H_2 gas.

As an alternative approach for alkali metal doping, Hupp and Hartman et al. independently performed postsynthetic modifications

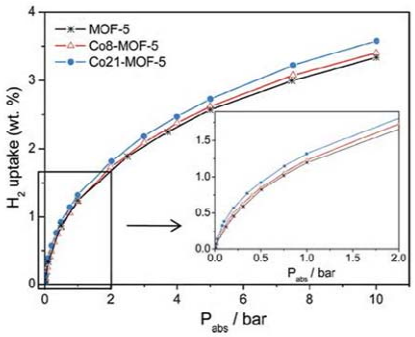

Figure 29. Hydrogen adsorption isotherms for Co8-MOF-5, Co21-MOF-5, and MOF-5 at 77 K. Reproduced with permission from ref 306. Copyright 2010 American Chemical Society.

of pendant-alcohol groups of the MOFs.[148,304] Hupp et al. exchanged the hydroxyl protons of the diol groups of the organic linker in the Zn(II) MOF (DO-MOF) with Li^+ and Mg^{2+} ions by using lithium and magnesium alkoxides (Figure 28).[148] They achieved this modification by exchanging (via soaking) the initially present guest solvent molecules (DMF) with more volatile THF and then stirring the MOF in an excess of $Li^+[O(CH_3)_3^-]$ in CH_3CN/THF. The extent of lithium loading was controlled by adjusting the stirring rate and time. When the Li^+/Zn^{2+} ratio was about 0.20, the BET surface area and the pore volume slightly increased, and the H_2 uptake also increased (1.32 wt % at 1 atm) with the increased isosteric heat of H_2 adsorption (6.3−6.6 kJ mol^{-1}) compared to the H_2 uptake capacity (1.23 wt % at 77 K and 1 atm) and the isosteric heat of H_2 adsorption (6.3−4.7 kJ mol^{-1}) of the original DO-MOF. It is not common that isosteric heat increases as the H_2 loading increases. However, as the Li^+/Zn^{2+} ratio became 2.62, the isosteric heat of H_2 adsorption as well as the surface area and pore volume diminished. Similar results were observed for the Mg^{2+} exchanged samples. When the Mg^{2+}/Zn^{2+} ratio was 0.86, the surface area and pore volume increased and the isosteric heat reached 6.2−6.9 kJ mol^{-1}, but the H_2 uptake capacity slightly decreased. When the Mg^{2+}/Zn^{2+} ratio increased to 2.02, the heat of H_2 adsorption slightly increased to 7.3−5.0 kJ mol^{-1}, although the H_2 uptake capacity decreased. At low to intermediate levels of metal ion substitution, the activated metals appear to be naked, apart from alkoxide anchoring, providing unusual Q_{st} behavior and modest enhancement of H_2 sorption.

Hartmann et al. also exchanged the protons of hydroxyl pendants in [Al(OH)(BDC-OH)], MIL-53(Al) with lithium by using lithium diisopropylamide (LDA).[304] By chemical analysis, it was found that 15% of the acidic framework protons were exchanged with lithium. The apparent Langmuir (BET) surface area of Li-MIL-53(Al) was 1450 $m^2\ g^{-1}$ (1384 $m^2\ g^{-1}$), which is 180 $m^2\ g^{-1}$ smaller than that of the original MOF. The H_2 uptake capacities at 77 K and 1 bar were 0.5 wt % and 1.7 wt % for nondoped MIL-53(Al)-OH and Li-doped Li-MIL-53(Al), respectively. The enhancement of the H_2 storage in Li-MIL-53(Al) was not only due to the lithium doping but also due to the temperature-induced structural transformation. The isosteric heat of H_2 adsorption clearly demonstrated the impact of Li^+ doping on hydrogen sorption. Compared with the undoped compound which has an adsorption enthalpy of 5.8−4.4 kJ mol^{-1},

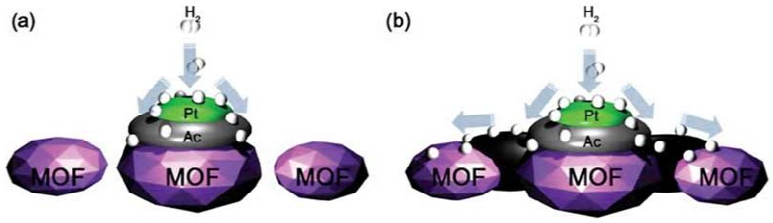

Figure 30. (a) Primary spillover of atomic hydrogen from Pt metal to the activated carbon support and secondary spillover to the MOF receptor that has limited contacts with the support. (b) Facilitated primary and secondary spillover by using carbon bridges (dark black zone).[308]

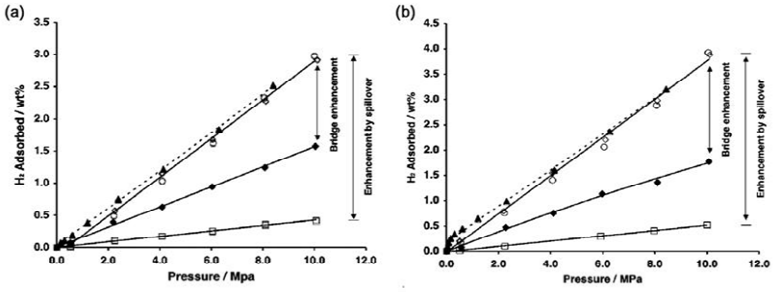

Figure 31. (a) High-pressure hydrogen isotherms at 298 K for pure IRMOF-1 (□), and physical mixture of Pt/AC and IRMOF-1 (1:9 weight ratio; ♦) and for a carbon-bridged sample of Pt/AC-bridges-IRMOF-1: first adsorption (○), desorption (▲), and second adsorption (◊). (b) High-pressure hydrogen isotherms at 298 K for pure IRMOF-8 (□), physical mixture (1:9 weight ratio) of Pt/AC and IRMOF-8 (♦) and for a sample of Pt/AC-bridges-IRMOF-8: first adsorption (○), desorption (▲), and second adsorption (◊). Reproduced with permission from ref 308. Copyright 2006 American Chemical Society.

Table 9. Hydrogen Uptake Capacities of MOFs Embedded with Pt Nanoparticles[310]

sample	Pt CVD condition	Pt content (wt%)	average Pt size (nm)	BET surface area ($m^2\ g^{-1}$)	pore volume ($cm^3\ g^{-1}$)	H_2 uptake at 298 K, 10 MPa (wt %)
IRMOF				1430	0.69	0.44
Pt/IRMOF-8-1	303 K, 6 h	4.8	2.2 ± 1.0	1175	0.59	0.85
Pt/IRMOF-8-2	308 K, 8 h	6.2	3.9 ± 1.9	1071	0.53	0.67
Pt/IRMOF-8-3	318 K, 11 h	7.7	9.1 ± 4.3	1014	0.55	0.49

Li-MIL-53(Al) has a heat of H_2 adsorption of 11.6−6.4 kJ mol^{-1}, which approaches the theoretical maximum value of ca. 13 kJ mol^{-1}.[305]

There has also been a report about the transition metal ion doping in a MOF. Botas et al. partially doped MOF-5 with Co^{2+} ions during the crystallization step of the solvothermal synthesis.[306] On the basis of the ICP analysis, the materials were characterized as $Zn_{3.68}Co_{0.32}O(BDC)_3(DEF)_{0.75}$ (Co8-MOF-5) containing 8% Co and 92% Zn and $Zn_{3.16}Co_{0.84}O(BDC)_3$-$(DEF)_{0.47}$ (Co21-MOF-5) having 21% Co and 79% Zn. The chemical compositions of Co-MOF-5 materials suggest that the substitution of more than one Co^{2+} ion in a given Zn_4O cluster is difficult. The PXRD data indicated that both undoped and Co-doped MOF-5 had an identical crystal phase. The pink color of the as-synthesized crystal changed to blue upon evacuation due to the removal of the guest solvent, indicating that the coordination geometry around Co^{2+} changed from octahedral to tetrahedral by the loss of two diethylformamide (DEF). The hydrogen uptake capacities at 77 K and 10 bar were in the order of Co21-MOF-5 > Co8-MOF-5 > MOF-5. Furthermore, the heat of adsorption in Co21-MOF-5 was ~7 kJ mol^{-1}, which is higher than that (5.5 kJ mol^{-1}) of MOF-5. Even though the increase in the absolute H_2 uptake was not so large, the H_2 uptake increased proportionally with the increased amount of Co^{2+}. This result suggests that Co^{2+} must be a good doping agent for enhancing the hydrogen storage capacity (Figure 29).

As discussed above, MOFs can be doped with alkali, alkaline earth, or transition metal ions at the ligand parts or at the metal centers. Although the metal doped MOFs showed enhanced H_2 uptakes, the enhancement was in general not so great. Because of the lack of H_2 storage data at ambient temperature, it is difficult to predict the impact of the metal doping on the H_2 storage at

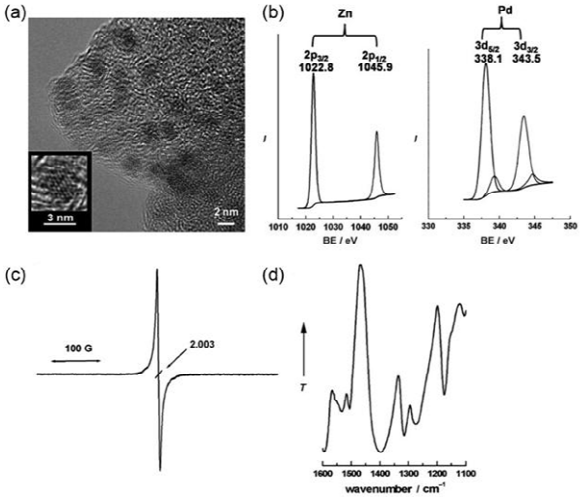

Figure 32. SNU-3 with embedded Pd nanoparticles. (a) FE-TEM image, (b) X-ray photoelectron spectrum, (c) EPR spectrum (powder, measured at 173 K), and (d) IR spectrum, for 3 wt % PdNPs@$[SNU\text{-}3]^{0.54+}(NO^{3-})_{0.54}$. Reproduced with permission from ref 134. Copyright 2009 WILEY-VCH Verlag GmbH & Co. KGaA, Weinheim.

room temperature, but based on the rather small values of the H_2 adsorption enthalpy, we may assume that it would be minor.

4.2.1.3. Spillover Effect of Palladium and Platinum. A hydrogen spillover effect has been known for a long time in the hydrogenation catalysts. It is defined as the dissociative chemisorption of hydrogen on the metal and the subsequent migration of atomic hydrogen onto the surface of the support such as alumina, carbon, etc.[307] The support can be considered as the primary receptor for atomic hydrogen. Spillover on a secondary material is referred to as secondary spillover.

Yang et al. reported significantly enhanced room temperature hydrogen storage in some MOFs, which was achieved simply by mixing Pt/AC (AC = active carbon) catalysts with IRMOF-1 or IRMOF-8.[69] For a spillover experiment, they utilized active carbon containing 5 wt % Pt that was ground with the secondary receptor (IRMOF-1 or IRMOF-8) in a weight ratio of 1:9. For this physical mixture, the active carbon and MOF were considered as the primary and secondary receptor, respectively. The high pressure gas sorption data at 298 K and 10 MPa indicated that the hydrogen adsorption capacity of Pt/AC was 1.0 wt % and those of unmodified IRMOF-1 and IRMOF-8 were ~0.4 wt % and ~0.5 wt %, respectively. The physical mixture of the Pt/AC catalyst and the MOF substantially increased the hydrogen uptake capacities by ca. three times that of the pure MOF, resulting in 1.56 wt % for modified the IRMOF-1 and 1.8 wt % for the modified IRMOF-8. Furthermore, these modified MOFs not only adsorbed 70% of the total H_2 uptake amount within 1 h, but also released over 60% of the adsorbed hydrogen in 10 min. Yang et al. also reported that a carbon bridge introduced in the mixture further increased H_2 uptake.[308] They used sucrose to build a carbon bridge to increase the contacts between the catalyst and the MOF. The three-component mixture of sucrose consisting of Pt/AC (5 wt % of Pt) and IRMOF-1 or IRMOF-8 (1:9 weight ratio of catalyst/MOF) was heated up to 473 K under helium for 3 h. This step allows sucrose to diffuse to the space between the particles of catalyst and MOF by melting, and enhances the secondary spillover (Figure 30). During the construction of the sucrose bridge, the MOFs did not decompose as confirmed by PXRD and the N_2 adsorption data. With a carbon bridge, the hydrogen uptake capacities of the modified IRMOF-1 and IRMOF-8 reached to ca. 3 wt % and 4 wt % (Figure 31), respectively, at ambient temperature and 10 MPa, which are 6−8 times higher than that of the original MOFs. The H_2 uptake amount of 4 wt % for IRMOF-8 is equivalent to ca. 34 hydrogen atoms per formula unit $[Zn_4O(NDC)_3]$. The isosteric heat of the H_2 adsorption estimated from the data at 298 and 323 K by using Clausius−Clapeyron equation was 20−23 kJ mol^{-1}, which was the highest value reported so far for the MOFs.

Table 10. The H_2 Adsorption Capacities of MOFs Embedded with Palladium Nanoparticles[134,152]

sample	amount of Pd NPs, wt %	condition	H_2 uptake amount, wt %
PdNPs@SNU-3	0	77 K, 1 bar 298 K, 95 bar	1.03 0.13
	1.70/5 min[a]	77 K, 1 bar	0.35
	2.60/10 min[a]	77 K, 1 bar	0.20
	2.94/30 min[a]	77 K, 1 bar	1.48
		298 K, 95 bar	0.3
	3.20/60 min[a]	77 K, 1 bar	1.10
MIL-100(Al)	0	77 K, 4 MPa	3.1
		298 K, 4 MPa	0.19
MIL-100(Al)/Pd	9.7	77 K, 4 MPa	1.3
		298 K, 4 MPa	0.35

[a] In the MeCN solution of 1.0×10^{-3} M $Pd(NO_3)_2 \cdot 2H_2O$ with a 1:1 mol ratio of Pd^{II}/MOF.

The report that physical mixing of Pt metal to the activated carbon support with MOF increased the H_2 storage has been reproduced by Liu et al.[309] According to this report, MIL-101 and MIL-53 were mixed with Pt/AC catalysts and carbon bridge. The H_2 storage capacities of the carbon bridge modified MIL-101 and MIL-53 became 1.14 wt % and 0.63 wt % at 293 K and 5.0 MPa, respectively, which were significantly higher than that of the pristine-MOFs.

Increased hydrogen storage by direct embedding of metal nanoparticles also has been reported for Pt-doped IRMOF-8,[310] Pt-doped MOF-177,[311] Ni-doped MIL-101,[312] Pd-doped redox-active MOF,[134] and Pd-doped MIL-100.[152] Recently, Yang et al. prepared Pt-doped IRMOF-8 by the chemical vapor deposition (CVD) of volatile platinum precursor, (trimethyl)methylcyclopentadienyl platinum(IV), and reported that the different Pt nanoparticle sizes in Pt-doped IRMOF-8 yielded different spillover effects on the hydrogen storage.[310] As shown in Table 9, the hydrogen storage capacities are in the order of Pt/IRMOF-8-1 > Pt/IRMOF-8-2 > Pt/IRMOF-8-3, which contain Pt nanoparticles of sizes, 2.2, 3.9, and 9.1 nm, respectively. The results indicate that smaller size nanoparticles afford better spillover effect.

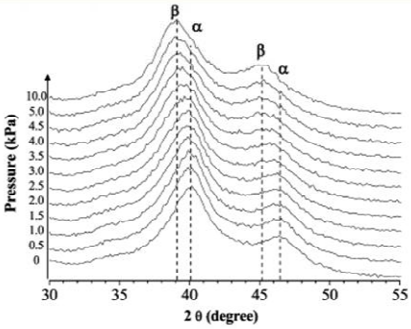

Figure 33. In situ PXRD for MIL-100(Al)/Pd (0.35 wt %) measured during the hydrogen absorption at room temperature and 10 kPa. The peak positions for the α- and β-phase of Pd NPs are shown by the straight lines in order to follow the phase transition during hydrogen adsorption. Reproduced with permission from ref 152. Copyright 2010 American Chemical Society.

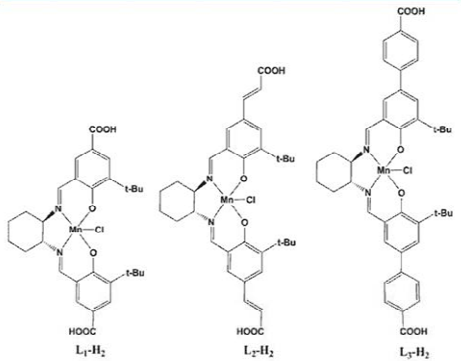

Figure 35. Schiff base complexes with dicarboxylic acid groups used in the synthesis of CMOFs.[321]

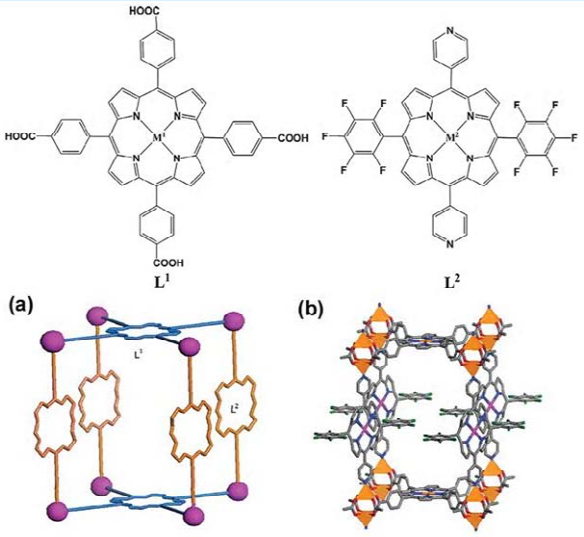

Figure 34. Structure of porphyrins and porphyrinic framework materials.[320] Porphyrinic tetraacid ligand (L^1) and pillaring dipyridylporphyrin strut (L^2). (a) Schematic diagram of porphyrinic framework. (b) Unit cell view of a porphyrinic framework.

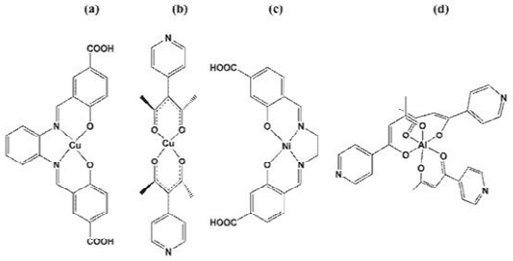

Figure 36. Schiff base complexes used in the synthesis of (a) $[Zn_3(OH)_2(L^{Cu})_2]\cdot 2DMF$,[322] (b) $[Cu_2(pzdc)_2L(H_2O)]\cdot 4H_2O$,[324] (c) $[Ln_2(L^{Ni})_3(DMF)(H_2O)_3]\cdot 4DMF\cdot 10H_2O$ (Ln = Er, Lu),[325] and (d) $[(ZnBr_2)_3(AlL_3)_2]$, $[Pd_6(AlL_3)_8](NO_3)_{12}$.[323]

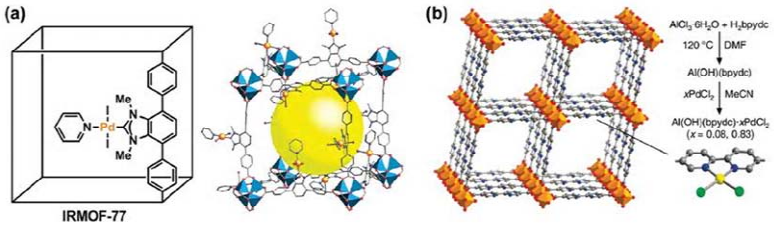

Figure 37. (a) Structure of IRMOF-77. Atom colors: blue tetrahedron, Zn; purple, I; orange, Pd; red, O; blue sphere, N. (b) Synthesis and representative structure of MOF-253. Post synthetic insertion of $PdCl_2$ into free bpy ligand sites. Atom colors: orange, yellow, green, red, blue, and gray spheres represent octahedral Al, Pd, Cl, O, N, and C atoms, respectively. Reproduced with permission from ref 329 and 330. Copyright 2010 American Chemical Society.

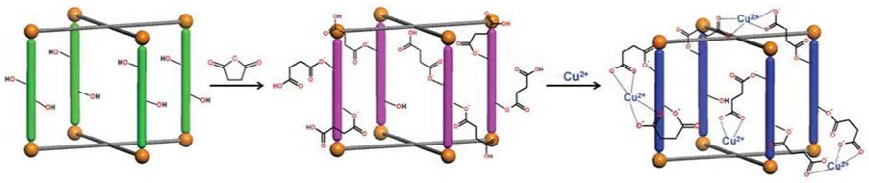

Figure 38. Schematic representation of generating open metal sites in the ligand part: postsynthetic reaction of $[Zn_2(TCPB)(DPG)]$ with succinic anhydride followed by the Cu^{2+} chelation.[331]

It should be noted here that nanoparticles embedded in MOFs were not so stable for many cycles of H_2 adsorption and desorption. It was reported that Pt@MOF-177 adsorbed 2.5 wt % of H_2 at room temperature and 144 bar in the first adsorption cycle.[311] However, in the second cycle, the storage capacity considerably decreased to 0.5 wt %, which was close to the value of pure MOF-177. This was due to the formation of Pt hydrides, from which hydrogen could not be desorbed at room-temperature.

Suh and co-workers have developed novel methods for producing metal nanoparticles in MOFs by using redox reactions between the redox-active MOFs and metal ions such as Ag(I), Au(III), and Pd(II).[95,130−134] They demonstrated that Pd nanoparticles (3.0 ± 0.4 nm, 3 wt % Pd) could be embedded in a redox-active MOF, $[Zn_3(NTB)_2]_n$ (SNU-3) simply by immersing the MOF in a MeCN solution of $Pd(NO_3)_2\cdot 2H_2O$ at room temperature without any extra reducing or capping agent.[134] The redox reaction between the redox-active organic building block (NTB^{3-}) in the MOF and the Pd(II) ions produced the positively charged framework that incorporated palladium nanoparticles (Pd NPs) and NO_3^- anions in the channels. The particle size was independent of immersion time and the concentration of the Pd(II) solution. The PXRD pattern indicated that the framework structure was maintained even after the formation of the Pd NPs. The amount of Pd NPs embedded in the MOF could be controlled by the immersion time of the MOF in the palladium(II) solution. The coexistence of Pd^0 nanoparticles and Zn^{II} in the MOF was supported by X-ray photoelectron spectroscopy (Figure 32). The H_2 adsorption capacity depended on the amount of Pd NPs loaded in the MOF. In particular, the MOF loaded with 3 wt % Pd NPs showed significantly increased H_2 sorption capacities (1.48 wt % at 77 K and 1 atm and 0.30 wt % at 298 K and 100 bar) compared to the respective 1.03 wt %

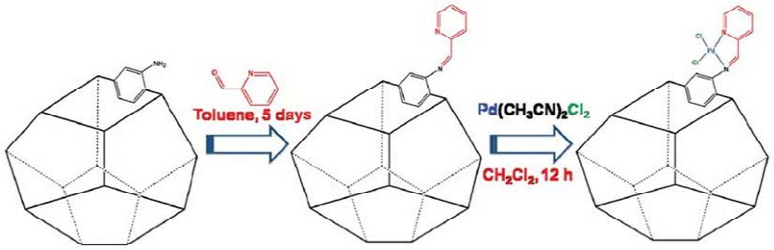

Figure 39. Covalent modification of UMCM-1-NH_2 for generating open metal sites on the struts of the MOFs.[332]

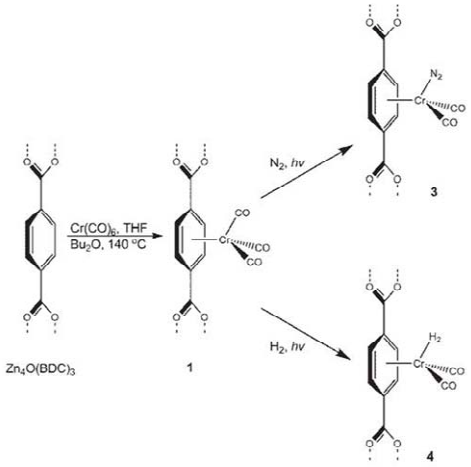

Figure 40. Reaction of $Zn_4O(BDC)_3$ with $Cr(CO)_6$ to generate $Zn_4O[(BDC)Cr(CO)_3]_3$, followed by photolysis under N_2 or H_2 to afford $Zn_4O[(BDC)Cr(CO)_2(N_2)]_3$ and $Zn_4O[(BDC)Cr(CO)_2(H_2)]_3$.[272]

and 0.13 wt % for $[Zn_3(NTB)_2]$ without Pd NPs, even though the surface area significantly decreased from 559 $m^2 g^{-1}$ to 242 $m^2 g^{-1}$ due to the Pd NPs and NO_3^- counter-anions occupying the pores. Interestingly, the zero coverage isosteric heat of 3 wt % Pd NPs loaded sample was 6.62 kJ mol^{-1}, which was significantly lower than that (8.11 kJ mol^{-1}) of $[Zn_3(NTB)_2]$.

Férey et al. also fabricated Pd NPs (size 2.5 ± 0.2 nm) into MIL-100(Al).[152] After embedding Pd NPs, the composite MIL-100(Al)/Pd (0.35 wt %) adsorbed 1.3 wt % H_2 at 77 K and 40 bar, which was lower than 1.8 wt % H_2 of MIL-100(Al) under the same condition due to the decrease in the specific surface area and pore volume. However, at room temperature and 4 MPa, it showed an H_2 uptake capacity (0.35 wt %) that was almost twice as high as that (0.19 wt %) of the pristine MIL-100(Al) (Table 10). The adsorption isotherm of MIL-100(Al)/Pd at ambient temperature and low pressure (below 0.1 MPa) displayed a steep increase, which was ascribed to the transformation of Pd to Pd hydride. Under a H_2 pressure of 4.5 kPa, PXRD peaks for Pd were shifted to the low angle region, suggesting the lattice expansion of Pd by the formation of Pd β-hydride (Figure 33).

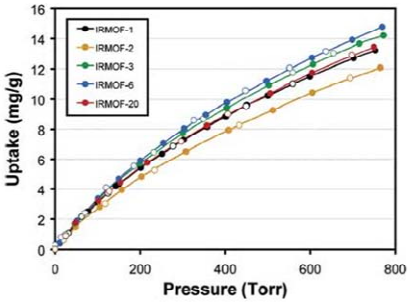

Figure 41. The H_2 adsorption isotherms at 77 K for noncatenated IRMOFs having various functional groups at the organic linker. Reproduced with permission from ref 61. Copyright 2006 American Chemical Society.

It was difficult to identify the pressure value where the phase transition of Pd hydride started to form Pd β-hydride because very broad PXRD peaks resulted from a convolution of the α- and β-phase of Pd hydride.

4.2.1.4. Other Possibilities: Open Metal Sites at Organic Linker Parts. Porous MOFs constructed of various types of porphyrin complexes have been known for many years.[313−316] Even though there has been no H_2 adsorption data reported for the porphyrin based MOFs, they have been suggested as possible H_2 storage materials since they contain open metal sites with respect to the square-planar coordination plane.[55,317−320] From multiple porphyrin ligands and various metal ions, porous robust porphyrinic materials (RPMs) (Figure 34) have been synthesized.[320]

Similarly, MOFs constructed from Schiff Base complexes also possess open metal sites. Lin and co-workers synthesized a series of isoreticular chiral metal−organic frameworks (CMOFs) from the chiral Mn-Salen-derived dicarboxylate ligands and $[Zn_4O]$ SBUs, which contained Mn(III) open metal sites (Figure 35).[321] The N_2 adsorption isotherm showed a negligible surface area due to the collapse of the framework on activation. There have been many reports for such networks, in which Schiff base complexes were used as the building blocks (Figure 36), although the H_2 gas sorption data were missing.[322−327]

The other approach for creating the open metal sites in the MOF is the synthesis of an organometallic MOF where the metal fragments are attached to the organic linker parts. This approach

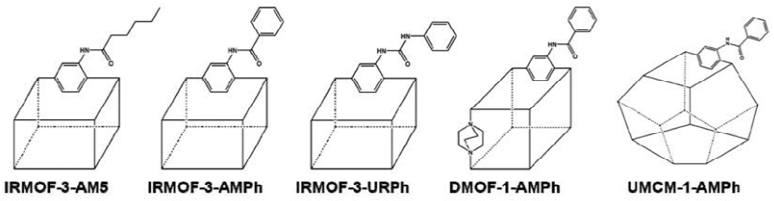

Figure 42. Schematic representation of the five postsynthetically modified MOFs. IRMOF-3, DMOF-1, UMCM-1 contain $-NH_2$ functional groups.[150]

involves covalent functionalization followed by metalation and photochemical attachment of organometallic complexes to the aromatic components of the struts. Although the H_2 uptake data in the materials have not been reported, their open metal sites might lead to enhanced isosteric heat of H_2 adsorption.

Lin and co-workers used (*R*)-6,6′-dichloro-2,2′-dihydroxy-1,1′-binaphthyl-4,4′-bipyridine (L) as a chiral bridging ligand containing orthogonal functional groups to make a MOF, $[Cd_3Cl_6L_3]\cdot 4DMF\cdot 6MeOH\cdot 3H_2O$,[328] The two pyridyl functional groups were linked with metal ions to form extended networks, whereas the orthogonal chiral 2,2′-dihydroxy secondary functional groups remained free and they were available for introduction of additional metal ions by postsynthetic modification using $Ti(O^iPr)_4$.

Yaghi and co-workers prepared a metalated ligand [4,7-bis(4-carboxylphenyl)-1,3-dimethylbenzimidazol-2-ylidene](pyridyl)-palladium(II) iodide and then assembled it into an IRMOF, which was denoted as IRMOF-77, $[Zn_4O(C_{28}H_{21}I_2N_3O_4Pd)_3]$ (Figure 37a).[329] They also reported a MOF with open 2,2′-bpy coordination sites, [Al(OH)(bpydc)] (MOF-253), synthesized from 2,2′-bipyridine-5,5′-dicarboxylic acid (H_2bpydc; Figure 37b).[330] Because of the accessibility of the chelating bpy units in MOF-253, they could insert $PdCl_2$ and $Cu(BF_4)_2$ in the MOF by soaking the MOF solid in acetonitrile solutions of $PdCl_2$ and $Cu(BF_4)_2$ respectively, which afforded MOF-253·$x$$PdCl_2$ (x = 0.08, 0.83) and MOF-253·0.97$Cu(BF_4)_2$.

In combining covalent and coordinate covalent postsynthetic modification, the MOF is covalently bound to a chelating group, and then metalated. Hupp, Nguyen, and co-workers synthesized the Zn-pillared paddle-wheel MOF, Zn_2(TCPB)(DPG) (TCPB = 1,2,4,5-tetrakis(4-carboxyphenyl)-benzene, and DPG = *meso*-1,2-bis(4-pyridyl)-1,2-ethanediol) and then reacted it with succinic anhydride (Figure 38).[331] The diols in the MOF readily reacted with succinic anhydride, resulting in a ring opened product having free carboxylic acid groups. The free carboxylic groups could be further modified by immersion in aqueous solution of $CuCl_2$.

Yaghi and co-workers reacted the amine-functionalized framework $[(Zn_4O)_3(BDC\text{-}NH_2)_3(BTB)_4]$, UMCM-1-$NH_2$ with 2-pyridinecarboxaldehyde to obtain the covalently bound iminopyridine chelate derivative $(Zn_4O)_3(BDC\text{-}C_6H_5N_2)_3(BTB)_4$, which was reacted with $PdCl_2(CH_3CN)_2$ to result the metal-complexed MOF $(Zn_4O)_3(BDC\text{-}C_6H_5N_2PdCl_2)_3(BTB)_4$ (Figure 39).[332]

Kaye and Long revealed that the benzene rings in $[Zn_4O(BDC)_3]$ (IRMOF-1) can be fully loaded with $Cr(CO)_3$ groups to afford $Zn_4O[(bdc)Cr(CO)_3]_3$.[70] The decarbonylated framework with three open coordination sites per metal was prepared by heating at 200 °C under a flow of nitrogen for 5 h, and low-pressure N_2 and H_2 adsorption measurements were performed at 298 K. It adsorbed

Table 11. Hydrogen Uptake Properties of a Series of MOFs (IRMOF-3, UMCM-1-NH_2, and DMOF-1-NH_2) upon Post-synthetic Modification[150]

compound	conversion	H_2 uptake, wt%[a]	Q_{st}[b] kJ mol^{-1}
IRMOF-3	N/A	1.52 ± 0.02	5.3 ± 0.3
IRMOF-3-AMP-a	32%	1.73	5.3
IRMOF-3-AMP-b	44%	1.73	5.7
IRMOF-3-AMP-c	70%	1.68	6.0
IRMOF-3-URPh	41 ± 5%	1.54 ± 0.06	5.7 ± 0.3
IRMOF-3-AM-5	86 ± 5%	1.21 ± 0.02	5.7 ± 0.3
UMCM-1-NH_2	N/A	1.35 ± 0.05	4.6 ± 0.4
UMCM-1-AMPh	76 ± 1%	1.54 ± 0.04	5.2 ± 0.2
DMOF-1-NH_2	N/A	2.08 ± 0.01	5.6
DMOF-1-AMPh	63 ± 1%	1.69 ± 0.05	7.0 ± 0.1

[a] Gravimetric uptake at 77 K and 1 atm. [b] Heat of H_2 adsorption at zero coverage was calculated by using a virial equation.

fewer than 0.2 molecules of H_2 per formula unit of MOF at 298 K due to the aggregation of Cr atoms. Gentle photolysis conditions enabled substitution of a single CO ligand per metal by N_2 and H_2 to give $Zn_4O[(bdc)Cr(CO)_2(N_2)]_3$ and $Zn_4O[(bdc)Cr(CO)_2(H_2)]_3$ (Figure 40), respectively, which was characterized by infrared spectroscopy. Considering the H_2 binding energy for $[(C_6H_6)Cr(CO)_2(H_2)]$ and $[(C_6H_5Me)Cr(CO)_2(H_2)]$, the H_2 binding energy for $Zn_4O[(bdc)Cr(CO)_2(H_2)]_3$ was expected to be 60−70 kJ mol^{-1}.[272]

4.2.2. Control of Pore Size and Functionalization of MOFs. As seen in Figure 19, some MOFs have high room temperature H_2 storage capacities even though they have relatively small surface areas and do not contain open metal sites (see the region marked by the yellow circle in Figure 19). This indicates that increasing the surface area and creating open metal sites cannot guarantee a high H_2 storage capacity at room temperature. Small pore size is also necessary to achieve high room temperature H_2 uptake, since the small pore enables the overlap of energy potentials between the opposing walls, leading to higher interaction energy with the H_2 molecules.[333,334] Two MOFs of M(HBTC)(4,4′-bpy) (M = Ni and Co) showed high H_2 storage capacities at 298 K and 70 bar, 1.20 wt % (Ni) and 0.96 wt % (Co), even though their BET surface areas were relatively low, 1590 m^2 g^{-1} (Ni) and 887 m^2 g^{-1} (Co).[89] The room temperature H_2 storage capacity of Ni(HBTC)(4,4′-bpy) is the highest among the MOFs reported so far. The frameworks have small pores: nonlinear honeycomb channels with only 5 Å at the narrowest and 8 Å at the widest spacing, and rectangular channels of size 7 Å × 6 Å.

The primitive cubic MOF, $[Co_3(NDC)_3(dabco)]$, based on trinuclear pinwheel motifs is another example having high H_2

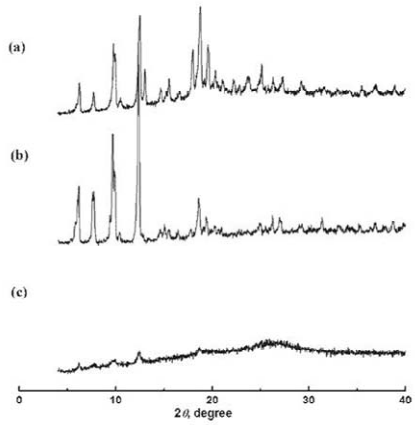

Figure 43. The PXRD patterns of SNU-5 having open metal sites.[76] (a) As-synthesized, (b) SNU-5 prepared by drying at 170 °C under a vacuum for 24 h, and (c) SNU-5 after exposure to air for 24 h.

sorption (0.89 wt % at 298 K and 17.2 bar). The high H_2 uptake is attributed to the combination of relatively high surface area (BET, 1502 $m^2 g^{-1}$) and narrow channels (4.5 Å).[187]

Control of interpenetration (or catenation) is one of the effective ways to adjust pore size. The 3D interpenetrating framework [Cu(hfipbb)$(H_2$hfipbb$)_{0.5}$] (H_2hfipbb = 4,4′-(hexafluoroisopropylidene)bis(benzoic acid)) contains two types of pores, small pores of ca. 3.5 Å × 3.5 Å size and large pores of 5.1 Å × 5.1 Å size.[197] At room temperature and 48 atm, it can adsorb about 1 wt % of H_2.

Lin and co-workers reported that 4-fold interpenetrating networks based Zn_4O clusters generated 3D channels of less than 5 Å. These materials showed BET surface areas of only 396 $m^2 g^{-1}$ and 502 $m^2 g^{-1}$, but they adsorbed 1.12 wt % and 0.98 wt % of H_2 at room temperature and 48 bar.[216]

As introduced in section 3.5, the chemical environment of the pore surface as well as the pore size can be tuned by functionalization of MOFs, which can enhance the hydrogen adsorption. Yaghi and co-workers prepared isoreticular structures from modified BDC with different functional groups. These structures include IRMOF-1, IRMOF-2 with -Br, IRMOF-3 with -NH_2, IRMOF-6 with C_2H_4, and IRMOF-20 with thieno[3,2-*b*]thiophene. They expected that the electronic character of the organic linkers might affect the amount of hydrogen uptake in the IRMOF.[61] Contrary to expectations, IRMOFs having different functional groups showed quite similar H_2 adsorption capacities (12−15 mg g^{-1}) at 77 K and 1 bar (Figure 41). Although the functionalized IRMOFs (IRMOF-3 and -6) have slightly enhanced H_2 uptake capacities up to 25% that of the unfunctionalized IRMOF-1, they are not attributed to the electronic effect of the functional groups. It is rather due to the reduction of pore size by the pendant groups: 9.6−9.8 Å for IRMOF-2, -3, and -6, compared to 12.1 Å of IRMOF-1. The observations were corroborated with some computational studies. According to second-order Møller−Plesset (MP2) calculations,[335] the H_2 molecule should be located above the center of the functionalized aromatic ring for optimal interaction geometry. The interaction energy could be enhanced by 15% by electron-donating groups such as amino and methyl group. The −Br substituent is a weak electron-withdrawing group and decreases the interaction energy between H_2 and the phenyl ring because of the stronger direct interaction between H_2 and Br since Br has greater polarizability than the phenyl ring.

Cohen et al. have tuned the H_2 adsorption properties of MOFs by postsynthetic modification.[150] They reacted NH_2-MOFs such as IRMOF-3, DMOF-1-NH_2, and UMCM-1-NH_2 with anhydrides or isocyanates to obtain amide groups (Figure 42). This type of postsynthetic modification could change the pore properties of the MOFs and alter not only the hydrogen uptake capacities but also the heats of the H_2 adsorption. The degree of conversion of the functional group (ranging from 32% to 76%) was controlled by reaction time. The resulting IRMOF-3-AMPh, IRMOF-3-URPh, and UMCM-1-AMPh exhibited enhanced H_2 storage capacities up to 1.73 wt %, 1.54 wt %, and 1.54 wt %, respectively, compared to those of IRMOF-3 (1.51 wt %) and UMCM-1-NH_2 (1.35 wt %). In addition, it was observed that the H_2 adsorption capacity and the heat of H_2 adsorption are higher for MOFs having aromatic ring substituents than those with alkyl chain substituents. The results support the hypothesis that the optimal interaction geometry between H_2 and the MOF is with the H_2 molecule located at the center of the phenyl ring. The hydrogen uptake capacities and the isosteric heats of the functionalized MOFs are summarized in Table 11.

5. TECHNIQUES AND METHODS FOR HYDROGEN SORPTION EXPERIMENTS

5.1. Preparation and Handling

It has been reported that the gas sorption properties of MOFs are significantly affected by the preparation and handling methods of as-synthesized samples, such as reaction temperature and reaction time during solvothermal synthesis. For example, it was reported that N_2 and H_2 uptake capacities of MOF-5, which was desolvated by guest-exchange with methylene chloride followed by evacuation at room temperature, depend on the reaction temperature, reaction time, and the type of solvent used in the solvothermal synthesis.[31]

The structural stability of MOFs against water vapor adsorption is an important issue for potential applications of MOFs in the gas storage because complete removal of H_2O from industrial gas resources is quite difficult. Unfortunately, the structure of some MOFs such as MOF-5,[31] MOF-177,[336] and SNU-5[76] were partially dissociated upon exposure to air as evidenced by the PXRD patterns (Figure 43), resulting in a significant decrease in the gas sorption capacities.

Li and Yang measured H_2O vapor adsorption isotherm at 298 K for MOF-177 to test the stability of MOF-177 upon H_2O adsorption. MOF-177 adsorbed up to ∼10 wt % H_2O, and ∼65% of the adsorbed H_2O could not be desorbed readily at room temperature. Therefore, trace amount of H_2O present in the hydrogen sources should be removed, and the MOFs should be handled with great care not to be exposed to air in order to achieve maximum H_2 storage capacities.

5.2. Activation Methods

In general, as-synthesized MOFs include the solvent molecules, from which the MOFs are synthesized, in the pores and channels. For applications of MOFs as porous materials, it is necessary to remove guest solvent molecules from the pores of the MOF without the loss of porosity, a process termed "activation".

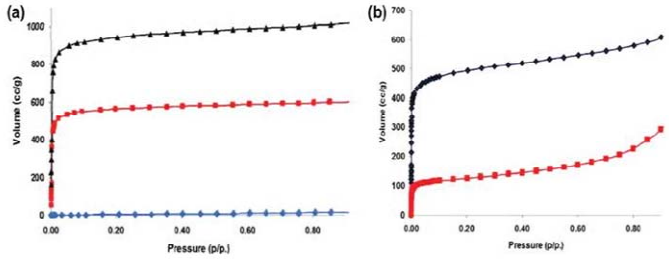

Figure 44. (a) The N_2 isotherms of IRMOF-3 at 77 K, after SCD activation (top), after the exchange with $CHCl_3$ followed by evacuation at 25 °C (middle), and conventional activation at 100 °C (bottom). (b) The N_2 isotherms of IRMOF-16 at 77 K, after SCD activation (top) and after exchange with $CHCl_3$ followed by activation at 25 °C (bottom). Reproduced with permission from ref 339. Copyright 2009 American Chemical Society.

In general, MOFs are activated by (1) heat-evacuation method based on the thermogravimetry data or (2) exchange of guest molecules with lower boiling point solvent followed by room temperature evacuation or heat-evacuation. When activating a MOF by guest exchange followed by evacuation, one must keep in mind that guest exchange often transforms the structure of the MOF, which depends on the type of solvent. In particular, the solvent molecules that form hydrogen bonds with MOF frameworks change the structure significantly,[337,338] and the desolvated structures are still affected by the guest-exchanged structures. Therefore, the choice of solvent to exchange with the guest solvent molecules of the as-synthesized sample is important and the potential structural changes caused by the guest exchange should be examined by powder X-ray diffraction data. Once the guest solvent molecules in the MOFs are exchanged with a low-boiling solvent, the MOF can be activated by room temperature evacuation, heat evacuation, or treatment with supercritical CO_2.

Unfortunately, the heat-evacuation method sometimes results in collapsed framework structures. In particular, MOFs with large pores (mesopores) are susceptible to incomplete activation, which leads to partial or even complete loss of porosity. Yaghi and co-workers reported that MOFs maintained their porosity in the absence of guests when they were activated by exchanging the guest solvent molecules with a lower boiling point solvent followed by evacuation under relatively mild conditions.[59]

Supercritical processing has been employed in aerogel fabrication to prevent collapse of the pores resulting from the elimination of surface tension upon removal of the solvent.[339] In supercritical CO_2 activation, the sample is treated through many cycles of the introduction of supercritical CO_2, commonly at 40 °C and 200 atm, followed by venting at 1 atm. Hupp and co-workers demonstrated that MOFs activated by the supercritical CO_2 drying (SCD) method adsorbed significantly greater amounts of gases than those activated by evacuation methods; thus SCD could be utilized as a potential activation method.[339] They reported the results on four MOFs that were comprised of dicarboxylate organic ligands and Zn_4O clusters as nodes. The MOFs exhibited instability under most activation conditions. As shown in Figure 44, the SCD method increases the internal surface areas of the MOFs compared with the other methods such as (a) thermal evacuation of the solvent used in the synthesis (DMF or DEF), a "conventional activation" method, and (b) guest exchange with liquid solvents with lower boiling points (e.g., DMF ↔ $CHCl_3$; DEF ↔ THF) followed by evacuation at moderate temperatures. For example, when IRMOF-3 was activated by the conventional heat-evacuation method and by the room-temperature evacuation method after the guest solvent was exchanged with $CHCl_3$, the surface areas obtained were 10 $m^2\ g^{-1}$ and 1800 $m^2\ g^{-1}$, respectively. However, when it was activated by supercritical CO_2, the N_2 accessible surface area became 2850 $m^2\ g^{-1}$. IRMOF-16 showed no porosity when it was activated through conventional methods, but the surface area became 470 $m^2\ g^{-1}$ when it was evacuated at room temperature after the solvent exchange. When IRMOF-16 was activated by SCD, it showed the surface area of 1910 $m^2\ g^{-1}$ (Figure 44b). The significant increase of the surface area through the supercritical CO_2 activation was explained by the inhibition of collapse of interparticle mesopores during the SCD activation.

Lin et al. reported that MOFs that had breathing properties adsorbed much higher amounts of gases when they were activated by a freeze-drying method compared to those activated by room temperature- or heat-evacuation methods.[340] They applied the freeze-drying method to activate MOFs that were constructed from tetracarboxylic acid and Cu_2 paddle-wheel units. The MOFs had breathing properties as evidenced by PXRD patterns. In the freeze-drying experiment, the guest solvent molecules with high boiling point were exchanged with benzene, which was subsequently removed by sublimation under a vacuum at temperatures below its freezing point. Higher internal surface areas and H_2 uptake capacities were obtained for the freeze-dried samples compared to those activated by the conventional activation method, since bypass of the liquid phase eliminated the detrimental effect where surface tension induces the mesopore collapse.

However, the compounds utilized by Hupp and Lin contained coordinated solvent molecules at the metal centers, and it was not fully characterized whether the coordinated solvent molecules were removed or not during the activation, something which must affect the gas sorption properties. In addition, there was no clear experimental evidence showing how the framework structure changed depending on the activation methods.

Recently, Suh and co-workers revealed by complete single-crystal X-ray analyses that the *guest-free* structures of a MOF are determined not only by the activation methods but also by temperature.[173] They synthesized a doubly interpenetrated Zn_4O-type MOF having PdF_2-net structure, SNU-77, from the solvothermal reaction of an extended carboxylic acid H_3TCBPA and $Zn(NO_3)_2 \cdot 6H_2O$ in DMA. Desolvated samples of SNU-77 exhibit high surface area (BET, 3670 $m^2\ g^{-1}$), high pore volume (1.52 $cm^3\ g^{-1}$), and exceptionally high uptake

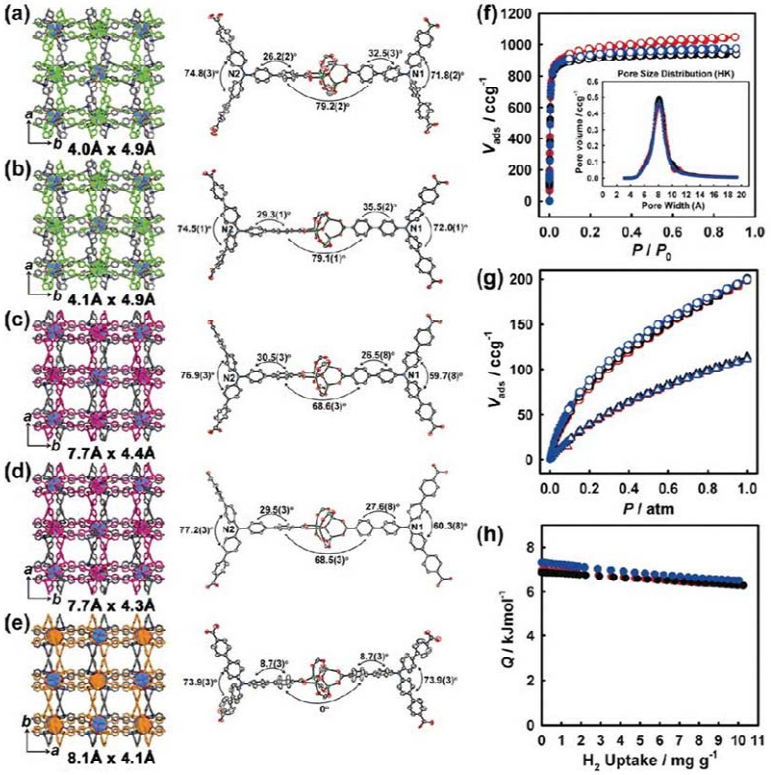

Figure 45. X-ray crystal structures of (a) SNU-77, (b) SNU-77′, (c) SNU-77R, (d) SNU-77S, and (e) SNU-77H. Doubly interpenetrated networks are represented in two different colors. The numbers below each structure represent the effective aperture size. (f) N_2 gas sorption isotherms at 77 K (Inset: pore-size distributions estimated by the Horvath−Kawazoe method), (g) H_2 gas sorption isotherms at 77 K (circles) and 87 K (triangles), and (h) isosteric heats of H_2 adsorption, for SNU-77R (black), SNU-77S (blue), and SNU-77H (red). Filled shapes: adsorption; open shapes: desorption. Reproduced with permission from ref 173. Copyright 2011 WILEY-VCH Verlag GmbH & Co. KGaA, Weinheim.

capacities for N_2, H_2, O_2, CO_2, and CH_4 gases. They activated the MOF by various activation methods such as room temperature evacuation, supercritical CO_2 drying, and high temperature evacuation. During these activation processes, SNU-77 underwent single-crystal to single-crystal transformations to afford single crystals of SNU-77R, SNU-77S, and SNU-77H, respectively (Figure 45). These *guest-free* MOFs exhibited different fine structures at room temperature, with different pore shapes and pore window sizes differing by several angstroms (Å's). Although their cell dimensions changed only slightly and Zn_4O units were located at similar positions, the organic ligands underwent rotational motion and changed the dihedral angles between the phenyl rings of the ligand. The variable-temperature synchrotron X-ray single-crystal analyses reveal that the guest-free structure is affected also by the temperature change. Interestingly, despite the different fine structures, SNU-77R, SNU-77S, and SNU-77H show similar gas sorption properties. The authors explained this phenomenon by the nonbreathing nature of the MOF as well as by the additional temperature-induced structural transformation that provided similar fine structures at the cryogenic gas sorption temperature. The results together with the reports by Hupp and Lin suggest that MOFs which collapse upon thermal evacuation or highly flexible MOFs, which exhibit a breathing effect will show increased gas sorption capacities when activated by supercritical CO_2 or by freeze-drying method compared to the thermal evacuation methods.

Suh's group proved this by preparation of a highly flexible MOF, which showed significantly increased surface area and gas sorption capacities on supercritical CO_2 treatment rather than evacuation methods.[259] They prepared a flexible non-interpenetrated MOF constructed from Cu(II) paddle-wheel units and tetrakis[4-(carboxyphenyl)oxamethyl]methane acid (H_4TCM). They activated the MOF by supercritical CO_2, which afforded [Cu_2(TCM)] (SNU-21S), and by the heat-evacuation method, which provided [Cu_2(TCM)] (SNU-21H). Both activation methods removed the coordinated solvent molecules from

the metal centers as well as the guest solvent molecules included in the pores. SNU-21S showed greater gas sorption capacities than SNU-21H. The Langmuir surface area and pore volume of SNU-21S were 905 $m^2 g^{-1}$ and 0.31 $cm^3 g^{-1}$, respectively, while those of SNU-21H were 695 $m^2 g^{-1}$ and 0.25 $cm^3 g^{-1}$. In addition, the H_2 uptake capacity and isosteric heat of the H_2 adsorption were higher in SNU-21S than in SNU-21H.

It must be quite difficult to prove whether the supercritical CO_2 treatment of MOFs would remove even the coordinated solvent molecules or not. In general, the MOFs with open metal sites pick up water molecules from the air as soon as they are exposed to air, and thus even if the method generates open metal sites, the handling of the sample, such as taking the sample out of the drying apparatus and transferring it to a gas sorption apparatus might involve exposure to air to result in the MOFs without open metal sites. Despite these difficulties, it has been reported that the coordinated solvent molecules were removed from SNU-21S[259] and NU-100[28] by the supercritical CO_2 drying method. In any case, the supercritical drying method is definitely milder than the heat-evacuation method. However, we cannot say clearly whether supercritical CO_2 treatment can always remove the coordinated solvent molecules or not until more data are accumulated to confirm this.

5.3. Gravimetric versus Volumetric Measurements

To characterize MOFs as H_2 storage materials, the H_2 uptake isotherms should be measured accurately during H_2 adsorption and desorption. There are two different methods for this measurement: gravimetric and volumetric. In the gravimetric method, the increased mass of the adsorbed H_2 in a MOF is directly estimated by using a highly sensitive microbalance.[334] The mass of the adsorbed H_2 decreases when high pressure is applied to the system, due to its buoyancy, and this weight loss is calculated using the skeletal volume of the MOF's framework and the density of H_2.[45] In the volumetric method, however, the pressure change of H_2 by the adsorption (or desorption) is measured in a closed chamber having a constant volume.[334] The volume of the adsorbed H_2 in the MOF is then calculated by subtracting the volume of H_2 in the free space from the total volume of dosed H_2.

The major disadvantage of the gravimetric method is that any H_2O impurity can lead to a significant error because the weight of a H_2O molecule is equal to the weight of nine H_2 molecules.[341] Even though the concentration of the H_2O impurity in H_2 is as low as several ppm, the sample is usually kept in a H_2 flow for a certain period of time to determine the weight change. As a result, the sample can adsorb a significant amount of H_2O, particularly when a small amount of sample is used during prolonged measurements.

On the contrary, the volumetric method determines the pressure change of H_2 during the adsorption (or desorption) in a closed chamber. As a result, the adsorption of H_2O can lead to a much lower error in the H_2 uptake capacity. The significant disadvantage of the volumetric method is the inherent errors caused by the indirect determination of the adsorbed quantities. The main sources of errors of this technique are the error in the determination of the pressure cell and adsorption cell volumes, the error in the pressure and temperature measurements, the error from the leakage of gas at high pressure, the error in the sample mass, and the error from the equation of state.[342] For ease of operation and availability of instrumentation, however, the volumetric method is more favorable in most cases discussed above.[34]

Yaghi and co-workers compared the H_2 sorption isotherms of MOF-177 measured by both volumetric and gravimetric methods at 77 K to establish the importance of calibrating gas adsorption instrumentation prior to evaluating the H_2 storage capacities.[45] The isotherms obtained by the volumetric method saturated at close to 60 bar with maximum excess amounts of 75 mg g^{-1} at 77 K. Gravimetric measurement provided a similar profile to the volumetric isotherm with an excess uptake capacity of 73 mg g^{-1} at a saturation pressure of 50 bar. They explained that the small difference between volumetric and gravimetric uptake is attributed to the difference in the apparent surface area of MOF-177 samples. The lower saturation pressure in the gravimetric measurements compared to that determined by volumetric measurements may be attributed to differences in the buoyancy correction made by He gas. Buoyancy correction cannot be made for the volume of adsorbed H_2 in the gravimetric measurement, which leads to an underestimation of H_2 uptake in the high pressure region.

5.4. Physical Methods for Characterization of Hydrogen-MOF Interaction

It is important to analyze carefully how the H_2 molecules interact with a framework so that one can modify the weakly interacting part of the framework with the strongly interacting functional groups. To find interaction sites of the MOF that are active toward H_2 molecules and to understand the mechanism of the interaction, neutron diffraction, inelastic neutron scattering, and infrared spectroscopy have been used.

5.4.1. Neutron Powder Diffraction. Neutron diffraction has been employed to find the exact position of light H_2 or D_2 molecules in a framework, since neutrons strongly scatter the nuclei of ^1H and ^2H, while X-ray is insensitive to such nuclei. To study the H_2 adsorption in a MOF, the neutron diffraction pattern of the guest-free framework as well as those patterns at various D_2-loading are obtained. The structure is then refined by using Fourier difference maps to locate the exact positions of D_2.

Yildirim and Hartman used neutron diffraction to find the adsorption sites in MOF-5.[343] The fully deuterated samples of MOF-5 were prepared and samples were finely ground in order to eliminate the effects of preferred orientation, and then adsorption experiments were conducted at 3.5 K. The first adsorption sites were near the center of the three ZnO_3 triangular faces, of which there are four such sites for each tetrahedral Zn_4O cluster. The second adsorption sites are at the top of the ZnO_3 triangles. The next two sites are occupied nearly equally as H_2 loading increases. The sites are just above the two oxygens and the top of the hexagonal linkers. The structural refinement indicates that these four adsorption sites are almost completely occupied to yield a 6.8 wt % H_2 uptake. This demonstrates that the metal-oxide cluster units are the main adsorption sites for H_2 at low temperature and high pressure. The adsorbed H_2 molecules form nanoclusters with intermolecular distances of 3.0 Å and the potential H_2 uptake is as high as 11 wt %.

Neutron powder diffraction studies were conducted by Long et al. on Mn-BTT at 3.5 K.[48] The strongest adsorption site at low loading was 2.27 Å from the Mn^{2+} ions, and the second binding site was a sodalite-like cage created by the chloride ion and the tetrazolate rings. The second sites adsorbed up to 48 H_2 molecules per formula unit, and they were fully occupied as the H_2 loading increases. The next strongest adsorption site was

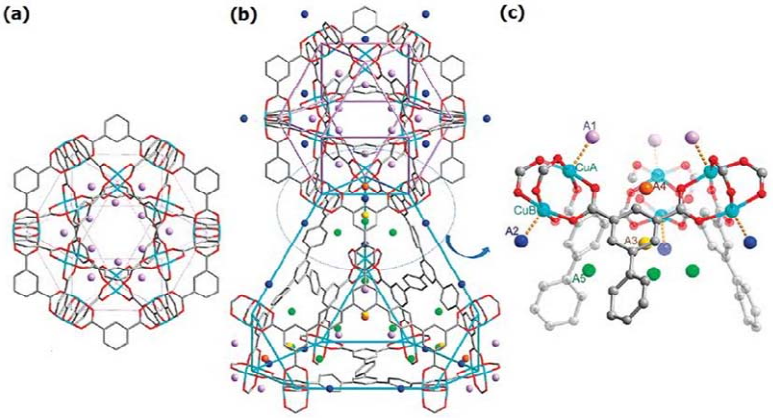

Figure 46. Views for the adsorbed D_2 positions in the desolvated sample of NOTT-112: (a) D_2 positions in the cuboctahedral cage at D_2 loading of $0.5D_2$/Cu; (b) D_2 positions in the cage A and cage B at D_2 loading of 2.0 D_2/Cu; (c) view of five D_2 positions (A1, A2, A3, A4, and A5) at 2.0 D_2/Cu; gray, carbon; red, oxygen; turquoise, copper. The D_2 positions are represented by colored spheres: A1, lavender; A2, blue; A3, yellow; A4, orange; A5, green. Reproduced with permission from ref 275. Copyright 2010 American Chemical Society.

situated inside the large framework cavity. The fourth site was located inside the smaller cavities and near carbon atoms of the tetrazolate ring. This work also confirmed that the open metal sites were one of the important factors for the creation of MOF for H_2 storage.

Kepert et al. reported the D_2 adsorption sites in HKUST-1 that has accessible Cu(II) sites.[288] The Rietveld analyses for the D_2 loaded sample showed six D_2 adsorption sites. The first adsorption site was at the open Cu(II) site of the paddle-wheel unit. The site was located 2.39 Å from the Cu atom, indicating a strong interaction between the H_2 molecule and the Cu(II). The distance is greater than that of σ-bonded η^2-dihydrogen complexes of group 6 metal ions. The next binding site was 3.29 Å from the benzene ring of BTC, and the third binding site was located 3.88 Å from the six BTC oxygen atoms and 3.90 Å from the three BTC carbon atoms. The remaining adsorption sites were located near the benzene carbon atoms and the carboxylate carbon atoms as well as the oxygen atoms. This also confirms that the open metal sites in the MOFs are important for H_2 storage.

Zhou et al. have also performed neutron diffraction studies to find the H_2 adsorption site in the rare earth MOF, Y(BTC)-$(H_2O)\cdot 4.3H_2O$.[245] The desolvated sample showed H_2 uptake capacities of 1.57 wt % at 77 K and 1 atm, and 2.1 wt % at 77 K and 10 bar. Powder neutron diffraction data upon dosing D_2 gas were measured at 4 K. Rietveld analyses indicated four different adsorption sites. Interestingly, the first adsorption site was near the BTC linkers instead of the metal centers. The H_2 adsorption site was 3.7 Å from the benzene rings and 4.27 Å from the exposed Y^{3+} ions. As H_2 loading increased, the site reached near-saturation and other sites were also occupied with H_2. The second site was located in the pores at a distance of 3.6 Å from the benzene ring and 3.9 Å from the open Y^{3+} ion. The third site was about 2.96 Å from the six BTC oxygen atoms and 4.3 Å from the Y^{3+} ions. The fourth adsorption was comparatively very weaker and located at 3.23 Å from the two BTC carboxylate oxygen atoms and 3.31 Å from two BTC carboxylate carbon atoms. This result demonstrates that an optimal pore size of about 6 Å enhances the interaction between the framework and H_2 molecules rather than the presence of open metal sites, giving a new direction in the synthesis of MOFs optimized for H_2 storage.

In situ neutron diffraction experiments have been conducted on MIL-53 (Cr) in order to identify the preferred adsorption sites as well as the mechanism of H_2 (deuterium) adsorption in the framework.[344] A fully deuterated sample of MIL-53 was used to eliminate the large incoherent background of the protons in the neutron diffraction experiment. The data for the powder samples collected at 10 K indicated that the sites near the Cr−O cluster were occupied first and then the site near the blunt corner. At higher loading, the D_2 molecules occupied the sides of the benzene rings, and the central part of the framework was occupied when D_2 adsorption reached saturation. The H_2 site occupations at various stages of loading were also measured at 25−140 K and 2 bar, and the results showed that the preferred site was independent of the temperature. The adsorption capacity reached saturation (5.5 wt %) at low temperature (below the freezing point of H_2), but many sites were still unoccupied because of the limited space and the van der Waals repulsions between the H_2 molecules.

Yildirim et al. revealed the H_2 adsorption sites in ZIF-8 at 3.5 K.[345] Contrary to MOFs, the strongest H_2 adsorption site was close to the C═C bond of the imidazolate organic linker. The other adsorption sites were at the center of the channel. This suggests that to increase the H_2 adsorption capacity, one must modify the organic linker instead of the central metal atom.

Powder neutron diffraction experiments were conducted at 4 K on Cu-BTT.[273] The framework showed a H_2 uptake capacity of 2.42 wt % at 77 K and 900 Torr. The diffraction data indicated that H_2 adsorption occurred 2.47 Å from the exposed Cu^{2+} ions. As the H_2 loading increased, the site occupancy reached about 93%. The next strong site also had similar binding energy as the

first site and was situated ca. 3.46 Å from the framework's Cl^- ions and within van der Waals contact with the tetrazolate rings. The other sites were located near the tetrazolate and the benzene rings.

The NPD measurement of NOTT-112 indicated that there were differences in the H_2−Cu(II) interaction among the exposed Cu(II) sites.[275] NOTT-112 has rht topology consisting of cuboctahedral cages (Figure 46). NPD studies were performed on the framework with different degrees of loading (0.5, 1.0, 1.5, and 2.0 D_2 per Cu). On loading 0.5 D_2 per Cu, the strongest site was near CuA (2.23 Å) and the second site was near CuB (2.41 Å) (Figure 46). It was found that 85% of the D_2 from the first dosing coordinates to CuA. The presence of CuA inside the cuboctahedral cage increases the CuA−D_2 interaction, while CuB is located outside the cage. On higher loading, sites A3 (near phenyl ring), A4, A5 start to be occupied. This is the first report showing the differences of the adsorption sites that are chemically equivalent.

According to above results reported by various research groups, the strongest adsorption sites are the open transition metal sites, although the strongest binding site for H_2 depends on the type of MOF. In the absence of open metal sites, the organic linkers become dominant binding sites for H_2 molecules.

5.4.2. Inelastic Neutron Scattering. Inelastic neutron scattering (INS) spectroscopy can be used to get information about the number of individual binding sites when H_2 molecules are loaded in a MOF. In INS, the energy transfer from neutrons to the host is measured. In a H_2 molecule, the lowest rotational transition from ortho (parallel ^{1}H spins) to para form (antiparallel ^{1}H spins) occurs at 14.7 meV. This transition is highly influenced by the chemical environment around the H_2 molecule. INS spectroscopy detects the change in the nuclear spin transition for the H_2 molecule, which provides fine details about the chemical environment of the adsorbed H_2 molecule. During the measurement, the sample is degassed and cooled to 15 K and a blank INS spectrum is measured. Then a measured amount of H_2 is loaded to the container and the sample is warmed to a temperature between 40 and 100 K to allow the H_2 to be adsorbed by the sample. Then the sample is cooled to 15 K and the INS spectrum is measured.

Yaghi et al. have used INS spectroscopy to find the specific H_2 binding sites in the series of IRMOF such as IRMOF-1, IRMOF-8, IRMOF-11, and MOF-177.[346] All of these MOFs are chemically similar and the relatively stronger adsorption sites are located near the carboxylate group and then near the $[Zn_4O]$ cluster units. The binding of H_2 at the inorganic cluster sites is affected by the nature of the organic linker and is strongest in IRMOF-11, coincident with the adsorption isotherm data. In MOFs, the sites on organic linkers have lower binding energies but a much greater capacity for H_2 loading. The results demonstrate the importance of the organic linker for H_2 storage in the MOFs.

Cheetham and co-workers have used INS spectra to analyze the H_2 sorption sites in a Ni MOF, $NaNi_3(OH)(SIP)_2$ [SIP = 5-sulfoisophthalate].[230] The INS spectra revealed that the first H_2 sorption sites were the unsaturated Ni^{2+} sites on the activated framework, where H_2 molecules were adsorbed via chemisorption. On higher H_2 loading, H_2 molecules were adsorbed on other parts by weak physisorption.

Zhou and co-workers have used INS spectroscopy to study and compare the binding sites in catenated and noncatenated frameworks.[242] The INS spectra of the two frameworks appear to be similar due to the similar chemical compositions. The INS spectra of both isomers indicate that the initial site of the H_2 adsorption is the open Cu center of the paddle-wheel SBU. The H_2 interaction with the organic linker increases as the H_2 loading increases. The interaction of H_2 with the organic linker in the catenated framework is stronger than the noncatenated framework, indicating that catenation favors H_2 adsorption by offering a higher number of effective H_2 binding sites.

5.4.3. Variable Temperature Infrared Spectroscopy. IR spectroscopy can be used to track the change in the H_2 molecules on adsorption at the active site of the MOFs. Normally, the H_2 molecule is IR inactive, but it becomes IR active when it is adsorbed on the MOF surface. The H−H bond becomes polarized and the H−H stretching mode is shifted to a lower frequency. The shifts observed for the different interaction sites are large because of the single bond perturbation in H_2. Therefore, the different adsorption sites can be easily identified, even if they have very similar interaction energies. That is, the different adsorption sites provide distinctly different IR peaks for the adsorbed molecule and the shift in the IR frequency depends on the strength of the binding site, and the binding energy of any specific site can be easily measured.

Variable-temperature infrared spectroscopy was used to verify the H_2−framework interaction in MOF-5 at 15 K.[347] Two doublets, at 4088−4093 and 4175−4181 cm^{-1}, were used to characterize the interaction. On H_2 adsorption in the MOF, the above bands were broadened and blue-shifted. New peaks appeared at 4110−4150 cm^{-1} and a doublet at 4112 and 4121 cm^{-1} dominated at low H_2 loading. With increasing the H_2 pressure, a new band at 4130 cm^{-1} became predominant. The binding enthalpies estimated for the low- and high-pressure sites were 7.4 and 3.5 kJ mol^{-1}, respectively.

By using IR spectroscopy, the interactions between H_2 and the HKUST-1 framework were studied.[348] As the temperature was decreased under an H_2 pressure of 50 mbar, parallel growth of two bands at 4097 and 4090 cm^{-1} was observed, indicating the *ortho*- and *para*-H_2 adsorption on Cu^{2+} sites. The adsorption energy was about 10 kJ mol^{-1} for the system.

Chabal and co-workers also detected the H_2 binding sites in various MOFs at 300 K and high pressures (27−55 bar) by using IR spectroscopy.[349] The study revealed that the organic linkers were weakly perturbed upon incorporation of guest molecules and that the H_2 stretch mode was red-shifted. With a structure of type $M(bdc)(ted)_{0.5}$ (ted = triethylenediamine), H_2 interacts with the benzene ring instead of the metal centers. The perturbation of H_2 molecules depends on the sensitivity of the binding sites. The H_2 perturbation increases linearly with increasing the H_2 pressure, and the IR intensity varies depending on the number of benzene rings interacting with the H_2 molecules.

6. CONCLUSION AND PROSPECTS

As reviewed in this article, MOFs have versatile structures, high surface areas, and high pore volumes, and thus can be regarded as good candidate materials for H_2 storage. There are many MOFs that have high H_2 adsorption capacities at low temperatures, typically at 77 or 87 K. The highest H_2 storage capacity reported so far is 99.5 mg g^{-1} at 77 K and 56 bar for NU-100. However, the high H_2 capacities of MOFs at cryogenic temperatures dramatically decrease as the temperature increases to room temperature. This is because the H_2 adsorption in MOFs is weak physisorption and the interaction energies between the H_2 molecules and frameworks are very low.

The H_2 adsorption capacities at 77 K and high pressures (up to 100 atm) have a qualitative relationship with the surface areas of MOFs: as surface area increases, the H_2 capacity at 77 K also increases. To increase the surface areas of MOFs, various strategies have been employed, such as using polycarboxylate ligands as organic building blocks, elongation of the ligands, creation of catenated frameworks, and employing mixed ligands in the synthesis of MOFs. MOFs constructed from hexacarboxylic acid have higher surface areas and pore volumes than those from corresponding di-, tri-, or tetracarboxylates and display relatively high H_2 storage capacities. Despite a relatively low isosteric heat of H_2 adsorption, the MOFs constructed from hexacarboxylic acid and with open copper sites have the highest excess H_2 uptake capacity at 77 K reported to date. MOFs synthesized from the extended organic building blocks provide increased surface areas but tend to interpenetrate or collapse after removal of guest solvent molecules, leading to a reduced surface area or even a nonporous structure.

In order to apply a MOF as a H_2 gas storage material, the MOF should store large amounts of H_2 at ambient temperature. The DOE targets that should be achieved by 2017 are 5.5 wt % and 45 g L^{-1} at −40−60 °C under the maximum delivery pressure of 100 atm. In order to achieve this, the framework should have a high H_2 adsorption enthalpy. Theoretical calculations have predicted that the material should have a 15−25 kJ mol^{-1} of isosteric heat of H_2 adsorption in order to store H_2 gas at ca. 30 bar and to release at ca. 1.5 bar,[170] but most of the porous MOFs reported so far have isosteric heat of the H_2 adsorption in the range of 5−12 kJ mol^{-1}.

To increase the interaction energy between H_2 molecules and MOFs surface, also known as Q_{st}, various methods have been employed such as generating open metal sites, constraining pore size, catenation, ligand functionalization, alkali metal ion or alkaline-earth metal ion inclusion, doping with metal ions, and embedding MOFs with Pd or Pt nanoparticles.

Creating open metal sites at the metal cluster nodes or in the organic linkers definitely increases the isosteric heat of H_2 adsorption, which may lead to improved H_2 storage at room temperature. The highest isosteric heat of H_2 adsorption reported so far is 15 kJ mol^{-1} for a Co(II) MOF where every Co(II) site contains an open metal site together with a Co−Co distance appropriate for the side-on interaction with a H_2 molecule.[168] In an effort to increase the isosteric heat of H_2 adsorption, one may also design and synthesize new MOFs by using the functional ligands having open metal sites such as porphyrins or macrocyclic complexes, which has never been proven to have good H_2 storage capacity. Another approach to increase the isosteric heat of H_2 adsorption is to constrain pore size. However, the relationship between pore sizes and surface areas of MOFs reported so far shows that MOFs with smaller pores have smaller surface areas and MOFs with larger pores have larger surface area. Therefore, more studies should be done for optimization of pore size and surface area. It is a challenge to generate a high concentration of open metal sites in a MOF and achieve the ideal case such that each metal binds more than one H_2 molecule.

Even though there has been no systematic study, initial studies reveal that catenation enhances room temperature H_2 storage capacities of MOFs.[242,243] Recent reports demonstrated that the degree of catenation can even be controlled by the design of molecular building blocks and the template molecules.

There have also been extensive efforts to increase the isosteric heat of H_2 adsorption in high surface area MOFs through postsynthetic modifications. Contrary to expectations, the incorporation of small metal ions with high charge density in the MOF could only slightly increase the isosteric heat of H_2 adsorption. This is because the solvent molecules bound to the introduced metal ions could not be removed by activation. In this respect, it is worthwhile trying the following approach: searching for suitable metal ions that can dope the MOFs without coordinating solvent molecules or developing MOFs that have extraordinary high thermal stability so that metal-doped MOFs can be activated at a high temperature without collapsing the frameworks. DFT-PBE calculations have shown that the binding energies to H_2 molecules are 21.9, 34.6, and 46.5 kJ mol^{-1} for Sc, Ti, and V in MOFs, respectively.[350] Therefore, one may synthesize MOFs constructed of these metal ions and then generate open metal sites to see their effects on H_2 storage.

The embedding of Pd or Pt nanoparticles definitely enhances room temperature H_2 storage, but problems arise from the reduced pore volume and surface area caused by blocking of the pores by the embedded nanoparticles, in addition to their sensitivity toward air.[134] However, doping MOFs with catalysts is still an effective approach to increase hydrogen storage capacities at ambient temperature because H_2 adsorption in MOFs promoted by metal-catalysts will take place by atomic hydrogen instead of molecular hydrogen, which will provide a high adsorption enthalpy much greater than 20 kJ mol^{-1}.

To achieve high H_2 storage at room temperature in a MOF, the MOF should have not only a high isosteric heat of H_2 adsorption but also a very high surface area and pore volume. There have been some MOFs with comparatively large isosteric heats of adsorption; however, their surface areas and the pore volumes were too low to store a large amount of H_2 gas.[134,235,351] A synthetic strategy should be developed to construct a MOF incorporating a highly interacting surface while generating a large surface area with low dead volume.

One must keep in mind that the discovery of a MOF with a large surface area and high H_2 adsorption energy at room temperature does not guarantee that it will be applied as a H_2 storage material. If a MOF is to be used in industry, it must be stable in the general working conditions. It should be comparatively inert toward moisture, air, and other gas impurities. Many MOFs, in particular, Zn(II)-carboxylate based MOFs, are unstable on contacting with the slightest amount of moisture in air and tend to adsorb much less amounts of H_2 gas once exposed to moisture, since weak metal-carboxylate bridges in the MOFs are easily dissociated by moisture.

For MOFs containing open metal sites, the exposure to moisture results in coordinating the water molecules from air, which leads to reduced H_2 uptake. Some MOFs are also decomposed in the presence of moisture due to the unstable SBUs. Most commonly reported MOFs are unstable to acids and bases and decompose immediately.[352] Recent research shows that ZIFs are relatively stable toward moisture and other harsh conditions, compared to the MOFs prepared from carboxylic acids. The stability may also depend on the metal ions employed in the synthesis of the MOFs, and therefore one has to find the right metal based MOFs. MOFs constructed of various metal ions belonging to group 1 through group 4 as well as other transition metal ions that have not been commonly used should be prepared, and their stabilities against moisture should be examined. Recently, it has been shown that MOFs synthesized from the ligands containing hydrophobic functional groups[353,354] and those with postsynthetically introduced hydrophobic functional groups enhance water resistance.[355] Therefore, when designing MOFs, one must keep in mind that strong metal−ligand bonds

should be made so that the MOF can be stable against moisture and also be thermally stable for complete desolvation to generate open metal sites without the collapse of the framework. One should also try to reduce the total cost of production of MOFs in a bulk scale synthesis by using readily available raw materials, instead of employing ligands that require a multistep organic synthesis.

To develop MOFs as H_2 storage materials that meet the U.S. DOE targets for an on-board hydrogen system, a serious challenge is still present in the design and synthesis of the MOF materials. We may expect that highly stable MOFs having a large surface area and pore volume, together with many open metal sites and embedded catalysts for hydrogen spillover, would provide some positive results for H_2 storage at ambient temperature.

AUTHOR INFORMATION

Corresponding Author

*Telephone: +82 2 880 7760; fax: +82 2 886 8516; e-mail: mpsuh@snu.ac.kr.

BIOGRAPHIES

Myunghyun Paik Suh is professor of Department of Chemistry at Seoul National University. She received her B.S. at Seoul National University (1971) and Ph.D. at the University of Chicago (1976), and she started her career as an assistant professor at the Seoul National University in 1977. Her current research interest is the development of energy and environment related materials based on coordination chemistry and nanoscience. She is a member of the Korean Academy of Science and Technology and has received the Korean Science Award offered by the President of Korea.

Hye Jeong Park received her B.S. (2006) and M.S. (2008) degrees in chemistry from Seoul National University. She is currently a Ph.D. student in inorganic chemistry at Seoul National University under the guidance of Prof. Myunghyun Paik Suh. Her research is focused on the design and synthesis of porous crystalline materials and their application in gas storage and separation as well as crystal dynamics.

Thazhe Kootteri Prasad received his Ph.D. in Chemistry in 2008 from the University of Hyderabad, India, under the guidance of Prof. M. V. Rajasekharan. In 2008, he joined the group of Prof. Myunghyun Paik Suh at Seoul National University as a post-doctoral researcher. From 2010 to 2011 he worked with Prof. Andrea Cornia at University of Modena and Reggio Emilia, Italy, researching single molecule based magnets. He is currently in Suh's lab, working on the porous materials suitable for sensing and gas storage applications.

Dae-Woon Lim received his B.S. (2009) degree in chemistry from DanKook University in Korea. He is currently a Ph.D. student at Seoul National University, working on porous materials and nanocomposites for hydrogen storage under the guidance of Prof. Myunghyun Paik Suh.

ACKNOWLEDGMENT

This work was supported by National Research Foundation of Korea (NRF) Grants funded by the Korean Government (MEST) (Nos. 2010-0029651 and 2011-0001341).

LIST OF ABBREVIATIONS

abtc	1,1′-azobenzene-3,3′,5,5′-tetracarboxylate
abtt	5,5′,5″-(2-aminobenzene-1,3,5-triyl)tris(ethyne-2,1-diyl)triisophthalic acid
acac	acetylacetonate

adc	9,10-anthracenedicarboxylate
abdc	4,4′-azobenzenedicarboxylate
adip	5,5′-(9,10-anthracenediyl)diisophthalate
aobtc	azoxybenzene-3,3′,5,5′-tetracarboxylate
APS	3-aminopropyltrialkoxysilane
azd	1,3-azulenedicarboxylate
BBC	4,4′,4″-[benzene-1,3,5-trily tris(benzene-4,1-diyl)]-tribenzoate
BDC	benzene-1,4-dicarboxylate
bdcppi	*N*,*N*′-bis(3,5-dicarboxyphenyl)pyromellitic diimide
bddc/bdi	5,5′-(buta-1,3-diyne-1,4-diyl)diisophthalate
BDP	1,4-benzenedi(4′-pyrazolyl)
BDT	1,4-benzeneditetrazolate
bdpb	1,3-bis(3,5-dicarboxylphenylethynyl)benzene
BHB	3,3′,3″,5,5′,5″-benzene-1,3,5-triyl-hexabenzoate
bhtc	biphenyl-3,4′,5-tricarboxylate
bpdc	4,4′-biphenyldicarboxylate
bpe	1,2-bis(4-pyridyl)ethane
BPnDC	4,4′-benzophenone dicarboxylate
bpta	3,6-di(4-pyridyl)-1,2,4,5-tetrazine
bptc	1,1′-biphenyl-3,3′,5,5′-tetracarboxylate
bpy	bipyridine
bpydc	2,2′-bipyridyl-5,5′-dicarboxylate
bpytc	4,4′-bipyridine-2,6,2′,6′-tetracarboxylate
Brbdc	2-bromobenzene-1,4-dicarboxylate
btatb	4,4′,4″,4‴-benzene-1,2,4,5-tetrayltetrabenzoate (same as TCPB)
BTDD	bis(1H-1,2,3-triazolo[4,5-b],-[4′,5′-i])dibenzo[1,4]-dioxin
BTB	4,4′,4″-benzene-1,3,5-triyl-tribenzoate
BTC	benzene-1,3,5-tricarboxylate
BTE	4,4′,4″-[benzene-1,3,5-triyl-tris(ethyne-2,1-diyl)]tribenzoate
btei	5,5′,5″-benzene-1,3,5-triyltris(1-ethynyl-2-isophthalate)
BTT	1,3,5-benzenetristetrazolate
btti	5,5′,5″-(benzene-1,3,5-triyl-tris(biphenyl-4,4′-diyl))triisophthalate
cdc	1,12-dicarboxyl-1,12-dicabra-closo-dodecarborane
CF_3Py	4-(α,α,α-trifluoromethyl)pyridine
CMOF	chiral metal−organic framework
cnc	4-carboxycinnamate
cyclam	1,4,8,11-tetraazacyclotetradecane
dabco	1,4-diazabicyclo[2.2.2]octane
dbdc	1,2-dihydrocyclobutabenzene-3,6-dicarboxylate
dcbBn	6,6′-dichloro-2,2′-dibenzyloxy-1,1′-binaphthyl-4,4′-dibenzoate
dccptp	3,5-dicyano-4-(4-carboxyphenyl)-2,2′:6,4″-terpyridine
dcdEt	6,6′-dichloro-2,2′-diethoxy-1,1′-binaphthyl-4,4′-dibenzoate
DEF	diethylformamide
DETA	diethylenetriamine
dhtp	2,5-dihydroxyterephthalate
diPyNI	*N*,*N*′-di-(4-pyridyl)-1,4,5,8-naphthalenetetracarboxydiimide
diPyTz	3,6-di(4-pyridyl)-1,2,4,5-tetrazine (same as bpta)
DMF	dimethylformamide
DMOF	1,4-diazabicyclo[2.2.2]octane−MOF
dobdc	2,5-dioxido-1,4-benzenedicarboxylate
DPG	meso-1,2-bis(4-pyridyl)-1,2-ethanediol
dpt	3,6-di(4-pyridyl)-1,2,4,5-tetrazine (same as bpta)
ebdc	5,5′-(1,2-ethynediyl)bis(1,3-benzenedicarboxylate)
ED	ethylene diamine
EMC	entatic metal centers
EtPy	4-ethylpyridine
hfipbb	4,4′-(idene hexafluoroisopropylidene)-dibenzoate
fma	fumarate
F-pymo	5-fluoropyrimidin-2-olate
2F-4-TBA	2-fluoro-4-(1H-tetrazole-5-yl)benzoate
GCMC	Grand Canonical Monte Carlo
HKUST	Hong Kong University of Science and Technology
hpdc	4,5,9,10-tetrahydropyrene-2,7-dicarboxylate
HPP	1,3,4,6,7,8-hexahydro-2H-pyrimido[1,2-a]pyrimidine
ICP	inductively coupled plasma
IM	imidazolates
ImDC	4,5-imidazoledicarboxylate
IN	isonicotinate
INS	inelastic neutron scattering
IRMOF	isoreticular metal−organic framework
mdip	5,5′-methylene diisophthalate
MeIM	1-methylimidazole
MePy	4-methylpyridine
MIL	material from Institut Lavoisier
mna	mercaptonicotinate
MOF	metal-organic framework
MTB	methanetetrabenzoate
NDC	naphthalenedicarboxylate
NH_2-bdc	2-aminobenzene-1,4-dicarboxylate
NP	nanoparticle
NPD	neutron powder diffraction
NTB	4,4′,4″-nitrilotrisbenzoate
ntbd	4′,4″,4‴-nitrilotribiphenyl-3,5-dicarboxylate
ntc	naphthalene-1,4,5,8-tetracarboxylate
ntei	5,5′,5″-(4,4′,4″-nitrilotris(benzene-4,1-diyl)tris(ethyne-2,1-diyl))triisophthalate
NU	Northwestern University
ox	oxalate
oxdc	oxidiacetate
PBA	4-(4-pyridyl) benzoate
pbpc	pyridine-3,5-bis(phenyl-4-carboxylate)
PCN	porous coordination network
pda	*p*-phenylenediacylate
pdc	pyridinedicarboxylate
peip	5-(pyridin-3-ylethynyl)isophthalate
PmDC	4,6-pyrimidinedicarboxylate
pmip	5-[(pyridin-3-ylmethyl)amino]isophthalate
PMTB	diphenylmethane-3,3′,5,5′-tetrakis(3,5-bisbenzoate)
ppz	piperazine
ptei	5,5′-((5′-(4-((3,5-dicarboxyphenyl)ethynyl)phenyl)-[1,1′:3′,1″-terphenyl]-4,4″-diyl)-bis(ethyne-2,1-diyl))diisophthalate
pydc	pyrene-2,7-dicarboxylate
pyen	5-methyl-4-oxo-1,4-dihydropyridine-3-carbaldehyde
pymc	2-pyrimidinecarboxylate
pymo	pyrimidinolate
pyrdc	pyrene-2,7-dicarboxylate
qptc	quaterphenyl-3,3‴,5,5‴-tetracarboxylate
Q_{st}	isosteric heats of H_2 adsorption
RPM	robust porphyrinic material
sbtc	*trans*-stilbene-3,3′,5,5′-tetracarboxylate
SCD	supercritical CO_2 drying
SIP	5-sulfoisophthalate
SNU	Seoul National University

TATB	4,4′,4″-*s*-triazine-2,4,6-triyltribenzoate
4-TBA	4-(1H-tetrazole-5-yl)benzoate
tbbdc	5-*tert*-butyl-1,3-benzenedicarboxylate
tbip	5-*t*-butyl isophthalate
tbtt	5,5′,5″-(2,4,6-trimethylbenzene-1,3,5-triyl)tris(ethyne-2,1-diyl)triisophthalate
TCBPA	tris(4-carboxybiphenyl)amine
TCM	tetrakis[4-(carboxyphenyl)-oxamethyl]methane
TCPB	1,2,4,5-tetrakis(4-carboxyphenyl)-benzene
TCPBDA	*N*,*N*,*N*′,*N*′-tetrakis(4-carboxyphenyl)biphenyl-4,4′-diamine
TDC	thiophene-2,5-dicarboxylate
tftpa	tetra-fluoroterephthalate
tcpdep	3,3′,5,5′-tetra(4-carboxyphenyl)-2,2′-diethoxylbiphenyl
TCPPDA	*N*,*N*,*N*′,*N*′-tetrakis(4-carboxyphenyl)-1,4-phenylenediamine
T^2DC	thieno[3,2-b]thiophene-2,5-dicarboxylate
ted	triethylenediamine
tfbdc	tetrafluoroterephthalate
THF	tetrahydrofuran
tmbdc	tetramethylterephthalate
TPB-3tz	1,3,5-tri-p-(tetrazol-5-yl)phenylbenzene
TPT-3tz	2,4,6-tri-p-(tetrazol-5-yl)phenyl-*s*-triazine
4,4′-tpcb	*rctt*-tetrakis (4-pyridyl)cyclobutane
3-tpt	2,4,6-tri(3-pyridyl)-1,3,5-triazine
4-tpt	2,4,6-tri(4-pyridyl)-1,3,5-triazine
tptc	terphenyl-3,3″,5,5″-tetracarboxylate
TPyP	5,10,15,20,-tetra-4-pyridyl-21*H*,23*H*-porphyrine
trz	1,2,4-triazolate
ttdc	thieno[3,2-b]thiophen-2,5-dicarboxylate
ttei	5,5′,5″-(((benzene-1,3,5-triyltris(ethyne-2,1-diyl))tris(benzene-4,1-diyl))tris-(ethyne-2,1-diyl))triisophthalate
ttpm	tetrakis(4-tetrazolylphenyl)methane
TUDMOF	Technical University of Dresden metal−organic framework
Tz	3,5-bis(trifluoromethyl)-1,2,4-triazolate
Tzc	tetrazolate-5-carboxylate
TZI	5-tetrazolylisophthalate
UMCM	University of Michigan crystalline material
UTSA	University of Texas at San Antonio
ViPy	4-vinylpyridine
ZIF	zeolitic imidazolate framework

REFERENCES

(1) http://www1.eere.energy.gov/hydrogenandfuelcells/ storage/current_technology.html.
(2) Sakintuna, B.; Lamari-Darkrimb, F.; Hirscher, M. *Int. J. Hydrogen Energy* **2007**, *32*, 1121.
(3) Schuth, F.; Bogdanovic, B.; Felderhoff, M. *Chem. Commun.* **2004**, 2249.
(4) Orimo, S.; Nakamori, Y.; Eliseo, J. R.; Züttel, A.; Jensen, C. M. *Chem. Rev.* **2007**, *107*, 4111.
(5) Grochala, W.; Edwards, P. P. *Chem. Rev.* **2004**, *104*, 1283.
(6) Christensen, C. H.; Sørensen, R. Z.; Johannessen, T.; Quaade, U. J.; Honkala, K.; Elmøe, T. D.; Køhler, R.; Nørskov, J. K. *J. Mater. Chem.* **2005**, *15*, 4106.
(7) Hugle, T.; Hartl, M.; Lentz, D. *Chem.—Eur. J.* **2011**, *17*, 10184.
(8) Alcaraz, G.; Sabo-Etienne, S. *Angew. Chem., Int. Ed.* **2010**, *49*, 7170.
(9) Hamilton, C. W.; Baker, R. T.; Staubitz, A.; Manners, I. *Chem. Soc. Rev.* **2009**, *38*, 279.
(10) Zhang, Y.-H. P. *Int. J. Hydrogen Energy* **2010**, *35*, 10334.
(11) Struzhkin, V. V.; Militzer, B.; Mao, W. L.; Mao, H.-k.; Hemley, R. J. *Chem. Rev.* **2007**, *107*, 4133.
(12) Chen, J.; Wu, F. *Appl. Phys. A: Mater. Sci. Process.* **2004**, *78*, 989.
(13) McKeown, N. B.; Budd, P. M. *Chem. Soc. Rev.* **2006**, *35*, 675.
(14) Cheng, H.-M.; Yang, Q.-H.; Liu, C. *Carbon* **2001**, *39*, 1447.
(15) Baughman, R. H.; Zakhidov, A. A.; de Heer, W. A. *Science* **2002**, *297*, 787.
(16) Strobel, R.; Garche, J.; Moseley, P. T.; Jorissen, L.; Wolf, G. *J. Power Sources* **2006**, *159*, 781.
(17) Yang, J.; Sudik, A.; Wolverton, C.; Siegel, D. J. *Chem. Soc. Rev.* **2010**, *39*, 656.
(18) Morris, R. E.; Wheatley, P. S. *Angew. Chem., Int. Ed.* **2007**, *47*, 4966.
(19) van den Berg, A. W. C.; Arean, C. O. *Chem. Commun.* **2008**, 668.
(20) David, W. I. F. *Faraday Discuss.* **2011**, *151*, 399.
(21) Fakioglu, E.; Yurum, Y.; Veziroglu, T. N. *Int. J. Hydrogen Energy* **2004**, *29*, 1371.
(22) Jena, P. *J. Phys. Chem. Lett.* **2011**, *2*, 206.
(23) Cohen, R. L.; Wernick, J. H. *Science* **1981**, *214*, 1081.
(24) Schlapbach, L.; Züttel, A. *Nature* **2001**, *414*, 353.
(25) Everett, D. H. *Pure Appl. Chem.* **1972**, *31*, 577.
(26) Burwell, R L, Jr. *Pure Appl. Chem.* **1976**, *46*, 71.
(27) Calvert, J. G. *Pure Appl. Chem.* **1990**, *62*, 2167.
(28) Farha, O. K.; Yazaydin, A. O.; Eryazici, I.; Malliakas, C. D.; Hauser, B. G.; Kanatzidis, M. G.; Nguyen, S. T.; Snurr, R. Q.; Hupp, J. T. *Nat. Chem.* **2010**, *2*, 944.
(29) Furukawa, H.; Ko, N.; Go, Y. B.; Aratani, N.; Choi, S. B.; Choi, E.; Yazaydin, A. O.; Snurr, R. Q.; O'Keeffe, M.; Kim, J.; Yaghi, O. M. *Science* **2010**, *329*, 424.
(30) Rosi, N. L.; Eckert, J.; Eddaoudi, M.; Vodak, D. T.; Kim, J.; O'Keeffe, M.; Yaghi, O. M. *Science* **2003**, *300*, 1127.
(31) Kaye, S. S.; Dailly, A.; Yaghi, O. M.; Long, J. R. *J. Am. Chem. Soc.* **2007**, *129*, 14176.
(32) Sculley, J.; Yuan, D.; Zhou, H.-C. *Energy Environ. Sci.* **2011**, *4*, 2721.
(33) Lin, X.; Champness, N. R.; Schröder, M. *Top. Curr. Chem.* **2010**, *293*, 35.
(34) Hu, Y. H.; Zhang, L. *Adv. Mater.* **2010**, *22*, E117.
(35) Ma, S.; Zhou, H.-C. *Chem. Commun.* **2010**, *46*, 44.
(36) Han, S. S.; Mendoza-Cortes, J. L.; Goddard, W. A. *Chem. Soc. Rev.* **2009**, *38*, 1460.
(37) Murray, L. J.; Dincă, M.; Long, J. R. *Chem. Soc. Rev.* **2009**, *38*, 1294.
(38) Dincă, M.; Long, J. R. *Angew. Chem., Int. Ed.* **2008**, *47*, 6766.
(39) Lin, X.; Jia, J.; Hubberstey, P.; Schröder, M.; Champness, N. R. *CrystEngComm* **2007**, *9*, 438.
(40) Lowell, S.; Shields, J. E.; Thomas, M. A.; Thommes, M. *Characterization of Porous Solids and Powders Surface Area, Pore Size and Density*; Springer (originally by Kluwer Academic Publishers): New York, 2004.
(41) Marsh, H. *Carbon* **1987**, *25*, 49.
(42) Walton, K. S.; Snurr, R. Q. *J. Am. Chem. Soc.* **2007**, *129*, 8552.
(43) Duren, T.; Millange, F.; Férey, G.; Walton, K. S.; Snurr, R. Q. *J. Phys. Chem. C* **2007**, *111*, 15350.
(44) Salem, M. M. K.; Braeuer, P.; Szombathely, M. v.; Heuchel, M.; Harting, P.; Quitzsch, K.; Jaroniec, M. *Langmuir* **1998**, *14*, 3376.
(45) Furukawa, H.; Miller, M. A.; Yaghi, O. M. *J. Mater. Chem.* **2007**, *17*, 3197.
(46) Sircar, S. *Ind. Eng. Chem. Res.* **1999**, *38*, 3670.
(47) Myers, A. L.; Calles, J. A.; Calleja, G. *Adsorption* **1997**, *3*, 107.
(48) Dincă, M.; Dailly, A.; Liu, Y.; Brown, C. M.; Neumann, D. A.; Long, J. R. *J. Am. Chem. Soc.* **2006**, *128*, 16876.
(49) Czepirski, L.; Jagiello, J. *Chem. Eng. Sci.* **1989**, *44*, 797.
(50) R program http://www.R-project.org.
(51) Cole, J. H.; Everett, D. H.; Marshall, C. T.; Paniego, A. R.; Powl, J. C; Rodriguez-Reinoso, F. *J. Chem. Soc. Faraday Trans.* **1974**, *70*, 2154.

(52) Yang, R. T. *Gas Separation by Adsorption Process*; Butterworth: Boston, 1997.
(53) Cahill, C. L.; de Lilla, D. T.; Frisch, M. *CrystEngComm* **2007**, *9*, 15.
(54) Wang, Y.; Cheng, P.; Chen, J.; Liao, D.-Z.; Yan, S.-P. *Inorg. Chem.* **2007**, *46*, 4530.
(55) Shultz, A. M.; Farha, O. K.; Hupp, J. T.; Nguyen, S. T. *J. Am. Chem. Soc.* **2009**, *131*, 4204.
(56) Chen, B.; Liang, C.; Yang, J.; Contreras, D. S.; Clancy, Y. L.; Lobkovsky, E. B.; Yaghi, O. M.; Dai, S. *Angew. Chem., Int. Ed.* **2006**, *45*, 1390.
(57) Park, H. J.; Suh, M. P. *Chem.—Eur. J.* **2008**, *14*, 8812.
(58) O'Keeffe, M.; Yaghi, O. M. *Chem. Rev.* **2012**, DOI: 10.1021/cr200205j.
(59) Eddaoudi, M.; Kim, J.; Rosi, N.; Vodak, D.; Wachter, J.; O'Keeffe, M.; Yaghi, O. M. *Science* **2002**, *295*, 469.
(60) Rowsell, J. L. C.; Millward, A. R.; Park, K. S.; Yaghi, O. M. *J. Am. Chem. Soc.* **2004**, *126*, 5666.
(61) Rowsell, J. L. C.; Yaghi, O. M. *J. Am. Chem. Soc.* **2006**, *128*, 1304.
(62) Wong-Foy, A. G.; Matzger, A. J.; Yaghi, O. M. *J. Am. Chem. Soc.* **2006**, *128*, 3494.
(63) Müller, M.; Turner, S.; Lebedev, O. I.; Wang, Y.; Tendeloo, G. v.; Fischer, R. A. *Eur. J. Inorg. Chem.* **2011**, *25*, 1878.
(64) Esken, D.; Zhang, X.; Lebedev, O. I.; Schröder, F.; Fischer, R. A. *J. Mater. Chem.* **2009**, *19*, 1314.
(65) Müller, M.; Hermes, S.; Khler, K.; van den Berg, M. W. E.; Muhler, M.; Fischer, R. A. *Chem. Mater.* **2008**, *20*, 4576.
(66) Schröder, F.; Esken, D.; Cokoja, M.; van den Berg, M. W. E.; Lebedev, O. I.; Tendeloo, G. V.; Walaszek, B.; Buntkowsky, G.; Limbach, H.-H.; Chaudret, B.; Fischer, R. A. *J. Am. Chem. Soc.* **2008**, *130*, 6119.
(67) Han, S.; Wei, Y.; Valente, C.; Lagzi, I.; Gassensmith, J. J.; Coskun, A.; Stoddart, J. F.; Grzybowski, B. A. *J. Am. Chem. Soc.* **2010**, *132*, 16358.
(68) Liu, B.; Shioyama, H.; Akita, T.; Xu, Q. *J. Am. Chem. Soc.* **2008**, *130*, 5390.
(69) Li, Y.; Yang, R. T. *J. Am. Chem. Soc.* **2006**, *128*, 726.
(70) Kaye, S. S.; Long, J. R. *J. Am. Chem. Soc.* **2008**, *130*, 806.
(71) Chae, H. K.; Siberio-Perez, D. Y.; Kim, J.; Go, Y.; Eddaoudi, M.; Matzger, A. J.; O'Keeffe, M.; Yaghi, O. M. *Nature* **2004**, *427*, 523.
(72) Koh, K.; Wong-Foy, A. G.; Matzger, A. J. *J. Am. Chem. Soc.* **2009**, *131*, 4184.
(73) Chui, S. S. Y.; Lo, S. M. F.; Charmant, J. P. H; Orpen, A. G.; Williams, I. D. *Science* **1999**, *283*, 1148.
(74) Zhou, W.; Wu, H.; Yildirim, T. *J. Am. Chem. Soc.* **2008**, *130*, 15268.
(75) Lin, X.; Telepeni, I.; Blake, A. J.; Dailly, A.; Brown, C. M.; Simmons, J. M.; Zoppi, M.; Walker, G. S.; Thomas, K. M.; Mays, T. J.; Hubberstey, P.; Champness, N. R.; Schröder, M. *J. Am. Chem. Soc.* **2009**, *131*, 2159.
(76) Lee, Y.-G.; Moon, H. R.; Cheon, Y. E.; Suh, M. P. *Angew. Chem., Int. Ed.* **2008**, *47*, 7741.
(77) Ma, B.- Q.; Mulfort, K. L.; Hupp, J. T. *Inorg. Chem.* **2005**, *44*, 4912.
(78) Park, H. J.; Cheon, Y. E.; Suh, M. P. *Chem.—Eur. J.* **2010**, *16*, 11662.
(79) Horike, S.; Matsuda, R.; Tanaka, D.; Matsubara, S.; Mizuno, M.; Endo, K.; Kitagawa, S. *Angew. Chem., Int. Ed* **2006**, *45*, 7226.
(80) Chen, B.; Ma, S.; Hurtado, E. J.; Lobkovsky, E. B.; Zhou, H. C. *Inorg. Chem.* **2007**, *46*, 8490.
(81) Henke, S.; Fischer, R. A. *J. Am. Chem. Soc.* **2011**, *133*, 2064.
(82) Férey, G.; Mellot-Draznieks, C.; Serre, C.; Millange, F.; Dutour, J.; Surble, S.; Margiolaki, I. *Science* **2005**, *309*, 2040.
(83) Férey, G.; Serre, C.; Mellot-Draznieks, C.; Millange, F.; Surble, S.; Dutour, J.; Margiolaki, I. *Angew. Chem., Int. Ed.* **2004**, *43*, 6296.
(84) Latroche, M.; Suble, S.; Serre, C.; Mellot-Draznieks, C.; Llewellyn, P. L.; Lee, J.-H.; Chang, J.-S.; Jhung, S. H.; Férey, G. *Angew. Chem., Int. Ed.* **2006**, *45*, 8227.
(85) Liu, Y.; Eubank, J. F.; Cairns, A. J.; Eckert, J.; Kravtsov, V. C.; Luebke, R.; Eddaoudi, M. *Angew. Chem., Int. Ed.* **2007**, *46*, 3278.
(86) Zheng, S.-T.; Bu, J.-T.; Li, Y.; Wu, T.; Zuo, F.; Feng, P.; Bu, X. *J. Am. Chem. Soc.* **2010**, *132*, 17062.
(87) Yang, S. H.; Lin, X.; Blake, A. J.; Walker, G. S.; Hubberstey, P.; Champness, N. R.; Schröder, M. *Nat. Chem.* **2009**, *1*, 487.
(88) Ma, S.; Zhou, H.-C. *J. Am. Chem. Soc.* **2006**, *128*, 11734.
(89) Li, Y.; Xie, L.; Liu, Y.; Yang, R.; Li, X. *Inorg. Chem.* **2008**, *47*, 10372.
(90) Mallick, A.; Saha, S.; Pachfule, P.; Roy, S.; Banerjee, R. *J. Mater. Chem.* **2010**, *20*, 9073.
(91) Senkovska, I.; Kaskel, S. *Eur. J. Inorg. Chem.* **2006**, *20*, 4564.
(92) Cheon, Y.-E.; Park, J.; Suh, M. P. *Chem. Commun.* **2009**, *45*, 5436.
(93) Gedrich, K.; Senkovska, I.; Klein, N.; Stoeck, U.; Henschel, A.; Lohe, M. R.; Baburin, I. A.; Mueller, U.; Kaskel, S. *Angew. Chem. Int. Ed.* **2010**, *49*, 8489.
(94) Lee, Y. E.; Jang, S. Y.; Suh, M. P. *J. Am. Chem. Soc.* **2005**, *127*, 6374.
(95) Suh, M. P.; Cheon, Y. E.; Lee, E. Y. *Chem.—Eur. J.* **2007**, *13*, 4208.
(96) Tian, Y.-Q.; Cai, C.-X.; Ji, Y.; You, X.-Z.; Peng, S.-M.; Lee, G.-H. *Angew. Chem., Int. Ed.* **2002**, *41*, 1384.
(97) Tian, Y.-Q.; Cai, C.-X.; Ren, X.-M.; Duan, C.-Y.; Xu, Y.; Gao, S.; You, X.-Z. *Chem.—Eur. J.* **2003**, *9*, 5673.
(98) Tian, Y.-Q.; Chen, Z.-X.; Weng, L.-H.; Guo, H.-B.; Gao, S.; Zhao, D.-Y. *Inorg. Chem.* **2004**, *43*, 4631.
(99) Tian, Y.-Q.; Zhao, Y.-M.; Chen, Z.-X.; Zhang, G.-N.; Weng, L.-H.; Zhao, D.-Y. *Chem.—Eur. J.* **2007**, *13*, 4146.
(100) Park, K. S.; Ni, Z.; Cote, A. P.; Choi, J. Y.; Huang, R.; Uribe-Romo, F. J.; Chae, H. K.; O'Keeffe, M.; Yaghi, O. M. *Proc. Natl. Acad. Sci. U.S.A.* **2006**, *103*, 10186.
(101) Banerjee, R.; Phan, A.; Wang, B.; Knobler, C.; Furukawa, H.; O'Keeffe, M.; Yaghi, O. M. *Science* **2008**, *319*, 939.
(102) Wang, B.; Côté, A. P.; Furukawa, H.; O'Keeffe, M.; Yaghi, O. M. *Nature* **2008**, *453*, 207.
(103) Hayashi, H.; Côté, A. P.; Furukawa, H.; O'Keeffe, M.; Yaghi, O. M. *Nat. Mater.* **2007**, *6*, 501.
(104) Phan, A.; Doonan, C.; Uribe-Romo, F. J.; Knobler, C. B.; O'keeffe, M.; Yaghi, O. M. *Acc. Chem. Res.* **2009**, *43*, 58.
(105) Choi, H. J.; Dincă, M.; Long, J. R. *J. Am. Chem. Soc.* **2008**, *130*, 7848.
(106) Aromi, G.; Barrios, L. A.; Gamez, P. *Coord. Chem. Rev.* **2011**, *255*, 485.
(107) Demessence, A.; D'Alessandro, D. M.; Foo, M. L.; Long, J. R. *J. Am. Chem. Soc.* **2009**, *131*, 8784.
(108) Yang, C.; Wang, X.; Omary, M. A. *J. Am. Chem. Soc.* **2007**, *129*, 1545.
(109) Zhang, J.-P.; Chen, X.-M. *J. Am. Chem. Soc.* **2008**, *130*, 6010.
(110) Zhang, J.-P.; Lin, Y.-Y.; Huang, X. -C.; Chen, X.-M. *J. Am. Chem. Soc.* **2005**, *127*, 5495.
(111) Zhu, A.-X.; Lin, J.-B.; Zhang, J.-P.; Chen, X.-M. *Inorg. Chem.* **2009**, *48*, 3882.
(112) Dincă, M.; Long, J. R. *J. Am. Chem. Soc.* **2007**, *129*, 11172.
(113) Dincă, M.; Dailly, A.; Tsay, C.; Long, J. R. *Inorg. Chem.* **2008**, *47*, 11.
(114) Dincă, M.; Yu, A. F.; Long, J. R. *J. Am. Chem. Soc.* **2006**, *128*, 8904.
(115) Chun, H.; Dybtsev, D. N.; Kim, H.; Kim, K. *Chem.—Eur. J.* **2005**, *11*, 3521.
(116) Park, H. J.; Suh, M. P. *Chem. Commun.* **2010**, *46*, 610.
(117) Koh, K.; Wong-Foy, A. G.; Matzger, A. J. *Angew. Chem., Int. Ed.* **2008**, *47*, 677.
(118) Koh, K.; Wong-Foy, A. G.; Matzger, A. J. *J. Am. Chem. Soc.* **2010**, *132*, 15005.
(119) Pichon, A.; Lazuen-Garay, A.; James, S. L. *CrystEngComm* **2006**, *8*, 211.
(120) Liu, Y.; Kravtsov, V. Ch.; Beauchamp, D. A.; Eubank, J. F.; Eddaoudi, M. *J. Am. Chem. Soc.* **2005**, *127*, 7266.
(121) Xiang, S.; Huang, J.; Li, L.; Zhang, J.; Jiang, L.; Kuang, X.; Su, C.-Y. *Inorg. Chem.* **2011**, *50*, 1743.

(122) Eubank, J. F.; Wojtas, L.; Hight, M. R.; Bousquet, T.; Kravtsov, V. Ch.; Eddaoudi, M. *J. Am. Chem. Soc.* 2011, *133*, 17532–17535.
(123) Das, M. C.; Xu, H; Xiang, S.; Zhang, Z.; Arman, H. D.; Qian, G.; Chen, B. *Chem.—Eur. J.* **2011**, *17*, 7817.
(124) Nouar, F.; Eubank, J. F.; Bousquet, T.; Wojtas, L.; Zaworotko, M. J.; Eddaoudi, M. *J. Am. Chem. Soc.* **2008**, *130*, 1833.
(125) Suh, M. P.; Moon, H. R. *Adv. Inorg. Chem.* **2007**, *59*, 39.
(126) Suh, M. P.; Cheon, Y. E.; Lee, E. Y. *Coord. Chem. Rev.* **2008**, *252*, 1007.
(127) Lee, E. Y.; Suh, M. P.; Ko, J. W.; Choi, H. J. *J. Am. Chem. Soc.* **2002**, *124*, 10976.
(128) Choi, H. J.; Suh, M. P. *J. Am. Chem. Soc.* **2004**, *126*, 15844.
(129) Lee, E. Y.; Suh, M. P. *Angew. Chem., Int. Ed.* **2004**, *43*, 2798.
(130) Moon, H. R.; Kim, J. H.; Suh, M. P. *Angew. Chem., Int. Ed.* **2005**, *44*, 1261.
(131) Suh, M. P.; Moon, H. R.; Lee, E. Y.; Jang, S. Y. *J. Am. Chem. Soc.* **2006**, *128*, 4710.
(132) Cheon, Y. E.; Suh, M. P. *Chem.—Eur. J.* **2008**, *14*, 3961.
(133) Moon, H. R.; Suh, M. P. *Eur. J. Inorg. Chem.* **2010**, *24*, 3795.
(134) Cheon, Y. E.; Suh, M. P. *Angew. Chem., Int. Ed.* **2009**, *48*, 2899.
(135) Choi, H. J.; Suh, M. P. *J. Am. Chem. Soc.* **1998**, *120*, 6309.
(136) Choi, H. J.; Suh, M. P. *Angew. Chem., Int. Ed.* **1999**, *38*, 1405.
(137) Ko, J. W.; Min, K. S.; Suh, M. P. *Inorg. Chem.* **2002**, *41*, 2151.
(138) Suh, M. P.; Choi, H. J.; So, S. M.; Kim, B. M. *Inorg. Chem.* **2003**, *42*, 676.
(139) Kim, H.; Suh, M. P. *Inorg. Chem.* **2005**, *44*, 810.
(140) Reguera, L.; Krap, C. P.; Balmaseda, J.; Reguera, E. *J. Phys. Chem. C* **2008**, *112*, 15893.
(141) Kaye, S. S.; Long, J. R. *Chem. Commun.* **2007**, *43*, 4486.
(142) Culp, J. T.; Matranga, C.; Smith, M.; Bittner, E. W.; Bockrath, B. *J. Phys. Chem. B* **2006**, *110*, 8325.
(143) Culp, J. T.; Natesakhawat, S.; Smith, M. R.; Bittner, E.; Matranga, C.; Bockrath, B. *J. Phys. Chem. C* **2008**, *112*, 7079.
(144) Kaye, S. S.; Long, J. R. *J. Am. Chem. Soc.* **2005**, *127*, 6506.
(145) Kaye, S. S.; Long, J. R. *Catal. Today* **2007**, *120*, 311.
(146) Reguera, L.; Balmaseda, J.; Krap, C. P.; Avila, M.; Reguera, E. *J. Phys. Chem. C* **2008**, *112*, 17443.
(147) Chapman, K. W.; Southon, P. D.; Weeks, C. L.; Kepert, C. J. *Chem. Commun.* **2005**, *41*, 3322.
(148) Mulfort, K. L.; Farha, O. K.; Stern, C. L.; Sarjeant, A. A.; Hupp, J. T. *J. Am. Chem. Soc.* **2009**, *131*, 3866.
(149) Nouar, F.; Eckert, J.; Eubank, J. F.; Forster, P.; Eddaoudi, M. *J. Am. Chem. Soc.* **2009**, *131*, 2864.
(150) Wang, Z.; Tanabe, K. K.; Cohen, S. M. *Chem.—Eur. J.* **2010**, *16*, 212.
(151) Mulfort, K. L.; Hupp, J. T. *J. Am. Chem. Soc.* **2007**, *129*, 9604.
(152) Zlotea, C.; Campesi, R.; Cuevas, F.; Leroy, E.; Dibandjo, P.; Volkringer, C.; Loiseau, T.; Férey, G.; Latroche, M. *J. Am. Chem. Soc.* **2010**, *132*, 2991.
(153) Hoskins, B. F.; Robson, R. *J. Am. Chem. Soc.* **1990**, *112*, 1546.
(154) Wang, Z.; Cohen, S. M. *J. Am. Chem. Soc.* **2007**, *129*, 12368.
(155) Wang, Z.; Cohen, S. M. *Chem. Soc. Rev.* **2009**, *38*, 1315.
(156) Tanabe, K. K.; Cohen, S. M. *Chem. Soc. Rev.* **2011**, *40*, 498.
(157) Hwang, Y. K.; Hong, D.-Y.; Chang, J.-S.; Jhung, S. H.; Seo, Y.-K.; Kim, J.; Vimont, A.; Daturi, M.; Serre, C.; Férey, G. *Angew. Chem., Int. Ed.* **2008**, *47*, 4144.
(158) Meilikhov, M.; Yusenko, K.; Esken, D.; Turner, S.; Tendeloo, G. V.; Fischer, R. A. *Eur. J. Inorg. Chem.* **2010**, 3701.
(159) Farha, O. K.; Mulfort, K. L.; Hupp, J. T. *Inorg. Chem.* **2008**, *47*, 10223.
(160) Costa, J. S.; Gamez, P.; Black, C. A.; Roubeau, O.; Teat, S. J.; Reedijk *Eur. J. Inorg. Chem.* **2008**, 1551.
(161) Kawamichi, T.; Kodama, T.; Kawano, M.; Fujita, M. *Angew. Chem., Int. Ed.* **2008**, *47*, 8030.
(162) Ingleson, M. J.; Barrio, J. P.; Guilbaud, J.-B.; Khimyak, Y. Z.; Rosseinsky, M. J. *Chem. Commun.* **2008**, *44*, 2680.
(163) Morris, W.; Doonan, C. J.; Furukawa, H.; Banerjee, R.; Yaghi, O. M. *J. Am. Chem. Soc.* **2008**, *130*, 12626.
(164) Burrows, A.; Frost, C.; Mahon, M.; Richardson, C. *Angew. Chem., Int. Ed.* **2008**, *47*, 8482.
(165) Jones, S. C.; Bauer, C. A. *J. Am. Chem. Soc.* **2009**, *131*, 12516.
(166) Goto, Y.; Sato, H.; Shinkai, S.; Sada, K. *J. Am. Chem. Soc.* **2008**, *130*, 14354.
(167) Gadzikwa, T.; Farha, O. K.; Malliakas, C. D.; Kanatzidis, M. G.; Hupp, J. T.; Nguyen, S. T. *J. Am. Chem. Soc.* **2009**, *131*, 13613.
(168) Cheon, Y. E.; Suh, M. P. *Chem. Commun.* **2009**, *45*, 2296.
(169) Lochan, R. C.; Head-Gordon, M. *Phys. Chem. Chem. Phys.* **2006**, *8*, 1357.
(170) Bhatia, S. K.; Myers, A. L. *Langmuir* **2006**, *22*, 1688.
(171) Frost, H.; Duren, T.; Snurr, R. Q. *J. Phys. Chem. B* **2006**, *110*, 9565.
(172) Frost, H.; Snurr, R. Q. *J. Phys. Chem. C* **2007**, *111*, 18794.
(173) Park, H. J.; Lim, D.-W.; Yang, W. S.; Oh, T.-R.; Suh, M. P. *Chem.—Eur. J.* **2011**, *17*, 7251.
(174) Sumida, K.; Hill, M. R.; Horike, S.; Dailly, A.; Long, J. R. *J. Am. Chem. Soc.* **2009**, *131*, 15120.
(175) Rood, J. A.; Noll, B. C.; Henderson, K. W. *Inorg. Chem.* **2006**, *45*, 5521.
(176) Férey, G.; Latroche, M.; Serre, C.; Millange, F.; Loiseau, T.; Percheron-Guegan, A. *Chem. Commun.* **2003**, *24*, 2976.
(177) Loiseau, T.; Lecroq, L.; Volkringer, C.; Marrot, J.; Férey, G.; Haouas, M.; Taulelle, F.; Bourrelly, S.; Llewellyn, P. L.; Latroche, M. *J. Am. Chem. Soc.* **2006**, *128*, 10223.
(178) Perles, J.; Iglesias, M.; Martín-Luengo, M.-Á.; Monge, M. Á.; Ruiz-Valero, C.; Snejko, N. *Chem. Mater.* **2005**, *17*, 5837.
(179) Ibarra, I. A.; Yang, S.; Lin, X.; Blake, A. J.; Rizkallah, P. J.; Nowell, H.; Allan, D. R.; Champness, N. R.; Hubberstey, P. *Chem. Commun.* **2011**, *47*, 8304.
(180) Dybtsev, D. N.; Chun, H.; Yoon, S. H.; Kim, D.; Kim, K. *J. Am. Chem. Soc.* **2004**, *126*, 32.
(181) Jia, J.; Lin, X.; Wilson, C.; Blake, A. J.; Champness, N. R.; Hubberstey, P.; Walker, G.; Cussen, E. J.; Schröder, M. *Chem. Commun.* **2007**, *43*, 840.
(182) Chen, B.; Ma, S.; Hurtado, E. J.; Lobkovsky, E. B.; Liang, C.; Zhu, H.; Dai, S. *Inorg. Chem.* **2007**, *46*, 8705.
(183) Lee, J. Y.; Li, J.; Jagiello, J. *J. Solid State Chem.* **2005**, *178*, 2527.
(184) Humphrey, S. M.; Chang, J.-S.; Jhung, S. H.; Yoon, J. W.; Wood, P. T. *Angew. Chem., Int. Ed.* **2007**, *46*, 272.
(185) Zhu, L.-G.; Xiao, H.-P. *Z. Anorg. Allg. Chem.* **2008**, *634*, 845.
(186) Takei, T.; Kawashima, J.; Ii, T.; Maeda, A.; Hasegawa, M.; Kitagawa, T.; Ohmura, T.; Ichikawa, M.; Hosoe, M.; Kanoya, I. *Bull. Chem. Soc. Jpn.* **2008**, *81*, 847.
(187) Chun, H.; Jung, H.; Koo, G.; Jeong, H.; Kim, D.-K. *Inorg. Chem.* **2008**, *47*, 5355.
(188) Lee, J. Y.; Pan, L.; Kelly, S. P.; Jagiello, J.; Emge, T. J.; Li, J. *Adv. Mater.* **2005**, *17*, 2703.
(189) Chang, Z.; Zhang, D.-S.; Hu, T.-L.; Bu, X.-H. *Cryst. Growth Des.* **2011**, *11*, 2050.
(190) Jiang, G.; Wu, T.; Zheng, S.-T.; Zhao, X.; Lin, Q.; Bu, X.; Feng, P. *Cryst. Growth Des.* **2011**, *11*, 3713.
(191) Ma, S.; Wang, X.-S.; Manis, E. S.; Collier, C. D.; Zhou, H.-C. *Inorg. Chem.* **2007**, *46*, 3432.
(192) Noguchi, D.; Tanaka, H.; Kondo, A.; Kajiro, H.; Noguchi, H.; Ohba, T.; Kanoh, H.; Kaneko, K. *J. Am. Chem. Soc.* **2008**, *130*, 6367.
(193) Yang, W.; Lin, X.; Jia, J.; Blake, A. J.; Wilson, C.; Hubberstey, P.; Champness, N. R.; Schröder, M. *Chem. Commun.* **2008**, *44*, 359.
(194) Chen, B.; Ma, S.; Zapata, F.; Fronczek, F. R.; Lobkovsky, E. B.; Zhou, H.-C. *Inorg. Chem.* **2007**, *46*, 1233.
(195) Navarro, J. A. R.; Barea, E.; Salas, J. M.; Masciocchi, N.; Galli, S.; Sironi, A.; Ania, C. O.; Parra, J. B. *Inorg. Chem.* **2006**, *45*, 2397.
(196) Navarro, J. A. R.; Barea, E.; Rodríguez-Diéguez, A.; Salas, J. M.; Ania, C. O.; Parra, J. B.; Masciocchi, N.; Galli, S.; Sironi, A. *J. Am. Chem. Soc.* **2008**, *130*, 3978.

(197) Pan, L.; Sander, M. B.; Huang, X.; Li, J.; Smith, M.; Bittner, E.; Bockrath, B.; Johnson, J. K. *J. Am. Chem. Soc.* **2004**, *126*, 1308.
(198) Lee, J. Y.; Olson, D. H.; Pan, L.; Emge, T. J.; Li, J. *Adv. Funct. Mater.* **2007**, *17*, 1255.
(199) Zhou, W.; Wu, H.; Hartman, M. R.; Yildirim, T. *J. Phys. Chem. C* **2007**, *111*, 16131.
(200) Chen, B.; Ma, S.; Zapata, F.; Lobkovsky, E. B.; Yang, J. *Inorg. Chem.* **2006**, *45*, 5718.
(201) Pan, L.; Parker, B.; Huang, X.; Olson, D. H.; Lee, J. Y.; Li, J. *J. Am. Chem. Soc.* **2006**, *128*, 4180.
(202) Krawiec, P.; Kramer, M.; Sabo, M.; Kunschke, R.; Fröde, H.; Kaskel, S. *Adv. Eng. Mater.* **2006**, *8*, 293.
(203) Hulvey, Z.; Sava, D. A.; Eckert, J.; Cheetham, A. K. *Inorg. Chem.* **2011**, *50*, 403.
(204) Lin, X.; Blake, A. J.; Wilson, C.; Sun, X. Z.; Champness, N. R.; George, M. W.; Hubberstey, P.; Mokaya, R.; Schröder, M. *J. Am. Chem. Soc.* **2006**, *128*, 10745.
(205) Xue, M.; Ma, S.; Jin, Z.; Schaffino, R. M.; Zhu, G.-Z.; Lobkovsky, E. B.; Qiu, S.-L.; Chen, B. *Inorg. Chem.* **2008**, *47*, 6825.
(206) Ma, L.; Lee, J. Y.; Li, J.; Lin, W. *Inorg. Chem.* **2008**, *47*, 3955.
(207) Sun, D.; Ke, Y.; Collins, D. J.; Lorigan, G. A.; Zhou, H.-C. *Inorg. Chem.* **2007**, *46*, 2725.
(208) Ma, S.; Wang, X.-S.; Collier, C. D.; Manis, E. S.; Zhou, H.-C. *Inorg. Chem.* **2007**, *46*, 8499.
(209) Barman, S.; Furukawa, H.; Blacque, O.; Venkatesan, K.; Yaghi, O. M.; Berke, H. *Chem. Commun.* **2010**, *46*, 7981.
(210) Panella, B.; Hirscher, M.; Pütter, H.; Müller, U. *Adv. Funct. Mater.* **2006**, *16*, 520.
(211) Panella, B.; Hirscher, M. *Adv. Mater.* **2005**, *17*, 538.
(212) Sabo, M.; Henschel, A.; Fröde, H.; Klemm, E.; Kaskel, S. *J. Mater. Chem.* **2007**, *17*, 3827.
(213) Dailly, A.; Vajo, J. J.; Ahn, C. C. *J. Phys. Chem. B* **2006**, *110*, 1099.
(214) Kim, H.; Das, S.; Kim, M. G.; Dybtsev, D. N.; Kim, Y.; Kim, K. *Inorg. Chem.* **2011**, *50*, 3691.
(215) Sun, D.; Collins, D. J.; Ke, Y.; Zuo, J.-L.; Zhou, H.-C. *Chem.—Eur. J.* **2006**, *12*, 3768.
(216) Kesanli, B.; Cui, Y.; Smith, M. R.; Bittner, E. W.; Bockrath, B. C.; Lin, W. *Angew. Chem., Int. Ed.* **2005**, *44*, 72.
(217) Park, H.; Britten, J. F.; Mueller, U.; Lee, J. Y.; Li, J.; Parise, J. B. *Chem. Mater.* **2007**, *19*, 1302.
(218) Han, D.; Jiang, F.-L.; Wu, M.-Y.; Chen, L.; Chen, Q.-X.; Hong, M.-C. *Chem. Commun.* **2011**, *47*, 9861.
(219) Fang, Q.-R.; Zhu, G.-S.; Xue, M.; Zhang, Q.-L.; Sun, J.-Y.; Guo, X.-D.; Qiu, S.-L.; Xu, S.-T.; Wang, P.; Wang, D.-J.; Wei, Y. *Chem.—Eur. J.* **2006**, *12*, 3754.
(220) Navarro, J. A. R.; Barea, E.; Salas, J. M.; Masciocchi, N.; Sironi, S.; Galli, A.; Ania, C. O.; Parra, J. B. *J. Mater. Chem.* **2007**, *17*, 1939.
(221) Yang, C.; Wang, X.; Omary, M. A. *J. Am. Chem. Soc.* **2007**, *129*, 15454.
(222) Fang, Q.-R.; Zhu, G.-S.; Jin, Z.; Ji, Y.-Y.; Ye, J.-W.; Xue, M.; Yang, H.; Wang, Y.; Qiu, S.-L. *Angew. Chem., Int. Ed.* **2007**, *46*, 6638.
(223) Sava, D. F.; Kravtsov, V. C.; Nouar, F.; Wojtas, L.; Eubank, J. F.; Eddaoudi, M. *J. Am. Chem. Soc.* **2008**, *130*, 3768.
(224) Gu, X.; Lu, Z.-H.; Xu, Q. *Chem. Commun.* **2010**, *46*, 7400.
(225) Zheng, S.-T.; Bu, J. J.; Wu, T.; Chou, C.; Feng, P.; Bu, X. *Angew. Chem., Int. Ed.* **2011**, *50*, 8858.
(226) Ma, S.; Wang, X.-S.; Yuan, D.; Zhou, H.-C. *Angew. Chem., Int. Ed.* **2008**, *47*, 4130.
(227) Sumida, K.; Brown, C. M.; Herm, Z. R.; Chavan, S.; Bordiga, S.; Long, J. R. *Chem. Commun.* **2011**, *47*, 1157.
(228) Moon, H. R.; Kobayashi, N.; Suh, M. P. *Inorg. Chem.* **2006**, *45*, 8672.
(229) Yoon, J. H.; Choi, S. B.; Oh, Y. J.; Seo, M. J.; Jhon, Y. H.; Lee, T.-B.; Kim, D.; Choi, S.-H.; Kim, J. *Catal. Today* **2007**, *120*, 324.
(230) Forster, P. M.; Eckert, J.; Heiken, B. D.; Parise, J. B.; Yoon, J. W.; Jhung, S. H.; Chang, J. S.; Cheetham, A. K. *J. Am. Chem. Soc.* **2006**, *128*, 16846.
(231) Dietzel, P. D. C.; Panella, B.; Hirscher, M.; Blom, R.; Fjellvåg, H. *Chem. Commun.* **2006**, *42*, 959.
(232) Liu, X.; Oh, M.; Lah, M. S. *Inorg. Chem.* **2011**, *50*, 5044.
(233) Liu, X.; Oh, M.; Lah, M. S. *Cryst. Growth Des.* 2011, *11*, 5064–5071.
(234) Liu, Y.; Kabbour, H.; Brown, C. M.; Neumann, D. A.; Ahn, C. C. *Langmuir* **2008**, *24*, 4772.
(235) Chen, B.; Zhao, X.; Putkham, A.; Hong, K.; Lobkovsky, E. B.; Hurtado, E. J.; Fletcher, A. J.; Thomas, K. M. *J. Am. Chem. Soc.* **2008**, *130*, 6411.
(236) Farha, O. K.; Spokoyny, A. M.; Mulfort, K. L.; Hawthorne, M. F.; Mirkin, C. A.; Hupp, J. T. *J. Am. Chem. Soc.* **2007**, *129*, 12680.
(237) Jia, J.; Lin, X.; Blake, A. J.; Champness, N. R.; Hubberstey, P.; Shao, L.; Walker, G. S.; Wilson, C.; Schröder, M. *Inorg. Chem.* **2006**, *45*, 8838.
(238) Sumida, K.; Her, J.-H.; Dincă, M.; Murray, L. J.; Schloss, J. M.; Pierce, C. J.; Thompson, B. A.; FitzGerald, S. A.; Brown, C. M.; Long, J. R. *J. Phys. Chem. C* **2011**, *115*, 8414.
(239) Surblé, S.; Millange, F.; Serre, C.; Düren, T.; Latroche, M.; Bourrelly, S.; Llewellyn, P. L.; Férey, G. *J. Am. Chem. Soc.* **2006**, *128*, 14889.
(240) Choi, S. B.; Seo, M. J.; Cho, M.; Kim, Y.; Jin, M. K.; Jung, D.-Y.; Choi, J.-S.; Ahn, W.-S.; Rowsell, J. L. C.; Kim, J. *Cryst. Growth Des.* **2007**, *7*, 2290.
(241) Sun, D.; Ma, S.; Ke, Y.; Collins, D. J.; Zhou, H.-C. *J. Am. Chem. Soc.* **2006**, *128*, 3896.
(242) Ma, S.; Eckert, J.; Forster, P. M.; Yoon, J. W.; Hwang, Y. K.; Chang, J.-S.; Collier, C. D.; Parise, J. B.; Zhou, H.-C. *J. Am. Chem. Soc.* **2008**, *130*, 15896.
(243) Zhou, H.-C.; Ma, S. Q.; Sun, D. F.; Ambrogio, M.; Fillinger, J. A.; Parkin, S. *J. Am. Chem. Soc.* **2007**, *129*, 1858.
(244) Wong-Foy, A. G.; Lebel, O.; Matzger, A. J. *J. Am. Chem. Soc.* **2007**, *129*, 15740.
(245) Luo, J.; Xu, H.; Liu, Y.; Zhao, Y.; Daemen, L. L.; Brown, C.; Timofeeva, T. V.; Ma, S.; Zhou, H.-C. *J. Am. Chem. Soc.* **2008**, *130*, 9626.
(246) Kramer, M.; Schwarz, U.; Kaskel, S. *J. Mater. Chem.* **2006**, *16*, 2245.
(247) Guo, X.; Zhu, G.; Li, Z.; Sun, F.; Yang, Z.; Qiu, S. *Chem. Commun.* **2006**, *42*, 3172.
(248) Zhang, P.; Li, B.; Zhao, Y.; Meng, X.; Zhang, T. *Chem. Commun.* **2011**, *47*, 7722.
(249) Chen, B.; Ockwig, N. W.; Millward, A. R.; Contreras, D. S.; Yaghi, O. M. *Angew. Chem., Int. Ed.* **2005**, *44*, 4745.
(250) Lin, X.; Jia, J.; Zhao, X.; Thomas, K. M.; Blake, A. J.; Walker, G. S.; Champness, N. R.; Hubberstey, P.; Schröder, M. *Angew. Chem., Int. Ed.* **2006**, *45*, 7358.
(251) Yang, S. H.; Lin, X.; Dailly, A.; Blake, A. J.; Hubberstey, P.; Champness, N. R.; Schröder, M. *Chem.—Eur. J.* **2009**, *15*, 4829.
(252) Wang, X. S.; Ma, S. Q.; Rauch, K.; Simmons, J. M.; Yuan, D. Q.; Wang, X. P.; Yildirim, T.; Cole, W. C.; Lopez, J. J.; de Meijere, A.; Zhou, H.-C. *Chem. Mater.* **2008**, *20*, 3145.
(253) Wang, X.-S.; Ma, S.; Forster, P. M.; Yuan, D.; Eckert, J.; López, J. L.; Murphy, B. J.; Parise, J. B.; Zhou, H.-C. *Angew. Chem., Int. Ed.* **2008**, *47*, 7263.
(254) Ma, S.; Simmons, J. M.; Sun, D.; Yuan, D.; Zhou, H. —C. *Inorg. Chem.* **2009**, *48*, 5263.
(255) Sun, D.; Ma, S.; Simmons, J. M.; Li, J.-R.; Yuan, D.; Zhou, H.-C. *Chem. Commun.* **2010**, *46*, 1329.
(256) Zhuang, W.; Ma, S.; Wang, X.-S.; Yuan, D.; Li, J.-R.; Zhao, D.; Zhou, H.-C. *Chem. Commun.* **2010**, *46*, 5223.
(257) Zhao, D.; Yuan, D.; Yakovenko, A.; Zhou, H.-C. *Chem. Commun.* **2010**, *46*, 4196.
(258) Xue, M.; Zhu, G.; Li, Y.; Zhao, X.; Jin, Z.; Kang, E.; Qiz, S. *Cryst. Growth Des.* **2008**, *8*, 2478.
(259) Kim, T. K.; Suh, M. P. *Chem. Commun.* **2011**, *47*, 4258.
(260) Prasad, T. K.; Hong, D. H.; Suh, M. P. *Chem.—Eur. J.* **2010**, *16*, 14043.
(261) Zheng, B.; Liang, Z.; Li, G.; HuO, Q.; Liu, Y. *Cryst. Growth Des.* **2010**, *10*, 3405.

(262) Sun, D.; Ke, Y.; Mattox, T. M.; Ooro, B. A.; Zhou, H.-C. *Chem. Commun.* **2005**, *41*, 5447.
(263) Yan, Y.; Blake, A. J.; Lewis, W.; Barnett, S. A.; Dailly, A.; Champness, N. R.; Schröder, M. *Chem.—Eur. J.* **2011**, *17*, 11162.
(264) Guo, Z.; Wu, H.; Srinivas, G.; Zhou, Y.; Xiang, S.; Chen, Z.; Yang, Y.; Zhou, W.; O'Keeffe, M.; Chen, B. *Angew. Chem., Int. Ed.* **2011**, *50*, 3178.
(265) Yuan, D.; Zhao, D.; Sun, D.; Zhou, H.-C. *Angew. Chem., Int. Ed.* **2010**, *49*, 5357.
(266) Yan, Y.; Yang, S.; Blake, A. J.; Lewis, W.; Poirier, E.; Barnett, S. A.; Champness, N. R.; Schröder, M. *Chem. Commun.* **2011**, *47*, 9995.
(267) Yuan, D.; Zhao, D.; Zhou, H.-C. *Inorg. Chem.* 2011, *50*, 10528–10530.
(268) Yan, Y.; Lin, X.; Yang, S.; Blake, A. J.; Dailly, A.; Champness, N. R.; Hubberstey, P.; Schröder, M. *Chem. Commun.* **2009**, *45*, 1025.
(269) Hong, S.; Oh, M.; Park, M.; Yoon, J. W.; Chang, J. −S.; Lah, M. S. *Chem. Commun.* **2009**, *45*, 5397.
(270) Tan, C.; Yang, S.; Champness, N. R.; Lin, X.; Blake, A. J.; Lewis, W.; Schröder, M. *Chem. Commun.* **2011**, *47*, 4487.
(271) Sumida, K.; Horike, S.; Kaye, S. S.; Herm, Z. R.; Queen, W. L.; Brown, C. M.; Grandjean, F.; Long, G. J.; Anne, D.; Long, J. R. *Chem. Sci.* **2010**, *1*, 184.
(272) Dincă, M.; Long, J. R. *Chem.—Eur. J.* **2008**, *14*, 10280.
(273) Dincă, M.; Han, W. S.; Liu, Y.; Dailly, A.; Brown, C. M.; Long, J. R. *Angew. Chem., Int. Ed.* **2007**, *46*, 1419.
(274) Denysenko, D.; Grzywa, M.; Tonigold, M.; Streppel, B.; Krkljus, I.; Hirscher, M.; Mugnaioli, E.; Kolb, U.; Hanss, J.; Volkmer, D. *Chem. Eur. J.* **2011**, *17*, 1837.
(275) Yan, Y.; Telepeni, I.; Yang, S.; Lin, X.; Kockelmann, W.; Dailly, A.; Blake, A. J.; Lewis, W.; Walker, G. S.; Allan, D. R.; Barnett, S. A.; Champness, N. R.; Schröder, M. *J. Am. Chem. Soc.* **2010**, *132*, 4092.
(276) Zhao, D.; Yuan, D. Q.; Sun, D. F.; Zhou, H. C. *J. Am. Chem. Soc.* **2009**, *131*, 9186.
(277) *Metal-Organic Frameworks: Design and Application*; MacGillivray, L. R., Ed.; Wiley: Hoboken, NJ, 2010.
(278) Rosi, N. L.; Eddaoudi, M.; Kim, J.; O'Keeffe, M.; Yaghi, O. M. *Angew. Chem., Int. Ed.* **2002**, *41*, 294.
(279) Batten, S. R. *CrystEngComm* **2001**, *3*, 67.
(280) Batten, S. R.; Robson, R. *Angew. Chem., Int. Ed.* **1998**, *37*, 1460.
(281) Farha, O. K.; Malliakas, C. D.; Kanatzidis, M. G.; Hupp, J. T. *J. Am. Chem. Soc.* **2010**, *132*, 950.
(282) Zhang, J.; Wojtas, L.; Larsen, R. W.; Eddaoudi, M.; Zaworotko, M. J. *J. Am. Chem. Soc.* **2009**, *131*, 17040.
(283) Shekhah, O.; Wang, H.; Paradinas, M.; Ocal, C.; Schupbach, B.; Terfort, A.; Zacher, D.; Fischer, R. A.; Woll, C. *Nat. Mater.* **2009**, *8*, 481.
(284) Rowsell, J. L.; Yaghi, O. M. *Angew. Chem., Int. Ed.* **2005**, *44*, 4670.
(285) Kanoo, P.; Matsuda, R.; Higuchi, M.; Kitagawa, S.; Maji, T. K. *Chem. Mater.* **2009**, *21*, 5860.
(286) Ryan, P.; Broadbelt, L. J.; Snurr, R. Q. *Chem. Commun.* **2008**, *44*, 4132.
(287) Bae, Y.-S.; Snurr, R. Q. *Microporous Mesoporous Mater.* **2010**, *132*, 300.
(288) Peterson, V. K.; Liu, Y.; Brown, C. M.; Kepert, C. J. *J. Am. Chem. Soc.* **2006**, *128*, 15578.
(289) Xiao, B.; Wheatley, P. S.; Zhao, X.; Fletcher, A. J.; Fox, S.; Rossi, A. G.; Megson, I. L.; Bordiga, S.; Regli, L.; Thomas, K. M.; Morris, R. E. *J. Am. Chem. Soc.* **2007**, *129*, 1203.
(290) S.; Deng, W.-Q.; Goddard, W. A. *Angew. Chem., Int. Ed.* **2007**, *46*, 6289.
(291) Dincă, M.; Long, J. R. *J. Am. Chem. Soc.* **2005**, *127*, 9376.
(292) Liu, Y.; Kravtsov, V. C.; Larsen, R.; Eddaoudi, M. *Chem. Commun.* **2006**, *42*, 1488.
(293) Mulfort, K. L.; Hupp, J. T. *Inorg. Chem.* **2008**, *47*, 7936.
(294) Mulfort, K. L.; Wilson, T. M.; Wasielewski, M. R.; Hupp, J. T. *Langmuir* **2009**, *25*, 503.
(295) Blomqvist, A.; Araffljo, C. M.; Srepusharawoot, P.; Ahuja, R. *Proc. Natl. Acad. Sci. U.S.A.* **2007**, *104*, 20173.
(296) Han, S. S.; Goddard, W. A. *J. Am. Chem. Soc.* **2007**, *129*, 8422.
(297) Han, S. S.; Goddard, W. A. *J. Phys. Chem. C* **2008**, *112*, 13431.
(298) Han, S. S.; Choi, S.-H.; Goddard, W. A. *J. Phys. Chem. C* **2011**, *115*, 3507.
(299) Mavrandonakis, A.; Klopper, W. *J. Phys. Chem. C* **2008**, *112*, 11580.
(300) Dalach, P.; Frost, H.; Snurr, R. Q.; Ellis, D. E. *J. Phys. Chem. C* **2008**, *112*, 9278.
(301) Mavrandonakis, A.; Tylianakis, E.; Stubos, A. K.; Froudakis, G. E. *J. Phys. Chem. C* **2008**, *112*, 7290.
(302) Huang, B.; Lee, H.; Duan, W.; Ihm, J. *Appl. Phys. Lett.* **2008**, *93*, 63107.
(303) Choi, Y. J.; Lee, J. W.; Choi, J. H.; Kang, J. K. *Appl. Phys. Lett.* **2008**, *92*, 173102.
(304) Himsl, D.; Wallacher, D.; Hartmann, M. *Angew. Chem., Int. Ed.* **2009**, *48*, 4639.
(305) Klontzas, E.; Mavrandonakis, A.; Tylianakis, E.; Froudakis, G. E. *Nano Lett.* **2008**, *8*, 1572.
(306) Botas, J. A.; Calleja, G.; Sánchez-Sánchez, M.; Orcajo, M. G. *Langmuir.* **2010**, *26*, 5300.
(307) Srinivas, S. T.; Rao, P. K. *J. Catal.* **1994**, *148*, 470.
(308) Li, Y.; Yang, R. T. *J. Am. Chem. Soc.* **2006**, *128*, 8136.
(309) Liu, Y.-Y.; Zeng, J.-L.; Zhang, J.; Xu, F.; Sun, L.-X. *Int. J. Hydrogen. Energy.* **2007**, *32*, 4005.
(310) Wang, L.; Stuckert, N. R.; Chen, H.; Yang, R. T. *J. Phys. Chem. C* **2011**, *115*, 4793.
(311) Proch, S.; Herrmannsdofer, J.; Kempe, R.; Kern, C.; Jess, A.; Seyfarth, L.; Senker, J. *Chem.—Eur. J.* **2008**, *14*, 8204.
(312) Liu, Y. Y.; Zhang, J.; Zeng, J. L.; Chu, H. L.; Xu, F.; Sun, L. X. *Chin. J. Catal.* **2008**, *29*, 655.
(313) Kosal, M. E.; Chou, J.-H.; Wilson, S. R.; Suslick, K. S. *Nat. Mater.* **2002**, *1*, 118.
(314) Zimmer, B.; Hutin, M.; Bulach, V.; Hosseini, M. W.; Cian, A. D.; Kyritsakas, N. *New. J. Chem.* **2002**, *26*, 1532.
(315) Deiters, E.; Bulach, V.; Hosseini, M. W. *Chem. Commun.* **2005**, 3906.
(316) Kuhn, E.; Bulach, V.; Hosseini, M. W. *Chem. Commun.* **2008**, 5104.
(317) Ohmura, T.; Usuki, A.; Fukumori, K.; Ohta, T.; Ito, M.; Tatsumi, K. *Inorg. Chem.* **2006**, *45*, 7988.
(318) Alkordi, M. H.; Liu, Y. L.; Larsen, R. W.; Eubank, J. F.; Eddaoudi, M. *J. Am. Chem. Soc.* **2008**, *130*, 12639.
(319) Chen, L.; Yang, Y.; Jiang, D. L. *J. Am. Chem. Soc.* **2010**, *132*, 9138.
(320) Farha, O. K.; Shultz, A. M.; Sarjeant, A. A.; Nguyen, S. T.; Hupp, J. T. *J. Am. Chem. Soc.* **2011**, *133*, 5652.
(321) Song, F.; Wang, C.; Falkowski, J. M.; Ma, L.; Lin, W. *J. Am. Chem. Soc.* **2010**, *132*, 15390.
(322) Kitaura, R.; Onoyama, G.; Sakamoto, H.; Matsuda, R.; Noro, S.; Kitagawa, S. *Angew. Chem., Int. Ed.* **2004**, *43*, 2684.
(323) Wu, H.-B.; Wang, Q.-M. *Angew. Chem., Int. Ed.* **2009**, *48*, 7343.
(324) Sakamoto, H.; Matsuda, R.; Bureekaew, S.; Tanaka, D.; Kitagawa, S. *Chem.—Eur. J.* **2009**, *15*, 4985.
(325) Roesky, P. W.; Bhunia, A.; Lan, Y.; Powell, A. K.; Kureti, S. *Chem. Commun.* **2011**, *47*, 2035.
(326) Shultz, A. M.; Farha, O. K.; Adhikari, D.; Sarjeant, A. A.; Hupp, J. T.; Nguyen, S. T. *Inorg. Chem.* **2011**, *50*, 3174.
(327) Shultz, A. M.; Sarjeant, A. A.; Farha, O. K.; Hupp, J. T.; Nguyen, S. T. *J. Am. Chem. Soc.* **2011**, *133*, 13252.
(328) Wu, C.-D.; Hu, A.; Zhang, L.; Lin, W. *J. Am. Chem. Soc.* **2005**, *127*, 8940.
(329) Oisaki, K.; Li, Q.; Furukawa, H.; Czaja, A. U.; Yaghi, O. M. *J. Am. Chem. Soc.* **2010**, *132*, 9262.
(330) Bloch, E. D.; Britt, D.; Lee, C.; Doonan, C.; Uribe-Romo, F. J.; Furukawa, H.; Long, J. R.; Yaghi, O. M. *J. Am. Chem. Soc.* **2010**, *132*, 14382.

(331) Gadzikwa, T.; Farha, O. K.; Mulfort, K. L.; Hupp, J. T.; Nguyen, S. T. *Chem. Commun.* **2009**, *45*, 3720.
(332) Doonan, C. J.; Morris, W.; Furukawa, H.; Yaghi, O. M. *J. Am. Chem. Soc.* **2009**, *131*, 9492.
(333) Everett, D. H.; Powl, J. C. *J. Chem. Soc., Faraday Trans.* **1976**, *72*, 619.
(334) Zhao, D.; Yan, D.; Zhou, H.-C. *Energy Environ. Sci.* **2008**, *1*, 225.
(335) Hubner, O.; Gloss, A.; Fichtner, M.; Klopper, W. *J. Phys. Chem. A* **2004**, *108*, 3019.
(336) Li, Y.; Yang, R. T. *Langmuir* **2007**, *23*, 12937.
(337) Millange, F.; Serre, C.; Guillou, N.; Férey, G.; Walton, R. I. *Angew. Chem., Int. Ed.* **2008**, *47*, 4100.
(338) Dybtsev, D. N.; Yutkin, M. P.; Samsonenko, D. G.; Fedin, V. P.; Nuzhdin, A. L.; Bezrukov, A. A.; Bryliakov, K. P.; Talsi, E. P.; Belosludov, R. V.; Mizuseki, H.; Kawazoe, Y.; Subbotin, O. S.; Belosludov, V. R. *Chem.—Eur. J.* **2010**, *16*, 10348.
(339) Nelson, A. P.; Farha, O. K.; Mulfort, K. L.; Hupp, J. T. *J. Am. Chem. Soc.* **2009**, *131*, 458.
(340) Ma, L.; Jin, A.; Xie, Z.; Lin, W. *Angew. Chem., Int. Ed.* **2009**, *48*, 9905.
(341) Broom, D. P. *Int. J. Hydrogen Energy* **2007**, *32*, 4871.
(342) Belmabkhout, Y.; Frere, M.; Weireld, G. D. *Meas. Sci. Technol.* **2004**, *15*, 848.
(343) Yildirim, T.; Hartman, M. R. *Phys. Rev. Lett.* **2005**, *95*, 215504.
(344) Mulder, F. M.; Assfour, B.; Huot, J.; Dingemans, T. J.; Wagemaker, M.; Ramirez-Cuesta, A. J. *J. Phys. Chem. C* **2010**, *114*, 10648.
(345) Wu, H.; Zhou, W.; Yildirm, T. *J. Am. Chem. Soc.* **2007**, *129*, 5314.
(346) Roswell, J. L. C.; Eckert, J.; Yaghi, O. M. *J. Am. Chem. Soc.* **2005**, *127*, 14904.
(347) Bordiga, S.; Vitillo, J.; Ricchiardi, G.; Regli, L.; Cocina, D.; Zecchina, A.; Arstad, B.; Bjorgen, M.; Hafizovic, J.; Lillerud, K. P. *J. Phys. Chem. B* **2005**, *109*, 18237.
(348) Bordiga, S.; Regli, L.; Bonino, F.; Groppo, E.; Lamberti, C.; Xiao, B.; Wheatley, P. S.; Morris, R. E.; Zecchina., A. *Phys. Chem. Chem. Phys.* **2007**, *9*, 2676.
(349) Nijem, N.; Veyan, J.-F.; Kong, L.; Li, K.; Pramanik, S.; Zhao, Y.; Li, J.; Langreth, D.; Chabal, Y. J. *J. Am. Chem. Soc.* **2010**, *132*, 1654.
(350) Sun, Y. Y.; Kim, Y. H.; Zhang, S. B. *J. Am. Chem. Soc.* **2007**, *129*, 12606.
(351) Vitillo, J. G.; Regli, L.; Chavan, S.; Ricchiardi, G.; Spoto, G.; Dietzel, P. D. C.; Bordiga, S.; Zecchina, A. *J. Am. Chem. Soc.* **2008**, *130*, 8386.
(352) Kang, I. J.; Khan, N. A.; Haque, E.; Jhung, S. H. *Chem. Eur. J.* **2011**, *17*, 6437.
(353) Ma, D.; Li, Y.; Li, Z. *Chem. Commun.* **2011**, *47*, 7377.
(354) Wu, T.; Shen, L.; Luebbers, M.; Hu, C.; Chen, Q.; Ni, Z.; Masel, R. I. *Chem. Commun.* **2010**, *46*, 6120.
(355) Nguyen, J. G.; Cohen, S. M. *J. Am. Chem. Soc.* **2010**, *132*, 4560.

DOI: 10.1002/chem.201003376

A Highly Porous Metal–Organic Framework: Structural Transformations of a Guest-Free MOF Depending on Activation Method and Temperature

Hye Jeong Park, Dae-Woon Lim, Woo Seung Yang, Tae-Rog Oh, and Myunghyun Paik Suh*[a]

Abstract: A doubly interpenetrating porous metal–organic framework (**SNU-77**) has been synthesized from the solvothermal reaction of the extended carboxylic acid tris(4′-carboxybiphenyl)amine (H_3TCBPA) and $Zn(NO_3)_2{\cdot}6H_2O$ in *N*,*N*-dimethylacetamide (DMA). **SNU-77** undergoes single-crystal-to-single-crystal transformations during various activation processes, such as room-temperature evacuation, supercritical CO_2 drying, and high temperature evacuation, to afford **SNU-77R**, **SNU-77S**, and **SNU-77H**, respectively. These guest-free MOFs exhibited different fine structures with different window shapes and different effective window sizes at room temperature. Variable-temperature synchrotron single-crystal X-ray analyses reveal that the guest-free structure is also affected by changes in temperature. Despite the different fine structures, **SNU-77R**, **SNU-77S**, and **SNU-77H** show similar gas sorption properties due to the nonbreathing nature of the framework and an additional structural change upon cooling to cryogenic gas sorption temperature. **SNU-77H** exhibits a large surface area (BET, 3670 $m^2 g^{-1}$), a large pore volume (1.52 $cm^3 g^{-1}$), and exceptionally high uptake capacities for N_2, H_2, O_2, CO_2, and CH_4 gases.

Keywords: adsorption · gas storage · metal–organic frameworks · structure elucidation · X-ray diffraction

Introduction

Porous metal–organic frameworks (MOFs) have received considerable attention because of their diverse chemical compositions and architectures as well as their potential applications in gas storage and separation,[1–5] catalysis,[6,7] and in the fabrication of metal nanoparticles.[8–11] The potential applications of MOFs are attributed to their permanent microporosity and large internal surface areas. It has been reported that the gas sorption capacities of desolvated MOFs are significantly affected by the method of preparation and the handling of the as-synthesized samples, such as reaction temperature and heating time during the solvothermal synthesis as well as the exposure of the products to air.[12,13] Furthermore, it has recently been reported that MOFs activated by treatment with supercritical CO_2 and freeze-drying adsorb much greater amounts of gases than those activated by thermal or room-temperature evacuation.[14,15] These observations have been explained by the inhibition of the collapse of interparticle mesopores and the breathing effect of the framework, respectively. However, there has been no clear experimental evidence showing how the structure of the framework changes depending on the activation method, although this must be an important factor determining the gas sorption properties. In particular, the compounds used in those experiments contained solvent molecules coordinated to the metal centers. Therefore, whether the coordinated solvent molecules are removed or not during the activation must affect the gas sorption properties, but this was not considered by the authors.[14,15] The single-crystal structures have not revealed how the structure of a guest-free MOF is changed by a change in temperature, although there have been some reports of temperature-dependent structural transformations of guest-free MOFs as evidenced from the powder X-ray diffraction patterns.[16,17]

To investigate how the guest-free structures of a MOF vary depending on the activation method and temperature, the crystal should retain its single-crystal nature throughout the process, but this rarely happens. Even though a considerable number of studies have been conducted on single-crystal-to-single-crystal (SCSC) transformations of MOFs,[8,18–22] to the best of our knowledge there has been no report of a single-crystal analysis revealing how the framework structure changes depending on the activation method.

In this study we have synthesized a new Zn_4O-type MOF that cannot coordinate solvent molecules to eliminate the possible ambiguities arising from the removal of coordinated solvent molecules during the activation process. We expected that the Zn_4O-type MOF may maintain its single-crystal nature during the various activation processes because of the rather rigid nature of the (6,3)-connected net. In the synthesis of the MOF, we have used an elongated organic building block, tris(4′-carboxybiphenyl)amine (H_3TCBPA), because a higher surface area can be achieved for an MOF constructed of an elongated organic building block.[23–25]

[a] H. J. Park, D.-W. Lim, W. S. Yang, T.-R. Oh, Prof. Dr. M. P. Suh
Department of Chemistry, Seoul National University
Seoul 151-747 (Republic of Korea)
Fax: (+82) 288-68-516
E-mail: mpsuh@snu.ac.kr

Supporting information for this article is available on the WWW under http://dx.doi.org/10.1002/chem.201003376.

Herein we report a porous MOF, $[Zn_4O(TCBPA)_2]\cdot 19DMA\cdot 4H_2O$ (**SNU-77**, DMA = *N*,*N*-dimethylacetamide), which undergoes SCSC transformations during various activation processes, such as room-temperature evacuation, supercritical CO_2 drying, and high-temperature evacuation, to afford **SNU-77R**, **SNU-77S**, and **SNU-77H**, respectively. The X-ray crystal data collected at room temperature for the three different activated samples indicate that the molecular components of the framework undergo rotational rearrangements and that the extent of the rearrangements depend significantly on the activation method to afford different effective window sizes and shapes. Synchrotron single-crystal X-ray studies on **SNU-77R** with sequential temperature changes (293→373→293→100 K) indicate that the structure of the guest-free framework also depends on the temperature. Despite the different fine structures at room temperature, the guest-free samples of **SNU-77** exhibit similar gas sorption properties due to the nonbreathing nature of the framework and additional structural transformation at the cryogenic gas adsorption temperature. **SNU-77H** shows an exceptionally large surface area (Langmuir, 4180 m^2g^{-1}; BET, 3670 m^2g^{-1}), large pore volume (1.52 cm^3g^{-1}), and high uptake capacities for N_2, H_2, O_2, CO_2, and CH_4 gases.

Results and Discussion

Synthesis and X-ray crystal structure of $[Zn_4O(TCBPA)_2]\cdot 19DMA\cdot 4H_2O$ (SNU-77): Brown crystals of **SNU-77** were obtained by heating a mixture of $Zn(NO_3)_2\cdot 6H_2O$ and H_3TCBPA in DMA at 115°C for 2 days. Thermogravimetric analysis (TGA) reveals 53.6% weight loss between 25 and 400°C, which corresponds to the loss of all the guest solvent molecules (calcd 53.8%), and no chemical decomposition occurs below 430°C (Figure S1). The X-ray crystal structure (Figure 1) indicates that a $Zn_4O(CO_2)_6$ cluster is formed as an octahedral secondary building unit (SBU), each of which is linked to six trigonal units of $TCBPA^{3-}$, giving rise to a (6,3)-connected net that mimics a PdF_2 net topology.[22,26] The network is doubly interpenetrating. In **SNU-77**, two crystallographically different $TCBPA^{3-}$ units, TCBPA1 and TCBPA2, are located in *trans* positions around a Zn_4O cluster and show a dihedral angle of 79.2(2)° between the outer phenyl rings of the ligand. The $TCBPA^{3-}$ unit resembles a propeller because the inner phenyl rings are tilted relative to each other, and the central nitrogen is sp^2-hybridized instead of sp^3-hybridized with C–N–C angles of approximately 120°. Edge-to-face π–π interactions exist between two interpenetrating nets [the shortest C–C distance, 3.675(9) Å; dihedral angle, 53.3(3)°; Figure S2]. Three-dimensional channels with an effective window size of 4.0×4.9 Å are generated along the three orthogonal directions. Because the guest molecules of **SNU-77** could not be located due to thermal disorder, the formula of **SNU-77** was determined on the basis of the IR, elemental analysis, and TGA data.

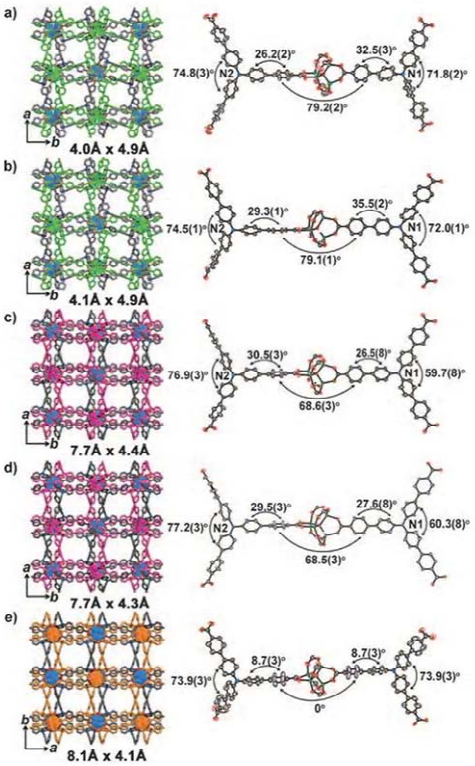

Figure 1. X-ray crystal structures of a) **SNU-77**, b) **SNU-77′**, c) **SNU-77R**, d) **SNU-77S**, and e) **SNU-77H**. Doubly interpenetrating networks are represented in two different colors. The numbers below each structure represent the effective aperture size.

Single-crystal-to-single-crystal transformations of SNU-77 through various activation processes: To remove the guest solvent molecules of **SNU-77**, we employed three different activation methods: 1) Guest–solvent exchange with toluene followed by evacuation at room temperature, 2) the direct activation of **SNU-77** by treatment with supercritical CO_2, and 3) evacuation of the guest-exchanged sample at high temperature. These processes yielded **SNU-77R**, **SNU-77S**, and **SNU-77H**, respectively. The chemical formulae of **SNU-77R**, **SNU-77S**, and **SNU-77H** are $[Zn_4O(TCBPA)_2]$, as characterized by IR spectroscopy, elemental analysis, and TGA. During these activation processes, the MOFs retained their single-crystal nature and the X-ray crystal structures of three different guest-free samples were elucidated (Figure 1). The X-ray crystal data for **SNU-77R**, **SNU-77S**, and **SNU-77H** are summarized in Table 1.

Table 1. Crystallographic data for **SNU-77**, **SNU-77′**, **SNU-77R**, **SNU-77S**, and **SNU-77H**.

	SNU-77[a]	**SNU-77′**[a]	**SNU-77R**	**SNU-77S**	**SNU-77H**[a]
formula	$Zn_4C_{78}H_{48}N_2O_{13}$	$Zn_4C_{78}H_{48}N_2O_{13}$	$Zn_4C_{78}H_{48}N_2O_{13}$	$Zn_4C_{78}H_{48}N_2O_{13}$	$Zn_4C_{78}H_{48}N_2O_{13}$
crystal system	cubic	cubic	cubic	cubic	cubic
space group	*Pa*-3	*Pa*-3	*Pa*-3	*Pa*-3	*Ia*-3
M_r	1482.76	1482.76	1482.76	1482.76	1482.76
a [Å]	32.6570(9)	32.5926(6)	32.407(5)	32.4053(7)	32.2713(18)
V [Å^3]	34828.0(17)	34622.4(11)	34034(9)	34028.9(13)	33609(3)
Z	8	8	8	8	8
ρ_{calcd} [g cm^{-3}]	0.566	0.569	0.579	0.579	0.586
T [K]	293	293	293	293	293
λ [Å]	0.71073	0.71073	0.71073	0.71073	0.71073
μ [mm^{-1}]	0.570	0.574	0.584	0.584	0.591
GOF (F^2)	0.703	0.796	1.072	1.053	0.868
R_1,[b] wR_2[c] [$I > 2\sigma(I)$]	0.0890, 0.2052	0.0522, 0.1337	0.0925, 0.2503	0.0883, 0.2459	0.0957, 0.2470
R_1,[b] wR_2[c] (all data)	0.2182, 0.2327	0.1222, 0.1465	0.2025, 0.3318	0.2219, 0.3348	0.2028, 0.2852

[a] The residual electron densities were flattened by using the SQUEEZE option of PLATON. [b] $R = \Sigma||F_o| - |Fc||/\Sigma|F_o|$. [c] $wR(F^2) = [\Sigma w(F_o^2 - F_c^2)^2/\Sigma w(F_o^2)^2]^{1/2}$ in which $w = 1/[\sigma^2(F_o^2) + (0.1160P)^2 + (0.000)P]$, $P = (F_o^2 + 2F_c^2)/3$ for **SNU-77**, $w = 1/[\sigma^2(F_o^2) + (0.0741P)^2 + (0.000)P]$, $P = (F_o^2 + 2F_c^2)/3$ for **SNU-77′**, $w = 1/[\sigma^2(F_o^2) + (0.1696P)^2 + (26.59)P]$, $P = (F_o^2 + 2F_c^2)/3$ for **SNU-77R**, $w = 1/[\sigma^2(F_o^2) + (0.1776P)^2 + (4.96)P]$, $P = (F_o^2 + 2F_c^2)/3$ for **SNU-77S**, and $w = 1/[\sigma^2(F_o^2) + (0.1569P)^2 + (0.000)P]$, $P = (F_o^2 + 2F_c^2)/3$ for **SNU-77H**.

When crystals of **SNU-77** were immersed in toluene for 24 h, the DMA guest molecules were exchanged with toluene to yield $[Zn_4O(TCBPA)_2]\cdot 14PhCH_3\cdot 3H_2O$ (**SNU-77′**), as characterized by IR spectroscopy, elemental analysis, and TGA. The X-ray crystal structure of **SNU-77′** is very similar to that of **SNU-77** (Figure 1).

When **SNU-77′** was activated at room temperature under a pressure of 10^{-5} torr for 24 h, $[Zn_4O(TCBPA)_2]$ (**SNU-77R**) resulted. The X-ray diffraction data of **SNU-77R** collected at room temperature indicates that many of its key dihedral angles are different to those of **SNU-77** and **SNU-77′**. In particular, the dihedral angle between the two outer phenyl rings of the ligands located in the *trans* positions around the Zn_4O cluster is 68.6(3)° compared with 79.1(1)° in **SNU-77′**, and the dihedral angles between the inner phenyl rings of TCBPA1 and TCBPA2 are 76.9(3) and 59.7(8)°, respectively, compared with 74.5(1) and 72.0(1)° in **SNU-77′** (Figure 1). These angles indicate that the phenyl rings in $TCBPA^{3-}$ in the framework rotate upon removal of the guests even at room temperature. **SNU-77R** exhibits edge-to-face π–π interactions between two interpenetrating nets [the shortest C–C distance, 3.806(30) Å], but the dihedral angle [24.6(7)°] is remarkably different to that in **SNU-77′** [48.3(1)°; Figure S2]. Due to these rotational rearrangements, the shape of the channel is different to that of **SNU-77′** and the effective window size is enlarged to 7.7×4.4 Å compared with 4.1×4.9 Å for **SNU-77′**. A few examples of enlarged pore windows on desolvation have been reported in the literature.[27,28] The void volume of **SNU-77R** estimated by PLATON[29] is 69.9% (1.21 cm^3 g^{-1}), similar to the value of 70.3% (1.24 cm^3 g^{-1}) for **SNU-77**.

Supercritical drying is a common washing method in polymer synthesis and aerogel production. Recently, supercritical CO_2 drying has been applied to MOFs as an efficient activation method that leads to increased surface areas of the MOFs.[14] In this study, when single crystals of **SNU-77** were activated by treatment with supercritical CO_2 (see the Experimental Section), a single crystal of $[Zn_4O(TCBPA)_2]$ (**SNU-77S**) resulted. The X-ray crystal structure of **SNU-77S** is similar to that of **SNU-77R**, as shown in Figure 1, which indicates that treatment with supercritical CO_2 is as mild as room-temperature evacuation and induces rather small structural rearrangements.

Interestingly, however, $[Zn_4O(TCBPA)_2]$ (**SNU-77H**), which was obtained by heating **SNU-77′** at 110 °C under a pressure of 10^{-5} torr for 2 h, exhibits a significantly different structure to those of **SNU-77**, **SNU-77′**, **SNU-77R**, and **SNU-77S**. The crystal space group is *Ia*-3, compared with *Pa*-3 for the others, and only one kind of $TCBPA^{3-}$ unit exists. Most importantly, the $TCBPA^{3-}$ unit within the structure exhibits large rotational rearrangements: The dihedral angle between the outer phenyl rings of the biphenyl groups located in the *trans* positions around the Zn_4O cluster is 0.0°, compared with 79.1(1)° in **SNU-77′** and 68.6(3)° in **SNU-77R**, and the dihedral angles between the two phenyl rings of the biphenyl groups in $TCBPA^{3-}$ are 8.7(3)°, compared with an average of 30.5(1)° in **SNU-77′** and an average of 30.3(3)° in **SNU-77R** (Figure 1). Face-to-face π–π interactions exist between two interpenetrating nets in **SNU-77H** [the shortest C–C distance, 3.693(2) Å; dihedral angle, 8.8(4)°], in contrast to edge-to-face π–π interactions in the others (Figure S2). The effective window size (8.1×4.1 Å) is larger than those of **SNU-77′**, **SNU-77R**, and **SNU-77S**. The void volume of **SNU-77H** estimated by PLATON[29] is 69.1% (1.18 cm^3 g^{-1}).

The major structural differences between **SNU-77′** (=**SNU-77**), **SNU-77R** (=**SNU-77S**), and **SNU-77H** are the effective window sizes and shapes, which are determined by the dihedral angles between the phenyl rings around a Zn_4O cluster (Table 2), although they have similar cell parameters and only 2.3–3.0% differences in cell volumes. **SNU-77R** and **SNU-77S** have intermediate structures between **SNU-77′** and **SNU-77H**. Despite the different fine structures revealed by the single-crystal X-ray data, the simulated powder X-ray diffraction (PXRD) patterns of **SNU-77R**, **SNU-77S**, and **SNU-77H** are very similar: Only the small peaks at $2\theta = 9.4$, 10.1, and 11.2° for **SNU-77** and **SNU-77′** are significantly weaker in the patterns of **SNU-77R** and **SNU-77S**, and they disappear in **SNU-77H** (Figure S3). This indicates that the rearrangements of the molecular components can barely be recognized by the PXRD patterns unless extremely careful attention is paid to the very small peaks.

Table 2. Comparison of crystal structures.

MOF	Dihedral angles between the phenyl rings [°]			π–π interaction	
	Biphenyls of $TCBPA^{3-}$	Inner rings of $TCBPA^{3-}$	Outer rings of $TCBPA^{3-}$[a]	Shortest C–C distance [Å]	Dihedral angle [°]
SNU-77	26.2(2), 32.5(3)	71.8(2), 74.8(3)	79.2(2)	3.675(9)	53.3(3)
SNU-77′	29.3(1), 35.5(2)	72.0(1), 74.5(1)	79.1(1)	3.559(4)	48.3(1)
SNU-77R	26.5(5), 30.5(3)	59.7(8), 76.9(3)	68.6(3)	3.806(30)	24.6(7)
SNU-77S	27.6(8), 29.5(3)	60.3(8), 77.2(3)	68.5(3)	3.787(32)	24.1(7)
SNU-77H	8.7(3)	73.9(3)	0.0(0)	3.693(2)	8.8(4)
SNU-77R					
293 K	29.8(2), 30.5(4)	64.1(4), 76.7(2)	79.2(2)	3.504(7)	34.7(2)
373 K	6.4(3)	74.8(2)	0.0(4)	3.990(12)	10.4(3)
293 K (2nd)	4.8(3)	74.8(2)	0.0(4)	3.926(12)	7.7(4)
100 K	34.3(1), 41.7(1)	65.6(1), 78.0(1)	76.6(1)	3.482(4)	37.5(1)

[a] Outer rings of two $TCBPA^{3-}$ located in *trans* positions around the Zn_4O cluster.

Structural transformations of a guest-free MOF upon temperature change: Previously we reported that the phenyl rings of NTB^{3-} in $[Zn_4O(NTB)_2]$, where NTB is 4,4′,4″-nitrilotrisbenzoate, underwent rotational motion when the as-synthesized MOF was activated at 400 °C and a pressure of 10^{-5} torr.[22] However, we could not verify whether the rotational motion occurred as a result of the applied heat or simply by removal of the guest molecules because we failed to exchange all the guest molecules with a lower-boiling-point solvent to obtain the crystal that could be activated at room temperature. The results presented herein indicate that the degree of rotational movement of the molecular components in the crystal actually depends on the activation temperature. On the basis that all X-ray diffraction data were collected at room temperature, including those of **SNU-77H**, it is evident that once the molecular components have rearranged during the removal of guests at high temperature, their positions do not easily change to those of **SNU-77R**, even after cooling to room temperature. This prompted us to investigate whether the structure of a guest-free MOF depends on the temperature or not.

We performed synchrotron single-crystal X-ray diffraction studies on **SNU-77R** by changing the temperature sequentially from 293 to 373 K, and then to 293 and 100 K (Table 3). As shown in Figure 2, on heating **SNU-77R** at 373 K for 2 h, the structure becomes similar to that of **SNU-77H**. This implies that the previously mentioned structural transformation of **SNU-77′** to **SNU-77R** is triggered mainly by guest removal and that of **SNU-77R** to **SNU-77H** is induced by thermal energy. Interestingly, cooling from 373 to 293 K for 2 h did not reverse the structure of **SNU-77H** to that of **SNU-77R**. However, on further cooling to 100 K, the structure was reversed and changed further. Figures 1 and 2 suggest that as the guests are removed and the temperature is elevated, decreases are observed in the dihedral angles between the outer phenyl rings of the biphenyl moieties located in the *trans* positions around the $Zn_4O(CO_2)_6$ unit as well as between the two phenyl rings of the biphenyl groups in $TCBPA^{3-}$. To the best of our knowledge, this is the first report of single-crystal structures revealing the temperature-induced structural transformation of a guest-free MOF rather than powder diffraction analyses.[16,17] The results suggest that at the cryogenic temperature of gas sorption measurements, the structures of **SNU-77R**, **SNU-77S**, and **SNU-77H** would become similar to each other as a result of temperature-induced structural transformations.

Table 3. Crystallographic data for **SNU-77R** upon temperature change.

	293 K	373 K	293 K (2nd)	100 K
formula	$Zn_4C_{78}H_{48}N_2O_{13}$	$Zn_4C_{78}H_{48}N_2O_{13}$	$Zn_4C_{78}H_{48}N_2O_{13}$	$Zn_4C_{78}H_{48}N_2O_{13}$
crystal system	cubic	cubic	cubic	cubic
space group	*Pa*-3	*Ia*-3	*Ia*-3	*Pa*-3
M_r	1482.76	1482.76	1482.76	1482.76
a [Å]	32.387(5)	32.374(5)	32.359(5)	32.443(4)
V [Å^3]	33971(9)	33930(9)	33883(9)	34148(7)
Z	8	8	8	8
ρ_{calcd} [g cm^{-3}]	0.580	0.580	0.581	0.577
T [K]	293	373	293	100
λ [Å]	0.77000	0.77000	0.77000	0.77000
μ [mm^{-1}]	0.585	0.585	0.586	0.582
GOF (F^2)	1.103	1.106	1.072	1.104
R_1,[a] wR_2[b] [$I>2\sigma(I)$]	0.0725, 0.2330	0.0956, 0.2993	0.1071, 0.3486	0.0740, 0.2153
R_1,[a] wR_2[b] (all data)	0.0993, 0.2568	0.1519, 0.3414	0.1426, 0.3826	0.0831, 0.2218

[a] $R=\Sigma||F_o|-|F_c||/\Sigma|F_o|$. [b] $wR(F^2)=[\Sigma w(F_o^2-F_c^2)^2/\Sigma w(F_o^2)^2]^{1/2}$ in which $w=1/[\sigma^2(F_o^2)+(0.1521P)^2+(10.47)P]$, $P=(F_o^2+2F_c^2)/3$ for the data at 293 K, $w=1/[\sigma^2(F_o^2)+(0.1879P)^2+(9.08)P]$, $P=(F_o^2+2F_c^2)/3$ for the data at 373 K, $w=1/[\sigma^2(F_o^2)+(0.2000P)^2+(0.00)P]$, $P=(F_o^2+2F_c^2)/3$ for the data at 293 K (2nd), and $w=1/[\sigma^2(F_o^2)+(0.1577P)^2+(0.00)P]$, $P=(F_o^2+2F_c^2)/3$ for the data at 100 K.

Luminescence properties: The solid samples of **SNU-77** and **SNU-77′** exhibit photoluminescence at $\lambda_{max}=477$ and 488 nm, respectively, whereas **SNU-77R**, **SNU-77S**, and **SNU-77H** show photoluminescence at $\lambda_{max}=512$, 510, and 506 nm, respectively, upon photoexcitation at 410 nm (Figure 3). This indicates that the photoluminescence of the host framework is strongly dependent upon the presence and absence of the guest solvent molecules as well as the type of guests, but scarcely on the rearrangement of the host framework caused by different activation methods. The luminescence seems to originate from the ligand because the luminescent spectra are comparable to that of Na_3TCBPA, which emits at 478 nm.

Gas sorption properties of SNU-77R, SNU-77S, and SNU-77H: The gas sorption isotherms were measured for N_2, H_2, O_2, CO_2, and CH_4 gases (Table 4). Because zinc MOFs con-

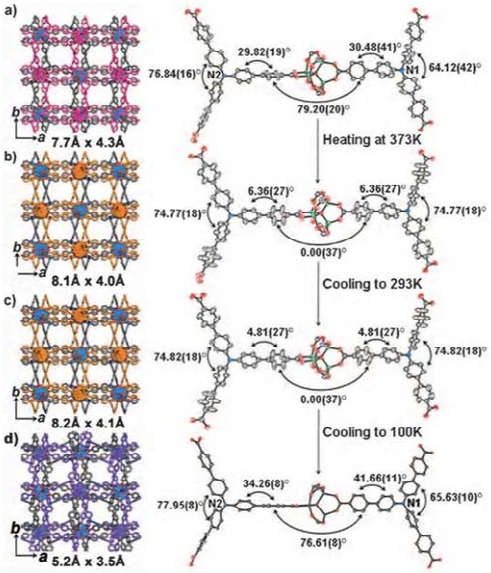

Figure 2. Structural transformations of **SNU-77R** upon sequential changes in temperature: a) 293, b) 373, c) 293 (2nd), and d) 100 K. The ORTEP views are drawn with the thermal ellipsoids at the 30% probability level. Zn, green; O, red; N, blue; C, black.

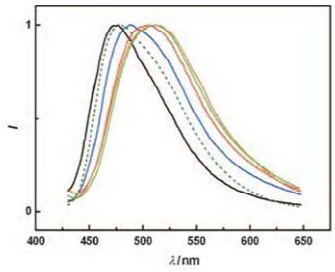

Figure 3. Luminescence spectra with normalized intensity: **SNU-77** (black), **SNU-77′** (blue), **SNU-77R** (orange), **SNU-77S** (green), **SNU-77H** (red), and solid Na_3TCBPA (olive) upon photoexcitation at 410 nm.

structed of carboxylates are frequently air- or moisture-sensitive and the gas sorption capacities decrease on exposure to air,[12,13] we took special care in handling the samples (see the Experimental Section).

In contrast to previous reports that treatment with supercritical CO_2 and freeze-drying significantly enhanced the gas adsorption capacities of MOFs compared with thermal or room-temperature evacuation methods,[14,15] all the desolvated solids of the present MOF show similar gas sorption properties (Figure 4). This can be attributed to the fact that the present doubly interpenetrating Zn_4O-type MOF exhibits no breathing effect and only its organic components perform rotational motion. Furthermore, all of them should have similar structures at the gas sorption temperature (77 or 87 K) due to temperature-induced structural transformation. If a MOF is much more flexible and exhibits a strong breathing effect, the guest-free MOF prepared by heat evacuation should be significantly different to that prepared by treatment with supercritical CO_2. In that case, their structures would hardly be similar, even at the gas adsorption temperature, leading to different gas sorption capacities.

Table 4. Gas uptake capacity data for **SNU-77H**.

Gas	T [K]	P [bar]	STP [$cm^3 g^{-1}$]	wt% gas	Gas adsorbed[a] [$g L^{-1}$]	v(STP)/v[a]
N_2	77	0.91	1050	131	768	615
	298	1.0	3.19	0.40	2.3	1.9
H_2	77	1.0	200	1.79	10.5	117
	87	1.0	112	1.01	5.90	65.6
	77	90	907 (1230)	8.10 (11.0)	47.4 (64.5)	532 (722)
	298	90	56.3 (133)	0.50 (1.19)	2.93 (6.97)	33.0 (77.9)
O_2	77	0.2	1201	172	1006	704
	298	1.0	3.56	0.51	3.0	2.1
CO_2	195	1.0	860	169	990	504
	231	1.0	660	130	760	387
	273	1.0	41.8	8.21	48.1	24.6
	298	1.0	20.1	3.94	23.1	11.8
	298	40	475 (523)	93.3 (103)	547 (601)	278 (306)
CH_4	195	1.0	122	8.70	50.9	71.5
	231	1.0	57.6	4.12	24.2	33.8
	273	1.0	17.0	1.20	7.00	10.0
	298	1.0	8.68	0.62	3.6	5.1
	298	35	199 (242)	14.2 (17.3)	83.2 (101)	117 (142)
	298	60	248 (308)	17.7 (22.0)	104 (129)	145 (180)

[a] Gas adsorbed per volume of sample: The values were calculated as mass of adsorbed gas × density of sample (586 $g L^{-1}$ for **SNU-77H**). The values in parentheses indicate the total amount of adsorbed gas.

SNU-77R, **SNU-77S**, and **SNU-77H** adsorb N_2 gas at 77 K, showing type I isotherms characteristic of microporous materials (Figure 4a). The BET surface areas of **SNU-77R**, **SNU-77S**, and **SNU-77H** estimated from the N_2 gas sorption data are similar: 3560, 3660, and 3670 $m^2 g^{-1}$ (Langmuir surface areas: 4020, 4120, and 4180 $m^2 g^{-1}$), respectively, which are comparable to those of MOF-5 (3800 $m^2 g^{-1}$)[12] and MOF-177 (4630 $m^2 g^{-1}$).[30] Their pore volumes, determined by the Dubinin–Radushkevich (DR) equation, are 1.45, 1.48, and 1.52 $cm^3 g^{-1}$, respectively. The plots of pore-size distribution based on the Horváth–Kawazoe (HK) method[31] indicate that all have pore sizes of 8.1 Å. The surface areas calculated from the X-ray crystal structures by using the Materials Studio program[32] with a probe radius of 1.82 Å and a grid interval of 0.25 Å are 4450 $m^2 g^{-1}$ for **SNU-77R** and **SNU-77S**, and 4390 $m^2 g^{-1}$ for **SNU-77H**.

SNU-77R, **SNU-77S**, and **SNU-77H** adsorb almost same amount of H_2 gas, up to 1.8 wt% at 77 K and 1 atm, and up to 1.0 wt% at 87 K and 1 atm (Figure 4b). The H_2 uptake capacities at 77 K are higher than that of MOF-177 (1.24 wt%) with larger pores (11.8 Å) in the noninterpene-

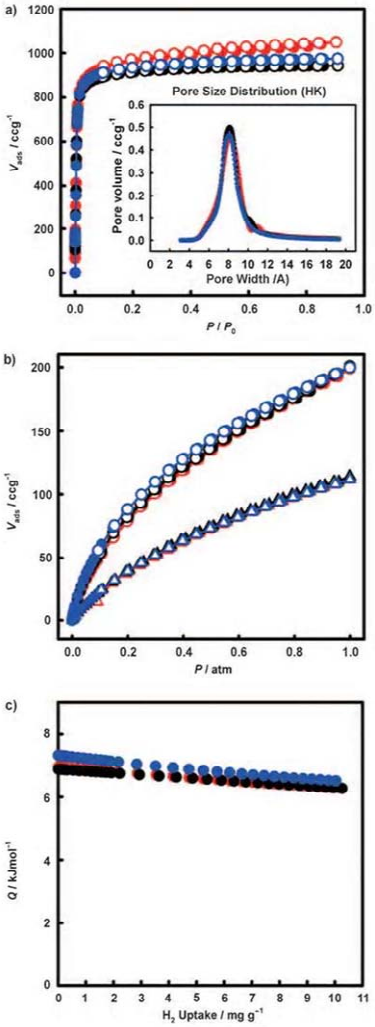

Figure 4. Gas sorption isotherms of **SNU-77R** (black), **SNU-77S** (blue), and **SNU-77H** (red). Filled shapes: adsorption; open shapes: desorption. a) N_2 at 77 K. Inset: pore-size distributions estimated by the Horváth–Kawazoe method. b) H_2 at 77 K (circles) and 87 K (triangles). c) Isosteric heats of H_2 adsorption.

trating (6,3)-connected net,[30] but lower than that of [Zn_4O-$(NTB)_2$] (1.9 wt%) with much smaller pores (5.0 Å) in the doubly interpenetrating nets.[22] The isosteric heats (Q_{st}) of H_2 adsorption estimated from the isotherms at 77 and 87 K by using the virial equation[33] are rather insensitive to the amount of H_2 loading (Figure 4c), which can be attributed to the interpenetration leading to a smaller pore size and an overlap of energy potentials between the opposing walls. The average zero coverage isosteric heats for the three desolvated samples is 7.05 kJ mol^{-1}, which is higher than those of noninterpenetrating Zn_4O-based MOFs such as MOF-5 (4.7 kJ mol^{-1})[34] and MOF-177 (4.4 kJ mol^{-1}).[30] When **SNU-77H** was exposed to air for 6 days, the H_2 uptake capacity was significantly reduced to 1.51 wt% at 77 K and 1 atm, similarly to previous reports,[12,13] even though the PXRD patterns indicate an intact framework structure (Figure S4).

Because the gas sorption properties of **SNU-77R**, **SNU-77S**, and **SNU-77H** are similar, the high-pressure H_2, CO_2, and CH_4 gas adsorption isotherms and the low-pressure O_2, CO_2, and CH_4 adsorption isotherms were measured only for **SNU-77H** (Figure 5). **SNU-77H** adsorbs large amounts of these gases (Table 4). In particular, the high-pressure H_2 gas uptake capacity at 77 K and 90 bar is exceptionally high (Figure 5a), with an excess of 8.1 wt% (47.4 g L^{-1}) and a total of 11.0 wt% (64.5 g L^{-1}). The best H_2 uptake at 77 K reported so far for MOFs is 9.95 wt% (total 16.4 wt%) at 56 bar for NU-100[35] and 8.6 wt% (total 16.7 wt%) at 70 bar for MOF-210.[36]

The O_2 adsorption capacity at 77 K and 0.2 atm (172 wt%, 1201 cm^3 g^{-1} at STP) is the best reported for MOFs because of the large void volume of the MOF (Figure 5b). It is close to the value (1280 cm^3 g^{-1}) calculated from the void volume of **SNU-77H** (1.52 cm^3 g^{-1}) and the density of liquid O_2 (1.205 g cm^{-3}) at 77 K over 0.2 atm. At room temperature, however, it falls to 3.56 cm^3 g^{-1} at 1 atm.

The CO_2 and CH_4 uptake capacities are also high, reaching 93.5 wt% at 298 K and 42 bar and 14.2 wt% [117 v-(STP)/v] at 298 K and 35 bar, respectively (Figure 5c and d). The isosteric heats of the CO_2 and CH_4 adsorption at low coverage are 19.9–19.4 and 14.3–14.2 kJ mol^{-1}, respectively, as estimated from the isotherms recorded at 195, 231, 273, and 298 K by using the Clausius–Clapeyron equation (Figure S6).

Conclusion

We have revealed for the first time through complete single-crystal X-ray analyses that the guest-free structures of a MOF are determined not only by the activation method but also by the temperature. For the doubly interpenetrating Zn_4O-type MOF studied herein, the different activation methods, such as room-temperature evacuation, treatment with supercritical CO_2, and high-temperature evacuation, provide different fine structures at room temperature with pore shapes and window sizes that differ by several Å. However, they show similar gas sorption properties because the framework does not breathe and the fine structures are similar to each other at the cryogenic gas sorption temperature due to further temperature-induced structural transformations. The results presented herein together with the pre-

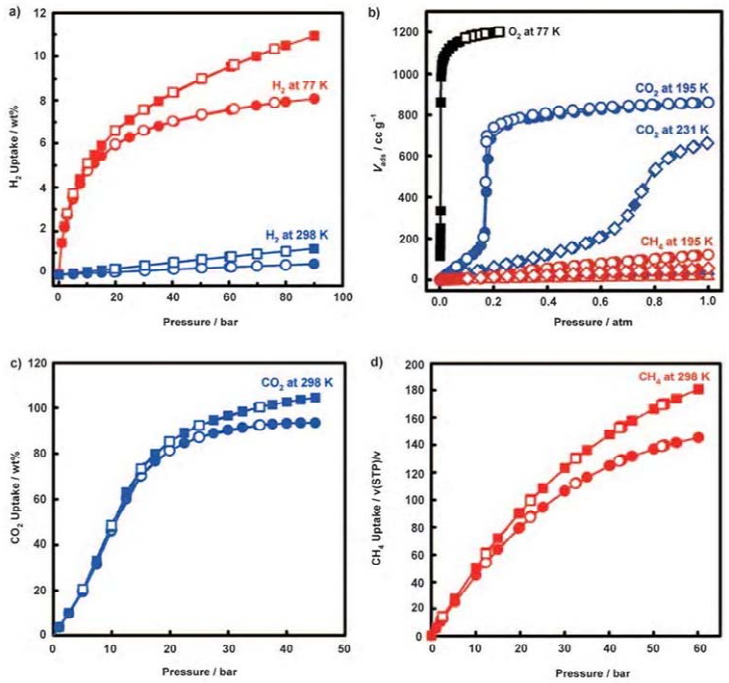

Figure 5. Gas sorption isotherms of **SNU-77H**. a) H_2 sorption at 77 (red) and 298 K (blue) at high pressures. b) O_2 (black) sorption at 77 K and CO_2 (blue) and CH_4 (red) sorption at 195 (●), 231 (◆), and 273 K (▲). c) CO_2 and d) CH_4 sorption at 298 K and high pressures. In a), c), and d), circles and squares represent the excess and the total adsorptions, respectively. Filled shapes: adsorption; open shapes: desorption.

vious reports by Hupp[14] and Lin[15] and their co-workers suggest that MOFs that collapse on thermal evacuation or highly flexible MOFs exhibiting a breathing effect would show increased gas sorption capacity when activated by treatment with supercritical CO_2 or freeze-drying than by thermal evacuation methods. The MOF described herein can be applied to the storage of gases as well as to the development of crystalline devices because of its exceptionally high porosity and ability to retain its single-crystal nature.

Experimental Section

General methods: All chemicals and solvents used in the syntheses were of reagent grade and used without further purification. Infrared spectra were recorded on a Perkin–Elmer Spectrum One FT-IR spectrophotometer. NMR spectra were measured on a Bruker Spectrospin 300 spectrometer. UV/Vis spectra were recorded with a Perkin–Elmer Lambda 35 UV/Vis spectrophotometer. Emission spectra were recorded with a Perkin–Elmer LS-55 luminescence spectrophotometer. Elemental analyses were performed with a Perkin–Elmer 2400 Series II CHN analyzer. Thermogravimetric analysis (TGA) and differential scanning calorimetry (DSC) were performed at a scan rate of 5 °C min^{-1} by using TGA Q50 and DSC Q10 of TA instruments. Powder X-ray diffraction (PXRD) data were recorded on a Bruker D5005 diffractometer at 40 kV and 40 mA with $Cu_{K\alpha}$ radiation ($\lambda = 1.54050$ Å) at a scan rate of 5° min^{-1} and a step size of 0.02° in 2θ.

Synthesis of the novel ligand, tris(4′-carboxybiphenyl)amine (H_3TCBPA): H_3TCBPA was synthesized by the Suzuki–Miyaura coupling reaction,[37] purified by column chromatography, and characterized by IR and NMR spectra. FTIR (KBr pellet): $\tilde{\nu} = 1687$ cm^{-1} (C=O); ^{1}H NMR (300 MHz, DMSO): $\delta = 7.23$ (s, 6H), 7.77 (s, 6H), 7.82 (s, 6H), 8.03 ppm (s, 6H).

Synthesis of $[Zn_4O(TCBPA)_2]$·19DMA·4H_2O (SNU-77): $Zn(NO_3)_2$·6H_2O (180 mg, 0.61 mmol) and tris(4-carboxybiphenyl)amine (40 mg, 0.070 mmol) were dissolved in anhydrous DMA (7 mL) and the mixture was then placed in a Teflon vessel within the autoclave and heated at 115 °C for 2 days. On cooling to room temperature, brown crystals were formed, which were filtered off, washed with anhydrous DMA, and dried briefly in air. Yield: 0.12 g, 54%. FTIR (KBr pellet): $\tilde{\nu} = 2929$ (C–H-(DMA)), 1633 (C=O(DMA)), 1600 (O–C=O), 1521 cm^{-1} (C=C); UV/Vis (diffuse reflectance): $\lambda_{max} = 410$ nm; luminescence (solid): $\lambda_{max} = 477$ nm (excitation at $\lambda_{max} = 410$ nm); elemental analysis calcd (%) for $Zn_4C_{154}H_{227}N_{21}O_{36}$: C 57.62, H 7.13, N 9.16; found: C 57.61, H 6.95, N 9.15.

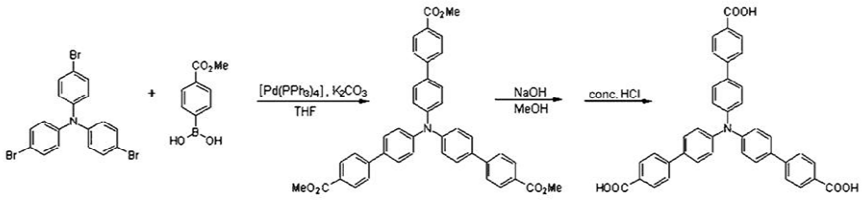

Preparation of $[Zn_4O(TCBPA)_2]\cdot 14PhCH_3\cdot 3H_2O$ (SNU-77′): Crystals of as-synthesized **SNU-77**, which were still in the mother liquor, were transferred into a 20 mL vial. The mother liquor was decanted and the crystals were washed with anhydrous DMA (2×20 mL). The product was immersed in anhydrous toluene (20 mL) for 2 days. During the guest-exchange process, toluene was replenished four times. FTIR (KBr pellet): $\tilde{\nu}$ = 3026 (C–H(toluene)), 1599 (O–C=O), 1521 cm^{-1} (C=C); UV/Vis (diffuse reflectance): λ_{max} = 410 nm; luminescence (solid): λ_{max} = 488 nm (excitation at λ_{max} = 410 nm); elemental analysis calcd (%) for $Zn_4C_{176}H_{166}O_{16}N_2$: C 74.73, H 5.99, N 0.99; found: C 74.61, H 5.93, N 0.99.

Preparation of $[Zn_4O(TCBPA)_2]$ (SNU-77R): Crystals of **SNU-77′** were introduced into a 9 mm cell of the gas sorption apparatus and evacuated at room temperature under a pressure of 10^{-5} torr for 24 h. FTIR (KBr pellet): $\tilde{\nu}$ = 1596 (O–C=O), 1522 cm^{-1} (C=C); UV/Vis (diffuse reflectance): λ_{max} = 410 nm; luminescence (solid): λ_{max} = 512 nm (excitation at λ_{max} = 410 nm); elemental analysis calcd (%) for $Zn_4C_{78}H_{48}O_{13}N_2$: C 63.18, H 3.26, N 1.89; found: C 62.73, H 3.18, N 2.03.

Preparation of $[Zn_4O(TCBPA)_2]$ (SNU-77S) by the supercritical drying method: Prior to drying, crystals of **1** as-synthesized, which were still in the mother liquor, were transferred into a vial (20 mL). The mother liquor was decanted and the crystals were washed briefly with anhydrous DMA (2×15 mL). The crystals were placed inside the supercritical dryer together with the solvent and the drying chamber was sealed. The temperature and pressure of the chamber were raised to 40 °C and 200 bar with CO_2, above the critical point (31 °C, 73 atm) of CO_2. The chamber was vented at a rate of 15 mL min^{-1} and then filled with CO_2 again. The cycles of refilling with CO_2, pressurizing, and venting were repeated for 4 h. After drying, the closed container with the dried crystals (**SNU-77S**) was transferred to a glove bag to prevent exposure of the crystals to air. The gas sorption isotherms were measured without further activation. FTIR (KBr pellet): $\tilde{\nu}$ = 1603 (O–C=O), 1521 cm^{-1} (C=C); UV/Vis (diffuse reflectance): λ_{max} = 410 nm; luminescence (solid): λ_{max} = 510 nm (excitation at λ_{max} = 410 nm); elemental analysis calcd (%) for $Zn_4C_{78}H_{48}O_{13}N_2$: C 63.18, H 3.26, N 1.89; found: C 62.96, H 3.20, N 2.01.

Preparation of $[Zn_4O(TCBPA)_2]$ (SNU-77H): Crystals of **SNU-77′** were evacuated in a Schlenk tube at a pressure of 10^{-5} torr at room temperature for 1 h and then heated at 110 °C for 12 h. FTIR (KBr pellet): $\tilde{\nu}$ = 1596 (O–C=O), 1521 cm^{-1} (C=C); UV/Vis (diffuse reflectance): λ_{max} = 410 nm; luminescence (solid): λ_{max} = 506 nm (excitation at λ_{max} = 410 nm); elemental analysis calcd (%) for $Zn_4C_{78}H_{48}O_{13}N_2$: C 63.18, H 3.26, N 1.89; found: C 62.82, H 3.01, N 1.97.

X-ray crystallography: The diffraction data of **SNU-77**, **SNU-77′**, **SNU-77R**, **SNU-77S**, and **SNU-77H** were collected at room temperature with an Enraf–Nonius Kappa CCD diffractometer ($Mo_{K\alpha}$, λ = 0.71073 Å, graphite monochromator). For the collection of X-ray diffraction data of **SNU-77**, the crystal was introduced into a glass capillary together with the mother liquor. To observe the SCSC transformation from **SNU-77** to **SNU-77′**, a crystal of **SNU-77** was removed from the capillary after its X-ray diffraction data were collected and then it was dropped into toluene in a 1.5 mL vial. After immersion in toluene for 1 day, the crystal (**SNU-77′**) was sealed in a glass capillary together with toluene and the X-ray diffraction data were collected. To observe the SCSC transformation from **SNU-77′** to **SNU-77R**, single crystals of **SNU-77′** were introduced into a 9 mm cell of the gas sorption apparatus and evacuated at room temperature and a pressure of 10^{-5} torr for 24 h. One of the crystals was coated with epoxy resin immediately and sealed in a glass capillary to prevent exposure of the crystal to air. To observe the SCSC transformation from **SNU-77** to **SNU-77S**, single crystals of **SNU-77** were desolvated by the supercritical drying method and then introduced into a glove bag in which one of the crystals was coated with epoxy resin and sealed in the glass capillary. For single-crystal X-ray crystallography of **SNU-77H**, a single crystal of **SNU-77′** was introduced into the empty space created at the bottom of the 0.5 mm glass capillary with an open end in which toluene was already filled and then the toluene was removed. The glass capillary with **SNU-77′** was placed in a Schlenk tube, heated at 110 °C under vacuum for 2 h, and then cooled to room temperature. The capillary was taken out from the Schlenk tube and immediately sealed for X-ray crystal data collection. Preliminary orientation matrices and unit cell parameters were obtained from the peaks of the first 10 frames and then refined by using the whole data set. Frames were integrated and corrected for Lorentzian and polarization effects using DENZO.[38] The scaling and global refinement of crystal parameters were performed by using SCALEPACK.[38] No correction for absorption was made. The crystal structures were solved by direct methods[39] and refined by full-matrix least-squares refinement using the SHELXS-97 computer program.[40] The positions of all non-hydrogen atoms were refined with anisotropic displacement factors. The hydrogen atoms were positioned geometrically and refined by using a riding model. In **SNU-77H**, all zinc and carboxylate oxygen atoms were statistically disordered over two sites. The site occupancy factors were given as 0.1667 for the Zn(1) atom, which sits on a three-fold crystallographic axis, and 0.5 for the Zn(2) atom, which sits in a general position. The site occupancy factors were given as 0.5 for all carboxylate oxygen atoms. For **SNU-77** and **SNU-77′**, the electron densities of the disordered guest molecules were flattened by using the SQUEEZE option of PLATON.[29] Therefore, the formula of **SNU-77** and **SNU-77′** were determined on the basis of IR spectroscopy, elemental analyses, and TGA. Although electron densities associated with guest molecules were not observed, two residual electron densities found around the phenyl rings of $TCBPA^{3-}$ in **SNU-77H** were flattened by using the SQUEEZE option of PLATON,[29] which provided a slightly lower R value than that determined without SQUEEZE. However, geometrical differences with and without the SQUEEZE procedure were not observed and the X-ray crystal structure of **SNU-77H** after SQUEEZE was the same as that before SQUEEZE.

CCDC-726040 (**SNU-77**), 726041 (**SNU-77′**), 771231 (**SNU-77R**), 771232 (**SNU-77S**), and 726042 (**SNU-77H**) contain the supplementary crystallographic data for this paper. These data can be obtained free of charge from the Cambridge Crystallographic Data Centre via www.ccdc.cam.ac.uk/data_request/cif.

In situ synchrotron single-crystal X-ray diffraction studies of SNU-77R: Variable-temperature single-crystal X-ray diffraction data were measured with λ = 0.77000 Å synchrotron radiation on a 6B MX-I ADSC Quantum-210 detector with a silicon (111) double-crystal monochromator at the Pohang Accelerator Laboratory (PAL), Korea. A crystal of **SNU-77R** was coated with epoxy resin immediately to prevent exposure to air, sealed in a glass capillary, and the X-ray diffraction data were collected at room temperature (293 K). To observe the structural transformation induced by the temperature change, the X-ray diffraction data were collected sequentially at 293, 373, 293, and then 100 K. The temperature was controlled by the cryostream and the sample was maintained at the re-

quired temperature for 2–2.5 h to attain an equilibrium before collecting the X-ray data. The ADSC Quantum-210 ADX program (Ver. 1.96)[41] was used for data collection and HKL2000 (Ver. 0.98.699)[38] was used for cell refinement, reduction, and absorption correction. The structures were solved by direct methods[39] and refined by full-matrix least-squares refinement using the SHELXS-97 computer program.[40] The positions of all non-hydrogen atoms were refined with anisotropic displacement factors. The hydrogen atoms were positioned geometrically by using a riding model. For the X-ray data measured at 373 and 293 K (2nd), all the zinc and oxygen atoms of TCPBA were statistically disordered over two sites. The site occupancy factors were given as 0.1667 for the Zn(1) atom, which sits on a three-fold crystallographic axis and as 0.5 for the Zn(2) atom, which sits in a general position.

CCDC-783398, -783399, -783400, and -783401 contain the corresponding supplementary crystallographic data. These data can be obtained free of charge from the Cambridge Crystallographic Data Centre via www.ccdc.cam.ac.uk/data_request/cif.

Low-pressure gas sorption measurements: The gas adsorption/desorption experiments were performed on **SNU-77R**, **SNU-77S**, and **SNU-77H** using an automated micropore gas analyzer Autosorb-3B (Quantachrome Instruments). All the gases used were of 99.999% purity. The N_2 and O_2 sorption isotherms were measured at 77 K. The H_2 sorption isotherms were measured at 77 and 87 K and the CO_2 and CH_4 gas sorption isotherms were measured at 195, 231, 273, and 298 K at each equilibrium pressure by the static volumetric method. During the preparation and handling of the samples we took great care to prevent them from being exposed to air. The samples for the gas sorption experiments were prepared as follows. For **SNU-77R** and **SNU-77H**, crystals of **SNU-77′** in a suspension of toluene were transferred into a 9 mm cell of the gas sorption apparatus by using a glass pipette to prevent exposure of the sample to air. The crystals were evacuated at 10^{-5} torr and room temperature for 24 h to afford **SNU-77R**. For **SNU-77H**, crystals were evacuated at 10^{-5} torr, first at room temperature for 1 h and then at 110 °C for 12 h. The outgassing procedure was repeated between every experiment. After the gas sorption measurement was finished, the weight of the sample was measured precisely. The surface area was determined from the N_2 adsorption isotherm at 77 K by using the Brunauer–Emmett–Teller (BET) and Langmuir models, taking the data in the range $P/P_0 = 0.01$–0.1. The pore volume was determined from the Dubinin–Radushkevich (DR) equation.

Estimation of the isosteric heats of the H_2 adsorption: The isosteric heats of H_2 adsorption were estimated for **SNU-77R**, **SNU-77S**, and **SNU-77H** from the H_2 sorption data measured at 77 and 87 K. A virial-type expression was used [Eq. (1)], which is composed of parameters a_i and b_i that are independent of temperature.[33,24] In Equation (1), P is the pressure in atm, N is the amount adsorbed H_2 gas in mg g^{-1}, T is the temperature in K, and m and n represent the number of coefficients required to adequately describe the isotherms. The equation was fitted by using the R statistical software package.[42]

$$\ln P = \ln N + \frac{1}{T}\sum_{i=0}^{m} a_i N^i + \sum_{i=0}^{n} b_i N^i \quad (1)$$

To estimate the values of the Q_{st} of H_2 adsorption, Equation (2) was applied in which R is the universal gas constant.

$$Q_{st} = -R\sum_{i=0}^{m} a_i N^i \quad (2)$$

Calculation of isosteric heats of the CO_2 and CH_4 adsorption: The isosteric heats of the CO_2 and CH_4 adsorptions by **SNU-77H** were calculated from the adsorption isotherms measured at 195, 231, 273, and 298 K by using the Clausius–Clapeyron equation [Eq. (3)].[33] As a result of the significantly reduced uptake with increasing temperature, the isosteric heats were estimated only at very low gas coverage range.

$$\frac{\partial(\ln P)}{\partial(1/T)} = -\frac{Q_{st}}{R} \quad (3)$$

High-pressure gas sorption measurements: High-pressure gas sorption isotherms of **SNU-77H** were measured by the gravimetric method using a Rubotherm MSB (magnetic suspension balance) apparatus. The H_2 sorption isotherms were measured at 77 and 298 K, and the CO_2 and CH_4 sorption isotherms were measured at 298 K. All the gases used were of 99.999% purity and the traces of moisture were removed by using a drying trap filled with 5 Å molecular sieves, which was purchased from the Chromatography Research Supplies (model 500). Desolvated solid **SNU-77H** (more than 200 mg) was quickly introduced into the apparatus and then activated by evacuation at 110 °C under vacuum. Prior to gas sorption measurement, the He isotherm (up to 90 bar) was measured at 298 K to obtain the volume of the framework skeleton. The excess sorption isotherms were measured and corrected for the buoyancy of the system and sample. The buoyancy correction of the sample was made by multiplying the volume of the framework skeleton by the density of the corresponding gas at each pressure and temperature.[43] In the unit conversion from gravimetric (wt%) to volumetric (g L^{-1}), the crystallographic density of the sample was applied.

Estimation of the total amount of adsorbed gas at high pressures: The total amount of adsorbed gas and the pore volume are expressed in Equations (4) and (5) in which N_{tot} is the total adsorption in wt%, N_{ex} is the excess adsorption in wt%, which is the quantity being measured, d_{gas} is the density of the compressed gas at given temperature and pressure in g cm^{-3}, V_{pore} is the pore volume in cm^3 g^{-1}, d_{bulk} is the crystallographic density of the sample, and $d_{skeletal}$ is the skeletal density of the material. The skeletal density can be calculated from Equation (6) in which m is the sample mass expressed in g and $V_{skeletal}$ is the sample volume in cm^3, which iss determined by using He expansion measured at 298 K up to 100 bar. The d_{bulk} and $d_{skeletal}$ values used to calculate the V_{pore} of **SNU-77H** are 0.586 and 1.491 g cm^{-3}, respectively.

$$N_{tot} = N_{ex} + 100 d_{gas} V_{pore} \quad (4)$$

$$V_{pore} = 1/d_{bulk} - 1/d_{skeletal} \quad (5)$$

$$d_{skeletal} = m/V_{skeletal} \quad (6)$$

Acknowledgements

This work was supported by a National Research Foundation of Korea (NRF) Grant funded by the Korean Government (MEST; Nos. 2010-0029651 and 2011-001341). H.J.P. acknowledges support from the Seoul Science Fellowship. The authors acknowledge the Pohang Accelerator Laboratory (PAL) for the use of the synchrotron beamline.

[1] L. J. Murray, M. Dincă, J. R. Long, *Chem. Soc. Rev.* **2009**, *38*, 1294–1314.
[2] H.-S. Choi, M. P. Suh, *Angew. Chem.* **2009**, *121*, 6997–7001; *Angew. Chem. Int. Ed.* **2009**, *48*, 6865–6869.
[3] Y. E. Cheon, M. P. Suh, *Angew. Chem.* **2009**, *121*, 2943–2947; *Angew. Chem. Int. Ed.* **2009**, *48*, 2899–2903.
[4] J.-R. Li, R. J. Kuppler, H.-C. Zhou, *Chem. Soc. Rev.* **2009**, *38*, 1477–1504.
[5] Y. E. Cheon, M. P. Suh, *Chem. Commun.* **2009**, 2296–2298.
[6] C.-D. Wu, W. Lin, *Angew. Chem.* **2007**, *119*, 1093–1096; *Angew. Chem. Int. Ed.* **2007**, *46*, 1075–1078.
[7] T. Uemura, R. Kitaura, Y. Ohta, M. Nagaoka, S. Kitagawa, *Angew. Chem.* **2006**, *118*, 4218–4222; *Angew. Chem. Int. Ed.* **2006**, *45*, 4112–4116.
[8] M. P. Suh, H. R. Moon, E. Y. Lee, S. Y. Jang, *J. Am. Chem. Soc.* **2006**, *128*, 4710–4718.
[9] H. R. Moon, J. H. Kim, M. P. Suh, *Angew. Chem.* **2005**, *117*, 1287–1291; *Angew. Chem. Int. Ed.* **2005**, *44*, 1261–1265.
[10] C. Liang, W. Xia, M. van den Berg, Y. Wang, H. Soltani-Ahmadi, O. Schluter, R. A. Fischer, M. Muhler, *Chem. Mater.* **2009**, *21*, 2360–2366.
[11] F. Schröder, D. Esken, M. Cokoja, M. W. E. van den Berg, O. I. Lebedev, G. Van Tendeloo, B. Walaszek, G. Buntkowsky, H.-H. Lim-

bach, B. Chaudret, R. A. Fischer, *J. Am. Chem. Soc.* **2008**, *130*, 6119–6130.
[12] S. S. Kaye, A. Dailly, O. M. Yaghi, J. R. Long, *J. Am. Chem. Soc.* **2007**, *129*, 14176–14177.
[13] Y. Li, R. T. Yang, *Langmuir* **2007**, *23*, 12937–12944.
[14] A. P. Nelson, O. K. Farha, K. L. Mulfort, J. T. Hupp, *J. Am. Chem. Soc.* **2009**, *131*, 458–460.
[15] L. Ma, A. Jin, Z. Xie, W. Lin, *Angew. Chem.* **2009**, *121*, 10089–10092; *Angew. Chem. Int. Ed.* **2009**, *48*, 9905–9908.
[16] Y. Liu, J.-H. Her, A. Dailly, A. J. Ramirez-Cuesta, D. A. Neumann, C. M. Brown, *J. Am. Chem. Soc.* **2008**, *130*, 11813–11818.
[17] A. Boutin, M.-A. Springuel-Huet, A. Nossov, A. Gédéon, T. Loiseau, C. Volkringer, G. Férey, F.-X. Coudert, A. H. Fuchs, *Angew. Chem.* **2009**, *121*, 8464–8467; *Angew. Chem. Int. Ed.* **2009**, *48*, 8314–8317.
[18] M. P. Suh, Y. E. Cheon, *Aus. J. Chem.* **2006**, *59*, 605–612.
[19] H. J. Choi, M. P. Suh, *J. Am. Chem. Soc.* **2004**, *126*, 15844–15851.
[20] M. P. Suh, Y. E. Cheon, E. Y. Lee, *Coord. Chem. Rev.* **2008**, *252*, 1007–1026.
[21] M. Kawano, M. Fujita, *Coord. Chem. Rev.* **2007**, *251*, 2592–2605.
[22] E. Y. Lee, S. Y. Jang, M. P. Suh, *J. Am. Chem. Soc.* **2005**, *127*, 6374–6381.
[23] M. Dinca, A. Dailly, C. Tsay, J. R. Long, *Inorg. Chem.* **2008**, *47*, 11–13.
[24] M. Dinca, A. Dailly, Y. Liu, C. M. Brown, D. A. Neumann, J. R. Long, *J. Am. Chem. Soc.* **2006**, *128*, 16876–16883.
[25] Y. Yan, I. Telepeni, S. Yang, X. Lin, W. Kockelmann, A. Dailly, A. J. Blake, W. Lewis, G. S. Walker, D. R. Allan, S. A. Barnett, N. R. Champness, M. Schröder, *J. Am. Chem. Soc.* **2010**, *132*, 4092–4094.
[26] H. K. Chae, J. Kim, O. D. Friedrichs, M. O'Keefe, O. M. Yaghi, *Angew. Chem.* **2003**, *115*, 4037–4039; *Angew. Chem. Int. Ed.* **2003**, *42*, 3907–3909.
[27] T. K. Maji, K. Uemura, H.-C. Chang, R. Matsuda, S. Kitagawa, *Angew. Chem.* **2004**, *116*, 3331–3334; *Angew. Chem. Int. Ed.* **2004**, *43*, 3269–3272.
[28] D. N. Dybtsev, H. Chun, K. Kim, *Angew. Chem.* **2004**, *116*, 5143–5146; *Angew. Chem. Int. Ed.* **2004**, *43*, 5033–5036.
[29] A. L. Spek, *PLATON99 A Multipurpose Crystallographic Tool*, Utrecht University: Utrecht, **1999**.
[30] H. Furukawa, M. Miller, O. M. Yaghi, *J. Mater. Chem.* **2007**, *17*, 3197–3204.
[31] G. Horváth, K. Kawazoe, *J. Chem. Eng. Jpn.* **1983**, *16*, 470–475.
[32] Materials Studio program, version 4.1, Accelrys, San Diego, **2006**.
[33] L. Czepirski, J. Jagiello, *Chem. Eng. Sci.* **1989**, *44*, 797–801.
[34] J. C. Rowsell, O. M. Yaghi, *J. Am. Chem. Soc.* **2006**, *128*, 1304–1315.
[35] O. K. Farha, A. Ö. Yazaydin, I. Eryazici, C. D. Malliakas, B. G. Hauser, M. G. Kanatzidis, S. T. Nguyen, R. Q. Snurr, J. T. Hupp, *Nat. Chem.* **2010**, *2*, 944–948.
[36] H. Furukawa, N. Ko, Y. B. Go, N. Aratani, S. B. Choi, E. Choi, A. Ö. Yazaydin, R. Q. Snurr, M. O'Keeffe, J. Kim, O. M. Yaghi, *Science* **2010**, *329*, 424–428.
[37] N. Miyaura, A. Suzuki, *Chem. Rev.* **1995**, *95*, 2457.
[38] Z. Otwinowski, W. Minor in *Processing of X-ray Diffraction Data Collected in Oscillation Mode, Methods in Enzymology Vol. 276 Part A*, (Ed. C. W .Carter Jr., R. M. Sweet), Academic Press, New York, **1997**, pp. 307-326.
[39] G. M. Sheldrick, *Acta Crystallogr. A* **1990**, *46*, 467–473.
[40] G. M. Sheldrick, SHELXS-97. Program for the crystal structure refinement, University of Göttingen, Göttingen, Germany, **1997**.
[41] A. J. Arvai, C. Nielsen, ADSC Quantum-210 ADX Program, Area Detector System Corporation, Poway, CA, USA, **1983**.
[42] The software package is available online at http://www.r-project.org.
[43] NIST chemistry webbook (thermophysical properties of fluid systems) http://webbook.nist.gov/chemistry/fluid.

Received: November 23, 2010
Revised: February 25, 2011
Published online: May 10, 2011

국문 초록

PART I. Crown ether를 포함한 리간드를 이용하여 합성한 금속-유기 골격체의 수소저장: 양이온 도입

18-crown-6 (18C6)를 유기 리간드 안에 포함하는 네 방향 카르복실레이트 리간드를 이용하여 이중으로 침투하는 삼차원 다공성 금속-유기골격체, $Zn_5(\mu_3\text{-}OH)_2(TBADB\text{-}18\text{-}Cr\text{-}6)_2\cdot 4DMF]\cdot 13DMF\cdot 4H_2O$ (SNU-200)를 합성하였다. SNU-20 의 다공 내에 다양한 양 이온 (K^+, NH_4^+, methyl viologen(MV^{2+}), and Eu^{3+})을 도입하였을 때, 도입된 양이온은 리간 내에 있는 18C6 에 결합 할 수 있을 뿐 아니라 SNU-200 은 도입된 양이온에 따라 다른 가스흡착의 특성을 보여준다. 동공 내에 도입된 양이온은 18C6 에 결합되어 구멍을 막지 않고 탈 용매에 따른 다공성 고체의 구조 변화를 줄여주며 금속-유기 골격체의 표면적을 증가 시키는 현상을 나타낸다. 그 뿐 아니라 SNU-200 은 양 이온을 도입하였을 때에도 단결정을 유지하고 있다. 유지된 단결정을 X-ray 분석을 통해 단결정에서 단결정으로의 변환을 확인 할 수 있었으며, 18C6 에 배위된 양이온과 금속 이온에 배위된 음이온 그리고 구멍에 위치한 음이온까지 확인하였다. 유기 리간드에 포함된 18C6 와 도입된 양이온이 가스흡착에 주는 영향을 확인하기 위하여 다양한 온도에서 N_2, H_2, CO_2, 그리고 CH_4 가스의 흡착과 탈착 실험을 수행 하였다. 18C6 를 포함하고 있는 SNU-200'는 7.70 $kJmol^{-1}$의 높은 수소 흡착열을 보여주며, 이는 일반적인 Zn(II)의 금속-유기 골격체와 비교하였을 때 1-3 $kJmol^{-1}$ 만큼 더 큰 값이다. 다양한 양이온이 도입된 화합물들 중에는 K^+가 도입된 화합물이 9.92 $kJmol^{-1}$ 까지 수소의 흡착열을 증가 시키며 수소와

상호작용을 하는 것을 알 수 있었다. 그 뿐 아니라 이산화탄소/질소가스의 선택 흡착에서도 22.6 의 높은 이산화탄소에 대한 선택성을 보여주었다.

주 요 어: 금속-유기 골격체 • 수소 저장 • 흡착열 • 크라운 이서 • 정전기장 • 양이온 도입 • 단결정에서 단결정으로의 변환

PART II. 물리적 화학적 흡착을 통한 하이브리드 수소 저장을 위한 다공성 배위 고분자 내의 마그네슘 나노 결정의 생성

$Zn(NO_3)_2$ 와 Aniline-2,4,6-tribenzoate (atb)를 이용하여 3차원 금속-유기 골격체를 $[Zn_4O(atb)_2]\cdot 22DMF\cdot 9H_2O$ (SNU-90), 합성하였다. SNU-90는 겹쳐져있지 않는 하나의 골격체로 *qom* topology를 갖는 (6,3)-connected net을 형성한다. 구조는 MOF-177 유사하며 3D채널을 갖고 있다. SNU-90는 4244 m^2g^{-1} 의 Brunauer-Emmett-Teller (BET) 표면적과 4914 m^2g^{-1}의 Langmuir 표면적을 나타 내었다.

Chemical vapor deposition의 방법을 이용하여 $Mg(cp)_2$ 전구체를 금속-유기 골격체 SNU-90의 구멍 안에 도입 시켰고, 동공 안에 마그네슘 전구체를 포함하고 있는 $Mg(cp)_2$@SNU-90를 아르곤 기류 하에서 473 K 온도로 가열하여 40-100 nm 육각 판형의 마그네슘 나노 결정을 SNU-90 안에 생성 시켰다. 마그네슘 나노 입자의 모양과 위치는 HRTEM 과 Tomography를 이용하여 확인 하였다. 마그네슘 나노 입자를 포함하고 있는 금속-유기 골격체는 (Mg@MOF) 물리적인 흡착은 물론 화학적인 흡착 방법으로 수소를 저장 할 수 특성을 보여주었다. 도입된 마그네슘의 양이 증가 할 수록 극저온(77 K)에서 물리적 수소저장의 양은 감소하지만 수소와 구조체와의 상호인력은 4.55 $kJmol^{-1}$에서 11.6 kJ mol^{-1}까지 증가하였다. 그 뿐 아니라 수소를 화학적 흡착방법으로 저장하는 마그네슘 입자가 금속 유기 골격체 안에서 나노 크기로 존재하기 때문에 50 - 100 μm 크기의 Mg powder와 비교하였을 때 마그네슘이 수소를 화학적 흡착 하기에 필요한 온도를 200 °C 가량 낮춰서 수소를 저장하는 현상을 나타내었다. 즉 10.5 wt%의 마그네슘을 포함하고 있는 Mg@SNU-90는 50 °C부터 마

그네슘 나노 결정에 수소가 흡착되며, 473 K and 30 bar에서 약 0.71 wt% 까지의 수소 저장능을 보여주었다.

Tetrakis (4-bromophenyl) methane와 $Ni(cod)_2$ 촉매를 사용한 cross-coupling 반응을 이용하여 다공성 유기 고분자 PAF-1 (Porous Aromatic Framework, PAF-1)을 합성하였다. PAF-1은 페닐링으로만 구성된 Diamondoid 구조를 갖고 있으며 5640 m^2g^{-1}의 넓은 BET 표면적을 나타낸다. PAF-1은 금속 원소가 없고 페닐링으로만 구성되어 있기 때문에 가볍고, 높은 열적/ 화학적 안정성을 나타내며 소수성 이다.

다공성 유기 고분자 (PAF-1)안에 chemical vapor deposition을 통해서 $MgCp_2$ 를 도입하여, 도입된 마그네슘 전구체를 Li-naphthalenide를 이용하여 화학적 방법으로 환원시킴으로써 다양한 크기를 갖는 마그네슘 나노 입자를 생성 하였다. 구조체 내에 산소 원자가 없으며, 소수성 특성을 지닌 다공성 유기 고분자 안에 마그네슘 나노 입자를 도입했을 때, 공기 중에 노출 되었을 때도 안정한 마그네슘 나노 입자를 합성 할 수 있었다. 극저온에서 물리적 수소흡착을 측정하였을 때, 마그네슘이 도입된 다공성 유기 고분자는 순수한 다공성 유기 고분자에 비해 1.82 $kJmol^{-1}$ 향상된 수소 흡착열을 보여주었다.

주 요 어: 금속-유기 골격체 • 공유결합성 유기 골격체 • 마그네슘• 나노 결정 • 수소저장 • 화학적 흡착 • 물리적 흡착

감사의 글

벌써 졸업이라는 시간을 맞이하게 되었습니다. 항상 선배들의 졸업 논문에서 읽었던 감사의 글을 직접 쓰는 시간을 맞이하니 감회가 새롭습니다. 이 자리를 빌려서 가장 먼저 좋은 학자의 자세를 몸소 가르쳐 주셨던 백명현 교수님께 진심으로 감사 드립니다. 입학 할 때 멀리만 보였던 선생님의 정년 시기가 이렇게 앞으로 다가왔다는 것이 실감 나지 않습니다. 지난 시간 동안 선생님께 배운 연구에 대한 열정과 가르침 그리고 격려가 헛되지 않도록 좋은 과학자로 사회적 책임을 갖고 평생 살겠습니다.

바쁘신 와중에도 학위 논문 심사를 맡아 주신 김관 교수님, 이동환 교수님, 숭실대 김자헌 교수님, 연세대 천진우 교수님께 깊은 감사를 드립니다. 많이 부족한 제가 이 실험실에서 박사학위를 마칠 수 있도록 아낌없이 많은 도움을 주신 선배님들, 문회리 교수님 태경이 누나, 우승이 형, 혜정이, 그리고 같은 시간을 함께해준 대호와 시영이, 지난 학기 졸업한 승안, 명호, 세용이, 그리고 입학부터 졸업까지 봤던 Prasad 박사님 실험실 모든 가족들에게 고마운 마음을 전합니다. 그리고 힘든 순간마다 생각나고 힘이 되어준 친구들 찬호, 대용이, 민혁이, 현호 모두 고맙습니다.

제가 항상 바쁘다는 핑계로 많이 신경 쓰지 못했던 가족들 끝없는 사랑과 믿음으로 저를 지켜 봐준 아버지, 어머니, 매형, 누나, 형에게 감사한 마음을 전합니다. 그리고 새로운 가족 장인어른, 장모님, 사라처제, 현민이 항상 든든한 지원군이 되주어서 고맙습니다. 마지막으로 가장 사랑하는 아내 한나에게 나를 믿어주고 함께 해줘서 고맙습니다. 그리고 앞으로 같이 할 날을 기대할 수 있게 해서 더욱 고맙고 사랑합니다. 지금까지 건강하게 학업을 잘 마치게 하신 하나님께 감사 드리고 앞으로 제가 더 좋은 도구가 되어 세상에 쓰임 받는 삶이 되길 간절히 바랍니다.

이제 다시 새로운 길을 시작 합니다. 지금까지 받았던 모든 격려들 다시 한 번 모든 분들께 감사 드립니다.

2014년 2월

임 대 운 드림